

ABSTRACT

NGUYEN, ALEXANDER KHOA. Toxicological and Materials Evaluation of Photopolymers for Use in Additively Manufactured Medical Devices (Under the direction of Dr. Roger J. Narayan).

Additive manufacturing of medical devices allows for patient-specific treatments and increases design freedom. Stereolithography (SLA) and two-photon polymerization (2PP) promise micrometer-scale resolution while retaining compatibility with a wide range of feedstock materials. SLA and 2PP use photopolymers that have inherent toxicological risks associated with the reactive polymerizable moiety, the photoinitiator, and light exposure; the synergistic toxic effect of concomitant photoinitiator and light exposure requires special attention. This dissertation details strategies to ameliorate the toxic effects of photopolymers. The first involves the replication of the 2PP master structure with a biocompatible alternative; drug delivery of amphotericin B for treatment of cutaneous leishmaniasis via soft-lithography replication of a 2PP microneedle array master structure is presented as an example. The second strategy involves post processing to reduce the toxicity of the photopolymer. Tissue engineering scaffolds produced from hydrogels using 2PP were post-processed and evaluated for their cytotoxicity and genotoxicity. Chips of various ceramic materials printed using SLA then conventionally sintered were evaluated for their ability to support osteogenic differentiation of human bone marrow stem cells. Neither of these strategies would be applicable if direct printing of cell encapsulating materials is required. In this case, the toxic effects should be characterized; alternatively, a more biocompatible alternative should be developed. Therefore, a Norrish Type II photoinitiator based on riboflavin was investigated as a potentially less cyto- and geno- toxic photoinitiator. Residual photocatalytic activity of crosslinked gelatin methacryloyl photoinitiated with lithium (2,4,6-trimethylbenzoyl)phosphinate (LAP) was investigated. The mutagenic potential of concomitant

405 nm light and LAP exposure was evaluated to understand the mutagenic risk to cells undergoing bioprinting.

© Copyright 2020 by Alexander Nguyen

All Rights Reserved

Toxicological and Materials Evaluation of Photopolymers for Use in Additively Manufactured
Medical Devices

by
Alexander Khoa Nguyen

A dissertation submitted to the Graduate Faculty of
North Carolina State University
in partial fulfillment of the
requirements for the degree of
Doctor of Philosophy

Biomedical Engineering

Raleigh, North Carolina
2020

APPROVED BY:

Dr. Roger J. Narayan
Committee Chair

Dr. Boris Chichkov

Dr. Albert Baner

Dr. Troy Nagle

Dr. Susan Schiffman

Dr. Harold Pillsbury

DEDICATION

To my colleagues. To those that carried passionate discussion walking to the cafeteria, in passing through the hallway, or over some coffee. To those with whom I've sweat with, laughed with, and literally bled with. I value your goodwill over all else.

BIOGRAPHY

Alexander Nguyen is currently an NSF-FDA Scholar in Residence from the UNC/NCSU Joint Department of Biomedical Engineering and is working with the FDA's Center for Devices and Radiological Health (CDRH) on projects revolving around the toxicology of Additively Manufactured devices. After graduating *magna cum laude* from the University of Alabama, Tuscaloosa with a B.S. in Biochemistry, Alex joined Prof. Roger Narayan's group and has since then collaborated with Laser Zentrum Hannover, Sandia Natl. Labs, and Argonne Natl. Labs along with the FDA. Through these projects, he developed expertise in Two Photon Polymerization, microfluidics, microwave-assisted chemical vapor deposition, and various *in vitro* methods to assess biocompatibility. He has been active in the academic community through peer review of manuscripts and has also participated in grant review for the Chilean National Fund for Scientific and Technological Development. Alex has also been an active member of the Society of Toxicology since 2015 and has won multiple awards from both the National Capital Area Chapter and the Medical Device and Combination Product Specialty Section for his work on nanotoxicology, and photopolymer toxicological evaluation. His work has attracted media interest with 3DPrint.com featuring his review on Two Photon Polymerization.

ACKNOWLEDGMENTS

It's easy to fly high if you know someone will catch you if you fall. I am blessed to have supportive parents and family that would, at the very least, put a roof over my head and put food in my belly. Also, thank you for taking care of Nadine for me these couple years. Peace of mind forms a strong launching point for success.

To my siblings and cousins (who might as well be siblings), thank you for all the shenanigans throughout the years. A special shout out to Cecilia Ong for being there when I had to rush back to Raleigh. Her door was always open, and by door, I mean for both the house and refrigerator (albeit full of vegetarian food).

When I share my stories of graduate school, people always comment on how atypical it was to travel to so many different places. Roger Narayan essentially gave me paid vacations to live in Hannover where I got to experience an entirely different culture, to Albuquerque in the middle of the Breaking Bad craze, and to Chicago in the winter (thanks for that). More importantly, he gave me intellectual freedom to explore many different projects at my own initiative. These unorthodox experiences have uniquely shaped me not only as a well-rounded researcher, but also as a well-travelled person with life experiences outside the academic bubble.

Thank you to my committee and hosts. I know I have made many mistakes and you have given me many opportunities to learn from them. Thanks especially to Boris Chichkov for being the first guinea pig host for a brand-new graduate student who didn't know the difference between a fume hood and biosafety hood. Olga gave me a good lecture on that.

I've worked with Peter Goering in DBCMS for the past couple years now and I couldn't ask for a better supervisor. This experience in DBCMS is probably giving me unrealistic expectations of future supervisors. Thanks also to Katherine Vorvolakos who has also been my

advocate on multiple occasions. Despite the intense crunch due to Covid-19, both Peter and Kat spent a good chunk of time navigating government bureaucracy for me.

To my comrades in science. The lessons both professional and unprofessional fueled my growth. Thanks to Paul Turner, David Wolloscheck, Erin Wood, Diane Smith, and presumably Keaton Nahan of the Fun and Games Administration for some welcome distraction. Jade Noble also helped me with TEM and brewing on multiple occasions. Thanks Teresa Palacios and Paco Delgado (and Frankie) for your friendship and letting me be part of so many important life events. Kotaro Obata and Arune Gaidukeviciute for discussions on laser technologies. I still have that tool steel happy face you gave me; it makes a surprisingly good bottle opener. Thanks Anastasia Koroleva for helping me make, not only scaffolds and microfluidic channels, but also “carbohydrate glass” and LN₂ ice cream.

Finally, all the members of the Narayan lab: Shaun Gittard, Phil Miller, Shelby Skoog, Ryan Boehm, Kai-Hung Yang, and Sina Machekposhti. We are bound by our common experience.

TABLE OF CONTENTS

LIST OF TABLES	viii
LIST OF FIGURES	ix
CHAPTER 1 – Introduction.....	1
Description of 2PP apparatus.....	6
Outline of the Dissertation	11
CHAPTER 2 – Two Photon Polymerization for Biological Applications	15
Abstract	15
Introduction.....	15
Excitation Mechanisms	18
Photopolymer Design Strategies.....	22
Optics Considerations	34
Conclusions.....	38
CHAPTER 3 – Microneedle-Based Delivery of Amphotericin B for Treatment of Cutaneous Leishmaniasis.....	49
Abstract	49
Introduction.....	50
Materials and Methods.....	52
Results.....	59
Discussion	68
Conclusions.....	73
CHAPTER 4 - Two-photon polymerization of polyethylene glycol diacrylate scaffolds with riboflavin and triethanolamine used as a water-soluble photoinitiator.....	84
Abstract	84
Introduction.....	85
Materials and Methods.....	91
Results and Discussion	98
Conclusion	109
CHAPTER 5 - Toxicity and photosensitizing assessment of gelatin methacryloyl-based hydrogels photoinitiated with lithium phenyl-2,4,6-trimethylbenzoylphosphinate in human primary renal proximal tubule epithelial cells	124
Abstract	124
Introduction.....	125
Materials and Methods.....	128
Results.....	132

Discussion	138
Conclusions.....	142
CHAPTER 6 – Lithium Phenyl (2,4,6-trimethylbenzoyl) phosphinate with exposure to 405 nm light is cytotoxic to mammalian cells but not mutagenic in bacterial reverse mutation assays..	152
Abstract	152
Introduction.....	153
Materials and Methods.....	156
Results.....	160
Discussion	167
Conclusion	172
CHAPTER 7 – Effects of Subcytotoxic Exposure of Silver Nanoparticles on Osteogenic Differentiation of Human Bone Marrow Stem Cells.....	185
Abstract	185
Introduction.....	186
Materials and Methods.....	188
Results.....	195
Discussion	204
Conclusions.....	209
CHAPTER 8 – Sintered Tape-cast 3YSZ Supports Human Bone Marrow Derived Stem Cell Osteogenic Differentiation.....	222
Abstract	222
Introduction.....	223
Materials and Methods.....	224
Results and Discussion	227
Conclusion	232
CHAPTER 9 - Physical characterization and in vitro evaluation of 3D printed hydroxyapatite, tricalcium phosphate, zirconia, alumina, and SiAlON structures made by lithographic ceramic manufacturing	242
Abstract	242
Introduction.....	242
Methods.....	245
Results and Discussion	248
Conclusions.....	255
CHAPTER 10 – Conclusions.....	266
Outlook and Future Directions.....	269
REFERENCES	271

LIST OF TABLES

Table 9.1 – Composition and RMS Roughness of Sintered LCM Ceramics	251
---	-----

LIST OF FIGURES

Figure 1.1 –SEM images of a 2PP microneedle replica produced from a Gantrez AN-169 and camphorquinone slurry via PDMS micromolding. Camphorquinone is insoluble in Gantrez AN-169 and acts as an analogue for insoluble drugs such as amphotericin B.....	4
Figure 1.2 – Beam path diagram of the 2PP apparatus.....	9
Figure 1.3 – (left) Mark trajectory driven by galvanoscanner for a single layer of a ring. The laser focus jumps (green) from the center to the outer contour. The laser is switched on and does a complete circle (red). Alternating arc commands with the arc center shifted a quarter the hatching value to the right (yellow) and the left (blue) compose a pseudo-Archimedian spiral with a pitch equal to the hatching distance. The spiral terminates at the inner contour, if applicable, where a full circle (red) completes the layer. Hatching distance in this depiction is exaggerated for clarity. (right) A single layer in a microneedle viewed through the CCD camera.....	11
Figure 2.1 - Structures of new 2PA photoinitiators and reference compounds. Reprinted (adapted) with permission from Nazir, R., Danilevicius, P., Ciuciu, A. I., Chatzinikolaidou, M., Gray, D., Flamigni, L., Farsari, M., Gryko, D. T. (2014). p-expanded ketocoumarins as efficient, biocompatible initiators for two photon-induced polymerization. <i>Chemistry of Materials</i> , 26(10), 3175–3184. doi:10.1021/cm500612w, Copyright 2014 American Chemical Society.....	24
Figure 2.2 - (a) Merged live/dead staining after five days of culture for a 50% polyethylene glycol diacrylate-riboflavin-triethanolamine scaffold seeded with endothelial cells. (b) polyethylene glycol diacrylate exhibits red autofluorescence; ethidium homodimer-1 (dead cell) fluorescence is distinct from the polyethylene glycol diacrylate fluorescence. Republished with permission of Future Medicine Ltd, from “Two-photon polymerization of polyethylene glycol diacrylate scaffolds with riboflavin and triethanolamine used as a water-soluble photoinitiator.” Nguyen, A. K., et al. Vol. 8 (6), 2011; permission conveyed through Copyright Clearance Center, Inc.....	25
Figure 2.3 - (a) Processing windows of investigated initiators in TPIP screening tests; (b) Classifications of the structures by the typical quality of their shapes. Republished with permission of Royal Society of Chemistry, from “Initiation efficiency and cytotoxicity of novel water-soluble two-photon photoinitiators for direct 3D microfabrication of hydrogels.” Li, Z. Q., et al. Vol. 3 (36), 2013; permission conveyed through Copyright Clearance Center, Inc.	26
Figure 2.4 - Double-bond conversion of formulation A. Reprinted from Cicha, K., et al. (2011). “Evaluation of 3D structures fabricated with two-photon photopolymerization by using FTIR spectroscopy.” <i>Journal of Applied Physics</i> 110 (6), with the permission of AIP Publishing.	30

Figure 2.5 - Cells on scaffolds after 21 days in osteogenic and control cultures: (a and c) human adipose derived stem cells and human bone marrow stromal cells from osteogenic culture; (e and g) human adipose derived stem cells and human bone marrow stromal cells from control culture. High magnification images showing calcium phosphate deposits of human adipose derived stem cell and human bone marrow stromal cell cultures on Zr-Si scaffolds in osteogenic (b and d) and control (f and h) conditions; (i-l) Energy-dispersive X-ray spectroscopy mapping confirming the presence of calcium and phosphorus in the accumulations. Scale bars: (a, c, e, g) 60 μ m, (b, d, f, h) 5 μ m, (i) 50 μ m and (j-l) 10 μ m. Reprinted from Ref. [40] licensed under Attribution 2.0 Generic (CC BY 2.0).....	33
Figure 2.6 - Optical setup of a femtosecond laser imaging and microfabrication system, which is capable of fluorescence lifetime imaging microscopy. Reprinted from Ref. [74].....	35
Figure 2.7 - Experimental generation of arbitrary light fields using one proposed method. The size is approximately 4.8 mm. Reprinted from Ref. [75].	36
Figure 2.8 - Tissue engineering scaffolds made by 2PP with single focus structuring (a) and four foci structuring (b). Image of bovine endothelial cells growing on scaffold made by multi-beam 2PP (c). Reprinted from Ref. [78].	38
Figure 3.1 - Scanning electron microscopy images of microneedles with nominal heights of 500 μ m (Panel A), 750 μ m (Panel B), and 1000 μ m (Panel C) obtained at a stage tilt angle of 45°. The scale bars for these images are 500 μ m.	60
Figure 3.2 - Lesions formed at the infection site in animals from vehicle control groups at the end of the 10 day dosing period for <i>L. mexicana</i> at 44 days post infection (Panel A) and <i>L. major</i> at 30 days post infection (Panel B).	61
Figure 3.3 - Nodule measurements for animals infected with <i>L. mexicana</i> . Panel A – Mice were treated topically at the site of the nodule with a solution of amphotericin B in DMSO (AmB, 25 mg/kg) either in the absence of microneedle application or after the application of microneedle arrays 500 μ m, 750 μ m, or 1000 μ m in nominal length as described in the methods section. Error bars represent the mean \pm standard error of the mean (SEM) (n = 5). The letters indicate a significant difference (p < 0.05, Tukey’s HSD tests) between the amphotericin B no needle group and (a) the amphotericin B 500 μ m needle group, (b) the amphotericin B 750 μ m needle group, or (c) the amphotericin B 1000 μ m needle group using ANOVA with repeated measurements. Differences of borderline significance (0.05 < p < 0.1) were observed between the amphotericin B no needle group and the amphotericin B 1000 μ m needle group on days 59 and 63, (p values = 0.06 and 0.08, respectively), which are not noted on the graph. Panel B – In the same experiment, mice received either PBS vehicle or AmBisome (20 mg/kg) by the IP route as outlined in the methods (a separate panel is included for these two groups for the sake of clarity). Error bars represent the mean \pm	

standard error of the mean (SEM) (n = 5). In the PBS control group, one animal became moribund and was euthanized on day 37 post infection, so n = 4 for this group from that point on. Asterisks (*) indicate a significant difference (p < 0.05, Tukey's HSD tests) between the PBS control group and the AmBisome group at specific post-infection time points. In both panels, the arrows pointing to the x-axis (↓) indicate the days on which treatment began and ended..... 63

Figure 3.4 - Limiting dilution assays were performed for the *L. mexicana* experiment in duplicate and parasite load per gram of tissue was determined as described in the methods section. Circles indicate determinations from individual nodules. Groupwise comparisons were conducted using U rank tests. Asterisks (*) indicate differences with statistical significance (p < 0.05) and hash symbols (#) indicate differences with borderline significance (p values = 0.06 and 0.07, respectively)..... 65

Figure 3.5 - Measurements of nodule area (Panel A) and ulcer area (Panel B) for animals infected with *L. major*. Mice were treated topically at the site of the nodule either with microneedles alone or with a solution of amphotericin B in DMSO (AmB, 25 mg/kg) either with or without application of microneedle arrays 750 μm in length, with AmBisome (20 mg/kg) by the IP route, or with IP 0.9% saline vehicle as described in the methods section. Error bars represent the mean ± standard error of the mean (SEM) (n = 5). Asterisks (*) indicate significant differences (p < 0.05, Tukey's HSD tests) between the saline control group and the AmBisome group at specific post-infection time points. The hash symbol (#) indicates a difference with borderline significance (p = 0.08, 0.06) at days 35 and 42 post infection, respectively. Additional details regarding significant differences in area between the AmBisome groups and the other groups is provided in the text but is not shown here for clarity. The arrows pointing to the x-axis (↓) in Panel A indicate the days on which treatment began and ended; these arrows are not shown in Panel B. In the AmB, 750 μm group, one animal met early removal criteria prior to the last measurement due to a large, ulcerated lesion..... 66

Figure 3.6 - Limiting dilution assays were performed for the *L. major* experiment in duplicate and parasite load per gram of tissue was determined as described in the methods section. Circles indicate determinations from individual nodules. The asterisk (*) indicates a significant difference in parasite load per gram of tissue between the saline control and AmBisome groups (p < 0.05, U rank test). Significant differences in parasite load per gram of tissue were also observed between the AmBisome group and all other non-AmBisome groups (p < 0.05); this is not shown for clarity. 68

Figure 4.1 - UV-visible absorption spectra of riboflavin and the riboflavin–triethanolamine mixture in distilled water. 98

Figure 4.2 - UV-Vis absorption spectrum of polyethylene glycol diacrylate and the 66% PEGda–riboflavin–triethanolamine mixture..... 99

Figure 4.3 - UV-visible transmission spectra of films normalized to a 500- μm path length. Light at 312, 365 and 405 nm is emitted by the UV curing chamber.....	101
Figure 4.4 - (A) Polyethylene glycol diacrylate (PEGda) with 2% Irgacure® 369; (B) 66% PEGda–riboflavin–triethanolamine (the lowest evaluated laser power was subthreshold and is not present within the image); (C) PEGda with 2% Irgacure 2959. Linear scan speed increases from top to bottom and average power increases from left to right.	103
Figure 4.5 - Optical images of 50% polyethylene glycol diacrylate–riboflavin–triethanolamine scaffolds in water.	103
Figure 4.6 - Scanning electron microscopy images of a tissue engineering scaffold made from 50% polyethylene glycol diacrylate–riboflavin–triethanolamine.	104
Figure 4.7 - Comet assay tail moments after 24 h of culture on photopolymer wafers. The error bars indicate the 95% CI.	105
Figure 4.8 - Cell proliferation of GM-7373 bovine aortic endothelial cells on polyethylene glycol diacrylate wafers after 24 h of culture in the presence of photopolymer extract solutions. The error bars indicate the 95% CI.....	106
Figure 4.9 - Cell viability of GM-7373 bovine aortic endothelial cells on polyethylene glycol diacrylate wafers after 24 h of culture in the presence of photopolymer extract solutions. The error bars indicate the 95% CI.	107
Figure 4.10 - Fluorescence images of GM-7373 bovine aortic endothelial cells on riboflavin–triethanolamine–polyethylene glycol diacrylate scaffolds. Merged Live/Dead staining after 5 days of culture of a 50% riboflavin–triethanolamine–polyethylene glycol diacrylate scaffold seeded with GM-7373 endothelial cells. Fluorescence of ethidium homodimer-1 (associated with dead cells) is distinct from dull red autofluorescence of PEGda (right).	108
Figure 4.11 - Calcein AM stain highlights live cells. Cell outgrowths were noted, which are similar to normal endothelial cell morphology.....	108
Figure 5.1 - UV-visible absorption spectra of Irgacure 2959 and LAP in ultrapure water superimposed on the fluorescent UV-A light source emission spectra normalized to the UV-A emission peak. The LAP absorbance peak at 370 nm matches the UV-A emission peak of the fluorescent light source. Irgacure 2959 has tail absorbance in this wavelength range.	133
Figure 5.2 - Viability of hRPTEC exposed for 24 h to GelMA-LAP extracts determined via (a) Alamar Blue and (b) CyQuant Direct Cell assay. Values represent $\bar{X} \pm \text{SD}$ of $n = 3$ independent experimental replicates. Ctrl– = cell media negative control; ctrl+ = 30 μM AgNO ₃ positive control. Values marked with an asterisk (*) are statistically different from the negative control.	134

Figure 5.3 - No effect on hRPTEC viability of LAP concentration in GelMA formulations was determined using the Alamar Blue assay on formulation extracts. Linear regression analysis determined a statistically significant correlation between viability from the CyQuant Direct Cell assay and LAP concentration. Values represent $\bar{X} \pm SD$ pooling the values from all UV exposure treatment groups for each tested LAP concentration. Dotted lines represent the 95% confidence band..... 135

Figure 5.4 - Ratio of NADH fluorescence intensity of NADH photocatalyzed to NAD⁺ in the presence of 0.01 mg/ml LAP to NADH alone. Samples were exposed to visible (>400 nm; 7 mW/cm²) or UV-A (350–400 nm; 5.5 mW/cm²) light, and the fluorescence intensity at 340 nm excitation and 460 nm emission wavelengths was determined at each timepoint. The derivative of the curve at t = 0 was used to calculate the photocatalytic activity toward NADH oxidation. Values represent $X \pm SD$ of n = 6 technical replicates..... 136

Figure 5.5 - Photocatalytic activity of GelMA-LAP extracts normalized to the activity of 0.01 mg/ml LAP in water. Values represent averages of n = 3 independent experimental replicates. 137

Figure 5.6 - Elastic moduli of 10% GelMA chips determined via nanoindentation. Values represent $X \pm SD$ of n = 7 measurements at different locations on the GelMA chips. 138

Figure 6.1 - Storage modulus of 10% GelMA with LAP photoinitiator tracked by photo-rheology; the 405 nm light source (3 mW/cm²) was switched on at 60 sec for all measurements. (Top Panel) Crosslinking of GelMA with 17 (red), 8.5 (green), 3.4 (blue), and 1.7 (purple) mmol/L LAP. (Bottom Panel) Crosslinking of non-nitrogen-purged (blue) and nitrogen-purged (orange) GelMA with 3.4 mmol/L LAP with a focus on the time between light exposure and a rise in storage modulus; the red line denotes the start of light exposure. 162

Figure 6.2 - Viability of mouse M-1 collecting duct cell monolayers exposed to varying concentrations of LAP (3.4, 5.1, 6.8, 17, 25.5, 34, or 68 mmol/L) and not-exposed (•) or exposed to 9.6 mW/cm² 405 nm light (o). LAP concentrations are represented as equivalent Li concentrations. Results are normalized to the viability of monolayers exposed only to PBS and not exposed to light. CdCl₂ (1 mmol/L) was used as the positive control; viability averaged 0% for both assays (data not shown). (Top Panel) Viability determined by the Alamar Blue assay. (Lower Panel) Viability determined by the Neutral Red Uptake assay. Values represent means \pm standard deviations of N = 3 independent replicate experiments. Values that appear to be missing error bars are cases where the standard deviation is smaller than the symbol size. Asterisks (*) denote treatments where the viability of monolayers exposed to LAP is significantly different (p < 0.05) from the viability of monolayers exposed to LAP and light.. 165

- Figure 6.3** - Mutagenicity assessment using bacterial reverse mutation assays. Reverse mutant colony counts of *E. coli* (WP2uvrA, left panel) and *S. typhimurium* (TA98 or TA100, right panel) exposed to PBS (negative control), 0.5 µg/plate 4-NQO or 0.4 µg/plate 2-NF (strain-specific positive controls), 18.5 mJ/cm² UV-C light, 34 mmol/L LAP, or various LAP concentrations with exposure to 10 min of 9.6 mW/cm² 405 nm light. For *E. coli* (left panel), values represent the average of N=2 independent replicate experiments. For *S. typhimurium* strains (right panel), values represent means ± standard deviations of N=3 independent replicate experiments..... 166
- Figure 7.1** - Schedule of AgNP dosing of hBMSC cultures for three separate exposure scenarios: single 24-hour exposure, repeated weekly 24-hour exposures, or continuous exposure. Each square represents a 24-hour period with red squares indicating periods of AgNP exposure. Cell proliferation, alkaline phosphatase expression, and hydroxyapatite content were measured on days 1, 7, 14, and 21 for all exposure scenarios. Fluorescence imaging of hydroxyapatite was performed on day 21 only. hBMSC, human bone marrow mesenchymal stem cells..... 191
- Figure 7.2** - Representative TEM image (top left) of 10 nm PVP-coated AgNP. AgNP core diameter was determined to be 9.95 nm with a 2.22 nm SD by image analysis of n = 140 particles. Cryo-TEM images of AgNP diluted in water (top right), OS– media (bottom left), and OS+ media (bottom right). AgNP, silver nanoparticles; SD, standard deviation; TEM, transmission electron microscope..... 195
- Figure 7.3** - Viability of hBMSC (MTT assay) cultured for 24 hours in the absence (OS–) or presence (OS+) of osteogenic supplements. Cells were exposed to various concentrations of 10 nm PVP-coated AgNP. Cells grown in media alone or media with 3 mmol/L AgNO₃ were used as the negative (ctrl–) and positive (ctrl+) controls, respectively. Values represent (n = 3 replicate experiments). Bars with asterisks are significantly different from the negative control (p < 0.05). SD, standard deviation. 196
- Figure 7.4** - Time-course responses for the proliferation of hBMSC (PicoGreen dsDNA assay) cultured in the absence (OS–) or presence (OS+) of osteogenic supplements under single, repeated, or continuous exposure (Fig. 1) to 1, 5, or 10 µg/mL of 10 nm PVP-coated AgNP. Note that hBMSC not exposed to OS (OS–) or AgNP proliferated over the entire 21-day period, whereas the proliferation of hBMSC exposed to OS (OS+) peaked around day 7 and then declined. Values represent (n = 3 replicate experiments). Statistical analysis of these data is displayed in Figure 7.5..... 197
- Figure 7.5** - Cell proliferation data from Figure 4 plotted separately for days 1, 7, 14, and 21 of culture to more clearly show statistical differences of exposure (single, repeated, continuous) scenarios and AgNP dose. Values represent (n = 3). Bars with no matching letters are statistically different (p < 0.05). 199

Figure 7.6 - Differences in ALP expression in hBMSC cultured in the presence (OS+) and absence of (OS-) of osteogenic supplements under single, repeated, or continuous exposure (Fig. 1) to 1, 5, or 10 µg/mL of 10 nm PVP-coated AgNP. Elevated ALP expression is an early marker of osteogenic differentiation. Values plotted were derived by subtracting the signal values from OS- cells from the signals from OS+ supplemented cells. Therefore, the values represent calculated as for n=3 replicate experiments. Bars with asterisks denote a statistically significant ($p < 0.05$) increase in ALP expression of OS+ supplemented cells over the corresponding OS- cells. Absent bars marked with ‡ are the result of negative values due to subtracting the signal values from OS- cells from near-baseline signals from OS+ supplemented cells. ALP, alkaline phosphatase..... 201

Figure 7.7 - Differences in hydroxyapatite content (OsteoImage Mineralization Assay) between TCPS with hBMSC cultured in the presence of osteogenic supplements (OS+) subtracted from TCPS with hBMSC cultured in the absence of osteogenic supplements (OS-) under single, repeated, or continuous exposure to 1, 5, or 10 µg/mL of 10 nm PVP-coated AgNP. Mineralization of the substrate is a late marker of osteogenic differentiation. Values plotted were derived by subtracting the signal values from OS- cells from the signals from OS+ supplemented cells. Therefore, the values plotted represent calculated as for n=3 replicate experiments. Bars with asterisks denote a significant ($p < 0.05$) increase in mineralization of the substrate from OS+ supplemented cells over the corresponding OS- cells. Absent bars marked with ‡ are the result of negative values due to subtracting signal values from OS- cells from near-baseline signal values from OS+ supplemented cells. TCPS, tissue culture polystyrene surfaces. 203

Figure 7.8 - Fluorescence microscopy images corresponding to the OsteoImage mineralization data summarized in Figure 7 for OS+ supplemented hBMSC cultured for 21 days and exposed to AgNP under single, repeated, or continuous exposure scenarios. No hydroxyapatite was detected with repeated or continuous exposure to 5 µg/mL AgNP or for any exposure to 10 µg/mL AgNP. 204

Figure 8.1 - X-ray diffraction spectra of a YSZ wafer (top), and the tetragonal ZrO₂ reference spectrum (bottom) from PDF Card 04-016-1792. 228

Figure 8.2 - Scanning electron microscopy image analysis of ENrG tape-cast zirconia (top). Scale bar = 2 µm. Summary data from 815 particles (bottom) reported a median grain size of 283 nm..... 229

Figure 8.3 - Atomic Force Microscopy of a YSZ wafer. Topographical image of a 10.00 µm scan size (bottom) and 3D rendering of a 1.0 µm region (top). RMS roughness values were 26.852 nm and 20.799 nm for the 10.00 µm and 1.0 µm regions respectively. 230

Figure 8.4 - Scanning electron micrographs of ENrG with hBMSC (top), and tissue-culture treated polyester with hBMSC (bottom). Scale bar = 200 µm 231

- Figure 8.5** - ALP activity per cell hBMSC cultured on glass without osteogenic media (Ctrl -), tape-cast zirconia (ENrG) with osteogenic media, and glass with osteogenic media (Ctrl +). Bars with asterisks (*) are significantly higher than the negative control. Values represent $\bar{X} \pm SD$ of n = 3 independent experimental replicates. 232
- Figure 9.1** - XRD spectra (black line) of the LCM ceramics after sintering. Colored highlights correspond to the reference spectra of tetragonal zirconia (green, ZrO₂, Powder Diffraction File# 00-050-1089), alumina (red, α -Al₂O₃, Powder Diffraction File# 04-007-4873), silicon nitride (orange, β -Si₃N₄, Powder Diffraction File# 00-033-1160), HA (purple, Ca₅(PO₄)₃(OH), Powder Diffraction File# 04-014-8416), and TCP (blue, Ca₃(PO₄)₂, Powder Diffraction File# 04-001-7220). 250
- Figure 9.2** - 3D renderings and topographical maps from AFM data from the sintered LCM ceramics. Scale bars are 2 μ m for the left image and 400 nm for the right image for each material. Roughness data is summarized in Table 9.1..... 252
- Figure 9.3** - ALP expression of hBMSC grown in the presence of osteogenic supplements and cultured on sintered LCM ceramics or glass and assayed at day 7 (black), day 14 (light gray), and day 21 (gray). ALP measured from the ALP Liquicolor® assay was normalized to cell count determined from the PicoGreen® assay. hBMSC cultured on borosilicate glass coverslips and grown in mesenchymal stem cell media and osteogenic media were used as the negative (Ctrl -) and positive (Ctrl +) controls respectively. Asterisks (*) represent values significantly different (p < 0.05) from the corresponding positive control at the same timepoint. Values represent the means and standard deviations of N = 3 independent replicates (except for ATZ day 14, which has N = 2). 253

CHAPTER 1 – Introduction

In a general sense, Additive Manufacturing (AM) increases geometrical design and manufacturing workflow freedom. Traditionally “impossible” designs, such as ball bearings printed as a single unit, are possible with fewer design considerations versus incumbent technologies such as Computer Numerical Control (CNC) milling. Additionally, modifications to the AM tool is generally not required when switching designs which allow for small-batch manufacturing. Applied to medical devices, AM allows for direct fabrication of complex geometries like porous structures generated in a patient-specific manner. Rapid Prototyping, a synonym for AM, has gone out-of-fashion in recent years but this ability stemming from the small-batch manufacturing capability represents AM’s largest strength. As a case study demonstrating patient-specific treatment, an endangered red-crowned crane was fitted with a prosthetic beak made from selectively laser sintered (SLS) titanium alloy; fused deposition modeling (FDM), the technology used in consumer-grade desktop 3D printers, was used to rapidly prototype the prosthesis geometry iteratively to ensure a good fit for the final titanium prosthesis [1]. The ability to rapidly and inexpensively make small changes to designs is famously leveraged in orthodontic aligners where the labor-intensive steps of adjusting a physical model and plaster casting were replaced with computer-aided design (CAD) modeling and stereolithography (SLA) [2]. Patient-specific AM surgical guides [3] and pre-operative planning models [4] are also used to improve procedure outcomes.

The resolution of AM processes such as inkjet printing [5], extrusion bioprinting, and SLA [6] have been demonstrated in the literature to have sub-millimeter or better resolution and can be smaller than the size of a single cell. Compared with a cell on the order of ten’s of microns, inkjet bioprinting has demonstrated 100 μm droplets with single cells [7] or 200 μm

linewidth when used to produce photopolymer grids. [8] Laser Induced Forward Transfer, an orifice-free version of inkjet printing deposited a keratinocyte grid with $<100\ \mu\text{m}$ linewidth [9]. Extrusion bioprinting has demonstrated linewidths typically $200\ \mu\text{m}$ and above. [10, 11]. The resolution of both these types of bioprinters is highly dependent on the ink rheological properties which vary widely depending on the application. In contrast, bioprinting with SLA is more limited by the optics and free radical diffusion. Resolutions down to $25\text{-}50\ \mu\text{m}$ have been demonstrated in cell-laden constructs which is the practical limit for digital light projection-based SLA. [12] The resolution can be reduced past the optical diffraction limit using two-photon polymerization (2PP), a type of laser-scanning SLA, where $0.5\ \mu\text{m}$ linewidths were achieved when encapsulating human adipose mesenchymal stem cells in gelatin methacrylate. [13] Since these lithographic processes have resolutions on par with or finer than the size of a single cell, the tissue engineering construct resolution is not limited by the photopolymer chemistry which makes this type of material attractive across multiple 3D printing apparatus types.

Despite these benefits, SLA medical devices used clinically are largely composed of limited or prolonged surface devices at worst. External communicating or implant devices such as osseointegrated transcutaneous prosthetic devices, with prolonged or permanent contact times, require much more stringent safety standards. Photopolymers used in SLA and 2PP have inherent toxicological risks associated with the reactive polymerizable moiety, the photoinitiator, and light exposure. The most severe use scenario would be in bioprinting of tissue engineering constructs [14] where cells are embedded within the photopolymer during crosslinking and would be present during the crosslinking process; potential adverse reactions from exposure to the conditions during crosslinking are under-characterized [15]. Photoinitiators commonly used

in bioprinting generate free radicals upon excitation by an appropriate wavelength of light which then initiates free-radical chain polymerization. However, these free radicals can form reactive oxygen species which are a cytotoxic and genotoxic risk. Genotoxicity from light exposure can occur in the presence of certain photosensitizers; photoexcitation of a chromophore can excite an intermediate compound that can continue to generate ROS even after the light source is removed. For example, excitation of melanin, the subsequent degradation of melanin into long-lived triplet-state lipophilic radicals, and the diffusion of these radicals through the nuclear membrane cause formation of cyclobutene pyrimidine dimers (CBD), a form of DNA damage, formation for multiple hours after UV-A irradiation [16]. This mechanism is similar to dark polymerization reactions where energy stored during illumination continues to initiate polymerization after removal of the light source. Singlet oxygen generated from photo-excitation of Rose Bengal can react with ascorbic acid to continuously form hydroxyl radicals which polymerized various acrylate polymers over the next 10 to 20 hours [17]. This effect was detected *in vivo* where UV-B light exposure immediately caused CBD formation, but CBD was also detected hours after UV-A irradiation in mice [18, 19]. Thus, risks from the photopolymer are not only present during the crosslinking process, but may also remain potent after crosslinking.

One strategy is to avoid the use of photopolymers in the final medical device altogether by using the SLA part as a model for casting or as the mold itself. The aforementioned orthodontic aligners use this strategy where the final device is a thermoformed plastic part using the SLA manufactured part as the model; the photopolymer never contacts the patient. Using AM parts as molds or models to be replicated confers the ease of changing designs with compatibility with a wider range of materials. In cases where many identical devices are required, it may even speed up process throughput. For example, “soft lithography” is used to

make microfluidic channels from master structures formed using 2D-lithography; replacing the 2D master with a 3D one is also applicable. For example, a multi-level microfluidic chip to generate droplets using flow-focusing was fabricated from a DLP-SLA fabricated master structure [20]. Instead of bonding the polydimethylsiloxane (PDMS) to glass to produce a microfluidic chip, the PDMS part could be used as a mold to replicate the master structure using a different material. A master structure produced from SU-8, a common negative photoresist, was replicated using polycaprolactone to produce tissue engineering scaffolds [21]. Because this process isolates the final medical device from the AM process, it can be attractive for applications like drug delivery where the drug may be damaged by the AM process. The microneedle pictured in Figure 1.1 was replicated from a 2PP pentaerythritol tetraacrylate master structure using a Gantrez AN-169 and camphorquinone slurry as an analogue for Amphotericin B; this pilot experiment was conducted to determine whether Gantrez AN-169 could still accurately reproduce structures with a high proportion of undissolved solids.

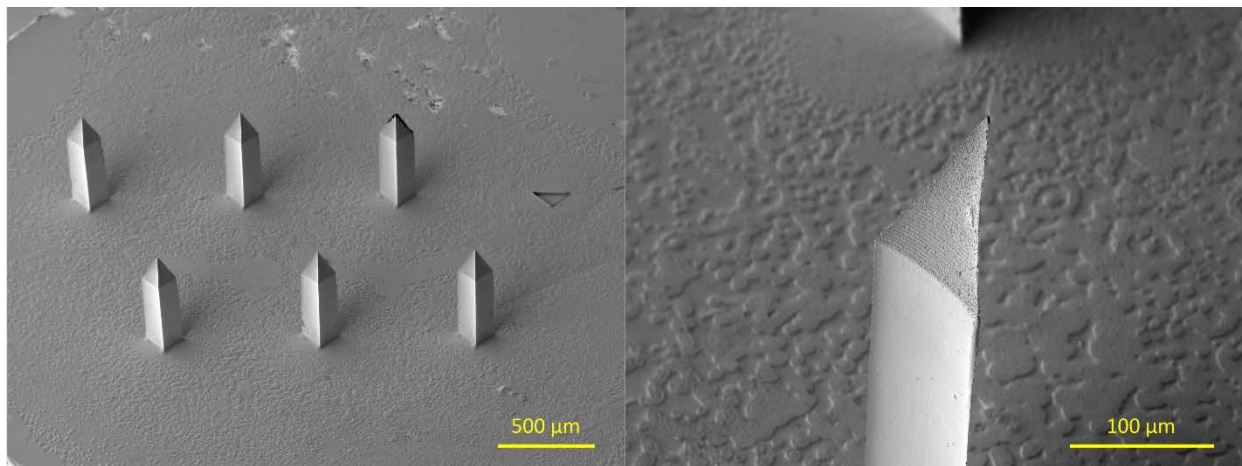


Figure 1.1 –SEM images of a 2PP microneedle replica produced from a Gantrez AN-169 and camphorquinone slurry via PDMS micromolding. Camphorquinone is insoluble in Gantrez AN-169 and acts as an analogue for insoluble drugs such as amphotericin B.

If the final part contains photopolymer, various post processing techniques can improve the biocompatibility of the device or confer additional properties before cell seeding or implantation. Leachable and Extractables testing for medical devices aim to assess the risk of physiologically relevant and exaggerated exposures to compounds that can be extracted from the finished device. Using similar procedures, extractables can be pre-extracted before the device is finished to reduce the quantity of extractables available in the finished device to cause toxicity. This can be achieved using multiple methods such as extended soaking in solvents [22] or even in supercritical carbon dioxide [23]. Alternatively, the photopolymeric component could be eliminated from the device in certain cases. Liquid Ceramic Manufacturing (LCM) is based on SLA where a slurry containing both photopolymer and ceramic is patterned to form a ceramic green body. Sintering eliminates the photopolymer leaving behind just the pure ceramic behind [24]. Toxicity originating from photopolymers can be reduced or eliminated using various post-processing techniques.

The high resolution of SLA and 2PP holds great promise for the manufacturing of medical devices but the many post-processing methods reveal that the use of photopolymers has inherent toxicity that various, application-specific, strategies must be taken to avoid adverse effects. In cases where post processing before contact with cells or tissue is not possible, the effects of light and photoinitiator exposure should be understood and characterized. Therefore, the aims of this dissertation are to 1) develop a 2PP apparatus and demonstrate strategies to avoid photopolymer toxicity, 3) investigate the applicability of LCM ceramic parts alongside other materials relevant to orthopedic devices, 4) characterize toxic effects of fully crosslinked photopolymers on biocompatibility, and 5) characterize the toxicities associated with the photocrosslinking reaction.

Description of 2PP apparatus

Attaining sufficient sample quantity for statistical significance in biological studies is a challenge for lower throughput processes like 2PP so methods to increase throughput was first explored. 2PP is often described as a technique that trades throughput for higher resolution versus traditional laser-scanning SLA but can be faster in certain applications. AM is often called a layer-by-layer manufacturing method but 2PP and certain other AM technologies can break this mold. As an example, consumer 3D printers based on FDM print layer-by-layer, however, this paradigm is bent when using the “spiral vase” method; the print extruder prints the vase contour with slight movement in the vertical direction so the extruder is shifted vertically by the layer height by the time it returns to the contour beginning. Continuing this helical print allows for a 3D structure composed entirely of a single line with no discrete layer shifts. This is possible because FDM can technically print anywhere within 3D space and is only practically limited by support material requirements. 3D “pens”, essentially hand-held FDM extruders, are also commercially available; artists are free to lay filament in any configuration. The “layer-by-layer” paradigm is a strategy to generalize the print process for FDM printers and is not a requirement. Unlike SLA where additional layers must be applied sequentially, 2PP shares the ability of FDM to print anywhere within the build volume and may not require support material if a solid photoresist such as SU-8 or zirconia-ormosil is used. Since 2PP can print equally fast in any direction, high aspect ratio structures such as microneedles or porous materials could have higher throughput with 2PP versus SLA.

Even if 2PP can print in all directions equally quickly, it still stands that the print voxel is a sub-micron diameter volume and would polymerize less material per second versus SLA where an entire cm-scale layer can be polymerized at a time using digital light projection technology.

However, the “dead time” required when moving between layers in SLA is considerable and brings down the average volume polymerized per second; SLA can print quickly in the horizontal plane but is limited in the vertical direction. 2PP does not have this limitation so strategies to improve the throughput involve increasing fabrication speed in the horizontal plane. This is accomplished by optimizing the print trajectory to minimize the amount of “dead time” within each layer. Laser raster-scanning is commonly used when a large 2-D area needs to be covered. For example, confocal microscopy has a resonant scan mode where a mirror vibrating at its resonant frequency translates the laser quickly in one axis while a second mirror scans more slowly in the perpendicular axis; fluorescence intensity data is collected for every location within the region of interest. Unlike confocal, 2PP fabrication only requires laser exposure where polymerized material is desired so scanning over the entire build area is suboptimal. If this resonant scanning is applied to 2PP, the laser would switch on and off rapidly whenever polymerization is desired. The laser focus position is scanned over the entire build volume whether the laser is switched on or not which leads to a large proportion of “dead time”; a solid cube would take the same time as a highly porous cube of the same external dimensions despite the large difference in polymerized volume. This can be solved by using vector scanning, rather than raster scanning, to minimize or eliminate “dead time” within each layer.

The 2PP apparatus designed to accomplish this is composed of five core components, 1) the Ti:sapphire laser, 2) laser shutter/power control, 3) beam spatial filtering, 4) laser focus position control, and 5) machine vision. The beam path diagram is depicted in Figure 1.2. Briefly, the laser is a Mai Tai (Newport, Irvine, CA) laser aimed directly into a half-wave plate and polarizing beam splitter; rotating the polarization with the wave plate allows for manual adjustment of the beam power after the polarizing beam splitter. This beam is focused into an

acousto-optical modulator (Gooch & Housego, Ilminster, UK) which accepts a 1V analog control voltage. When properly aligned, this component diffracts the beam mainly into the 0th order and 1st order beam. When unpowered, only the 0th order beam is present. Increasing the control signal voltage increases the efficiency of the diffraction grating produced by the acousto-optical effect thereby diverting power into the 1st order beam; the acousto-optical modulator combines the function of power control and shutter and can be computer controlled. The beam is then passed through a pinhole spatial filter to remove high spatial frequencies that would be detrimental to resolution. The collimating lens used in this assembly expands the beam to a diameter greater than the back aperture diameter of the microscope objective to make full use of the objective numerical aperture. Finally, the beam passes through a galvanoscanner (Scanlab, Puchheim, Germany) and microscope objective which focuses the laser into the sample. In this apparatus, no scan relay is used which avoids group velocity dispersion caused by transmissive optics and simplifies beam alignment albeit at the cost of a smaller field-of-view of the microscope objective. An XPS-Q8 motion controller and associated stages (Newport, Irvine, CA) are used for large moves (i.e., between unit structures within an array) while the galvanoscanner is used for laser movement within each structure. Machine vision is accomplished by placing a CCD camera behind a dichroic mirror behind the scanner. An RTC5 scanner control card (Scanlab, Puchheim, Germany) controls and synchronizes the activities of the acousto-optical modulator and galvanoscanner. The various instruments were controlled by a custom-made C# program with wrappers to integrate and standardize the manufactures' methods into two main control classes, laser control (print trajectory controlled by the scanner, speed, and laser power) and stage control (sample trajectory controlled by stages, speed).

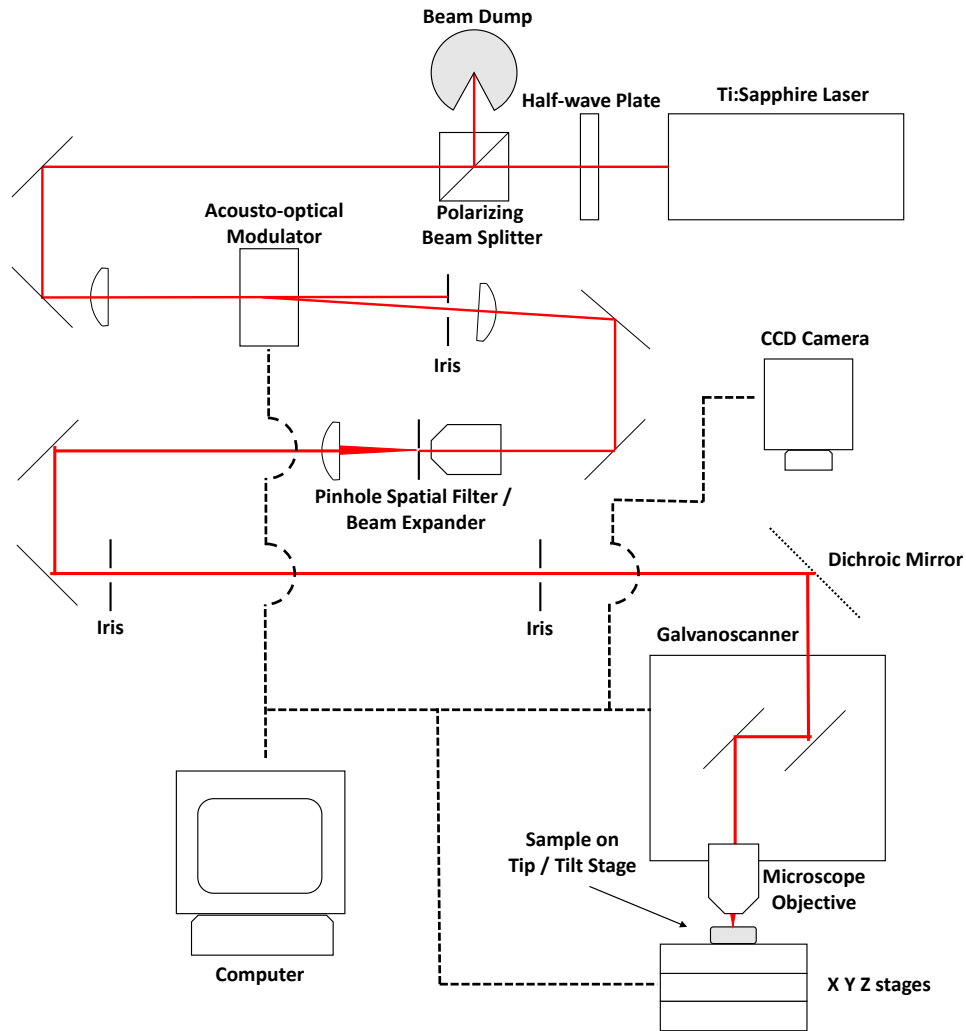


Figure 1.2 – Beam path diagram of the 2PP apparatus.

The fabrication logic within each layer was designed to avoid the “dead time” associated with raster scanning. For example, the unit structure of both tissue engineering ring scaffolds (**Figure 4.5**) and microneedle arrays described in this dissertation (i.e., cylinders or microneedles) are composed of multiple layers of rings with varying inner and outer diameters. These cylinders can be defined parametrically by the unit structure parameters (outer diameter, inner diameter, height), layer parameters (hatching, layer height), and laser parameters (laser power, speed); hatching in this dissertation refers to the line-to-line spacing and is derived from

the artistic method of shading an area with parallel lines. To produce a ring, the laser first draws a circle at the outer diameter followed by a pseudo-Archimedean spiral that ends at the inner diameter, or the center for a solid circle; the spiral is composed of a series of arc commands (equivalent to G02 or G03) with small shifts in the arc center position and arc endpoint to slowly reduce the radius with each revolution. Versus a raster scan where the laser would have to scan through the empty center area, the laser only turns off when jumping to the outer diameter and when the linear stage shifts between the layers or to the next unit structure. This minimizes “deadtime” so the fabrication time for each structure is proportional to the polymerized volume rather than the total structure volume. This optimization enabled an *in vitro* study investigating the osteogenic differentiation of human stem cells on 5 mm diameter porous zirconia-ormosil scaffolds; each scaffold took 50 min to fabricate [25] so sample fabrication required only weeks versus the greater part of a year required previously. Similar logic also applies to other cross-sectional shapes such as hexagons for a honeycomb-like structure or triangles. A microneedle design with a flat face perpendicular to the substrate is presented in Figure 1.1 which was produced from stacked isosceles triangles with the triangle center shifted to stack the long edge vertically; this geometry was intended for the inkjet printing of pharmaceuticals on the perpendicular face.

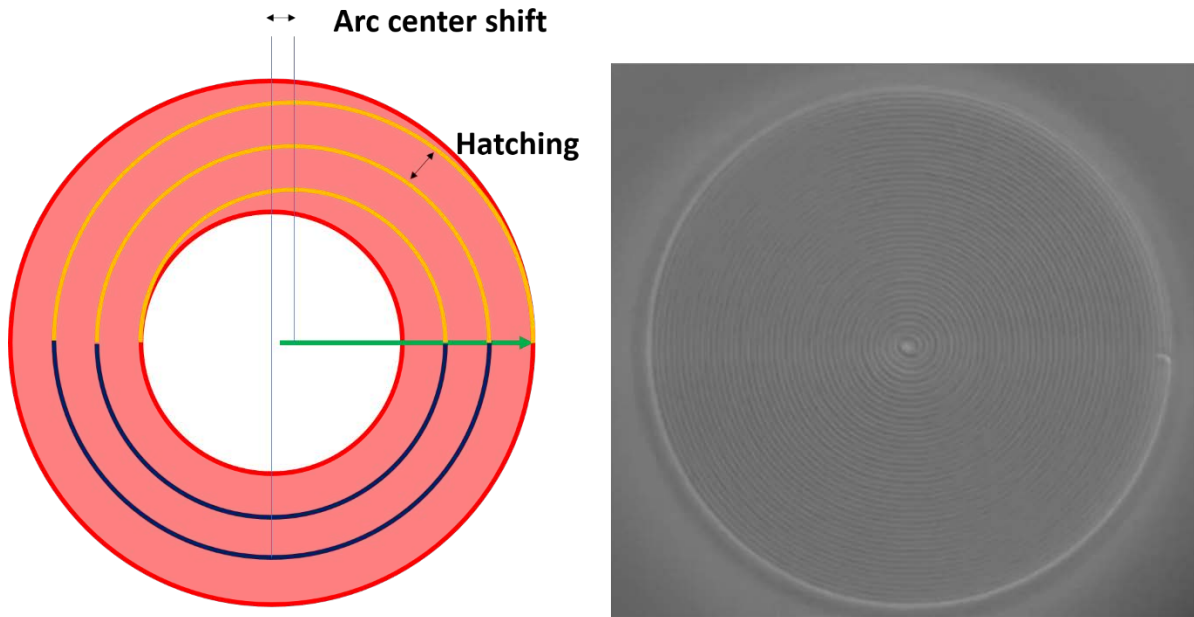


Figure 1.3 – (left) Mark trajectory driven by galvanoscanner for a single layer of a ring. The laser focus jumps (green) from the center to the outer contour. The laser is switched on and does a complete circle (red). Alternating arc commands with the arc center shifted a quarter the hatching value to the right (yellow) and the left (blue) compose a pseudo-Archimedean spiral with a pitch equal to the hatching distance. The spiral terminates at the inner contour, if applicable, where a full circle (red) completes the layer. Hatching distance in this depiction is exaggerated for clarity. (right) A single layer in a microneedle viewed through the CCD camera.

Outline of the Dissertation

The first section of this dissertation discusses the background of 2PP and its use in both a drug delivery microneedle array and for tissue engineering. Although 2PP has a throughput advantage versus SLA for high aspect ratio structures, direct fabrication of multiple identical devices is not the best use of this technology. Microneedle arrays can be fabricated using multiple methods. Isotropic reactive ion etching could be used to sharpen silicon pillars into needles [26]. SLA-fabricated needles are also possible but are difficult to manufacture with sharp tips at the sub-millimeter level [27]. The use of 2PP in this dissertation describes the direct fabrication of microneedle array masters with micron-scale tip radii with sub-millimeter needle

heights. By using soft lithography to replicate these masters, and using the replicas to generate additional molds, each master structure was able to generate the hundreds of “secondary replicas” required for use in an *in vivo* study investigating microneedle-based delivery of amphotericin B into leishmaniasis lesions in mice. This study replaced the toxic photopolymer used in 2PP with a biocompatible material but did not address the toxicity of the photopolymer. The other 2PP-related project proposed the use of riboflavin and triethanolamine as an alternative, water-soluble photoinitiator for tissue engineering applications. Most photoinitiators were not developed with tissue engineering in mind and therefore are cytotoxic, but more importantly, not water-soluble; this precludes their use in hydrogels. An aqueous riboflavin and triethanolamine mixture was able to polymerize polyethyleneglycol diacrylate (PEGda) in the presence of both UV light and with 2PP. The polymerized material extract was less genotoxic and cytotoxic in GM-7373 bovine aortic endothelial cells versus extracts generated from PEGda photoinitiated with Irgacure 369 or even Irgacure 2959, one of the most common water-soluble photoinitiators used in bioprinting. However, this came at the cost of requiring higher laser power and slower scan speeds.

The second section investigates the biocompatibility gelatin methacryloyl (GelMA) photoinitiated with lithium phenyl(2,4,6-trimethylbenzoyl) phosphinate (LAP), a common and commercially available photopolymer primarily used in bioprinting. The first study investigates crosslinked GelMA which best models acellular scaffolds meant to be seeded with cells after fabrication. GelMA extracts generated from any combination of LAP concentration and light exposure were not significantly cytotoxic but the risk of photosensitization was detected. The elastic modulus of photopolymers could be adjusted by partially crosslinking the polymer but extracts generated from under-crosslinked material in this study had considerable photocatalytic

activity towards the photo-oxidation of NADH to NAD⁺; this assay is used to screen for potential phototoxic compounds. Thus, fully crosslinking the photopolymer would lower its photosensitizing potential. Photo-oxidation would be more intense during the crosslinking reaction where cells could be exposed to free radicals generated from light-exposed photoinitiator. In the next study, light exposure conditions found to fully crosslink GelMA containing bioprinting-relevant concentrations of LAP were determined using photorheology. LAP up to 0.5 wt% was found to be non-cytotoxic but when considering light exposure, the lowest LAP concentration of 0.1 wt% was found to be cytotoxic. Despite these conditions being highly cytotoxic to mammalian cells, these conditions were not found to be mutagenic to multiple strains of bacteria in the Ames assay. These results warrant further investigation into the mutagenicity in mammalian cell models.

The final set of studies focuses on substrates supporting osteogenic differentiation. AM orthopedic implants are usually produced using SLS since laser sintering can achieve the temperatures required to melt metals. However, ceramics are much more difficult to sinter using this process. LCM is an alternative process based on SLA which, after sintering, produces a pure ceramic part while retaining the resolution of SLA [24]. Ceramics such as tricalciumphosphate are also compatible with this process which makes it attractive for orthopedic applications [28]. One current challenge of orthopedic implants is the risk of infection which is the second most prevalent cause of revision surgeries [29] so incorporation of silver nanoparticles is being investigated as an antimicrobial agent in medical devices [30, 31] and can be incorporated into AM materials with intended orthopedic uses [32, 33]. However silver nanoparticles may be cytotoxic and/or affect osteogenic differentiation which would affect osseointegration. Impaired osseointegration would lead to prolonged healing or loosening of the implant which is the

leading cause of revision surgery [29]. The first in this series of studies investigates the effect of silver nanoparticle dose and exposure scenario on the ability of human bone marrow stem cells (hBMSC) to undergo osteogenic differentiation by assaying their proliferation, alkaline phosphatase expression, and hydroxyapatite deposition. Yttria-stabilized zirconia ceramic was also investigated in this manner as a potential orthopedic material. Finally, LCM samples including alumina-toughened zirconia, silicon nitride, and hydroxyapatite were evaluated for their mechanical properties, topography, and ability to support osteogenic differentiation.

This dissertation covers multiple manufacturing strategies and use scenarios that involve photopolymers and characterizes potential toxic effects. The first strategy involving the use of 2PP to directly fabricate a microneedle array master structure and subsequent replication demonstrates the ability of this process to quickly generate large numbers of devices with fine features out of a biocompatible material. Direct use of photopolymers is sometimes unavoidable such as in bioprinting so the use of a mixture of riboflavin and triethanolamine as an alternative, less cytotoxic and genotoxic photoinitiator was investigated. GelMA and LAP photopolymer, a common and commercially available bioprinting ink was also investigated for its cytotoxicity, photosensitization risk, and mutagenicity. Finally, the applicability of AM in orthopedics was investigated by observing osteogenic differentiation of hBMSC exposed to silver nanoparticles, a potential antimicrobial, and LCM samples.

CHAPTER 2 – Two Photon Polymerization for Biological Applications

Alexander K. Nguyen¹ and Roger J. Narayan¹

1. UNC/NCSU Joint Department of Biomedical Engineering, North Carolina State University, Raleigh, NC

Reference: Nguyen, A.K.; Narayan, R.J. Two-photon polymerization for biological applications. *Materials Today* **2017**, *20*, 314-322, doi:<https://doi.org/10.1016/j.mattod.2017.06.004>.

Abstract

Two-photon polymerization (2PP) leverages the two-photon absorption (TPA) of near-infrared (NIR) radiation for additive manufacturing with sub-diffraction limit resolution within the bulk of a photosensitive material. This technology draws heavily on photosensitive polymers from the microelectronics industry, which were not optimized for TPA or for biocompatibility. 2PP with sub 100 nm resolution has been repeatedly demonstrated; however, this level of fabrication resolution comes at the expense of long fabrication times. Manufacturing of medical devices beyond surface texturing would be prohibitively slow using the current state of the art 2PP technology. Current research into TPA-sensitive photopolymers with good biocompatibility and holographic projections using spatial light modulators address current technological limitations by providing materials specifically formulated for biological applications and by making better use of available laser power for applications in which nanoscale resolution is not required.

Introduction

Additive manufacturing (AM) techniques are freed from many of the practical concerns associated with incumbent fabrication techniques such as computerized numerical control (CNC) milling; however, additive manufacturing techniques commonly face limitations associated with the tool path. For example, in ultraviolet light-based stereolithography (SLA), light as the

“tool” is “bound” by its interaction with the photopolymer surface. For this reason, AM techniques are often described as “layer-by-layer” techniques. Two-photon polymerization (2PP) breaks free from this paradigm due to the absence of this tool path limitation. 2PP utilizes the two-photon absorption of near infrared (NIR) light to excite the same energy transition as ultraviolet (UV) photons. Since the 2PP photopolymer is transparent to this fundamental wavelength, the 2PP “tool” is essentially an unsupported floating point that is able to process material within the photopolymer. This process is not diffraction limited, allowing for sub-wavelength fabrication; structures with dimensions below 100 nm have been fabricated out of a chemically modified zirconium-based sol-gel composite material using this approach [34]. Just as stereolithography evolved from a laser-scanning approach to a two-dimensional digital-light projection approach, laser-scanning 2PP has the ability to evolve into a three-dimensional holographic projection approach.

The unique capabilities associated with 2PP stem from the capability for sub-micrometer resolution materials processing and from the unsupported voxel; intricate features can be made in regions of structures that are impossible to access using other fabrication techniques. One set of interesting applications of 2PP is fabrication within a microfluidic channel. 2PP-based structuring is performed within a photopolymer-filled channel, followed by exposure to the developing solution. For example, Wu et al. not only generated Fresnel lenses within a microfluidic channel but also fabricated a porous filter, which would have been difficult to conventionally fabricate and place within the channel. The lenses in combination with the filter were used as a white-light cell counter[35]. 2PP was also used to generate porous microchannels for the study of chemotaxis in dendritic cells. The 500 nm pores in the channels generated within the microfluidic channel were too small for the cells to grow

into but large enough for transport of the desired chemokine[36]. A 2PP-fabricated hypodermic microneedle was integrated with a microfluidic device; this device was able to uptake solutions containing physiologically-relevant K^+ solutions for detection with an ion-selective electrode[37]. Producing structures on the cellular size scale opens up many opportunities to determine the cellular response to substrate geometry; for example, neuronal cells have been shown to extend neurites along channels with features on the micrometer scale[38]. In another study, a biomimetic scaffold was produced fromOrmocomp®, an organically modified ceramic, using computed tomography images of human trabecular bone; good adhesion of SaOS-2 osteoblast-like cells to the scaffold surfaces was demonstrated[39].

At this time, 2PP is not commonly used for biological applications due to the toxicity of many feedstock materials and the difficulty of producing mesoscale structures that are relevant for biological applications. Since most 2PP polymers have been adopted from established SLA technologies, they were not formulated for either 2PP or biological applications. In addition, the nano-scale precision offered by 2PP is a source of weakness; structures with small-scale features require relatively long fabrication speeds. Strategies such as soft lithography replication of a 2PP fabricated master structure have been demonstrated[40, 41]; however, these strategies are stop gap measures and do not overcome existing weaknesses. Novel photopolymers exhibiting increased 2PP sensitivity and optics that are able to process larger volumes must be developed to enable large-scale commercial translation. In this paper, the excitation mechanisms associated with 2PP, innovations in photosensitive materials for 2PP, and innovations in optical setups for 2PP will be considered.

Excitation Mechanisms

Despite having “two-photon” in its name, 2PP proceeds by multiple mechanisms, only one of which involves two-photon absorption. In the traditional one-photon case, the photoinitiator is excited to a higher singlet state and decays through an intersystem crossing to the triplet state. Due to this forbidden transition, the triplet state has a much longer lifetime; the long half-life of the triplet species allows for emission even seconds after excitation. These triplet species can form free radicals, which initiate polymerization; as such, photoinitiator designs having long triplet lifetimes are beneficial to UV lithography and 2PP by extension. Unlike UV lithography, 2PP involves extremely intense laser radiation on the order of terawatts per cm^2 , which is associated with the possibility of multiphoton ionization and subsequent dielectric breakdown.

Dielectric breakdown, also known as avalanche ionization, occurs in regions of highly intense electric fields and causes a normally insulating species to become locally conductive. Electrons in the conduction band of a material can be accelerated by the electric field and transfer energy to other electrons in the valence band, promoting those electrons to the conduction band. These child electrons can also be accelerated, generating conduction band electrons within the laser focus in an exponential manner. Order of magnitude estimations of multiphoton and avalanche ionization that were calculated for SZ2080 zirconium Ormosil®, a photoresist used both for photonics and biological applications, revealed that the contribution from avalanche ionization is much greater than from two-photon absorption near the 2PP threshold[42]. Since dielectric breakdown would also take place within the monomer, it is possible to perform 2PP without photoinitiators. Eliminating photoinitiators would be very

attractive from a biocompatibility viewpoint; however, the working range of the 2PP process would be severely narrowed.

The working range is informally limited by (a) the 2PP threshold, the average laser power found in practice to initiate polymerization, and (b) the burning threshold, the power at which the material breaks down and generates bubbles that destroy the sample. Dielectric breakdown requires a conductive electron to be accelerated; such electrons are exceedingly rare in insulators and the vast majority of polymers. A photoinitiator with a quasistable excited state has multiple seeds for dielectric breakdown. Malinauskas et al. reported 2PP structuring without a photoinitiator in Ormosil®; the 2PP threshold was cut in one-third and the working range was tripled with addition of 1% by weight Irgacure® 369 or Michler's ketone[42].

Simple heating of a photopolymer can cause polymerization, which can result in unwanted voxel spread. For example, SU-8, a polymer from the microelectronics industry that is commonly used in biological studies, will thermally polymerize when exposed to temperatures above 167 °C [43]. It was calculated that a 0.5 nJ pulse, which approximates the energy from a 50 mW Ti:Sapphire laser operating at 80 MHz, would generate an equilibrium temperature of 227 °C within the focal volume (assuming insufficient time for heat diffusion) [44]. Considering a typical 80 MHz repetition rate and a 1 mm voxel size, the laser focus would have to scan at above 80 m/s to have no voxel overlap. Since 2PP experiments commonly typically take place with scan speeds in the range of millimeters per second, heat-initiated polymerization is a major contributor to the final dimensions of a 2PP-fabricated structure. Baldacchini et al. used a pulse width modulated (PWM) acousto-optical modulator to chop the 80 MHz laser into bursts with variable repetition rates. Decreasing the repetition rate (at a constant average laser power and burst width) increased the resolution of the 2PP-fabricated structures [45]. Although an identical

average power is experienced by the sample, allowing the local regions to cool by spacing out the pulses reduces the effect of thermal polymerization.

Drawing multiple lines simultaneously is one method to increase the fabrication speed; this approach is possible with laser technologies but it is associated with voxel spread via diffusion of the polymerization propagating species. Cross-talk between fine features (e.g., diffraction gratings or wave guides) occurs when the scanning process is rapid. Much of this phenomenon can be explained by heat buildup within the substrate; however, a linewidth increase of up to 25% was noted in experiments in which thermal effects were considered negligible. The effects of spatial and temporal proximity were investigated by scanning two foci separated by an x and y distance; when scanning parallel to the y -axis, the x separation constituted spatial separation between the two lines and the y -separation formed the temporal delay. The focus trailing behind the other contained a higher concentration of initiating species, which diffused from the leading pulse and caused broadening. This effect was significant out to 100 ms temporally and 3000 nm spatially [46]. Current fabrication strategies such as raster scanning often involve marking parallel lines spatially and temporally shorter than these values; as such, this ‘‘proximity effect’’ must be considered when tight tolerances are required.

Since two-photon absorption (TPA) is the mechanism that seeds polymerization, maximizing the TPA coefficient is an important factor in 2PP photopolymer design. In single photon absorption, the intensity of the transmitted light is dependent on the linear absorption coefficient (α), concentration, and path length as per the Beer–Lambert law. The non-linear absorption coefficient (β) becomes a non-negligible factor at high intensities; it can be negative for saturation of absorbance or positive for multi-photon absorbance. This phenomenon is measured using the Z-scan technique, in which a sample is translated along the axis of a

converging laser while the transmitted light intensity is measured. In the typical Z-scan apparatus, the non-linear absorption coefficient is measured in an open aperture configuration in which all of the transmitted light is collected; any change in transmittance while scanning through the focus would be due to non-linear (e.g., two-photon absorption) effects. The theoretical calculations behind this technique incorporate three main assumptions to simplify the calculations: (1) only the third-order non-linearity (two-photon processes) are considered, (2) the sample thickness is shorter than the Rayleigh range of the focus, and (3) the laser is a TEM00 Gaussian beam. If one approximates the sample to be a ‘‘thin’’ sample, then the laser focal region dimensions do not vary significantly within the sample while being translated within the beam. This approach enables use of the slowly varying envelope approximation; higher order differentials in the equation representing electric field can be ignored. Using a Gaussian beam simplifies the calculations since the Fourier transform of a Gaussian distribution is also Gaussian. At the endpoint of the calculations, the change in normalized transmission through the sample can be represented by the Taylor series:

$$T(z) = \sum_{m=0}^{\infty} \frac{[-q_0(z, 0)]^m}{(m + 1)^{3/2}}$$

Where $q_0(z, 0)$ is:

$$q_0(z, 0) = \frac{\beta I_0 L_{eff}}{1 + (z^2/z_R^2)}$$

In this equation, z_R is the Rayleigh range, L_{eff} is the effective path length represented by $L_{eff} = [(1 - e^{-\alpha L})/\alpha]$, and I_0 is the peak irradiance at the focus of the sample[47]. Since photopolymers used with 2PP should be transparent to the laser radiation, α will be very small, which makes $L_{eff} \approx L$. For a perfectly Gaussian beam, I_0 can be given by [48]:

$$I_0 = \frac{4P_{Avg}}{\pi\omega_0^2 R\tau} \sqrt{\frac{\ln(2)}{\pi}} = \frac{4P_{Avg}}{M^2\lambda z_R R\tau} \sqrt{\frac{\ln(2)}{\pi}}$$

where R is the repetition rate, τ is the pulse duration, ω_0 is the beam waist, and M^2 is the beam quality. All parameters in I_0 are either defined by the experimenter (i.e., average power P_{Avg} and Rayleigh length z_R) or the characteristics of the laser. L_{eff} is an experimental parameter, leaving the value for β unknown. β , the non-linear absorption coefficient, can be numerically fit to the Taylor series. Further approximating the value by only considering them = 1 term in the series, using L in place of L_{eff} , and subtracting the $m = 0$ term (which is simply 1 in any case), a greatly simplified equation in terms of the change in the normalized transmittance can be obtained:

$$T(z) - 1 = \Delta T(z) = \frac{-\beta I_0 L}{2\sqrt{2}[1 + (z^2/z_R^2)]}$$

Although the highest change in transmittance will always be found at $z = 0$, noise in the data can make it difficult to find the exact values for $\Delta T(z)$ and z_R . That said, a good starting point to qualitatively compare different photoinitiator formulations would be to measure the relative change in transmittance at $z = 0$ while accounting for potential differences in the sample path lengths. Finding photoinitiator formulations with high TPA cross-sections generates a list of moieties that are highly efficient absorbers.

Photopolymer Design Strategies

Designing an efficient 2PP photoinitiator differs from designing an efficient ultraviolet photoinitiator since the TPA cross-section is not considered during development of an ultraviolet photoinitiator; however, designing an efficient 2PP photoinitiator and designing an efficient ultraviolet photoinitiator share many strategies. In general, high TPA cross-section

photoinitiators commonly consist of an extended p-system chromophore that is flanked by multiple electron donating or withdrawing groups [49, 50]. For example, Ethyl Michler's ketone is composed of a benzophenone with a diethyl amino group at each of the para positions. Another consideration is the efficiency of the radical species that initiate polymerization. Furthermore, there must be a bridge between these two criteria in which the excited state can form the radical species[49].

The mechanism by which the free-radical species is formed splits photoinitiators into two classes. Type 1 photoinitiators are cleaved from the triplet state, forming two free radicals that can initiate chain polymerization. In contrast, the triplet excited state of type 2 photoinitiator chromophores must react with a coinitiator, which subsequently forms the radical species. Type 1 photoinitiators are more common since photocleavage is a monomolecular reaction; type 2 photoinitiators utilize bi-molecular reactions and are less efficient. It should be noted that type 2 photoinitiator formulations in which the chromophore is covalently bonded with the co-initiator allow for formation of a free radical species in a mono-molecular reaction without cleavage[51].

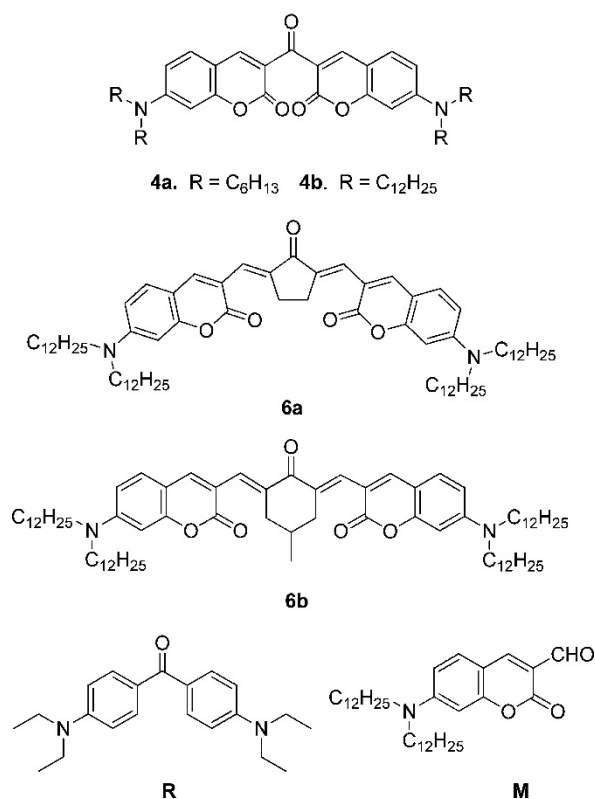


Figure 2.1 - Structures of new 2PA photoinitiators and reference compounds. Reprinted (adapted) with permission from Nazir, R., Danilevicius, P., Ciuciu, A. I., Chatzinikolaïdou, M., Gray, D., Flamigni, L., Farsari, M., Gryko, D. T. (2014). p-expanded ketocoumarins as efficient, biocompatible initiators for two photon-induced polymerization. *Chemistry of Materials*, 26(10), 3175–3184. doi:10.1021/cm500612w, Copyright 2014 American Chemical Society.

Considering the TPA cross-section, the mechanism of radical formation, and the initiation efficiency leaves few 2PP feedstock materials with appropriate features for biological applications. Photoinitiators are generally toxic materials since reactive oxygen species are harmful to cellular function. As such, type 1 photoinitiators designed to easily cleave are not the most biocompatible class of materials. For this reason, recent research efforts have been geared toward the development of biocompatible type 2 photoinitiators. For example, high TPA cross-section chromophores (shown in **Figure 2.1**) were produced from two different p-extended

ketocoumarins and modified with different diacylamino- groups; these materials were shown to exhibit 100% cell viability and similar proliferation rates to the glass control [52]. The combination of riboflavin and triethanolamine has been used as a UV photoinitiator [53] and has been successfully used for 2PP [54]. No statistically significant difference in cell viability was noted between riboflavin- triethanolamine wafers and glass. Growth of bovine aortic endothelial cells on a polyethylene glycol-riboflavin-triethanolamine scaffold processed using 2PP was demonstrated (**Figure 2.2**); a LIVE/DEAD™ stain of a five day culture of GM7373 endothelial cells demonstrated a significant number of live cells and few dead cells. It should be noted that riboflavin-triethanolamine was less efficient than conventional photoinitiators (e.g., Irgacure® 369 and Irgacure® 2959) in terms of the laser fluence required for 2PP. The higher laser fluence required for this photoinitiator formulation is affected by the TPA cross section and radical generation from the excited state.

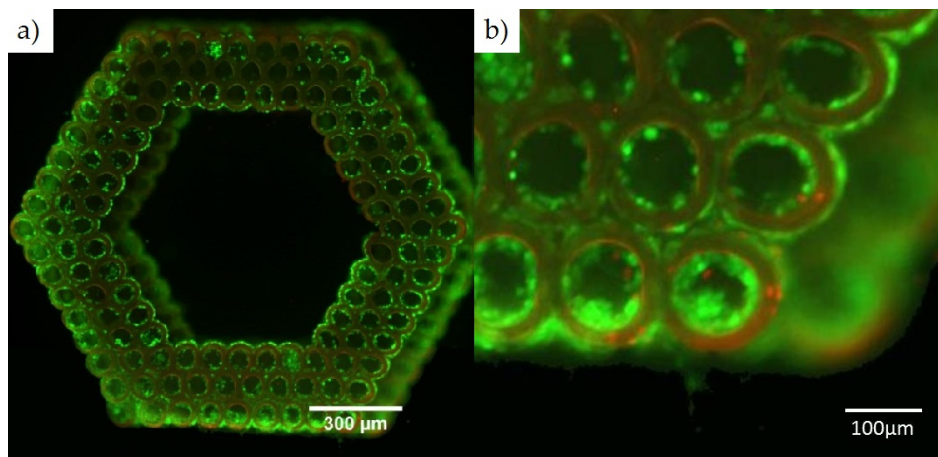


Figure 2.2 - (a) Merged live/dead staining after five days of culture for a 50% polyethylene glycol diacrylate-riboflavin-triethanolamine scaffold seeded with endothelial cells. (b) polyethylene glycol diacrylate exhibits red autofluorescence; ethidium homodimer-1 (dead cell) fluorescence is distinct from the polyethylene glycol diacrylate fluorescence. Republished with permission of Future Medicine Ltd, from “Two-photon polymerization of polyethylene glycol diacrylate scaffolds with riboflavin and triethanolamine used as a water-soluble photoinitiator.” Nguyen, A. K., et al. Vol. 8 (6), 2011; permission conveyed through Copyright Clearance Center, Inc.

While each parameter is important individually, all of the factors can be summed up by the processing window. Qualitatively speaking, the processing window is related to the scanning speed and the laser power, the product of which gives the laser dosage exposed to a volume. A more effective photoinitiator would have a wide range of speed and a power at which good structuring is observed. The gold standard to evaluate the processing window is a parametric study that evaluates each speed-power combination. An example parameter search array is given in **Figure 2.3**, in which both parameters are serially tested [55]. In areas with high power and low speed, poor structuring is observed since the polymer burns from the high irradiation. Areas with high speed and low power are underexposed, which results in weak or missing structures. A wide processing window between these two zones indicates an easy-to-use photopolymer.

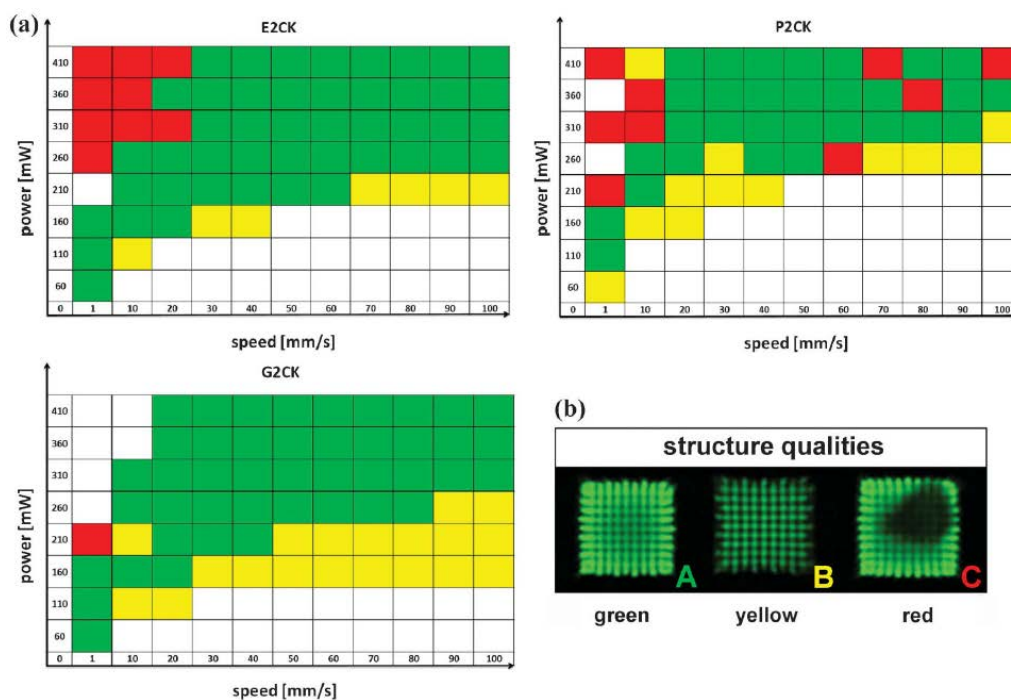


Figure 2.3 - (a) Processing windows of investigated initiators in TPIP screening tests; (b) Classifications of the structures by the typical quality of their shapes. Republished with permission of Royal Society of Chemistry, from "Initiation efficiency and cytotoxicity of novel water-soluble two-photon photoinitiators for direct 3D microfabrication of hydrogels." Li, Z. Q., et al. Vol. 3 (36), 2013; permission conveyed through Copyright Clearance Center, Inc.

Water insoluble photoinitiators make up the majority of available products on the market; however, their insolubility does not rule out their use in hydrogels. Pawar et al. used 2,4,6-trimethylbenzoyldiphenylphosphine oxide (TPO) as a model water insoluble photoinitiator to process aqueous acrylamide in an SLA setup. The TPO was prepared as an oil-in-water microemulsion and then spray dried to produce a dry nanoparticle powder; dispersing this powder into water yielded a clear solution [56]. TPO and ethyl Michler's ketone are well established photoinitiators that are also unfortunately water insoluble, preventing their traditional use in hydrogels. Preparing these photoinitiators in nanoparticle form would be one method for photosensitizing hydrogel monomers. Although these materials are not highly biocompatible, post processing steps and the insolubility of these materials would reduce the amount of material that enters the biological environment during use.

Appropriate photopolymers for biological applications would ideally have a high degree of conversion to minimize the amount of residual monomer and fast polymerization kinetics to reduce the required laser dwell time necessary to achieve full polymerization. Being able to tune the mechanical properties and degradation characteristics would be an ideal characteristic for several tissue engineering applications. Biological uses of photopolymers are already commonplace albeit not with photopolymers that are processed using additive manufacturing approaches. Dental applications draw heavily on methacrylates that are commonly initiated by Type II photoinitiators due to their compatibility with visible light; however, Type I photoinitiators may also be used. Further examination of dental photopolymer systems may suggest appropriate methacrylate formulations for use with 2PP.

The Degree of Conversion (DC) determines the final mechanical properties and the biocompatibility of the structure (e.g., the biocompatibility of the structure may be reduced by

leaching of unreacted monomer). Changes in Fourier transform infrared spectra (e.g., changes in the vinyl peak) are commonly used to determine the DC value. For example, the DC value for a 55:45 molar ratio of 2,2-bis[4-(2-hydroxy-3-methacryloxypropoxy)phenylpropane (BisGMA) and 2-hydroxyethylmethacrylate (HEMA) mixture was monitored with an Attenuated Total Reflectance FTIR (ATFTIR). The ratio of the 1637 cm^{-1} peak (associated with aliphatic C=C) to the 1608 cm^{-1} peak (associated with aromatic C=C) was evaluated. Measurements obtained at multiple times during polymerization were compared to the initial ratio of the monomer solution; these measurements were used to calculate the DC values for the system [57]. This approach was also used to examine a 7:3 mass ratio of BisGMA and triethyleneglycoldimethacrylate (TEGDMA) [58]. Both studies evaluated the effect of several photoinitiators and illumination conditions on camphorquinone (CQ)-based photoinitiators. DC values for these systems, which exhibit 20–70% conversion, are heavily influenced by the choice of photoinitiator. Additional photoinitiator systems based on 9,10-phenanthrenequinone (PQ), TPO, and phenylbis(2,4,6-trimethylbenzoyl) phosphine oxide (BAPO) were investigated for a 55:45 BisGMA:HEMA monomer mixture under wet and dry conditions [59]. A study that investigated the reaction kinetics for several ratios of BisGMA and TEGDMA with a CQ-based Type II photoinitiator or a monoacylphosphine (MAPO) Type I photoinitiator showed changes in the DC value from variations in the monomer ratio and the photoinitiator type. The use of MAPO resulted in a higher final DC value, with polymerization requiring one-fourth to one-sixth the amount of time to reach 95% of the final DC value. High performance liquid chromatography analysis of monomer eluted after one week in a 75% ethanol solution revealed a steep slope between the total monomer eluted and the DC value (e.g., 12% by weight eluted at 40% DC versus 3% eluted at 50% DC) [60]. Both photoinitiators used in this study are not biocompatible; however, the

marked difference between the DC values (and the amount of elutable monomer by extension) raises questions about the trade-off between photoinitiator toxicity and DC value. Since a high DC value is associated with less residual monomer and less toxicity, the effect of laser-material interaction on DC should also be considered. Cica et al. demonstrated 2PP of a 1:1 mixture by weight of trimethylolpropane triacrylate and ethoxylated(20) trimethylolpropane triacrylate, which was photoinitiated by either 2,7-bis[[(4-dibutylamino)phenyl]ethynyl]-9Hfluoren-9-one (B3FL) or E,E-1,4-bis[40-(N,N-di-n-butylamino)styryl]-2,5-dimethoxybenzene (R1) at a 6.3 mmol/g concentration; several scan speeds and average laser powers were evaluated in this study. The DC values of the 50 μm x 50 μm x 30 μm structures were calculated using data from the 810 cm^{-1} peak, which was attributed to carbon double bonds; the carbon double bond data was normalized using data from the 1730 cm^{-1} carbonyl peak (**Figure 2.4**). Scan speed was found to have an effect on the DC value near the 2PP threshold, the lowest laser power at which polymerization is observed. The correlation between scan speed and DC value was not significant at high power values; changing the scan speed from 100 to 800 mm/s at the threshold reduced the DC value from 61% to 56%. A DC value of 74% was obtained for structures within this scan speed range when using power values above 1.75x the threshold were utilized [61].

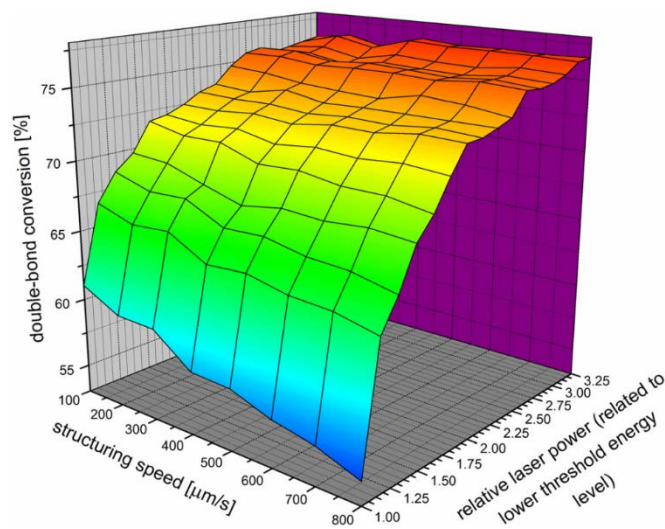


Figure 2.4 - Double-bond conversion of formulation A. Reprinted from Cicha, K., et al. (2011). "Evaluation of 3D structures fabricated with two-photon photopolymerization by using FTIR spectroscopy." *Journal of Applied Physics* 110 (6), with the permission of AIP Publishing.

Hydrogels are commonly polymerized with 2PP since this class of materials is commonly used in studies involving soft tissue regeneration. In addition, several types of biological polymers, including carbohydrate- and protein- based materials, can be modified with photopolymerizable groups to make them feedstock materials for the 2PP process. It is also common to incorporate growth factors or other compounds within the polymer chain that alter its mechanical properties. The general procedure for modifying the backbones of synthetic and biological polymers with pre-polymer groups is similar.

The addition of methacrylate groups can be undertaken with glycidyl methacrylate, which can react with carboxyl, hydroxyl, and amine groups to form a corresponding carbonyl linkage that terminates in a methacrylate group [62, 63]. Methacrylation of hyaluronic acid using this approach is straightforward due to its water solubility. Chitosan must be modified with succinic anhydride to become soluble in water; reaction with an amine group on the chitosan backbone forms an amide linkage that terminates in a carboxylate group. Incubation of either hyaluronic

acid or N-succinylated chitosan with glycidyl methacrylate over ten days yielded a photopolymerizable hydrogel. Purification was performed by precipitation in acetone, dialysis in pure water, and lyophilization. The mechanical properties of the methacrylated polymer can be modified by the addition of polyethylene glycol diacrylate. Lactate dehydrogenase and cell proliferation assays indicated that both the base methacrylated polymer and the copolymer containing polyethylene glycol diacrylate possess biocompatibility similar to that of the tissue culture polystyrene control [62, 63].

A process utilizing the more reactive methacrylic anhydride was described for methacrylation of gelatin; the degree of substitution can be controlled by varying the concentration of the methacrylic anhydride in the solution. The procedure is relatively simple, involving the addition of methacrylic anhydride to a 50 °C gelatin solution in phosphate buffered saline over a period of one hour. Dialysis over twenty-four hours and lyophilization completed the purification of the material [64]. 2PP was used to process material into a woodpile-style scaffold; human adipose-derived stem cells were able to proliferate through the structure and differentiate into adipocytes [65]. The reactive methacrylating agent has also been used to modify a biodegradable polylactic acid base polymer with organic solvents [54]. The photopolymer that was obtained using this approach was seeded with a human SH-SY5Y human neuronal cell line and with primary rat Schwann cells [66].

All of the photopolymers mentioned thus far have been negative photoresists; it should be noted that positive photoresists, for which illumination causes polymer cleaving, are also compatible with multiphoton absorption technology. For example, Kloxin et al. produced a photocleavable PEG-based polymer using 4-[4-(1-hydroxyethyl)-2-methoxy-5-nitrophenoxy]butanoic acid as the photolabile group. The addition of an acrylate group produced

the photodegradable acrylate. Ammonium persulfate and tetramethylenediamine were used for radical-mediated polymerization of the bulk polymer. Exposure to 365 nm light, or two-photon excitation by 740 nm light commonly produced by a Ti:sapphire femtosecond laser, caused hydrolysis of the ester group adjacent to the acrylate group. Kloxin et al. also provided a procedure for cell encapsulation within the crosslinked polymer [67]. One important advantage of using a positive photoresist with encapsulated cells is that UV phototoxicity is not an issue; the cell-laden polymer exposed to in-focus NIR light is washed away during development; the out-of-focus NIR light should have little effect on cells compared to the UV light that is used in traditional lithography.

While not a traditional polymerization reaction, certain proteins can be crosslinked without modification through a complex reaction that involves singlet oxygen generation from a chromophore. Crosslinking of collagen using UV light is well known and is commonly utilized by ophthalmologists for the treatment of keratoconus [68]. A 40% increase in the stiffness of collagen-rich tissue cultured in vitro from murine embryonic fibroblasts and neonatal rat cardiomyocytes was demonstrated using this approach [69]. Singlet oxygen can also be generated using TPA from aromatic amino acids within the proteins themselves; this mechanism enables crosslinking of protein solutions without the inclusion of additional photosensitizers [70]. The addition of a chromophore such as methylene blue, rose bengal, or flavin adenine dinucleotide can improve the crosslinking performance [71]. Robust 3D structures such as small cantilevers or chambers may be processed using this approach. By precisely measuring the mechanical properties of crosslinked avidin structures using atomic force microscopy, Khripin et al. was able to measure the pressure of proliferating *E. coli* within a chamber; this approach can be potentially used to predict pressures within cancerous tumors [72].

Tissue engineering of orthopedic implants requires relatively stiff materials, which facilitate the differentiation pathway of undifferentiated cells into the osteocyte lineage. Organically-modified ceramic (Ormocer®) materials are popular materials for orthopedic applications. For example, the zirconium–silicon based hybrid solgel photopolymer (ORMOSIL SZ2080) has been used for orthopedic applications due to its biocompatibility; 1% w/w ethyl Michler’s ketone is a popular photoinitiator for use with this polymer. Extensive washing is commonly used to remove the unreacted monomer and the photoinitiator. Human adipose- and bone marrow-derived stem cells have been grown on this material in three-dimensional scaffold [25] (**Figure 2.5**) and two-dimensional textured surface [73] formats to examine the effect of scaffold geometry on osteogenic differentiation.

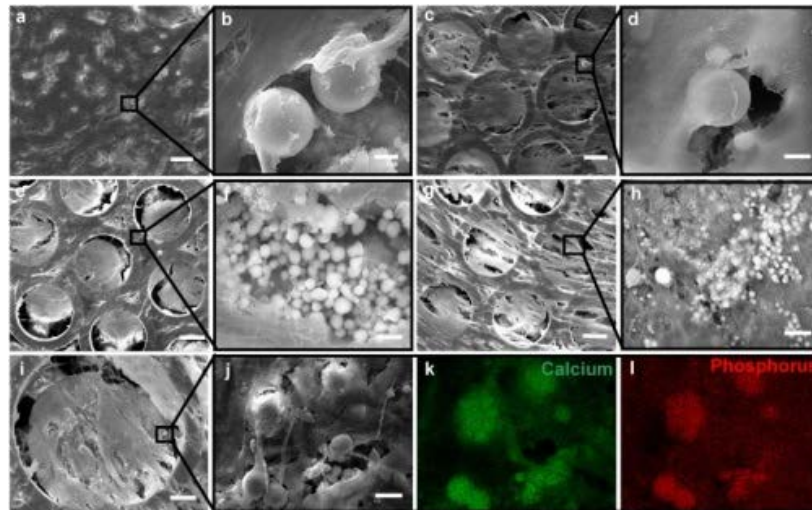


Figure 2.5 - Cells on scaffolds after 21 days in osteogenic and control cultures: (a and c) human adipose derived stem cells and human bone marrow stromal cells from osteogenic culture; (e and g) human adipose derived stem cells and human bone marrow stromal cells from control culture. High magnification images showing calcium phosphate deposits of human adipose derived stem cell and human bone marrow stromal cell cultures on Zr-Si scaffolds in osteogenic (b and d) and control (f and h) conditions; (i–l) Energy-dispersive X-ray spectroscopy mapping confirming the presence of calcium and phosphorus in the accumulations. Scale bars: (a, c, e, g) 60 μ m, (b, d, f, h) 5 μ m, (i) 50 μ m and (j–l) 10 μ m. Reprinted from Ref. [40] licensed under Attribution 2.0 Generic (CC BY 2.0).

2PP is a unique tool to perform additive manufacturing for biological applications since structures of arbitrary geometry on the size scale of the cell or of sub-cellular structures can be reliably reproduced. Due to the fabrication speed limitations of 2PP, the most promising current applications of 2PP have been for in vitro assays that examine cellular behavior rather than for implantable tissue engineering scaffolds.

Optics Considerations

The 2PP apparatus is used to (a) tightly focus the laser into the sample while allowing for cleaning or shaping of the beam and (b) translate the focal point within the sample.

Titanium:sapphire lasers are the most commonly used for 2PP experiments; however, other types of femtosecond lasers (e.g. frequency doubled Nd:glass lasers) or even some picosecond lasers may be used for 2PP. The most simple 2PP setup consists of a laser source, a focusing objective, a translational stage, a laser power control system, and a shutter; most of these components are also found on microscopes. As such, building a 2PP system on an existing two-photon fluorescence microscope is commonly undertaken. Additions to the setup can improve the resolution and fabrication speed. Using the scanning mirrors as the primary method for moving the laser focus results in orders of magnitude faster fabrication versus using the translational stages (although this approach is limited to the field of view of the objective). Controlling the group velocity dispersion using optics such as prism compressors or chirped mirrors can reduce the pulse duration; with a shorter pulse duration, 2PP threshold intensities can be achieved with lower average laser power values. An example 2PP beam path is given in **Figure 2.6**, which contains all of the aforementioned components.

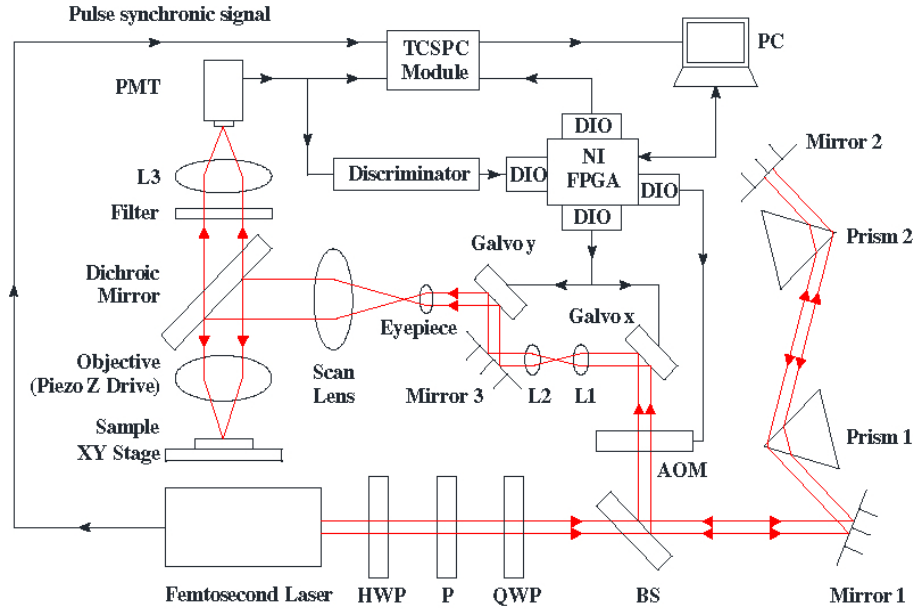


Figure 2.6 - Optical setup of a femtosecond laser imaging and microfabrication system, which is capable of fluorescence lifetime imaging microscopy. Reprinted from Ref. [74].

Use of a spatial light modulator (SLM) is similar to use of projection SLA in that the beam is shaped to present more than a one-dimensional point for fabrication [75]. Unlike ultraviolet lithography, in which the projection of any two-dimensional image will suffice, manipulating a three-dimensional focal volume is more challenging from hardware and computational standpoints. While a two-dimensional mask suffices for ultraviolet illumination, amplitude and phase modulation within the beam must be manipulated to form the desired voxel shape for projection of a three-dimensional image. This parameter is achieved by inserting a mask within the $4f$ system Fourier plane, the plane in between the two lenses. The simplest case would be a pinhole spatial filter, in which low spatial frequencies that focus closer to the optical axis are allowed through. Computer-controlled SLMs placed at the first conjugate plane can introduce phase delays within certain regions of the beam. Currently available SLMs are essentially small liquid crystal displays and are usually controlled via a Digital Visual Interface

(DVI) input; instead of controlling the color intensity, each pixel on this device changes the phase of the incident light. The current approach is to generate a holographic image, which generates the desired pattern after a Fourier transformation. Many algorithms are available, including ab initio ones; in general, the highest precision will be obtained using iterative algorithms. One example of the image generation capabilities of the SLM utilized the Gerchberg-Saxton (GS) iterative algorithm combined with the angular spectrum method to allow for faster calculation of images that deviated from the focal plane. One stated limitation of this approach is that the out-of-focus light from one component image was visible at the focus of another component image. For 2PP, this limitation is not consequential since the photopolymer is transparent to the unfocused light. As shown in **Figure 2.7**, Hilario et al. projected different letters that were each independently mobile in all three axes [75].

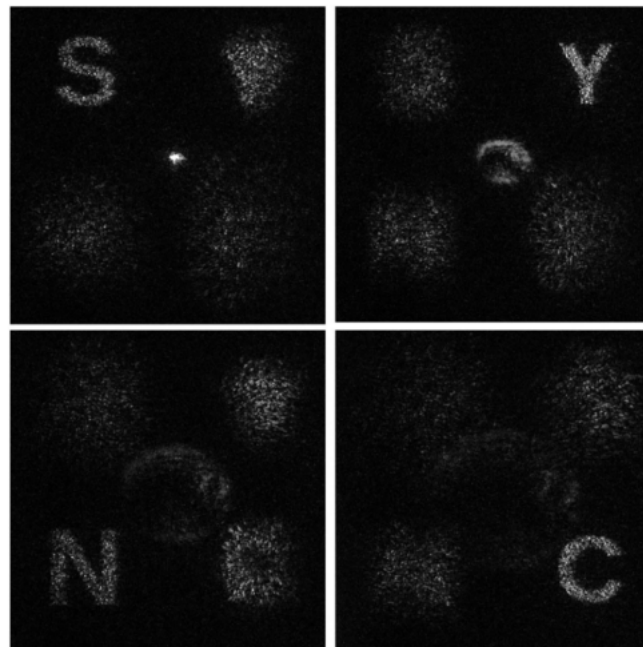


Figure 2.7 - Experimental generation of arbitrary light fields using one proposed method. The size is approximately 4.8 mm. Reprinted from Ref. [75].

Using a SLM for 2PP is currently limited by the need to provide sufficient laser power that initiates polymerization. When projecting a point source, a 1 μm voxel requires only a couple milliwatts of power and nanoseconds of exposure. Illuminating a 10 μm cubic region would require on the order of watts of power, which would be difficult to achieve considering that this amount of power is the entire power of many currently available titanium:sapphire lasers; in addition, significant power loss is associated with the spatial light modulator and other elements in the beam path. Yang et al. generated structures using two-dimensional projections in a layer-by-layer fashion; this approach involved 560 mW of power and multiple seconds of exposure [76]. In contrast, solid-state three-dimensional 2PP was utilized to produce a tetrahedron using only static hardware to scan a single focus in all three dimensions [77]. Making a three-dimensional structure using only solid-state hardware means that it is theoretically possible to project an entire structure instead of a single layer (as with a two-dimensional projection). This technology is limited by both laser power and current hologram generation capabilities; however, useful applications of this currently incomplete technology have been described. For example, Gittard et al. utilized multiple static foci, which were scanned separately by a galvanoscanner, to produce multiple structures in parallel. Additionally, four ring-shaped unit cells (**Figure 2.8**) of a tissue engineering scaffold were produced simultaneously from polyethylene glycol diacrylate; this structure was geometrically identical to one fabricated using a single-beam approach. In addition, an array of thirty-six rocket-shaped microneedles was produced from an Ormocer[®] material using a multibeam approach [78].

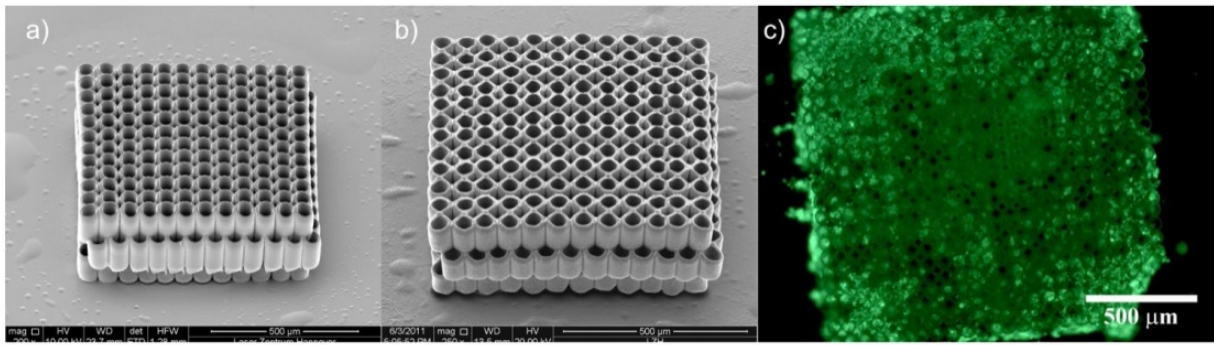


Figure 2.8 - Tissue engineering scaffolds made by 2PP with single focus structuring (a) and four foci structuring (b). Image of bovine endothelial cells growing on scaffold made by multi-beam 2PP (c). Reprinted from Ref. [78].

Conclusions

Several innovations involving the use of 2PP for biological applications have been described in recent years. Many recent studies have drawn from techniques and materials that were originally utilized in more well-established lithographic techniques. Although many bulk polymers that are commonly utilized in lithographic techniques are not toxic, the unreacted monomers, oligomers, and photoinitiators can present biocompatibility issues; extensive post-2PP washing is commonly used when processing photopolymers that were not designed for biomedical applications. The precise geometrical requirements for medical devices and the often toxic chemistries used in photopolymerization are unique challenges for 2PP. Biocompatible photopolymers have been synthesized from biological polymers such as chitosan and gelatin; these materials have been polymerized using novel photoinitiator designs that were formulated for a large TPA cross-section and for water solubility. Advances in the mechanical/optical side have primarily focused on increasing the fabrication speed to address the commercial and clinical requirements for higher throughput.

Despite the unique opportunities that it offers for biological applications, 2PP technology has yet to sufficiently distinguish itself from incumbent technologies. Since it utilizes materials

and technologies that were originally developed for other fields, an interdisciplinary approach is required to utilize 2PP technology for biological applications. Since tissues require specific physical, chemical, and geometrical conditions to perform their intended functions, biologists must collaborate with polymer chemists to design polymers that exhibit appropriate biological properties. The development of photoinitiators with higher TPA efficiency is also needed.

Optimizing the laser beam path for throughput rather than for high resolution processing requires an intimate knowledge of optics for modulating the laser at great angular deviations, in which the paraxial approximation cannot be used to achieve a large build volume. SLMs promise to be a key component in 2PP technology but must overcome several limitations, such as the low pixel fill factor that introduces unintended spatial frequencies into the beam. In addition, software and algorithms to run the SLM need to be improved to obtain real-time hologram generation.

Calculating the phase and amplitude deviations within a beam to project the desired three-dimensional image of an arbitrary structure is far removed from engineering the cellular environment or other biological applications. The individual components of a biologically-relevant 2PP system have been published; however, to this point, a single system that is capable of processing biocompatible materials on the centimeter-scale with sub-micrometer resolution has yet to be demonstrated.



Two-photon polymerization for biological applications

Alexander K. Nguyen and Roger J. Narayan*

UNC/NCSU Joint Department of Biomedical Engineering, North Carolina State University, Raleigh, NC 27695-7115, USA

Two-photon polymerization (2PP) leverages the two-photon absorption (TPA) of near-infrared (NIR) radiation for additive manufacturing with sub-diffraction limit resolution within the bulk of a photosensitive material. This technology draws heavily on photosensitive polymers from the microelectronics industry, which were not optimized for TPA or for biocompatibility. 2PP with sub 100 nm resolution has been repeatedly demonstrated; however, this level of fabrication resolution comes at the expense of long fabrication times. Manufacturing of medical devices beyond surface texturing would be prohibitively slow using the current state of the art 2PP technology. Current research into TPA-sensitive photopolymers with good biocompatibility and holographic projections using spatial light modulators address current technological limitations by providing materials specifically formulated for biological applications and by making better use of available laser power for applications in which nanoscale resolution is not required.

Introduction

Additive manufacturing (AM) techniques are freed from many of the practical concerns associated with incumbent fabrication techniques such as computerized numerical control (CNC) milling; however, additive manufacturing techniques commonly face limitations associated with the tool path. For example, in ultraviolet light-based stereolithography (SLA), light as the “tool” is “bound” by its interaction with the photopolymer surface. For this reason, AM techniques are often described as “layer-by-layer” techniques. Two-photon polymerization (2PP) breaks free from this paradigm due to the absence of this tool path limitation. 2PP utilizes the two-photon absorption of near infrared (NIR) light to excite the same energy transition as ultraviolet (UV) photons. Since the 2PP photopolymer is transparent to this fundamental wavelength, the 2PP “tool” is essentially an unsupported floating point that is able to process material within the photopolymer. This process is not diffraction limited, allowing for sub-wavelength fabrication; structures with dimensions below 100 nm have been fabricated out of a chemically modified zirconium-based sol-gel composite material using

this approach [1]. Just as stereolithography evolved from a laser-scanning approach to a two-dimensional digital-light projection approach, laser-scanning 2PP has the ability to evolve into a three-dimensional holographic projection approach.

The unique capabilities associated with 2PP stem from the capability for sub-micrometer resolution materials processing and from the unsupported voxel; intricate features can be made in regions of structures that are impossible to access using other fabrication techniques. One set of interesting applications of 2PP is fabrication within a microfluidic channel. 2PP-based structuring is performed within a photopolymer-filled channel, followed by exposure to the developing solution. For example, Wu et al. not only generated Fresnel lenses within a microfluidic channel but also fabricated a porous filter, which would have been difficult to conventionally fabricate and place within the channel. The lenses in combination with the filter were used as a white-light cell counter [2]. 2PP was also used to generate porous microchannels for the study of chemotaxis in dendritic cells. The 500 nm pores in the channels generated within the microfluidic channel were too small for the cells to grow into but large enough for transport of the desired chemokine [3]. A 2PP-fabricated hypodermic microneedle was integrated with a microfluidic device; this device was able to

*Corresponding author. Narayan, R.J. (roger_narayan@unc.edu)

uptake solutions containing physiologically-relevant K^+ solutions for detection with an ion-selective electrode [4]. Producing structures on the cellular size scale opens up many opportunities to determine the cellular response to substrate geometry; for example, neuronal cells have been shown to extend neurites along channels with features on the micrometer scale [5]. In another study, a biomimetic scaffold was produced from Ormocomp[®], an organically modified ceramic, using computed tomography images of human trabecular bone; good adhesion of SaOS-2 osteoblast-like cells to the scaffold surfaces was demonstrated [6].

At this time, 2PP is not commonly used for biological applications due to the toxicity of many feedstock materials and the difficulty of producing mesoscale structures that are relevant for biological applications. Since most 2PP polymers have been adopted from established SLA technologies, they were not formulated for either 2PP or biological applications. In addition, the nano-scale precision offered by 2PP is a source of weakness; structures with small-scale features require relatively long fabrication speeds. Strategies such as soft lithography replication of a 2PP-fabricated master structure have been demonstrated [7,8]; however, these strategies are stop gap measures and do not overcome existing weaknesses. Novel photopolymers exhibiting increased 2PP sensitivity and optics that are able to process larger volumes must be developed to enable large-scale commercial translation. In this paper, the excitation mechanisms associated with 2PP, innovations in photosensitive materials for 2PP, and innovations in optical setups for 2PP will be considered.

Excitation mechanisms

Despite having “two-photon” in its name, 2PP proceeds by multiple mechanisms, only one of which involves two-photon absorption. In the traditional one-photon case, the photoinitiator is excited to a higher singlet state and decays through an intersystem crossing to the triplet state. Due to this forbidden transition, the triplet state has a much longer lifetime; the long half-life of the triplet species allows for emission even seconds after excitation. These triplet species can form free radicals, which initiate polymerization; as such, photoinitiator designs having long triplet lifetimes are beneficial to UV lithography and 2PP by extension. Unlike UV lithography, 2PP involves extremely intense laser radiation on the order of terawatts per cm^2 , which is associated with the possibility of multiphoton ionization and subsequent dielectric breakdown.

Dielectric breakdown, also known as avalanche ionization, occurs in regions of highly intense electric fields and causes a normally insulating species to become locally conductive. Electrons in the conduction band of a material can be accelerated by the electric field and transfer energy to other electrons in the valence band, promoting those electrons to the conduction band. These child electrons can also be accelerated, generating conduction band electrons within the laser focus in an exponential manner. Order of magnitude estimations of multiphoton and avalanche ionization that were calculated for SZ2080 zirconium Ormosil[®], a photoresist used both for photonics and biological applications, revealed that the contribution from avalanche ionization is much greater than from two-photon absorption near the 2PP threshold [9]. Since dielectric breakdown would also take place within the monomer, it is possible to perform 2PP without photoinitiators. Eliminating photoinitiators would be very attractive

from a biocompatibility viewpoint; however, the working range of the 2PP process would be severely narrowed.

The working range is informally limited by (a) the 2PP threshold, the average laser power found in practice to initiate polymerization, and (b) the burning threshold, the power at which the material breaks down and generates bubbles that destroy the sample. Dielectric breakdown requires a conductive electron to be accelerated; such electrons are exceedingly rare in insulators and the vast majority of polymers. A photoinitiator with a quasi-stable excited state has multiple seeds for dielectric breakdown. Malinauskas et al. reported 2PP structuring without a photoinitiator in Ormosil[®]; the 2PP threshold was cut in one-third and the working range was tripled with addition of 1% by weight Irgacure[®] 369 or Michler's ketone [9].

Simple heating of a photopolymer can cause polymerization, which can result in unwanted voxel spread. For example, SU-8, a polymer from the microelectronics industry that is commonly used in biological studies, will thermally polymerize when exposed to temperatures above 167 °C [10]. It was calculated that a 0.5 nJ pulse, which approximates the energy from a 50 mW Ti:Sapphire laser operating at 80 MHz, would generate an equilibrium temperature of 227 °C within the focal volume (assuming insufficient time for heat diffusion) [11]. Considering a typical 80 MHz repetition rate and a 1 μm voxel size, the laser focus would have to scan at above 80 m/s to have no voxel overlap. Since 2PP experiments commonly typically take place with scan speeds in the range of millimeters per second, heat-initiated polymerization is a major contributor to the final dimensions of a 2PP-fabricated structure. Baldacchini et al. used a pulse width modulated (PWM) acousto-optical modulator to chop the 80 MHz laser into bursts with variable repetition rates. Decreasing the repetition rate (at a constant average laser power and burst width) increased the resolution of the 2PP-fabricated structures [12]. Although an identical average power is experienced by the sample, allowing the local regions to cool by spacing out the pulses reduces the effect of thermal polymerization.

Drawing multiple lines simultaneously is one method to increase the fabrication speed; this approach is possible with laser technologies but it is associated with voxel spread via diffusion of the polymerization propagating species. Cross-talk between fine features (e.g., diffraction gratings or wave guides) occurs when the scanning process is rapid. Much of this phenomenon can be explained by heat buildup within the substrate; however, a linewidth increase of up to 25% was noted in experiments in which thermal effects were considered negligible. The effects of spatial and temporal proximity were investigated by scanning two foci separated by an x and y distance; when scanning parallel to the y -axis, the x separation constituted spatial separation between the two lines and the y -separation formed the temporal delay. The focus trailing behind the other contained a higher concentration of initiating species, which diffused from the leading pulse and caused broadening. This effect was significant out to 100 ms temporally and 3000 nm spatially [13]. Current fabrication strategies such as raster scanning often involve marking parallel lines spatially and temporally shorter than these values; as such, this “proximity effect” must be considered when tight tolerances are required.

Since two-photon absorption (TPA) is the mechanism that seeds polymerization, maximizing the TPA coefficient is an important

factor in 2PP photopolymer design. In single photon absorption, the intensity of the transmitted light is dependent on the linear absorption coefficient (α), concentration, and path length as per the Beer-Lambert law. The non-linear absorption coefficient (β) becomes a non-negligible factor at high intensities; it can be negative for saturation of absorbance or positive for multi-photon absorbance. This phenomenon is measured using the Z-scan technique, in which a sample is translated along the axis of a converging laser while the transmitted light intensity is measured. In the typical Z-scan apparatus, the non-linear absorption coefficient is measured in an open aperture configuration in which all of the transmitted light is collected; any change in transmittance while scanning through the focus would be due to non-linear (e.g., two-photon absorption) effects. The theoretical calculations behind this technique incorporate three main assumptions to simplify the calculations: (1) only the third-order non-linearity (two-photon processes) are considered, (2) the sample thickness is shorter than the Rayleigh range of the focus, and (3) the laser is a TEM₀₀ Gaussian beam. If one approximates the sample to be a "thin" sample, then the laser focal region dimensions do not vary significantly within the sample while being translated within the beam. This approach enables use of the slowly varying envelope approximation; higher order differentials in the equation representing electric field can be ignored. Using a Gaussian beam simplifies the calculations since the Fourier transform of a Gaussian distribution is also Gaussian. At the endpoint of the calculations, the change in normalized transmission through the sample can be represented by the Taylor series:

$$T(z) = \sum_{m=0}^{\infty} \frac{[-q_0(z,0)]^m}{(m+1)^{3/2}}$$

where $q_0(z,0)$ is:

$$q_0(z,0) = \frac{\beta I_0 L_{\text{eff}}}{(1 + (z^2/z_R^2))}$$

In this equation, z_R is the Rayleigh range, L_{eff} is the effective path length represented by $L_{\text{eff}} = ((1 - e^{-\alpha L})/\alpha)$, and I_0 is the peak irradiance at the focus of the sample [14]. Since photopolymers used with 2PP should be transparent to the laser radiation, α will be very small, which makes $L_{\text{eff}} \approx L$. For a perfectly Gaussian beam, I_0 can be given by [15]:

$$I_0 = \frac{4P_{\text{avg}}}{\pi \omega_0^2 R \tau} \sqrt{\frac{\ln(2)}{\pi}} = \frac{4P_{\text{avg}}}{M^2 \lambda z_R R \tau} \sqrt{\frac{\ln(2)}{\pi}}$$

where R is the repetition rate, τ is the pulse duration, ω_0 is the beam waist, and M^2 is the beam quality. All parameters in I_0 are either defined by the experimenter (i.e., average power P_{avg} and Rayleigh length z_R) or the characteristics of the laser. L_{eff} is an experimental parameter, leaving the value for β unknown. β , the non-linear absorption coefficient, can be numerically fit to the Taylor series. Further approximating the value by only considering the $m = 1$ term in the series, using L in place of L_{eff} , and subtracting the $m = 0$ term (which is simply 1 in any case), a greatly simplified equation in terms of the change in the normalized transmittance can be obtained:

$$T(z) - 1 = \Delta T(z) = \frac{-\beta I_0 L}{2\sqrt{2}(1 + (z^2/z_R^2))}$$

Although the highest change in transmittance will always be found at $z = 0$, noise in the data can make it difficult to find the exact values for $\Delta T(0)$ and z_R . That said, a good starting point to

qualitatively compare different photoinitiator formulations would be to measure the relative change in transmittance at $z = 0$ while accounting for potential differences in the sample path lengths. Finding photoinitiator formulations with high TPA cross-sections generates a list of moieties that are highly efficient absorbers.

Photopolymer design strategies

Designing an efficient 2PP photoinitiator differs from designing an efficient ultraviolet photoinitiator since the TPA cross-section is not considered during development of an ultraviolet photoinitiator; however, designing an efficient 2PP photoinitiator and designing an efficient ultraviolet photoinitiator share many strategies. In general, high TPA cross-section photoinitiators commonly consist of an extended π -system chromophore that is flanked by multiple electron donating or withdrawing groups [16,17]. For example, Ethyl Michler's ketone is composed of a benzophenone with a diethyl amino group at each of the para-positions. Another consideration is the efficiency of the radical species that initiate polymerization. Furthermore, there must be a bridge between these two criteria in which the excited state can form the radical species [16].

The mechanism by which the free-radical species is formed splits photoinitiators into two classes. Type 1 photoinitiators are cleaved from the triplet state, forming two free radicals that can initiate chain polymerization. In contrast, the triplet excited state of type 2 photoinitiator chromophores must react with a co-initiator, which subsequently forms the radical species. Type 1 photoinitiators are more common since photocleavage is a mono-molecular reaction; type 2 photoinitiators utilize bi-molecular reactions and are less efficient. It should be noted that type 2 photoinitiator formulations in which the chromophore is covalently bonded with the co-initiator allow for formation of a free radical species in a mono-molecular reaction without cleavage [18].

Considering the TPA cross-section, the mechanism of radical formation, and the initiation efficiency leaves few 2PP feedstock materials with appropriate features for biological applications. Photoinitiators are generally toxic materials since reactive oxygen species are harmful to cellular function. As such, type 1 photoinitiators designed to easily cleave are not the most biocompatible class of materials. For this reason, recent research efforts have been geared toward the development of biocompatible type 2 photoinitiators. For example, high TPA cross-section chromophores (shown in Fig. 1) were produced from two different π -extended ketocoumarins and modified with different dialkylamino- groups; these materials were shown to exhibit 100% cell viability and similar proliferation rates to the glass control [19]. The combination of riboflavin and triethanolamine has been used as a UV photoinitiator [20] and has been successfully used for 2PP [21]. No statistically significant difference in cell viability was noted between riboflavin- triethanolamine wafers and glass. Growth of bovine aortic endothelial cells on a polyethylene glycol-riboflavin-triethanolamine scaffold processed using 2PP was demonstrated (Fig. 2); a LIVE/DEAD™ stain of a five day culture of GM7373 endothelial cells demonstrated a significant number of live cells and few dead cells. It should be noted that riboflavin-triethanolamine was less efficient than conventional photoinitiators (e.g., Irgacure® 369 and Irgacure® 2959) in terms of the laser fluence

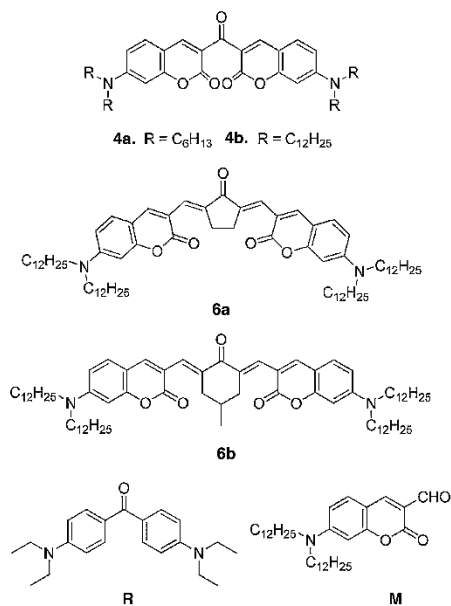


FIGURE 1

Structures of new 2PA photoinitiators and reference compounds. Reprinted (adapted) with permission from Nazir, R., Danilevicius, P., Ciuciu, A. I., Chatzinikolaïdou, M., Gray, D., Flamigni, L., Farsari, M., Gryko, D. T. (2014). π -expanded ketocoumarins as efficient, biocompatible initiators for two-photon-induced polymerization. *Chemistry of Materials*, 26(10), 3175–3184. doi:10.1021/cm500612w, Copyright 2014 American Chemical Society.

required for 2PP. The higher laser fluence required for this photoinitiator formulation is affected by the TPA cross section and radical generation from the excited state. While each parameter is important individually, all of the factors can be summed up by the processing window. Qualitatively speaking, the processing window is related to the scanning speed and the laser power,

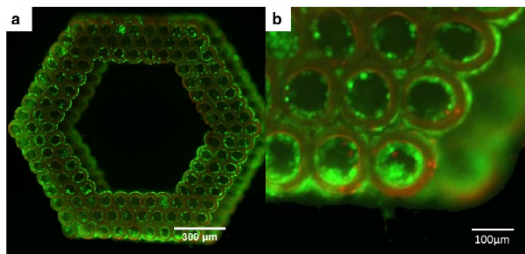


FIGURE 2

(a) Merged live/dead staining after five days of culture for a 50% polyethylene glycol diacrylate-riboflavin-triethanolamine scaffold seeded with endothelial cells. (b) polyethylene glycol diacrylate exhibits red autofluorescence; ethidium homodimer-1 (dead cell) fluorescence is distinct from the polyethylene glycol diacrylate fluorescence. Republished with permission of Future Medicine Ltd, from "Two-photon polymerization of polyethylene glycol diacrylate scaffolds with riboflavin and triethanolamine used as a water-soluble photoinitiator." Nguyen, A. K., et al. Vol. 8 (6), 2011; permission conveyed through Copyright Clearance Center, Inc.

the product of which gives the laser dosage exposed to a volume. A more effective photoinitiator would have a wide range of speed and a power at which good structuring is observed. The gold standard to evaluate the processing window is a parametric study that evaluates each speed-power combination. An example parameter search array is given in Fig. 3, in which both parameters are serially tested [22]. In areas with high power and low speed, poor structuring is observed since the polymer burns from the high irradiation. Areas with high speed and low power are underexposed, which results in weak or missing structures. A wide processing window between these two zones indicates an easy-to-use photopolymer.

Water insoluble photoinitiators make up the majority of available products on the market; however, their insolubility does not rule out their use in hydrogels. Pawar et al. used 2,4,6-trimethylbenzoyl-diphenylphosphine oxide (TPO) as a model water insoluble photoinitiator to process aqueous acrylamide in an SLA setup. The TPO was prepared as an oil-in-water microemulsion and then spray dried to produce a dry nanoparticle powder; dispersing this powder into water yielded a clear solution [23]. TPO and ethyl Michler's ketone are well established photoinitiators that are also unfortunately water insoluble, preventing their traditional use in hydrogels. Preparing these photoinitiators in nanoparticle form would be one method for photosensitizing hydrogel monomers. Although these materials are not highly biocompatible, post processing steps and the insolubility of these materials would reduce the amount of material that enters the biological environment during use.

Appropriate photopolymers for biological applications would ideally have a high degree of conversion to minimize the amount of residual monomer and fast polymerization kinetics to reduce the required laser dwell time necessary to achieve full polymerization. Being able to tune the mechanical properties and degradation characteristics would be an ideal characteristic for several tissue engineering applications. Biological uses of photopolymers are already commonplace albeit not with photopolymers that are processed using additive manufacturing approaches. Dental applications draw heavily on methacrylates that are commonly initiated by Type II photoinitiators due to their compatibility with visible light; however, Type I photoinitiators may also be used. Further examination of dental photopolymer systems may suggest appropriate methacrylate formulations for use with 2PP.

The Degree of Conversion (DC) determines the final mechanical properties and the biocompatibility of the structure (e.g., the biocompatibility of the structure may be reduced by leaching of unreacted monomer). Changes in Fourier transform infrared spectra (e.g., changes in the vinyl peak) are commonly used to determine the DC value. For example, the DC value for a 55:45 molar ratio of 2,2-bis[4-(2-hydroxy-3-methacryloxypropoxy)phenyl]propane (BisGMA) and 2-hydroxyethylmethacrylate (HEMA) mixture was monitored with an Attenuated Total Reflectance FTIR (AT-FTIR). The ratio of the 1637 cm⁻¹ peak (associated with aliphatic C=C) to the 1608 cm⁻¹ peak (associated with aromatic C=C) was evaluated. Measurements obtained at multiple times during polymerization were compared to the initial ratio of the monomer solution; these measurements were used to calculate the DC values for the system [24]. This approach was also used to examine a 7:3 mass ratio of BisGMA and triethyleneglycoldimethacrylate

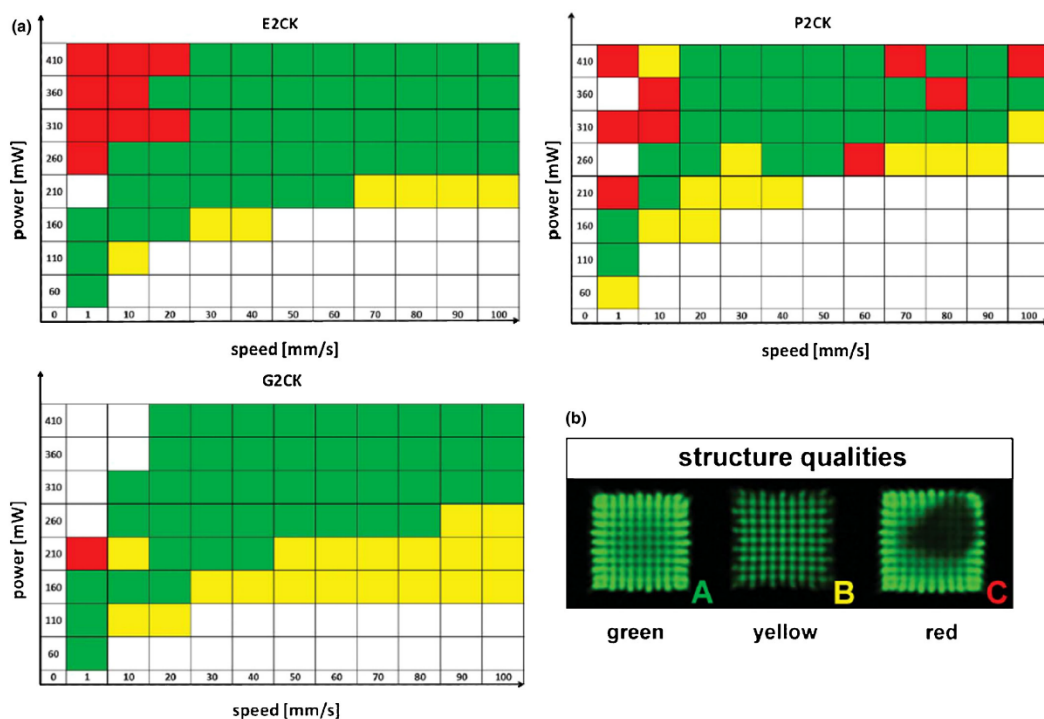


FIGURE 3

(a) Processing windows of investigated initiators in TPIP screening tests; (b) Classifications of the structures by the typical quality of their shapes. Republished with permission of Royal Society of Chemistry, from "Initiation efficiency and cytotoxicity of novel water-soluble two-photon photoinitiators for direct 3D microfabrication of hydrogels." Li, Z. Q., et al. Vol. 3 (36), 2013; permission conveyed through Copyright Clearance Center, Inc.

(TEGDMA) [25]. Both studies evaluated the effect of several photoinitiators and illumination conditions on camphorquinone (CQ)-based photoinitiators. DC values for these systems, which exhibit 20–70% conversion, are heavily influenced by the choice of photoinitiator. Additional photoinitiator systems based on 9,10-phenanthrenequinone (PQ), TPO, and phenylbis(2,4,6-trimethylbenzoyl)phosphine oxide (BAPO) were investigated for a 55:45 BisGMA:HEMA monomer mixture under wet and dry conditions [26]. A study that investigated the reaction kinetics for several ratios of BisGMA and TEGDMA with a CQ-based Type II photoinitiator or a monoacylphosphine (MAPO) Type I photoinitiator showed changes in the DC value from variations in the monomer ratio and the photoinitiator type. The use of MAPO resulted in a higher final DC value, with polymerization requiring one-fourth to one-sixth the amount of time to reach 95% of the final DC value. High performance liquid chromatography analysis of monomer eluted after one week in a 75% ethanol solution revealed a steep slope between the total monomer eluted and the DC value (e.g., 12% by weight eluted at 40% DC versus 3% eluted at 50% DC) [27]. Both photoinitiators used in this study are not biocompatible; however, the marked difference between the DC values (and the amount of elutable monomer by extension) raises questions about the trade-off between photoinitiator toxicity and

DC value. Since a high DC value is associated with less residual monomer and less toxicity, the effect of laser-material interaction on DC should also be considered. Cica et al. demonstrated 2PP of a 1:1 mixture by weight of trimethylolpropane triacrylate and ethoxylated(20) trimethylolpropane triacrylate, which was photoinitiated by either 2,7-bis[(4-dibutylamino)phenyl]ethynyl]-9H-fluoren-9-one (B3FL) or E,E-1,4-bis[4'-(N,N-di-n-butylamino)styryl]-2,5-dimethoxybenzene (R1) at a 6.3 $\mu\text{mol/g}$ concentration; several scan speeds and average laser powers were evaluated in this study. The DC values of the $50 \mu\text{m} \times 50 \mu\text{m} \times 30 \mu\text{m}$ structures were calculated using data from the 810 cm^{-1} peak, which was attributed to carbon double bonds; the carbon double bond data was normalized using data from the 1730 cm^{-1} carbonyl peak (Fig. 4). Scan speed was found to have an effect on the DC value near the 2PP threshold, the lowest laser power at which polymerization is observed. The correlation between scan speed and DC value was not significant at high power values; changing the scan speed from 100 to 800 $\mu\text{m/s}$ at the threshold reduced the DC value from 61% to 56%. A DC value of 74% was obtained for structures within this scan speed range when using power values above 1.75 \times the threshold were utilized [28].

Hydrogels are commonly polymerized with 2PP since this class of materials is commonly used in studies involving soft tissue

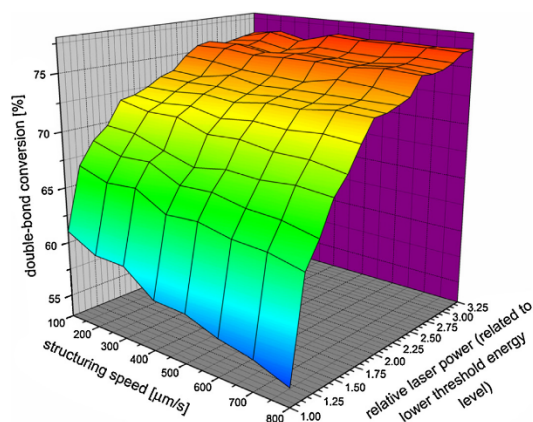


FIGURE 4

Double-bond conversion of formulation A. Reprinted from Cicha, K., et al. (2011). "Evaluation of 3D structures fabricated with two-photon-photopolymerization by using FTIR spectroscopy." *Journal of Applied Physics* **110** (6), with the permission of AIP Publishing.

regeneration. In addition, several types of biological polymers, including carbohydrate- and protein- based materials, can be modified with photopolymerizable groups to make them feed-stock materials for the 2PP process. It is also common to incorporate growth factors or other compounds within the polymer chain that alter its mechanical properties. The general procedure for modifying the backbones of synthetic and biological polymers with pre-polymer groups is similar.

The addition of methacrylate groups can be undertaken with glycidyl methacrylate, which can react with carboxyl, hydroxyl, and amine groups to form a corresponding carbonyl linkage that terminates in a methacrylate group [29,30]. Methacrylation of hyaluronic acid using this approach is straightforward due to its water solubility. Chitosan must be modified with succinic anhydride to become soluble in water; reaction with an amine group on the chitosan backbone forms an amide linkage that terminates in a carboxylate group. Incubation of either hyaluronic acid or N-succinylated chitosan with glycidyl methacrylate over ten days yielded a photopolymerizable hydrogel. Purification was performed by precipitation in acetone, dialysis in pure water, and lyophilization. The mechanical properties of the methacrylated polymer can be modified by the addition of polyethylene glycol diacrylate. Lactate dehydrogenase and cell proliferation assays indicated that both the base methacrylated polymer and the copolymer containing polyethylene glycol diacrylate possess biocompatibility similar to that of the tissue culture polystyrene control [29,30].

A process utilizing the more reactive methacrylic anhydride was described for methacrylation of gelatin; the degree of substitution can be controlled by varying the concentration of the methacrylic anhydride in the solution. The procedure is relatively simple, involving the addition of methacrylic anhydride to a 50 °C gelatin solution in phosphate buffered saline over a period of one hour. Dialysis over twenty-four hours and lyophilization completed the purification of the material [31]. 2PP was used to process material

into a woodpile-style scaffold; human adipose-derived stem cells were able to proliferate through the structure and differentiate into adipocytes [32]. The reactive methacrylating agent has also been used to modify a biodegradable polylactic acid base polymer with organic solvents [21]. The photopolymer that was obtained using this approach was seeded with a human SH-SY5Y human neuronal cell line and with primary rat Schwann cells [33].

All of the photopolymers mentioned thus far have been negative photoresists; it should be noted that positive photoresists, for which illumination causes polymer cleaving, are also compatible with multiphoton absorption technology. For example, Kloxin et al. produced a photocleavable PEG-based polymer using 4-[4-(1-hydroxyethyl)-2-methoxy-5-nitrophenoxy]butanoic acid as the photolabile group. The addition of an acrylate group produced the photodegradable acrylate. Ammonium persulfate and tetramethylenediamine were used for radical-mediated polymerization of the bulk polymer. Exposure to 365 nm light, or two-photon excitation by 740 nm light commonly produced by a Ti:sapphire femtosecond laser, caused hydrolysis of the ester group adjacent to the acrylate group. Kloxin et al. also provided a procedure for cell encapsulation within the crosslinked polymer [34]. One important advantage of using a positive photoresist with encapsulated cells is that UV phototoxicity is not an issue; the cell-laden polymer exposed to in-focus NIR light is washed away during development; the out-of-focus NIR light should have little effect on cells compared to the UV light that is used in traditional lithography.

While not a traditional polymerization reaction, certain proteins can be crosslinked without modification through a complex reaction that involves singlet oxygen generation from a chromophore. Crosslinking of collagen using UV light is well known and is commonly utilized by ophthalmologists for the treatment of keratoconus [35]. A 40% increase in the stiffness of collagen-rich tissue cultured in vitro from murine embryonic fibroblasts and neonatal rat cardiomyocytes was demonstrated using this approach [36]. Singlet oxygen can also be generated using TPA from aromatic amino acids within the proteins themselves; this mechanism enables crosslinking of protein solutions without the inclusion of additional photosensitizers [37]. The addition of a chromophore such as methylene blue, rose bengal, or flavin adenine dinucleotide can improve the crosslinking performance [38]. Robust 3D structures such as small cantilevers or chambers may be processed using this approach. By precisely measuring the mechanical properties of crosslinked avidin structures using atomic force microscopy, Khripin et al. was able to measure the pressure of proliferating *E. coli* within a chamber; this approach can be potentially used to predict pressures within cancerous tumors [39].

Tissue engineering of orthopedic implants requires relatively stiff materials, which facilitate the differentiation pathway of undifferentiated cells into the osteocyte lineage. Organically-modified ceramic (Ormocer®) materials are popular materials for orthopedic applications. For example, the zirconium-silicon based hybrid sol-gel photopolymer (ORMOSIL SZ2080) has been used for orthopedic applications due to its biocompatibility; 1% w/w ethyl Michler's ketone is a popular photoinitiator for use with this polymer. Extensive washing is commonly used to remove the unreacted monomer and the photoinitiator. Human adipose- and bone marrow-derived stem cells have been grown on this material in three-dimensional scaffold [40] (Fig. 5) and two-dimensional textured surface [41]

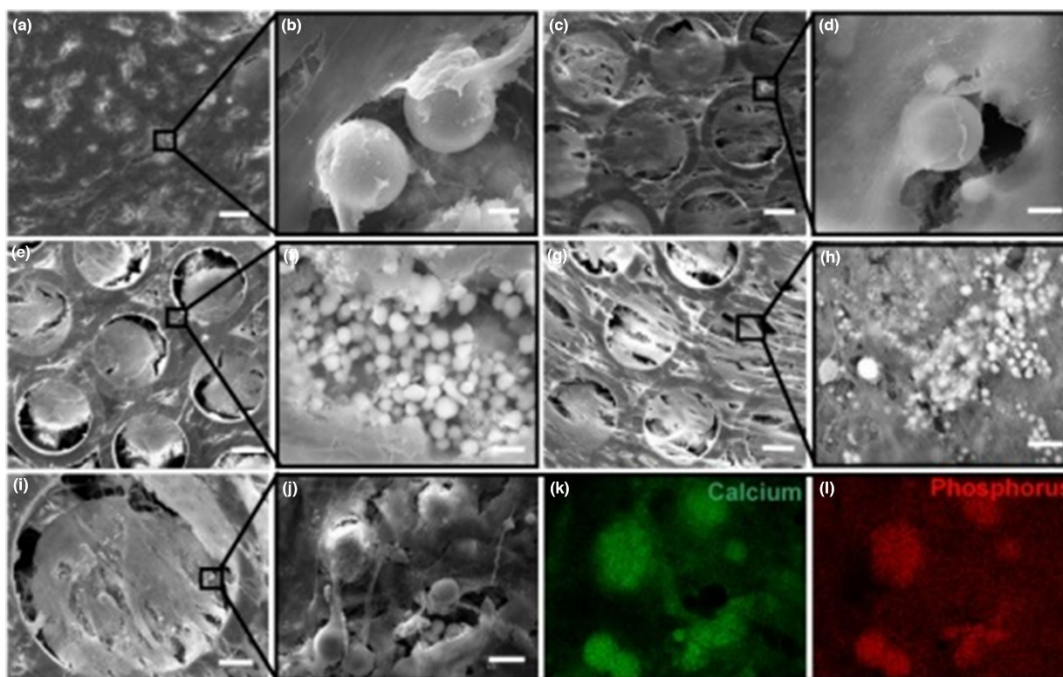


FIGURE 5

Cells on scaffolds after 21 days in osteogenic and control cultures: (a and c) human adipose derived stem cells and human bone marrow stromal cells from osteogenic culture; (e and g) human adipose derived stem cells and human bone marrow stromal cells from control culture. High magnification images showing calcium phosphate deposits of human adipose derived stem cell and human bone marrow stromal cell cultures on Zr-Si scaffolds in osteogenic (b and d) and control (f and h) conditions; (i–l) Energy-dispersive X-ray spectroscopy mapping confirming the presence of calcium and phosphorus in the accumulations. Scale bars: (a, c, e, g) 60 μm , (b, d, f, h) 5 μm , (i) 50 μm and (j–l) 10 μm . Reprinted from Ref. [40] licensed under Attribution 2.0 Generic (CC BY 2.0).

formats to examine the effect of scaffold geometry on osteogenic differentiation.

2PP is a unique tool to perform additive manufacturing for biological applications since structures of arbitrary geometry on the size scale of the cell or of sub-cellular structures can be reliably reproduced. Due to the fabrication speed limitations of 2PP, the most promising current applications of 2PP have been for in vitro assays that examine cellular behavior rather than for implantable tissue engineering scaffolds.

Optics considerations

The 2PP apparatus is used to (a) tightly focus the laser into the sample while allowing for cleaning or shaping of the beam and (b) translate the focal point within the sample. Titanium:sapphire lasers are the most commonly used for 2PP experiments; however, other types of femtosecond lasers (e.g. frequency doubled Nd:glass lasers) or even some picosecond lasers may be used for 2PP. The most simple 2PP setup consists of a laser source, a focusing objective, a translational stage, a laser power control system, and a shutter; most of these components are also found on microscopes. As such, building a 2PP system on an existing two-photon fluorescence microscope is commonly undertaken. Additions to the setup can improve the resolution and fabrication speed. Using the

scanning mirrors as the primary method for moving the laser focus results in orders of magnitude faster fabrication versus using the translational stages (although this approach is limited to the field of view of the objective). Controlling the group velocity dispersion using optics such as prism compressors or chirped mirrors can reduce the pulse duration; with a shorter pulse duration, 2PP threshold intensities can be achieved with lower average laser power values. An example 2PP beam path is given in Fig. 6, which contains all of the aforementioned components.

Use of a spatial light modulator (SLM) is similar to use of projection SLA in that the beam is shaped to present more than a one-dimensional point for fabrication [42]. Unlike ultraviolet lithography, in which the projection of any two-dimensional image will suffice, manipulating a three-dimensional focal volume is more challenging from hardware and computational standpoints. While a two-dimensional mask suffices for ultraviolet illumination, amplitude and phase modulation within the beam must be manipulated to form the desired voxel shape for projection of a three-dimensional image. This parameter is achieved by inserting a mask within the 4f system Fourier plane, the plane in between the two lenses. The simplest case would be a pinhole spatial filter, in which low spatial frequencies that focus closer to the optical axis are allowed through. Computer-controlled SLMs

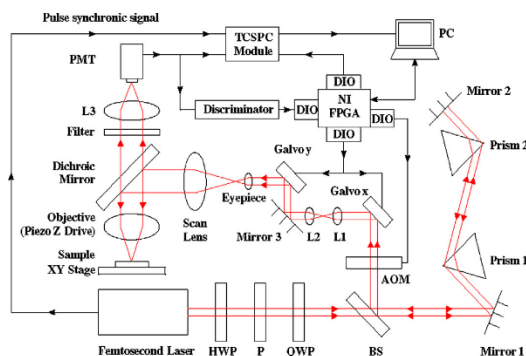


FIGURE 6

Optical setup of a femtosecond laser imaging and microfabrication system, which is capable of fluorescence lifetime imaging microscopy. Reprinted from Ref. [46].

placed at the first conjugate plane can introduce phase delays within certain regions of the beam. Currently available SLMs are essentially small liquid crystal displays and are usually controlled via a Digital Visual Interface (DVI) input; instead of controlling the color intensity, each pixel on this device changes the phase of the incident light. The current approach is to generate a holographic image, which generates the desired pattern after a Fourier transformation. Many algorithms are available, including ab initio ones; in general, the highest precision will be obtained using iterative algorithms. One example of the image generation capabilities of the SLM utilized the Gerchberg-Saxton (GS) iterative algorithm combined with the angular spectrum method to allow for faster calculation of images that deviated from the focal plane. One stated limitation of this approach is that the out-of-focus light from one component image was visible at the focus of another component image. For 2PP, this limitation is not consequential since the photopolymer is transparent to the unfocused light. As shown in Fig. 7, Hillario et al. projected different letters that were each independently mobile in all three axes [42].

Using a SLM for 2PP is currently limited by the need to provide sufficient laser power that initiates polymerization. When projecting a point source, a $1\ \mu\text{m}$ voxel requires only a couple milliwatts

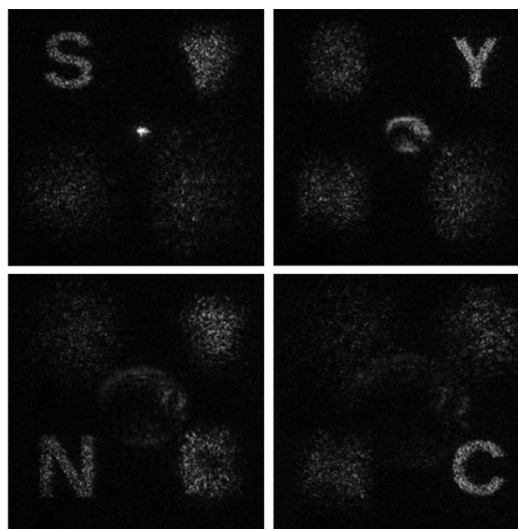


FIGURE 7

Experimental generation of arbitrary light fields using one proposed method. The size is approximately 4.8 mm. Reprinted from Ref. [42].

of power and nanoseconds of exposure. Illuminating a $10\ \mu\text{m}$ cubic region would require on the order of watts of power, which would be difficult to achieve considering that this amount of power is the entire power of many currently available titanium:sapphire lasers; in addition, significant power loss is associated with the spatial light modulator and other elements in the beam path. Yang et al. generated structures using two-dimensional projections in a layer-by-layer fashion; this approach involved 560 mW of power and multiple seconds of exposure [43]. In contrast, solid-state three-dimensional 2PP was utilized to produce a tetrahedron using only static hardware to scan a single focus in all three dimensions [44]. Making a three-dimensional structure using only solid-state hardware means that it is theoretically possible to project an entire structure instead of a single layer (as with a two-dimensional projection). This technology is limited

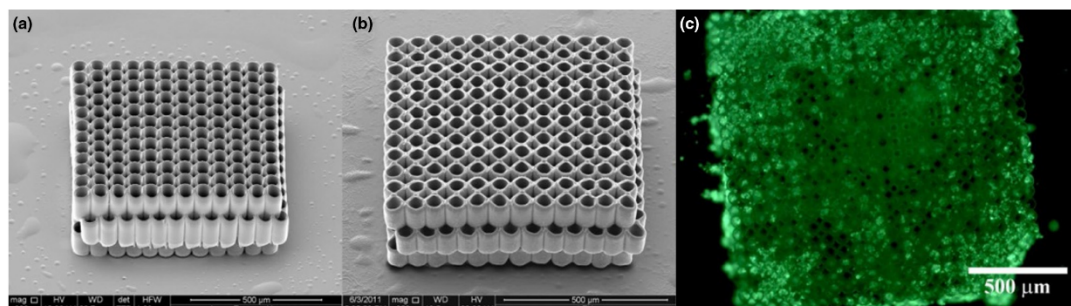


FIGURE 8

Tissue engineering scaffolds made by 2PP with single focus structuring (a) and four foci structuring (b). Image of bovine endothelial cells growing on scaffold made by multi-beam 2PP (c). Reprinted from Ref. [45].

by both laser power and current hologram generation capabilities; however, useful applications of this currently incomplete technology have been described. For example, Gittard et al. utilized multiple static foci, which were scanned separately by a galvanoscanner, to produce multiple structures in parallel. Additionally, four ring-shaped unit cells (Fig. 8) of a tissue engineering scaffold were produced simultaneously from polyethylene glycol diacrylate; this structure was geometrically identical to one fabricated using a single-beam approach. In addition, an array of thirty-six rocket-shaped microneedles was produced from an Ormocer® material using a multibeam approach [45].

Conclusions

Several innovations involving the use of 2PP for biological applications have been described in recent years. Many recent studies have drawn from techniques and materials that were originally utilized in more well-established lithographic techniques. Although many bulk polymers that are commonly utilized in lithographic techniques are not toxic, the unreacted monomers, oligomers, and photoinitiators can present biocompatibility issues; extensive post-2PP washing is commonly used when processing photopolymers that were not designed for biomedical applications. The precise geometrical requirements for medical devices and the often toxic chemistries used in photopolymerization are unique challenges for 2PP. Biocompatible photopolymers have been synthesized from biological polymers such as chitosan and gelatin; these materials have been polymerized using novel photoinitiator designs that were formulated for a large TPA cross-section and for water solubility. Advances in the mechanical/optical side have primarily focused on increasing the fabrication speed to address the commercial and clinical requirements for higher throughput.

Despite the unique opportunities that it offers for biological applications, 2PP technology has yet to sufficiently distinguish itself from incumbent technologies. Since it utilizes materials and technologies that were originally developed for other fields, an interdisciplinary approach is required to utilize 2PP technology for biological applications. Since tissues require specific physical, chemical, and geometrical conditions to perform their intended functions, biologists must collaborate with polymer chemists to design polymers that exhibit appropriate biological properties. The development of photoinitiators with higher TPA efficiency is also needed. Optimizing the laser beam path for throughput rather than for high resolution processing requires an intimate knowledge of optics for modulating the laser at great angular deviations, in which the paraxial approximation cannot be used to achieve a large build volume. SLMs promise to be a key component in 2PP technology but must overcome several limitations, such as the low pixel fill factor that introduces unintended spatial

frequencies into the beam. In addition, software and algorithms to run the SLM need to be improved to obtain real-time hologram generation. Calculating the phase and amplitude deviations within a beam to project the desired three-dimensional image of an arbitrary structure is far removed from engineering the cellular environment or other biological applications. The individual components of a biologically-relevant 2PP system have been published; however, to this point, a single system that is capable of processing biocompatible materials on the centimeter-scale with sub-micrometer resolution has yet to be demonstrated.

References

- [1] M. Emons, et al. *Opt. Mater. Express* 2 (7) (2012) 942.
- [2] D. Wu, et al. *Light Sci. Appl.* (2015) 4.
- [3] G.M. Hjortto, et al. *Biomed. Microdevices* 17 (2) (2015).
- [4] P.R. Miller, et al. *Adv. Healthc. Mater.* 3 (6) (2014) 876.
- [5] S. Turunen, et al. *Opt. Laser Eng.* 55 (2014) 197.
- [6] A. Marino, et al. *Acta Biomater.* 10 (10) (2014) 4304.
- [7] S.D. Gittard, et al. *J. Diabetes Sci. Technol.* 3 (2) (2009) 304.
- [8] A. Koroleva, et al. *Biofabrication* 4 (1) (2012).
- [9] M. Malinauskas, et al. *Opt. Express* 18 (10) (2010) 10209.
- [10] B.H. Ong, et al. *Opt. Lett.* 31 (10) (2006) 1367.
- [11] K.K. Seet, et al. *Appl. Phys. Lett.* 89 (2) (2006).
- [12] T. Baldacchini, et al. *Opt. Express* 20 (28) (2012) 29890.
- [13] E. Waller, G. von Freymann, *Polymers-Basel* 8 (8) (2016) 297.
- [14] M. Sheikbahae, et al. *IEEE J. Quant. Elect.* 26 (4) (1990) 760.
- [15] A. Ajami, et al. *J. Opt. Soc. Am. B* 27 (11) (2010) 2290.
- [16] B.H. Campston, et al. *Nature* 398 (6722) (1999) 51.
- [17] M. Pawlicki, et al. *Angew. Chem. Int. Ed.* 48 (18) (2009) 3244.
- [18] M. Aydin, et al. *Macromol. Rapid Commun.* 24 (12) (2003) 718.
- [19] R. Nazir, et al. *Chem. Mater.* 26 (10) (2014) 3175.
- [20] B. Orellana, et al. *Macromolecules* 32 (20) (1999) 6570.
- [21] A.K. Nguyen, et al. *Regen. Med.* 8 (6) (2013) 725.
- [22] Z.Q. Li, et al. *RSC Adv.* 3 (36) (2013) 15939.
- [23] A.A. Pawar, et al. *Sci. Adv.* 2 (4) (2016) e1501381.
- [24] L. Song, et al. *Dent. Mater.* 32 (1) (2016) 102.
- [25] A.B. Denis, et al. *J. Spectrosc.* 2016 (2016) 1.
- [26] V.E. Salgado, et al. *Int. J. Adhes Adhes.* 72 (2017) 6.
- [27] L.D. Randolph, et al. *Dent. Mater.* 32 (2) (2016) 136.
- [28] K. Cicha, et al. *J. Appl. Phys.* 110 (6) (2011).
- [29] O. Kufelt, et al. *Acta Biomater.* 18 (2015) 186.
- [30] O. Kufelt, et al. *Biomacromolecules* 15 (2) (2014) 650.
- [31] A.I. Van den Bulcke, et al. *Biomacromolecules* 1 (1) (2000) 31.
- [32] A. Ovsianikov, et al. *Materials* 4 (1) (2011) 288.
- [33] A. Koroleva, et al. *Biofabrication* 4 (2) (2012).
- [34] A.M. Kloxin, et al. *Nat. Protoc.* 5 (12) (2010) 1867.
- [35] L. Mastropasqua, *Eye Vis. (Lond.)* 2 (2015) 19.
- [36] K. Kuetermeyer, et al. *Opt. Express* 19 (17) (2011) 15996.
- [37] B. Kaehr, et al. *Anal. Chem.* 78 (9) (2006) 3198.
- [38] B. Kaehr, J.B. Shear, *Proc. Natl. Acad. Sci. U.S.A.* 105 (26) (2008) 8850.
- [39] C.Y. Khrpin, et al. *Soft Matter* 6 (12) (2010) 2842.
- [40] A. Koroleva, et al. *PLoS ONE* 10 (2) (2015).
- [41] S.A. Skoog, et al. *Biointerphases* 9 (2) (2014).
- [42] P.L. Hilario, et al. *Opt. Lett.* 39 (7) (2014) 2036.
- [43] L. Yang, et al. *Opt. Commun.* 331 (2014) 82.
- [44] A.D. Zalesskii, et al. *Russ. J. Phys. Chem. B* 6 (3) (2012) 357.
- [45] S.D. Gittard, et al. *Biomed. Opt. Express* 2 (11) (2011) 3167.
- [46] C.Y. Lin, et al. *Opt. Express* 20 (13) (2012) 13669.

CHAPTER 3 – Microneedle-Based Delivery of Amphotericin B for Treatment of Cutaneous Leishmaniasis

Alexander K. Nguyen¹, Kai-Hung Yang¹, Kelsey Bryant², Junan Li³, April C. Joyce², Karl A. Werbovetz², and Roger J. Narayan¹

1. UNC/NCSU Joint Department of Biomedical Engineering, North Carolina State University, Raleigh, NC
2. Division of Medicinal Chemistry and Pharmacognosy, College of Pharmacy, The Ohio State University, Columbus, OH
3. College of Pharmacy, The Ohio State University, Columbus, OH

Reference: Nguyen, A.K.; Yang, K.H.; Bryant, K.; Li, J.; Joice, A.C.; Werbovetz, K.A.; Narayan, R.J. Microneedle-Based Delivery of Amphotericin B for Treatment of Cutaneous Leishmaniasis. *Biomed Microdevices* **2019**, *21*, 8, doi:10.1007/s10544-018-0355-8.

Abstract

Current therapeutic options against cutaneous leishmaniasis are plagued by several weaknesses. The effective topical delivery of an antileishmanial drug would be useful in treating some forms of cutaneous leishmaniasis. Toward this end, a microneedle-based delivery approach for the antileishmanial drug amphotericin B was investigated in murine models of both New World (*Leishmania mexicana*) and Old World (*Leishmania major*) infection. In the *L. mexicana* model, ten days of treatment began on day 35 post infection, when the area of nodules averaged 9–15 mm². By the end of the experiment, a significant difference in nodule area was observed for all groups receiving topical amphotericin B at 25 mg/kg/day after application of microneedle arrays of 500, 750, and 1000 µm in nominal length compared to the group that received this dose of topical amphotericin B alone. In the *L. major* model, ten days of treatment began on day 21 post infection when nodule area averaged 51–65 mm² in the groups. By the end of the

experiment, there was no difference in nodule area between the group receiving 25 mg/kg of topical amphotericin B after microneedle application and any of the non-AmBisome groups. These results show the promise of topical delivery of amphotericin B via microneedles in treating relatively small nodules caused by *L. mexicana*. These data also show the limitations of the approach against a disseminated *L. major* infection. Further optimization of microneedle delivery is needed to fully exploit this strategy for cutaneous leishmaniasis treatment.

Introduction

Leishmaniasis has been designated by the World Health Organization to be one of the most significant tropical diseases; 350 million individuals worldwide are at risk of being affected by this condition [79]. Leishmaniasis is caused by several species of flagellated protozoans that belong to the genus *Leishmania*; the protozoans are transmitted to humans by several types of sand flies [80] that are commonly found in areas where leishmaniasis is endemic [81].

Leishmaniasis is associated with a broad array of clinical manifestations; the infection can take the following forms: (a) an absence of clinical symptoms, (b) a self-limited cutaneous infection, or (c) a disseminated infection that can manifest as either cutaneous, mucocutaneous, or visceral disease, which is potentially fatal in the case of visceral disease [80, 82, 83]. Cutaneous leishmaniasis typically presents as one or more ulcerated nodules [84, 85]. These nodules may reach several centimeters in length and may cause significant scarring as well as concomitant social effects [84-86].

Conventional leishmaniasis treatment approaches (e.g., parenteral administration of pentavalent antimonial agents or amphotericin B) are associated with several shortcomings, including long treatment times, repeated dosing, and toxicity [87, 88]. Other shortcomings associated with conventional leishmaniasis treatment approaches include unpredictable

therapeutic responses, high cost, and poor patient compliance [88, 89]. For example, side effects of sodium stibogluconate, a pentavalent antimonial agent, include arthralgia, cytopenia, fatigue, headache, hematologic suppression, myalgia, pancreatitis, rash, and transaminitis; the development of these side effects commonly leads to interruption of treatment [90, 91].

A liposomal formulation of amphotericin B has recently been used for treating cutaneous leishmaniasis. Solomon et al. showed that liposomal amphotericin B was well tolerated and effective for treating *Leishmania tropica* [92]. Although other successes have been noted in the treatment of cutaneous leishmaniasis with liposomal amphotericin B, there is no consensus on an optimal treatment regimen [93]. It should be noted that the development of cognitive side effects (e.g., confusion and memory difficulties) have been associated with the use of the liposomal formulation of amphotericin B [94]. In addition, Hervás et al. described treatment failure for intravenous liposomal amphotericin B against *Leishmania infantum*; they described a case of cutaneous leishmaniasis that did not respond to two courses of the liposomal formulation [95]. Furthermore, liposomal amphotericin B is expensive; as such, liposomal amphotericin B may be of limited use in developing countries or among individuals with limited resources. The development of alternative delivery mechanisms, including the use of microscale devices for transdermal drug delivery, may be useful for improving topical delivery of amphotericin B and other antileishmanial agents.

In this paper, the use of microscale needle-shaped devices, which will be referred to as microneedles, for transdermal delivery of amphotericin B to cutaneous leishmaniasis lesions is considered. Microneedle devices are used to generate microscale pores in the topmost 15 μm -thick layer of the skin, which is known as the stratum corneum layer of the epidermis [96, 97]. The stratum corneum impedes the transport of several types of pharmacologic agents, including

many types of large, charged, and/or polar pharmacologic agents. By physically disrupting the stratum corneum layer, topical delivery for the treatment of cutaneous leishmaniasis may be obtained.

In previous work, Gittard et al. demonstrated that a combination of two photon polymerization (2PP) and poly(dimethyl siloxane) (PDMS) micromolding-photopolymerization was an appropriate approach for fabricating microneedle devices [40]. The material used to create the microneedle devices, eShell 200, is an acrylate-based polymer that exhibits a Young's modulus of 2400 GPa and a glass transition temperature of 109 °C [40] per the manufacturer's product specifications. The viability of human epidermal keratinocytes on eShell 200 surfaces was shown to be similar to that on polystyrene surfaces [40]. The eShell 200 microneedle device was able to successfully create 58 μm diameter pores in human stratum corneum and epidermis [40]. The results of this study indicate that two photon polymerization and PDMS micromolding-photopolymerization can be used for high throughput replication of eShell 200 microneedle devices with appropriate properties for transdermal drug delivery. In this manuscript, eShell 200 microneedle arrays are evaluated as a delivery vehicle for amphotericin B in two murine models of cutaneous leishmaniasis to examine the feasibility of this approach for the topical treatment of this infection.

Materials and Methods

2PP master structure fabrication 1 cm diameter hexagonal array master structures composed of 250 μm base radius conical microneedles of 500, 750, or 1000 μm nominal heights were fabricated using two-photon polymerization (2PP); the nominal microneedle spacings were 295.45, 361.11, or 423.91 μm for the 500, 750, or 1000 μm nominal microneedle heights, respectively. A Mai-Tai titanium:sapphire laser (Newport Corporation, Irvine, CA) was used to

generate femtosecond laser pulses (780 nm wavelength, <80 fs pulse duration, 80 MHz repetition rate, $M^2 < 1.1$). All optics were sourced from Newport Corporation (Irvine, CA) unless otherwise specified. The laser beam path includes a half-waveplate / polarizing beamsplitter pair for manual power control, an acousto-optical modulator (Gooch & Housego, Ilminster, UK) for computer power control / electronic shutter, a pinhole spatial filter to remove high-order spatial modes and to expand the beam to 1 cm diameter, a galvano-scanner (Intelliscan14, Scanlab GmbH, Munich, Germany) for fine laser positioning, and finally a 20x, 0.5 NA microscope objective (Carl Zeiss AG, Oberkochen, Germany). An XPS-Q8 motion controller was used to control stages and achieve sample translation in the linear axes. Machine vision was achieved by observation through a dichroic mirror directly behind the scanner using a monochrome CMOS image sensor (Flea3, FLIR, Richmond, Canada). Laser power measurement was performed before the scanner.

Pentaerythritol triacrylate (Sigma-Aldrich, St. Louis, MO) with 2% w/w Irgacure® 369 (Ciba, Basel, Switzerland) was mixed, degassed under vacuum, and subsequently syringe filtered through a 0.4 μm membrane. This photopolymer was sandwiched between a glass slide functionalized with 3-(trimethoxysilyl)propyl methacrylate (MAPTMS, Sigma-Aldrich, St. Louis, MO), and a #1 coverslip using 1.5 mm thick PDMS (Sylgard 184, Dow Corning, Midland, MI) spacers.

Microneedles were produced in a layer by layer manner using the galvano-scanner to translate the laser focus in the horizontal plane and the Z-axis stage to translate between layers; the linear stages were used to move between microneedle positions in the array. The toolpath used in each layer of a microneedle was composed of a circle to form the exterior contour, then an Archimedean spiral with a 2 μm pitch that terminates at the center. A scan speed of 20 mm/s

at 200 mW of laser power was used to polymerize the photopolymer. It must be noted that a scan relay was not used; as such, the laser diameter must be larger than the microscope objective entrance diameter. In addition, an uncharacterized amount of power attenuation takes place within the objective itself; the reported laser power should not be taken as an optimal setting for use on a different 2PP apparatus. The sample was moved 5 μm between each layer until the complete microneedle was fabricated. Following completion of a single microneedle, the stages were moved to the next position in the hexagonal array, and the microneedle fabrication process was repeated.

Microneedle array masters were developed in 4-methyl-2-pentanone (MIBK, Sigma-Aldrich, St. Louis, MO). The microscope slide containing the microneedles surrounded in liquid photopolymer was inverted above a watch glass, and the glass was filled with MIBK. Master structures were washed in this manner for 5 min to remove the bulk of the liquid photopolymer, 15 min or until the photopolymer was absent by visual inspection, and then rinsed in excess MIBK.

Soft lithography replication Master structures were treated with trichloro(1H,1H,2H,2H-perfluorooctyl)silane (PTFE-silane) to aid in demolding. 10 μL of the PTFE-silane was placed in a watch glass, and the master structure was inverted over the top. The entire assembly was placed into a vacuum desiccator and held under vacuum for 3 h. Treated master structures were molded in PDMS using pre-cured PDMS rings to contain the liquid PDMS. The PDMS was cured for at least 3 h at 60 $^{\circ}\text{C}$ before demolding. PDMS molds generated directly from the master structure are designated as the primary molds. eShell 200 (Envisiontec, Dearborn, MI) was applied to the mold and degassed over multiple vacuum cycles. Filled molds were contacted to MAPTMS-functionalized slides and polymerized using an Envisiontec

Otoflash® post curing light pulsing unit; the primary molds were subsequently removed.

Replicas generated from the primary molds are designated the primary replicas. Primary replicas were used to generate additional molds, which were designated as the secondary molds. The replicas generated from the secondary molds were designated as the secondary replicas.

Images of the secondary replicas were obtained using a S-3200 variable pressure scanning electron microscope with a Robinson back-scattered electron detector attachment (Hitachi, Tokyo, Japan). Prior to imaging, the microneedle devices were coated with 60% gold-40% palladium using a Technics Hummer II instrument (Anatech, Battle Creek, MI). The chemical composition of the microneedle devices was evaluated via energy dispersive x-ray spectroscopy; analysis was performed in charge reduction mode. In charge reduction mode, a small amount of He gas is introduced into the microscope chamber, which is ionized by electrons in the microscope chamber. The ions are attracted to regions of opposite charge on the surface of the sample, thereby canceling any charging. Microneedle dimensions were measured in ImageJ (National Institutes of Health, Bethesda, MD) using a topdown view to characterize the needle base diameter and a side-view for the needle height. The secondary replicas were also used for the *in vivo* studies described below.

Reagents for biological studies USP grade 0.9% sodium chloride and AmBisome (a liposomal formulation of amphotericin B) were obtained through the Department of Pharmacy at The Ohio State University Wexner Medical Center from Baxter Health Corporation (Deerfield, IL) and Astellas Pharma (Tokyo, Japan), respectively. USP grade amphotericin B was purchased from VWR Life Science (Sanborn, NY). Schneider's *Drosophila* medium and penicillin-streptomycin were obtained from Thermo Fisher (Waltham, MA). *HaeIII* was purchased from New England Biolabs (Ipswich, MA). USP grade dimethyl sulfoxide (DMSO), phosphate

buffered saline (PBS) tablets, and fetal bovine serum were obtained from Sigma-Aldrich (St. Louis, MO). If not otherwise indicated, other reagents were purchased from Sigma-Aldrich.

Parasites *Leishmania mexicana* (MNYC/BZ/62/M379) parasites were generously provided by the Satoskar lab at The Ohio State University as lesion-derived parasites harvested from infected female BALB/c mice as indicated below. Parasites were maintained in Schneider's *Drosophila* medium containing 10% heat-inactivated fetal bovine serum, 50 units / mL penicillin, and 50 µg/mL streptomycin. *Leishmania major* (NIH173 [MHOM/IR/-/173]) parasites were kindly provided by Dr. Brian Vesely at the Walter Reed Army Institute of Research. These parasites were passaged through female BALB/c mice by injection at the base of the tail and harvested from the lesions that subsequently formed. Lesion-derived amastigotes were transformed into promastigotes by suspension in Schneider's *Drosophila* medium containing 20% heat inactivated fetal bovine serum, 50 units/mL penicillin, and 50 µg/mL streptomycin and incubation at 26 °C. The species identity of both parasites was confirmed by PCR amplification of the ribosomal internal transcribed spacer region from parasite genomic DNA followed by restriction fragment length polymorphism (RFLP) analysis of the PCR product digested with the restriction enzyme HaeIII [98].

***Leishmania mexicana in vivo* model** *In vivo* studies in murine cutaneous leishmaniasis models were performed according to a protocol approved by The Ohio State University IACUC. Female 7–8 week old BALB/c mice (Envigo, Somerset, NJ) were infected with 10⁷ stationary phase, low pass *Leishmania mexicana* promastigotes by subcutaneous injection at the base of the tail. When infected animals bore nodules of at least 2 mm in one direction (at 35 days post infection in this case), animals were randomly sorted into groups of five (www.randomization.com, animals randomized into 1 block), then treated once a day for ten days with

either a) AmBisome (20 mg/kg by the intraperitoneal (IP) route), b) PBS vehicle in water (IP), c) topical amphotericin B dissolved in DMSO, or topical amphotericin B dissolved in DMSO after application of microneedle arrays d) 500 μm , e) 750 μm , or f) 1000 μm in length. All topical amphotericin B groups received a dose of 25 mg/kg/day. Nodules caused by infection with parasites were measured twice weekly throughout treatment continuing through three weeks post treatment. Nodules were measured in two dimensions using digital calipers (Fisher Scientific, Hampton, NH) and nodule areas were calculated based on the formula $A = \pi \times r1 \times r2$ (the area of an ellipse). After the final measurement was made, animals were euthanized by CO₂ asphyxiation followed by cervical dislocation to confirm death.

Lesions were excised using surgical scissors, weighed, cut into small pieces, and homogenized using the rubber end of a syringe plunger. The homogenate (3 mL in Schneider's *Drosophila* medium containing 10% heat-inactivated fetal bovine serum, 50 units/mL penicillin, and 50 $\mu\text{g/mL}$ streptomycin) was strained with a cell strainer, centrifuged at 1800 \times g for 10 min at 4 °C, and the resulting pellet was resuspended in 400 μL of the medium described above. A limiting dilution assay using the same medium was then performed in duplicate for each sample. In this limiting dilution assay, 200 μL portions of resuspended pellets from tissue homogenates were placed into the first well of a 96-well plate, then tenfold serial dilutions were performed to provide 24 wells for analysis of the parasite burden derived from each duplicate sample. Plates were sealed around the edges with parafilm and then incubated for 7 days at 26 °C. The parasite load was then estimated after seven days of incubation based on the well of greatest dilution that contained viable parasites observed by microscopy. The log₁₀ values of the parasite load in each duplicate were averaged for each animal. The antilog of this average was then divided by the weight of the sample to determine the average parasite load per gram of tissue for each animal.

Leishmania major in vivo model Female 8–9 week old BALB/c mice were infected with 10^7 stationary phase *Leishmania major* promastigotes by subcutaneous injection at the base of the tail as described above for *L. mexicana*. When infected animals bore nodules of at least 2 mm in one direction (at 21 days post infection in this case), animals were randomly sorted into groups of five as mentioned earlier, then were treated once daily for ten days with either a) AmBisome (20 mg/kg IP), b) 0.9% saline vehicle (IP), c) topical amphotericin B dissolved in DMSO, d) topical amphotericin B dissolved in DMSO after application of microneedle arrays 750 μm in length, or e) application of 750 μm microneedle arrays alone. Both topical amphotericin B groups received a 25 mg/kg/day dose of this drug. Nodules and ulcers caused by infection with parasites were measured in two dimensions as indicated above twice weekly throughout treatment continuing through two weeks post treatment. After two weeks post treatment, early removal criteria were met for a subset of animals due to ulcer size and the experiment was terminated. Animals were euthanized, nodules were removed, tissue homogenates were prepared, and a limiting dilution assay was performed as described above, with the minor modification that the medium used contained 20% heat-inactivated fetal bovine serum rather than 10% heat-inactivated fetal bovine serum. Plates were viewed at days 7 and 11 for the appearance of promastigotes. The results of this limiting dilution assay were identical on days 7 and 11, except that one additional well in one of the duplicates for a single sample was observed as positive on day 11 that was not read as positive on day 7. Parasite load per gram of tissue based on the day 11 observations were then calculated and plotted as described earlier.

Data analyses The treatment effects on nodule area and ulcer area were analyzed using ANOVA with repeated measurements. At different post-infection time points, groupwise comparisons of nodule area and ulcer area were conducted using Tukey's Honestly Significant

Difference (HSD) tests. Since values for parasite burden per gram of tissue deviated from a normal distribution, U rank tests were used to compare the medians between any two treatment groups. All statistical tests were two-sided and the significance level was 0.05. Borderline significance was defined as $0.05 < p < 0.1$. R3.3 software (The R project for statistical computing, CRAN.Rproject.org) was used in all statistical analyses.

Results

Secondary replicas of each microneedle array type were characterized using scanning electron microscopy and energy dispersive x-ray spectroscopy. Scanning electron micrographs of each type of secondary replica are shown in **Figure 3.1**. Arrays of microneedles with a 500 μm nominal height contained $571.8 \pm 5.6 \mu\text{m}$ tall microneedles with a microneedle base diameter of $201.0 \pm 2.3 \mu\text{m}$, and a microneedle-to-microneedle spacing of $299.9 \pm 2.4 \mu\text{m}$. Arrays of microneedles with a 750 μm nominal height contained $808.4 \pm 4.2 \mu\text{m}$ tall microneedles with a microneedle base diameter of $161.9 \pm 3.6 \mu\text{m}$, and a microneedle-to-microneedle spacing of $360.9 \pm 4.6 \mu\text{m}$. Arrays of microneedles of 1000 μm nominal height contained $1044.2 \pm 6.0 \mu\text{m}$ tall microneedles with a microneedle base diameter of $145.9 \pm 4.1 \mu\text{m}$ and a microneedle-to-microneedle spacing of $423.1 \pm 9.7 \mu\text{m}$. Energy-dispersive x-ray spectroscopy studies of the secondary replicas of the microneedle devices indicated that the microneedle devices with 500 μm nominal height, 750 μm nominal height, and 1000 μm nominal height contained carbon, oxygen, and titanium. In addition, the microneedle device with 750 μm nominal height contained trace amounts of phosphorus and silicon. All of these elements are either found in biological tissues (e.g., carbon, oxygen, and phosphorus) or have good compatibility with human tissues (e.g., silicon and titanium) [99]. No trace amounts of elements with known toxicity were found.

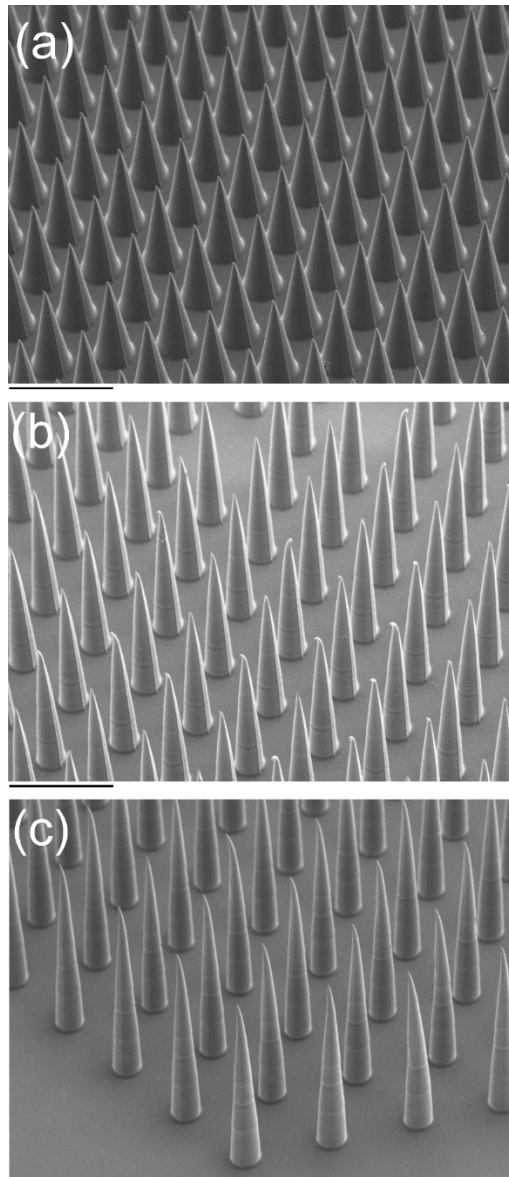


Figure 3.1 - Scanning electron microscopy images of microneedles with nominal heights of 500 μm (Panel A), 750 μm (Panel B), and 1000 μm (Panel C) obtained at a stage tilt angle of 45°. The scale bars for these images are 500 μm .

Comparison of the *L. mexicana* and *L. major* models For both Leishmania species, subcutaneous injection of late log phase promastigotes at the base of the tail of female BALB/c mice resulted in the formation of a nodule at the site of inoculation. The progression of infection was more rapid in the *L. major* model compared to the *L. mexicana* model as detailed below. In

addition, the nodules resulting from *L. major* infection ulcerated to a much greater degree than in the *L. mexicana* study, allowing for measurement of both nodules and ulcers for the former. A visual comparison of typical lesions observed in the two models is provided in **Figure 3.2**.

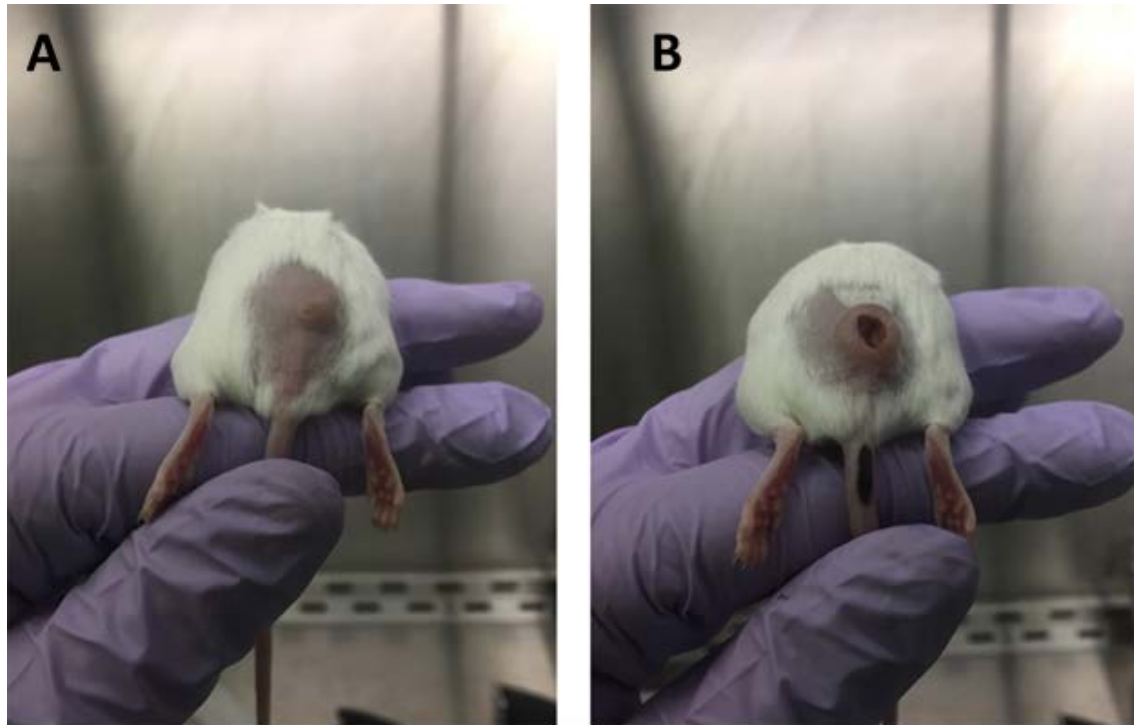


Figure 3.2 - Lesions formed at the infection site in animals from vehicle control groups at the end of the 10 day dosing period for *L. mexicana* at 44 days post infection (Panel A) and *L. major* at 30 days post infection (Panel B).

Effect of the poke and apply approach in the *L. Mexicana* model

In an initial experiment in BALB/c mice infected with *L. mexicana*, the effect of topical amphotericin B after the application of microneedle arrays of 500, 750, and 1000 μm nominal length was examined. A topical amphotericin B control group, an IP AmBisome group, and an IP PBS vehicle control group were also included for reference. Average nodule areas ranged from 9 to 15 mm^2 in the six groups at the beginning of treatment and ranged from 13 to 66 mm^2 at the end of the experiment (65 days post infection, **Figure 3.3A** and B). Statistically significant

differences in nodule area were observed between both the 500 μm and the 750 μm needle plus amphotericin B groups and the topical amphotericin B group starting on day 49 post infection (**Figure 3.3A**, $p < 0.05$). On days 59 and 63 post infection, differences with borderline significance were observed in nodule area between the 1000 μm needle plus amphotericin B group and the topical amphotericin B group (p values = 0.06 and 0.08, respectively); these differences were statistically significant ($p < 0.05$) on day 65 post infection (**Figure 3.3A**). Significant differences were observed between the AmBisome group and the PBS control group starting on day 45 post infection ($p < 0.05$ **Figure 3.3B**).

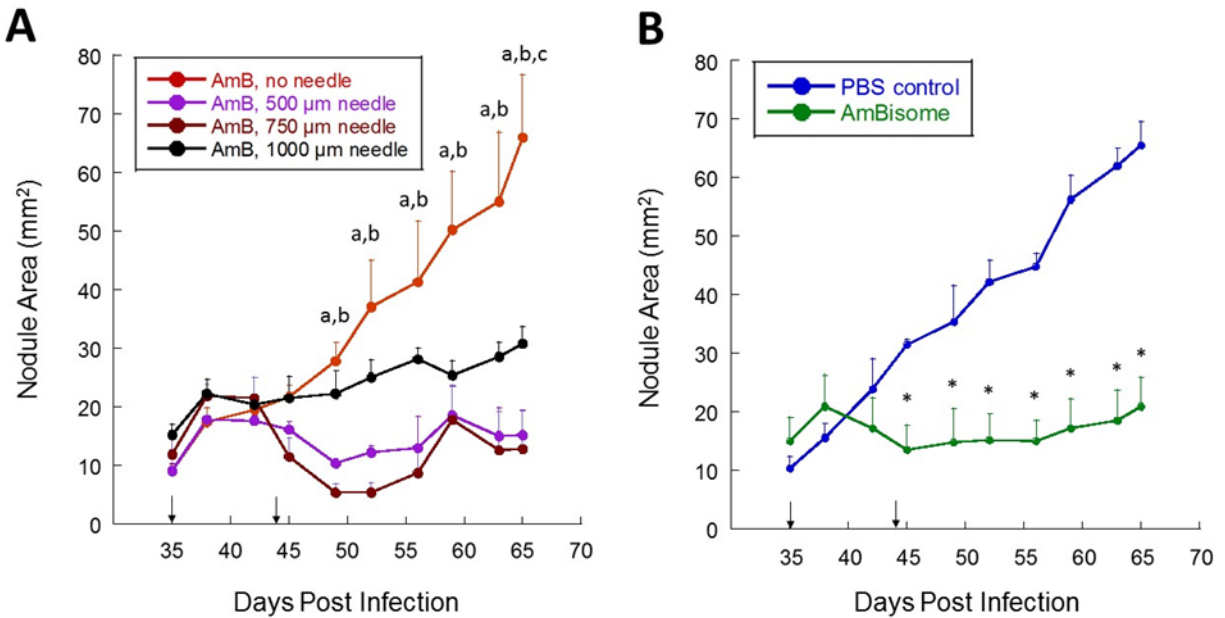


Figure 3.3 - Nodule measurements for animals infected with *L. mexicana*. Panel A – Mice were treated topically at the site of the nodule with a solution of amphotericin B in DMSO (AmB, 25 mg/kg) either in the absence of microneedle application or after the application of microneedle arrays 500 µm, 750 µm, or 1000 µm in nominal length as described in the methods section. Error bars represent the mean ± standard error of the mean (SEM) (n = 5). The letters indicate a significant difference (p < 0.05, Tukey’s HSD tests) between the amphotericin B no needle group and (a) the amphotericin B 500 µm needle group, (b) the amphotericin B 750 µm needle group, or (c) the amphotericin B 1000 µm needle group using ANOVA with repeated measurements. Differences of borderline significance (0.05 < p < 0.1) were observed between the amphotericin B no needle group and the amphotericin B 1000 µm needle group on days 59 and 63, (p values = 0.06 and 0.08, respectively), which are not noted on the graph. Panel B – In the same experiment, mice received either PBS vehicle or AmBisome (20 mg/kg) by the IP route as outlined in the methods (a separate panel is included for these two groups for the sake of clarity). Error bars represent the mean ± standard error of the mean (SEM) (n = 5). In the PBS control group, one animal became moribund and was euthanized on day 37 post infection, so n = 4 for this group from that point on. Asterisks (*) indicate a significant difference (p < 0.05, Tukey’s HSD tests) between the PBS control group and the AmBisome group at specific post-infection time points. In both panels, the arrows pointing to the x-axis (↓) indicate the days on which treatment began and ended.

As for parasite burden per gram of tissue, significant differences were observed between the 750 μm needle plus amphotericin B group and the topical amphotericin B group and between the 1000 μm needle plus amphotericin B group and the topical amphotericin B group (**Figure 3.4**, $p < 0.05$). Differences with borderline significance were found between the 500 μm needle plus amphotericin B group and the topical amphotericin B group and between the AmBisome group and the PBS control group (**Figure 3.4**, p values = 0.06 and 0.07, respectively). For one lesion in the 500 μm needle group in this assay, a parasite load of slightly less than 10^4 parasites/g of tissue was measured, by far the lowest parasite load recorded in this experiment. One of the duplicate samples used in this determination had no detectable parasites, resulting in the point that was much lower than the rest.

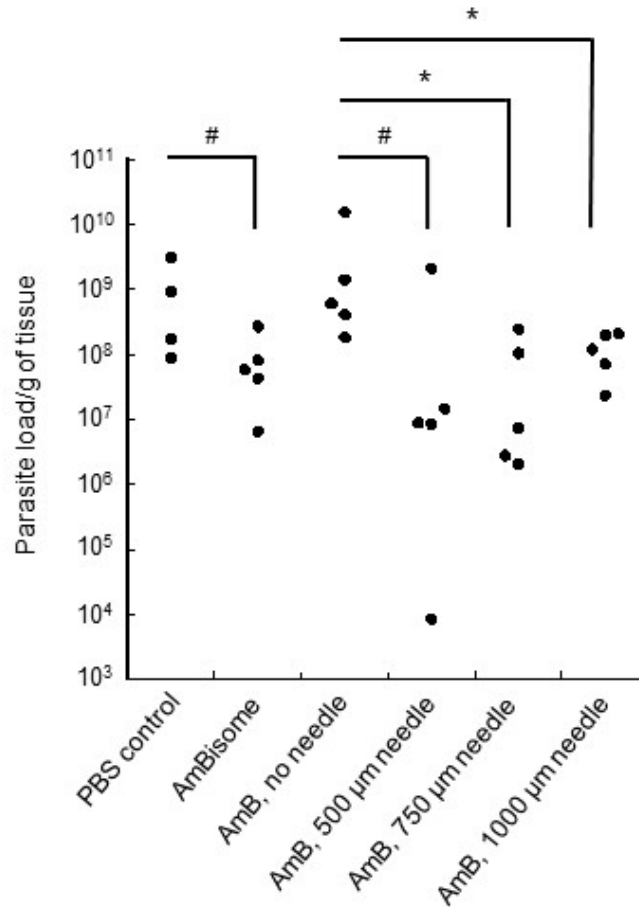


Figure 3.4 - Limiting dilution assays were performed for the *L. mexicana* experiment in duplicate and parasite load per gram of tissue was determined as described in the methods section. Circles indicate determinations from individual nodules. Groupwise comparisons were conducted using U rank tests. Asterisks (*) indicate differences with statistical significance ($p < 0.05$) and hash symbols (#) indicate differences with borderline significance (p values = 0.06 and 0.07, respectively).

Effect of the poke and apply approach in the *L. major* model Female BALB/c mice infected with *L. major* were used to examine the effect of topical amphotericin B after the application of 750 µm nominal length microneedle arrays in a different model of cutaneous leishmaniasis infection. Groups receiving topical amphotericin B alone and needles alone were also included along with IP AmBisome and IP 0.9% saline vehicle groups for reference. Average nodule areas ranged from 51 to 65 mm² in the five groups at the beginning of treatment (21 days

post infection) and from 57 to 134 mm² one day prior to the end of the experiment (44 days post infection, **Figure 3.5A**). Beginning on day 31 post infection, a statistically significant difference was observed in the area of nodules for the AmBisome group compared to the saline control group ($p < 0.05$).

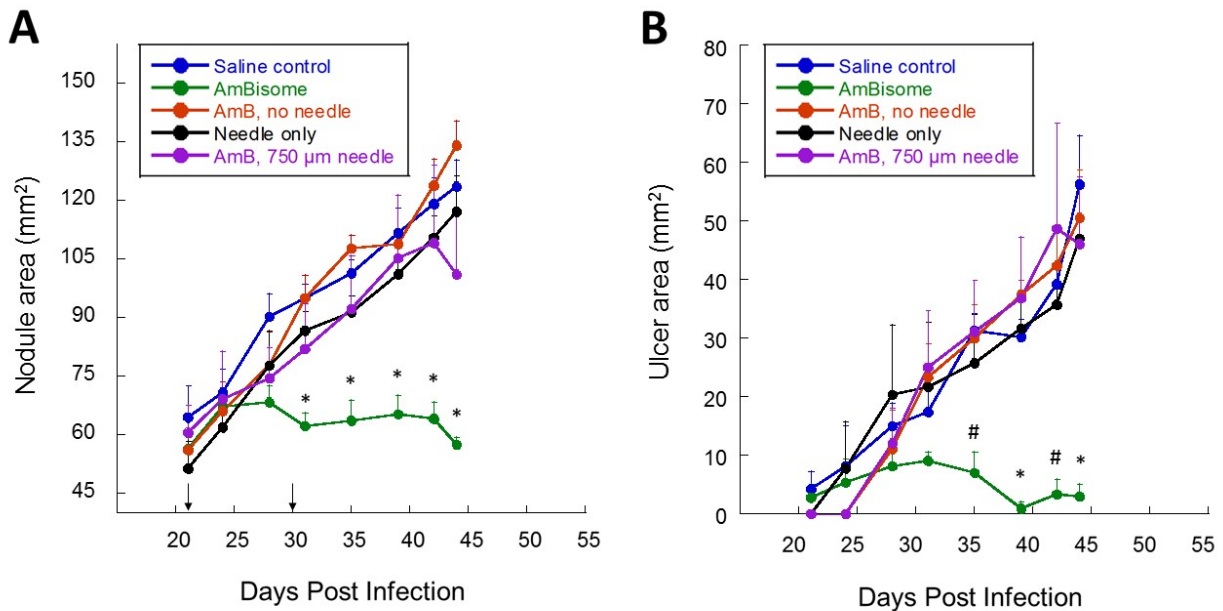


Figure 3.5 - Measurements of nodule area (Panel A) and ulcer area (Panel B) for animals infected with *L. major*. Mice were treated topically at the site of the nodule either with microneedles alone or with a solution of amphotericin B in DMSO (AmB, 25 mg/kg) either with or without application of microneedle arrays 750 µm in length, with AmBisome (20 mg/kg) by the IP route, or with IP 0.9% saline vehicle as described in the methods section. Error bars represent the mean \pm standard error of the mean (SEM) ($n = 5$). Asterisks (*) indicate significant differences ($p < 0.05$, Tukey's HSD tests) between the saline control group and the AmBisome group at specific post-infection time points. The hash symbol (#) indicates a difference with borderline significance ($p = 0.08, 0.06$) at days 35 and 42 post infection, respectively. Additional details regarding significant differences in area between the AmBisome groups and the other groups is provided in the text but is not shown here for clarity. The arrows pointing to the x-axis (↓) in Panel A indicate the days on which treatment began and ended; these arrows are not shown in Panel B. In the AmB, 750 µm group, one animal met early removal criteria prior to the last measurement due to a large, ulcerated lesion.

For ulcer area, statistically significant differences were found on days 39 and 44 between the AmBisome group and the saline control group ($p < 0.05$), while differences with borderline significance were found between these two groups on days 35 and 42 ($p = 0.08$ and 0.06 , respectively). By day 42 post infection for nodule area and on days 39 and 44 post infection for ulcer area, significant differences were observed between the AmBisome group and all other groups ($p < 0.05$). However, no significant differences were observed between the needle plus amphotericin B group and any of the other non-AmBisome groups. For the limiting dilution assay (**Figure 3.6**), a significant difference in parasite load per gram of tissue was found between the AmBisome group and all other groups ($p < 0.05$), while differences between the needle plus amphotericin B group and any of the other non-AmBisome groups were not statistically significant.

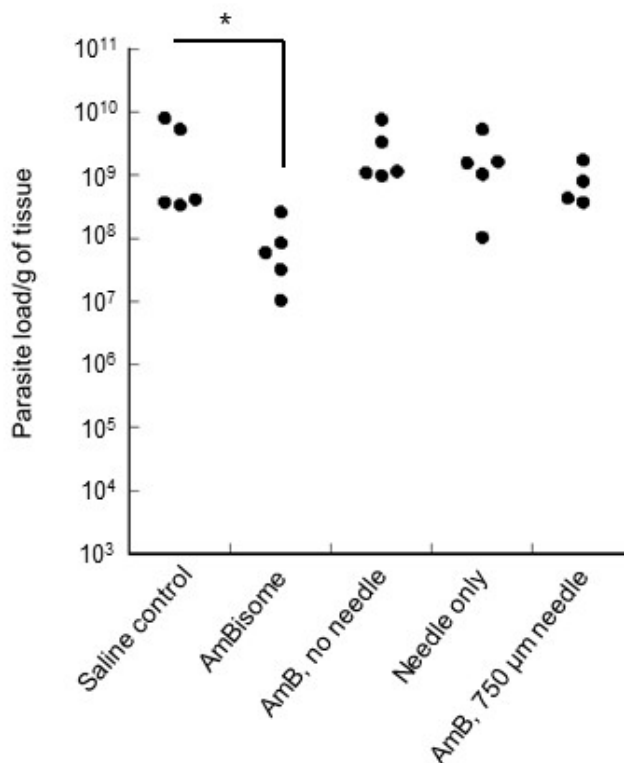


Figure 3.6 - Limiting dilution assays were performed for the *L. major* experiment in duplicate and parasite load per gram of tissue was determined as described in the methods section. Circles indicate determinations from individual nodules. The asterisk (*) indicates a significant difference in parasite load per gram of tissue between the saline control and AmBisome groups ($p < 0.05$, U rank test). Significant differences in parasite load per gram of tissue were also observed between the AmBisome group and all other non-AmBisome groups ($p < 0.05$); this is not shown for clarity.

Discussion

For localized cutaneous leishmaniasis, effective topical treatment is preferred to injectable therapy. A safe and effective topical agent to treat cutaneous leishmaniasis could also offer advantages compared to thermotherapy, which can lead to hyperpigmentation and secondary infections, and cryotherapy, which can also lead to secondary infections, can cause “burns,” and results in moderate cure rates [100]. The available topical drug therapy for cutaneous leishmaniasis is based on the aminoglycoside paromomycin; creams containing

paromomycin have shown good efficacy in some trials [101], but such topical preparations have not been broadly tested against a variety of *Leishmania* species and are not widely available [100, 101]. Given that amphotericin B is a potent antileishmanial drug that is used successfully in treating visceral leishmaniasis, the activity of various amphotericin B formulations has been tested in animal models of cutaneous leishmaniasis. Arabinogalactan conjugates of amphotericin B given subcutaneously to BALB/c mice infected at the base of the tail with *L. major* were effective in delaying lesion appearance in these animals [102]. Liposomal amphotericin B containing 1,2-distigmasterylhemisuccinoyl-sn-glycero-3-phosphocholine as one of the liposomal components was as effective as AmBisome in BALB/c mice bearing *L. major* footpad infections when both were given by the IP route [103]. Intradermal injection of an amphotericin B-polymethacrylic acid (PMA) complex led to healing of *L. major* footpad lesions in both early and established BALB/c mouse infection models [104]. While these experimental amphotericin B formulations were effective in animal models, all were administered by injection. In a seminal study showing the efficacy of topical paromomycin against cutaneous leishmaniasis, topical amphotericin B (15%) in white soft paraffin was ineffective against *L. major* lesions in BALB/c mice [105], while application of lipid formulations of amphotericin B dispersed in 5% ethanol was effective in reducing lesion size in *L. major*-infected CBA mice [106]. Topical application of the skin penetrable nanoliposomal formulation of amphotericin B termed SinaAmphoLeish caused a temporary reduction in lesion sizes in 129SVE mice infected with *L. mexicana*, but there was no significant difference between the size of lesions in these animals compared to controls at the end of the experiment [107]. No reduction in lesion size was observed in *L. mexicana*-infected BALB/c mice receiving topical SinaAmphoLeish and the control group receiving topical Vaseline [107]. Thus, an effective topical amphotericin B formulation could be

of great interest for treating cutaneous leishmaniasis and could compete with paromomycin creams depending on efficacy and cost.

In the present study, AmBisome administered by the IP route was chosen as the treatment control in experiments with both *L. mexicana* and *L. major* based both on the efficacy of this formulation in previous studies [108-111] and because the effectiveness of the active pharmaceutical ingredient, amphotericin B, could be compared between the two methods of administration. The effect of AmBisome on nodule area in both studies and on ulcer area in the *L. major* study was significant compared to the vehicle control group (**Figure 3.3B**, **Figure 3.5**). A statistically significant reduction in tissue parasite burden was observed between the AmBisome and vehicle control groups in the *L. major* study (**Figure 3.6**), while borderline significance was observed between these two groups in the *L. mexicana* study (**Figure 3.4**). Although parasite burden was not measured in their study, Yardley and Croft demonstrated that complete resolution of lesions was initially observed in 2/5 *L. major*-infected BALB/c mice treated with 25 mg/kg AmBisome every other day for six days by the IV route, although recurrence of lesions eventually occurred [108]. Fortin et al. observed a statistically significant reduction in ulcer size and parasite burden when *L. major*-infected animals were treated for ten consecutive days with 25 mg/kg AmBisome administered IP when ulcer area reached ~50 mm² [110]. In BALB/c mice infected with *L. major*, the administration of IPAmBisome at 12.5 mg/kg and 25 mg/kg for ten consecutive days resolved lesions in 4/5 and 5/5 animals, respectively, when treatment began after lesion area reached an average of 50 mm² [111]. Thus, we believe that our results with AmBisome are consistent with previous studies in murine cutaneous leishmaniasis models.

In the *L. mexicana* study, nodule area was reduced in animals receiving topical amphotericin B after microneedle application (**Figure 3.3A**) and differences in parasite burden per gram of tissue were noted between the needle plus amphotericin B groups and the topical amphotericin B alone group (**Figure 3.4**). Overall, the 500 μm and 750 μm needles outperformed the 1000 μm needles in terms of nodule suppression ($p < 0.05$) but not in terms of parasite burden ($p > 0.1$). Cutaneous leishmaniasis is caused by infection of macrophages in the dermal layer of the skin [112, 113]. To the best of our knowledge, the depth of the dermal layer in mice infected with *L. mexicana* or any other cutaneous leishmaniasis species has not been measured, but the depth of the dermal layer in female mice has been estimated to be approximately 200 μm [114, 115]. Since the 1000 μm needles were inferior in performance to the shorter needles in terms of nodule suppression, these needles may have been too long to optimally target the parasites in the dermal layer with amphotericin B.

In the *L. major* study, no significant differences were observed in nodule or ulcer area between the needle plus topical amphotericin B group and the topical amphotericin B alone group or between the needle plus topical amphotericin group and the needle alone group (**Figure 3.5**). Likewise, differences between the amphotericin B plus needle group and the non-AmBisome groups were not significant in the *L. major* limiting dilution assay (**Figure 3.6**). Several explanations are possible for the more favorable response to the poke and apply approach in the *L. mexicana* model compared to the *L. major* model: 1) *L. major* infections developed more rapidly than *L. mexicana* infections, resulting in larger nodules (compare **Figure 3.3** with **Figure 3.5**). *L. major* infections disseminate in susceptible BALB/c mice [116, 117], likely making it more difficult for the microneedle plus amphotericin B treatment to influence nodule development. In the clinical treatment of cutaneous leishmaniasis, topical approaches are

not recommended for treating cutaneous infections that consist of large or multiple lesions or that have spread to the lymphatic system [118]. Despite its widespread use as a cutaneous leishmaniasis model, *L. major* infections in BALB/c mice may more closely resemble human visceral leishmaniasis than cutaneous leishmaniasis in humans [119]. In contrast, AmBisome delivered by the IP route is more likely to interfere with the spread of infection due to its systemic availability. While BALB/c mice infected subcutaneously with *L. mexicana* also acquire visceral infections, the development of these infections is slower than with *L. major* [120], as observed here. 2) The hexagonal needle arrays used for these experiments measured approximately 10 mm in diameter. During the course of treatment, the area of some *L. major* nodules surpassed the area of the microneedle arrays and continued to expand. This is in contrast with the *L. mexicana* nodules, which remained smaller in area than the microneedle arrays for the duration of treatment. Thus, the topical treatment with amphotericin B after the application of microneedles may have been more effective for the smaller nodules. 3) While *L. mexicana* nodules were essentially smooth with little ulceration over the course of the study, *L. major* nodules developed ulcers that formed scabs and eventually presented an uneven surface (**Figure 3.2**). Both the accumulation of necrotic tissue [111] and changes to the surface of the lesion in the *L. major* model may have affected the delivery of topical amphotericin B after microneedle application.

Differences in experimental design between the *L. mexicana* and *L. major* studies reported here merit explanation. Phosphate buffered saline was the isotonic IP injection control in the *L. mexicana* experiment; USP saline was used in this role in the *L. major* study upon advisement by the IACUC that USP grade reagents are preferred. Separate needle alone groups were not included in the *L. mexicana* study because of the time and expense of preparing twice

as many needle arrays and the need to limit the number of animals in this experiment to a manageable size while still exploring different needle lengths. A needle alone control was included in the *L. major* study, where the 750 μm needle length that appeared to provide optimal activity in the *L. mexicana* experiment (although this cannot be shown statistically) was employed. As detailed above, the lack of efficacy of the approach in the *L. major* model is likely due to the more rapid progression of infection. Considering that this is the first report of microneedle delivery for treating cutaneous leishmaniasis, additional studies are needed to assess the full potential of this approach.

Conclusions

A statistically significant reduction of nodule size and parasite burden was observed in mice infected with *L. mexicana* after applying microneedle arrays followed by topical amphotericin B. While this approach was not effective in the *L. major* study described here, the more rapid progression and dissemination of infection and the development of ulcers may help to explain the lack of efficacy of the microneedle plus topical amphotericin B approach against *L. major*. While the efficacy of the microneedle approach in the *L. mexicana* model provides proof of concept for microneedle delivery of amphotericin B to treat cutaneous leishmaniasis, efficacy in a range of models is needed to identify new approaches for broad treatment of this disease endemic to different parts of the world. Other microneedle-based approaches that avoid a DMSO vehicle and that are capable of directly delivering high levels of the drug to the site of infection are being explored as candidate therapeutic strategies against cutaneous leishmaniasis.



Microneedle-Based Delivery of Amphotericin B for Treatment of Cutaneous Leishmaniasis

Alexander K. Nguyen¹ · Kai-Hung Yang¹ · Kelsey Bryant² · Junan Li³ · April C. Joice² · Karl A. Werbovetz² · Roger J. Narayan¹

Published online: 7 January 2019
© Springer Science+Business Media, LLC, part of Springer Nature 2019

Abstract

Current therapeutic options against cutaneous leishmaniasis are plagued by several weaknesses. The effective topical delivery of an antileishmanial drug would be useful in treating some forms of cutaneous leishmaniasis. Toward this end, a microneedle based delivery approach for the antileishmanial drug amphotericin B was investigated in murine models of both New World (*Leishmania mexicana*) and Old World (*Leishmania major*) infection. In the *L. mexicana* model, ten days of treatment began on day 35 post infection, when the area of nodules averaged 9–15 mm². By the end of the experiment, a significant difference in nodule area was observed for all groups receiving topical amphotericin B at 25 mg/kg/day after application of microneedle arrays of 500, 750, and 1000 μM in nominal length compared to the group that received this dose of topical amphotericin B alone. In the *L. major* model, ten days of treatment began on day 21 post infection when nodule area averaged 51–65 mm² in the groups. By the end of the experiment, there was no difference in nodule area between the group receiving 25 mg/kg of topical amphotericin B after microneedle application and any of the non-AmBisome groups. These results show the promise of topical delivery of amphotericin B via microneedles in treating relatively small nodules caused by *L. mexicana*. These data also show the limitations of the approach against a disseminated *L. major* infection. Further optimization of microneedle delivery is needed to fully exploit this strategy for cutaneous leishmaniasis treatment.

Keywords Microneedle · Drug delivery · Amphotericin B · Leishmaniasis

1 Introduction

Leishmaniasis has been designated by the World Health Organization to be one of the most significant tropical diseases; 350 million individuals worldwide are at risk of being affected by this condition (Neghina and Neghina 2010). Leishmaniasis is caused by several species of flagellated

protozoans that belong to the genus *Leishmania*; the protozoans are transmitted to humans by several types of sand flies (Murray et al. 2005) that are commonly found in areas where leishmaniasis is endemic (Jacobson 2011). Leishmaniasis is associated with a broad array of clinical manifestations; the infection can take the following forms: (a) an absence of clinical symptoms, (b) a self-limited cutaneous infection, or (c) a disseminated infection that can manifest as either cutaneous, mucocutaneous, or visceral disease, which is potentially fatal in the case of visceral disease (Murray et al. 2005; Ameen 2010; Matheson et al. 2012). Cutaneous leishmaniasis typically presents as one or more ulcerated nodules (David and Craft 2009; Torres-Guerrero et al. 2017). These nodules may reach several centimeters in length and may cause significant scarring as well as concomitant social effects (Bari and Rahman 2003; David and Craft 2009; Torres-Guerrero et al. 2017).

Conventional leishmaniasis treatment approaches (e.g., parenteral administration of pentavalent antimonial agents or amphotericin B) are associated with several shortcomings, including long treatment times, repeated dosing, and toxicity (Cameiro et al. 2012; López et al. 2012). Other shortcomings

Alexander K. Nguyen, Kai-Hung Yang, Kelsey Bryant contributed equally.

✉ Roger J. Narayan
roger_narayan@ncsu.edu

¹ Joint Department of Biomedical Engineering, University of North Carolina and North Carolina State University, Box 7115, Raleigh, NC 27695-7115, USA

² Division of Medicinal Chemistry and Pharmacognosy, College of Pharmacy, The Ohio State University, Columbus, OH, USA

³ College of Pharmacy, The Ohio State University, Columbus, OH, USA

associated with conventional leishmaniasis treatment approaches include unpredictable therapeutic responses, high cost, and poor patient compliance (Frézard and Demicheli 2010; López et al. 2012). For example, side effects of sodium stibogluconate, a pentavalent antimonial agent, include arthralgia, cytopenia, fatigue, headache, hematologic suppression, myalgia, pancreatitis, rash, and transaminitis; the development of these side effects commonly leads to interruption of treatment (Aronson et al. 1998, 2010).

A liposomal formulation of amphotericin B has recently been used for treating cutaneous leishmaniasis. Solomon et al. showed that liposomal amphotericin B was well-tolerated and effective for treating *Leishmania tropica* (Solomon et al. 2011). Although other successes have been noted in the treatment of cutaneous leishmaniasis with liposomal amphotericin B, there is no consensus on an optimal treatment regimen (Mosimann et al. 2018). It should be noted that the development of cognitive side effects (e.g., confusion and memory difficulties) have been associated with the use of the liposomal formulation of amphotericin B (Glasser and Murray 2011). In addition, Hervás et al. described treatment failure for intravenous liposomal amphotericin B against *Leishmania infantum*; they described a case of cutaneous leishmaniasis that did not respond to two courses of the liposomal formulation (Hervás et al. 2012). Furthermore, liposomal amphotericin B is expensive; as such, liposomal amphotericin B may be of limited use in developing countries or among individuals with limited resources. The development of alternative delivery mechanisms, including the use of microscale devices for transdermal drug delivery, may be useful for improving topical delivery of amphotericin B and other antileishmanial agents.

In this paper, the use of microscale needle-shaped devices, which will be referred to as microneedles, for transdermal delivery of amphotericin B to cutaneous leishmaniasis lesions is considered. Microneedle devices are used to generate microscale pores in the topmost 15 μm -thick layer of the skin, which is known as the stratum corneum layer of the epidermis (Henry et al. 1998; Gittard et al. 2010). The stratum corneum impedes the transport of several types of pharmacologic agents, including many types of large, charged, and/or polar pharmacologic agents. By physically disrupting the stratum corneum layer, topical delivery for the treatment of cutaneous leishmaniasis may be obtained.

In previous work, Gittard et al. demonstrated that a combination of two photon polymerization (2PP) and poly(dimethyl siloxane) (PDMS) micromolding-photopolymerization was as an appropriate approach for fabricating microneedle devices (Gittard et al. 2009). The material used to create the microneedle devices, eShell 200, is an acrylate-based polymer that exhibits a Young's modulus of 2400 GPa and a glass transition temperature of 109 $^{\circ}\text{C}$ (Gittard et al. 2009) per the manufacturer's product specifications. The viability of human

epidermal keratinocytes on eShell 200 surfaces was shown to be similar to that on polystyrene surfaces (Gittard et al. 2009). The eShell 200 microneedle device was able to successfully create 58 μm diameter pores in human stratum corneum and epidermis (Gittard et al. 2009). The results of this study indicate that two photon polymerization and PDMS micromolding-photopolymerization can be used for high throughput replication of eShell 200 microneedle devices with appropriate properties for transdermal drug delivery. In this manuscript, eShell 200 microneedle arrays are evaluated as a delivery vehicle for amphotericin B in two murine models of cutaneous leishmaniasis to examine the feasibility of this approach for the topical treatment of this infection.

2 Materials and Methods

2PP master structure fabrication 1 cm diameter hexagonal array master structures composed of 250 μm base radius conical microneedles of 500, 750, or 1000 μm nominal heights were fabricated using two-photon polymerization (2PP); the nominal microneedle spacings were 295.45, 361.11, or 423.91 μm for the 500, 750, or 1000 μm nominal microneedle heights, respectively. A Mai-Tai titanium:sapphire laser (Newport Corporation, Irvine, CA) was used to generate femtosecond laser pulses (780 nm wavelength, <80 fs pulse duration, 80 MHz repetition rate, $M^2 < 1.1$). All optics were sourced from Newport Corporation (Irvine, CA) unless otherwise specified. The laser beam path includes a half-waveplate / polarizing beamsplitter pair for manual power control, an acousto-optical modulator (Gooch & Housego, Ilminster, UK) for computer power control / electronic shutter, a pinhole spatial filter to remove high-order spatial modes and to expand the beam to 1 cm diameter, a galvano-scanner (Intelliscan14, Scanlab GmbH, Munich, Germany) for fine laser positioning, and finally a 20x, 0.5 NA microscope objective (Carl Zeiss AG, Oberkochen, Germany). An XPS-Q8 motion controller was used to control stages and achieve sample translation in the linear axes. Machine vision was achieved by observation through a dichroic mirror directly behind the scanner using a monochrome CMOS image sensor (Flea3, FLIR, Richmond, Canada). Laser power measurement was performed before the scanner.

Pentaerythritol triacrylate (Sigma-Aldrich, St. Louis, MO) with 2% w/w Irgacure® 369 (Ciba, Basel, Switzerland) was mixed, degassed under vacuum, and subsequently syringe filtered through a 0.4 μm membrane. This photopolymer was sandwiched between a glass slide functionalized with 3-(trimethoxysilyl)propyl methacrylate (MAPTMS, Sigma-Aldrich, St. Louis, MO), and a #1 coverslip using 1.5 mm thick PDMS (Sylgard 184, Dow Corning, Midland, MI) spacers.

Microneedles were produced in a layer by layer manner using the galvano-scanner to translate the laser focus in the horizontal plane and the Z-axis stage to translate between layers; the linear stages were used to move between microneedle positions in the array. The toolpath used in each layer of a microneedle was composed of a circle to form the exterior contour, then an Archimedean spiral with a 2 μm pitch that terminates at the center. A scan speed of 20 mm/s at 200 mW of laser power was used to polymerize the photopolymer. It must be noted that a scan relay was not used; as such, the laser diameter must be larger than the microscope objective entrance diameter. In addition, an uncharacterized amount of power attenuation takes place within the objective itself; the reported laser power should not be taken as an optimal setting for use on a different 2PP apparatus. The sample was moved 5 μm between each layer until the complete microneedle was fabricated. Following completion of a single microneedle, the stages were moved to the next position in the hexagonal array, and the microneedle fabrication process was repeated.

Microneedle array masters were developed in 4-methyl-2-pentanone (MIBK, Sigma-Aldrich, St. Louis, MO). The microscope slide containing the microneedles surrounded in liquid photopolymer was inverted above a watch glass, and the glass was filled with MIBK. Master structures were washed in this manner for 5 min to remove the bulk of the liquid photopolymer, 15 min or until the photopolymer was absent by visual inspection, and then rinsed in excess MIBK.

Soft lithography replication Master structures were treated with trichloro(1H,1H,2H,2H-perfluorooctyl)silane (PTFE-silane) to aid in demolding. 10 μL of the PTFE-silane was placed in a watch glass, and the master structure was inverted over the top. The entire assembly was placed into a vacuum desiccator and held under vacuum for 3 h. Treated master structures were molded in PDMS using pre-cured PDMS rings to contain the liquid PDMS. The PDMS was cured for at least 3 h at 60 $^{\circ}\text{C}$ before demolding. PDMS molds generated directly from the master structure are designated as the primary molds. eShell 200 (Envisiontec, Dearborn, MI) was applied to the mold and degassed over multiple vacuum cycles. Filled molds were contacted to MAPTMS-functionalized slides and polymerized using an Envisiontec Otoflash[®] post curing light pulsing unit; the primary molds were subsequently removed. Replicas generated from the primary molds are designated the primary replicas. Primary replicas were used to generate additional molds, which were designated as the secondary molds. The replicas generated from the secondary molds were designated as the secondary replicas.

Images of the secondary replicas were obtained using a S-3200 variable pressure scanning electron microscope with a Robinson back-scattered electron detector attachment (Hitachi, Tokyo, Japan). Prior to imaging, the microneedle devices were coated with 60% gold-40% palladium using a

Technics Hummer II instrument (Anatech, Battle Creek, MI). The chemical composition of the microneedle devices was evaluated via energy dispersive x-ray spectroscopy; analysis was performed in charge reduction mode. In charge reduction mode, a small amount of He gas is introduced into the microscope chamber, which is ionized by electrons in the microscope chamber. The ions are attracted to regions of opposite charge on the surface of the sample, thereby canceling any charging. Microneedle dimensions were measured in ImageJ (National Institutes of Health, Bethesda, MD) using a top-down view to characterize the needle base diameter and a side-view for the needle height. The secondary replicas were also used for the *in vivo* studies described below.

Reagents for biological studies USP grade 0.9% sodium chloride and AmBisome (a liposomal formulation of amphotericin B) were obtained through the Department of Pharmacy at The Ohio State University Wexner Medical Center from Baxter Health Corporation (Deerfield, IL) and Astellas Pharma (Tokyo, Japan), respectively. USP grade amphotericin B was purchased from VWR Life Science (Sanborn, NY). Schneider's *Drosophila* medium and penicillin-streptomycin were obtained from Thermo Fisher (Waltham, MA). *HaeIII* was purchased from New England Biolabs (Ipswich, MA). USP grade dimethyl sulfoxide (DMSO), phosphate buffered saline (PBS) tablets, and fetal bovine serum were obtained from Sigma-Aldrich (St. Louis, MO). If not otherwise indicated, other reagents were purchased from Sigma-Aldrich.

Parasites *Leishmania mexicana* (MNYC/BZ/62/M379) parasites were generously provided by the Satoskar lab at The Ohio State University as lesion-derived parasites harvested from infected female BALB/c mice as indicated below. Parasites were maintained in Schneider's *Drosophila* medium containing 10% heat-inactivated fetal bovine serum, 50 units/mL penicillin, and 50 $\mu\text{g}/\text{mL}$ streptomycin. *Leishmania major* (NIH173 [MHOM/IR/-/173]) parasites were kindly provided by Dr. Brian Vesely at the Walter Reed Army Institute of Research. These parasites were passaged through female BALB/c mice by injection at the base of the tail and harvested from the lesions that subsequently formed. Lesion-derived amastigotes were transformed into promastigotes by suspension in Schneider's *Drosophila* medium containing 20% heat-inactivated fetal bovine serum, 50 units/mL penicillin, and 50 $\mu\text{g}/\text{mL}$ streptomycin and incubation at 26 $^{\circ}\text{C}$. The species identity of both parasites was confirmed by PCR amplification of the ribosomal internal transcribed spacer region from parasite genomic DNA followed by restriction fragment length polymorphism (RFLP) analysis of the PCR product digested with the restriction enzyme *HaeIII* (Schönián et al. 2003).

Leishmania mexicana in vivo model *In vivo* studies in murine cutaneous leishmaniasis models were performed according to

a protocol approved by The Ohio State University IACUC. Female 7–8 week old BALB/c mice (Envigo, Somerset, NJ) were infected with 10^7 stationary phase, low pass *Leishmania mexicana* promastigotes by subcutaneous injection at the base of the tail. When infected animals bore nodules of at least 2 mm in one direction (at 35 days post infection in this case), animals were randomly sorted into groups of five (www.randomization.com, animals randomized into 1 block), then treated once a day for ten days with either a) AmBisome (20 mg/kg by the intraperitoneal (IP) route), b) PBS vehicle in water (IP), c) topical amphotericin B dissolved in DMSO, or topical amphotericin B dissolved in DMSO after application of microneedle arrays d) 500 μm , e) 750 μm , or f) 1000 μm in length. All topical amphotericin B groups received a dose of 25 mg/kg/day. Nodules caused by infection with parasites were measured twice weekly throughout treatment continuing through three weeks post treatment. Nodules were measured in two dimensions using digital calipers (Fisher Scientific, Hampton, NH) and nodule areas were calculated based on the formula $A = \pi \times r_1 \times r_2$ (the area of an ellipse). After the final measurement was made, animals were euthanized by CO_2 asphyxiation followed by cervical dislocation to confirm death.

Lesions were excised using surgical scissors, weighed, cut into small pieces, and homogenized using the rubber end of a syringe plunger. The homogenate (3 mL in Schneider's *Drosophila* medium containing 10% heat-inactivated fetal bovine serum, 50 units/mL penicillin, and 50 $\mu\text{g}/\text{mL}$ streptomycin) was strained with a cell strainer, centrifuged at $1800 \times g$ for 10 min at 4 $^\circ\text{C}$, and the resulting pellet was resuspended in 400 μL of the medium described above. A limiting dilution assay using the same medium was then performed in duplicate for each sample. In this limiting dilution assay, 200 μL portions of resuspended pellets from tissue homogenates were placed into the first well of a 96-well plate, then tenfold serial dilutions were performed to provide 24 wells for analysis of the parasite burden derived from each duplicate sample. Plates were sealed around the edges with parafilm and then incubated for 7 days at 26 $^\circ\text{C}$. The parasite load was then estimated after seven days of incubation based on the well of greatest dilution that contained viable parasites observed by microscopy. The \log_{10} values of the parasite load in each duplicate were averaged for each animal. The antilog of this average was then divided by the weight of the sample to determine the average parasite load per gram of tissue for each animal.

Leishmania major in vivo model Female 8–9 week old BALB/c mice were infected with 10^7 stationary phase *Leishmania major* promastigotes by subcutaneous injection at the base of the tail as described above for *L. mexicana*. When infected animals bore nodules of at least 2 mm in one direction (at 21 days post infection in this case), animals were randomly sorted into groups of five as mentioned earlier, then

were treated once daily for ten days with either a) AmBisome (20 mg/kg IP), b) 0.9% saline vehicle (IP), c) topical amphotericin B dissolved in DMSO, d) topical amphotericin B dissolved in DMSO after application of microneedle arrays 750 μm in length, or e) application of 750 μm microneedle arrays alone. Both topical amphotericin B groups received a 25 mg/kg/day dose of this drug. Nodules and ulcers caused by infection with parasites were measured in two dimensions as indicated above twice weekly throughout treatment continuing through two weeks post treatment. After two weeks post treatment, early removal criteria were met for a subset of animals due to ulcer size and the experiment was terminated. Animals were euthanized, nodules were removed, tissue homogenates were prepared, and a limiting dilution assay was performed as described above, with the minor modification that the medium used contained 20% heat-inactivated fetal bovine serum rather than 10% heat-inactivated fetal bovine serum. Plates were viewed at days 7 and 11 for the appearance of promastigotes. The results of this limiting dilution assay were identical on days 7 and 11, except that one additional well in one of the duplicates for a single sample was observed as positive on day 11 that was not read as positive on day 7. Parasite load per gram of tissue based on the day 11 observations were then calculated and plotted as described earlier.

Data analyses The treatment effects on nodule area and ulcer area were analyzed using ANOVA with repeated measurements. At different post-infection time points, groupwise comparisons of nodule area and ulcer area were conducted using Tukey's Honestly Significant Difference (HSD) tests. Since values for parasite burden per gram of tissue deviated from a normal distribution, U rank tests were used to compare the medians between any two treatment groups. All statistical tests were two-sided and the significance level was 0.05. Borderline significance was defined as $0.05 < p < 0.1$. R3.3 software (The R project for statistical computing, CRAN.R-project.org) was used in all statistical analyses.

3 Results

Secondary replicas of each microneedle array type were characterized using scanning electron microscopy and energy dispersive x-ray spectroscopy. Scanning electron micrographs of each type of secondary replica are shown in Fig. 1. Arrays of microneedles with a 500 μm nominal height contained 571.8 ± 5.6 μm tall microneedles with a microneedle base diameter of 201.0 ± 2.3 μm , and a microneedle-to-microneedle spacing of 299.9 ± 2.4 μm . Arrays of microneedles with a 750 μm nominal height contained 808.4 ± 4.2 μm tall microneedles with a microneedle base diameter of 161.9 ± 3.6 μm , and a microneedle-to-microneedle spacing of 360.9 ± 4.6 μm . Arrays of microneedles of 1000 μm nominal height contained

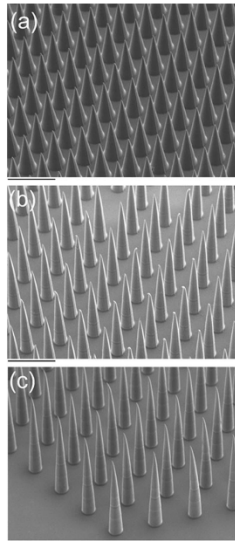
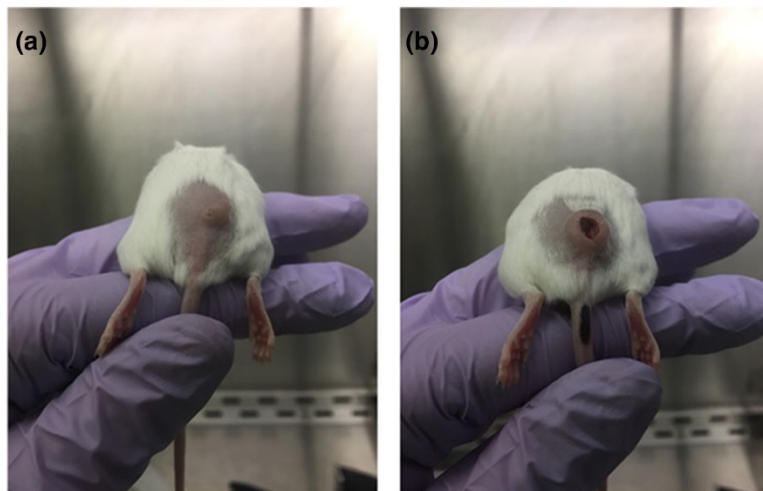


Fig. 1 Scanning electron microscopy images of microneedles with nominal heights of 500 μm (Panel A), 750 μm (Panel B), and 1000 μm (Panel C) obtained at a stage tilt angle of 45°. The scale bars for these images are 500 μm

1044.2 \pm 6.0 μm tall microneedles with a microneedle base diameter of 145.9 \pm 4.1 μm and a microneedle-to-microneedle spacing of 423.1 \pm 9.7 μm . Energy-dispersive x-ray spectroscopy studies of the secondary replicas of the microneedle devices indicated that the microneedle devices with 500 μm nominal height, 750 μm nominal height, and 1000 μm nominal height contained carbon, oxygen, and titanium. In addition, the microneedle device with 750 μm

Fig. 2 Lesions formed at the infection site in animals from vehicle control groups at the end of the 10 day dosing period for *L. mexicana* at 44 days post infection (Panel A) and *L. major* at 30 days post infection (Panel B)



nominal height contained trace amounts of phosphorus and silicon. All of these elements are either found in biological tissues (e.g., carbon, oxygen, and phosphorus) or have good compatibility with human tissues (e.g., silicon and titanium) (Fine et al. 2013, Sidambe 2014). No trace amounts of elements with known toxicity were found.

Comparison of the *L. mexicana* and *L. major* models For both *Leishmania* species, subcutaneous injection of late log phase promastigotes at the base of the tail of female BALB/c mice resulted in the formation of a nodule at the site of inoculation. The progression of infection was more rapid in the *L. major* model compared to the *L. mexicana* model as detailed below. In addition, the nodules resulting from *L. major* infection ulcerated to a much greater degree than in the *L. mexicana* study, allowing for measurement of both nodules and ulcers for the former. A visual comparison of typical lesions observed in the two models is provided in Fig. 2.

Effect of the poke and apply approach in the *L. mexicana* model In an initial experiment in BALB/c mice infected with *L. mexicana*, the effect of topical amphotericin B after the application of microneedle arrays of 500, 750, and 1000 μm nominal length was examined. A topical amphotericin B control group, an IP AmBisome group, and an IP PBS vehicle control group were also included for reference. Average nodule areas ranged from 9 to 15 mm^2 in the six groups at the beginning of treatment and ranged from 13 to 66 mm^2 at the end of the experiment (65 days post infection, Fig. 3A and B). Statistically significant differences in nodule area were observed between both the 500 μm and the 750 μm needle plus amphotericin B groups and the topical amphotericin B group starting on day 49 post infection (Fig. 3A, $p < 0.05$). On days

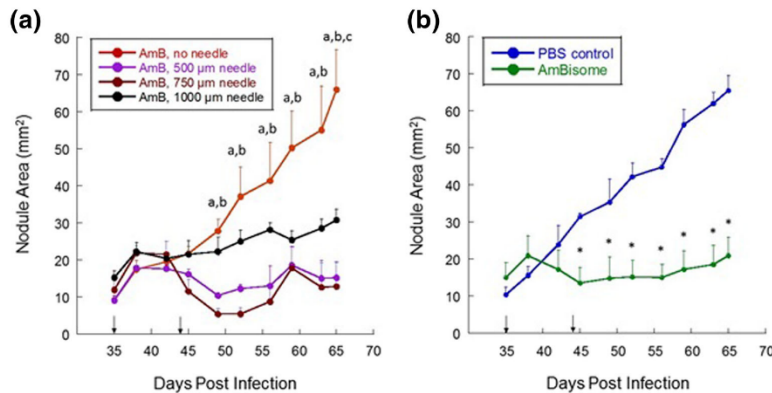


Fig. 3 Nodule measurements for animals infected with *L. mexicana*. **Panel A** – Mice were treated topically at the site of the nodule with a solution of amphotericin B in DMSO (AmB, 25 mg/kg) either in the absence of microneedle application or after the application of microneedle arrays 500 μ m, 750 μ m, or 1000 μ m in nominal length as described in the methods section. Error bars represent the mean \pm standard error of the mean (SEM) ($n = 5$). The letters indicate a significant difference ($p < 0.05$, Tukey's HSD tests) between the amphotericin B no needle group and (a) the amphotericin B 500 μ m needle group, (b) the amphotericin B 750 μ m needle group, or (c) the amphotericin B 1000 μ m needle group using ANOVA with repeated measurements. Differences of borderline significance ($0.05 < p < 0.1$) were observed between the amphotericin B no needle group and the

amphotericin B 1000 μ m needle group on days 59 and 63, (p values = 0.06 and 0.08, respectively), which are not noted on the graph. **Panel B** – In the same experiment, mice received either PBS vehicle or AmBisome (20 mg/kg) by the IP route as outlined in the methods (a separate panel is included for these two groups for the sake of clarity). Error bars represent the mean \pm standard error of the mean (SEM) ($n = 5$). In the PBS control group, one animal became moribund and was euthanized on day 37 post infection, so $n = 4$ for this group from that point on. Asterisks (*) indicate a significant difference ($p < 0.05$, Tukey's HSD tests) between the PBS control group and the AmBisome group at specific post-infection time points. In both panels, the arrows pointing to the x-axis (\downarrow) indicate the days on which treatment began and ended

59 and 63 post infection, differences with borderline significance were observed in nodule area between the 1000 μ m needle plus amphotericin B group and the topical amphotericin B group (p values = 0.06 and 0.08, respectively); these differences were statistically significant ($p < 0.05$) on day 65 post infection (Fig. 3A). Significant differences were observed between the AmBisome group and the PBS control group starting on day 45 post infection ($p < 0.05$, Fig. 3B). As for parasite burden per gram of tissue, significant differences were observed between the 750 μ m needle plus amphotericin B group and the topical amphotericin B group and between the 1000 μ m needle plus amphotericin B group and the topical amphotericin B group (Fig. 4, $p < 0.05$). Differences with borderline significance were found between the 500 μ m needle plus amphotericin B group and the topical amphotericin B group and between the AmBisome group and the PBS control group (Fig. 4, p values = 0.06 and 0.07, respectively). For one lesion in the 500 μ m needle group in this assay, a parasite load of slightly less than 10^4 parasites/g of tissue was measured, by far the lowest parasite load recorded in this experiment. One of the duplicate samples used in this determination had no detectable parasites, resulting in the point that was much lower than the rest.

Effect of the poke and apply approach in the *L. major* model Female BALB/c mice infected with *L. major* were

used to examine the effect of topical amphotericin B after the application of 750 μ m nominal length microneedle arrays in a different model of cutaneous leishmaniasis infection. Groups receiving topical amphotericin B alone and needles alone were also included along with IP AmBisome and IP 0.9% saline vehicle groups for reference. Average nodule areas ranged from 51 to 65 mm^2 in the five groups at the beginning of treatment (21 days post infection) and from 57 to 134 mm^2 one day prior to the end of the experiment (44 days post infection, Fig. 5A). Beginning on day 31 post infection, a statistically significant difference was observed in the area of nodules for the AmBisome group compared to the saline control group ($p < 0.05$). For ulcer area, statistically significant differences were found on days 39 and 44 between the AmBisome group and the saline control group ($p < 0.05$), while differences with borderline significance were found between these two groups on days 35 and 42 ($p = 0.08$ and 0.06, respectively). By day 42 post infection for nodule area and on days 39 and 44 post infection for ulcer area, significant differences were observed between the AmBisome group and all other groups ($p < 0.05$). However, no significant differences were observed between the needle plus amphotericin B group and any of the other non-AmBisome groups. For the limiting dilution assay (Fig. 6), a significant difference in parasite load per gram of tissue was found between the AmBisome group and all other groups ($p < 0.05$), while differences between the

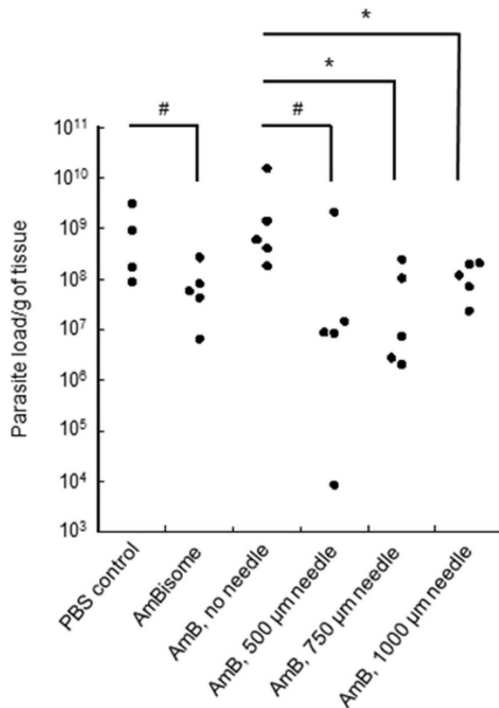


Fig. 4 Limiting dilution assays were performed for the *L. mexicana* experiment in duplicate and parasite load per gram of tissue was determined as described in the methods section. Circles indicate determinations from individual nodules. Groupwise comparisons were conducted using U rank tests. Asterisks (*) indicate differences with statistical significance ($p < 0.05$) and hash symbols (#) indicate differences with borderline significance (p values = 0.06 and 0.07, respectively)

needle plus amphotericin B group and any of the other non-AmBisome groups were not statistically significant.

4 Discussion

For localized cutaneous leishmaniasis, effective topical treatment is preferred to injectable therapy. A safe and effective topical agent to treat cutaneous leishmaniasis could also offer advantages compared to thermotherapy, which can lead to hyperpigmentation and secondary infections, and cryotherapy, which can also lead to secondary infections, can cause “burns,” and results in moderate cure rates (Wolf Nassif et al. 2017). The available topical drug therapy for cutaneous leishmaniasis is based on the aminoglycoside paromomycin; creams containing paromomycin have shown good efficacy in some trials (Ben Salah et al. 2013), but such topical preparations have not been broadly tested against a variety of

Leishmania species and are not widely available (Wolf Nassif et al. 2017; Ben Salah et al. 2014). Given that amphotericin B is a potent antileishmanial drug that is used successfully in treating visceral leishmaniasis, the activity of various amphotericin B formulations has been tested in animal models of cutaneous leishmaniasis. Arabinogalactan conjugates of amphotericin B given subcutaneously to BALB/c mice infected at the base of the tail with *L. major* were effective in delaying lesion appearance in these animals (Golenser et al. 1999). Liposomal amphotericin B containing 1,2-distigmasterylhemisuccinoyl-sn-glycero-3-phosphocholine as one of the liposomal components was as effective as AmBisome in BALB/c mice bearing *L. major* footpad infections when both were given by the IP route (Iman et al. 2017). Intradermal injection of an amphotericin B-polymethacrylic acid (PMA) complex led to healing of *L. major* footpad lesions in both early and established BALB/c mouse infection models (Corware et al. 2011). While these experimental amphotericin B formulations were effective in animal models, all were administered by injection. In a seminal study showing the efficacy of topical paromomycin against cutaneous leishmaniasis, topical amphotericin B (15%) in white soft paraffin was ineffective against *L. major* lesions in BALB/c mice (El-On et al. 1984), while application of lipid formulations of amphotericin B dispersed in 5% ethanol was effective in reducing lesion size in *L. major*-infected CBA mice (Frankenburg et al. 1998). Topical application of the skin penetrable nanoliposomal formulation of amphotericin B termed SinaAmphoLeish caused a temporary reduction in lesion sizes in 129SVE mice infected with *L. mexicana*, but there was no significant difference between the size of lesions in these animals compared to controls at the end of the experiment (Varikuti et al. 2017). No reduction in lesion size was observed in *L. mexicana*-infected BALB/c mice receiving topical SinaAmphoLeish and the control group receiving topical Vaseline (Varikuti et al. 2017). Thus, an effective topical amphotericin B formulation could be of great interest for treating cutaneous leishmaniasis and could compete with paromomycin creams depending on efficacy and cost.

In the present study, AmBisome administered by the IP route was chosen as the treatment control in experiments with both *L. mexicana* and *L. major* based both on the efficacy of this formulation in previous studies (Yardley and Croft 1997; Grogl et al. 2013; Fortin et al. 2014; Caridha et al. 2017) and because the effectiveness of the active pharmaceutical ingredient, amphotericin B, could be compared between the two methods of administration. The effect of AmBisome on nodule area in both studies and on ulcer area in the *L. major* study was significant compared to the vehicle control group (Fig. 3B, Fig. 5). A statistically significant reduction in tissue parasite burden was observed between the AmBisome and vehicle control groups in the *L. major* study (Fig. 6), while borderline significance was observed between these two groups

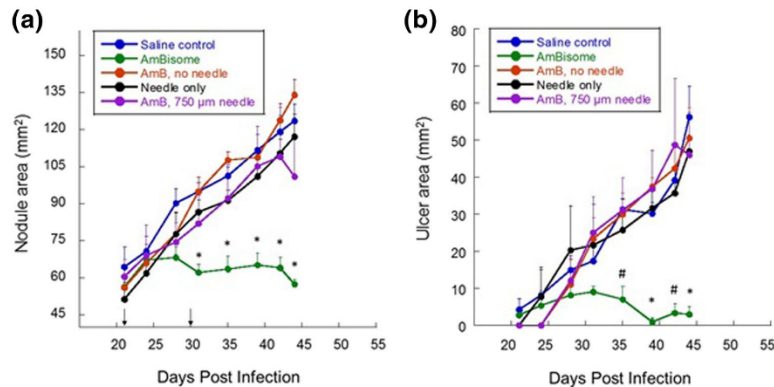


Fig. 5 Measurements of nodule area (*Panel A*) and ulcer area (*Panel B*) for animals infected with *L. major*. Mice were treated topically at the site of the nodule either with microneedles alone or with a solution of amphotericin B in DMSO (AmB, 25 mg/kg) either with or without application of microneedle arrays 750 µm in length, with AmBisome (20 mg/kg) by the IP route, or with IP 0.9% saline vehicle as described in the methods section. Error bars represent the mean \pm standard error of the mean (SEM) ($n = 5$). Asterisks (*) indicate significant differences ($p < 0.05$, Tukey's HSD tests) between the saline control group and the

AmBisome group at specific post-infection time points. The hash symbol (#) indicates a difference with borderline significance ($p = 0.08$, 0.06) at days 35 and 42 post infection, respectively. Additional details regarding significant differences in area between the AmBisome groups and the other groups is provided in the text but is not shown here for clarity. The arrows pointing to the x-axis (\downarrow) in *Panel A* indicate the days on which treatment began and ended; these arrows are not shown in *Panel B*. In the AmB, 750 µM group, one animal met early removal criteria prior to the last measurement due to a large, ulcerated lesion

in the *L. mexicana* study (Fig. 4). Although parasite burden was not measured in their study, Yardley and Croft demonstrated that complete resolution of lesions was initially observed in 2/5 *L. major*-infected BALB/c mice treated with 25 mg/kg AmBisome every other day for six days by the IV route, although recurrence of lesions eventually occurred (Yardley and Croft 1997). Fortin et al. observed a statistically significant reduction in ulcer size and parasite burden when *L. major*-infected animals were treated for ten consecutive days with 25 mg/kg AmBisome administered IP when ulcer area reached ~ 50 mm² (Fortin et al. 2014). In BALB/c mice infected with *L. major*, the administration of IP AmBisome at 12.5 mg/kg and 25 mg/kg for ten consecutive days resolved lesions in 4/5 and 5/5 animals, respectively, when treatment began after lesion area reached an average of 50 mm² (Caridha et al. 2017). Thus, we believe that our results with AmBisome are consistent with previous studies in murine cutaneous leishmaniasis models.

In the *L. mexicana* study, nodule area was reduced in animals receiving topical amphotericin B after microneedle application (Fig. 3A) and differences in parasite burden per gram of tissue were noted between the needle plus amphotericin B groups and the topical amphotericin B alone group (Fig. 4). Overall, the 500 µm and 750 µm needles outperformed the 1000 µm needles in terms of nodule suppression ($p < 0.05$) but not in terms of parasite burden ($p > 0.1$). Cutaneous leishmaniasis is caused by infection of macrophages in the dermal layer of the skin (Grevelink and Lerner 1996; Venkataram et al. 2001). To the best of our knowledge, the depth of the

dermal layer in mice infected with *L. mexicana* or any other cutaneous leishmaniasis species has not been measured, but the depth of the dermal layer in female mice has been estimated to be approximately 200 µm (Calabro et al. 2011; Wei et al. 2017). Since the 1000 µm needles were inferior in performance to the shorter needles in terms of nodule suppression, these needles may have been too long to optimally target the parasites in the dermal layer with amphotericin B.

In the *L. major* study, no significant differences were observed in nodule or ulcer area between the needle plus topical amphotericin B group and the topical amphotericin B alone group or between the needle plus topical amphotericin group and the needle alone group (Fig. 5). Likewise, differences between the amphotericin B plus needle group and the non-AmBisome groups were not significant in the *L. major* limiting dilution assay (Fig. 6). Several explanations are possible for the more favorable response to the poke and apply approach in the *L. mexicana* model compared to the *L. major* model: 1) *L. major* infections developed more rapidly than *L. mexicana* infections, resulting in larger nodules (compare Fig. 3 with Fig. 5). *L. major* infections disseminate in susceptible BALB/c mice (Schilling and Glaichenhaus 2001; Laskay et al. 1997), likely making it more difficult for the microneedle plus amphotericin B treatment to influence nodule development. In the clinical treatment of cutaneous leishmaniasis, topical approaches are not recommended for treating cutaneous infections that consist of large or multiple lesions or that have spread to the lymphatic system (Blum et al. 2014). Despite its widespread use as a cutaneous

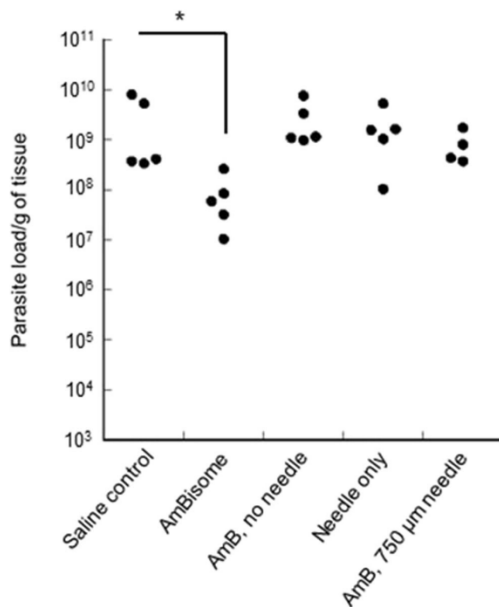


Fig. 6 Limiting dilution assays were performed for the *L. major* experiment in duplicate and parasite load per gram of tissue was determined as described in the methods section. Circles indicate determinations from individual nodules. The asterisk (*) indicates a significant difference in parasite load per gram of tissue between the saline control and AmBisome groups ($p < 0.05$, U rank test). Significant differences in parasite load per gram of tissue were also observed between the AmBisome group and all other non-AmBisome groups ($p < 0.05$); this is not shown for clarity

leishmaniasis model, *L. major* infections in BALB/c mice may more closely resemble human visceral leishmaniasis than cutaneous leishmaniasis in humans (Mears et al. 2015). In contrast, AmBisome delivered by the IP route is more likely to interfere with the spread of infection due to its systemic availability. While BALB/c mice infected subcutaneously with *L. mexicana* also acquire visceral infections, the development of these infections is slower than with *L. major* (Torrentera et al. 2002), as observed here. 2) The hexagonal needle arrays used for these experiments measured approximately 10 mm in diameter. During the course of treatment, the area of some *L. major* nodules surpassed the area of the microneedle arrays and continued to expand. This is in contrast with the *L. mexicana* nodules, which remained smaller in area than the microneedle arrays for the duration of treatment. Thus, the topical treatment with amphotericin B after the application of microneedles may have been more effective for the smaller nodules. 3) While *L. mexicana* nodules were essentially smooth with little ulceration over the course of the study, *L. major* nodules developed ulcers that formed scabs and eventually presented an uneven surface (Fig. 2). Both the

accumulation of necrotic tissue (Caridha et al. 2017) and changes to the surface of the lesion in the *L. major* model may have affected the delivery of topical amphotericin B after microneedle application.

Differences in experimental design between the *L. mexicana* and *L. major* studies reported here merit explanation. Phosphate buffered saline was the isotonic IP injection control in the *L. mexicana* experiment; USP saline was used in this role in the *L. major* study upon advisement by the IACUC that USP grade reagents are preferred. Separate needle alone groups were not included in the *L. mexicana* study because of the time and expense of preparing twice as many needle arrays and the need to limit the number of animals in this experiment to a manageable size while still exploring different needle lengths. A needle alone control was included in the *L. major* study, where the 750 µm needle length that appeared to provide optimal activity in the *L. mexicana* experiment (although this cannot be shown statistically) was employed. As detailed above, the lack of efficacy of the approach in the *L. major* model is likely due to the more rapid progression of infection. Considering that this is the first report of microneedle delivery for treating cutaneous leishmaniasis, additional studies are needed to assess the full potential of this approach.

5 Conclusions

A statistically significant reduction of nodule size and parasite burden was observed in mice infected with *L. mexicana* after applying microneedle arrays followed by topical amphotericin B. While this approach was not effective in the *L. major* study described here, the more rapid progression and dissemination of infection and the development of ulcers may help to explain the lack of efficacy of the microneedle plus topical amphotericin B approach against *L. major*. While the efficacy of the microneedle approach in the *L. mexicana* model provides proof of concept for microneedle delivery of amphotericin B to treat cutaneous leishmaniasis, efficacy in a range of models is needed to identify new approaches for broad treatment of this disease endemic to different parts of the world. Other microneedle-based approaches that avoid a DMSO vehicle and that are capable of directly delivering high levels of the drug to the site of infection are being explored as candidate therapeutic strategies against cutaneous leishmaniasis.

Acknowledgments The authors would like to acknowledge support from the National Institutes of Health (R21 AI117748 02). We thank Abhay Satoskar and Chad Rappleye for helpful discussions and Ben Russell for assistance with the animal studies and for authenticating the *Leishmania* parasites. We thank Chuck Mooney and the Analytical Instrumentation Facility for assistance with scanning electron microscopy and energy dispersive X-ray spectroscopy.

Publisher's Note Springer Nature remains neutral with regard to jurisdictional claims in published maps and institutional affiliations.

References

- M. Ameen, *Clin. Exp. Dermatol.* **35**, 699 (2010)
- N.E. Aronson, G.W. Wortmann, S.C. Johnson, J.E. Jackson, R.A. Gasser Jr., A.J. Magill, T.P. Endy, P.E. Coyne, M. Grogl, P.M. Benson, J.S. Beard, J.D. Tally, J.M. Gambel, R.D. Kreutzer, C.N. Oster, *Clin. Infect. Dis.* **27**, 1457 (1998)
- N.E. Aronson, G.W. Wortmann, W.R. Byrne, R.S. Howard, W.B. Bernstein, M.A. Marovich, M.E. Polhemus, I.K. Yoon, K.A. Hummer, R.A. Gasser Jr., C.N. Oster, P.M. Benson, *PLoS Negl. Trop. Dis.* **4**, e628 (2010)
- A.U. Bari, S.B. Rahman, *J. Coll. Physicians Surg. Pak.* **13**, 471 (2003)
- A. Ben Salah, N. Ben Messaoud, E. Guedri, A. Zaatour, N. Ben Alaya, J. Bettaieb, A. Gharbi, N. Belhadj Hamida, A. Boukthir, S. Chlif, K. Abdelhamid, Z. El Ahmadi, H. Louzir, M. Mokni, G. Morizot, P. Buffet, P. Smith, K. Kopydlowski, M. Kreishman-Deitrick, K. Smith, C. Nielsen, D. Ullman, J. Norwood, G. Thorne, W. McCarthy, R. Adams, R. Rice, D. Tang, J. Berman, J. Ransom, A. Magill, M. Grogl, *N. Engl. J. Med.* **368**, 524 (2013)
- A. Ben Salah, A. Zaïtour, N. Ben Messaoud, A. Kidar, P. Smith, K. Kopydlowski, M. Kreishman-Deitrick, C. Nielsen, A. Novitt-Moreno, J. Ransom, G. Morizot, M. Grogl, P. Buffet, *PLoS Negl. Trop. Dis.* **8**, e2749 (2014)
- J. Blum, P. Buffet, L. Visser, G. Harms, M. Bailey, E. Caumes, J. Clerinx, P. van Thiel, G. Morizot, C. Hatz, T. Dorlo, D. Lockwood, *J Travel Med* **21**, 116 (2014)
- K. Calabro, A. Curtis, T. J-R Galarneau, I.J.B. Krucker, *J. Biomed. Opt.* **16**, 011008 (2011)
- D. Caridha, S. Parriot, T. Hudson, T. Lang, F. Ngundam, S. Leed, J. Sena, M. Harris, M. O'Neil, R. Sciotti, L. Read, H. Lecoet, M. Hickman, M. Grogl, *Antimicrob. Agents Chemother.* **61**, e02048 (2017)
- G. Carneiro, M.G. Aguiar, A.P. Fernandes, L.A. Ferreira, *Expert Opin Drug Deliv* **9**, 1083 (2012)
- K. Corware, D. Harris, I. Teo, M. Rogers, K. Naresh, I. Müller, S. Shaunak, *Biomaterials* **32**, 8029 (2011)
- C.V. David, N. Craft, *Dermatol. Ther.* **22**, 491 (2009)
- J. El-On, G.P. Jacobs, E. Witznum, C.L. Greenblatt, *Antimicrob. Agents Chemother.* **26**, 745 (1984)
- D. Fine, A. Grattoni, R. Goodall, S.S. Bansal, C. Chiappini, S. Hosali, A.L. van de Ven, S. Srinivasan, X. Liu, B. Godin, L. Brousseau, I.K. Yazdi, J. Fernandez-Moure, E. Tasciotti, H.-J. Wu, Y. Hu, S. Klemm, M. Ferrari, *Adv Health Mater* **2**, 632 (2013)
- A. Fortin, D. Caridha, S. Leed, F. Ngundam, J. Sena, T. Bosschaerts, S. Parriott, M. Hickman, T. Hudson, M. Grogl, *PLoS Negl. Trop. Dis.* **8**, e3144 (2014)
- S. Frankenburg, D. Glick, S. Klaus, Y. Barenholz, *Antimicrob. Agents Chemother.* **42**, 3092 (1998)
- F. Frézard, C. Demicheli, *Expert Opin Drug Deliv* **7**, 1343 (2010)
- S.D. Gittard, A. Ovsianikov, N.A. Monteiro-Riviere, J. Lusk, P. Morel, P. Minghetti, C. Lenardi, B.N. Chichkov, R.J. Narayan, *J. Diabetes Sci. Technol.* **3**, 304 (2009)
- S.D. Gittard, A. Ovsianikov, B.N. Chichkov, A. Doraiswamy, R.J. Narayan, *Expert Opin Drug Deliv* **7**, 1 (2010)
- J.S. Glasser, C.K. Murray, *Am. J. Trop. Med. Hyg.* **84**, 566 (2011)
- J. Golenser, S. Frankenburg, T. Ehrenfreund, A. Domb, *Antimicrob. Agents Chemother.* **43**, 2209 (1999)
- S. Grevelink, E. Lerner, *J. Am. Acad. Dermatol.* **34**, 257 (1996)
- M. Grogl, M. Hickman, W. Ellis, T. Hudson, J. Lazo, E. Sharlow, J. Johnson, J. Berman, R. Sciotti, *Am. J. Trop. Med. Hyg.* **88**, 216 (2013)
- S. Henry, D.V. McAllister, M.G. Allen, M.R. Prausnitz, *J. Pharm. Sci.* **87**, 922 (1998)
- J.A. Hervás, A. Martín-Santiago, D. Hervás, E. Rojo, A. Mena, V. Rocamora, J. Dueñas, *Pediatr. Infect. Dis. J.* **31**, 97 (2012)
- M. Iman, Z. Huang, S.H. Alavizadeh, F.C. Szoka, M.R. Jaafari, *Antimicrob. Agents Chemother.* **61**, e02525 (2017)
- R.L. Jacobson, *Vector-Borne and Zoonotic Diseases* **11**, 247 (2011)
- T. Laskay, I. Wittmann, A. Diefenbach, M. Rollinghoff, W. Solbach, *J. Immunol.* **158**, 1246 (1997)
- L. López, M. Robayo, M. Vargas, I.D. Vélez, *Trials* **13**, 58 (2012)
- A. Matheson, R. Williams, M.S. Bailey, *J. R. Army Med. Corps* **158**, 221 (2012)
- E. Mears, F. Modabber, R. Don, G. Johnson, *PLoS Negl. Trop. Dis.* **9**, e0003889 (2015)
- V. Mosimann, A. Neumayr, D.H. Paris, J. Blum, *Acta Trop.* **182**, 246 (2018)
- H.W. Murray, J.D. Berman, C.R. Davies, N.G. Saravia, *Lancet* **366**, 1561 (2005)
- R. Neghina, A.M. Neghina, *Scand. J. Infect. Dis.* **42**, 563 (2010)
- S. Schilling, N. Glaichenhaus, *Infect. Immun.* **69**, 1212 (2001)
- G. Schönián, A. Nasereddin, N. Dinse, C. Schweynoch, H. Schallig, W. Presber, C. Jaffe, *Diagn. Microbiol. Infect. Dis.* **47**, 349 (2003)
- A.T. Sidambe, *Materials* **7**, 8168 (2014)
- M. Solomon, F. Pavlotsky, E. Leshem, M. Ephros, H. Trau, E. Schwartz, *J. Eur. Acad. Dermatol. Venereol.* **25**, 973 (2011)
- F.A. Torrentera, M. Lambot, J. Laman, M. Van Meurs, R. Kiss, J. Noël, Y. Carlier, *Am. J. Trop. Med. Hyg.* **66**, 273 (2002)
- E. Torres-Guerrero, M.R. Quintanilla-Cedillo, J. Ruiz-Esmenjaud, R. Arenas, *Fl000Res* **6**, 750 (2017)
- S. Varikuti, S. Oghumu, N. Saljoughian, M. Pioso, B. Sedmak, A. Khamesipour, A. Satoskar, *Acta Trop.* **173**, 102 (2017)
- M. Venkataram, M. Moosa, L. Devi, *Indian J Dermatol Venereol Leprol* **67**(294) (2001)
- J.C.J. Wei, G.A. Edwards, D.J. Martin, H. Huang, M.L. Crichton, M.A.F. Kendall, *Sci Report* **7**, 15885 (2017)
- P. Wolf Nassif, T. De Mello, T. Navasconi, C. Mota, I. Demarchi, S. Aristides, M. Lonardoni, J. Teixeira, T. Silveira, *Parasitology* **144**, 995 (2017)
- V. Yardley, S. Croft, *Antimicrob. Agents Chemother.* **41**, 752 (1997)

CHAPTER 4 - Two-photon polymerization of polyethylene glycol diacrylate scaffolds with riboflavin and triethanolamine used as a water-soluble photoinitiator

Alexander K. Nguyen¹, Shaun D. Gittard², Anastasia Koroleva², Sabrina Schlie², Arune Gaidukeviciute², Boris N. Chichkov², and Roger J. Narayan¹

1. UNC/NCSU Joint Department of Biomedical Engineering, North Carolina State University, Raleigh, NC
2. Nanotechnology Department, Laser Zentrum Hannover e. V., Hannover, Germany

Full Reference: Nguyen, A.K.; Gittard, S.D.; Koroleva, A.; Schlie, S.; Gaidukeviciute, A.; Chichkov, B.N.; Narayan, R.J. Two-photon polymerization of polyethylene glycol diacrylate scaffolds with riboflavin and triethanolamine used as a water-soluble photoinitiator. *Regen Med* **2013**, *8*, 725-738, doi:10.2217/rme.13.60.

Abstract

Aim: In this study, the suitability of a mixture containing riboflavin (vitamin B2) and triethanolamine (TEOHA) as a novel biocompatible photoinitiator for two-photon polymerization (2PP) processing was investigated. **Materials & methods:** Polyethylene glycol diacrylate was crosslinked using Irgacure® 369, Irgacure 2959 or a riboflavin–TEOHA mixture; biocompatibility of the photopolymer extract solutions was subsequently assessed via endothelial cell proliferation assay, endothelial cell viability assay and single-cell gel electrophoresis (comet) assay. Use of a riboflavin–TEOHA mixture as a photoinitiator for 2PP processing of a tissue engineering scaffold and subsequent seeding of this scaffold with GM-7373 bovine aortic endothelial cells was also demonstrated.

Results: The riboflavin–TEOHA mixture was found to produce much more biocompatible scaffolds than those produced with Irgacure 369 or Irgacure 2959.

Conclusion: The results suggest that riboflavin is a promising component of photoinitiators for 2PP fabrication of tissue engineering scaffolds and other medically relevant structures (e.g., biomicroelectromechanical systems).

Introduction

Two-photon polymerization (2PP) is a rapid prototyping approach in which a 3D computer-aided design model is used to direct selective curing of a photosensitive material by means of nearly simultaneous absorption of ultrashort (e.g., femtosecond) laser pulses. This approach provides many possibilities for fabricating 3D microscale structures, including biomicroelectromechanical systems [121], microfluidic devices [122], biomedical implants [123], microneedles for transdermal drug delivery [124] and scaffolds for tissue engineering [125-134].

Control of the cell environment (e.g., spatial constraints, mechanical properties and chemical factors) is essential to the field of tissue engineering and, in particular, the fabrication of niches for stem cell differentiation. The flexibility of 2PP in creating structures with well-controlled geometries and feature sizes ranging from below one micrometer to hundreds of micrometers makes this technique particularly appealing for fabrication of 3D tissue engineering scaffolds [41, 65, 66, 125-135]. In addition, patient-specific scaffolds for tissue engineering may be created using 2PP from patient imaging data (e.g., microcomputed tomography data or MRI data) [127].

Biocompatible materials (e.g., photoinitiators) that are compatible with 2PP are necessary to improve the acceptance of this approach for fabrication of 3D tissue engineering scaffolds. For example, Ovsianikov et al. evaluated the cytotoxicity of several 2PP photoinitiators [136]. Aqueous extracts of polyethylene glycol (PEG) diacrylate (PEGda) formulations with molecular

weights of 302 and 742 were polymerized using three photoinitiators: Michler's ketone; Irgacure® 369 and Irgacure 2959 (BASF Schweiz AG, Switzerland). The photopolymerized materials contained water-soluble molecules that were toxic to L929 fibroblasts. Aging the PEGda material with a molecular weight of 742 that had been polymerized with Irgacure 2959 in water for a period of 7 days reduced the amount of the watersoluble toxic components to a level such that no cytotoxic effect was noted. Arcaute et al. found that PEG polymerized with the photoinitiators Irgacure 2959 and 2-hydroxy-2-methyl-1-phenyl-1-propanone was cytotoxic at a photoinitiator concentration of 0.5%; toxicity was noted to increase with exposure time and photoinitiator concentration [137]. Owing to photoinitiator leaching, the authors noted that a concentration of 0.5% Irgacure 2959 may be utilized without inducing severe cytotoxicity. Williams et al. examined the cytotoxicity of Irgacure 184, Irgacure 2959 and Irgacure 651 against a variety of cell lines that are utilized in tissue engineering, including chondrocytes, corneal epithelial cells, mesenchymal stem cells, osteoblasts and embryonic germ cells [138]. At concentrations below 0.1% Irgacure 2959 was noted to be well tolerated by all cell types; on the other hand, the other two evaluated photoinitiators were toxic for all cell types at a concentration of 0.02%. In addition, they suggested that rapidly dividing cells were more sensitive to the photoinitiators. Rouillard et al. noted significant cytotoxicity (i.e., viability under 70%) for an alginate–chondrocyte hydrogel containing a methacrylate-modified alginate that had been crosslinked using Irgacure 2959 [139]. It is important to note that cytotoxicity was assessed by means of proliferation rate or LIVE/DEAD® (Invitrogen, CA, USA) staining studies in these studies.

Potential sources of biocompatible photoinitiators include free-radical-generating molecules that are naturally found in biological systems. Riboflavin, also known as vitamin B2,

is a molecule that has potential use as a biological photoinitiator. Flavins have the ability to easily undergo reduction–oxidation reactions, including transport of electrons by FADH₂ in the electron transport chain of cellular respiration. Riboflavin is excited by photon absorption and can form either the singlet- or triplet-excited states. It should be noted that the triplet state exhibits a longer lifetime in solution and, as such, is more available for molecular interactions than the singlet state. In a nitrogen-purged solution, triplet riboflavin was found to exist for several microseconds after excitation. On the other hand, singlet riboflavin was only observed for 20 ns after excitation [140]. Triplet riboflavin quenched by a monomer was not found to result in polymerization; however, the addition of triethanolamine (TEOHA) as a coinitiator did result in polymerization [53]. It is believed that triplet state riboflavin is oxidized by TEOHA to form the semioxidized radical of riboflavin and the semireduced amine. Donation of a proton from the amine to the riboflavin radical forms the long-lived neutral amine radical, which was found to initiate polymerization.

Several previous studies have reported on the use of riboflavin as a photoinitiator for polymerization of polymers. For example, Orellana et al. used riboflavin and a coinitiator, TEOHA, for crosslinking 2-hydroxyethyl methacrylate (HEMA) [53]. The polymerization rate was found to be highest for a TEOHA concentration of 0.01 M. Encinas et al. investigated crosslinking of HEMA with riboflavin and several amine coinitiators; their experiments indicated that TEOHA was one of the most efficient of the evaluated coinitiators [141]. In these studies, HEMA was polymerized using a mercury lamp with a center wavelength of 366 nm. Turunen et al. reported on use of flavin mononucleotide as a photosensitizer in pico- and femto-second laser-induced photocrosslinking of avidin, bovine serum albumin and biotinylated bovine serum albumin [142].

Riboflavin has been considered for use in several other biomedical applications. For example, Husain and Naseem demonstrated that photochemically activated riboflavin is able to counteract the effect of cisplatin, a chemotherapeutic agent that induces oxidative DNA strand breakage, in murine epidermal keratinocytes [143]. A combination of riboflavin and UV light treatment was shown to be effective for inactivating pathogens in platelet concentrates [144]. Riboflavin has also been used to induce crosslinking of collagen within the cornea for the treatment of keratoconus [145-148]. The therapeutic use of riboflavin in high doses or with UV exposure has already been shown to be compatible with living organisms. As such, addition of riboflavin to a tissue engineering scaffold is hypothesized to not result in a significant change in biocompatibility.

Production of tissue engineering scaffolds from PEGda by 2PP has been demonstrated by several groups. Liao et al. noted that PEGda hydrogels are appropriate scaffold materials for some biomedical applications (e.g., vocal fold applications) because their mechanical properties can be altered by modifying the concentration and/or molecular weight [149]. Bulick et al. and Munoz-Pinto et al. noted that PEGda is commonly utilized as a 'model' scaffold material for growth of fibroblast-like cells or smooth muscle-like cells [150, 151]. Bulick et al. developed PEGda scaffolds for tissue engineering that contained smooth muscle cells, in which the crosslinking of PEGda and the slow degradation rate of PEGda facilitated cell immobilization within the scaffold [150].

Ovsianikov et al. produced porous 3D tissue engineering scaffolds using PEGda by 2PP [130]. A ring-shaped scaffold was produced by 2P, which was then seeded with endothelial cells along the interior edge and smooth muscle cells along the outer edge by laser-induced forward transfer. Gittard reported using 2PP of PEGda to produce a 6 mm-long tubular tissue engineering

scaffold for vascular applications [133, 135]. Musumeci et al. recently encapsulated chondrocytes in PEGda hydrogels and showed that the encapsulated cells expressed lower levels of the apoptosis effector caspase-3 than control cartilage after 5 weeks [152]. In addition, increased cell growth, extracellular matrix formation and hyaline cartilage production were noted in the PEGda-cultured chondrocytes after 5 weeks. Lin et al. noted that PEGda hydrogels may be useful for cartilage tissue engineering since cells are embedded by the crosslinked material; chondrocyte photoencapsulation for cartilage tissue engineering has been shown using in vitro and in vivo studies [153]. Use of PEGda scaffolds for encapsulation of human mesenchymal stem cells has also been demonstrated [154].

As noted by Weiss et al., PEGda is a biologically inert material [131]. PEGda hydrogels may be useful as model materials for tissue engineering since they do not exert a biological effect on cells [154]. An unmodified PEGda hydrogel scaffold provides the encapsulated cells with a nonadhesive environment [155]. Although PEG resists cell attachment in its unmodified form, cell responses can be obtained via attachment of biologically active molecules [131]. For example, Lee et al. controlled cell growth within a tissue engineering scaffold by patterning conjugated RGD, a cell adhesion peptide, in collagenase sensitive poly(ethylene glycol-co-peptide) diacrylate hydrogels by 2PP [156]. Procedures exist to modify the PEG backbone with groups to facilitate cell adhesion (e.g., RGD sequences) or with groups that enable photopolymerization (e.g., the diacrylate group used in this study) [156].

Degradation of PEGda hydrogels is commonly associated with hydrolytic cleavage of ester bonds between the crosslinking units and the backbone; oxidation of the ether backbone may also play a role [149, 157]. Xin et al. performed an in vitro study involving degradation of PEGda in phosphate buffered saline solution and found that PEGda undergoes a small but

significant amount of degradation; polymers with less photocrosslinking were shown to undergo higher degradation [158]. PEGda hydrogels stored in phosphate-buffered saline over a period of 8 weeks showed a statistically significant but small change in Young's modulus and compressive strength. Browning et al. noted that the ester linkages in PEGda undergo slow hydrolytic cleavage within the body, which may occur within months to years after implantation [157]. They noted no significant change in swelling of PEGda hydrogels within phosphate buffered saline solution over 6 weeks; however, a linear regression analysis was able to reveal an increase in swelling over time. On the other hand, they observed complete dissolution of PEGda hydrogels by 80 h in an 'accelerated' (0.1 M) NaOH solution that was intended to reflect longer implantation times. As noted by Browning et al., PEGda degradation products, similar to all synthetic materials, are subject to protein adsorption and macrophage activation [157].

In addition to use as a tissue engineering scaffold material, PEGda hydrogel structures may have other in vivo applications. For example, Browning et al. noted that PEGda may find use in wound dressings and vascular graft coatings [158]. In addition, PEGda is an appropriate material for use as a filler material for soft tissue restoration since it is low in cost, nonpyrogenic and nonallergenic [159]. It can also be injected into a small tissue defect and molded in place to form a solid structure. Patel et al. showed that PEGda is able to withstand forces that are associated with use as a soft tissue filler [159].

In this study, we investigated the suitability of using a riboflavin-TEOHA mixture as a photoinitiator for producing PEGda tissue engineering scaffolds. The ability of this riboflavin-based mixture to initiate 2PP was evaluated by comparing the laser parameters and the scaffold morphology produced with the novel photoinitiator with scaffolds produced with the commercial photoinitiators Irgacure 369 and Irgacure 2959. According to ISO10993 guidelines,

biocompatibility was examined relative to conventionally produced scaffolds by using a single-cell gel electrophoresis (comet) assay to assess cytotoxicity as well as by measuring GM-7373 bovine aortic endothelial cell (Leibniz Institute DSMZ, Germany) proliferation and viability in the various polymer extract solutions [160]. Finally, LIVE/DEAD staining was performed on a model riboflavin–TEOHA initiated PEGda scaffold that had been seeded with GM-7373 cells to directly determine the suitability of this material for cell culture.

Materials and Methods

Photopolymers Scaffolds were produced from SR610 (Sartomer, France), a PEGda material that has a molecular weight of 742 g/mol; this material has previously been used to create tissue engineering scaffolds and small-scale medical devices [129, 143]. 4-(2-hydroxyethoxy) phenyl-(2-hydroxy-2-propyl)ketone (BASF Schweiz AG), more commonly known as Irgacure 2959, and 2-benzyl-2-dimethylamino-1-(4-morpholinophenyl)-butanone (BASF Schweiz AG), more commonly known as Irgacure 369, were used as comparison photoinitiators.

A novel photopolymer was developed that contains PEGda as the polymer, riboflavin as the photoinitiator and TEOHA as the coinitiator. An aqueous solution of 4.2 mM riboflavin-5-phosphate (Sigma-Aldrich, MO, USA) and 4.2 M TEOHA (Sigma-Aldrich) was prepared; the solution was purged with nitrogen to minimize oxygen content. A photopolymer solution with 200 μ M riboflavin and 200 mM TEOHA was produced by combining 50 μ l of the concentrated riboflavin–TEOHA solution with every milliliter of the final photopolymer volume. For example, a 50% PEGda mixture was made by combining 4 ml of PEGda, 3.800 ml of distilled water, and 0.200 ml of the riboflavin–TEOHA solution. The resulting mixture was purged with

nitrogen and kept in darkness or in yellow light. The PEGda dilutions examined in this study contained 50 and 66% PEGda by volume.

UV-Visible Spectroscopy In order to determine an optimal laser wavelength for polymerization, UV-visible (UV-Vis) spectroscopy was utilized to obtain absorption spectra of the photoinitiator and the photopolymer. The absorbance spectra of 66% PEGda–riboflavin–TEOHA, pure PEGda, riboflavin, the riboflavin–TEOHA mixture and the various films were collected from 190 to 1000 nm using SpectraSuite software (Ocean Optics, Germany). The emission spectra of a UV curing chamber (PEQLAB Biotechnologie GmbH, Erlangen, Germany) used for bulk polymerization of material were collected using an HR2000+ spectrophotometer (Ocean Optics, FL, USA). In addition, free-standing films of polymerized 50% PEGda–riboflavin–TEOHA and PEGda containing 2% wt Irgacure 369 or 2% wt Irgacure 2959 were measured to determine the transmittance of the polymerized material to the postcuring light. Three 140- μm glass coverslips were used as spacers to control the film thickness. In order to normalize the transmittance spectra, the actual thickness was determined directly after UV-Vis spectrometry by means of optical microscopy; the average thickness was noted to be approximately 425 μm . The thickness values were used to normalize the transmission spectra using Beer's Law to a 500- μm path length, the maximum depth at which double-sided illumination within the mirrored UV curing chamber would have to reach.

2PP of structures Scaffolds were produced by 2PP of a 66 or 50% PEGda–riboflavin–TEOHA solution using a 780-nm ChameleonTMTi:sapphire femtosecond laser (Coherent, CA, USA); a 140 fs pulse and a 80-MHz repetition rate were used in this study. Parameter search arrays were fabricated with the 66% PEGda–riboflavin–TEHOA solution; these arrays were compared with undiluted PEGda solutions containing 2% wt Irgacure 369 or 2% wt Irgacure

2959 that were polymerized using a 780-nm femtosecond laser and 515-nm light from a frequency-doubled Yb:glass laser (1 MHz, 200 fs, High Q Laser, Austria), respectively.

The unpolymerized resin was placed between two glass coverslips in a 6-mm diameter by 1-mm tall polydimethylsiloxane ring. 2PP processing of the resin was performed by scanning the laser, which was focused by a 20× Epiplan objective (Carl Zeiss AG, Jena, Germany) within this resin reservoir. Lateral scanning of small-scale components (e.g., individual cylinders) was achieved using a hurrySCAN® galvano scan head (Scanlab, Germany). The height of the laser focus was adjusted using a C-843 linear translation stage (PhysikInstrumente, Germany); two additional linear stages were used to control lateral motion from one component in the structure to the next. Custom written software was used to produce cylinders with an inner diameter of 100 μm , an outer diameter of 120 μm and a height of 100 μm . The individual cylinders were placed in a hexagonal honeycomb configuration with nine cylinders composing the outer wall and seven cylinders composing the inner wall; the total width of the structure was 2.2 mm. Array cylinders had larger dimensions, with inner diameters of 160 μm , outer diameters of 200 μm and heights of 50 μm . In the case of the 515-nm laser system, rectangular prisms in the ‘woodpile’ configuration (i.e., linear arrays in which the line direction alternates from one layer to the next layer) were produced with a 100- μm side length and a 50- μm height. Production of the structures proceeded in a layer-by-layer fashion, in which each layer was composed of concentric circles or straight lines that were separated by a distance of 2 μm . Each line or circle was scanned five times at a linear speed of 2.50 mm/s for scaffold elements or at 1.25, 2.50 or 3.75 mm/s for structures in the parameter search array before moving onto the next component. After a complete layer was exposed, the sample was moved 5 μm away from the objective before starting the next layer. The average laser power was controlled by a liquid crystal polarizer in the

case of the 780-nm laser or a motorized quarter wave plate in the case of the 515-nm laser. The minimum average laser power was selected by finding a power close to the 2PP threshold and then increasing the power in regular intervals. Power levels of 90, 128, 167, 212 and 256 mW were used for the Irgacure 369 containing solutions and 193, 244, 292, 343 and 403 mW were used for the 66% PEGda–riboflavin–TEOHA-containing solutions. Irgacure 2959 solutions were polymerized with 515-nm light and are thus on a different scale. Average laser powers of 60, 70, 80, 90 and 100 mW were used in this case.

The parameter search arrays were imaged before development in order to eliminate the effect of shrinkage or swelling during imaging and to prevent the loss of underpolymerized structures. Scaffolds were developed by placing the scaffolds in deionized water to remove the remaining unpolymerized material. The scaffolds were subsequently exposed to broad spectrum (full width at half maximum: 570 ± 70 nm) light from an ELC-410 UV lamp (Electro-Lite, CT, USA) for approximately 1 min in order to facilitate polymerization throughout the structure.

Scaffold Imaging After fabrication, scaffolds and parameter search arrays were imaged by optical microscopy and/or scanning electron microscopy (SEM). The scaffolds and arrays were inspected with a light microscope (Carl Zeiss AG) while immersed in water and liquid prepolymer, respectively. SEM imaging of the scaffolds was performed with a Quanta 400F scanning electron microscope (FEI, OR, USA). Scaffolds were sputter coated with approximately 200 nm of gold prior to SEM imaging.

UV polymerization of wafers Cylindrical wafers with 6-mm diameters and 1-mm thicknesses were produced using 50% PEGda–riboflavin–TEOHA, 66% PEGda–riboflavin–TEOHA, PEGda with 2% wt Irgacure 369 and PEGda with 2% wt Irgacure 2959; these wafers were used for biocompatibility testing. The wafers were made by filling polydimethylsiloxane

wells with the various PEGda compositions, sandwiching them between glass coverslips and then polymerizing them in the UV curing chamber. Briefly, the samples were suspended approximately 20 cm from the overhead bulbs; owing to the mirrored interior, polymerization can proceed from both top and bottom. The eight bulbs draw a combined power of 40 W and emit mainly at 254 nm; additional peaks with one order of magnitude lower intensity at 312, 365, 405, 436, 546 and 577 nm are also emitted. Following UV polymerization, the wafers were washed in distilled water for 1 h to simulate the development process after 2PP fabrication.

Genotoxicity Testing The comet assay was used to examine the genotoxicity of the photochemically crosslinked PEGda–photoinitiator compounds by means of a protocol that has been previously described [161]. Cylindrical wafers of 50% PEGda–riboflavin–TEOHA, 66% PEGda–riboflavin–TEOHA, PEGda with 2% wt Irgacure 369, and PEGda with 2% wt Irgacure 2959 were used as the test materials. Circular glass coverslips of the same size were used as a negative control. To ensure total DNA damage, H₂O₂ was applied to cells as a positive control.

Bovine aortic GM-7373 endothelial cells (Institute of Biophysics, Leibniz University of Hanover, Germany) were cultured on the wafers and the glass coverslips for 24 h. To obtain a positive control of DNA damage, a subset of glass coverslips with a cell monolayer were treated with a 0.15 mM H₂O₂ phosphate buffer saline solution for 30 min at 37°C. The cells on all of the samples were then trypsinized, harvested and centrifuged at 800 × g for 10 min. After centrifugation, the pellets were resuspended in phosphate-buffered saline in order to obtain a density of 2 × 10⁶ cells/ml. A total of 50 µl of this suspension was added to 100 µl of low-melting agarose (0.6%). Then, 100 µl of this mixture was placed on agarose-coated glass slides, covered with coverslips and cooled to 4°C for 10 min. After solidification, the coverslip was removed and an additional 100 µl of agarose was added. A second round of solidification at 4°C

was subsequently performed. The slides were next incubated for 90 min in a pH 10 lysis buffer, which contained 2.5 M NaCl, 100 mM Na₂EDTA, 10 mM Tris, 1% lauryl sarcosin, 1% Triton X-100 and 10% dimethylsulfoxide. The coverslips were then placed into a horizontal gel electrophoresis chamber that had been filled with the comet assay electrophoresis buffer (1 mM Na₂EDTA and 300 mM NaOH, pH >13). After 40 min, electrophoresis was performed for 20 min at 25 V, 300 mA and 4°C. The slides were then neutralized by washing three times with a Tris buffer solution (400 mM Tris, pH 7.4). The resulting comets were viewed using ethidium bromide staining (20 µg/ml) by means of fluorescence microscopy (magnification: 200×) with a xenon lamp and an ethidium bromide filter set (Zeiss, Germany). The tail moment was evaluated using Autocomet comet scoring software (Tri-Tek Corp., VA, USA) in order to quantitatively determine the degree of DNA breakage.

Extract Cytotoxicity The toxicity of extracts from the crosslinked PEGda wafers was also examined. This technique was previously used to evaluate the toxicity of extracts from PEGda-based photopolymers [129]. Wafers of 50% PEGda–riboflavin–TEOHA, PEGda with 2% wt Irgacure 369 and PEGda with 2% wt Irgacure 2959 were used as the test materials. After UV crosslinking, the wafers were washed in deionized water for 1 h to simulate the developing process that is commonly utilized for 2PP of this polymer. The pellets were then exposed to light from an UV lamp and soaked in 80 µl of DMEM with fetal calf serum for 24 h at 37°C. The amount of culture media was determined by using a test material surface area to culture media ratio of 6 cm²/ml. The resulting solution was used as the extract solution for determining cytotoxicity. GM-7373 bovine endothelial cells were seeded at a density of 15,000 cells per well in a 96-well plate and incubated for 24 h. After incubation, the culture media was replaced with a mixture of 1:1 extract solution to fresh media and cultured for an additional 48 h. Fresh media

was used as a control. Using a Neubauer cell counting chamber (Brand GmbH, Germany), cell viability was determined by counting dead and live cells stained with trypan blue. The effect on cell proliferation was also determined by seeding a 24-well plate with 100,000 cells per well and culturing in 1:1 extract solution to fresh media (DMEM) for 48 h. After removal from the media, the cells were trypsinized and counted using a CASY cell counter device (Roche Innovatis AG, Germany). GM-7373 cells were also cultured in fresh media in order to obtain control data.

Statistical analysis All tests for statistical significance were performed using a two-tailed, homoscedastic Student's t-test. Results were considered significantly different when p-values were lower than 0.05. The number of samples measured per experiment was six for each photoinitiator type. For the comet assay, over 200 cells per sample were evaluated.

Cell seeding 2PP-fabricated PEGda scaffolds were sterilized in 70% ethanol solution for 1 h and were subsequently washed twice in sterile distilled water for 30 min. The scaffolds were then incubated in cell culture media for 3 h prior to cell seeding. The GM-7373 bovine aortic endothelial cells for scaffold seeding were maintained in DMEM-F12 Ham's DMEM (Sigma-Aldrich, Germany) supplemented with 10% fetal bovine serum, 500 U penicillin and 100 mg/ml streptomycin. The cells were incubated at 37°C in a 5% CO₂ environment until a cell monolayer was obtained. The cell culture was then harvested, counted and diluted to a concentration of 1,000,000 cells/ml. The scaffolds were seeded via centrifugation within the cell suspension. Tubes containing scaffolds in media received a 1 ml cell suspension containing 1×10^6 cells. The tubes were loaded into the centrifuge rotor and rotated at 450 rpm for 10 min in order to force the cells into the interior of the scaffold. The scaffolds were then removed and placed into sterile cell culture dishes containing 2 ml of DMEM and cultured for 5 days.

LIVE/DEAD assay A LIVE/DEAD assay (Invitrogen, Life Technologies, Germany) was performed after the 5-day culture period. Seeded scaffolds were stained with 4- μ M ethidium homodimer-1 and 2- μ M calcein AM solutions. Fluorescence imaging was performed using a 645-nm wavelength, which enabled imaging of dead cells that were labeled with ethidium homodimer-1. Fluorescence imaging using a wavelength of 530 nm enabled imaging of live cells that were labeled with calcein AM.

Results and Discussion

UV-Vis spectroscopy UV-Vis spectroscopy was performed with riboflavin-TEOHA in distilled water and with 66% PEGda-riboflavin-TEOHA solution. The absorption spectra of riboflavin-TEOHA and riboflavin alone in distilled water are presented in **Figure 4.1**. Riboflavin-TEOHA in water showed two strong absorption peaks that were centered at 365 nm and 448 nm; no significant absorption occurred at below 300 nm and above 500 nm.

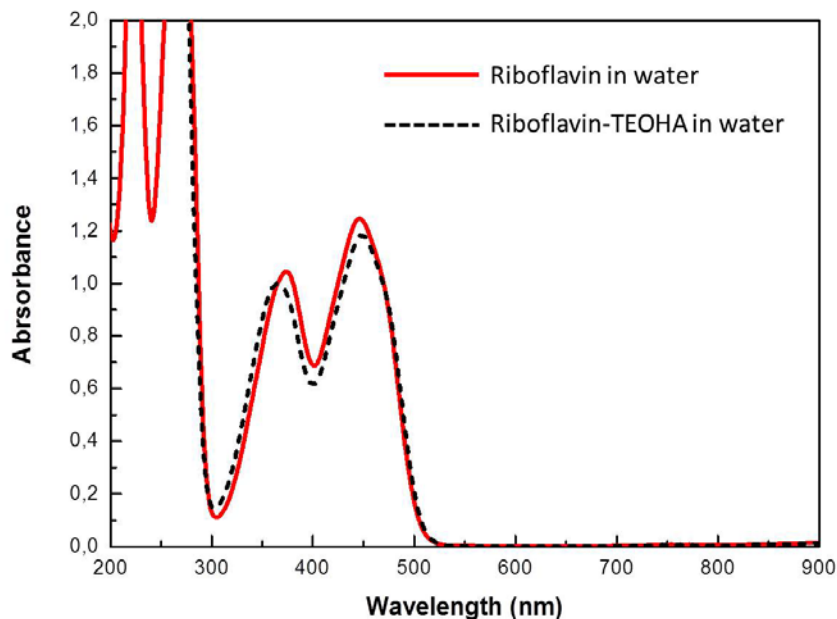


Figure 4.1 - UV-visible absorption spectra of riboflavin and the riboflavin-triethanolamine mixture in distilled water.

The UV-Vis absorption spectrum of PEGda and the 66% PEGda–riboflavin–TEOHA solution is provided in **Figure 4.2**. The PEGda–riboflavin–TEOHA solution exhibited weak absorption above 500 nm; pronounced absorption peaks at 355 nm and 448 nm were noted. Since pure PEGda only exhibited significant absorption below 500 nm, it can be surmised that the light source used in 2PP (excitation wavelength: 780 nm) does not induce chemical changes in this material. Since simultaneous absorption of two 780-nm photons would be equivalent to one 390-nm photon, the spectra for the 66% PEGda–riboflavin–TEOHA solution confirms that the laser wavelength of 780 nm normally used for 2PP experiments is suitable for riboflavin-based photopolymer solutions.

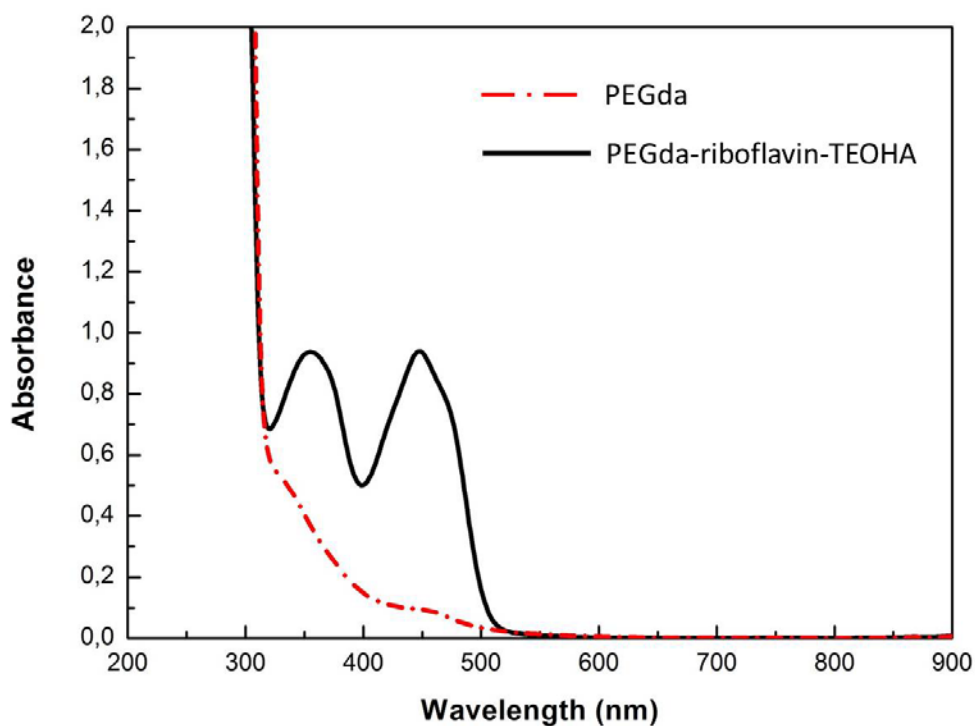


Figure 4.2 - UV-Vis absorption spectrum of polyethylene glycol diacrylate and the 66% PEGda–riboflavin–triethanolamine mixture.

Since the presence of unreacted compounds in the wafers used for biocompatibility testing may increase the apparent cytotoxicity and genotoxicity, UV-Vis spectrometry of polymerized PEGda films, each containing one of the three photoinitiator materials, was performed to determine the ability of the light emitted by the UV oven to fully penetrate the entire volume of the material. Results summarized in **Figure 4.3** show negligible transmission for all three formulations at 254 nm, the peak emission wavelength of the UV curing chamber. Furthermore, the 254-nm light would be further blocked by the glass coverslips that were used to contain the material during wafer or film fabrication. Emission bands with one order of magnitude lower intensity than the 254-nm peak are also emitted by the lamp and would not be blocked by the glass or the PEGda films. Emissions at 312, 365 and 405 nm are highly absorbed by the riboflavin-based photoinitiator (**Figure 4.1**) and were noted to have high transmission through PEGda (**Figure 4.2**), suggesting that these wavelengths are mainly responsible for polymerization. Since the transmissions of some or all these wavelengths are above 70% for a pathlength of 500 μm through the photopolymer films, 1-mm wafers illuminated from both sides will have received ample light for complete polymerization.

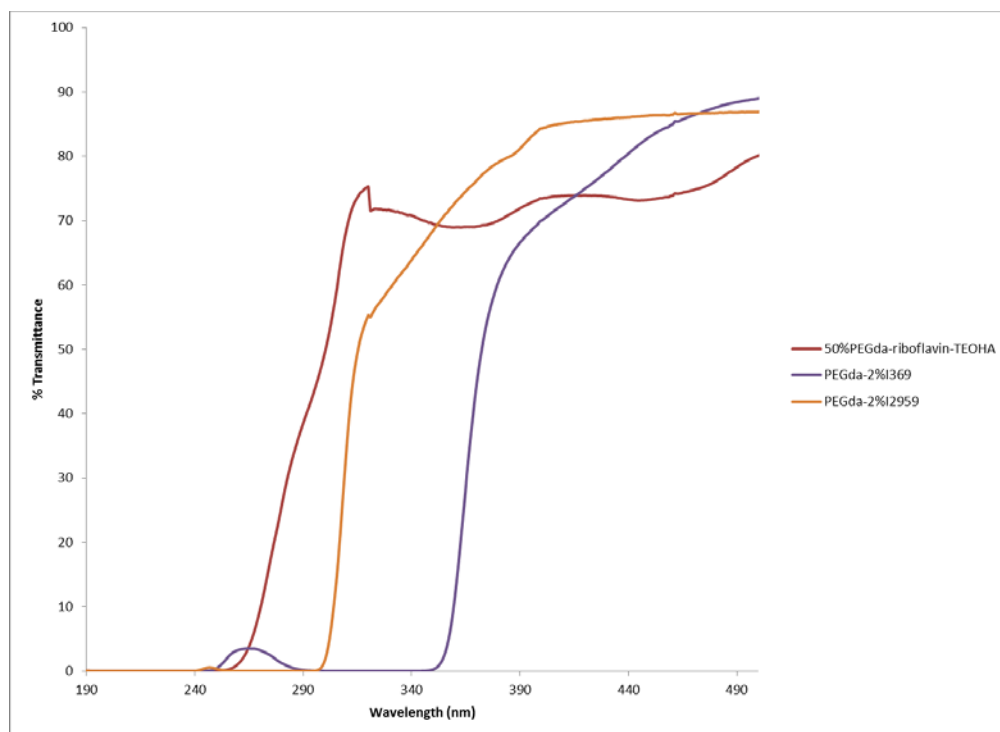


Figure 4.3 - UV-visible transmission spectra of films normalized to a 500- μm path length. Light at 312, 365 and 405 nm is emitted by the UV curing chamber.

2PP of scaffolds 2PP processing of materials is affected by material parameters and processing parameters. Two photon absorption proceeds where and when the laser fluence is sufficient to provide an appreciable probability of simultaneous absorption of photons. The voxel can be shaped by the use of different objectives; for example, the use of a 50 \times magnification objective would provide a much finer voxel than the use of a 20 \times objective. A higher numerical aperture would shrink the vertical resolution. Scaffold processing was performed using laser parameters that enabled a 2- μm line to be produced during scanning, providing a balance between processing resolution and processing speed. Although parameters could be found yielding a smaller voxel, the polymerized fragments would be too far away from one another to form a cohesive structure and would not appear in a parameter search array. The material characteristics directly affect the threshold fluences for 2PP as well as the burning threshold at

which excessive excitation causes degradation of the photopolymer chemical structure. The burning threshold is usually evidenced by the production of bubbles from gaseous decomposition products. As such, the highest resolution for the process would be found where the peak laser intensity is just above the 2PP threshold. Higher fluences can be used to increase the voxel size and shorten fabrication times; however, the structure would be lost if the burning threshold is breached. The available fluence range for each photopolymer was estimated using the parameter search array to find a suitable average laser power above the 2PP threshold that would not cause burning.

The effect of linear scan speed and average laser power on polymerization of the riboflavin-based photopolymer, riboflavin-TEOHA, as well as photopolymers containing Irgacure 369 and Irgacure 2959 was evaluated (**Figure 4.4**). PEGda containing 2% Irgacure 369 was noted to be the most efficient solution and enabled production of viable scaffold structures with a large range of laser fluences. Cylinders were still produced at an average laser power of 90 mW; burning of the polymer was still not observed at 256 mW. The 66% PEGda-riboflavin-TEOHA polymer required significantly higher power inputs for structure fabrication. Polymerization as evidenced by structuring was not observed until 244 mW; slight burning was observed at 403 mW. In addition, 2PP was observed only at 780 nm and was not noted at 515 nm. Conversely, 2PP of PEGda containing 2% Irgacure 2959 with 780-nm light was prohibitively slow, which necessitated use of the 515-nm laser system. Although the parameter search would not be directly comparable to those obtained with the 780-nm laser, structuring was possible from 60 to 100 mW, the maximum available power of the system. These results suggest that Irgacure 369 and Irgacure 2959 are more efficient photoinitiators than the riboflavin-based photoinitiator. It should be mentioned that the effect of water on the 2PP and burning thresholds

could not be compared owing to the insolubility of the Irgacure photoinitiator in water. Since the fabrication throughput is dependent on laser power and scanning speed, fabrication throughput may be diminished for situations in which laser power is limited.

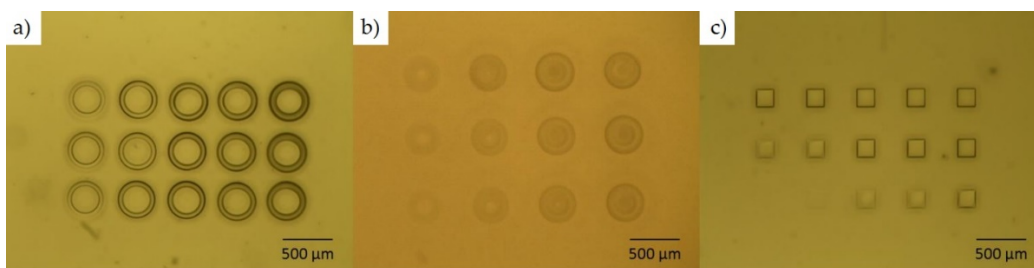


Figure 4.4 - (A) Polyethylene glycol diacrylate (PEGda) with 2% Irgacure® 369; (B) 66% PEGda–riboflavin–triethanolamine (the lowest evaluated laser power was subthreshold and is not present within the image); (C) PEGda with 2% Irgacure 2959. Linear scan speed increases from top to bottom and average power increases from left to right.

Scaffold imaging Optical (**Figure 4.5**) and SEM (**Figure 4.6**) images of the scaffold demonstrate the ability of the photopolymer to accurately form structures with small features. SEM images of the scaffold showed extensive shrinkage of the scaffold structure, which can be attributed to desiccation from exposure to vacuum in the sputtering instrument and within the scanning electron microscope (**Figure 4.6**). However, shrinkage did not occur when the scaffold was kept in an aqueous liquid; optical images of the scaffold in water confirm that the scaffold geometry is composed of regular cylinders as intended and does not exhibit shrinking.

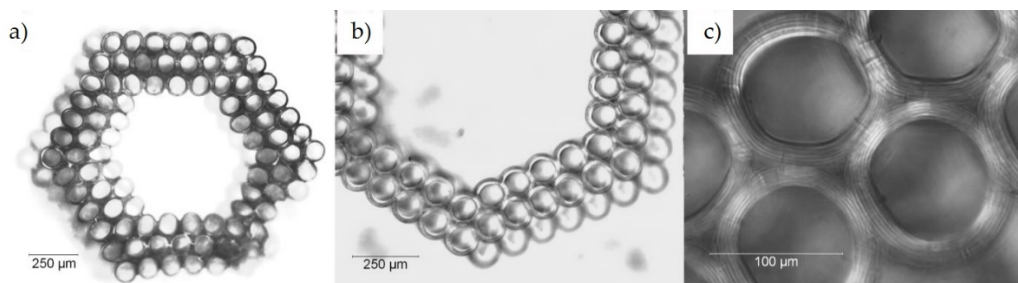


Figure 4.5 - Optical images of 50% polyethylene glycol diacrylate–riboflavin–triethanolamine scaffolds in water.

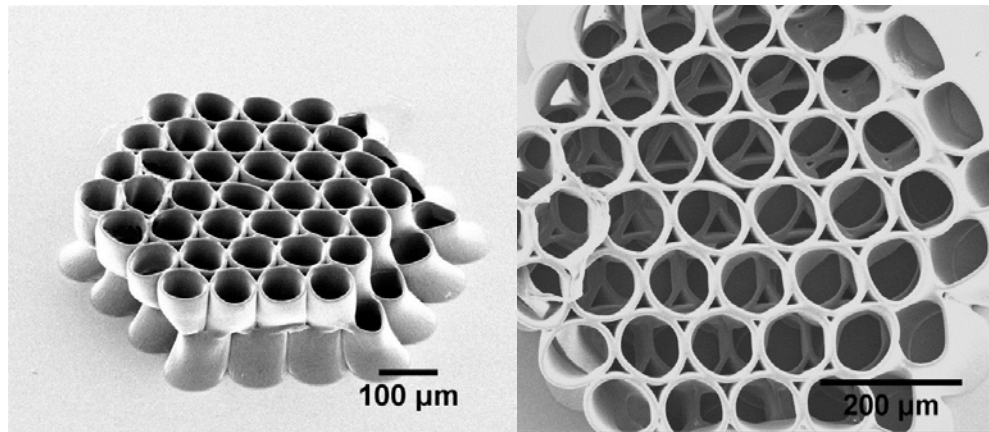


Figure 4.6 - Scanning electron microscopy images of a tissue engineering scaffold made from 50% polyethylene glycol diacrylate–riboflavin–triethanolamine.

Biocompatibility testing Sources of cytotoxicity and genotoxicity in polymer scaffolds include the scaffold material itself, the unpolymerized monomer and the photoinitiator(s). Ovsianikov et al. have shown that PEGda processed with several commercial photoinitiators (e.g., Milcher’s ketone, Irgacure 369 and Irgacure 2959) is cytotoxic and that the cytotoxic components in this material can be removed by extensive washing [136]. The washing process was most effective for PEGda containing Irgacure 2969. In this study, 6-mm diameter by 1-mm thick wafers of PEGda containing riboflavin–TEOHA, Irgacure 2959 or Irgacure 369 were produced by polymerization with a UV curing lamp and were evaluated for genotoxicity and cytotoxicity.

The comet assay assesses genotoxicity by detecting single and double strand DNA breaks; the degree of DNA damage corresponds to the length of the tail moment. The tail moments for PEGda wafers with 2% wt Irgacure 369, PEGda with 2% wt Irgacure 2959, glass as a negative control and H₂O₂ treatment as a positive control are presented in **Figure 4.7**. 50% PEGda–riboflavin–TEOHA was noted to be the least genotoxic material. This material had a tail moment value of 1.45 ± 0.24 , which was lower than that of the negative control (tail moment:

1.74 ± 0.10). In addition, 66% PEGda–riboflavin–TEOHA had a low tail moment value (2.21 ± 0.38). In comparison, PEGda containing Irgacure photoinitiators showed significantly higher tail moment values. PEGda with 2% wt Irgacure 369 had a tail moment value of 4.81 ± 0.80 and PEGda with 2% wt Irgacure 2959 had a tail moment value of 6.81 ± 0.58. The tail moment value of cells treated with H₂O₂ (positive control) was 10.34 ± 1.18. These results indicate that riboflavin–EOHA exhibits little genotoxicity in comparison to Irgacure 369 and Irgacure 2959.

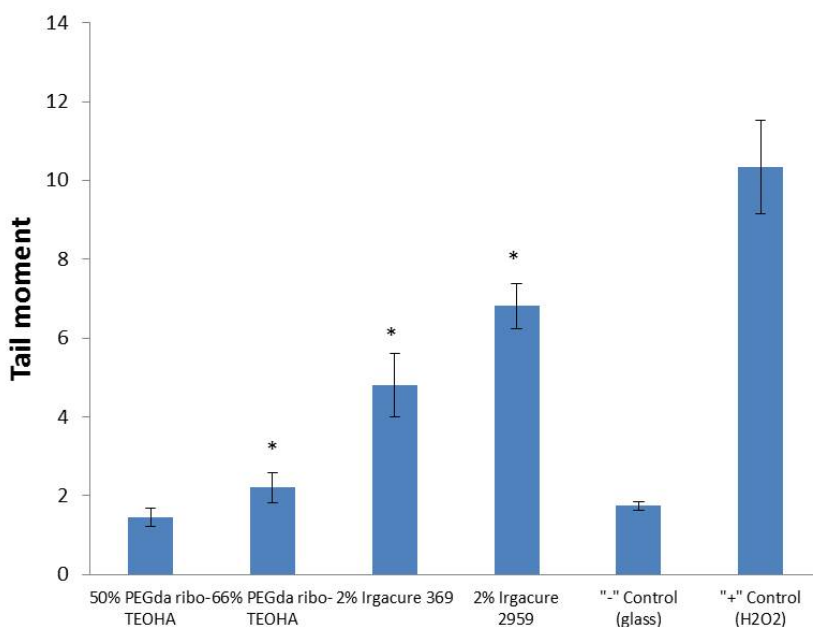


Figure 4.7 - Comet assay tail moments after 24 h of culture on photopolymer wafers. The error bars indicate the 95% CI.

The results for cell proliferation and viability are summarized in **Figure 4.8** and **Figure 4.9**, respectively. PEGda has previously been demonstrated to have potential use as a tissue engineering scaffold material [65]. The extracts were obtained from photopolymerized PEGda pellets in an identical manner to the ones used in the comet assay. The difference in cell proliferation rates between PEGda processed using the riboflavinbased photoinitiator and PEGda processed using Irgacure photoinitiators was statistically insignificant. On the other hand, the

difference between the viability of cells cultured in riboflavin-containing extracts (83%) and cells cultured in glass extracts (87%) was statistically significant. Cells cultured on the Irgacure 369 and Irgacure 2959 scaffolds had significantly lower viability than the riboflavin–TEOHA scaffolds or the glass control. This suggests that the use of riboflavin and TEOHA as a photoinitiator has little negative effect on cell viability compared with the commercial photoinitiators Irgacure 369 and Irgacure 2959.

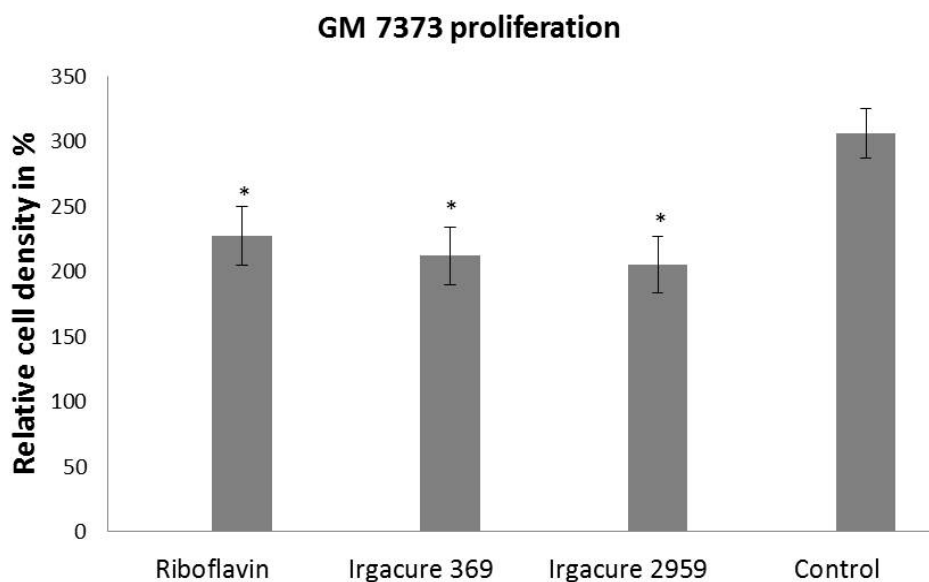


Figure 4.8 - Cell proliferation of GM-7373 bovine aortic endothelial cells on polyethylene glycol diacrylate wafers after 24 h of culture in the presence of photopolymer extract solutions. The error bars indicate the 95% CI.

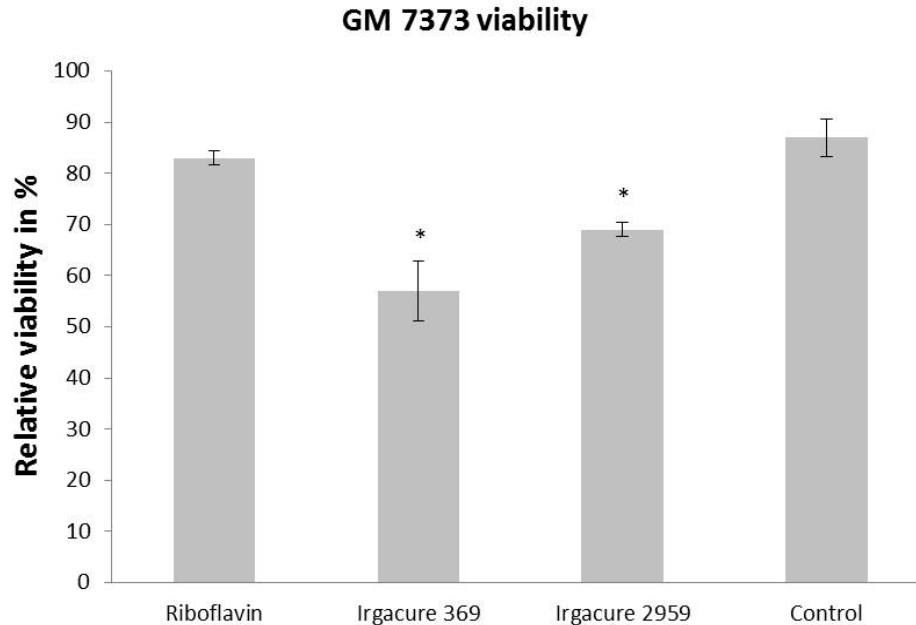


Figure 4.9 - Cell viability of GM-7373 bovine aortic endothelial cells on polyethylene glycol diacrylate wafers after 24 h of culture in the presence of photopolymer extract solutions. The error bars indicate the 95% CI.

LIVE/DEAD staining of the scaffolds As a qualitative demonstration of the ability of the riboflavin–TEOHA photoinitiator to undergo 2PP processing and support cell growth, a tissue engineering scaffold was fabricated from the 50% PEGda–riboflavin–TEOHA solution and subsequently seeded with GM-7373 bovine aortic endothelial cells (**Figure 4.10**). Staining with calcein AM (live cells) and ethidium homodimer-1 (dead cells), was performed to visualize the cells grown on the scaffold. Merged images from the LIVE/DEAD stain demonstrate that most of the seeded bovine aortic endothelial cells remained viable; few dead cells were noted on the scaffold (**Figure 4.10B**). The LIVE/DEAD stain data correlates well with the cell viability data for GM-7373 bovine aortic endothelial cells on PEGda wafers processed using the riboflavin-based photoinitiator. Cell outgrowths and development of extensions indicated

assembly of cell-to-cell contacts and formation of an endothelial monolayer on both the outer and inner surfaces of the scaffold (**Figure 4.11**).

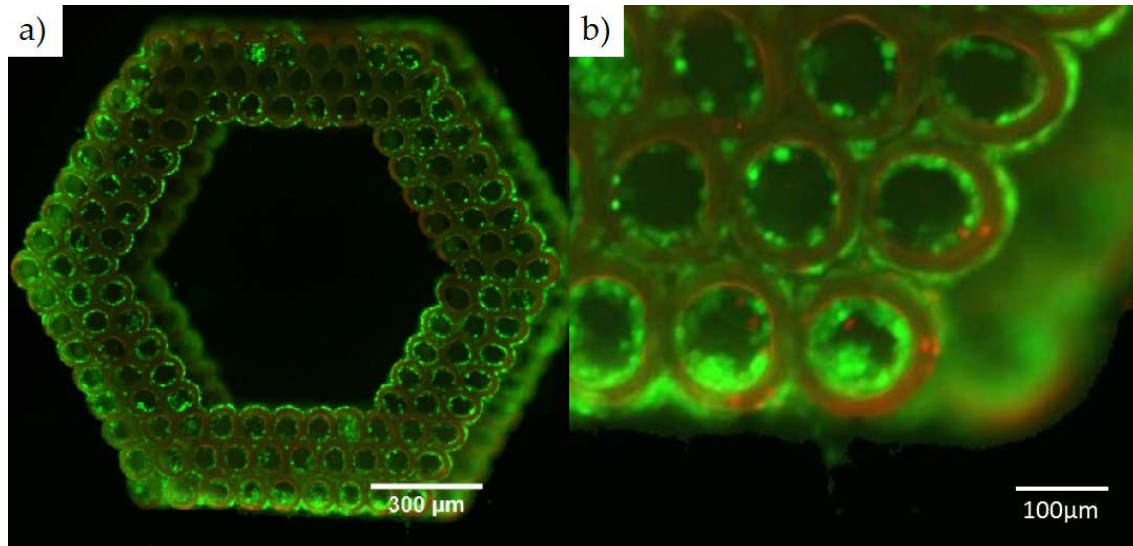


Figure 4.10 - Fluorescence images of GM-7373 bovine aortic endothelial cells on riboflavin–triethanolamine–polyethylene glycol diacrylate scaffolds. Merged Live/Dead staining after 5 days of culture of a 50% riboflavin–triethanolamine–polyethylene glycol diacrylate scaffold seeded with GM-7373 endothelial cells. Fluorescence of ethidium homodimer-1 (associated with dead cells) is distinct from dull red autofluorescence of PEGda (right).

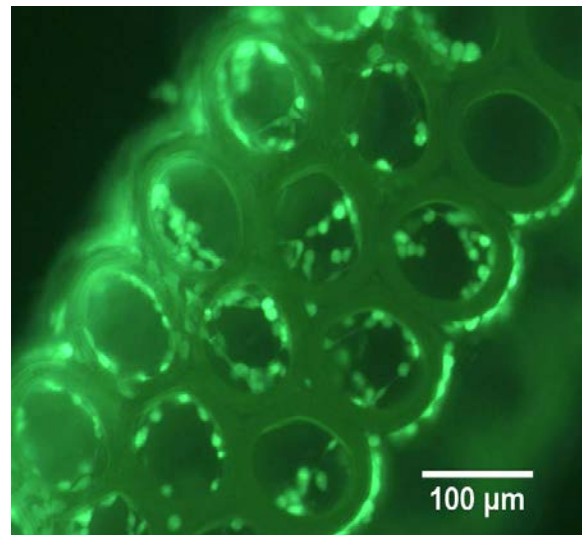


Figure 4.11 - Calcein AM stain highlights live cells. Cell outgrowths were noted, which are similar to normal endothelial cell morphology.

Conclusion

In this study, the use of riboflavin as a water-soluble photoinitiator for fabrication of tissue engineering scaffolds out of PEGda was explored. 2PP structuring with the riboflavin–TEOHA mixture was noted to exhibit lower photosensitivity than the commercially available photoinitiators Irgacure 2959 and Irgacure 369; however, genotoxicity measured via the comet assay indicated that the two tested riboflavin-based photopolymers were significantly less genotoxic than the conventionally produced photopolymers. Additionally, extracts from the riboflavin–TEOHA photopolymers were found to have viability on par with the glass control. Differences in proliferation were not significantly different between the tested materials. A 2PP-fabricated 50% PEGda–riboflavin–TEOHA scaffold was shown to support the growth of bovine aortic endothelial cells via a LIVE/DEAD stain.

High-precision lithographic methods that are adapted for biomedical applications currently employ conventional photoinitiators, which were not designed for use with cells. The issue of cytotoxicity is partially circumvented by minimizing photoinitiator exposure to cells via extensive washing or use of low photoinitiator concentrations. Novel photoinitiators for biological applications must be developed to facilitate use of photopolymers in clinical medicine. The riboflavin–TEOHA photoinitiator system described in this study exhibits excellent biocompatibility; however, it exhibits low efficiency in terms of the laser fluence required for 2PP. With further improvement of the photoinitiator properties, the riboflavin–TEOHA photoinitiator could be a powerful tool for realizing the two-photon or UV polymerization of completely biocompatible scaffolds or other medically relevant structures without extensive postprocessing.



For reprint orders, please contact: reprints@futuremedicine.com

Two-photon polymerization of polyethylene glycol diacrylate scaffolds with riboflavin and triethanolamine used as a water-soluble photoinitiator

Aim: In this study, the suitability of a mixture containing riboflavin (vitamin B2) and triethanolamine (TEOHA) as a novel biocompatible photoinitiator for two-photon polymerization (2PP) processing was investigated. **Materials & methods:** Polyethylene glycol diacrylate was crosslinked using Irgacure® 369, Irgacure 2959 or a riboflavin–TEOHA mixture; biocompatibility of the photopolymer extract solutions was subsequently assessed via endothelial cell proliferation assay, endothelial cell viability assay and single-cell gel electrophoresis (comet) assay. Use of a riboflavin–TEOHA mixture as a photoinitiator for 2PP processing of a tissue engineering scaffold and subsequent seeding of this scaffold with GM-7373 bovine aortic endothelial cells was also demonstrated. **Results:** The riboflavin–TEOHA mixture was found to produce much more biocompatible scaffolds than those produced with Irgacure 369 or Irgacure 2959. **Conclusion:** The results suggest that riboflavin is a promising component of photoinitiators for 2PP fabrication of tissue engineering scaffolds and other medically relevant structures (e.g., biomicroelectromechanical systems).

KEYWORDS: biocompatibility polyethylene glycol diacrylate riboflavin tissue engineering scaffolds triethanolamine two-photon polymerization

Two-photon polymerization (2PP) is a rapid prototyping approach in which a 3D computer-aided design model is used to direct selective curing of a photosensitive material by means of nearly simultaneous absorption of ultrashort (e.g., femtosecond) laser pulses. This approach provides many possibilities for fabricating 3D microscale structures, including biomicroelectromechanical systems [1], microfluidic devices [2], biomedical implants [3], microneedles for transdermal drug delivery [4] and scaffolds for tissue engineering [5–14].

Control of the cell environment (e.g., spatial constraints, mechanical properties and chemical factors) is essential to the field of tissue engineering and, in particular, the fabrication of niches for stem cell differentiation. The flexibility of 2PP in creating structures with well-controlled geometries and feature sizes ranging from below one micrometer to hundreds of micrometers makes this technique particularly appealing for fabrication of 3D tissue engineering scaffolds [5–18]. In addition, patient-specific scaffolds for tissue engineering may be created using 2PP from patient imaging data (e.g., microcomputed tomography data or MRI data) [7].

Biocompatible materials (e.g., photoinitiators) that are compatible with 2PP are necessary to improve the acceptance of this approach for fabrication of 3D tissue engineering scaffolds. For example, Ovsianikov *et al.* evaluated the cytotoxicity of several 2PP photoinitiators [19].

Aqueous extracts of polyethylene glycol (PEG) diacrylate (PEGda) formulations with molecular weights of 302 and 742 were polymerized using three photoinitiators: Michler's ketone; Irgacure® 369 and Irgacure 2959 (BASF Schweiz AG, Switzerland). The photopolymerized materials contained water-soluble molecules that were toxic to L929 fibroblasts. Aging the PEGda material with a molecular weight of 742 that had been polymerized with Irgacure 2959 in water for a period of 7 days reduced the amount of the water-soluble toxic components to a level such that no cytotoxic effect was noted. Arcaute *et al.* found that PEG polymerized with the photoinitiators Irgacure 2959 and 2-hydroxy-2-methyl-1-phenyl-1-propanone was cytotoxic at a photoinitiator concentration of 0.5%; toxicity was noted to increase with exposure time and photoinitiator concentration [20]. Owing to photoinitiator leaching, the authors noted that a concentration of 0.5% Irgacure 2959 may be utilized without inducing severe cytotoxicity. Williams *et al.* examined the cytotoxicity of Irgacure 184, Irgacure 2959 and Irgacure 651 against a variety of cell lines that are utilized in tissue engineering, including chondrocytes, corneal epithelial cells, mesenchymal stem cells, osteoblasts and embryonic germ cells [21]. At concentrations below 0.1% Irgacure 2959 was noted to be well tolerated by all cell types; on the other hand, the other two evaluated photoinitiators were toxic for all cell types at a concentration of 0.02%. In addition,

Alexander K Nguyen¹,
Shaun D Gittard²,
Anastasia Koroleva²,
Sabrina Schlie²,
Arune Gaidukeviciute²,
Boris N Chichkov²
& Roger J Narayan*¹

¹JUNC/NCSSU Joint Department of Biomedical Engineering, University of North Carolina, Campus Box 7575, Chapel Hill, NC 27599-7575, USA

²Nanotechnology Department, Laser Zentrum Hannover e. V., Hollerithallee 8, D-30419 Hannover, Germany

*Author for correspondence: roger_narayan@ncsu.edu

 Regenerative
Medicine

they suggested that rapidly dividing cells were more sensitive to the photoinitiators. Rouillard *et al.* noted significant cytotoxicity (i.e., viability under 70%) for an alginate–chondrocyte hydrogel containing a methacrylate-modified alginate that had been crosslinked using Irgacure 2959 [22]. It is important to note that cytotoxicity was assessed by means of proliferation rate or LIVE/DEAD® (Invitrogen, CA, USA) staining studies in these studies.

Potential sources of biocompatible photoinitiators include free-radical-generating molecules that are naturally found in biological systems. Riboflavin, also known as vitamin B₂, is a molecule that has potential use as a biological photoinitiator. Flavins have the ability to easily undergo reduction–oxidation reactions, including transport of electrons by FADH₂ in the electron transport chain of cellular respiration. Riboflavin is excited by photon absorption and can form either the singlet- or triplet-excited states. It should be noted that the triplet state exhibits a longer lifetime in solution and, as such, is more available for molecular interactions than the singlet state. In a nitrogen-purged solution, triplet riboflavin was found to exist for several microseconds after excitation. On the other hand, singlet riboflavin was only observed for 20 ns after excitation [23]. Triplet riboflavin quenched by a monomer was not found to result in polymerization; however, the addition of triethanolamine (TEOHA) as a coinitiator did result in polymerization [24]. It is believed that triplet state riboflavin is oxidized by TEOHA to form the semioxidized radical of riboflavin and the semireduced amine. Donation of a proton from the amine to the riboflavin radical forms the long-lived neutral amine radical, which was found to initiate polymerization.

Several previous studies have reported on the use of riboflavin as a photoinitiator for polymerization of polymers. For example, Orellana *et al.* used riboflavin and a coinitiator, TEOHA, for crosslinking 2-hydroxyethyl methacrylate (HEMA) [24]. The polymerization rate was found to be highest for a TEOHA concentration of 0.01 M. Encinas *et al.* investigated crosslinking of HEMA with riboflavin and several amine coinitiators; their experiments indicated that TEOHA was one of the most efficient of the evaluated coinitiators [25]. In these studies, HEMA was polymerized using a mercury lamp with a center wavelength of 366 nm. Turunen *et al.* reported on use of flavin mononucleotide as a photosensitizer in pico- and femto-second laser-induced photocrosslinking of avidin, bovine

serum albumin and biotinylated bovine serum albumin [26].

Riboflavin has been considered for use in several other biomedical applications. For example, Husain and Naseem demonstrated that photochemically activated riboflavin is able to counteract the effect of cisplatin, a chemotherapeutic agent that induces oxidative DNA strand breakage, in murine epidermal keratinocytes [27]. A combination of riboflavin and UV light treatment was shown to be effective for inactivating pathogens in platelet concentrates [28]. Riboflavin has also been used to induce crosslinking of collagen within the cornea for the treatment of keratoconus [29–32]. The therapeutic use of riboflavin in high doses or with UV exposure has already been shown to be compatible with living organisms. As such, addition of riboflavin to a tissue engineering scaffold is hypothesized to not result in a significant change in biocompatibility.

Production of tissue engineering scaffolds from PEGda by 2PP has been demonstrated by several groups. Liao *et al.* noted that PEGda hydrogels are appropriate scaffold materials for some biomedical applications (e.g., vocal fold applications) because their mechanical properties can be altered by modifying the concentration and/or molecular weight [33]. Bulick *et al.* and Munoz-Pinto *et al.* noted that PEGda is commonly utilized as a ‘model’ scaffold material for growth of fibroblast-like cells or smooth muscle-like cells [34,35]. Bulick *et al.* developed PEGda scaffolds for tissue engineering that contained smooth muscle cells, in which the crosslinking of PEGda and the slow degradation rate of PEGda facilitated cell immobilization within the scaffold [34].

Ovsianikov *et al.* produced porous 3D tissue engineering scaffolds using PEGda by 2PP [12]. A ring-shaped scaffold was produced by 2P, which was then seeded with endothelial cells along the interior edge and smooth muscle cells along the outer edge by laser-induced forward transfer. Gittard reported using 2PP of PEGda to produce a 6 mm-long tubular tissue engineering scaffold for vascular applications [10,36]. Musumeci *et al.* recently encapsulated chondrocytes in PEGda hydrogels and showed that the encapsulated cells expressed lower levels of the apoptosis effector caspase-3 than control cartilage after 5 weeks [37]. In addition, increased cell growth, extracellular matrix formation and hyaline cartilage production were noted in the PEGda-cultured chondrocytes after 5 weeks. Lin *et al.* noted that PEGda hydrogels may be useful for cartilage tissue engineering since cells are embedded by the crosslinked material; chondrocyte

photoencapsulation for cartilage tissue engineering has been shown using *in vitro* and *in vivo* studies [38]. Use of PEGda scaffolds for encapsulation of human mesenchymal stem cells has also been demonstrated [39].

As noted by Weiss *et al.*, PEGda is a biologically inert material [13]. PEGda hydrogels may be useful as model materials for tissue engineering since they do not exert a biological effect on cells [39]. An unmodified PEGda hydrogel scaffold provides the encapsulated cells with a nonadhesive environment [40]. Although PEG resists cell attachment in its unmodified form, cell responses can be obtained via attachment of biologically active molecules [13]. For example, Lee *et al.* controlled cell growth within a tissue engineering scaffold by patterning conjugated RGD, a cell adhesion peptide, in collagenase-sensitive poly(ethylene glycol-co-peptide) diacrylate hydrogels by 2PP [41]. Procedures exist to modify the PEG backbone with groups to facilitate cell adhesion (e.g., RGD sequences) or with groups that enable photopolymerization (e.g., the diacrylate group used in this study) [41].

Degradation of PEGda hydrogels is commonly associated with hydrolytic cleavage of ester bonds between the crosslinking units and the backbone; oxidation of the ether backbone may also play a role [33,42]. Xin *et al.* performed an *in vitro* study involving degradation of PEGda in phosphate-buffered saline solution and found that PEGda undergoes a small but significant amount of degradation; polymers with less photocrosslinking were shown to undergo higher degradation [43]. PEGda hydrogels stored in phosphate-buffered saline over a period of 8 weeks showed a statistically significant but small change in Young's modulus and compressive strength. Browning *et al.* noted that the ester linkages in PEGda undergo slow hydrolytic cleavage within the body, which may occur within months to years after implantation [42]. They noted no significant change in swelling of PEGda hydrogels within phosphate-buffered saline solution over 6 weeks; however, a linear regression analysis was able to reveal an increase in swelling over time. On the other hand, they observed complete dissolution of PEGda hydrogels by 80 h in an 'accelerated' (0.1 M) NaOH solution that was intended to reflect longer implantation times. As noted by Browning *et al.*, PEGda degradation products, similar to all synthetic materials, are subject to protein adsorption and macrophage activation [42].

In addition to use as a tissue engineering scaffold material, PEGda hydrogel structures may have other *in vivo* applications. For example,

Browning *et al.* noted that PEGda may find use in wound dressings and vascular graft coatings [43]. In addition, PEGda is an appropriate material for use as a filler material for soft tissue restoration since it is low in cost, nonpyrogenic and nonallergenic [44]. It can also be injected into a small tissue defect and molded in place to form a solid structure. Patel *et al.* showed that PEGda is able to withstand forces that are associated with use as a soft tissue filler [44].

In this study, we investigated the suitability of using a riboflavin-TEOHA mixture as a photoinitiator for producing PEGda tissue engineering scaffolds. The ability of this riboflavin-based mixture to initiate 2PP was evaluated by comparing the laser parameters and the scaffold morphology produced with the novel photoinitiator with scaffolds produced with the commercial photoinitiators Irgacure 369 and Irgacure 2959. According to ISO10993 guidelines, biocompatibility was examined relative to conventionally produced scaffolds by using a single-cell gel electrophoresis (comet) assay to assess cytotoxicity as well as by measuring GM-7373 bovine aortic endothelial cell (Leibniz Institute DSMZ, Germany) proliferation and viability in the various polymer extract solutions [10]. Finally, LIVE/DEAD staining was performed on a model riboflavin-TEOHA initiated PEGda scaffold that had been seeded with GM-7373 cells to directly determine the suitability of this material for cell culture.

Materials & methods

■ Photopolymers

Scaffolds were produced from SR610 (Sartomer, France), a PEGda material that has a molecular weight of 742 g/mol; this material has previously been used to create tissue engineering scaffolds and small-scale medical devices [11,27]. 4(2-hydroxyethoxy)phenyl-(2-hydroxy-2-propyl)ketone (BASF Schweiz AG), more commonly known as Irgacure 2959, and 2-benzyl-2-dimethylamino-1-(4-morpholinophenyl)-butanone (BASF Schweiz AG), more commonly known as Irgacure 369, were used as comparison photoinitiators.

A novel photopolymer was developed that contains PEGda as the polymer, riboflavin as the photoinitiator and TEOHA as the coinitiator. An aqueous solution of 4.2 mM riboflavin-5-phosphate (Sigma-Aldrich, MO, USA) and 4.2 M TEOHA (Sigma-Aldrich) was prepared; the solution was purged with nitrogen to minimize oxygen content. A photopolymer solution with 200 μ M riboflavin and 200 mM TEOHA was produced by combining 50 μ l of the concentrated riboflavin-TEOHA solution with every

milliliter of the final photopolymer volume. For example, a 50% PEGda mixture was made by combining 4 ml of PEGda, 3.800 ml of distilled water, and 0.200 ml of the riboflavin-TEOHA solution. The resulting mixture was purged with nitrogen and kept in darkness or in yellow light. The PEGda dilutions examined in this study contained 50 and 66% PEGda by volume.

■ UV-visible spectroscopy

In order to determine an optimal laser wavelength for polymerization, UV-visible (UV-Vis) spectroscopy was utilized to obtain absorption spectra of the photoinitiator and the photopolymer. The absorbance spectra of 66% PEGda-riboflavin-TEOHA, pure PEGda, riboflavin, the riboflavin-TEOHA mixture and the various films were collected from 190 to 1000 nm using SpectraSuite software (Ocean Optics, Germany). The emission spectra of a UV curing chamber (PEQLAB Biotechnologie GmbH, Erlangen, Germany) used for bulk polymerization of material were collected using an HR2000+ spectrophotometer (Ocean Optics, FL, USA). In addition, free-standing films of polymerized 50% PEGda-riboflavin-TEOHA and PEGda containing 2% wt Irgacure 369 or 2% wt Irgacure 2959 were measured to determine the transmittance of the polymerized material to the post-curing light. Three 140- μm glass coverslips were used as spacers to control the film thickness. In order to normalize the transmittance spectra, the actual thickness was determined directly after UV-Vis spectrometry by means of optical microscopy; the average thickness was noted to be approximately 425 μm . The thickness values were used to normalize the transmission spectra using Beer's Law to a 500- μm path length, the maximum depth at which double-sided illumination within the mirrored UV curing chamber would have to reach.

■ 2PP of structures

Scaffolds were produced by 2PP of a 66 or 50% PEGda-riboflavin-TEOHA solution using a 780-nm ChameleonTMTi:sapphire femtosecond laser (Coherent, CA, USA); a 140 fs pulse and a 80-MHz repetition rate were used in this study. Parameter search arrays were fabricated with the 66% PEGda-riboflavin-TEOHA solution; these arrays were compared with undiluted PEGda solutions containing 2% wt Irgacure 369 or 2% wt Irgacure 2959 that were polymerized using a 780-nm femtosecond laser and 515-nm light from a frequency-doubled Yb:glass laser (1 MHz, 200 fs, High Q Laser, Austria), respectively.

The unpolymerized resin was placed between two glass coverslips in a 6-mm diameter by 1-mm tall polydimethylsiloxane ring. 2PP processing of the resin was performed by scanning the laser, which was focused by a 20 \times Epiplan objective (Carl Zeiss AG, Jena, Germany) within this resin reservoir. Lateral scanning of small-scale components (e.g., individual cylinders) was achieved using a hurrySCAN[®] galvano scan head (Scanlab, Germany). The height of the laser focus was adjusted using a C-843 linear translation stage (PhysikInstrumente, Germany); two additional linear stages were used to control lateral motion from one component in the structure to the next. Custom written software was used to produce cylinders with an inner diameter of 100 μm , an outer diameter of 120 μm and a height of 100 μm . The individual cylinders were placed in a hexagonal honeycomb configuration with nine cylinders composing the outer wall and seven cylinders composing the inner wall; the total width of the structure was 2.2 mm. Array cylinders had larger dimensions, with inner diameters of 160 μm , outer diameters of 200 μm and heights of 50 μm . In the case of the 515-nm laser system, rectangular prisms in the 'woodpile' configuration (i.e., linear arrays in which the line direction alternates from one layer to the next layer) were produced with a 100- μm side length and a 50- μm height. Production of the structures proceeded in a layer-by-layer fashion, in which each layer was composed of concentric circles or straight lines that were separated by a distance of 2 μm . Each line or circle was scanned five times at a linear speed of 2.50 mm/s for scaffold elements or at 1.25, 2.50 or 3.75 mm/s for structures in the parameter search array before moving onto the next component. After a complete layer was exposed, the sample was moved 5 μm away from the objective before starting the next layer. The average laser power was controlled by a liquid crystal polarizer in the case of the 780-nm laser or a motorized quarter wave plate in the case of the 515-nm laser. The minimum average laser power was selected by finding a power close to the 2PP threshold and then increasing the power in regular intervals. Power levels of 90, 128, 167, 212 and 256 mW were used for the Irgacure 369 containing solutions and 193, 244, 292, 343 and 403 mW were used for the 66% PEGda-riboflavin-TEOHA-containing solutions. Irgacure 2959 solutions were polymerized with 515-nm light and are thus on a different scale. Average laser powers of 60, 70, 80, 90 and 100 mW were used in this case.

The parameter search arrays were imaged before development in order to eliminate the effect

of shrinkage or swelling during imaging and to prevent the loss of underpolymerized structures. Scaffolds were developed by placing the scaffolds in deionized water to remove the remaining unpolymerized material. The scaffolds were subsequently exposed to broad spectrum (full width at half maximum: 570 ± 70 nm) light from an ELC-410 UV lamp (Electro-Lite, CT, USA) for approximately 1 min in order to facilitate polymerization throughout the structure.

■ Scaffold imaging

After fabrication, scaffolds and parameter search arrays were imaged by optical microscopy and/or scanning electron microscopy (SEM). The scaffolds and arrays were inspected with a light microscope (Carl Zeiss AG) while immersed in water and liquid prepolymer, respectively. SEM imaging of the scaffolds was performed with a Quanta 400F scanning electron microscope (FEI, OR, USA). Scaffolds were sputter coated with approximately 200 nm of gold prior to SEM imaging.

■ UV polymerization of wafers

Cylindrical wafers with 6-mm diameters and 1-mm thicknesses were produced using 50% PEGda-riboflavin-TEOHA, 66% PEGda-riboflavin-TEOHA, PEGda with 2% wt Irgacure 369 and PEGda with 2% wt Irgacure 2959; these wafers were used for biocompatibility testing. The wafers were made by filling polydimethylsiloxane wells with the various PEGda compositions, sandwiching them between glass coverslips and then polymerizing them in the UV curing chamber. Briefly, the samples were suspended approximately 20 cm from the overhead bulbs; owing to the mirrored interior, polymerization can proceed from both top and bottom. The eight bulbs draw a combined power of 40 W and emit mainly at 254 nm; additional peaks with one order of magnitude lower intensity at 312, 365, 405, 436, 546 and 577 nm are also emitted. Following UV polymerization, the wafers were washed in distilled water for 1 h to simulate the development process after 2PP fabrication.

■ Genotoxicity testing

The comet assay was used to examine the genotoxicity of the photochemically crosslinked PEGda-photoinitiator compounds by means of a protocol that has been previously described [45]. Cylindrical wafers of 50% PEGda-riboflavin-TEOHA, 66% PEGda-riboflavin-TEOHA, PEGda with 2% wt Irgacure 369, and PEGda with 2% wt Irgacure 2959 were used as the test

materials. Circular glass coverslips of the same size were used as a negative control. To ensure total DNA damage, H_2O_2 was applied to cells as a positive control.

Bovine aortic GM-7373 endothelial cells (Institute of Biophysics, Leibniz University of Hanover, Germany) were cultured on the wafers and the glass coverslips for 24 h. To obtain a positive control of DNA damage, a subset of glass coverslips with a cell monolayer were treated with a 0.15 mM H_2O_2 phosphate buffer saline solution for 30 min at 37°C. The cells on all of the samples were then trypsinized, harvested and centrifuged at $800 \times g$ for 10 min. After centrifugation, the pellets were resuspended in phosphate-buffered saline in order to obtain a density of 2×10^6 cells/ml. A total of 50 μ l of this suspension was added to 100 μ l of low-melting agarose (0.6%). Then, 100 μ l of this mixture was placed on agarose-coated glass slides, covered with coverslips and cooled to 4°C for 10 min. After solidification, the coverslip was removed and an additional 100 μ l of agarose was added. A second round of solidification at 4°C was subsequently performed. The slides were next incubated for 90 min in a pH 10 lysis buffer, which contained 2.5 M NaCl, 100 mM Na_2EDTA , 10 mM Tris, 1% lauryl sarcosine, 1% Triton X-100 and 10% dimethylsulfoxide. The coverslips were then placed into a horizontal gel electrophoresis chamber that had been filled with the comet assay electrophoresis buffer (1 mM Na_2EDTA and 300 mM NaOH, pH >13). After 40 min, electrophoresis was performed for 20 min at 25 V, 300 mA and 4°C. The slides were then neutralized by washing three times with a Tris buffer solution (400 mM Tris, pH 7.4). The resulting comets were viewed using ethidium bromide staining (20 μ g/ml) by means of fluorescence microscopy (magnification: 200 \times) with a xenon lamp and an ethidium bromide filter set (Zeiss, Germany). The tail moment was evaluated using Autocomet comet scoring software (Tri-Tek Corp., VA, USA) in order to quantitatively determine the degree of DNA breakage.

■ Extract cytotoxicity

The toxicity of extracts from the crosslinked PEGda wafers was also examined. This technique was previously used to evaluate the toxicity of extracts from PEGda-based photopolymers [11]. Wafers of 50% PEGda-riboflavin-TEOHA, PEGda with 2% wt Irgacure 369 and PEGda with 2% wt Irgacure 2959 were used as the test materials. After UV crosslinking, the wafers were washed in deionized water for 1 h to simulate the developing process that is commonly

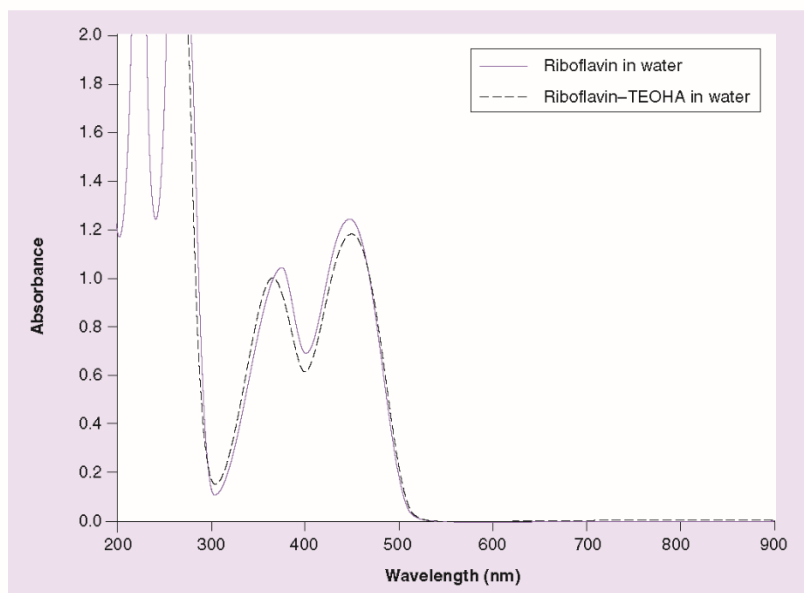


Figure 1. UV-visible absorption spectra of riboflavin and the riboflavin-triethanolamine mixture in distilled water.
TEOHA: Triethanolamine.

utilized for 2PP of this polymer. The pellets were then exposed to light from an UV lamp and soaked in 80 μ l of DMEM with fetal calf serum for 24 h at 37°C. The amount of culture

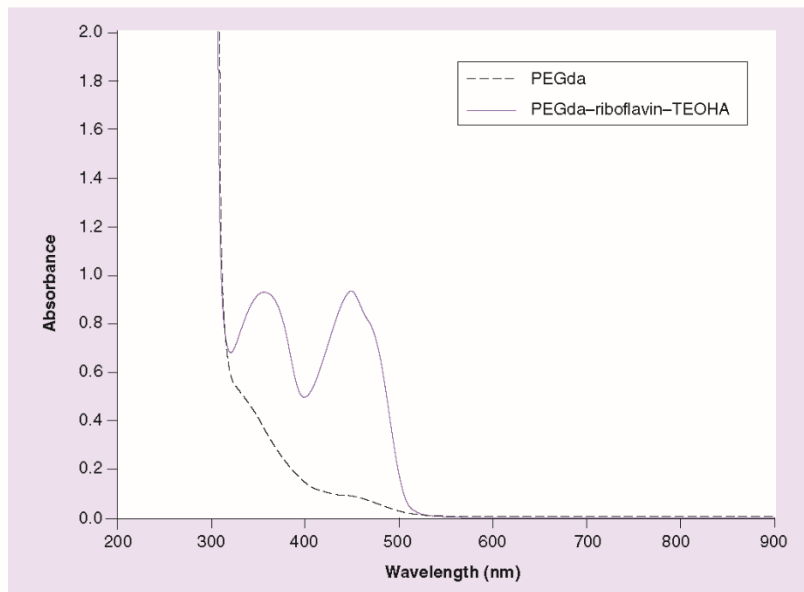


Figure 2. UV-Vis absorption spectrum of polyethylene glycol diacrylate and the 66% PEGda-riboflavin-triethanolamine mixture.
PEGda: Polyethylene glycol diacrylate; TEOHA: Triethanolamine.

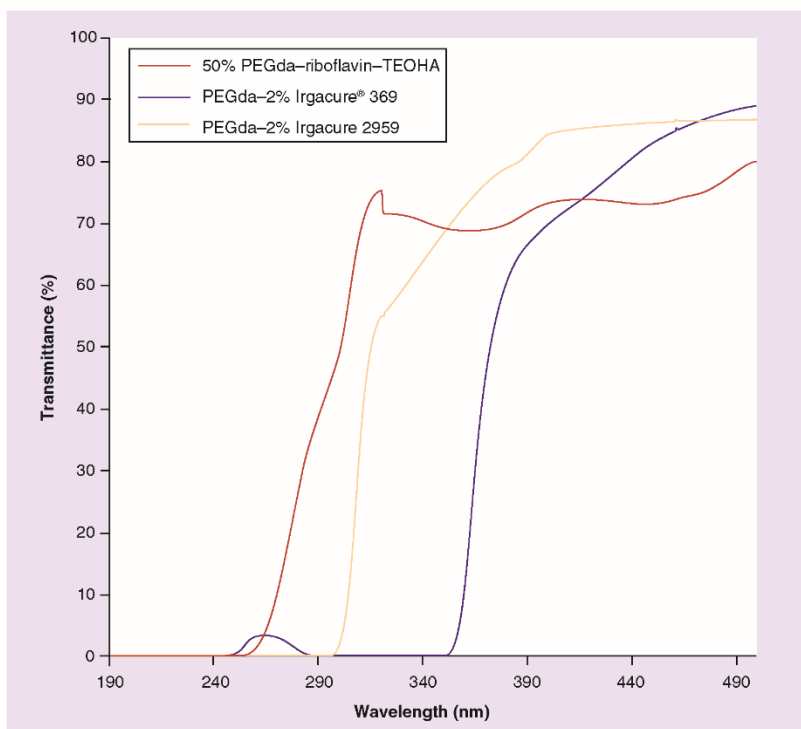


Figure 3. UV-visible transmission spectra of films normalized to a 500- μm path length. Light at 312, 365 and 405 nm is emitted by the UV curing chamber. PEGda: Polyethylene glycol diacrylate; TEOHA: Triethanolamine.

media was determined by using a test material surface area to culture media ratio of 6 cm^2/ml . The resulting solution was used as the extract solution for determining cytotoxicity. GM-7373 bovine endothelial cells were seeded at a density of 15,000 cells per well in a 96-well plate and incubated for 24 h. After incubation, the culture media was replaced with a mixture of 1:1 extract solution to fresh media and cultured for an additional 48 h. Fresh media was used as a control. Using a Neubauer cell counting chamber (Brand

GmbH, Germany), cell viability was determined by counting dead and live cells stained with trypan blue. The effect on cell proliferation was also determined by seeding a 24-well plate with 100,000 cells per well and culturing in 1:1 extract solution to fresh media (DMEM) for 48 h. After removal from the media, the cells were trypsinized and counted using a CASY cell counter device (Roche Innovatis AG, Germany). GM-7373 cells were also cultured in fresh media in order to obtain control data.



Figure 4. Parameter search arrays. (A) Polyethylene glycol diacrylate (PEGda) with 2% Irgacure® 369; (B) 66% PEGda-riboflavin-triethanolamine (the lowest evaluated laser power was subthreshold and is not present within the image); (C) PEGda with 2% Irgacure 2959. Linear scan speed increases from top to bottom and average power increases from left to right.

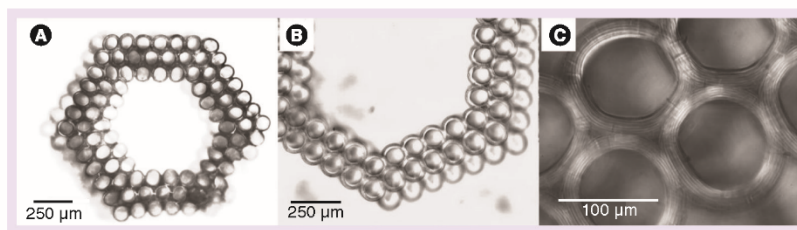


Figure 5. Optical images of 50% polyethylene glycol diacrylate-riboflavin-triethanolamine scaffolds in water.

■ Statistical analysis

All tests for statistical significance were performed using a two-tailed, homoscedastic Student's *t*-test. Results were considered significantly different when *p*-values were lower than 0.05. The number of samples measured per experiment was six for each photoinitiator type. For the comet assay, over 200 cells per sample were evaluated.

■ Cell seeding

2PP-fabricated PEGda scaffolds were sterilized in 70% ethanol solution for 1 h and were subsequently washed twice in sterile distilled water for 30 min. The scaffolds were then incubated in cell culture media for 3 h prior to cell seeding. The GM-7373 bovine aortic endothelial cells for scaffold seeding were maintained in DMEM-F12 Ham's DMEM (Sigma-Aldrich, Germany) supplemented with 10% fetal bovine serum, 500 U penicillin and 100 mg/ml streptomycin. The cells were incubated at 37°C in a 5% CO₂ environment until a cell monolayer was obtained. The cell culture was then harvested, counted and diluted to a concentration of 1,000,000 cells/ml. The scaffolds were seeded via centrifugation within the cell suspension. Tubes containing scaffolds in media received a 1 ml cell suspension containing

1 × 10⁶ cells. The tubes were loaded into the centrifuge rotor and rotated at 450 rpm for 10 min in order to force the cells into the interior of the scaffold. The scaffolds were then removed and placed into sterile cell culture dishes containing 2 ml of DMEM and cultured for 5 days.

■ LIVE/DEAD assay

A LIVE/DEAD assay (Invitrogen, Life Technologies, Germany) was performed after the 5-day culture period. Seeded scaffolds were stained with 4-µM ethidium homodimer-1 and 2-µM calcein AM solutions. Fluorescence imaging was performed using a 645-nm wavelength, which enabled imaging of dead cells that were labeled with ethidium homodimer-1. Fluorescence imaging using a wavelength of 530 nm enabled imaging of live cells that were labeled with calcein AM.

Results & discussion

■ UV-Vis spectroscopy

UV-Vis spectroscopy was performed with riboflavin-TEOHA in distilled water and with 66% PEGda-riboflavin-TEOHA solution. The absorption spectra of riboflavin-TEOHA and riboflavin alone in distilled water are presented in FIGURE 1. Riboflavin-TEOHA in water showed two strong absorption peaks that were centered at 365 nm and 448 nm; no significant absorption occurred at below 300 nm and above 500 nm.

The UV-Vis absorption spectrum of PEGda and the 66% PEGda-riboflavin-TEOHA solution is provided in FIGURE 2. The PEGda-riboflavin-TEOHA solution exhibited weak absorption above 500 nm; pronounced absorption peaks at 355 nm and 448 nm were noted. Since pure PEGda only exhibited significant absorption below 500 nm, it can be surmised that the light source used in 2PP (excitation wavelength: 780 nm) does not induce chemical changes in this material. Since simultaneous absorption of two 780-nm photons would be equivalent to one 390-nm photon, the spectra for the 66%

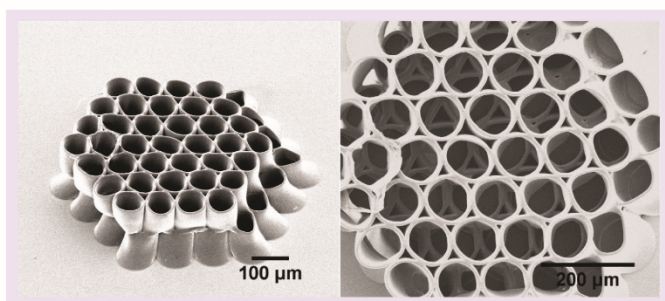


Figure 6. Scanning electron microscopy images of a tissue engineering scaffold made from 50% polyethylene glycol diacrylate-riboflavin-triethanolamine.

PEGda–riboflavin–TEOHA solution confirms that the laser wavelength of 780 nm normally used for 2PP experiments is suitable for riboflavin-based photopolymer solutions.

Since the presence of unreacted compounds in the wafers used for biocompatibility testing may increase the apparent cytotoxicity and genotoxicity, UV-Vis spectrometry of polymerized PEGda films, each containing one of the three photoinitiator materials, was performed to determine the ability of the light emitted by the UV oven to fully penetrate the entire volume of the material. Results summarized in FIGURE 3 show negligible transmission for all three formulations at 254 nm, the peak emission wavelength of the UV curing chamber. Furthermore, the 254-nm light would be further blocked by the glass coverslips that were used to contain the material during wafer or film fabrication. Emission bands with one order of magnitude lower intensity than the 254-nm peak are also emitted by the lamp and would not be blocked by the glass or the PEGda films. Emissions at 312, 365 and 405 nm are highly absorbed by the riboflavin-based photoinitiator (FIGURE 1) and were noted to have high transmission through PEGda (FIGURE 2), suggesting that these wavelengths are mainly responsible for polymerization. Since the transmissions of some or all these wavelengths are above 70% for a pathlength of 500 μm through the photopolymer films, 1-mm wafers illuminated from both sides will have received ample light for complete polymerization.

■ 2PP of scaffolds

2PP processing of materials is affected by material parameters and processing parameters. Two-photon absorption proceeds where and when the laser fluence is sufficient to provide an appreciable probability of simultaneous absorption of photons. The voxel can be shaped by the use of different objectives; for example, the use of a 50 \times magnification objective would provide a much finer voxel than the use of a 20 \times objective. A higher numerical aperture would shrink the vertical resolution. Scaffold processing was performed using laser parameters that enabled a 2- μm line to be produced during scanning, providing a balance between processing resolution and processing speed. Although parameters could be found yielding a smaller voxel, the polymerized fragments would be too far away from one another to form a cohesive structure and would not appear in a parameter search array. The material characteristics directly affect the threshold fluences for 2PP as well as the burning threshold

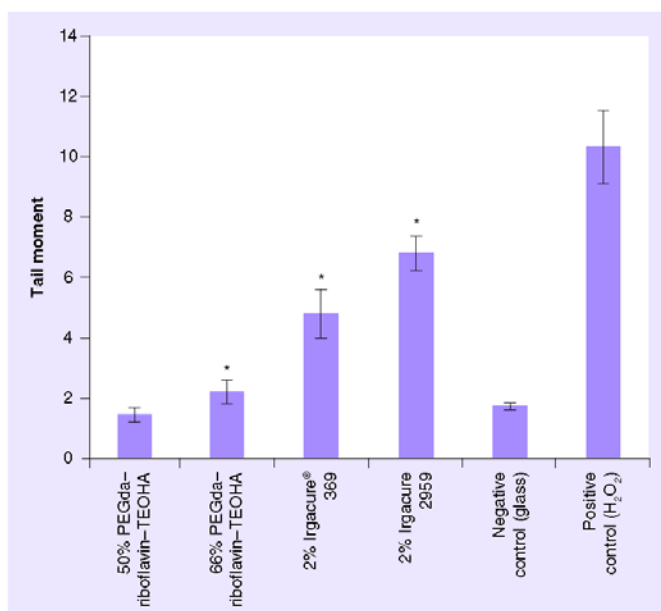


Figure 7. Comet assay tail moments after 24 h of culture on photopolymer wafers. The error bars indicate the 95% CI.

* $p < 0.05$.

PEGda: Polyethylene glycol diacrylate; TEOHA: Triethanolamine.

at which excessive excitation causes degradation of the photopolymer chemical structure. The burning threshold is usually evidenced by the production of bubbles from gaseous decomposition products. As such, the highest resolution for the process would be found where the peak laser intensity is just above the 2PP threshold. Higher fluences can be used to increase the voxel size and

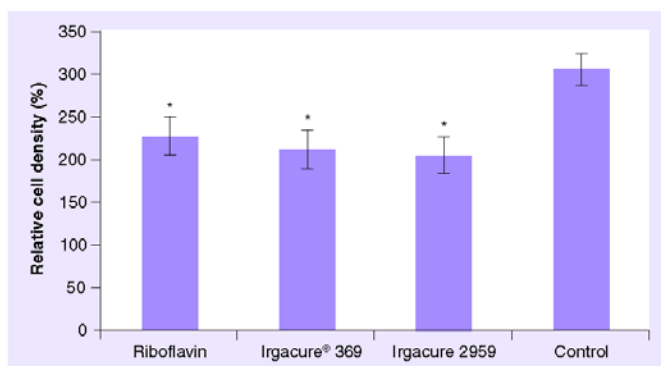


Figure 8. Cell proliferation of GM-7373 bovine aortic endothelial cells on polyethylene glycol diacrylate wafers after 24 h of culture in the presence of photopolymer extract solutions. The error bars indicate the 95% CI.

* $p < 0.05$.

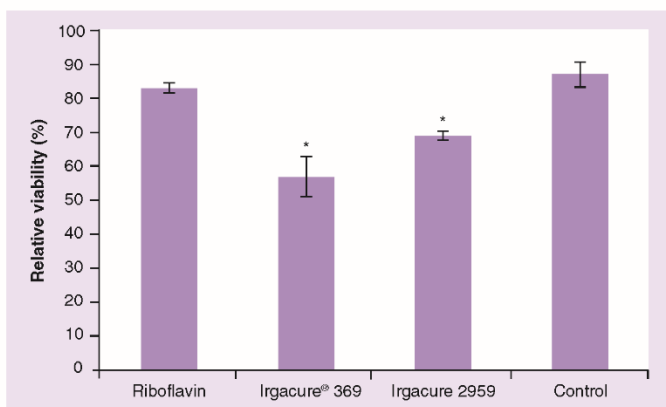


Figure 9. Cell viability of GM-7373 bovine aortic endothelial cells on polyethylene glycol diacrylate wafers after 24 h of culture in the presence of photopolymer extract solutions. The error bars indicate the 95% CI. * $p < 0.05$.

shorten fabrication times; however, the structure would be lost if the burning threshold is breached. The available fluence range for each photopolymer was estimated using the parameter search array to find a suitable average laser power above the 2PP threshold that would not cause burning.

The effect of linear scan speed and average laser power on polymerization of the riboflavin-based photopolymer, riboflavin-TEOHA, as well as photopolymers containing Irgacure 369 and Irgacure 2959 was evaluated (FIGURE 4). PEGda containing 2% Irgacure 369 was noted to be the most efficient solution and enabled production of viable scaffold structures with a large range of laser fluences. Cylinders were still produced at an average laser power of 90 mW; burning of

the polymer was still not observed at 256 mW. The 66% PEGda-riboflavin-TEOHA polymer required significantly higher power inputs for structure fabrication. Polymerization as evidenced by structuring was not observed until 244 mW; slight burning was observed at 403 mW. In addition, 2PP was observed only at 780 nm and was not noted at 515 nm. Conversely, 2PP of PEGda containing 2% Irgacure 2959 with 780-nm light was prohibitively slow, which necessitated use of the 515-nm laser system. Although the parameter search would not be directly comparable to those obtained with the 780-nm laser, structuring was possible from 60 to 100 mW, the maximum available power of the system. These results suggest that Irgacure 369 and Irgacure 2959 are more efficient photoinitiators than the riboflavin-based photoinitiator. It should be mentioned that the effect of water on the 2PP and burning thresholds could not be compared owing to the insolubility of the Irgacure photoinitiator in water. Since the fabrication throughput is dependent on laser power and scanning speed, fabrication throughput may be diminished for situations in which laser power is limited.

■ Scaffold imaging

Optical (FIGURE 5) and SEM (FIGURE 6) images of the scaffold demonstrate the ability of the photopolymer to accurately form structures with small features. SEM images of the scaffold showed extensive shrinkage of the scaffold structure, which can be attributed to desiccation from exposure to vacuum in the sputtering instrument and within the scanning electron microscope (FIGURE 6). However, shrinkage did not occur when the scaffold was kept in an aqueous liquid; optical images of the scaffold in water confirm that the scaffold geometry is composed of regular cylinders as intended and does not exhibit shrinking.

■ Biocompatibility testing

Sources of cytotoxicity and genotoxicity in polymer scaffolds include the scaffold material itself, the unpolymerized monomer and the photoinitiator(s). Ovsianikov *et al.* have shown that PEGda processed with several commercial photoinitiators (e.g., Milcher's ketone, Irgacure 369 and Irgacure 2959) is cytotoxic and that the cytotoxic components in this material can be removed by extensive washing [19]. The washing process was most effective for PEGda containing Irgacure 2969. In this study, 6-mm diameter by 1-mm thick wafers of PEGda containing riboflavin-TEOHA, Irgacure 2959 or Irgacure 369 were produced by polymerization with a UV curing

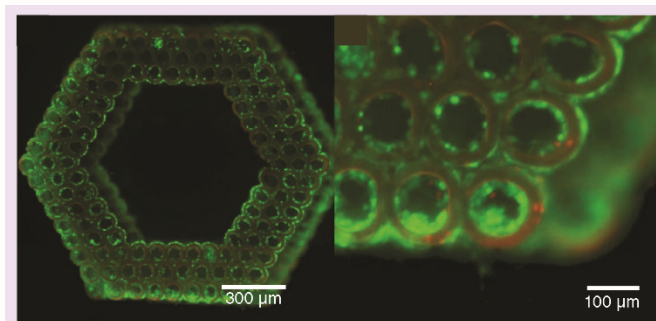


Figure 10. Fluorescence images of GM-7373 bovine aortic endothelial cells on riboflavin-triethanolamine-polyethylene glycol diacrylate scaffolds. Merged LIVE/DEAD staining after 5 days of culture of a 50% riboflavin-triethanolamine-polyethylene glycol diacrylate scaffold seeded with GM-7373 endothelial cells. Fluorescence of ethidium homodimer-1 (associated with dead cells) is distinct from dull red autofluorescence of PEGda (right). Please see color figure at www.futuremedicine.com/doi/pdf/10.2217/rme.13.60.

lamp and were evaluated for genotoxicity and cytotoxicity.

The comet assay assesses genotoxicity by detecting single and double strand DNA breaks; the degree of DNA damage corresponds to the length of the tail moment. The tail moments for PEGda wafers with 2% wt Irgacure 369, PEGda with 2% wt Irgacure 2959, glass as a negative control and H_2O_2 treatment as a positive control are presented in FIGURE 7. 50% PEGda-riboflavin-TEOHA was noted to be the least genotoxic material. This material had a tail moment value of 1.45 ± 0.24 , which was lower than that of the negative control (tail moment: 1.74 ± 0.10). In addition, 66% PEGda-riboflavin-TEOHA had a low tail moment value (2.21 ± 0.38). In comparison, PEGda containing Irgacure photoinitiators showed significantly higher tail moment values. PEGda with 2% wt Irgacure 369 had a tail moment value of 4.81 ± 0.80 and PEGda with 2% wt Irgacure 2959 had a tail moment value of 6.81 ± 0.58 . The tail moment value of cells treated with H_2O_2 (positive control) was 10.34 ± 1.18 . These results indicate that riboflavin-TEOHA exhibits little genotoxicity in comparison to Irgacure 369 and Irgacure 2959.

The results for cell proliferation and viability are summarized in FIGURE 8 and FIGURE 9, respectively. PEGda has previously been demonstrated to have potential use as a tissue engineering scaffold material [8]. The extracts were obtained from photopolymerized PEGda pellets in an identical manner to the ones used in the comet assay. The difference in cell proliferation rates between PEGda processed using the riboflavin-based photoinitiator and PEGda processed using Irgacure photoinitiators was statistically insignificant. On the other hand, the difference between the viability of cells cultured in riboflavin-containing extracts (83%) and cells cultured in glass extracts (87%) was statistically significant. Cells cultured on the Irgacure 369 and Irgacure 2959 scaffolds had significantly lower viability than the riboflavin-TEOHA scaffolds or the glass control. This suggests that the use of riboflavin and TEOHA as a photoinitiator has little negative effect on cell viability compared with the commercial photoinitiators Irgacure 369 and Irgacure 2959.

■ LIVE/DEAD staining of scaffolds

As a qualitative demonstration of the ability of the riboflavin-TEOHA photoinitiator to undergo 2PP processing and support cell growth, a tissue engineering scaffold was fabricated from the 50% PEGda-riboflavin-TEOHA solution

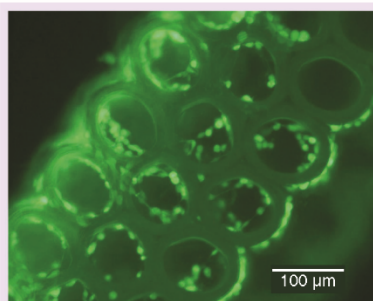


Figure 11. Calcein AM stain highlights live cells. Cell outgrowths were noted, which are similar to normal endothelial cell morphology. Please see color figure at www.futuremedicine.com/doi/pdf/10.2217/rme.13.60.

and subsequently seeded with GM-7373 bovine aortic endothelial cells (FIGURE 10). Staining with calcein AM (live cells) and ethidium homodimer-1 (dead cells), was performed to visualize the cells grown on the scaffold. Merged images from the LIVE/DEAD stain demonstrate that most of the seeded bovine aortic endothelial cells remained viable; few dead cells were noted on the scaffold (FIGURE 10B). The LIVE/DEAD stain data correlates well with the cell viability data for GM-7373 bovine aortic endothelial cells on PEGda wafers processed using the riboflavin-based photoinitiator. Cell outgrowths and development of extensions indicated assembly of cell-to-cell contacts and formation of an endothelial monolayer on both the outer and inner surfaces of the scaffold (FIGURE 11).

Conclusion

In this study, the use of riboflavin as a water-soluble photoinitiator for fabrication of tissue engineering scaffolds out of PEGda was explored. 2PP structuring with the riboflavin-TEOHA mixture was noted to exhibit lower photosensitivity than the commercially available photoinitiators Irgacure 2959 and Irgacure 369; however, genotoxicity measured via the comet assay indicated that the two tested riboflavin-based photopolymers were significantly less genotoxic than the conventionally produced photopolymers. Additionally, extracts from the riboflavin-TEOHA photopolymers were found to have viability on par with the glass control. Differences in proliferation were not significantly different between the tested materials. A 2PP-fabricated 50% PEGda-riboflavin-TEOHA scaffold was shown to support the growth of bovine aortic endothelial cells via a LIVE/DEAD stain.

High-precision lithographic methods that are adapted for biomedical applications currently employ conventional photoinitiators, which were not designed for use with cells. The issue of cytotoxicity is partially circumvented by minimizing photoinitiator exposure to cells via extensive washing or use of low photoinitiator concentrations. Novel photoinitiators for biological applications must be developed to facilitate use of photopolymers in clinical medicine. The riboflavin–TEOHA photoinitiator system described in this study exhibits excellent biocompatibility; however, it exhibits low efficiency in terms of the laser fluence required for 2PP. With further improvement of the photoinitiator properties, the riboflavin–TEOHA photoinitiator could be a powerful tool for realizing the two-photon or UV polymerization of completely biocompatible scaffolds or other medically relevant structures without extensive postprocessing.

Financial & competing interests disclosure

This work was supported by the Deutsche Forschungsgemeinschaft (DFG), the Cluster of Excellence REBIRTH, SFB TR 37, and the US National Science Foundation (Grant 0936110). The authors have no other relevant affiliations or financial involvement with any organization or entity with a financial interest in or financial conflict with the subject matter or materials discussed in the manuscript apart from those disclosed.

No writing assistance was utilized in the production of this manuscript.

Ethical conduct of research

The authors state that they have obtained appropriate institutional review board approval or have followed the principles outlined in the Declaration of Helsinki for all human or animal experimental investigations. In addition, for investigations involving human subjects, informed consent has been obtained from the participants involved.

Executive summary

Photopolymer characterization

- The 780-nm wavelength is valid for two-photon polymerization (2PP) crosslinking of the polyethylene glycol diacrylate (PEGda)–riboflavin–triethanolamine (TEOHA) photopolymer.
- UV-Vis spectrum of the PEGda–riboflavin–TEOHA photopolymer indicates significant absorbance in the 300–500-nm range.
- Simultaneous absorption of two 780-nm photons is equal to absorption of a 390-nm photon, which is within the 300–500-nm range.
- The riboflavin–TEOHA photoinitiator is less efficient in terms of laser fluence required for 2PP than the conventional photoinitiators Irgacure® 369 and Irgacure® 2959.
- The 2PP laser fluence threshold was much higher for riboflavin–TEOHA than for Irgacure 369.
- The viable fluence range between the 2PP threshold and burning was smaller for the riboflavin–TEOHA photoinitiator than for the conventional photoinitiators.
- Riboflavin–TEOHA is not able to undergo 2PP with 515-nm light.
- The transmission spectra of the three materials show very good transmittance for UV curing chamber emission bands near 400 nm, a wavelength close to the 2PP excitation wavelength.

Biocompatibility testing

- Riboflavin–TEOHA UV-crosslinked wafers have significantly higher biocompatibility than Irgacure 369- or Irgacure 2959-crosslinked wafers.
- Tail moments from a comet assay show that the 50% PEGda–riboflavin–TEOHA is less genotoxic than the glass control. The 66% PEGda–riboflavin–TEOHA solution was similar to the control.
- Both Irgacure 369 and Irgacure 2959 photopolymers have significantly larger tail moments than the riboflavin–TEOHA photopolymers and the glass control.
- The difference in cell viability on a riboflavin–TEOHA wafer or on the glass control was found to be statistically insignificant. The Irgacure materials exhibited significantly lower viability.
- No statistical difference was noted for cell proliferation rates on all of the tested photoinitiators.
- Growth of cells on a 50% PEGda–riboflavin–TEOHA scaffold processed using 2PP was demonstrated.
- A LIVE/DEAD® stain of a 5-day culture of GM-7373 endothelial cells showed a significant number of live cells; only a few dead cells were noted.
- Outgrowths were observed, indicative of normal endothelial cell morphology.

Conclusion

- A water-soluble riboflavin–TEOHA-based photoinitiator system has viable 2PP photoinitiator functionality; improvements in photoinitiator efficiency (i.e., the laser fluence required for 2PP) are necessary.
- PEGda–riboflavin–TEOHA photopolymers are significantly more biocompatible than the traditional photoinitiators Irgacure 369 and Irgacure 2959.
- Growth of cells on a 2PP-fabricated 50% PEGda–riboflavin–TEOHA scaffold was demonstrated; most of the GM-7373 endothelial cells seeded on a PEGda–riboflavin–TEOHA 2PP scaffold were noted to be viable.

References

Papers of special note have been highlighted as:
 * of interest
 ** of considerable interest

- Zukauskas A, Tikuisis KK, Sciuka M *et al.* Single-step direct laser fabrication of complex shaped microoptical components. *Proc. SPIE* 8428, 84280K (2012).
- Stoneman M, Fox M, Zeng C, Raicu V. Real-time monitoring of two-photon photopolymerization for use in fabrication of microfluidic devices. *Lab Chip* 9(6), 819–827 (2009).
- Ovsianikov A, Chichkov B, Adunka O, Pillsbury H, Doraiswamy A, Narayan RJ. Rapid prototyping of ossicular replacement prostheses. *Appl. Surface Sci.* 253, 6603–6607 (2007).
- Gittard SD, Ovsianikov A, Akar H *et al.* Two-photon polymerization-micromolding of polyethylene glycol-gentamicin sulfate microneedles. *Adv. Eng. Mater.* 12, B77–B82 (2010).
- Kasko AM, Wong DY. Two-photon lithography in the future of cell-based therapeutics and regenerative medicine: a review of techniques for hydrogel patterning and controlled release. *Future Med. Chem.* 2, 1669–1680 (2010).
- Farsari M, Chichkov BN. Materials processing: two-photon fabrication. *Nat. Photon* 3, 450–452 (2009).
- Narayan RJ, Doraiswamy A, Chrisey DB, Chichkov BN. Medical prototyping using two-photon polymerization. *Mater. Today* 13, 44–50 (2010).
- Ovsianikov A, Deiwick A, Van Vlierberghe S *et al.* Laser fabrication of three-dimensional CAD scaffolds from photosensitive gelatin for applications in tissue engineering. *Biomacromol.* 12, 851–858 (2011).
- Raimondi MT, Eaton SM, Nava MM, Lagana M, Cerullo G, Osellame R. Three-dimensional structural niches engineered via two-photon laser polymerization promote cell homing. *Acta Biomater.* 9 (1), 4579–4584 (2013).
- Gittard SD, Koroleva A, Nguyen AK *et al.* Two-photon polymerization microstructuring in regenerative medicine. *Front. Biosci. (Elite Ed.)* 5, 602–609 (2013).
- Raimondi MT, Eaton SM, Nava MM, Lagana M, Cerullo G, Osellame R. Two-photon laser polymerization: from fundamentals to biomedical application in tissue engineering and regenerative medicine. *J. Appl. Biomater. Funct. Mater.* 10(1), 55–65 (2012).
- Ovsianikov A, Gruene M, Pflaum M *et al.* Laser printing of cells into 3D scaffolds. *Biofabrication* 2(1), 014104 (2010).
- Weiss T, Schade R, Laube T *et al.* Two-photon polymerization of biocompatible photopolymers for microstructures 3d biointerfaces. *Adv. Eng. Mater.* 13(9), B264–B273 (2011).
- Koskela JE, Turunen S, Ylae-Outinen L, Narkilahti S, Kellomaki M. Two-photon microfabrication of poly(ethylene glycol) diacrylate and a novel biodegradable photopolymer – comparison of processability for biomedical applications. *Polym. Adv. Technol.* 23, 992–1001 (2012).
- Ovsianikov A, Deiwick A, Van Vlierberghe S *et al.* Laser fabrication of 3D gelatin scaffolds for the generation of bioartificial tissues. *Materials* 4, 288–299 (2011).
- Koroleva A, Gill AA, Ortega JW *et al.* Two-photon polymerization-generated and micromolding-replicated 3-D scaffolds for peripheral neural tissue engineering applications. *Biofabrication* 4(2), 025005 (2012).
- Koroleva A, Gittard SD, Schlie S, Deiwick A, Jockenhoevel S, Chichkov BN. Fabrication of fibrin scaffolds with controlled microscale architecture by a two-photon polymerization-micromolding technique. *Biofabrication* 4(1), 015001 (2012).
- Raimondi MT, Eaton SM, Lagana M *et al.* Three-dimensional structural niches engineered via two-photon laser polymerization promote stem cell homing. *Acta Biomater.* 9(1), 4579–4584 (2013).
- Ovsianikov A, Malinauskas M, Schlie S *et al.* Three-dimensional laser micro- and nanostructuring of acrylated poly(ethylene glycol) materials and evaluation of their cytotoxicity for tissue engineering applications. *Acta Biomater.* 7, 967–974 (2011).
- Direct comparison of a similar scaffold, that was crosslinked using Irgacure® 369.
- Arcaute K, Mann BK, Wicker RB. Stereolithography of three-dimensional bioactive poly(ethylene glycol) constructs with encapsulated cells. *Ann. Biomed. Eng.* 34, 1429–1441 (2006).
- Biocompatibility testing of Irgacure 2959 and generation of a seeded scaffold. Not directly comparable owing to the much lower photoinitiator concentration and use of stereolithography instead of two-photon polymerization.
- Williams CG, Malik AN, Kim TK, Manson PN, Elisseff JH. Variable cytocompatibility of six cell lines with photoinitiators used for polymerizing hydrogels and cell encapsulation. *Biomaterials* 26, 1211–1218 (2005).
- Reports on biocompatibility tests for Irgacure materials, highlighting their cytotoxicity for several cell lines.
- Rouillard AD, Berglund CM, Lee JY *et al.* Methods for photocrosslinking alginate hydrogel scaffolds with high cell viability. *Tissue Eng. C* 17, 173–179 (2011).
- Lu CY, Wang WF, Lin WZ, Han ZH, Yao SD, Lin NY. Generation and photosensitization properties of the oxidized radical of riboflavin: a laser flash photolysis study. *J. Photochem. Photobiol.* B52, 111–116 (1999).
- Chemical background of the photoinitiation process. Demonstrated that the nitrogen purge step in photoinitiator preparation improves polymerization performance.
- Orellana B, Ruf AM, Encinas MV, Previtali CM, Bertolotti S. The photoinitiation mechanism of vinyl polymerization by riboflavin/triethanolamine in aqueous medium. *Macromolecules* 32, 6570–6573 (1999).
- Source reference for the riboflavin–triethanolamine photoinitiator adapted for use with two-photon polymerization in the present study.
- Encinas MV, Ruf AM, Bertolotti S, Previtali CM. Free radical polymerization photoinitiated by riboflavin/amines. Effect of the amine structure. *Macromolecules* 34, 2845–2847 (2001).
- Investigation of different amine types compatible with photopolymerization. Confirms triethanolamine was appropriate for use as a coinitiator.
- Turunen S, Kapyla E, Terzaki K *et al.* Pico- and femtosecond laser-induced crosslinking of protein microstructures: evaluation of processability and bioactivity. *Biofabrication* 3, 045002 (2011).
- Suggests riboflavin can also be used for multiphoton structuring of proteins, albeit at a much slower rate.
- Husain E, Naseem I. Riboflavin-mediated cellular photoinhibition of cisplatin-induced oxidative DNA breakage in mice epidermal keratinocytes. *Photodermatol. Photoimmunol. Photomed.* 24, 301–307 (2008).
- Hardwick CC, Herivel TR, Hernandez SC, Ruane PH, Goodrich RP. Separation, identification and quantification of riboflavin and its photoproducts in blood products using high-performance liquid chromatography with fluorescence detection: a method to support pathogen reduction technology. *Photochem. Photobiol.* 80, 609–615 (2004).
- Wollensak G, Wilsch M, Spoerl E, Seiler T. Collagen fiber diameter in the rabbit cornea after collagen crosslinking by riboflavin/UVA. *Cornea* 23, 503–507 (2004).
- Spoerl E, Mrochen M, Sliney D, Trokel S, Seiler T. Safety of UVA–riboflavin crosslinking of the cornea. *Cornea* 26, 385–389 (2007).

- 31 Hovakimyan M, Guthoff R, Knappe S *et al.* Short-term corneal response to cross-linking in rabbit eyes assessed by *in vivo* confocal laser scanning microscopy and histology. *Cornea* 30, 196–203 (2011).
- 32 Knappe S, Stachs O, Zihivov A, Hovakimyan M, Guthoff R. Results of confocal microscopy examinations after collagen cross-linking with riboflavin and UVA light in patients with progressive keratoconus. *Ophthalmologica* 225, 95–104 (2011).
- 33 Liao H, Munoz-Pinto D, Qu X, Hou Y, Grunlan MA, Hahn MS. Influence of hydrogel mechanical properties and mesh size on vocal fold fibroblast extracellular matrix production and phenotype. *Acta Biomater.* 4(5), 1161–1171 (2008).
- 34 Bulick AS, Muñoz-Pinto DJ, Qu X *et al.* Impact of endothelial cells and mechanical conditioning on smooth muscle cell extracellular matrix production and differentiation. *Tissue Eng. Part A* 15(4), 815–825 (2009).
- 35 Munoz-Pinto DJ, Bulick AS, Hahn MS. Uncoupled investigation of scaffold modulus and mesh size on smooth muscle cell behavior. *J. Biomed. Mater. Res. A* 90(1), 303–316 (2009).
- 36 Gittard SD. *Light-based Rapid Prototyping of Micro- and Nanoscale Medical Devices for Drug Delivery and Regenerative Medicine (PhD thesis)*. North Carolina State University, NC, USA (2011).
- 37 Musumeci G, Loreto C, Carnazza ML, Strehin I, Elisseff J. OA cartilage derived chondrocytes encapsulated in poly(ethylene glycol) diacrylate (PEGDA) for the evaluation of cartilage restoration and apoptosis in an *in vitro* model. *Histol. Histopathol.* 26(10), 1265–1278 (2011).
- 38 Lin S, Sangaj N, Razafarison T, Zhang C, Varghese S. Influence of physical properties of biomaterials on cellular behavior. *Pharm Res.* 28(6), 1422–1430 (2011).
- 39 Bahney CS, Lujan TJ, Hsu CW, Bottlang M, West JL, Johnstone B. Visible light photoinitiation of mesenchymal stem cell-laden bioresponsive hydrogels. *Eur. Cell Mater.* 22, 43–55 (2011).
- 40 Williams CG, Kim TK, Taboas A, Malik A, Manson P, Elisseff J. *In vitro* chondrogenesis of bone marrow-derived mesenchymal stem cells in a photopolymerizing hydrogel. *Tissue Eng.* 9(4), 679–688 (2003).
- 41 Lee SH, Moon JJ, West JL. Three-dimensional micropatterning of bioactive hydrogels via two-photon laser scanning photolithography for guided 3D cell migration. *Biomaterials* 29 (20), 2962–2968 (2008).
- 42 Browning MB, Cosgriff-Hernandez E. Development of a Biostable replacement for PEGDA hydrogels. *Biomacromolecules* 13, 779–786 (2012).
- 43 Xin AX, Gaydos C, Mao JJ. *In vitro* degradation behavior of photopolymerized PEG hydrogels as tissue engineering scaffold. Presented at: *EMBS Annual International Conference*. New York City, NY, USA, 30 August–3 September 2006.
- 44 Patel PN, Smith CK, Patrick CW Jr. Rheological and recovery properties of poly(ethylene glycol) diacrylate hydrogels and human adipose tissue. *J. Biomed. Mater. Res. A* 73(3), 313–319 (2005).
- 45 Schlie S, Ngezahayo A, Ovsianikov A *et al.* Three-dimensional cell growth on structures fabricated from ORMOCER by two-photon polymerization technique. *J. Biomater. Appl.* 22, 275–287 (2007).

■ Website

- 101 ISO 10993-5:2009. Biological evaluation of medical devices – Part 5: tests for *in vitro* cytotoxicity. www.iso.org/iso/catalogue_detail.htm?csnumber=36406

CHAPTER 5 - Toxicity and photosensitizing assessment of gelatin methacryloyl-based hydrogels photoinitiated with lithium phenyl-2,4,6-trimethylbenzoylphosphinate in human primary renal proximal tubule epithelial cells

Alexander K. Nguyen^{1,2}, Peter L. Goering², Vytas Reipa³, and Roger J. Narayan¹

1. UNC/NCSU Joint Department of Biomedical Engineering, North Carolina State University, Raleigh, NC
2. Division of Biology Chemistry and Materials Science, US Food and Drug Administration, Silver Spring, MD
3. Biosystems and Biomaterials Division, National Institute for Standards and Technology, Gaithersburg, MD

Reference: Nguyen, A.K.; Goering, P.L.; Reipa, V.; Narayan, R.J. Toxicity and photosensitizing assessment of gelatin methacryloyl-based hydrogels photoinitiated with lithium phenyl-2,4,6-trimethylbenzoylphosphinate in human primary renal proximal tubule epithelial cells. *Biointerphases* **2019**, *14*, 021007, doi:10.1116/1.5095886.

Abstract

Gelatin methacryloyl (GelMA) and lithium phenyl-2,4,6-trimethylbenzoylphosphinate (LAP) photoinitiator are commonly used in combination to produce a photosensitive polymer but there are concerns that must be addressed: the presence of unreacted monomer is well known to be cytotoxic, and lithium salts are known to cause acute kidney injury. In this study, acellular 10% GelMA hydrogels cross-linked with different LAP concentrations and cross-linking illumination times were evaluated for their cytotoxicity, photosensitizing potential, and elastic moduli. Alamar Blue and CyQuant Direct Cell viability assays were performed on human primary renal proximal tubule epithelial cells (hRPTECs) exposed to extracts of each formulation. UV exposure during cross-linking was not found to affect extract cytotoxicity in either assay. LAP concentration did not affect extract cytotoxicity as determined by the Alamar

Blue assay but reduced hRPTEC viability in the CyQuant Direct cell assay. Photocatalytic activity of formulation extracts toward NADH oxidation was used as a screening method for photosensitizing potential; longer UV exposure durations yielded extracts with less photocatalytic activity. Finally, elastic moduli determined using nanoindentation was found to plateau to approximately 20–25 kPa after exposure to 342 mJ/cm² at 2.87 mW of UV-A exposure regardless of LAP concentration. LAP at concentrations commonly used in bioprinting (<0.5% w/w) was not found to be cytotoxic although the differences in cytotoxicity evaluation determined from the two viability assays imply cell membrane damage and should be investigated further. Complete cross-linking of all formulations decreased photocatalytic activity while maintaining predictable final elastic moduli.

Introduction

Precise control of device geometry and mechanical properties in tissue engineering constructs is required to recapitulate stem cell behavior as to elicit the intended cellular response. Many additive manufacturing materials and methods are detrimental to cell viability due to extreme conditions such as heat, pressure, and/or chemical toxicity. Novel developments in photosensitive polymers bridge this gap by avoiding excessive heat and pressure, such as those found in fused deposition modeling, while reducing the impact of chemical toxicity. Photosensitive, cell-laden tissue engineering constructs have been fabricated using methods including bulk polymerization [162] and micromolding [163]. Beyond the direct injection or casting of the liquid cell-laden photopolymer for implantation, additive manufacturing using stereolithography [164, 165] or especially extrusion bioprinting [166-168] of these gels is a popular method to impart needed features such as pores for nutrient exchange.

There are two general strategies to bioprinted constructs: fabrication of an acellular scaffold followed by seeding with cells or direct fabrication of the constructs with cells in situ. Both methods come with their own benefits and drawbacks but share many common challenges. In either case, the base polymer and photoinitiator have highly reactive chemical moieties that allow them to participate in the cross-linking reaction. The base materials and their reaction by-products can be materials of toxicological concern especially with polymerization with cells in situ. In this case, there would be no postprocessing step that would allow these potentially toxic materials to leach out before exposure to cells or tissue. The second concern unique to photosensitive polymers is potential adverse responses resulting from photosensitization; cells seeded in the presence of UV and/or visible light dyes could be at greater risk to phototoxicity. This possibility is compounded further in the direct fabrication of cell constructs due to the exposure of the cells to UV and/or visible radiation. Finally, this photopolymer system must retain practical polymerization rates and mechanical properties to be a workable candidate for bioprinting.

Photopolymers are composed of a base monomer or oligomer combined with a photoinitiator. This type of polymer is commonly a simple mixture of the two compounds although it is possible to integrate the photoinitiator into the polymer itself [169]. Popular reactive moieties include epoxy [170], thiol-ene [171-173], and acrylate chemistries and are matched with a compatible photoinitiator chemistry. For example, SU-8 is a popular biocompatible polymer designed for the microelectronics industry but has found uses in biomedical research; this polymer uses epoxy ring-opening chemistries combined with a photoacid generator. However, the most popular reactive group in bioprinting is the acrylate

group which undergoes radical chain polymerization and can be photoinitiated by free radical-generating photoinitiators.

Gelatin methacryloyl (GelMA) contains acrylate groups on a gelatin backbone and can therefore be cross-linked in the presence of free-radical photoinitiators for use in bioprinting. It is also one of the most popular, commercially-available photosensitive hydrogels for bioprinting because of its facile synthesis methods, tunability of mechanical properties, and cytocompatibility [64, 174]. This material is normally used with Irgacure 2959, which provides such advantages as water-solubility and acceptable cytotoxicity [138, 175]. Even so, Irgacure 2959 is not ideal for use because it has peak absorption at 280 nm with tail absorption in the UV-A spectrum. In addition, UV-B light emitting diodes (LEDs) are much more expensive, have shorter life spans versus UV-A LEDs, and have a greater potential to produce genotoxic effects [176]; use of UV-A or visible light for cross-linking is preferred for these reasons. Lithium phenyl-2,4,6-trimethylbenzoylphosphinate (LAP) is an alternative photoinitiator that is more water soluble than Irgacure 2959 and has peak absorption in the UV-A spectrum and tail absorption in the visible spectrum. Direct comparison of Irgacure 2959 and LAP as photoinitiators for polyethyleneglycol diacrylate as a model acrylate hydrogel revealed gelation times 10× faster with LAP versus Irgacure 2959 using 365 nm light at similar concentrations and UV-A exposures [177]. Exposure of PEGda gels with LAP to 405 nm light was also faster than the corresponding Irgacure 2959 gel exposed to 365 nm light with a gelation time of 120 s vs 212 s, respectively.

Due to its promise as a photopolymer formulation for bioprinting, GelMA with LAP should be closely evaluated for its compatibility with cells and tissue. LAP is a lithium salt and would expose incorporated cells and surrounding tissues to lithium ions. Ionic lithium is a

treatment for bipolar disorder with a narrow therapeutic blood serum concentration between 0.4 and 0.75 mmol/l with excursions to as much as 1.2 mmol/L [178]. Serum lithium of 1.4 mmol/l is the lower threshold of acute toxicity while concentrations exceeding 3.5 mmol/l are considered toxic to patients. The main adverse effects are neurological; however, renal tubulointerstitial nephropathy and nephrogenic diabetes insipidus have been noted [179]. A small hydrogel implant would not raise blood serum levels to these thresholds which makes adverse neurological effects unlikely, but local concentrations of lithium range from 1.7 mmol/l for gels containing 0.05% w/w LAP to 34 mmol/l for 1% LAP gels, which is of potential concern to the embedded cells and surrounding tissue. Although lithium has been shown to cause diabetes insipidus by affecting membrane localization of aquaporin-2 in kidney nephron collecting duct cells [180], acute tubulointerstitial nephropathy caused by proximal tubule cell damage can cause irreversible reduction in kidney function [181]. Therefore, the goal of this study was to evaluate toxicity in human renal proximal tubule endothelial cells (hRPTECs) that were acutely exposed to different formulations of GelMA hydrogel extracts using various LAP concentrations and UV-A exposures used during cross-linking to model proximal tubule tissue in close proximity to a GelMA-LAP hydrogel implant.

Materials and Methods

UV-vis spectroscopy of LAP and Irgacure 2959 Solutions (0.1% w/w) of LAP and Irgacure 2959 were serially diluted to produce 1, 0.2, 0.04, and 0.008 mg/ml solutions in ultrapure water. Aliquots (200 μ l) of each solution were loaded into a UV-transparent, 96-well plate (Greiner Bio-One GmbH, Frickenhausen, Germany) and the absorbance read from 190 to 850 nm on a SpectraMax190 plate reader (Molecular Devices, San Jose, CA). Emission spectra of the fluorescent UV-A light source within the UV curing oven (CL-1000L, Analytik Jena US,

Upland, CA), modified with a soda lime glass plate in front of the light source to filter out UV-B wavelengths, were characterized with a spectrometer (Ocean Optics, Largo, FL).

Cell Culture hRPTECs (PCS-400-010, lot 63010943, ATCC, Manassas, VA) were received from the manufacturer cryopreserved at passage 2 and cultured using renal epithelial cell basal medium (PCS-400-030) with the renal epithelial cell growth kit (PCS-400-040). hRPTECs were cultured through an additional passage then cryopreserved at passage 4 in media with 10% v/v dimethyl sulfoxide and 15% fetal bovine serum at 3.85×10^6 cells/ml. Each experimental replicate used a passage 4 cryopreserved vial grown through one passage before seeding. Thus, hRPTECs used in the study were at passage 5.

10 % w/w GelMA-LAP formulations and extraction LAP and GelMA were purchased from Allevi (Philadelphia, PA). GelMA used in this study is sourced from type A, 300 bloom gelatin sourced from porcine skin and has a 50% degree of methacrylation. GelMA (10% w/w) was produced by weighing dry GelMA on an analytical balance (M-220, Denver Instrument, Bohemia, NY), adding the appropriate mass of water, then sonicating the mixture for 30 min at 40 °C. LAP was weighed on a six-point balance (XP56, Mettler Toledo, Columbus, OH), the appropriate mass of 10% GelMA added to form a 1% w/w LAP concentration, and the mixture sonicated for 30 min at 40 °C. Both the plain 10% GelMA solution and the 10% GelMA containing 1% LAP were sterile-filtered through a 0.2 µm PES membrane (Millipore, Burlington, MA). Appropriate volumes of each were mixed to produce 0.1%, 0.25%, 0.5%, and 1% w/w LAP in 10% GelMA and exposed to one of three UV-A exposure durations: 30, 120, or 300 s in a CL-1000L UV cross-linking oven; these exposure times correspond to 86, 342, or 855 mJ/cm² of UV-A radiation. Thus, a test matrix composed of four LAP concentrations and three UV-A exposure durations was created for a total of 12 formulations.

GelMA solutions (1 ml) with 0.1%, 0.25%, 0.5%, or 1% w/w LAP were deposited on polystyrene petri-dishes and exposed to 86, 342, or 855 mJ/cm² of UV-A according to the experimental design. Gels were removed from the polystyrene using a polytetrafluoroethylene (PTFE) cell scraper and transferred to preweighed 15 ml conical centrifuge tubes and the gel mass measured on an analytical balance. Gels were extracted in cell culture media containing additional penicillin and streptomycin (30-2300, ATCC, Manassas, VA) at a 0.1 g/ml gel mass to media volume ratio for 24 h at 37 °C on a shaker plate. This extraction ratio is suggested for irregularly shaped porous devices by ISO 10993-12:2012 [160]. Following extraction, gel extracts were aliquoted and stored at -20 °C until use for the cytotoxicity and photocatalysis assays.

Alamar Blue / CyQuant Direct Cell viability assays Three wells per treatment group were seeded with 1.0×10^4 cells/well and incubated for 24 h before toxicant addition. Media within seeded wells were aspirated and replaced with 100 μ l of GelMA formulation extract. Media, or media with 30 μ M AgNO₃, was added as the negative and positive cytotoxicity controls, respectively; an additional 100 μ l of each solution was added to cell-free wells as the assay blank. hRPTECs were exposed to the toxicants for 24 h before addition of 10 μ l of Alamar Blue dye. All plates were incubated for 4 h before reading on a fluorescent plate reader at 570 nm emission and 585 nm emission wavelengths. CyQuant dye and background suppression compound were added to the wells after the Alamar Blue data were collected and the plate incubated for an additional 30 min before reading at 480 nm excitation and 535 nm excitation wavelengths. Three independent replicate experiments of the described procedure were performed.

NADH photocatalysis assay Photocatalytic activity of the LAP extracts toward NADH oxidation was measured using UV-A or visible illumination based on a method, described by Lee et al. [182] Photogenerated reactive oxygen species (ROS) converts the fluorescent NADH molecule to NAD⁺ which is nonfluorescent. A clear-bottomed, black 96-well plate (Sigma Aldrich, St. Louis, MO), containing GelMA-LAP extracts or LAP at several concentrations in triplicate, was filled with a 150 μ M NADH (Sigma Aldrich, St. Louis, MO) solution in phosphate-buffered saline (PBS). The plate was exposed to either UV-A light at 5.5 mW/cm² by placing it on a transilluminator (Model 2UV, UVP Inc., Upland, CA) or visible light at 7 mW/cm²; light from a 300 W Xenon arc lamp (Oriel Instruments, Stratford, CT) was filtered through a 1 in. thick quartz flask filled with water to filter out infrared wavelengths, and a 400 nm longpass filter (10LWF-400-B, Oriel Instruments, Stratford, CT). A fluorescence reading at 340 nm excitation and 460 nm emission wavelengths was recorded every minute. The NADH oxidation rate is calculated from the linear portion of the NADH fluorescence decay curve.

GelMA chips for assessment of elastic moduli by nanoindentation testing GelMA chips (12 mm diameter, 1 mm thick) of each formulation were polymerized on 3-(trimethoxysilyl)propylmethacrylate (MAPTMS, Sigma Aldrich, St. Louis, MO) functionalized glass slides. In brief, glass microscope slides were etched with 2.8M NaOH at 60 °C, rinsed in de-ionized water, then sonicated in toluene containing 3% v/v MAPTMS for 30 min. Silanized slides were rinsed in toluene then heated at 150 °C for 1 h under vacuum. MAPTMS-functionalized slides were stored under vacuum until use.

PTFE molds containing a 12 mm diameter \times 1 mm deep cavity were used for GelMA chip polymerization. For each gel formulation, molds were filled with the corresponding GelMA-LAP solution, capped with an MAPTMS-functionalized slide, then exposed to UV-A for the

prescribed duration. The PTFE molds were removed and the glass slides with attached GelMA chips stored in PBS at 4 °C.

GelMA chips of each formulation underwent nanoindentation testing through the Bio Hardness Tester (Anton Paar, Graz, Austria) with a 500 µm radius spherical ruby tip, and the testing was performed at 23 °C in ambient air condition. Loading/unloading cycles consisted of a 1.2 milliNewton per minute (mN/min) loading rate to a maximum of 0.2 mN, a 30 s pause maintaining 0.2 mN force, followed by a 1.2 mN/min unloading rate to 0 mN. Elastic moduli (EIT) were calculated using the Hertz solution for spherical contact assuming a 0.5 Poisson's ratio and that the reduced modulus is equal to EIT due to the indenter modulus being much greater than the gel modulus. EIT was calculated using the formula [183]

$$P = \frac{4}{3} E_{IT} \sqrt{r h^3}$$

where P is the indentation load, r is the indenter tip radius, and h is the indentation depth. Seven measurements at different locations on the surfaces were performed on a chip representative of each formulation.

Statistical analyses Statistical analysis and graphics generation were performed using Graphpad Prism 6 (La Jolla, CA). Two-way ANOVA was performed on the Alamar Blue and CyQuant Direct Cell datasets with grouping by LAP concentration and UV exposure used in the fabrication of the GelMA chips. Dunnett's multiple comparison post hoc test was performed to compare each of the formulations to the negative control. Linear regression was also performed on Alamar Blue and CyQuant Direct Cell datasets after pooling the measurements from the UV exposure treatment groups to display cell viability versus LAP concentration in the photopolymer formulation.

Results

LAP has peak absorbance in the UV-A spectrum with tail absorbance in the visible spectrum UV-visible spectra of the fluorescent UV-A source emission, LAP absorbance, and Irgacure 2959 absorbance are presented in **Figure 5.1**. The light source emits sharp 436 nm and 405 nm peaks corresponding to the typical Hg visible emission peaks and a broad peak at 370 nm with a full width at half maximum of 20 nm. LAP exhibits an absorbance peak centered at 370 nm with 14.1% remaining at 405 nm. Irgacure 2959 exhibits peak absorbance at 280 nm and trails off to less than 0.5% of peak absorbance values at 370 nm.

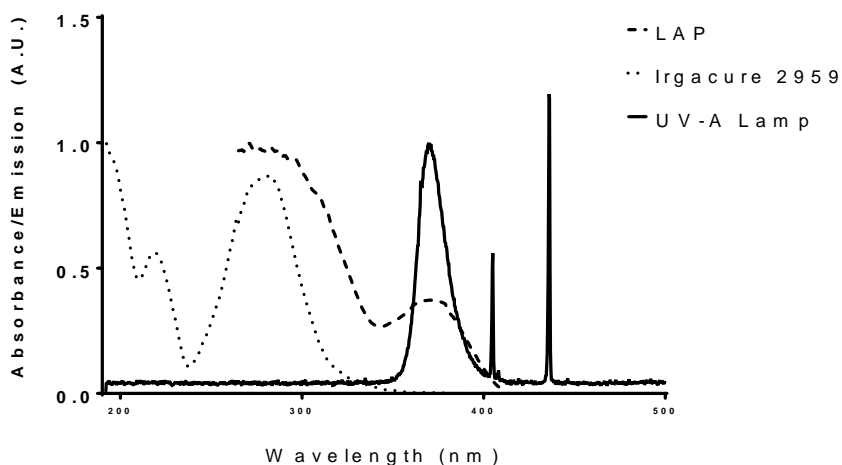


Figure 5.1 - UV-visible absorption spectra of Irgacure 2959 and LAP in ultrapure water superimposed on the fluorescent UV-A light source emission spectra normalized to the UV-A emission peak. The LAP absorbance peak at 370 nm matches the UV-A emission peak of the fluorescent light source. Irgacure 2959 has tail absorbance in this wavelength range.

Cross-linking duration has no effect on cytotoxicity of GelMA-LAP extracts; LAP concentration is negatively correlated with cell viability in the CyQuant Direct Cell assay Viability of hRPTEC after 24 h exposure to a GelMA formulation extracts was evaluated using Alamar Blue and CyQuant Direct Cell assays (**Figure 5.2**). Alamar Blue is a resazurin-based assay correlating the generation of highly-fluorescent resorufin resulting from cell metabolism to cell viability. CyQuant Direct Cell Proliferation assay is based on the CyQuant DNA stain but is

performed on whole cells instead of cell lysates; the fluorescent stain is membrane-permeable but the background suppression reagent is not; thus, only DNA in live cells with intact membranes will fluoresce. Using viability assays dependent on different mechanisms, i.e., metabolism versus membrane integrity, also gives insight into the mechanism of cytotoxicity. Neither LAP concentration in the GelMA photopolymer nor UV exposure used during cross-linking was identified as a significant source of variation in hRPTEC viability as judged by the Alamar Blue assay with all formulation extracts resulting in viability not significantly different from the negative control. Viability as judged by the CyQuant Direct Cell assay was not affected by the UV exposure used during cross-linking. Viabilities for the 0.1%, 0.25%, 0.5%, and 1% LAP formulations were 92.5%, 85.4%, 78.9%, and 67.1%, respectively, when averaging results from the three UV exposure scenarios. Viability of hRPTECs exposed to extracts from GelMA formulations containing 1% LAP in all UV exposure scenarios and those from the formulation containing 0.5% LAP exposed to 855 mJ/cm² UV-A was statistically different from the negative control.

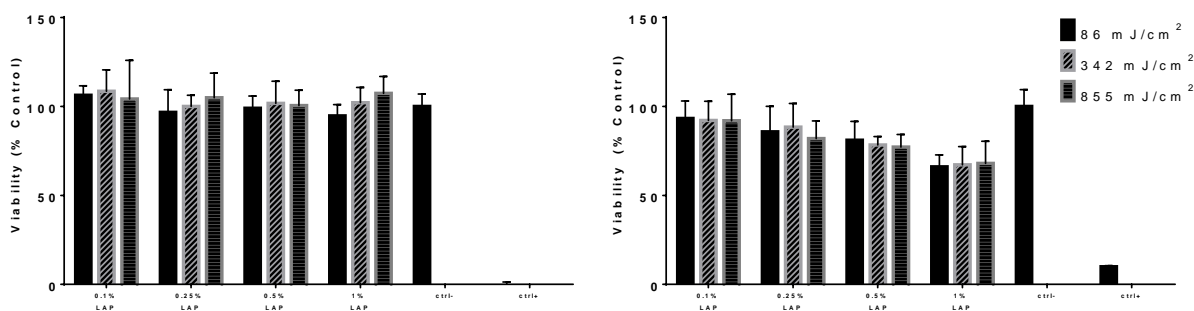


Figure 5.2 - Viability of hRPTEC exposed for 24 h to GelMA-LAP extracts determined via (a) Alamar Blue and (b) CyQuant Direct Cell assay. Values represent $\bar{X} \pm \text{SD}$ of $n = 3$ independent experimental replicates. Ctrl⁻ = cell media negative control; ctrl⁺ = 30 μM AgNO₃ positive control. Values marked with an asterisk (*) are statistically different from the negative control.

Because UV-A exposure used in cross-linking did not have a significant effect on extract cytotoxicity as determined from ANOVA, measurements from the UV-A exposure treatment groups were pooled for linear regression analysis (**Figure 5.3**). The concentration-response curve for hRPTEC viability as a function of LAP concentration in the GelMA formulation as determined by the Alamar Blue assay did not have a significant nonzero slope while the concentration-response curve as determined by the CyQuant Direct Cell assay revealed decreasing viability with increasing LAP concentration in the investigated region.

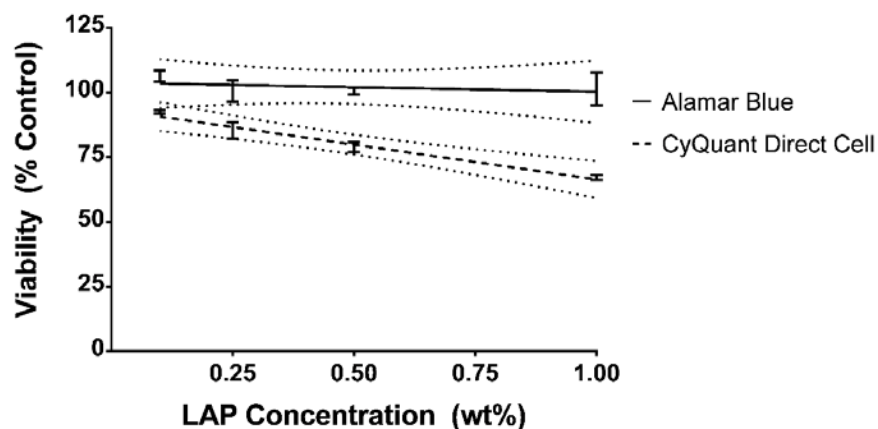


Figure 5.3 - No effect on hRPTEC viability of LAP concentration in GelMA formulations was determined using the Alamar Blue assay on formulation extracts. Linear regression analysis determined a statistically significant correlation between viability from the CyQuant Direct Cell assay and LAP concentration. Values represent $\bar{X} \pm SD$ pooling the values from all UV exposure treatment groups for each tested LAP concentration. Dotted lines represent the 95% confidence band.

Increasing cross-linking duration yields extracts with lower photocatalytic potential

Photocatalytic activity toward the oxidation of NADH to NAD⁺ was measured for LAP (**Figure 5.4**) and the formulation extracts (**Figure 5.5**). Solutions of LAP (0.01 mg/ml) exposed to 7 mW/cm² of visible (>400 nm) light did not have any measurable photocatalytic effect but exhibited a 1011 ± 210 mol/(min g) catalytic rate when exposed to 5.5 mW/cm² UV-A (350–

400 nm) light. Photocatalytic properties of all extracts exposed to UV-A light were generally within an order of magnitude of the photocatalytic rate of 0.01 mg/ml LAP. Increasing LAP concentration in the GelMA photopolymer formulation was associated with increasing photocatalytic activity of the extract. Conversely, increasing UV exposure during cross-linking was associated with a decrease in the extract's photocatalytic activity.

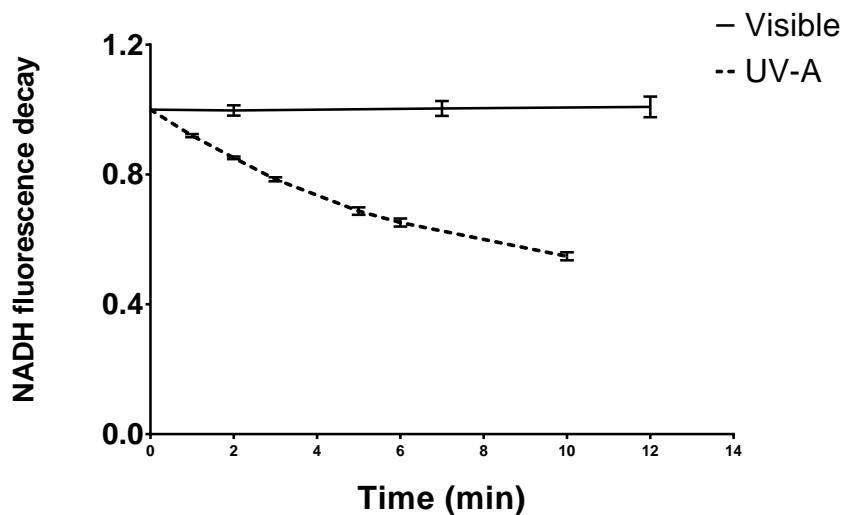


Figure 5.4 - Ratio of NADH fluorescence intensity of NADH photocatalyzed to NAD⁺ in the presence of 0.01 mg/ml LAP to NADH alone. Samples were exposed to visible (>400 nm; 7 mW/cm²) or UV-A (350–400 nm; 5.5 mW/cm²) light, and the fluorescence intensity at 340 nm excitation and 460 nm emission wavelengths was determined at each timepoint. The derivative of the curve at t = 0 was used to calculate the photocatalytic activity toward NADH oxidation. Values represent $\bar{X} \pm \text{SD}$ of n = 6 technical replicates.

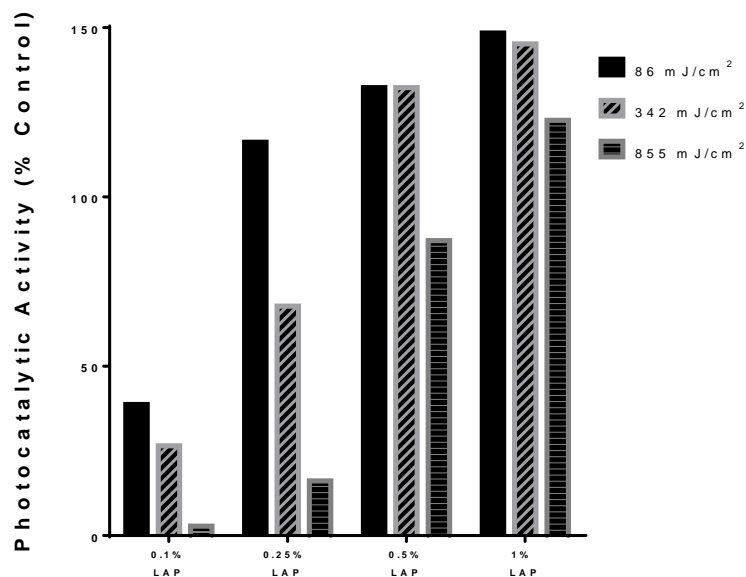


Figure 5.5 - Photocatalytic activity of GelMA-LAP extracts normalized to the activity of 0.01 mg/ml LAP in water. Values represent averages of $n = 3$ independent experimental replicates.

GelMA reaches stable elastic moduli after 120 s UV-A exposure Elastic moduli (EIT) were determined using nanoindentation from an average of seven measurements performed on a representative GelMA chip from each of the 12 formulations (**Figure 5.6**). Nanoindentation can be applied to wide array of material types and can precisely measure elastic modulus and hardness without having to measure the postindentation impression [184]. Nanoindentation is also widely applied to biological materials with larger indenters to avoid piercing the sample [185]. In this study, use of a 500 μm spherical tip was appropriate for softer substrates such as GelMA and avoids edge stresses associated with flat-tip geometries. Measurement at multiple locations on the GelMA surfaces reduced error from time-dependent changes in the material and made measurements representative of the entire surface rather than that of a single point. Within each tested LAP concentration, EIT increased between the 86 and 342 mJ/cm^2 UV-A exposures. However, for all samples except for the 0.1% w/w LAP concentration group, the elastic moduli

between the 342 and 855 mJ/cm² exposures were similar. A slight downward trend in elastic modulus was noted with increasing LAP concentration with the 0.25%, 0.5%, and 1.0% LAP gels at 25.2, 23.1, and 19.1 kPa, respectively, for the 855 mJ/cm² exposure and 11.9, 10.3, and 7.6 kPa for the 86 mJ/cm² exposure.

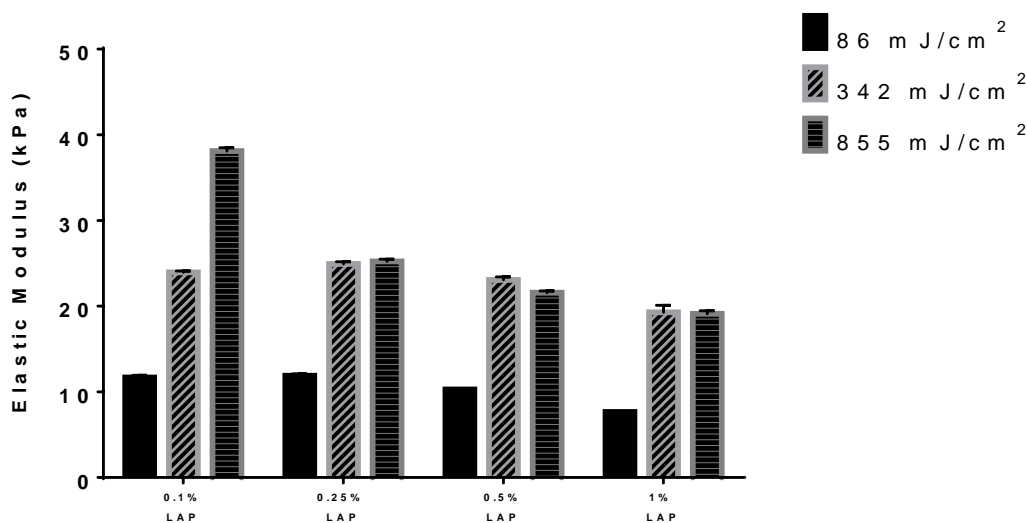


Figure 5.6 - Elastic moduli of 10% GelMA chips determined via nanoindentation. Values represent $\bar{X} \pm SD$ of $n = 7$ measurements at different locations on the GelMA chips.

Discussion

When considering materials for tissue engineering applications, hydrogel parameters such as mechanical properties, solidification mechanism, and cytocompatibility must be understood. Photosensitive polymers are attractive for tissue engineering because of their tunable mechanical properties and their ability to be precisely patterned. The benefits of photopolymers in tissue engineering are balanced by the reduced cytocompatibility stemming from the presence of ROS-generating photoinitiators and monomers involved in the cross-linking process. For these reasons, this study evaluated a common GelMA hydrogel with LAP photoinitiator by examining not only its cytocompatibility and mechanical properties, but also its photosensitizing potential.

Fabrication of tissue engineering constructs proceeds in one of two paradigms: fabrication of an acellular scaffold followed by cell seeding or direct fabrication with cells in situ. In the former case, cells are isolated from the cross-linking process and could be further protected by aging the scaffold in solvents to leach out toxic substances. In the latter case, cells would be exposed to potential toxicant agents in any, or combination of, four phases: (1) chemical exposure when suspended within the unreacted photopolymer, (2) light exposure in the presence of photoinitiator, (3) exposure to by-products of the cross-linking reaction, and (4) exposure to degradation products during long-term culture. In this study, hRPTECs were exposed to GelMA photopolymer extracts to assess cytotoxic responses in phase 3 and is an experimental model that is more relevant to assess the effects of freshly implanted GelMA on surrounding tissues.

Alamar Blue and CyQuant were performed as viability assays but demonstrated contrasting results. The metabolism-based Alamar Blue assay showed no reduction in cell viability for any extract, but the CyQuant assay showed reduced viability correlated with the LAP concentration in the photopolymer formulation. This unexpected outcome might be related to the difference in the mechanistic basis of each assay. Since hRPTEC metabolism is unaffected, one possible explanation is injury of the cell membrane allowing the fluorescence suppression dye to enter. Cells with damaged cell membranes are generally necrotic, which is the assumption of the CyQuant Direct Cell assay and other assays that operate on a similar membrane-damage mechanism, such as Neutral Red or Trypan Blue. However, membrane permeabilization without significant loss of viability is possible and is sometimes sought after for applications like drug delivery. For example, ultrasound was used to deliver 70 kDa dextran into KHT-C murine fibrosarcoma cells; viability above 90% was observed with successful permeabilization of approximately 20% of the cells [186]. Investigation of the effect of

membrane properties on extracellular or intracellular ROS-induced cell death revealed viability on par with the control of MDA-MB-231 breast cancer cells permeabilized with 0.002% saponin [187]. The mechanism of phospholipid bi-layer poration due to lipid oxidation was also determined with model 1,2-dioleoyl-sn-glycero-3-phosphocholine vesicles with exposure to methylene blue and phenothiazinium photosensitizers [188]. It is possible that the differences in results observed for these two viability assays are due to membrane poration.

Oxidative stress due to ROS from photoinitiator is a major concern during bioprinting with photopolymers and LAP could cause membrane poration. This oxidative potential was measured by the photosensitization screening method that tracks the oxidation of NADH to NAD⁺. Significant quantities of photocatalytic material remained in all extracts with the photocatalytic potential increasing with increasing LAP concentration in the gel that represents a possible mechanism of membrane poration. However, increasing UV exposure decreased the photocatalytic potential consistent with photobleaching and should have affected the CyQuant signal. One explanation is that the cells in this study were not exposed to light and extract simultaneously, so the photoactive by-products of cross-linking were not activated.

Elastic moduli of the gels exposed to 342 and 866 mJ/cm² 365 nm light were comparable for formulations containing 0.25%, 0.5%, and 1.0% LAP. These data contradict other studies reporting increasing elastic modulus or storage modulus with increasing photoinitiator concentrations and UV exposures exceeding multiple minutes [166]. Notably, many of these studies used Irgacure 2959 as the photoinitiator that has lower sensitivity to 365 nm light. For example, Fairbanks et al. reported gelation points for polyethyleneglycol diacrylate (PEGda) photoinitiated with 2.2 mmol/l Irgacure 2959 or LAP (corresponding approximately to 0.05% w/w) and cross-linked with 10 mW/cm² 365 nm light [177]. Irgacure 2959 required ten times the

light exposure duration versus LAP with a gelation time of 212 s vs 20 s. In addition, 0.22 mmol/l LAP using 365 nm light and 2.2 mmol/l LAP using 405 nm light had comparable gelation times at 141 and 120 s, respectively. Since a gelation time on the order of several minutes was required using Irgacure 2959, it is possible that other studies that report increasing gel stiffness with increasing UV exposure could be examining the region where cross-linking is still taking place. Duchi et al. also reported that increasing LAP concentration in a GelMA and hyaluronic acid gel correlated with increased storage modulus in an in situ photorheometry study [189]. However, gels containing 0.05% and 0.1% LAP exposed to continuous 365 nm light asymptotically reached the same storage modulus. When investigating the effect of different light exposure times on 0.1% LAP gels, 10 s of 100 mW/cm² illumination asymptotically reached the same ultimate storage modulus as the continuously illuminated sample. This result was corroborated by another photorheology study investigating GelMA with Irgacure 2959 to develop an empirical model predicting storage modulus. Equilibrium storage moduli obtained during in situ UV illumination was precisely predicted by GelMA concentration. UV light intensity and photoinitiator concentration were not found to precisely predict the final storage modulus but instead predicted the cross-linking rate; the total UV exposure energy was proportional to the square root of intensity and inversely proportional to the square root of photoinitiator concentration [190].

In the current study, 10% GelMA chips were exposed to UV in vast excess of the gelation point and should be expected to be fully cross-linked although the elastic modulus for sample D1, 10% GelMA with 0.1% w/w LAP and exposed to 855 mJ/cm² UV-A light, was significantly higher than the modulus for other gels at the same UV exposure. Given that this sample contained the lowest photoinitiator concentration, the elastic modulus should be equal to

or less than the modulus of the other samples at equivalent UV-A exposure. GelMA at a 10% w/w concentration tend to have elastic moduli around 10–25 kPa depending on gelatin origin and degree of methacrylation [191-193]. Considering all other investigated LAP concentrations yielded similar elastic moduli when fully cross-linked, the uncharacteristically high elastic modulus of 38 kPa for 10% GelMA, especially with the lowest investigated LAP concentration, is atypical of this material. GelMA containing all other investigated LAP concentrations was fully cross-linked by the 342 mJ/cm² exposure corresponding to 120 s. GelMA with LAP photoinitiator should reach predictable elastic moduli using shorter cross-linking times practical for bioprinting applications.

Conclusions

Viability measurements of hRPTEC differed depending on whether the assay measured metabolic activity or membrane integrity. These cells, exposed to GelMA extracts generated from chips containing 1% LAP, exhibited viability on par with the negative control when measured with the Alamar Blue assay but had 67% viability when measured with the CyQuant Direct Cell assay. A cell viability of <70% is considered the threshold for cytotoxic potential as described in an international standard for biocompatibility assessment [160]. Further investigation on whether this GelMA + LAP material causes membrane poration would help understand more precisely the potential adverse cell interactions. Increasing cross-linking duration decreases the photopolymer extract's photocatalytic potential without significantly affecting the final elastic modulus; exhaustive cross-linking should be performed on acellular gels. Based on the results of the current study, cross-linking at 405 nm instead of 370 nm would be greatly preferred for cell-laden constructs. The commercial availability and widespread use of GelMA and LAP in bioprinting is a testament to its cytocompatibility but bioprinted and cell-

laden photocrosslinkable hydrogels have been slow to reach a marketable form. High cell viability has been reported in the literature for GelMA and LAP and is mirrored in this study except for the highest LAP concentration, which is beyond the typical concentration used in bioprinting. The focus of future studies should shift to tissue function in different tissue models.

Toxicity and photosensitizing assessment of gelatin methacryloyl-based hydrogels photoinitiated with lithium phenyl-2,4,6-trimethylbenzoylphosphinate in human primary renal proximal tubule epithelial cells

Alexander K. Nguyen,^{1,2} Peter L. Goering,^{2,a)} Vytas Reipa,³ and Roger J. Narayan^{1,a)}

¹UNC/NCSSU Joint Department of Biomedical Engineering, North Carolina State University, Campus Box 7115, 911 Oval Drive, Raleigh, North Carolina 27695

²Division of Biology, Chemistry, and Materials Science, US Food and Drug Administration, 10903 New Hampshire Ave., Silver Spring, Maryland 20993

³Biosystems and Biomaterials Division, National Institute for Standards and Technology, 100 Bureau Drive, Gaithersburg, Maryland 20899

(Received 13 March 2019; accepted 17 April 2019; published 3 May 2019)

Gelatin methacryloyl (GelMA) and lithium phenyl-2,4,6-trimethylbenzoylphosphinate (LAP) photoinitiator are commonly used in combination to produce a photosensitive polymer but there are concerns that must be addressed: the presence of unreacted monomer is well known to be cytotoxic, and lithium salts are known to cause acute kidney injury. In this study, acellular 10% GelMA hydrogels cross-linked with different LAP concentrations and cross-linking illumination times were evaluated for their cytotoxicity, photosensitizing potential, and elastic moduli. Alamar Blue and CyQuant Direct Cell viability assays were performed on human primary renal proximal tubule epithelial cells (hRPTECs) exposed to extracts of each formulation. UV exposure during cross-linking was not found to affect extract cytotoxicity in either assay. LAP concentration did not affect extract cytotoxicity as determined by the Alamar Blue assay but reduced hRPTEC viability in the CyQuant Direct cell assay. Photocatalytic activity of formulation extracts toward NADH oxidation was used as a screening method for photosensitizing potential; longer UV exposure durations yielded extracts with less photocatalytic activity. Finally, elastic moduli determined using nanoindentation was found to plateau to approximately 20–25 kPa after exposure to 342 mJ/cm² at 2.87 mW of UV-A exposure regardless of LAP concentration. LAP at concentrations commonly used in bioprinting (<0.5% w/w) was not found to be cytotoxic although the differences in cytotoxicity evaluation determined from the two viability assays imply cell membrane damage and should be investigated further. Complete cross-linking of all formulations decreased photocatalytic activity while maintaining predictable final elastic moduli. *Published by the AVS.* <https://doi.org/10.1116/1.5095886>

I. INTRODUCTION

Precise control of device geometry and mechanical properties in tissue engineering constructs is required to recapitulate stem cell behavior as to elicit the intended cellular response. Many additive manufacturing materials and methods are detrimental to cell viability due to extreme conditions such as heat, pressure, and/or chemical toxicity. Novel developments in photosensitive polymers bridge this gap by avoiding excessive heat and pressure, such as those found in fused deposition modeling, while reducing the impact of chemical toxicity. Photosensitive, cell-laden tissue engineering constructs have been fabricated using methods including bulk polymerization¹ and micromolding.² Beyond the direct injection or casting of the liquid cell-laden photopolymer for implantation, additive manufacturing using stereolithography^{3,4} or especially extrusion bioprinting^{5–7} of these gels is a popular method to impart needed features such as pores for nutrient exchange.

There are two general strategies to bioprinted constructs: fabrication of an acellular scaffold followed by seeding with cells or direct fabrication of the constructs with cells *in situ*. Both methods come with their own benefits and drawbacks but share many common challenges. In either case, the base polymer and photoinitiator have highly reactive chemical moieties that allow them to participate in the cross-linking reaction. The base materials and their reaction by-products can be materials of toxicological concern especially with polymerization with cells *in situ*. In this case, there would be no postprocessing step that would allow these potentially toxic materials to leach out before exposure to cells or tissue. The second concern unique to photosensitive polymers is potential adverse responses resulting from photosensitization; cells seeded in the presence of UV and/or visible light dyes could be at greater risk to phototoxicity. This possibility is compounded further in the direct fabrication of cell constructs due to the exposure of the cells to UV and/or visible radiation. Finally, this photopolymer system must retain practical polymerization rates and mechanical properties to be a workable candidate for bioprinting.

^{a)}Authors to whom correspondence should be addressed: Peter.Goering@fda.hhs.gov and rjnaraya@ncsu.edu

Photopolymers are composed of a base monomer or oligomer combined with a photoinitiator. This type of polymer is commonly a simple mixture of the two compounds although it is possible to integrate the photoinitiator into the polymer itself.⁸ Popular reactive moieties include epoxy,⁹ thiol-ene,¹⁰⁻¹² and acrylate chemistries and are matched with a compatible photoinitiator chemistry. For example, SU-8 is a popular biocompatible polymer designed for the microelectronics industry but has found uses in biomedical research; this polymer uses epoxy ring-opening chemistries combined with a photoacid generator. However, the most popular reactive group in bioprinting is the acrylate group which undergoes radical chain polymerization and can be photoinitiated by free radical-generating photoinitiators.

Gelatin methacryloyl (GelMA) contains acrylate groups on a gelatin backbone and can therefore be cross-linked in the presence of free-radical photoinitiators for use in bioprinting. It is also one of the most popular, commercially-available photosensitive hydrogels for bioprinting because of its facile synthesis methods, tunability of mechanical properties, and cytocompatibility.^{13,14} This material is normally used with Irgacure 2959, which provides such advantages as water-solubility and acceptable cytotoxicity.^{15,16} Even so, Irgacure 2959 is not ideal for use because it has peak absorption at 280 nm with tail absorption in the UV-A spectrum. In addition, UV-B light emitting diodes (LEDs) are much more expensive, have shorter life spans versus UV-A LEDs, and have a greater potential to produce genotoxic effects;¹⁷ use of UV-A or visible light for cross-linking is preferred for these reasons. Lithium phenyl-2,4,6-trimethylbenzoylphosphine (LAP) is an alternative photoinitiator that is more water soluble than Irgacure 2959 and has peak absorption in the UV-A spectrum and tail absorption in the visible spectrum. Direct comparison of Irgacure 2959 and LAP as photoinitiators for polyethyleneglycol diacrylate as a model acrylate hydrogel revealed gelation times 10x faster with LAP versus Irgacure 2959 using 365 nm light at similar concentrations and UV-A exposures.¹⁸ Exposure of PEGda gels with LAP to 405 nm light was also faster than the corresponding Irgacure 2959 gel exposed to 365 nm light with a gelation time of 120 s vs 212 s, respectively.

Due to its promise as a photopolymer formulation for bioprinting, GelMA with LAP should be closely evaluated for its compatibility with cells and tissue. LAP is a lithium salt and would expose incorporated cells and surrounding tissues to lithium ions. Ionic lithium is a treatment for bipolar disorder with a narrow therapeutic blood serum concentration between 0.4 and 0.75 mmol/l with excursions to as much as 1.2 mmol/l.¹⁹ Serum lithium of 1.4 mmol/l is the lower threshold of acute toxicity while concentrations exceeding 3.5 mmol/l are considered toxic to patients. The main adverse effects are neurological; however, renal tubulointerstitial nephropathy and nephrogenic diabetes insipidus have been noted.²⁰ A small hydrogel implant would not raise blood serum levels to these thresholds which makes adverse neurological effects unlikely, but local concentrations of lithium range from 1.7 mmol/l for gels containing

0.05% w/w LAP to 34 mmol/l for 1% LAP gels, which is of potential concern to the embedded cells and surrounding tissue. Although lithium has been shown to cause diabetes insipidus by affecting membrane localization of aquaporin-2 in kidney nephron collecting duct cells,²¹ acute tubulointerstitial nephropathy caused by proximal tubule cell damage can cause irreversible reduction in kidney function.²² Therefore, the goal of this study was to evaluate toxicity in human renal proximal tubule endothelial cells (hRPTECs) that were acutely exposed to different formulations of GelMA hydrogel extracts using various LAP concentrations and UV-A exposures used during cross-linking to model proximal tubule tissue in close proximity to a GelMA-LAP hydrogel implant.

II. EXPERIMENT

A. UV-vis spectrometry of LAP and Irgacure 2959

Solutions (0.1% w/w) of LAP and Irgacure 2959 were serially diluted to produce 1, 0.2, 0.04, and 0.008 mg/ml solutions in ultrapure water. Aliquots (200 μ l) of each solution were loaded into a UV-transparent, 96-well plate (Greiner Bio-One GmbH, Frickenhausen, Germany) and the absorbance read from 190 to 850 nm on a SpectraMax190 plate reader (Molecular Devices, San Jose, CA). Emission spectra of the fluorescent UV-A light source within the UV curing oven (CL-1000L, Analytik Jena US, Upland, CA), modified with a soda lime glass plate in front of the light source to filter out UV-B wavelengths, were characterized with a spectrometer (Ocean Optics, Largo, FL).

B. Cell culture

hRPTECs (PCS-400-010, lot 63010943, ATCC, Manassas, VA) were received from the manufacturer cryopreserved at passage 2 and cultured using renal epithelial cell basal medium (PCS-400-030) with the renal epithelial cell growth kit (PCS-400-040). hRPTECs were cultured through an additional passage then cryopreserved at passage 4 in media with 10% v/v dimethyl sulfoxide and 15% fetal bovine serum at 3.85×10^6 cells/ml. Each experimental replicate used a passage 4 cryopreserved vial grown through one passage before seeding. Thus, hRPTECs used in the study were at passage 5.

C. 10% w/w GelMA-LAP formulations and extraction

LAP and GelMA were purchased from Allevi (Philadelphia, PA). GelMA used in this study is sourced from type A, 300 bloom gelatin sourced from porcine skin and has a 50% degree of methacrylation. GelMA (10% w/w) was produced by weighing dry GelMA on an analytical balance (M-220, Denver Instrument, Bohemia, NY), adding the appropriate mass of water, then sonicating the mixture for 30 min at 40 °C. LAP was weighed on a six-point balance (XP56, Mettler Toledo, Columbus, OH), the appropriate mass of 10% GelMA added to form a 1% w/w LAP concentration, and the mixture sonicated for 30 min at 40 °C.

Both the plain 10% GelMA solution and the 10% GelMA containing 1% LAP were sterile-filtered through a 0.2 μm PES membrane (Millipore, Burlington, MA). Appropriate volumes of each were mixed to produce 0.1%, 0.25%, 0.5%, and 1% w/w LAP in 10% GelMA and exposed to one of three UV-A exposure durations: 30, 120, or 300 s in a CL-1000L UV cross-linking oven; these exposure times correspond to 86, 342, or 855 mJ/cm^2 of UV-A radiation. Thus, a test matrix composed of four LAP concentrations and three UV-A exposure durations was created for a total of 12 formulations.

GelMA solutions (1 ml) with 0.1%, 0.25%, 0.5%, or 1% w/w LAP were deposited on polystyrene petri-dishes and exposed to 86, 342, or 855 mJ/cm^2 of UV-A according to the experimental design. Gels were removed from the polystyrene using a polytetrafluoroethylene (PTFE) cell scraper and transferred to preweighed 15 ml conical centrifuge tubes and the gel mass measured on an analytical balance. Gels were extracted in cell culture media containing additional penicillin and streptomycin (30-2300, ATCC, Manassas, VA) at a 0.1 g/ml gel mass to media volume ratio for 24 h at 37 °C on a shaker plate. This extraction ratio is suggested for irregularly shaped porous devices by ISO 10993-12:2012.²³ Following extraction, gel extracts were aliquoted and stored at -20 °C until use for the cytotoxicity and photocatalysis assays.

D. Alamar Blue/CyQuant Direct Cell viability assays

Three wells per treatment group were seeded with 1.0×10^4 cells/well and incubated for 24 h before toxicant addition. Media within seeded wells were aspirated and replaced with 100 μl of GelMA formulation extract. Media, or media with 30 μM AgNO_3 , was added as the negative and positive cytotoxicity controls, respectively; an additional 100 μl of each solution was added to cell-free wells as the assay blank. hRPTECs were exposed to the toxicants for 24 h before addition of 10 μl of Alamar Blue dye. All plates were incubated for 4 h before reading on a fluorescent plate reader at 570 nm emission and 585 nm emission wavelengths. CyQuant dye and background suppression compound were added to the wells after the Alamar Blue data were collected and the plate incubated for an additional 30 min before reading at 480 nm excitation and 535 nm excitation wavelengths. Three independent replicate experiments of the described procedure were performed.

E. NADH photocatalysis assay

Photocatalytic activity of the LAP extracts toward NADH oxidation was measured using UV-A or visible illumination based on a method, described by Lee *et al.*²⁴ Photogenerated reactive oxygen species (ROS) converts the fluorescent NADH molecule to NAD^+ which is nonfluorescent. A clear-bottomed, black 96-well plate (Sigma Aldrich, St. Louis, MO), containing GelMA-LAP extracts or LAP at several concentrations in triplicate, was filled with a 150 μM NADH (Sigma Aldrich, St. Louis, MO) solution in phosphate-

buffered saline (PBS). The plate was exposed to either UV-A light at 5.5 mW/cm^2 by placing it on a transilluminator (Model 2UV, UVP Inc., Upland, CA) or visible light at 7 mW/cm^2 ; light from a 300 W Xenon arc lamp (Orion Instruments, Stratford, CT) was filtered through a 1 in. thick quartz flask filled with water to filter out infrared wavelengths, and a 400 nm longpass filter (10LWF-400-B, Orion Instruments, Stratford, CT). A fluorescence reading at 340 nm excitation and 460 nm emission wavelengths was recorded every minute. The NADH oxidation rate is calculated from the linear portion of the NADH fluorescence decay curve.

F. GelMA chips for assessment of elastic moduli by nanoindentation testing

GelMA chips (12 mm diameter, 1 mm thick) of each formulation were polymerized on 3-(trimethoxysilyl)propylmethacrylate (MAPTMS, Sigma Aldrich, St. Louis, MO) functionalized glass slides. In brief, glass microscope slides were etched with 2.8M NaOH at 60 °C, rinsed in de-ionized water, then sonicated in toluene containing 3% v/v MAPTMS for 30 min. Silanized slides were rinsed in toluene then heated at 150 °C for 1 h under vacuum. MAPTMS-functionalized slides were stored under vacuum until use.

PTFE molds containing a 12 mm diameter \times 1 mm deep cavity were used for GelMA chip polymerization. For each gel formulation, molds were filled with the corresponding GelMA-LAP solution, capped with an MAPTMS-functionalized slide, then exposed to UV-A for the prescribed duration. The PTFE molds were removed and the glass slides with attached GelMA chips stored in PBS at 4 °C.

GelMA chips of each formulation underwent nanoindentation testing through the Bio Hardness Tester (Anton Paar, Graz, Austria) with a 500 μm radius spherical ruby tip, and the testing was performed at 23 °C in ambient air condition. Loading/unloading cycles consisted of a 1.2 milliNewton per minute (mN/min) loading rate to a maximum of 0.2 mN, a 30 s pause maintaining 0.2 mN force, followed by a 1.2 mN/min unloading rate to 0 mN. Elastic moduli (E_{IT}) were calculated using the Hertz solution for spherical contact assuming a 0.5 Poisson's ratio and that the reduced modulus is equal to E_{IT} due to the indenter modulus being much greater than the gel modulus. E_{IT} was calculated using the formula²⁵

$$P = \frac{4}{3} E_{\text{IT}} \sqrt{r h^3},$$

where P is the indentation load, r is the indenter tip radius, and h is the indentation depth. Seven measurements at different locations on the surfaces were performed on a chip representative of each formulation.

G. Statistical analyses

Statistical analysis and graphics generation were performed using Graphpad Prism 6 (La Jolla, CA). Two-way ANOVA was performed on the Alamar Blue and CyQuant

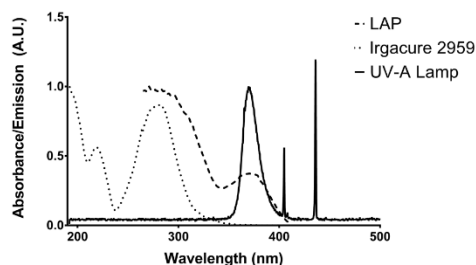


FIG. 1. UV-visible absorption spectra of Irgacure 2959 and LAP in ultrapure water superimposed on the fluorescent UV-A light source emission spectra normalized to the UV-A emission peak. The LAP absorbance peak at 370 nm matches the UV-A emission peak of the fluorescent light source. Irgacure 2959 has tail absorbance in this wavelength range.

Direct Cell datasets with grouping by LAP concentration and UV exposure used in the fabrication of the GelMA chips. Dunnett's multiple comparison *post hoc* test was performed to compare each of the formulations to the negative control. Linear regression was also performed on Alamar Blue and CyQuant Direct Cell datasets after pooling the measurements from the UV exposure treatment groups to display cell viability versus LAP concentration in the photopolymer formulation.

III. RESULTS AND DISCUSSION

A. LAP has peak absorbance in the UV-A spectrum with tail absorbance in the visible spectrum

UV-visible spectra of the fluorescent UV-A source emission, LAP absorbance, and Irgacure 2959 absorbance are presented in Fig. 1. The light source emits sharp 436 nm and 405 nm peaks corresponding to the typical Hg visible emission peaks and a broad peak at 370 nm with a full width at half maximum of 20 nm. LAP exhibits an absorbance peak centered at 370 nm with 14.1% remaining at 405 nm. Irgacure 2959 exhibits peak absorbance at 280 nm and trails off to less than 0.5% of peak absorbance values at 370 nm.

B. Cross-linking duration has no effect on cytotoxicity of GelMA-LAP extracts; LAP concentration is negatively correlated with cell viability in the CyQuant Direct Cell assay

Viability of hRPTEC after 24 h exposure to a GelMA formulation extracts was evaluated using Alamar Blue and CyQuant Direct Cell assays (Fig. 2). Alamar Blue is a resazurin-based assay correlating the generation of highly-fluorescent resorufin resulting from cell metabolism to cell viability. CyQuant Direct Cell Proliferation assay is based on the CyQuant DNA stain but is performed on whole cells instead of cell lysates; the fluorescent stain is membrane-permeable but the background suppression reagent is not; thus, only DNA in live cells with intact membranes will fluoresce. Using viability assays dependent on different mechanisms, i.e., metabolism versus membrane integrity, also gives insight into the mechanism of cytotoxicity.

Neither LAP concentration in the GelMA photopolymer nor UV exposure used during cross-linking was identified as a significant source of variation in hRPTEC viability as judged by the Alamar Blue assay with all formulation extracts resulting in viability not significantly different from the negative control. Viability as judged by the CyQuant Direct Cell assay was not affected by the UV exposure used during cross-linking. Viabilities for the 0.1%, 0.25%, 0.5%, and 1% LAP formulations were 92.5%, 85.4%, 78.9%, and 67.1%, respectively, when averaging results from the three UV exposure scenarios. Viability of hRPTECs exposed to extracts from GelMA formulations containing 1% LAP in all UV exposure scenarios and those from the formulation containing 0.5% LAP exposed to 855 mJ/cm² UV-A was statistically different from the negative control. Because UV-A exposure used in cross-linking did not have a significant effect on extract cytotoxicity as determined from ANOVA, measurements from the UV-A exposure treatment groups were pooled for linear regression analysis (Fig. 3). The concentration-response curve for hRPTEC viability as a function of LAP concentration in the GelMA formulation as determined by the Alamar Blue assay did not have a significant nonzero slope while the concentration-response curve as determined by the CyQuant Direct Cell assay revealed

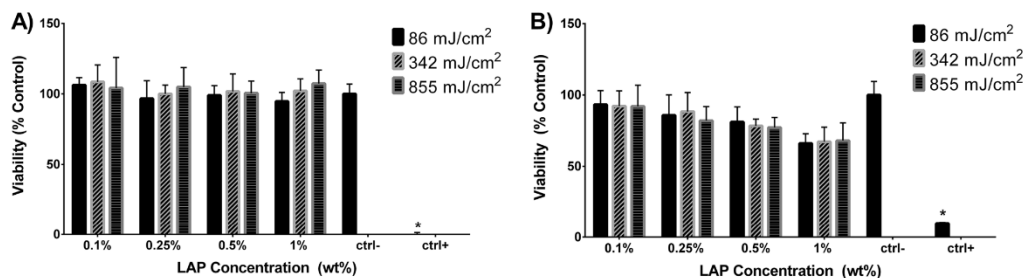


FIG. 2. Viability of hRPTEC exposed for 24 h to GelMA-LAP extracts determined via (a) Alamar Blue and (b) CyQuant Direct Cell assay. Values represent $\bar{X} \pm SD$ of $n = 3$ independent experimental replicates. Ctrl- = cell media negative control; ctrl+ = 30 μ M AgNO₃ positive control. Values marked with an asterisk (*) are statistically different from the negative control.

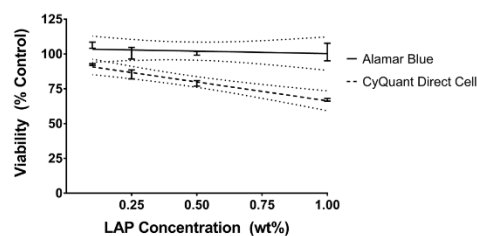


Fig. 3. No effect on hRPTEC viability of LAP concentration in GelMA formulations was determined using the Alamar Blue assay on formulation extracts. Linear regression analysis determined a statistically significant correlation between viability from the CyQuant Direct Cell assay and LAP concentration. Values represent $\bar{X} \pm SD$ pooling the values from all UV exposure treatment groups for each tested LAP concentration. Dotted lines represent the 95% confidence band.

decreasing viability with increasing LAP concentration in the investigated region.

C. Increasing cross-linking duration yields extracts with lower photocatalytic potential

Photocatalytic activity toward the oxidation of NADH to NAD^+ was measured for LAP (Fig. 4) and the formulation extracts (Fig. 5). Solutions of LAP (0.01 mg/ml) exposed to 7 mW/cm^2 of visible ($>400 \text{ nm}$) light did not have any measurable photocatalytic effect but exhibited a $1011 \pm 210 \text{ mol}/(\text{min g})$ catalytic rate when exposed to 5.5 mW/cm^2 UV-A (350–400 nm) light.

Photocatalytic properties of all extracts exposed to UV-A light were generally within an order of magnitude of the photocatalytic rate of 0.01 mg/ml LAP. Increasing LAP concentration in the GelMA photopolymer formulation was associated with increasing photocatalytic activity of the extract. Conversely, increasing UV exposure during cross-linking was associated with a decrease in the extract's photocatalytic activity.

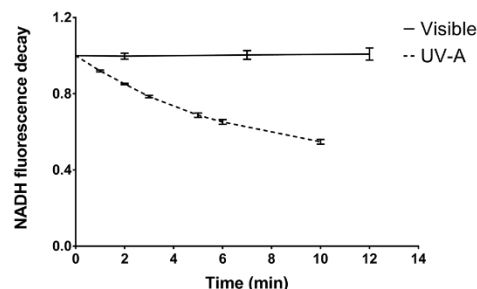


Fig. 4. Ratio of NADH fluorescence intensity of NADH photocatalyzed to NAD^+ in the presence of 0.01 mg/ml LAP to NADH alone. Samples were exposed to visible ($>400 \text{ nm}$; 7 mW/cm^2) or UV-A (350–400 nm; 5.5 mW/cm^2) light, and the fluorescence intensity at 340 nm excitation and 460 nm emission wavelengths was determined at each timepoint. The derivative of the curve at $t=0$ was used to calculate the photocatalytic activity toward NADH oxidation. Values represent $\bar{X} \pm SD$ of $n=6$ technical replicates.

Biointerphases, Vol. 14, No. 2, Mar/Apr 2019

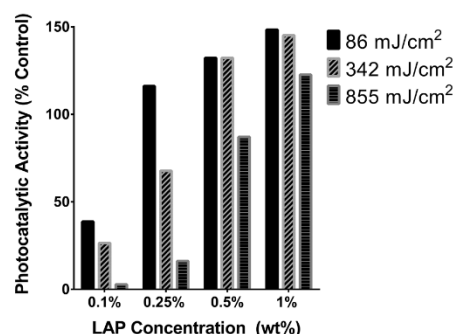


Fig. 5. Photocatalytic activity of GelMA-LAP extracts normalized to the activity of 0.01 mg/ml LAP in water. Values represent averages of $n=3$ independent experimental replicates.

D. GelMA reaches stable elastic moduli after 120 s UV-A exposure

Elastic moduli (E_{IT}) were determined using nanoindentation from an average of seven measurements performed on a representative GelMA chip from each of the 12 formulations (Fig. 6). Nanoindentation can be applied to wide array of material types and can precisely measure elastic modulus and hardness without having to measure the postindentation impression.²⁶ Nanoindentation is also widely applied to biological materials with larger indenters to avoid piercing the sample.²⁷ In this study, use of a $500 \mu\text{m}$ spherical tip was appropriate for softer substrates such as GelMA and avoids edge stresses associated with flat-tip geometries. Measurement at multiple locations on the GelMA surfaces reduced error from time-dependent changes in the material and made measurements representative of the entire surface rather than that of a single point. Within each tested LAP concentration, E_{IT} increased between the 86 and 342 mJ/cm^2 UV-A exposures. However, for all samples except for the 0.1% w/w LAP concentration group, the elastic moduli between the 342 and 855 mJ/cm^2 exposures were similar. A slight downward trend in elastic modulus was noted with increasing LAP concentration with the 0.25%, 0.5%, and

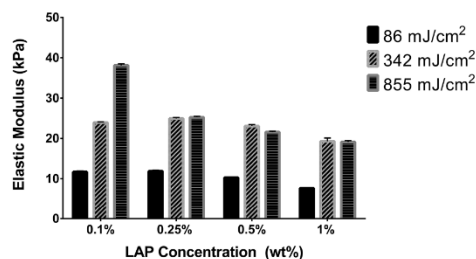


Fig. 6. Elastic moduli of 10% GelMA chips determined via nanoindentation. Values represent $\bar{X} \pm SD$ of $n=7$ measurements at different locations on the GelMA chips.

1.0% LAP gels at 25.2, 23.1, and 19.1 kPa, respectively, for the 855 mJ/cm² exposure and 11.9, 10.3, and 7.6 kPa for the 86 mJ/cm² exposure.

IV. DISCUSSION

When considering materials for tissue engineering applications, hydrogel parameters such as mechanical properties, solidification mechanism, and cytocompatibility must be understood. Photosensitive polymers are attractive for tissue engineering because of their tunable mechanical properties and their ability to be precisely patterned. The benefits of photopolymers in tissue engineering are balanced by the reduced cytocompatibility stemming from the presence of ROS-generating photoinitiators and monomers involved in the cross-linking process. For these reasons, this study evaluated a common GelMA hydrogel with LAP photoinitiator by examining not only its cytocompatibility and mechanical properties, but also its photosensitizing potential. Fabrication of tissue engineering constructs proceeds in one of two paradigms: fabrication of an acellular scaffold followed by cell seeding or direct fabrication with cells *in situ*. In the former case, cells are isolated from the cross-linking process and could be further protected by aging the scaffold in solvents to leach out toxic substances. In the latter case, cells would be exposed to potential toxicant agents in any, or combination of, four phases: (1) chemical exposure when suspended within the unreacted photopolymer, (2) light exposure in the presence of photoinitiator, (3) exposure to by-products of the cross-linking reaction, and (4) exposure to degradation products during long-term culture. In this study, hRPTECs were exposed to GelMA photopolymer extracts to assess cytotoxic responses in phase 3 and is an experimental model that is more relevant to assess the effects of freshly implanted GelMA on surrounding tissues.

Alamar Blue and CyQuant were performed as viability assays but demonstrated contrasting results. The metabolism-based Alamar Blue assay showed no reduction in cell viability for any extract, but the CyQuant assay showed reduced viability correlated with the LAP concentration in the photopolymer formulation. This unexpected outcome might be related to the difference in the mechanistic basis of each assay. Since hRPTEC metabolism is unaffected, one possible explanation is injury of the cell membrane allowing the fluorescence suppression dye to enter. Cells with damaged cell membranes are generally necrotic, which is the assumption of the CyQuant Direct Cell assay and other assays that operate on a similar membrane-damage mechanism, such as Neutral Red or Trypan Blue. However, membrane permeabilization without significant loss of viability is possible and is sometimes sought after for applications like drug delivery. For example, ultrasound was used to deliver 70 kDa dextran into KHT-C murine fibrosarcoma cells; viability above 90% was observed with successful permeabilization of approximately 20% of the cells.²⁸ Investigation of the effect of membrane properties on extracellular or intracellular ROS-induced cell death revealed viability on par with the

control of MDA-MB-231 breast cancer cells permeabilized with 0.002% saponin.²⁹ The mechanism of phospholipid bi-layer poration due to lipid oxidation was also determined with model 1,2-dioleoyl-sn-glycero-3-phosphocholine vesicles with exposure to methylene blue and phenothiazinium photosensitizers.³⁰ It is possible that the differences in results observed for these two viability assays are due to membrane poration.

Oxidative stress due to ROS from photoinitiator is a major concern during bioprinting with photopolymers and LAP could cause membrane poration. This oxidative potential was measured by the photosensitization screening method that tracks the oxidation of NADH to NAD⁺. Significant quantities of photocatalytic material remained in all extracts with the photocatalytic potential increasing with increasing LAP concentration in the gel that represents a possible mechanism of membrane poration. However, increasing UV exposure decreased the photocatalytic potential consistent with photobleaching and should have affected the CyQuant signal. One explanation is that the cells in this study were not exposed to light and extract simultaneously, so the photoactive by-products of cross-linking were not activated.

Elastic moduli of the gels exposed to 342 and 866 mJ/cm² 365 nm light were comparable for formulations containing 0.25%, 0.5%, and 1.0% LAP. These data contradict other studies reporting increasing elastic modulus or storage modulus with increasing photoinitiator concentrations and UV exposures exceeding multiple minutes.⁵ Notably, many of these studies used Irgacure 2959 as the photoinitiator that has lower sensitivity to 365 nm light. For example, Fairbanks *et al.* reported gelation points for polyethyleneglycol diacrylate (PEGda) photoinitiated with 2.2 mmol/l Irgacure 2959 or LAP (corresponding approximately to 0.05% w/w) and cross-linked with 10 mW/cm² 365 nm light.¹⁸ Irgacure 2959 required ten times the light exposure duration versus LAP with a gelation time of 212 s vs 20 s. In addition, 0.22 mmol/l LAP using 365 nm light and 2.2 mmol/l LAP using 405 nm light had comparable gelation times at 141 and 120 s, respectively. Since a gelation time on the order of several minutes was required using Irgacure 2959, it is possible that other studies that report increasing gel stiffness with increasing UV exposure could be examining the region where cross-linking is still taking place. Duchi *et al.* also reported that increasing LAP concentration in a GelMA and hyaluronic acid gel correlated with increased storage modulus in an *in situ* photorheometry study.³¹ However, gels containing 0.05% and 0.1% LAP exposed to continuous 365 nm light asymptotically reached the same storage modulus. When investigating the effect of different light exposure times on 0.1% LAP gels, 10 s of 100 mW/cm² illumination asymptotically reached the same ultimate storage modulus as the continuously illuminated sample. This result was corroborated by another photorheology study investigating GelMA with Irgacure 2959 to develop an empirical model predicting storage modulus. Equilibrium storage moduli obtained during *in situ* UV illumination was precisely predicted by GelMA

concentration. UV light intensity and photoinitiator concentration were not found to precisely predict the final storage modulus but instead predicted the cross-linking rate; the total UV exposure energy was proportional to the square root of intensity and inversely proportional to the square root of photoinitiator concentration.³²

In the current study, 10% GelMA chips were exposed to UV in vast excess of the gelation point and should be expected to be fully cross-linked although the elastic modulus for sample D1, 10% GelMA with 0.1% w/w LAP and exposed to 855 mJ/cm² UV-A light, was significantly higher than the modulus for other gels at the same UV exposure. Given that this sample contained the lowest photoinitiator concentration, the elastic modulus should be equal to or less than the modulus of the other samples at equivalent UV-A exposure. GelMA at a 10% w/w concentration tend to have elastic moduli around 10–25 kPa depending on gelatin origin and degree of methacrylation.^{33–35} Considering all other investigated LAP concentrations yielded similar elastic moduli when fully cross-linked, the uncharacteristically high elastic modulus of 38 kPa for 10% GelMA, especially with the lowest investigated LAP concentration, is atypical of this material. GelMA containing all other investigated LAP concentrations was fully cross-linked by the 342 mJ/cm² exposure corresponding to 120 s. GelMA with LAP photoinitiator should reach predictable elastic moduli using shorter cross-linking times practical for bioprinting applications.

V. SUMMARY AND CONCLUSIONS

Viability measurements of hRPTEC differed depending on whether the assay measured metabolic activity or membrane integrity. These cells, exposed to GelMA extracts generated from chips containing 1% LAP, exhibited viability on par with the negative control when measured with the Alamar Blue assay but had 67% viability when measured with the CyQuant Direct Cell assay. A cell viability of <70% is considered the threshold for cytotoxic potential as described in an international standard for biocompatibility assessment.²³ Further investigation on whether this GelMA + LAP material causes membrane poration would help understand more precisely the potential adverse cell interactions. Increasing cross-linking duration decreases the photopolymer extract's photocatalytic potential without significantly affecting the final elastic modulus; exhaustive cross-linking should be performed on acellular gels. Based on the results of the current study, cross-linking at 405 nm instead of 370 nm would be greatly preferred for cell-laden constructs. The commercial availability and widespread use of GelMA and LAP in bioprinting is a testament to its cytocompatibility but bioprinted and cell-laden photocrosslinkable hydrogels have been slow to reach a marketable form. High cell viability has been reported in the literature for GelMA and LAP and is mirrored in this study except for the highest LAP concentration, which is beyond the typical concentration used in bioprinting. The focus of future studies should shift to tissue function in different tissue models.

DISCLAIMER

The findings and conclusions in this paper have not been formally disseminated by the Food and Drug Administration and should not be construed to represent any agency determination or policy. The mention of commercial products, their sources, or their use in connection with material reported herein is not to be construed as either an actual or implied endorsement of such products by Department of Health and Human Services.

ACKNOWLEDGMENTS

The project is funded by the National Institutes of Health (NIH) under Grant No. R21-A1117748. The authors acknowledge Anton Paar's Mihaela Dubisson, Brandon Frye, and Nate Newbury for technical expertise and instrumentation (Biointenter UNHT3 Bio).

¹X. Zheng Shu, Y. Liu, F. S. Palumbo, Y. Luo, and G. D. Prestwich, *Biomaterials* **25**, 1339 (2004).

²J. Yeh, Y. Ling, J. M. Karp, J. Gantz, A. Chandawarkar, G. Eng, J. Blumling Iii, R. Langer, and A. Khademhosseini, *Biomaterials* **27**, 5391 (2006).

³K. S. Lim et al., *Biofabrication* **10**, 034101 (2018).

⁴Z. Wang, H. Kumar, Z. Tian, X. Jin, J. F. Holzman, F. Menard, and K. Kim, *ACS Appl. Mater. Interfaces* **10**, 26859 (2018).

⁵I. Pepelanova, K. Kruppa, T. Scheper, and A. Lavrentieva, *Bioengineering* **5**, 55 (2018).

⁶C. McBeth, J. Lauer, M. Ottersbach, J. Campbell, A. Sharon, and A. F. Sauer-Budge, *Biofabrication* **9**, 015009 (2017).

⁷W. Liu et al., *Adv. Healthc. Mater.* **6**, 1601451 (2017).

⁸S. R. Govindarajan, T. Jain, J.-W. Choi, A. Joy, I. Isayeva, and K. Vorvolakos, *Polymer* **152**, 9 (2018).

⁹Y. Lin, C. Gao, D. Gritsenko, R. Zhou, and J. Xu, *Microfluid. Nanofluid.* **22**, 97 (2018).

¹⁰S. Bertlein et al., *Adv. Mater.* **29**, 1703404 (2017).

¹¹H. W. Ooi, C. Mota, A. T. ten Cate, A. Calore, L. Moroni, and M. B. Baker, *Biomacromolecules* **19**, 3390 (2018).

¹²S. Zheng, M. Zlatin, P. R. Selvaganapathy, and M. A. Brook, *Addit. Manuf.* **24**, 86 (2018).

¹³A. I. Van Den Bulcke, B. Bogdanov, N. De Rooze, E. H. Schacht, M. Cornelissen, and H. Berghmans, *Biomacromolecules* **1**, 31 (2000).

¹⁴H. Shirahama, B. H. Lee, L. P. Tan, and N. J. Cho, *Sci. Rep.* **6**, 31036 (2016).

¹⁵C. G. Williams, A. N. Malik, T. K. Kim, P. N. Manson, and J. H. Elisseeff, *Biomaterials* **26**, 1211 (2005).

¹⁶T. Mironi-Harpaz, D. Y. Wang, S. Venkatraman, and D. Seliktar, *Acta Biomater.* **8**, 1838 (2012).

¹⁷H. Ikehata et al., *J. Invest. Dermatol.* **133**, 1850 (2013).

¹⁸B. D. Fairbanks, M. P. Schwartz, C. N. Bowman, and K. S. Anseth, *Biomaterials* **30**, 6702 (2009).

¹⁹W. E. Severus, N. Kleindienst, F. Seemüller, S. Frangou, H. J. Möller, and W. Greil, *Bipolar Disord.* **10**, 231 (2008).

²⁰J. Baird-Gunning, T. Lea-Henry, L. C. G. Hoegberg, S. Gosselin, and D. M. Roberts, *J. Intensive Care Med.* **32**, 249 (2016).

²¹D. Marples, S. Christensen, E. I. Christensen, P. D. Ottosen, and S. Nielsen, *J. Clin. Invest.* **95**, 1838 (1995).

²²K. S. Hodgkins and H. W. Schnaper, *Pediatr. Nephrol.* **27**, 901 (2012).

²³International Organization for Standardization, see: <https://www.iso.org/standard/36406.html> for "Biological Evaluation of Medical Devices (ISO Standard No. 10993:2009)."

²⁴N. A. Lee, S. J. Kim, B. J. Park, H. M. Park, M. Yoon, B. H. Chung, and N. W. Song, *Photochem. Photobiol. Sci.* **10**, 1979 (2011).

²⁵K. L. Johnson, *Contact Mechanics* (Cambridge University, Cambridge, 1985).

²⁶W. C. Oliver and G. M. Pharr, *J. Mater. Res.* **7**, 1564 (2011).

- ²⁷L. Qian and H. Zhao, *Micromachines* **9**, 654 (2018).
- ²⁸R. Karshafian, P. D. Bevan, R. Williams, S. Samac, and P. N. Burns, *Ultrasound Med. Biol.* **35**, 847 (2009).
- ²⁹H. R. Molavian, A. Goldman, C. J. Phipps, M. Kohandel, B. G. Wouters, S. Sengupta, and S. Sivaloganathan, *Sci. Rep.* **6**, 27439 (2016).
- ³⁰I. O. L. Bacellar, M. S. Baptista, H. C. Junqueira, M. Wainwright, F. Thalmann, C. M. Marques, and A. P. Schroder, *Biochim. Biophys. Acta Biomembranes* **1860**, 2366 (2018).
- ³¹S. Duchi *et al.*, *Sci. Rep.* **7**, 5837 (2017).
- ³²C. O'Connell *et al.*, *Soft Matter* **14**, 2142 (2018).
- ³³G. Eng, B. W. Lee, H. Parsa, C. D. Chin, J. Schneider, G. Linkov, S. K. Sia, and G. Vunjak-Novakovic, *Proc. Natl. Acad. Sci. U.S.A.* **110**, 4551 (2013).
- ³⁴Z. Wang, Z. Tian, F. Menard, and K. Kim, *Biofabrication* **9**, 044101 (2017).
- ³⁵X. Zhao *et al.*, *Adv. Healthc. Mater.* **5**, 108 (2016).

CHAPTER 6 – Lithium Phenyl (2,4,6-trimethylbenzoyl) phosphinate with exposure to 405 nm light is cytotoxic to mammalian cells but not mutagenic in bacterial reverse mutation assays

Alexander K. Nguyen^{1,2}, Peter L. Goering², Rosalie K. Elespuru², Srilekha Sarkar Das², and Roger J. Narayan¹

1. UNC/NCSU Joint Department of Biomedical Engineering, North Carolina State University, Raleigh, NC
2. Division of Biology Chemistry and Materials Science, US Food and Drug Administration, Silver Spring, MD

Reference: Nguyen, A.K.; Goering, P.L.; Elespuru, R.K.; Sarkar Das, S.; Narayan, R.J. The Photoinitiator Lithium Phenyl (2,4,6-Trimethylbenzoyl) Phosphinate with Exposure to 405 nm Light Is Cytotoxic to Mammalian Cells but Not Mutagenic in Bacterial Reverse Mutation Assays. *Polymers* **2020**, *12*, 1489.

Abstract

Lithium phenyl (2,4,6-trimethylbenzoyl) phosphinate (LAP) is a free radical photoinitiator used to initiate free radical chain polymerization upon light exposure and is combined with gelatin methacryloyl (GelMA) to produce a photopolymer used in bioprinting. The free radicals produced under bioprinting conditions are potentially cytotoxic and mutagenic. Since these photo-generated free radicals are highly-reactive but short-lived, toxicity assessments should be conducted with light exposure. In this study, photo-rheology determined that 10 min exposure to 9.6 mW/cm² 405 nm light from an LED light source fully crosslinked 10 wt% GelMA with >3.4 mmol/L LAP, conditions that were used for subsequent cytotoxicity and mutagenicity assessments. These conditions were cytotoxic to M-1 mouse kidney collecting duct cells, a cell type susceptible to lithium toxicity. Exposure to ≤ 17 mmol/L (0.5 wt%) LAP

without light was not cytotoxic; however, concurrent exposure to ≥ 3.4 mmol/L LAP and light was cytotoxic. No condition of LAP and/or light exposure evaluated was mutagenic in bacterial reverse mutation assays using *S. typhimurium* strains TA98, TA100 and *E. coli* WP2 uvrA. These data indicate that the combination of LAP and free radicals generated from photo-excited LAP is cytotoxic but mutagenicity was not observed in bacteria under typical bioprinting conditions.

Introduction

The growing waiting list for tissue and organ transplants is a critical and oft-cited reason for the importance of tissue engineering research. 3D bioprinting using photopolymers takes a front role due to its ability to manufacture patient-specific device geometries.

Photopolymerization provides several advantages in bioprinting, such as biocompatibility, high resolution lithography, and tunable viscoelastic properties [194-196]. Thus, extrusion bioprinting of a photopolymer containing cells is one popular method of creating tissue engineering constructs [14]. Despite the promise, photopolymer-based 3D bioprinting has not developed enough to find commercial success beyond *in vitro* models due, in part, to the complexity of the tissues and the large number of uncharacterized variables [15].

While different 3D printing apparatuses have unique considerations that affect outcomes such as cell settling or high shear strains, use of photopolymers during printing would expose cells to the photopolymer components and light characteristics used during crosslinking. Photopolymers are composed of a base polymer containing a reactive crosslinking moiety (e.g., acrylate, epoxide, and thiol-ene chemistries) and an appropriate photoinitiator compatible with this moiety (e.g., free radical generators, photoacid generators) [197]. Overall, acrylate and thiol-ene chemistries are the prevalent reactive moiety, both of which are used with free radical-

generating photoinitiators [198, 199]; upon exposure to light, these types of photoinitiators generate free radicals to initiate the crosslinking reaction that can also be cytotoxic to encapsulated cells. Many studies demonstrate low cytotoxicity related to their bioprinting process [198] but there is a dearth of reports that specifically focus on the toxic effects of light exposure in the presence of photopolymer. Similar studies primarily focus on topical photosensitizers with existing *in vitro* methods such as the KeratinoSens [200] or hCLAT [201] assays, both of which are being recognized by the Interagency Coordinating Committee on the Validation of Alternative Methods for human skin sensitizer screening [202]. However, systematic investigations focusing on light exposure and photoinitiator concentrations for the bioprinting field are absent.

Current studies reported in the literature are often demonstrations of a specific bioprinting apparatus or process; therefore, toxicity results are difficult to generalize to other systems. For example, Sabnis et al. investigated concurrent exposure of Irgacure 2959 photoinitiator and 365 nm light showing a cytotoxic dose-response correlated with only Irgacure 2959 concentration. Addition of 50 mg/L ascorbic acid, a radical scavenger, prevented cytotoxicity, which suggests that the mechanism of toxicity is related to free radical generation [203]. This study only investigated cell viability after exposing cells to photopolymer extracts and did not assay encapsulated cells. Leonhardt et al. investigated the cytotoxicity and genotoxicity of photopolymer extracts showing minimal toxicities for the visible-light polymerized acrylate polymer [204]. Use of photopolymer extracts, as in these studies, is generally amenable to biocompatibility testing but does not consider the initial burst of ROS generated when the photoinitiator is first exposed to light. Therefore, use of extracts for biocompatibility testing of photopolymers may not accurately reflect risks in bioprinting where cells are exposed directly to

photo-generated ROS. The photopolymer combination of GelMA and LAP is commercially available and widely cited for various biomedical applications but there is very little investigation of the mutagenicity potential of this material, especially considering the effect of light exposure during crosslinking. Given the literature demonstrating and proposing mechanisms of free-radical mediated mutagenicity [16, 205], it is surprising that almost no studies have investigated the mutagenicity of the GelMA + LAP photopolymer, or of photoinitiators in general, despite the large number of studies evaluating this specific combination.

Kidney collecting duct cells are a well-known target of lithium [206, 207], with kidney injury and disease being a common side effect of lithium treatment for psychiatric disorders [208, 209]. The mechanism of lithium toxicity to collecting duct cells is related to the epithelial sodium channels [210] (passive transport into the cell) having a greater affinity for lithium versus sodium and the sodium efflux ATPase pump having a lower affinity for lithium leading to accumulation within the cell [211]. Fibrosis is a late response to acute kidney injury [212] and is also observed after exposure to lithium chloride [213]; thus, LAP, a lithium salt, may be more cytotoxic to collecting duct cells versus other cell types. While alternative versions of this photoinitiator type exist, i.e., with a sodium instead of a lithium ion, with similar crosslinking efficiencies, changing the cation to sodium decreases solubility and increases cytotoxicity [214]. In this study, confluent M-1 mouse kidney collecting duct cells were considered because these cells 1) serve as a lithium target cell model, 2) exhibit epithelial polarity when cultured in well plates, and 3) form “domes” indicative of water transport [215]. LAP in cell culture medium is exposed to the *in vitro* equivalent of the apical membrane of collecting duct cells. Additionally, use of this cell model would expand the scope to technologies that could directly contact native

tissue such as tissue adhesives [216], injectable wound dressings [217], or hand-held extrusion printers for bioprinting during surgery [218]. Therefore, the objectives of this study were to 1) characterize light exposure conditions typical of bioprinters using LEDs as a light source 2) assess whether LAP with concurrent light exposure enhances cytotoxicity in confluent M-1 cells, and 3) determine if exaggerated exposure conditions associated with high cytotoxicity are mutagenic using bacterial reverse mutation assays.

Materials and Methods

Light source characterization and photorheology Two different LED light sources with a 405 nm nominal peak emission wavelength were evaluated for their emission spectra and irradiance using a HR4000 spectrometer (Ocean Insight, Largo, FL) and an Ophir Vega with a PD-300UV photodiode detector (Ophir, Jerusalem, Israel) respectively. To characterize the beam profile of a M405LP1 LED (Thorlabs, Newton, NJ) used for photo-rheology, the photodiode was masked with an approximately 1-mm pinhole and moved through the center of the beam; the LED chip was placed 150 mm vertically from the detector. Relative power was measured every 1 mm through the center of the beam. To illuminate the larger area required for the mammalian and bacterial assays, a higher power 405 nm LED array (Amazon, Seattle, WA) was used. The array was embedded into the bottom of a polystyrene box and oriented upward. A 55 x 70 mm cutout on top of the box allowed light to illuminate well plates from the bottom.

Photo-rheology measurements of 10 wt% GelMA (Cellink, Boston, MA) formulations were made using an MCR302 rheometer (Anton Paar, Ashland, VA) with a fused silica lower plate and a 20-mm parallel plate geometry. GelMA used in this study was derived from 300 bloom porcine gelatin with a 54% degree of methacrylation, and was sterile filtered through a 0.22 μm PES membrane by the manufacturer before lyophilization. The temperature was

maintained at 37°C and the gap distance set at 0.5 mm; this distance was varied during the experiment to maintain a constant 0.0 N normal force. The M405LP1 LED was set to 3.0 mW/cm². The linear viscoelastic region (LVER) was determined with a pair of pilot tests on 10 wt% GelMA containing 17 mmol/L LAP exposed to >10 min of light before measurement; a frequency sweep from 0.2 – 20 Hz at a constant 1% shear strain followed by a shear strain sweep between 0.01 and 1000% were performed. The photo-rheology experiments were conducted with a 60-sec pre-shear at 5% shear strain followed by triggering of the light source and simultaneous oscillatory measurement at 5% strain and 5 Hz for 15 min. An additional run investigated the crosslinking kinetics of 10% GelMA with 3.4 mmol/L LAP after a nitrogen purge through the solution for ~2 min.

Cytotoxicity Assays M-1 mouse collecting duct cells (ATCC, Manassas, VA) were incubated (37°C, 5% CO₂, 95% RH) in DMEM:F12 medium with 5 vol% FBS and 5 μmol/L dexamethasone (Sigma Aldrich, St. Louis, MO) for 10 days in 96-well plates with media changes every 2 or 3 days. Cell layers cultured for at least 10 days were observed to form domes indicative of ion transport; this observation is qualitative but is typical of healthy confluent layers [215].

Alamar Blue (AB) and Neutral Red Uptake (NRU) cytotoxicity assays were conducted on M-1 collecting duct cells exposed to LAP (Sigma Aldrich, St. Louis, MO) with or without light exposure. The first set of assays without light exposure was performed by exposing cell layers to 3.4, 5.1, 6.8, 17, 25.5, 34, 51, or 68 mmol/L LAP or lithium chloride (LiCl) (Sigma Aldrich, St. Louis, MO) in cell culture medium for 24 hr before conducting the AB and NRU assays. The second set of experiments with light exposure was conducted by adding 0, 3.4, 5.1, 6.8, 17 mmol/L of either agent to cell culture medium followed immediately with exposure to 10

min of 9.6 mW/cm² 405 nm light from the LED array. Both sets of plates were incubated for 24 hr before the AB and NRU assays were performed. In both sets of experiments, cell layers exposed to cell culture medium but not exposed to light, or cell culture medium containing 1 mmol/L cadmium chloride, were used as the negative and positive cytotoxicity controls, respectively.

For the AB assay, contents of all wells were aspirated and replaced with cell culture medium containing 10 vol% AB dye (ThermoFisher, Waltham, MA). Plates were incubated for 2 hr before fluorescence measurements were taken on a Tecan M1000 at 560 nm excitation and 585 nm emission wavelengths.

For the NRU assay, a 4 mg/mL Neutral Red (Sigma Aldrich, St. Louis, MO) stock solution in PBS was diluted to 40 µg/mL in cell culture medium and placed at 37°C overnight prior to assay. Neutral Red solutions were centrifuged at 600 g for 10 min the day of the assay and the supernatant retained to produce the NRU working solution. NRU desorb solution was produced by mixing 12.5 mL of ultrapure water (Millipore, Burlington, MA), 12.5 mL of 200-proof ethanol (Decon Labs, King of Prussia, PA), and 250 µL glacial acetic acid (Acros Organics, Fair Lawn, NJ). The contents of all wells were aspirated, the cell layers rinsed with 150 µL PBS, then 100 µL of NRU working solution added. After 2 hr incubation, plates were inspected under a phase contrast microscope to check for unintended crystallization of the dye. The cell layers were rinsed 2x with 150 µL PBS, then 150 µL of the NRU desorb solution was added. The plates were agitated for >10 min on a shaker before fluorescent reading at 534 nm excitation and 616 nm emission wavelengths.

Within each replicate experiment, the signal from 4 or 5 identical wells for each toxicant concentration were averaged. Results are reported as the means and standard deviations of N = 3

independent replicate experiments. Statistically significant differences ($p < 0.05$) were determined by multiple two-tailed t-tests (Graphpad Prism 6, Graphpad Software, San Diego, CA).

Ames Bacterial Reverse Mutation Assay The Ames bacterial assay used in this study consists of exposing the bacteria to both the potential mutagen and light in a 96-well plate and plating on minimal glucose plates using an overlay method [219]. Minimal glucose agar was composed of 16 g/L agar (Difco, Detroit, MI), 20 mL/L of 50x VBE salt (Moltox, Boone NC), and 21.5 g/L glucose (Sigma Aldrich, St. Louis, MO) in DI water; VBE salts and previously autoclaved 40% w/v glucose were added to the autoclaved agar solution once cooled to approximately 50 - 60°C, then poured in volumes of ~30 ml each into 100 mm polystyrene petri dishes and allowed to solidify. Plates were stored at 4-8°C until use. Top agar was composed of 6 g/L agar, and 5 g/L NaCl (Sigma Aldrich, St. Louis, MO) which was autoclaved; histidine/biotin (His/Bio) or tryptophan (Trp) was added to a final concentration of 4.6 mg/L once the solution cooled to approximately 50-60°C. Aliquots of top agar containing His/Bio or Trp were stored at room temperature until use. Before each replicate experiment, bottom agar plates were placed in an incubator at 37°C and the top agar melted then cooled to 45°C on a heating block. Stock solutions of strain-specific positive control compounds, 500 µg/mL 4-nitroquinoline-1-oxide (4-NQO) (Sigma Aldrich, St. Louis, MO) for *E. coli* or 200 µg/mL 2-nitrofluorene (2-NF) (Sigma Aldrich, St. Louis, MO) for *S. typhimurium*, were made in DMSO and stored frozen until use.

S. typhimurium (strains TA98 and TA100) and *E. coli* (strain WP2 uvrA) (Moltox, Boone NC) from stocks frozen at -70°C were cultured overnight in Oxoid, or Luria broth (ThermoFisher Scientific, Waltham, MA) respectively with 12 hr agitation at 37°C in fluted flasks on a shakeplate. Prior to any replicate experiment, optical density measurements at 600 nm (OD_{600}) of

the overnight cultures were taken with a Genesys 20 spectrophotometer (ThermoFisher Scientific, Waltham, MA); all overnight cultures had an OD₆₀₀ of approximately 1 prior to use in each assay. A 2x bacteria suspension was made by centrifuging 4 mL of the overnight culture at 8500 g for 30 sec and resuspending the pellet in 2 mL of PBS.

On 48-well plates, one well for each treatment and control condition was designated: well 1) PBS (negative control) alone; well 2) 0.5 µg/plate 4-NQO or 0.4 µg/plate 2-NF; well 3) 18.5 mJ/cm² UV-C exposure, 4) LAP 34 mmol/L alone; and wells 5-10) LAP (0, 3.4, 8.5, 17, 25.5, and 34 mmol/L) + 10 min 9.6 mW/cm² 405 nm light. Each well received 150 µL of 2x bacteria suspension and 150 µL of a solution containing PBS, positive control compound, or 102 mmol/L LAP to achieve the appropriate concentrations. A separate plate containing the bacteria and PBS for UV-C treatment was exposed to 3 s of UV-C radiation in a UV crosslinker (Spectronics Corporation, New Cassel, NY) corresponding to a radiant exposure of 18.5 mJ/cm². The plate containing the remaining treatment groups were exposed to 10 min 9.6 mW/cm² 405 nm light. Immediately after light exposure, 150 µL of the appropriate nutrient broth was added to all wells and the plates incubated for 30 min at 37°C for mutant expression before plating.

Within each replicate, duplicate plates were produced from each well with each plate made by adding 150 µL of the well contents to 2 mL of top agar prewarmed to 45°C followed by immediate plating on bottom agar plates prewarmed to 37°C. Plates were flipped once solid and incubated for 2 days before counting colonies on a SphereFlash automated colony counter (IUL Micro, Barcelona, Spain). Results are reported as the means and standard deviations of N = 3 or N=2 independent replicate experiments.

Results

Light source characterization and photorheology Since achieving even illumination of all samples was a major concern, a LED light source and an in-house light box containing a consumer LED array were characterized for their irradiance over the sample area and emission spectra. The Thorlabs M405LP1 and consumer LED array had a narrow, symmetrical emission spectrum with peak emission of $409 \text{ nm} \pm 7 \text{ nm}$ full width half maximum (FWHM) and $406 \text{ nm} \pm 7 \text{ nm}$ FWHM respectively. The M405LP1 exhibited peak irradiance in the center of the beam and decreased to 99% of peak values 10 mm from the center when the LED chip is 150 mm above the detector. Irradiance over the entire 20 mm diameter parallel plate geometry would be within 1% of the set value. Irradiance at the sample platform over the consumer LED array had unpredictable hotspots due to the array and multiple diffuse reflections inside the box, but maximum and minimum irradiance readings were 9.8 and 9.4 mW/cm^2 over the entire 55×70 mm area with no ability to alter the intensity of the light source after lightbox assembly. Irradiance over any sample in the biological assays should deviate within 2% of 9.6 mW/cm^2 .

The LVER of fully crosslinked 10% GelMA was determined first with a frequency sweep from 0.2 – 20 Hz at a constant 1% shear strain. The approximately 5500 Pa storage modulus value was found to be on par with the final storage modulus determined in the main crosslinking experiment and was indicative of a fully crosslinked gel. A subsequent sweep between 0.01% and 1000% strain at 5 Hz revealed a drop in the storage modulus starting at approximately 10% shear strain. Therefore, 5% shear strain at 5 Hz was determined to be within the LVER of 10% GelMA and was used for the main photo-rheology experiment to track the rate of crosslinking.

Figure 6.1 summarizes four features of the photo-rheology results: 1) lag time between start of light exposure and increase of the storage modulus, 2) the final storage modulus after excess light exposure, 3) the rate of increase of the storage modulus, and 4) an artifact starting

immediately after triggering the light source. This artifact is attributed to a software error where shear strain readings reached between 700 and 1700% and torque readings reached extremely high levels (up to 0.03 N·m) following an invalid data point. This caused the storage modulus calculations to be artificially high, but these readings stabilized to baseline levels within 13 seconds. This artifact was not present on the nitrogen purged sample that was collected after an equipment reset and did not have the invalid data point.

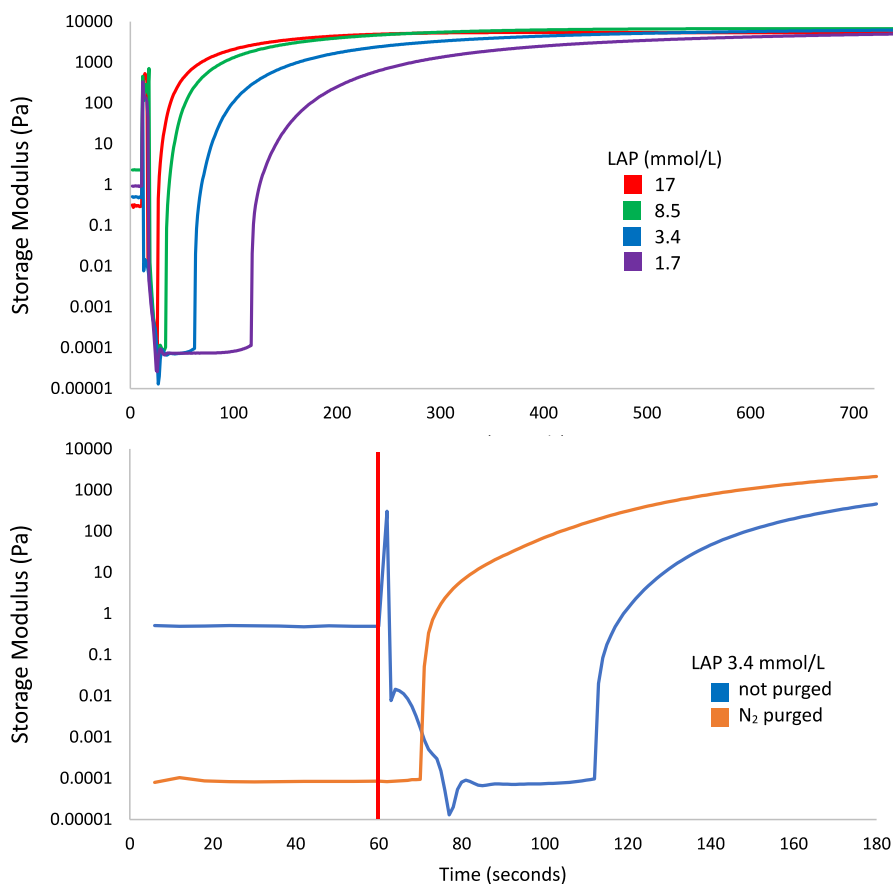


Figure 6.1 - Storage modulus of 10% GelMA with LAP photoinitiator tracked by photo-rheology; the 405 nm light source (3 mW/cm^2) was switched on at 60 sec for all measurements. (Top Panel) Crosslinking of GelMA with 17 (red), 8.5 (green), 3.4 (blue), and 1.7 (purple) mmol/L LAP. (Bottom Panel) Crosslinking of non-nitrogen-purged (blue) and nitrogen-purged (orange) GelMA with 3.4 mmol/L LAP with a focus on the time between light exposure and a rise in storage modulus; the red line denotes the start of light exposure.

The lag time is inversely proportional to the LAP concentration with gels containing 17, 8.4, 3.4, and 1.7 mmol/L LAP taking 17, 25, 53, and 108 sec after initiating light exposure and before any marked increase of storage modulus. This lag time is greatly reduced after nitrogen purging; comparing the storage modulus curves of GelMA + 3.4 mmol/L LAP with and without nitrogen purging in **Figure 6.1b**, the lag time was shortened from 53 sec to 10 sec. The final storage modulus of all gels approached the same value at approximately 6000 Pa. Times to reach > 95% of the final storage modulus for each gel were 319, 473, 720, or 995 sec for 10% GelMA with 17, 8.4, 3.4, or 1.7 mmol/L LAP exposed to 3.0 mW/cm² 405 nm light, respectively. The light exposure condition of 600 sec of 9.6 mW/cm² light used in the cytotoxicity and Ames assays would be sufficient to fully crosslink GelMA containing ≥ 3.4 mmol/L LAP and would be a representative light exposure scenario for cells undergoing bioprinting using an LED light source.

Cytotoxicity Assays Confluent M-1 collecting duct cell layers were exposed to various concentrations of LAP or LiCl with or without 9.6 mW/cm² 405 nm light exposure and the cell viability assessed with both the AB and NRU assays (**Figure 6.2**). The dose range for the cytotoxicity assays without light were centered around 17 mmol/L (0.5 wt% LAP), which is a common LAP concentration used in bioprinting. Cytotoxicity of LiCl was measured in parallel.

Exposure to LiCl with or without light slightly reduced viability. Cells exposed to the maximum investigated LiCl concentration (68 mmol/L) reduced viability down to 80% and 94% viability measured by the AB and NRU assays, respectively (data not shown). No differences in viability were observed between the treatments with LiCl alone and LiCl plus light exposure (data not shown).

Generally, the viability as reported in both assays for the LAP dose response curve was extremely sensitive with concentrations yielding near 100% or near 0% viability flanking a single inflection point. Between 3.4 and 17 mmol/L LAP without exposure to light, viability in the AB assay was above 100% viability and had an increasing trend over this concentration range while viability in the NRU assay remained below 100% and had a decreasing trend. AB and NRU assays both reported a sharp drop in viability at 25.5 mmol/L LAP; at higher concentrations, all cells were dead as viability was essentially zero %.

Cells exposed to light alone (no LAP) exhibited no change in viability compared to controls. Cell viability at 3.4 mmol/L LAP, the lowest investigated dose, with concomitant light exposure diminished to 68% and 48% for the AB and NRU assays, respectively. Only the result of the NRU assay was significant at this point, however, the results show that the EC₅₀ (effective concentration that kills 50% of the cells) for both assays was approximately 10-fold more potent for LAP + light compared to LAP alone. Both assays showed that for cells exposed to LAP concentrations higher than 3.4 mmol/L LAP with concomitant exposure to light, viability was near zero.

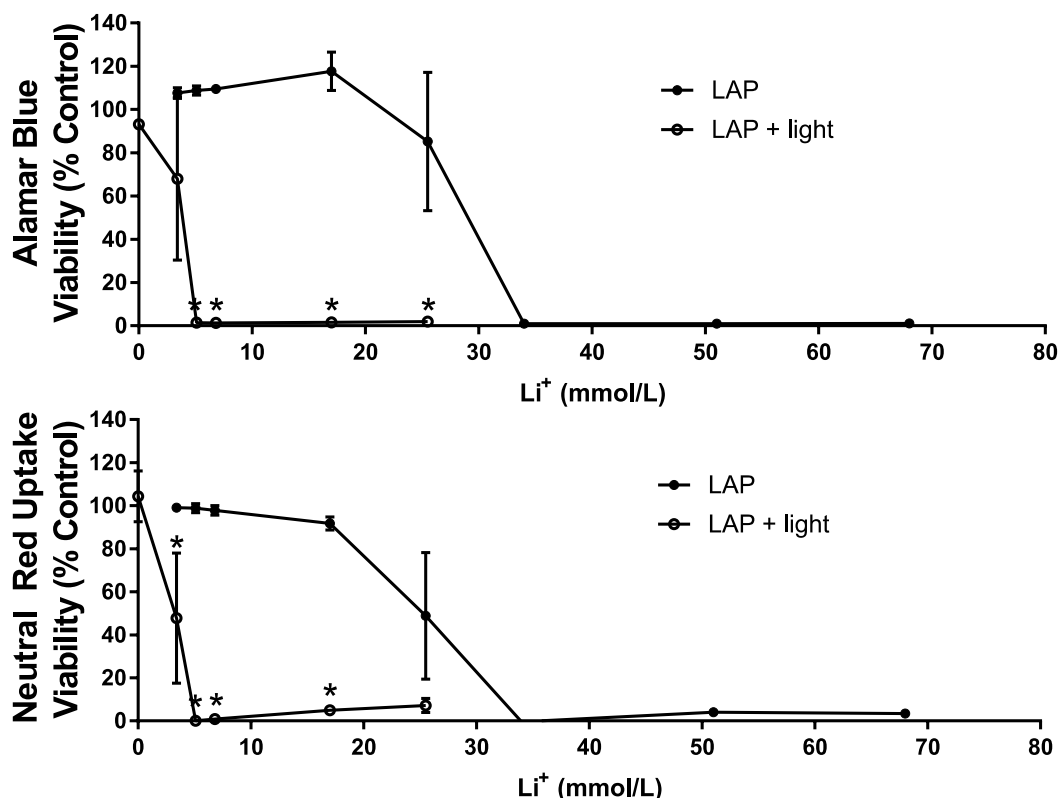


Figure 6.2 - Viability of mouse M-1 collecting duct cell monolayers exposed to varying concentrations of LAP (3.4, 5.1, 6.8, 17, 25.5, 34, or 68 mmol/L) and not-exposed (●) or exposed to 9.6 mW/cm² 405 nm light (○). LAP concentrations are represented as equivalent Li concentrations. Results are normalized to the viability of monolayers exposed only to PBS and not exposed to light. CdCl₂ (1 mmol/L) was used as the positive control; viability averaged 0% for both assays (data not shown). (Top Panel) Viability determined by the Alamar Blue assay. (Lower Panel) Viability determined by the Neutral Red Uptake assay. Values represent means ± standard deviations of N = 3 independent replicate experiments. Values that appear to be missing error bars are cases where the standard deviation is smaller than the symbol size. Asterisks (*) denote treatments where the viability of monolayers exposed to LAP is significantly different (p < 0.05) from the viability of monolayers exposed to LAP and light.

Ames Bacterial Reverse Mutagenicity Assay

Bacterial reverse mutagenicity assay results are summarized in **Figure 6.3**. All plates had an intact bacterial lawn which indicated the lack of overt cytotoxicity; colonies present on the plates are attributed to reverse mutation.

Baseline reverse mutation rates of WP2uvrA, TA98, and TA100 were 34, 38, and 89 revertant

colonies, respectively. Strain-specific positive controls (i.e., 4-NQO for WP2uvrA and 2-NF for TA98 and TA100) resulted in a marked increase in colony counts. For all strains, either the control chemical mutagen, UV-C positive control, or both resulted in a positive mutagenicity assessment. In contrast, all treatments with LAP with or without light in all strains tested resulted in no apparent mutagenicity; colony counts were on par with the negative control.

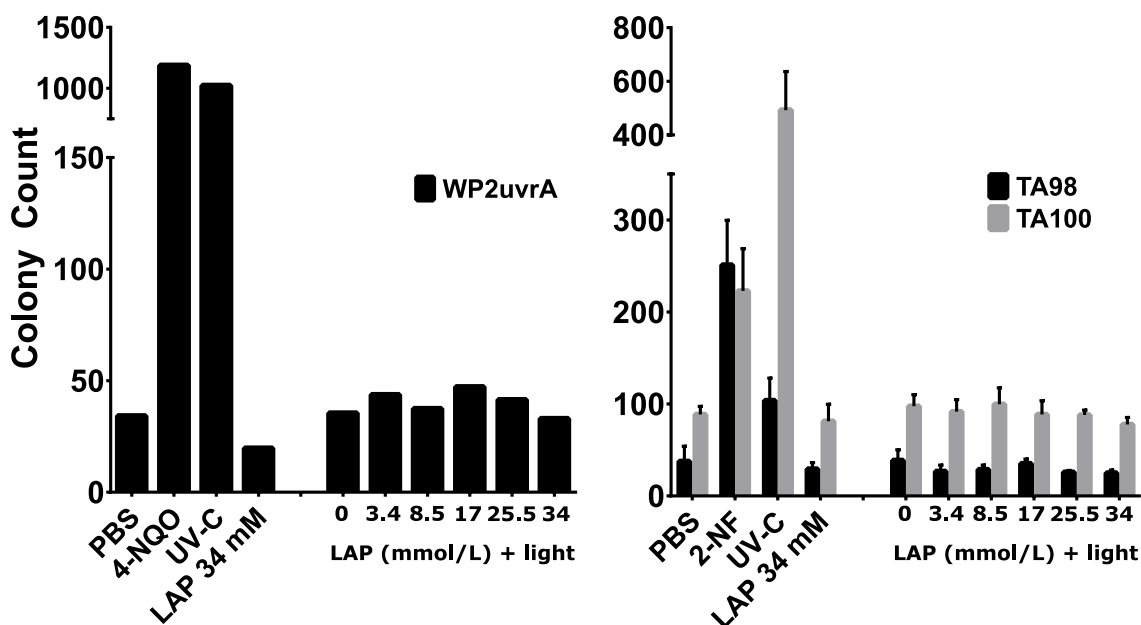


Figure 6.3 - Mutagenicity assessment using bacterial reverse mutation assays. Reverse mutant colony counts of *E. coli* (WP2uvrA, left panel) and *S. typhimurium* (TA98 or TA100, right panel) exposed to PBS (negative control), 0.5 $\mu\text{g}/\text{plate}$ 4-NQO or 0.4 $\mu\text{g}/\text{plate}$ 2-NF (strain-specific positive controls), 18.5 mJ/cm^2 UV-C light, 34 mmol/L LAP, or various LAP concentrations with exposure to 10 min of 9.6 mW/cm^2 405 nm light. For *E. coli* (left panel), values represent the average of N=2 independent replicate experiments. For *S. typhimurium* strains (right panel), values represent means \pm standard deviations of N=3 independent replicate experiments.

Discussion

GelMA is made photosensitive with addition of LAP photoinitiator and is crosslinked with exposure to 405 nm light. Crosslinked GelMA is solid at cell culture temperatures (37°C) and has a shear elastic modulus proportional to its concentration when fully crosslinked. Both LAP concentration and 405 nm light intensity are positively correlated with crosslinking rate but do not affect final elastic modulus [220]. Photo-crosslinking has been traditionally performed with curing lamps such as mercury or xenon arc lamps with filtered outputs [221] for their high output power, but the high heat generation, high power draw, large volume, and relatively high cost of these lamps have pushed for the use of LEDs in portable light sources, such as dental curing lights [222, 223] and commercially-available bioprinters. The use of 405 nm LEDs in this study is typical of bioprinters using LAP for these reasons. The use of 3 mW/cm² irradiance in the photo-rheology studies was mainly limited by the desire to achieve even illumination over the entire 20 mm geometry. Most of the LED power is discarded to result in only a small emission angle to the sample; increasing the irradiance by moving the LED closer or by including focusing optics is associated with decreasing evenness of the irradiance field. Since polymerization rate is proportional to the square root of light intensity [220], use of this lower irradiance can justify exposure conditions using the 9.6 mW/cm² irradiance used in the biological assays.

Photo-rheology results were evaluated mainly for the light exposure time required to reach 95% of the maximum achieved storage modulus for each LAP concentration investigated. However, the lag time between the start of light exposure and the beginning of polymerization is an important artifact. This lag time is inversely proportional to the photoinitiator concentration and is attributed to radical scavenging by oxygen [224]. To test this hypothesis, nitrogen purging

of the 3.4 mmol/L LAP gel reduced the lag time compared to the 17 mmol/L LAP gel. While nitrogen purging is a common method to improve the polymerization performance of acrylate photopolymers [225], this process is not compatible with cell-laden gels used in bioprinting. Nevertheless, the result that the 3.4 mmol/L LAP gel required 720 sec to fully polymerize justifies the exaggerated exposure from the higher 9.6 mW/cm² irradiance for 600 sec used in the subsequent studies.

Since studies have shown that both photoinitiator concentration [203] and light exposure [226] are associated with toxic effects, conventional wisdom states that these parameters should be carefully controlled. For example, underexposure would result in imprecise control of the mechanical properties and an increase in the concentration of unreacted monomer, while overexposure would expose cells to additional phototoxic effects while not significantly affecting the mechanical properties. Multiple studies report photopolymer tissue engineering constructs with low cytotoxicity [227, 228], and/or the ability of cells to proliferate within the construct after printing [223]. The success of this technique is contrary to the assumption that free-radical generating photoinitiators produce toxic effects, including genotoxicity, from reactive oxygen species [16, 19]. Therefore, the second and third objectives of this study were to determine whether concomitant exposures to LAP and light under conditions typical of bioprinting were cytotoxic and/or mutagenic.

Cytotoxicity assays were performed using confluent mouse kidney M-1 collecting duct cell layers, which exhibited evidence of active water transport, i.e., “domes” attributed to water transport between the cell layer and wellplate bottom were observed [215]. Lithium ion is a known nephrotoxicant, whose mechanism of toxicity is related to the inhibition of AQP-2 transport to the cell membrane, thereby causing diabetes insipidus [229]. However, diabetes

insipidus isn't the major concern in this study versus lithium accumulation within the kidney [211], risk of renal fibrosis [230], and damage to various organelles; karyolysis and cell fragmentation were observed in the kidneys of rats exposed to lithium chloride [213]. Results in both the Alamar Blue and Neutral Red Uptake assays agree that lithium ion concentrations typically associated with LAP can be mildly cytotoxic; However, 95% viability from 17 mmol/L LiCl exposure (i.e., equivalent to 0.5 wt% LAP) determined with the NRU assay is a generally accepted viability for cells grown *in vitro*; this effect should be less pronounced in other cell models not as sensitive to lithium. At LAP concentrations and exposure times typically used in bioprinting, lithium ions were not identified as a significant cytotoxic factor.

In contrast, LAP exposure to M-1 collecting duct layers in the absence of light was cytotoxic at 17 mmol/L corresponding to 0.5 wt% LAP, a commonly used concentration in bioprinting. The exposure duration was 24 hr, which represents an exaggerated exposure compared to bioprinted constructs where LAP would be diluted by cell culture medium after crosslinking. With exposure to light, an immediate reduction in viability was observed at the lowest LAP concentration corresponding to 0.1 wt% LAP. This result is corroborated in a study by Duchi et al. where sheep adipose derived stem cells exhibited around 20% viability after exposure to 0.1% LAP albeit with 700 mW/cm² 365 nm light for 10 sec [218]. Bioprinting with similar LAP and light conditions generally does not elicit this cytotoxic response so this discrepancy is attributed to a protective effect of GelMA and cell media used during bioprinting. For example, the presence of antioxidants, such as N-acetylcysteine, was shown to be protective against oxidative damage [231]. This strategy was also used to develop a photoprotective supplement composed of antioxidants which prevented light-induced cytotoxicity in neuronal culture exposed to 360 kJ/m² 470 nm light [232]. This protective effect was also observed in

bone marrow stromal cells encapsulated with methacrylated hyaluronic acid or polyglycerol; neither Irgacure 2959 concentration or radiant exposure from 6 mW/cm² 365 nm light for 5 min caused any statistically significant differences in cell viability or proliferation versus the non-irradiated control [233]. In the absence of the encapsulating polymer, increasing light exposure and/or Irgacure 2959 concentration caused drops in viability and proliferation [233]. High viability (~96%) was also observed in human neonate foreskin fibroblasts embedded in polyethyleneglycoldiacrylate with 2.2 mmol/L LAP exposed to 5-10 minutes of 10 mW/cm² 405 nm light [220]. In the present study, *in vitro* assays performed in the absence of GelMA likely exaggerated cytotoxicity typically observed when using this material in bioprinting. All investigated LAP concentrations with exposure to light were highly cytotoxic to the M-1 collecting duct cells compared to LAP alone and confirms the hypothesis that concurrent LAP and light exposure is more cytotoxic than LAP exposure alone.

A modified Ames bacterial mutagenicity assay was conducted with LAP and light exposures that were cytotoxic to M-1 cells to determine whether these exposures are mutagenic. This modification involves light exposure to the bacteria and toxicant prior to incubation and has been previously used to determine mutagenicity from concomitant light and exposure to sunscreen [234] and cosmetic [235] compounds. Results in the present study showed that the positive and negative controls performed adequately within defined parameters, resulting in valid assays; however, mutagenicity assessment for LAP concentrations ranging from 0 to 34 mmol/L with or without 10 min of 9.6 mW/cm² 405 nm light exposure were negative. OECD TG471 guidelines recommend a battery of four *S. typhimurium* strains (including TA98 and TA100) and additional choice of strain (including WP2 uvrA) which detects “oxidizing mutagens, cross-linking agents and hydrazines” [219]. While this study only used two *S. typhimurium* strains and

one *E. coli* strain, recent studies showed that using only TA98 and TA100 detected 93% of the >10000 compound database [236]. Since ROS is expected to be an oxidizing mutagen, the TA100, TA98, and WP2 uvrA test battery used in this assay should have a high chance of detecting mutagenicity. Thus, the negative result observed is surprising. Although addition of S9 metabolic activation is a customary procedure for testing chemicals that might require metabolic activation for genotoxicity, S9 was not deemed relevant to this study because we are exploring another mode of activation, light-based photo-activation. The Ames assay is widely-used and is predictive of 70-90% of carcinogens [237] but use of the Ames assay alone for a negative mutagenicity assessment is insufficient as a definitive stand-alone result [238]. Reasons for negative results include inadequate dosing (e.g. failure of uptake), failure to detect mammalian-specific mutagens, or chemical-specific requirements not met, in addition to a true lack of mutagenicity. Further investigations are needed to define the mutagenic status of LAP plus light, especially given the cytotoxicity observed.

Despite being a popular, well-cited, and commercially-available photoinitiator for use with bioprinting, there are no reports of studies evaluating the mutagenicity of LAP to the authors' knowledge. However, an EU report on the chemically similar trimethylbenzoyl diphenyl phosphine oxide (TPO), which is used primarily in photo-crosslinkable nail polish, finds that TPO is not mutagenic based on data from multiple *in vitro* and *in vivo* assays; however, no study took light exposure into account [239]. TPO was also investigated alongside camphorquinone in combination with various acrylate-based polymers and found to be marginally genotoxic determined with the Comet assay, although light exposure was not assessed [240]. Based on these studies, LAP was not expected to be mutagenic in the absence of light exposure, but our results thus far do not support our hypothesis that LAP with light exposure would be mutagenic,

given the expected generation of reactive oxygen species and the toxicity observed in mammalian cells.

Conclusion

The cytotoxicity of LAP to confluent M-1 collecting duct cells was significantly enhanced with exposure to 405 nm light with increased cytotoxicity observed at concomitant exposures of > 3.4 mmol/L LAP (0.1 wt% LAP) and 10 min of 9.6 mW/cm² light, conditions occurring during LAP use as a photoinitiator. However, LAP concentrations up to 34 mmol/L (1.0 wt%), an atypically high concentration for bioprinting, were not mutagenic in bacteria even after exposure to light. This study supports that use of LAP photoinitiator and free radicals generated from photo-excited LAP can be cytotoxic to cells undergoing bioprinting. Further studies are needed to more definitively demonstrate the lack of mutagenicity of LAP and light exposure conditions typical in bioprinting.

Article

The Photoinitiator Lithium Phenyl (2,4,6-Trimethylbenzoyl) Phosphinate with Exposure to 405 nm Light Is Cytotoxic to Mammalian Cells but Not Mutagenic in Bacterial Reverse Mutation Assays

Alexander K. Nguyen ^{1,2} , Peter L. Goering ², Rosalie K. Elespuru ², Srilekha Sarkar Das ² and Roger J. Narayan ^{1,*}

¹ Joint UNC/NCSU Department of Biomedical Engineering, North Carolina State University, Raleigh, NC 27695, USA; aknguye2@ncsu.edu

² Office of Science and Engineering Laboratories, Center for Devices and Radiological Health, U.S. Food and Drug Administration, Silver Spring, MD 20993, USA; Peter.Goering@fda.hhs.gov (P.L.G.); Rosalie.Elespuru@fda.hhs.gov (R.K.E.); Srilekha.Das@fda.hhs.gov (S.S.D.)

* Correspondence: roger_narayan@unc.edu

Received: 8 June 2020; Accepted: 1 July 2020; Published: 3 July 2020



Abstract: Lithium phenyl (2,4,6-trimethylbenzoyl) phosphinate (LAP) is a free radical photo-initiator used to initiate free radical chain polymerization upon light exposure, and is combined with gelatin methacryloyl (GelMA) to produce a photopolymer used in bioprinting. The free radicals produced under bioprinting conditions are potentially cytotoxic and mutagenic. Since these photo-generated free radicals are highly-reactive but short-lived, toxicity assessments should be conducted with light exposure. In this study, photorheology determined that 10 min exposure to 9.6 mW/cm² 405 nm light from an LED light source fully crosslinked 10 wt % GelMA with >3.4 mmol/L LAP, conditions that were used for subsequent cytotoxicity and mutagenicity assessments. These conditions were cytotoxic to M-1 mouse kidney collecting duct cells, a cell type susceptible to lithium toxicity. Exposure to ≤17 mmol/L (0.5 wt %) LAP without light was not cytotoxic; however, concurrent exposure to ≥3.4 mmol/L LAP and light was cytotoxic. No condition of LAP and/or light exposure evaluated was mutagenic in bacterial reverse mutation assays using *S. typhimurium* strains TA98, TA100 and *E. coli* WP2 uvrA. These data indicate that the combination of LAP and free radicals generated from photo-excited LAP is cytotoxic, but mutagenicity was not observed in bacteria under typical bioprinting conditions.

Keywords: lithium phenyl (2,4,6-trimethylbenzoyl) phosphinate; gelatin methacryloyl; bioprinting; photoinitiator; light exposure; mutagenicity; cytotoxicity; photorheology

1. Introduction

The growing waiting list for tissue and organ transplants is a critical and oft-cited reason for the importance of tissue engineering research. Three-dimensional bioprinting using photopolymers takes a front role, due to its ability to manufacture patient-specific device geometries. Photopolymerization provides several advantages in bioprinting, such as biocompatibility, high resolution lithography, and tunable viscoelastic properties [1–3]. Thus, extrusion bioprinting of a photopolymer containing cells is one popular method of creating tissue engineering constructs [4]. Despite the promise, photopolymer-based 3D bioprinting has not developed enough to find commercial success beyond in vitro models due, in part, to the complexity of the tissues and the large number of uncharacterized variables [5].

While different 3D printing apparatuses have unique considerations that affect outcomes, such as cell settling or high shear strains, the use of photopolymers during printing would expose cells to the photopolymer components and light characteristics used during crosslinking. Photopolymers are composed of a base polymer containing a reactive crosslinking moiety (e.g., acrylate, epoxide, and thiol-ene chemistries) and an appropriate photoinitiator compatible with this moiety (e.g., free radical generators, photoacid generators) [6]. Overall, acrylate and thiol-ene chemistries are the prevalent reactive moiety, both of which are used with free radical-generating photoinitiators; upon exposure to light, these types of photoinitiators generate free radicals to initiate the crosslinking reaction that can also be cytotoxic to encapsulated cells [7,8]. Many studies demonstrate low cytotoxicity related to their bioprinting process, but there is a dearth of reports that specifically focus on the toxic effects of light exposure in the presence of photopolymer [7]. Similar studies primarily focus on topical photosensitizers with existing *in vitro* methods, such as the KeratinoSens or hCLAT assays, both of which are being recognized by the Interagency Coordinating Committee on the Validation of Alternative Methods for human skin sensitizer screening [9–11]. However, systematic investigations focusing on light exposure and photoinitiator concentrations for the bioprinting field are absent.

Current studies reported in the literature are often demonstrations of a specific bioprinting apparatus or process; therefore, toxicity results are difficult to generalize to other systems. For example, Sabnis et al. investigated concurrent exposure of Irgacure 2959 photoinitiator and 365 nm light showing a cytotoxic dose-response correlated with only Irgacure 2959 concentration. The addition of 50 mg/L ascorbic acid, a radical scavenger, prevented cytotoxicity, which suggests that the mechanism of toxicity is related to free radical generation [12]. This study only investigated cell viability after exposing cells to photopolymer extracts, and did not assay encapsulated cells. Leonhardt et al. investigated the cytotoxicity and genotoxicity of photopolymer extracts showing minimal toxicities for the visible-light polymerized acrylate polymer [13]. The use of photopolymer extracts, as in these studies, is generally amenable to biocompatibility testing, but does not consider the initial burst of reactive oxygen species (ROS) generated when the photoinitiator is first exposed to light. Therefore, the use of extracts for biocompatibility testing of photopolymers may not accurately reflect the risks in bioprinting, where cells are exposed directly to photo-generated ROS. The photopolymer combination of gelatin methacryloyl (GelMA) and lithium phenyl (2,4,6-trimethylbenzoyl) phosphinate (LAP) is commercially available and widely cited for various biomedical applications, but there has been very little investigation into the mutagenicity potential of this material, especially considering the effect of light exposure during crosslinking. Given the literature demonstrating and proposing mechanisms of free-radical mediated mutagenicity, it is surprising that almost no studies have investigated the mutagenicity of the GelMA + LAP photopolymer, or of photoinitiators in general, despite the large number of studies evaluating this specific combination [14,15].

Kidney collecting duct cells are a well-known target of lithium, with kidney injury and disease being a common side effect of lithium treatment for psychiatric disorders [16–19]. The mechanism of lithium toxicity to collecting duct cells is related to the epithelial sodium channels (passive transport into the cell) having a greater affinity for lithium versus sodium and the sodium efflux ATPase pump having a lower affinity for lithium leading to accumulation within the cell [20,21]. Fibrosis is a late response to acute kidney injury, and is also observed after exposure to lithium chloride; thus, LAP, a lithium salt, may be more cytotoxic to collecting duct cells versus other cell types [22,23]. While alternative versions of this photoinitiator type exist, i.e., with a sodium instead of a lithium ion, with similar crosslinking efficiencies, changing the cation to sodium decreases solubility and increases cytotoxicity [24]. In this study, confluent M-1 mouse kidney collecting duct cells were considered, because these cells: (1) serve as a lithium target cell model, (2) exhibit epithelial polarity when cultured in well plates, and (3) form “domes” indicative of water transport [25]. LAP in cell culture medium is exposed to the *in vitro* equivalent of the apical membrane of collecting duct cells. Additionally, the use of this cell model would expand the scope to technologies that could directly contact native tissue, such as tissue adhesives, injectable wound dressings, or hand-held extrusion printers for bioprinting

during surgery [26–28]. Therefore, the objectives of this study were to: (1) characterize light exposure conditions typical of bioprinters, using LEDs as a light source; (2) assess whether LAP with concurrent light exposure enhances cytotoxicity in confluent M-1 cells; and (3) determine if exaggerated exposure conditions associated with high cytotoxicity are mutagenic using bacterial reverse mutation assays.

2. Materials and Methods

2.1. Light Source Characterization and Photorheology

Two different LED light sources with a 405 nm nominal peak emission wavelength were evaluated for their emission spectra and irradiance using a HR4000 spectrometer (Ocean Insight, Largo, FL, USA) and an Ophir Vega with a PD-300UV photodiode detector (Ophir, Jerusalem, Israel), respectively. To characterize the beam profile of a M405LP1 LED (Thorlabs, Newton, NJ, USA) used for photorheology, the photodiode was masked with an approximately 1-mm pinhole and moved through the center of the beam; the LED chip was placed 150 mm vertically from the detector. Relative power was measured every 1 mm through the center of the beam. To illuminate the larger area required for the mammalian and bacterial assays, a higher power 405 nm LED array (Amazon, Seattle, WA, USA) was used. The array was embedded into the bottom of a polystyrene box and oriented upward. A $55 \times 70 \text{ mm}^2$ cutout on top of the box allowed light to illuminate well plates from the bottom.

Photorheology measurements of 10 wt % GelMA (Cellink, Boston, MA, USA) formulations were made using an MCR302 rheometer (Anton Paar, Ashland, VA, USA) with a fused silica lower plate and a 20-mm parallel plate geometry. GelMA used in this study was derived from 300 bloom porcine gelatin with a 54% degree of methacrylation, and was sterile filtered through a $0.22 \mu\text{m}$ polyethersulfone membrane by the manufacturer before lyophilization. The temperature was maintained at 37°C , and the gap distance was set at 0.5 mm; this distance was varied during the experiment to maintain a constant 0.0 N normal force. The M405LP1 LED was set to 3.0 mW/cm^2 . The linear viscoelastic region (LVER) was determined with a pair of pilot tests on 10 wt % GelMA containing 17 mmol/L LAP exposed to >10 min of light before measurement; a frequency sweep from 0.2–20 Hz at a constant 1% shear strain, followed by a shear strain sweep between 0.01% and 1000%, were performed. The photorheology experiments were conducted with a 60 s pre-shear at 5% shear strain, followed by triggering of the light source and simultaneous oscillatory measurement at 5% strain and 5 Hz for 15 min. An additional run investigated the crosslinking kinetics of 10% GelMA with 3.4 mmol/L LAP, after a nitrogen purge through the solution for ~2 min.

2.2. Cytotoxicity Assays

M-1 mouse collecting duct cells (ATCC, Manassas, VA, USA) were incubated (37°C , 5% CO_2 , 95% RH) in DMEM:F12 medium with 5 vol % FBS and 5 $\mu\text{mol/L}$ dexamethasone (Sigma Aldrich, St. Louis, MO, USA) for 10 days in 96-well plates with media changes every 2 or 3 days. Cell layers cultured for at least 10 days were observed to form domes indicative of ion transport; this observation is qualitative but is typical of healthy confluent layers [25].

Alamar Blue (AB) and Neutral Red Uptake (NRU) cytotoxicity assays were conducted on M-1 collecting duct cells exposed to LAP (Sigma Aldrich, St. Louis, MO, USA), with or without light exposure. The first set of assays without light exposure was performed by exposing cell layers to 3.4, 5.1, 6.8, 17, 25.5, 34, 51, or 68 mmol/L LAP or lithium chloride (LiCl) (Sigma Aldrich, St. Louis, MO, USA) in cell culture medium for 24 h, before conducting the AB and NRU assays. The second set of experiments with light exposure was conducted by adding 0, 3.4, 5.1, 6.8, 17 mmol/L of either agent to cell culture medium, followed immediately by exposure to 10 min of 9.6 mW/cm^2 405 nm light from the LED array. Both sets of plates were incubated for 24 h, before the AB and NRU assays were performed. In both sets of experiments, cell layers exposed to cell culture medium, but not exposed to light, or cell culture medium containing 1 mmol/L cadmium chloride, were used as the negative and positive cytotoxicity controls, respectively.

For the AB assay, contents of all wells were aspirated and replaced with cell culture medium containing 10 vol % AB dye (ThermoFisher, Waltham, MA, USA). Plates were incubated for 2 h before fluorescence measurements were taken on a Tecan M1000 at 560 nm excitation and 585 nm emission wavelengths.

For the NRU assay, a 4 mg/mL Neutral Red (Sigma Aldrich, St. Louis, MO, USA) stock solution in PBS was diluted to 40 µg/mL in cell culture medium and placed at 37 °C overnight prior to assay. Neutral Red solutions were centrifuged at 600 g for 10 min the day of the assay, and the supernatant was retained to produce the NRU working solution. NRU desorb solution was produced by mixing 12.5 mL of ultrapure water (Millipore, Burlington, MA, USA), 12.5 mL of 200-proof ethanol (Decon Labs, King of Prussia, PA, USA), and 250 µL glacial acetic acid (Acros Organics, Fair Lawn, NJ, USA). The contents of all wells were aspirated, the cell layers rinsed with 150 µL PBS, then 100 µL of NRU working solution added. After 2 h incubation, plates were inspected under a phase contrast microscope to check for unintended crystallization of the dye. The cell layers were rinsed 2× with 150 µL PBS, then 150 µL of the NRU desorb solution was added. The plates were agitated for >10 min on a shaker, before fluorescent reading at 534 nm excitation and 616 nm emission wavelengths.

Within each replicate experiment, the signal from 4 or 5 identical wells for each toxicant concentration were averaged. Results are reported as the means and standard deviations of $N = 3$ independent replicate experiments. Statistically significant differences ($p < 0.05$) were determined by multiple two-tailed t-tests (Graphpad Prism 6, Graphpad Software, San Diego, CA, USA).

2.3. Ames Bacterial Reverse Mutation Assay

The Ames bacterial assay used in this study consists of exposing the bacteria to both the potential mutagen and light in a 96-well plate and plating on minimal glucose plates, using an overlay method [29]. Minimal glucose agar was composed of 16 g/L agar (Difco, Detroit, MI, USA), 20 mL/L of 50× VBE salt (Moltox, Boone NC, USA), and 21.5 g/L glucose (Sigma Aldrich, St. Louis, MO, USA) in DI water; VBE salts and previously autoclaved 40 % *w/v* glucose were added to the autoclaved agar solution once cooled to approximately 50–60 °C, then poured in volumes of ~30 mL each into 100 mm polystyrene petri dishes and allowed to solidify. Plates were stored at 4–8 °C until use. Top agar was composed of 6 g/L agar, and 5 g/L NaCl (Sigma Aldrich, St. Louis, MO, USA) which was autoclaved; histidine/biotin (His/Bio) or tryptophan (Trp) was added to a final concentration of 4.6 mg/L, once the solution cooled to approximately 50–60 °C. Aliquots of top agar containing His/Bio or Trp were stored at room temperature until use. Before each replicate experiment, bottom agar plates were placed in an incubator at 37 °C, and the top agar melted then cooled to 45 °C on a heating block. Stock solutions of strain-specific positive control compounds, 500 µg/mL 4-nitroquinoline-1-oxide (4-NQO) (Sigma Aldrich, St. Louis, MO, USA) for *E. coli* or 200 µg/mL 2-nitrofluorene (2-NF) (Sigma Aldrich, St. Louis, MO, USA) for *S. typhimurium*, were made in dimethylsulfoxide and stored frozen until use.

S. typhimurium (strains TA98 and TA100) and *E. coli* (strain WP2 uvrA) (Moltox, Boone NC, USA) from stocks frozen at –70 °C were cultured overnight in Oxoid, or Luria broth (ThermoFisher Scientific, Waltham, MA, USA), respectively, with 12 h agitation at 37 °C in fluted flasks on a shakeplate. Prior to any replicate experiment, optical density measurements at 600 nm (OD_{600}) of the overnight cultures were taken with a Genesys 20 spectrophotometer (ThermoFisher Scientific, Waltham, MA, USA); all overnight cultures had an OD_{600} of approximately 1 prior to use in each assay. A 2× bacteria suspension was made by centrifuging 4 mL of the overnight culture at 8500 g for 30 a, and resuspending the pellet in 2 mL of PBS.

On 48-well plates, one well for each treatment and control condition was designated: well (1) PBS (negative control) alone; well (2) 0.5 µg/plate 4-NQO or 0.4 µg/plate 2-NF; well (3) 18.5 mJ/cm² UV-C exposure, (4) LAP 34 mmol/L alone; and wells (5–10) LAP (0, 3.4, 8.5, 17, 25.5, and 34 mmol/L) + 10 min 9.6 mW/cm² 405 nm light. Each well received 150 µL of 2× bacteria suspension and 150 µL of a solution containing PBS, positive control compound, or 102 mmol/L LAP, to achieve the appropriate concentrations. A separate plate containing the bacteria and PBS for UV-C treatment was exposed to 3 s

of UV-C radiation in a UV crosslinker (Spectronics Corporation, New Cassel, NY, USA) corresponding to a radiant exposure of 18.5 mJ/cm^2 . The plate containing the remaining treatment groups were exposed to 10 min 9.6 mW/cm^2 405 nm light. Immediately after light exposure, $150 \mu\text{L}$ of the appropriate nutrient broth was added to all wells and the plates incubated for 30 min at 37°C for mutant expression before plating.

Within each replicate, duplicate plates were produced from each well with each plate made by adding $150 \mu\text{L}$ of the well contents to 2 mL of top agar prewarmed to 45°C , followed by immediate plating on bottom agar plates prewarmed to 37°C . Plates were flipped once solid and incubated for 2 days before counting colonies on a SphereFlash automated colony counter (IUL Micro, Barcelona, Spain). Results are reported as the means and standard deviations of $N = 3$ or 2 independent replicate experiments.

3. Results

3.1. Light Source Characterization and Photorheology

Since achieving even illumination of all samples was a major concern, a LED light source and an in-house light box containing a consumer LED array were characterized for their irradiance over the sample area and emission spectra. The Thorlabs M405LP1 and consumer LED array had a narrow, symmetrical emission spectrum with peak emission of $409 \pm 7 \text{ nm}$ full width half maximum (FWHM) and $406 \pm 7 \text{ nm}$ FWHM respectively. The M405LP1 exhibited peak irradiance in the center of the beam and decreased to 99% of peak values 10 mm from the center when the LED chip is 150 mm above the detector. Irradiance over the entire 20 mm diameter parallel plate geometry would be within 1% of the set value. Irradiance at the sample platform over the consumer LED array had unpredictable hotspots due to the array and multiple diffuse reflections inside the box, but maximum and minimum irradiance readings were 9.8 and 9.4 mW/cm^2 over the entire $55 \times 70 \text{ mm}^2$ area, with no ability to alter the intensity of the light source after lightbox assembly. Irradiance over any sample in the biological assays should deviate within 2% of 9.6 mW/cm^2 .

The LVER of fully crosslinked 10% GelMA was determined first with a frequency sweep from 0.2–20 Hz at a constant 1% shear strain. The approximately 5500 Pa storage modulus value was found to be on par with the final storage modulus determined in the main crosslinking experiment, and was indicative of a fully crosslinked gel. A subsequent sweep between 0.01% and 1000% strain at 5 Hz revealed a drop in the storage modulus starting at approximately 10% shear strain. Therefore, 5% shear strain at 5 Hz was determined to be within the LVER of 10% GelMA and was used for the main photorheology experiment to track the rate of crosslinking.

Figure 1 summarizes four features of the photorheology results: (1) lag time between start of light exposure and increase of the storage modulus, (2) the final storage modulus after excess light exposure, (3) the rate of increase of the storage modulus, and (4) an artifact starting immediately after triggering the light source. This artifact is attributed to a software error where shear strain readings reached between 700% and 1700%, and torque readings reached extremely high levels (up to 0.03 N-m) following an invalid data point. This caused the storage modulus calculations to be artificially high, but these readings stabilized to baseline levels within 13 s. This artifact was not present on the nitrogen purged sample that was collected after an equipment reset, and did not have the invalid data point.

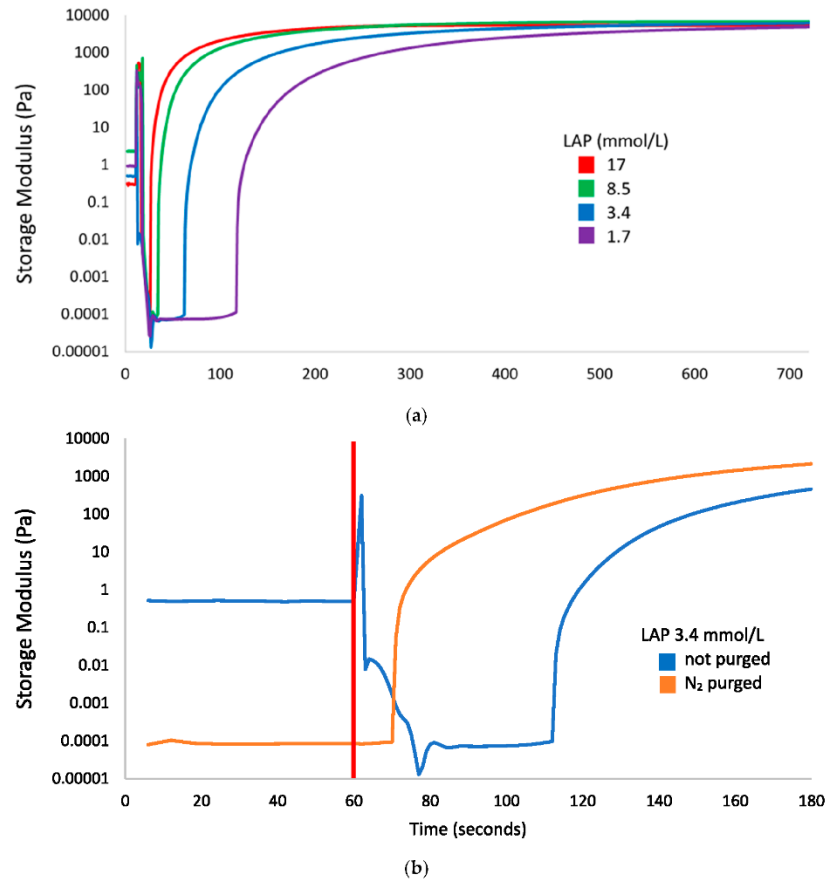


Figure 1. Storage modulus of 10% gelatin methacryloyl (GelMA) with lithium phenyl (2,4,6-trimethylbenzoyl) phosphinate (LAP) photoinitiator tracked by photorheology; the 405 nm light source (3 mW/cm²) was switched on at 60 s for all measurements. (a) Crosslinking of GelMA with 17 (red), 8.5 (green), 3.4 (blue), and 1.7 (purple) mmol/L LAP. (b) Crosslinking of non-nitrogen-purged (blue) and nitrogen-purged (orange) GelMA with 3.4 mmol/L LAP, with a focus on the time between light exposure and a rise in storage modulus; the red line denotes the start of light exposure.

The lag time is inversely proportional to the LAP concentration with gels containing 17, 8.4, 3.4, and 1.7 mmol/L LAP taking 17, 25, 53, and 108 s after initiating light exposure and before any marked increase of storage modulus. This lag time is greatly reduced after nitrogen purging; comparing the storage modulus curves of GelMA + 3.4 mmol/L LAP with and without nitrogen purging in Figure 1b, the lag time was shortened from 53 to 10 s. The final storage modulus of all gels approached the same value at approximately 6000 Pa. Times to reach >95% of the final storage modulus for each gel were 319, 473, 720, or 995 s for 10% GelMA with 17, 8.4, 3.4, or 1.7 mmol/L LAP exposed to 3.0 mW/cm² 405 nm light, respectively. The light exposure condition of 600 s of 9.6 mW/cm² light used in the cytotoxicity and Ames assays would be sufficient to fully crosslink GelMA containing ≥ 3.4 mmol/L LAP, and would be a representative light exposure scenario for cells undergoing bioprinting using an LED light source.

3.2. Cytotoxicity Assays

Confluent M-1 collecting duct cell layers were exposed to various concentrations of LAP or LiCl with or without 9.6 mW/cm² 405 nm light exposure and the cell viability assessed with both the AB and NRU assays (Figure 2). The dose range for the cytotoxicity assays without light were centered around 17 mmol/L (0.5 wt % LAP), which is a common LAP concentration used in bioprinting. Cytotoxicity of LiCl was measured in parallel.

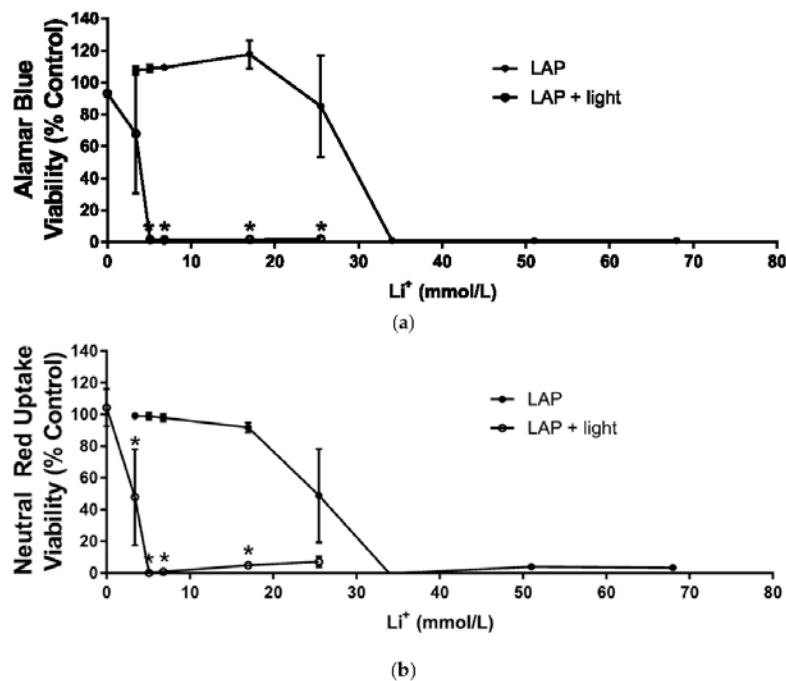


Figure 2. Viability of mouse M-1 collecting duct cell monolayers exposed to varying concentrations of LAP (3.4, 5.1, 6.8, 17, 25.5, 34, or 68 mmol/L) and not-exposed (●) or exposed to 9.6 mW/cm² 405 nm light (○). LAP concentrations are represented as equivalent Li concentrations. Results are normalized to the viability of monolayers exposed only to PBS and not exposed to light. CdCl₂ (1 mmol/L) was used as the positive control; viability averaged 0% for both assays (data not shown). (a) Viability determined by the Alamar Blue assay. (b) Viability determined by the Neutral Red Uptake assay. Values represent means ± standard deviations of N = 3 independent replicate experiments. Values that appear to be missing error bars are cases where the standard deviation is smaller than the symbol size. Asterisks (*) denote treatments where the viability of monolayers exposed to LAP is significantly different ($p < 0.05$) from the viability of monolayers exposed to LAP and light.

Exposure to LiCl with or without light slightly reduced viability. Cells exposed to the maximum investigated LiCl concentration (68 mmol/L) reduced viability down to 80% and 94% viability measured by the AB and NRU assays, respectively (data not shown). No differences in viability were observed between the treatments with LiCl alone and LiCl plus light exposure (data not shown).

Generally, the viability, as reported in both assays for the LAP dose response curve, was extremely sensitive, with concentrations yielding near 100% or near 0% viability flanking a single inflection point. Between 3.4 and 17 mmol/L LAP without exposure to light, viability in the AB assay was above 100%

viability, and had an increasing trend over this concentration range, while viability in the NRU assay remained below 100% and had a decreasing trend. AB and NRU assays both reported a sharp drop in viability at 25.5 mmol/L LAP; at higher concentrations, all cells were dead as viability was essentially zero %.

Cells exposed to light alone (no LAP) exhibited no change in viability compared to controls. Cell viability at 3.4 mmol/L LAP, the lowest investigated dose, with concomitant light exposure diminished to 68% and 48% for the AB and NRU assays, respectively. Only the result of the NRU assay was significant at this point, however, the results show that the EC_{50} (effective concentration that kills 50% of the cells) for both assays was approximately 10-fold more potent for LAP + light, compared to LAP alone. Both assays showed that for cells exposed to LAP concentrations higher than 3.4 mmol/L LAP with concomitant exposure to light, viability was near zero.

3.3. Ames Bacterial Reverse Mutagenicity Assay

Bacterial reverse mutagenicity assay results are summarized in Figure 3. All plates had an intact bacterial lawn, which indicated the lack of overt cytotoxicity; colonies present on the plates are attributed to reverse mutation. Baseline reverse mutation rates of WP2uvrA, TA98, and TA100 were 34, 38, and 89 revertant colonies, respectively. Strain-specific positive controls (i.e., 4-NQO for WP2uvrA and 2-NF for TA98 and TA100) resulted in a marked increase in colony counts. For all strains, either the control chemical mutagen, UV-C positive control, or both resulted in a positive mutagenicity assessment. In contrast, all treatments with LAP with or without light in all strains tested resulted in no apparent mutagenicity; colony counts were on par with the negative control.

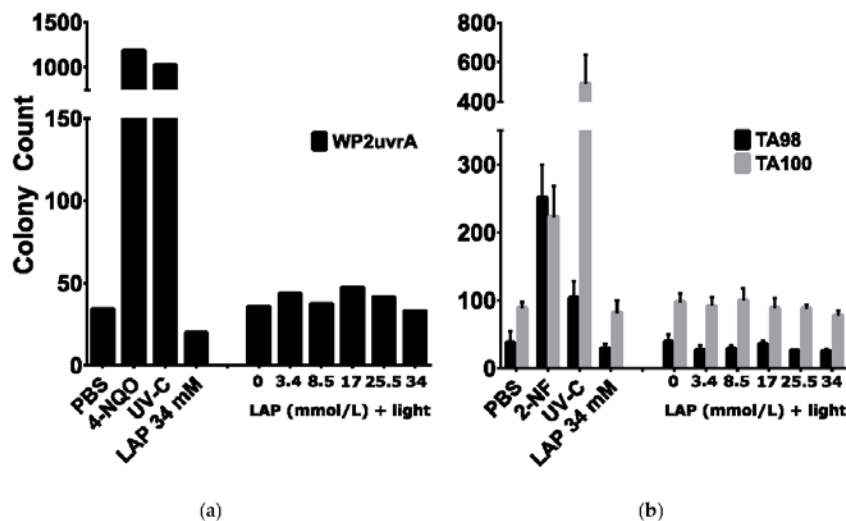


Figure 3. Mutagenicity assessment using bacterial reverse mutation assays. Reverse mutant colony counts of *E. coli* (WP2uvrA, (a)) and *S. typhimurium* (TA98 or TA100, (b)) exposed to PBS (negative control), 0.5 μ g/plate 4-NQO or 0.4 μ g/plate 2-NF (strain-specific positive controls), 18.5 mJ/cm² UV-C light, 34 mmol/L LAP, or various LAP concentrations with exposure to 10 min of 9.6 mW/cm² 405 nm light. For *E. coli* (a), values represent the average of N = 2 independent replicate experiments. For *S. typhimurium* strains (b), values represent means \pm standard deviations of N = 3 independent replicate experiments.

4. Discussion

GelMA is made photosensitive with addition of LAP photoinitiator and is crosslinked with exposure to 405 nm light. Crosslinked GelMA is solid at cell culture temperatures (37 °C) and has a shear elastic modulus proportional to its concentration when fully crosslinked. Both LAP concentration and 405 nm light intensity are positively correlated with crosslinking rate, but do not affect final elastic modulus [30]. Photo-crosslinking has been traditionally performed with curing lamps, such as mercury or xenon arc lamps with filtered outputs for their high output power, but the high heat generation, high power draw, large volume, and relatively high cost of these lamps have pushed for the use of LEDs in portable light sources, such as dental curing lights and commercially-available bioprinters [28,31,32]. The use of 405 nm LEDs in this study is typical of bioprinters using LAP for these reasons. The use of 3 mW/cm² irradiance in the photorheology studies was mainly limited by the desire to achieve even illumination over the entire 20 mm geometry. Most of the LED power is discarded to result in only a small emission angle to the sample; increasing the irradiance by moving the LED closer or by including focusing optics is associated with decreasing the evenness of the irradiance field. Since the polymerization rate is proportional to the square root of light intensity, the use of this lower irradiance can justify exposure conditions using the 9.6 mW/cm² irradiance used in the biological assays [30].

Photorheology results were evaluated mainly for the light exposure time required to reach 95% of the maximum achieved storage modulus for each LAP concentration investigated. However, the lag time between the start of light exposure and the beginning of polymerization is an important artifact. This lag time is inversely proportional to the photoinitiator concentration, and is attributed to radical scavenging by oxygen [33]. To test this hypothesis, nitrogen purging of the 3.4 mmol/L LAP gel reduced the lag time, compared to the 17 mmol/L LAP gel. While nitrogen purging is a common method to improve the polymerization performance of acrylate photopolymers, this process is not compatible with cell-laden gels used in bioprinting [34]. Nevertheless, the result that the 3.4 mmol/L LAP gel required 720 s to fully polymerize justifies the exaggerated exposure from the higher 9.6 mW/cm² irradiance for 600 s used in the subsequent studies.

Since studies have shown that both photoinitiator concentration and light exposure are associated with toxic effects, conventional wisdom states that these parameters should be carefully controlled [12,35]. For example, underexposure would result in imprecise control of the mechanical properties and an increase in the concentration of unreacted monomer, while overexposure would expose cells to additional phototoxic effects while not significantly affecting the mechanical properties. Multiple studies report photopolymer tissue engineering constructs with low cytotoxicity, and/or the ability of cells to proliferate within the construct after printing [28,36,37]. The success of this technique is contrary to the assumption that free-radical generating photoinitiators produce toxic effects, including genotoxicity, from reactive oxygen species [14,38]. Therefore, the second and third objectives of this study were to determine whether concomitant exposures to LAP and light under conditions typical of bioprinting were cytotoxic and/or mutagenic.

Cytotoxicity assays were performed using confluent mouse kidney M-1 collecting duct cell layers, which exhibited evidence of active water transport, i.e., “domes”, attributed to water transport between the cell layer and wellplate bottom [25]. Lithium ion is a known nephrotoxicant, whose mechanism of toxicity is related to the inhibition of AQP-2 transport to the cell membrane, thereby causing diabetes insipidus [39]. However, diabetes insipidus isn't the major concern in this study versus lithium accumulation within the kidney, risk of renal fibrosis, and damage to various organelles; karyolysis and cell fragmentation were observed in the kidneys of rats exposed to lithium chloride [21,23,40]. Results in both the Alamar Blue and Neutral Red Uptake assays agree that lithium ion concentrations typically associated with LAP can be mildly cytotoxic; However, 95% viability from 17 mmol/L LiCl exposure (i.e., equivalent to 0.5 wt % LAP) determined with the NRU assay is a generally accepted viability for cells grown in vitro; this effect should be less pronounced in other cell models not as sensitive to lithium. At LAP concentrations and exposure times typically used in bioprinting, lithium ions were not identified as a significant cytotoxic factor.

In contrast, LAP exposure to M-1 collecting duct layers in the absence of light was cytotoxic at 17 mmol/L corresponding to 0.5 wt % LAP, a commonly used concentration in bioprinting. The exposure duration was 24 h, which represents an exaggerated exposure compared to bioprinted constructs, where LAP would be diluted by cell culture medium after crosslinking. With exposure to light, an immediate reduction in viability was observed at the lowest LAP concentration corresponding to 0.1 wt % LAP. This result is corroborated in a study by Duchi et al. where sheep adipose derived stem cells exhibited around 20% viability after exposure to 0.1% LAP, albeit with 700 mW/cm² 365 nm light for 10 s [28]. Bioprinting with similar LAP and light conditions generally does not elicit this cytotoxic response, so this discrepancy is attributed to a protective effect of GelMA and cell media used during bioprinting. For example, the presence of antioxidants, such as N-acetylcysteine, was shown to be protective against oxidative damage [41]. This strategy was also used to develop a photoprotective supplement composed of antioxidants, which prevented light-induced cytotoxicity in neuronal culture exposed to 360 kJ/m² 470 nm light [42]. This protective effect was also observed in bone marrow stromal cells encapsulated with methacrylated hyaluronic acid or polyglycerol; neither Irgacure 2959 concentration or radiant exposure from 6 mW/cm² 365 nm light for 5 min caused any statistically significant differences in cell viability or proliferation versus the non-irradiated control [43]. In the absence of the encapsulating polymer, increasing light exposure and/or Irgacure 2959 concentration caused drops in viability and proliferation [44]. High viability (~96%) was also observed in human neonate foreskin fibroblasts embedded in polyethylene glycol diacrylate with 2.2 mmol/L LAP exposed to 5–10 min of 10 mW/cm² 405 nm light [30]. In the present study, in vitro assays performed in the absence of GelMA likely exaggerated cytotoxicity typically observed when using this material in bioprinting. All investigated LAP concentrations with exposure to light were highly cytotoxic to the M-1 collecting duct cells compared to LAP alone, and this confirms the hypothesis that concurrent LAP and light exposure is more cytotoxic than LAP exposure alone.

A modified Ames bacterial mutagenicity assay was conducted with LAP and light exposures that were cytotoxic to M-1 cells, to determine whether these exposures are mutagenic. This modification involves light exposure to the bacteria and toxicant prior to incubation, and has been previously used to determine mutagenicity from concomitant light and exposure to sunscreen and cosmetic [44,45] compounds. The results in the present study show that the positive and negative controls performed adequately within defined parameters, resulting in valid assays; however, mutagenicity assessment for LAP concentrations ranging from 0 to 34 mmol/L with or without 10 min of 9.6 mW/cm² 405 nm light exposure were negative. OECD TG471 guidelines recommend a battery of four *S. typhimurium* strains (including TA98 and TA100) and additional choice of strain (including WP2 uvrA) which detects “oxidizing mutagens, cross-linking agents and hydrazines” [29]. While this study only used two *S. typhimurium* strains and one *E. coli* strain, recent studies showed that using only TA98 and TA100 detected 93% of the >10000 compound database [46]. Since ROS is expected to be an oxidizing mutagen, the TA100, TA98, and WP2 uvrA test battery used in this assay should have a high chance of detecting mutagenicity. Thus, the negative result observed is surprising. Although the addition of S9 metabolic activation is a customary procedure for testing chemicals that might require metabolic activation for genotoxicity, S9 was not deemed relevant to this study, because we are exploring another mode of activation: light-based photo-activation. The Ames assay is widely-used and is predictive of 70–90% of carcinogens, but the use of the Ames assay alone for a negative mutagenicity assessment is insufficient as a definitive stand-alone result [47,48]. The reasons for negative results include inadequate dosing (e.g., failure of uptake), failure to detect mammalian-specific mutagens, or chemical-specific requirements not met, in addition to a true lack of mutagenicity. Further investigations are needed to define the mutagenic status of LAP plus light, especially given the cytotoxicity observed.

Despite being a popular, well-cited, and commercially-available photoinitiator for use with bioprinting, there are no reports of studies evaluating the mutagenicity of LAP to the authors' knowledge. However, an EU report on the chemically similar trimethylbenzoyl diphenyl phosphine oxide (TPO), which is used primarily in photo-crosslinkable nail polish, finds that TPO is not mutagenic

based on data from multiple in vitro and in vivo assays; however, no study took light exposure into account [49]. TPO was also investigated alongside camphorquinone, in combination with various acrylate-based polymers, and found to be marginally genotoxic determined with the Comet assay, although light exposure was not assessed [50]. Based on these studies, LAP was not expected to be mutagenic in the absence of light exposure, but our results thus far do not support our hypothesis that LAP with light exposure would be mutagenic, given the expected generation of reactive oxygen species and the toxicity observed in mammalian cells.

5. Conclusions

The cytotoxicity of LAP to confluent M-1 collecting duct cells was significantly enhanced with exposure to 405 nm light with increased cytotoxicity observed at concomitant exposures of >3.4 mmol/L LAP (0.1 wt % LAP) and 10 min of 9.6 mW/cm² light, conditions occurring during LAP use as a photoinitiator. However, LAP concentrations up to 34 mmol/L (1.0 wt %), an atypically high concentration for bioprinting, were not mutagenic in bacteria, even after exposure to light. This study supports that use of LAP photoinitiator and free radicals generated from photo-excited LAP can be cytotoxic to cells undergoing bioprinting. Further studies are needed to more definitively demonstrate the lack of mutagenicity of LAP and light exposure conditions typical in bioprinting.

Author Contributions: Investigation, A.K.N., R.K.E., and S.S.D.; writing—original draft preparation, A.K.N.; resources, R.K.E. and S.S.D.; writing—review & editing, supervision, P.L.G.; funding acquisition, R.J.N. All authors have reviewed/edited the manuscript and agree to the published version. All authors have read and agreed to the published version of the manuscript.

Funding: This research was funded by NSF award #1762202.

Acknowledgments: Photorheology data was collected using an Anton Paar MCR302 rheometer with assistance from David Wysocki. Light source irradiance and emission spectra was collected with help from Ilko Ilev from FDA's Division of Biomedical Physics.

Conflicts of Interest: The authors declare no conflict of interest.

Disclaimer: The findings and conclusions in this paper have not been formally disseminated by the Food and Drug Administration and should not be construed to represent any agency determination or policy. The mention of commercial products, their sources, or their use in connection with material reported herein is not to be construed as either an actual or implied endorsement of such products by Department of Health and Human Services.

References

1. Stampfl, J.; Baudis, S.; Heller, C.; Liska, R.; Neumeister, A.; Kling, R.; Ostendorf, A.; Spitzbart, M. Photopolymers with tunable mechanical properties processed by laser-based high-resolution stereolithography. *J. Micromech. Microeng.* **2008**, *18*, 125014. [[CrossRef](#)]
2. Larsen, E.K.U.; Larsen, N.B.; Almdal, K.; Larsen, E.K.U.; Larsen, N.B.; Almdal, K. Multimaterial hydrogel with widely tunable elasticity by selective photopolymerization of PEG diacrylate and epoxy monomers. *J. Polym. Sci. Part B Polym. Phys.* **2016**, *54*, 1195–1201. [[CrossRef](#)]
3. Jeon, O.; Bouhadir, K.H.; Mansour, J.M.; Alsberg, E. Photocrosslinked alginate hydrogels with tunable biodegradation rates and mechanical properties. *Biomaterials* **2009**, *30*, 2724–2734. [[CrossRef](#)] [[PubMed](#)]
4. Ning, L.; Chen, X. A brief review of extrusion-based tissue scaffold bio-printing. *Biotechnol. J.* **2017**, *12*, 1600671. [[CrossRef](#)]
5. Correia Carreira, S.; Begum, R.; Perriman, A.W. 3D Bioprinting: The Emergence of Programmable Biodesign. *Adv. Healthc. Mater.* **2019**, 1900554. [[CrossRef](#)] [[PubMed](#)]
6. Crivello, J.V.; Reichmanis, E. Photopolymer Materials and Processes for Advanced Technologies. *Chem. Mater.* **2014**, *26*, 533–548. [[CrossRef](#)]
7. Pereira, R.F.; Bártolo, P.J. 3D Photo-Fabrication for Tissue Engineering and Drug Delivery. *Engineering* **2015**, *1*, 90–112. [[CrossRef](#)]
8. Lin, C.-C.; Ki, C.S.; Shih, H. Thiol-norbornene photo-click hydrogels for tissue engineering applications. *J. Appl. Polym. Sci.* **2015**, *132*, 41563. [[CrossRef](#)]
9. OECD. *Test No. 442D: In Vitro Skin Sensitisation*; OECD Publishing: Paris, France, 2018. [[CrossRef](#)]

10. OECD. *Test No. 442E: In Vitro Skin Sensitisation*; OECD Publishing: Paris, France, 2018. [[CrossRef](#)]
11. Strickland, J.; Zang, Q.; Paris, M.; Lehmann, D.M.; Allen, D.; Choksi, N.; Matheson, J.; Jacobs, A.; Casey, W.; Kleinstreuer, N. Multivariate models for prediction of human skin sensitization hazard. *J. Appl. Toxicol.* **2017**, *37*, 347–360. [[CrossRef](#)]
12. Sabnis, A.; Rahimi, M.; Chapman, C.; Nguyen, K.T. Cytocompatibility studies of an in situ photopolymerized thermoresponsive hydrogel nanoparticle system using human aortic smooth muscle cells. *J. Biomed. Mater. Res. A* **2009**, *91*, 52–59. [[CrossRef](#)]
13. Leonhardt, S.; Klare, M.; Scheer, M.; Fischer, T.; Cordes, B.; Eblenkamp, M. Biocompatibility of photopolymers for additive manufacturing. *Curr. Dir. Biomed. Eng.* **2016**, *2*, 113–116. [[CrossRef](#)]
14. Premi, S.; Wallisch, S.; Mano, C.M.; Weiner, A.B.; Bacchiocchi, A.; Wakamatsu, K.; Bechara, E.J.; Halaban, R.; Douki, T.; Brash, D.E. Photochemistry. Chemiexcitation of melanin derivatives induces DNA photoproducts long after UV exposure. *Science* **2015**, *347*, 842–847. [[CrossRef](#)]
15. Moody, C.S.; Hassan, H.M. Mutagenicity of oxygen free radicals. *Proc. Natl. Acad. Sci. USA* **1982**, *79*, 2855–2859. [[CrossRef](#)] [[PubMed](#)]
16. Rookmaaker, M.B.; van Gerven, H.A.J.M.; Goldschmeding, R.; Boer, W.H. Solid renal tumours of collecting duct origin in patients on chronic lithium therapy. *Clin. Kidney J.* **2012**, *5*, 412–415. [[CrossRef](#)]
17. Trepiccione, F.; Pisitkun, T.; Hoffert, J.D.; Poulsen, S.B.; Capasso, G.; Nielsen, S.; Knepper, M.A.; Fenton, R.A.; Christensen, B.M. Early targets of lithium in rat kidney inner medullary collecting duct include p38 and ERK1/2. *Kidney Int.* **2014**, *86*, 757–767. [[CrossRef](#)] [[PubMed](#)]
18. Roque, A.; Herédia, V.; Ramalho, M.; de Campos, R.; Ferreira, A.; Azevedo, R.; Semelka, R. MR findings of lithium-related kidney disease: Preliminary observations in four patients. *Abdom. Imaging* **2012**, *37*, 140–146. [[CrossRef](#)]
19. Aiff, H.; Attman, P.-O.; Aurell, M.; Bendz, H.; Ramsauer, B.; Schön, S.; Svedlund, J. Effects of 10 to 30 years of lithium treatment on kidney function. *J. Psychopharmacol.* **2015**, *29*, 608–614. [[CrossRef](#)] [[PubMed](#)]
20. Christensen, B.M.; Zuber, A.M.; Loffing, J.; Stehle, J.-C.; Deen, P.M.T.; Rossier, B.C.; Hummler, E. α ENaC-Mediated Lithium Absorption Promotes Nephrogenic Diabetes Insipidus. *J. Am. Soc. Nephrol.* **2011**, *22*, 253–261. [[CrossRef](#)]
21. Davis, J.; Desmond, M.; Berk, M. Lithium and nephrotoxicity: Unravelling the complex pathophysiological threads of the lightest metal. *Nephrology (Carlton)* **2018**, *23*, 897–903. [[CrossRef](#)]
22. Hiatt, M.J.; Matsell, D.G. Chapter 25-Plasticity within the Collecting Ducts: What Role Does This Play in Response to Injury? In *Kidney Development, Disease, Repair and Regeneration*; Little, M.H., Ed.; Academic Press: Cambridge, MA, USA, 2016; pp. 335–350.
23. Efrati, S.; Averbukh, M.; Berman, S.; Feldman, L.; Dishy, V.; Kachko, L.; Weissgarten, J.; Golik, A.; Averbukh, Z. N-Acetylcysteine ameliorates lithium-induced renal failure in rats. *Nephrol. Dial. Transpl.* **2005**, *20*, 65–70. [[CrossRef](#)]
24. Benedikt, S.; Wang, J.; Markovic, M.; Moszner, N.; Dietliker, K.; Ovsianikov, A.; Grützmacher, H.; Liska, R. Highly efficient water-soluble visible light photoinitiators. *J. Polym. Sci. Part A Polym. Chem.* **2016**, *54*, 473–479. [[CrossRef](#)]
25. Korbmacher, C.; Segal, A.S.; Fejes-Toth, G.; Giebisch, G.; Boulpaep, E.L. Whole-cell currents in single and confluent M-1 mouse cortical collecting duct cells. *J. Gen. Physiol.* **1993**, *102*, 761–793. [[CrossRef](#)] [[PubMed](#)]
26. Gillman, N.; Lloyd, D.; Bindra, R.; Ruan, R.; Zheng, M. Surgical applications of intracorporeal tissue adhesive agents: Current evidence and future development. *Expert Rev. Med. Devices* **2020**, *17*, 443–460. [[CrossRef](#)] [[PubMed](#)]
27. Sun, A.; He, X.; Li, L.; Li, T.; Liu, Q.; Zhou, X.; Ji, X.; Li, W.; Qian, Z. An injectable photopolymerized hydrogel with antimicrobial and biocompatible properties for infected skin regeneration. *NPG Asia Mater.* **2020**, *12*, 25. [[CrossRef](#)]
28. Duchi, S.; Onofrillo, C.; O’Connell, C.D.; Blanchard, R.; Augustine, C.; Quigley, A.F.; Kapsa, R.M.I.; Pivonka, P.; Wallace, G.; Di Bella, C.; et al. Handheld Co-Axial Bioprinting: Application to in situ surgical cartilage repair. *Sci. Rep.* **2017**, *7*, 5837. [[CrossRef](#)] [[PubMed](#)]
29. OECD. *Test No. 471: Bacterial Reverse Mutation Test*; OECD Publishing: Paris, France, 1997. [[CrossRef](#)]
30. Fairbanks, B.D.; Schwartz, M.P.; Bowman, C.N.; Anseth, K.S. Photoinitiated polymerization of PEG-diacrylate with lithium phenyl-2,4,6-trimethylbenzoylphosphinate: Polymerization rate and cytocompatibility. *Biomaterials* **2009**, *30*, 6702–6707. [[CrossRef](#)] [[PubMed](#)]

CHAPTER 7 – Effects of Subcytotoxic Exposure of Silver Nanoparticles on Osteogenic Differentiation of Human Bone Marrow Stem Cells

Alexander K. Nguyen^{1,2}, Reema Patel², Jade M. Noble³, Jiwen Zheng², Roger J. Narayan¹, Girish Kumar², and Peter L. Goering²

1. UNC/NCSU Joint Department of Biomedical Engineering, North Carolina State University, Raleigh, NC
2. Division of Biology Chemistry and Materials Science, US Food and Drug Administration, Silver Spring, MD
3. Office of Generic Drugs, Center for Drug Evaluation and Research, US Food and Drug Administration, Silver Spring, MD

Reference: Nguyen, A.K.; Patel, R.; Noble, J.M.; Zheng, J.; Narayan, R.J.; Kumar, G.; Goering, P.L. Effects of Subcytotoxic Exposure of Silver Nanoparticles on Osteogenic Differentiation of Human Bone Marrow Stem Cells. *Applied In Vitro Toxicology* **2019**, *5*, 123-133, doi:10.1089/aivt.2019.0001.

Abstract

Introduction: In vitro toxicology evaluations utilizing human stem cell models represent attractive alternatives to conventional animal models, which are not always predictive of human responses. Silver nanoparticles (AgNP) are a potent antimicrobial for use in orthopedic devices. However, AgNP exposure may alter the behavior of stem cells within the bone marrow. The aim of this study was to determine if differences in cell proliferation, early, and late osteogenic differentiation markers can be detected in osteogenically differentiating human bone marrow mesenchymal stem cells (hBMSC) over a 21-day period at AgNP concentrations that are not considered cytotoxic after 24-hour exposure per ISO 10993-5 cytotoxicity testing guidelines.

Materials and Methods: Polyvinylpyrrolidone (PVP)-coated 10 nm AgNP were evaluated for their short-term (24-hour) cytotoxicity to hBMSC using the MTT assay to

determine subcytotoxic concentrations for the subsequent long-term study investigating osteogenic differentiation. hBMSC were exposed to 1, 5, or 10 $\mu\text{g/mL}$ AgNP in three different exposure scenarios: single (24-hour), repeated (24-hour at 1, 7, and 14 days), or continuous (21-day) exposure. Alkaline phosphatase (early osteogenic differentiation marker), hydroxyapatite deposition (late marker), and cell proliferation were measured at days 1, 7, 14, and 21.

Results: AgNP exposure reduced cell proliferation for all treatments. Neither differentiation marker expression was observed at any timepoint in hBMSC exposed to AgNP at 10 $\mu\text{g/mL}$ for any exposure scenario or in cells exposed to 5 $\mu\text{g/mL}$ in the repeated or continuous exposure scenarios.

Conclusions: Differences in proliferation and osteogenic marker expression were detected in the different exposure scenarios at AgNP concentrations identified as subcytotoxic in a 24-hour exposure assay.

Introduction

Infections associated with medical devices such as orthopedic implants are a common complication, which often necessitates explantation of the device. Recently published statistics for total knee arthroplasty performed between 1999 and 2015 revealed infection in 1.0%–1.5% of all orthopedic surgeries and was a close-second cause of revision surgeries [29].

Staphylococcus was found to be the leading organism in orthopedic surgeries at 29% [241]. This also includes methicillin-resistant Staphylococcus aureus, which does not respond well to antibiotic treatment. Due to the increasing risk of antibiotic resistance, silver as an alternate mechanism for infection control would be advantageous. Incorporation of silver into medical devices is shown to reduce concentrations of various microbes, including *S. aureus*, and inhibit the formation of biofilms [242, 243]. Both ionic and particulate forms of silver are used in skin-

contacting medical devices, such as wound dressings [244] or dermal reconstruction matrices [245], and multiple external-communicating devices, such as Foley catheters containing silver are commercially available.

Despite the beneficial antimicrobial properties, silver could have adverse effects on human cells if released in sufficient doses to the systemic circulation. For example, uncoated 35 nm silver nanoparticles (AgNP) were found to exceed the 5% hemolysis threshold in ASTM E2524-08 at 70 $\mu\text{g}/\text{mL}$.⁷ AgNP (12.5 nm diameter) were also found to significantly alter several hematologic parameters at a 30 $\mu\text{g}/\text{mL}$ threshold concentration in a blood loop model [246].

Long-term silver exposure resulting from device implantation could raise the possibility of adverse local responses in the surrounding tissue. Stem cells in bone marrow play a role in a wide array of tissue regeneration tasks, such as the growth of new bone, fat, and blood cells. While impairment of any of these functions might negatively influence patient treatment outcomes, adverse effects on differentiation into the osteocyte lineage would slow or prevent osseointegration of the implant. This could lead to loosening, which is the leading cause of revision surgery [29].

AgNP characteristics such as size, coating type, and surface chemistry influence biological outcomes such as cytotoxicity, nanoparticle uptake, and intracellular localization [247, 248] and the change of any one of these parameters can have drastic effects. For example, equimolar concentrations of 3, 10, 50, and 100 nm diameter AgNP had different effects on zebrafish mortality and a number of sublethal effects such as malformation of different parts [249]. Thus, the large number of possible combinations would be a challenge to test with conventional animal models. An alternative in vitro model using human stem cells and allowing for long-term exposure to the toxicant of interest would not only be more relevant to human

biological and toxicological responses but also be more practical to evaluate a large number of potential toxicants.

Therefore, the objective of this study was to assess the effect of prolonged AgNP exposure on osteogenic differentiation of human bone marrow mesenchymal stem cells (hBMSC) at subcytotoxic AgNP concentrations. Additionally, different exposure scenarios up to 21 days were investigated to model various degrees of duration (e.g., acute, moderate, and prolonged) of implant tissue contact. Thus, the hypothesis that differences in cell proliferation, early, and late osteogenic differentiation markers can be detected in differentiating hBMSC over a 21-day period at AgNP concentrations that are not considered cytotoxic after 24-hour exposure per ISO 10993-5 cytotoxicity testing guidelines was tested. Findings from this in vitro model can help inform further understanding of how human stem cells respond to subcytotoxic AgNP concentrations for extended exposures with additional benefits of (1) reducing the necessity of some animal testing and (2) contributing to understanding risks and benefits of this material for medical device implant applications.

Materials and Methods

hBMSC (PCS-500-012; ATCC, Manassas, VA) were cultured in mesenchymal stem cell basal medium (PCS-500-030; ATCC) supplemented with the mesenchymal stem cell growth kit (PCS-500-041; ATCC) and incubated at 37°C, 5.0% CO₂, and 90% relative humidity. Osteogenic differentiation was performed using the Osteocyte Differentiation Tool (PCS-500-052; ATCC) in place of the medium. The mesenchymal stem cell medium and Osteogenic Differentiation Tool are referred to as osteogenic supplement negative (OS⁻) and positive (OS⁺) respectively in this study. Other reagents included Trypsin-EDTA (9002-07-7; Sigma–Aldrich, St. Louis, MO), Dulbecco's phosphate-buffered saline (PBS; 14190-xxx; Thermo Scientific,

Waltham, MA), Triton X-100 (Sigma–Aldrich), 37% formaldehyde (252549; Sigma–Aldrich), and ultrapure water from a NANOpure Diamond water purifier (APS Water Services Corp., Van Nuys, CA).

AgNP characterization Polyvinylpyrrolidone (PVP)-coated, 10 nm diameter AgNP (BioPure; NanoComposix, San Diego, CA) were used in this study. AgNP stock solutions were received as a 1 mg/mL solution in water and were characterized using a JEM 2010F (JEOL, Tokyo, Japan) transmission electron microscope (TEM). AgNP were also diluted in cell culture medium immediately before application to the cryo-TEM grids and the cells per experimental design.

Dynamic light scattering analysis was performed with a Zetasizer Nano ZS (Malvern Panalytical, Malvern, United Kingdom). Hydrodynamic diameter measurements were performed on 20 µg/mL AgNP in 0.02 µm filtered ultrapure water (MilliporeSigma, Burlington, MA). Zeta potential measurements were performed on 100 µg/mL AgNP in 10 mM NaCl inside a DTS1070-folded capillary cell (Malvern Panalytical).

Cryo-TEM was performed on a JEOL 1400 (JEOL USA, Inc., Acworth, GA) operated at 80 kV and equipped with an Orius SC1000 CCD camera (Gatan, Pleasanton, CA). Aliquots (5 µL) of 100 µg/mL AgNP in ultrapure water, OS⁻ media, or OS⁺ media were pipetted onto glow discharged copper Quantifoil (Electron Microscopy Sciences, Hatfield, PA) grids and plunge-frozen using a Leica EM GP automatic plunge freezer (Leica Microsystems, Wetzlar, Germany). Images were binned by 1, resulting in pixel sizes of 0.4 nm.

Cell Culture For each experiment replicate, 1×10^6 hBMSC stored in liquid nitrogen at passage 4 were thawed and seeded into a T-150 flask and incubated overnight. A media change was performed the following day to remove the dimethylsulfoxide cryopreservative and

dead/unattached cells and then allowed to divide for ~1 week to reach 80% confluence. Cells were trypsinized, centrifuged at 200 g for 5 minutes, and resuspended in media. The hBMSC suspension cell density was measured with a hemocytometer and diluted to 5.0×10^4 cells/mL for seeding. Cells used in both the 24-hour exposure and 21-day culture procedures were therefore used at passage 5; passage 6 is the highest passage recommended by ATCC for osteogenic differentiation with the Osteocyte Differentiation Tool.

Viability of hBMSC after a single 24-hour exposure to AgNP Cytotoxicity of AgNP in a single 24-hour exposure was measured via the MTT assay (CellTiter 96 Non-radioactive Cell Proliferation Assay, G4000; Promega, Madison, WI) and read with an OptiMax plate reader (Molecular Devices, Sunnyvale, CA). Three wells per treatment in a 96-well plate were seeded with 1.0×10^4 cells per well in 200 μ L medium and allowed to attach over 24 hours. Cells were then exposed to 1, 5, 10, 25, or 50 μ g/mL AgNP for 24 hours in either OS⁻ or OS⁺ media. Medium alone and medium with 3 mM AgNO₃ were used as negative and positive controls, respectively. Cell-free wells of the corresponding solution were used as the background. An aliquot of 15 μ L MTT dye was added to each well and allowed to metabolize for 3 hours. The kit surfactant solution was used to stop the reaction and dissolve the colored metabolite. The plates were read after 30 minutes of incubation and 30 minutes on a shake plate. For each well, absorbance at 650 nm was subtracted from the absorbance at 570 nm. Viability is calculated as a percent of the negative control and reported as the means and standard deviations (SD) of three independent replicate experiments.

Long-term hBMSC culture using three dosing/exposure scenarios Three long-term subcytotoxic exposure scenario studies involved monitoring hBMSC with a combination of the following treatment conditions: (1) exposure to one of the three AgNP dosing/exposure

scenarios, (2) exposure to one of the three different AgNP concentrations, and (3) culture in media with or without osteogenic supplements. The exposure scenarios are summarized in **Figure 7.1**: a single 24-hour exposure (single), three 24-hour exposures performed on days 1, 7, and 14 (repeated), and continuous exposure to AgNP for 21 days with AgNP refreshed $3 \times$ per week (continuous). AgNP concentrations of 1, 5, or 10 $\mu\text{g}/\text{mL}$ in media with (OS+) or without (OS-) osteogenic supplements were prepared immediately before exposure to the cells.

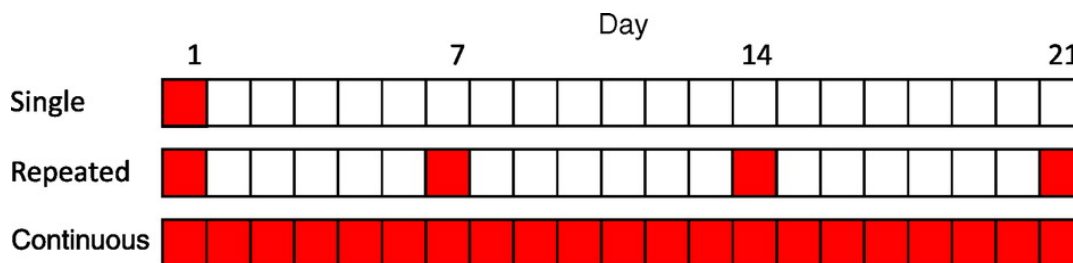


Figure 7.1 - Schedule of AgNP dosing of hBMSC cultures for three separate exposure scenarios: single 24-hour exposure, repeated weekly 24-hour exposures, or continuous exposure. Each square represents a 24-hour period with red squares indicating periods of AgNP exposure. Cell proliferation, alkaline phosphatase expression, and hydroxyapatite content were measured on days 1, 7, 14, and 21 for all exposure scenarios. Fluorescence imaging of hydroxyapatite was performed on day 21 only. hBMSC, human bone marrow mesenchymal stem cells.

For each of four sampling timepoints (1, 7, 14, and 21 days), six 96-well plates were used corresponding to one of the three exposure conditions, and the use of media with or without osteogenic supplements. On each plate, two wells per AgNP concentration (1, 5, or 10 $\mu\text{g}/\text{mL}$) for each of the planned assays were seeded with 1.0×10^4 cells per well in 200 μL medium and incubated for 24 hours before starting the prescribed exposure scenario; hBMSC at the day 1 AgNP exposure was $\sim 50\%$ confluent. hBMSC grown with or without osteogenic supplements and in the absence of AgNP were used as the negative controls. Data from the negative controls are shared between all exposure scenarios but are included on all subcharts in **Figure 7.4** -

Figure 7.7 for ease of comparison. Media were changed three times a week for the 21-day culture period with either media or media with AgNP applied to the cells according to the relevant exposure scenario (**Figure 7.1**). If a well in the single or repeated exposure scenarios received media with AgNP, the particles were removed 24 hours later and replaced with the corresponding media.

For each timepoint, plates were processed for the different assays: Quant-iT PicoGreen, Alkaline Phosphatase (ALP) Liquicolor, and OsteoImage Mineralization assays. ALP was measured immediately at each timepoint, but PicoGreen and OsteoImage assays were performed in bulk after all plates had been harvested. In preparation for storage, media were aspirated from all wells; OsteoImage wells were fixed with 3.7% formaldehyde in PBS for 30 minutes, rinsed 2 × with PBS, and then, the PBS aspirated before storage at −80°C.

PicoGreen assay Cells designated for the PicoGreen assay (Quant-iT PicoGreen dsDNA assay kit, P7589; Thermo Scientific) were previously frozen at −80°C at each timepoint so were thawed to room temperature before digestion with a papain suspension (lot 32J13550, LS003127; Worthington, Lakewood, NJ). Papain was dissolved at a 0.21 U/mL concentration in 1.75 mg/mL l-cysteine in PBS, and 200 µL of this solution was added to each well. The entire plate was sealed with aluminum sealing tape and heated at 60°C for 18 hours. After digestion, the plates were cooled to room temperature over 1 hour. From each well, three aliquots of 50 µL were transferred to three wells on a separate 96-well plate for measurement in triplicate. A double-stranded DNA concentration series (0, 40, 100, 200, 400, 600, 1000, 1400, 1600, and 2000 ng/mL) was prepared by diluting the kit dsDNA stock solution in Tris-EDTA buffer. For each dsDNA ladder concentration, 50 µL was added to two wells for measurement in duplicate. PicoGreen dye in Tris-EDTA buffer was mixed according to the manufacturer's specifications,

and 50 μL was added to all wells and the samples stained for 5–10 minutes. The plate was read in a fluorescent plate reader using 485 nm excitation and 538 nm emission wavelengths. For each set of three measurement wells corresponding to a single well on the initial plate, the average fluorescence intensity was fit to the DNA standard curve and multiplied by the 200- μL volume used in the papain digestion to calculate the DNA mass within the well.

ALP assay ALP was measured using the Alkaline Phosphatase Liquicolor kit (2900-430; Stanbio, Boerne, TX) using SER-T-FY 1 Level 1 Control Serum (lot 151631, G427-86; Stanbio) for controls. Kinetic measurements for this assay were performed on a SpectraMax 190 plate reader (Molecular Devices). Media from ALP assay wells were aspirated and replaced with 100 μL 0.2% Triton X-100 in PBS for 20 minutes. A new 96-well plate was prepared where three wells each were allocated for negative and positive controls: 0.2% Triton X-100, 5 μL serum, 15 μL serum, and 35 μL serum. These control wells were diluted to 75 μL total volume with additional 0.2% Triton X-100. The permeabilized cells were diluted with an additional 100 μL of 0.2% Triton X-100 and mixed thoroughly. Two 75 μL aliquots from each of these solutions were added to two wells on the new plate for measurement in duplicate. A 75 μL aliquot of the kit working reagent was added to each well; the plate was then immediately placed into a fluorescent plate reader for kinetic measurements. Absorbance at 405 nm was read once per minute over 5 hours. The rate of generation of the colored compound is initially linear and proportional to the ALP content. For each well, the linear region of the curve was determined between the start of data collection and the timepoint when the R^2 value of the linear regression was greater than 0.98. The slope of the linear region was compared with the slope of the serum control wells to calculate the ALP concentration.

OsteoImage fluorescent microscopy/mineralization quantification assay

Mineralization quantification was performed with the OsteoImage Mineralization Assay (PA-1503; Lonza, Walkersville, MD) that specifically stains hydroxyapatite; fluorescence quantification using a plate reader and fluorescence microscopy was performed in the same well. The hBMSC were previously fixed in 3.7% formaldehyde and stored frozen at -80°C . OsteoImage dye was diluted 1:100 in the supplied wash buffer per the manufacturer's instructions; 100 μL was added to each well, the samples stained for 30 minutes, and then washed $3 \times$ with the wash buffer. The hydroxyapatite fluorescence signal was read at 492 nm excitation and 520 nm emission wavelengths. Fluorescent images of the wells after 21 days in culture were obtained using an Eclipse TE2000-U fluorescence microscope (Nikon, Tokyo, Japan).

Statistical Analysis Statistical analysis and graphing were performed using GraphPad Prism 6 (San Diego, CA). Cytotoxicity after 24-hour AgNP exposure was analyzed by multiple Student's t-tests comparing each treatment with the negative control. Proliferation during the 21-day study measured by the PicoGreen DNA assay was analyzed using two-way analysis of variance between AgNP concentrations and exposure scenarios within each timepoint; statistical significance was determined using the Tukey post hoc analysis ($p < 0.05$). Detection of ALP and mineralization, early and late markers of osteogenic differentiation, respectively, was analyzed by comparing OS⁺ supplemented cells with the corresponding OS⁻ treatment for each timepoint using a one-tailed Student's t-test. Since both ALP expression and hydroxyapatite deposition were near baseline levels for all OS⁻ cells, data were summarized as the difference between the OS⁺ and OS⁻ supplemented groups for clarity. Thus, the resulting means and SDs were calculated using .

Results

AgNP characterization Particles ($n = 140$) in one TEM image (**Figure 7.2**) were analyzed using the ImageJ (NIH, Bethesda, MD). Particle diameter averaged 9.95 nm with a SD of 2.22 nm. The morphology was approximately circular with average major and minor elliptical axes of 10.52 and 9.44 nm, respectively. AgNP Z-average hydrodynamic diameter was measured to be 18.33 nm, with a SD of 0.73 nm over six measurements. Zeta potential was measured to be -15.6 mV, with a SD of 0.95 mV over four measurements.

Cryo-TEM (**Figure 7.2**) was performed on AgNP in both OS⁻ and OS⁺ media to image the state of AgNP that the hBMSC were exposed to. AgNP dispersed in water was found to be monodisperse. In both media types, AgNP appeared as single particles or as small agglomerates of less than 10 particles.

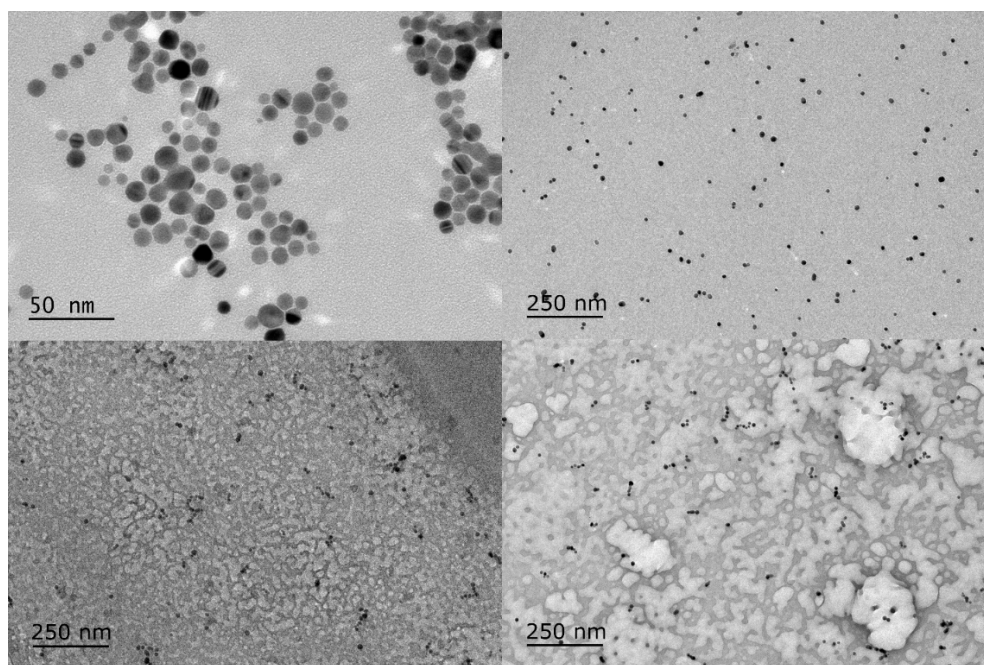


Figure 7.2 - Representative TEM image (top left) of 10 nm PVP-coated AgNP. AgNP core diameter was determined to be 9.95 nm with a 2.22 nm SD by image analysis of $n = 140$ particles. Cryo-TEM images of AgNP diluted in water (top right), OS⁻ media (bottom left), and OS⁺ media (bottom right). AgNP, silver nanoparticles; SD, standard deviation; TEM, transmission electron microscope.

Dose-finding for cytotoxicity of AgNP after a single 24-hour exposure An AgNP concentration-dependent decrease in hBMSC viability was observed using the MTT assay (**Figure 7.3**). Based on the international standard ISO 10993-5 [160], a chemical is noted to have cytotoxic potential if the viability falls below 70%. The viability of hBMSC exposed to 1 or 5 $\mu\text{g/mL}$ AgNP for 24 hours was not statistically different from the negative control. hBMSC exposed to 10 $\mu\text{g/mL}$ AgNP exhibited viabilities of 80% and 71% of control when cultured in the absence and presence of osteogenic supplements, respectively. Concentrations of 25 and 50 $\mu\text{g/mL}$ resulted in statistically significant decreases in viability, and the values were below the 70% cytotoxicity threshold. Therefore, concentrations of 1 and 5 $\mu\text{g/mL}$ were included in the 21-day study as concentrations with no detected 24 hours of cytotoxicity, and 10 $\mu\text{g/mL}$ AgNP included as the concentration that meets the criteria for nonsignificant cytotoxic potential according to the ISO 10993-5 standard.

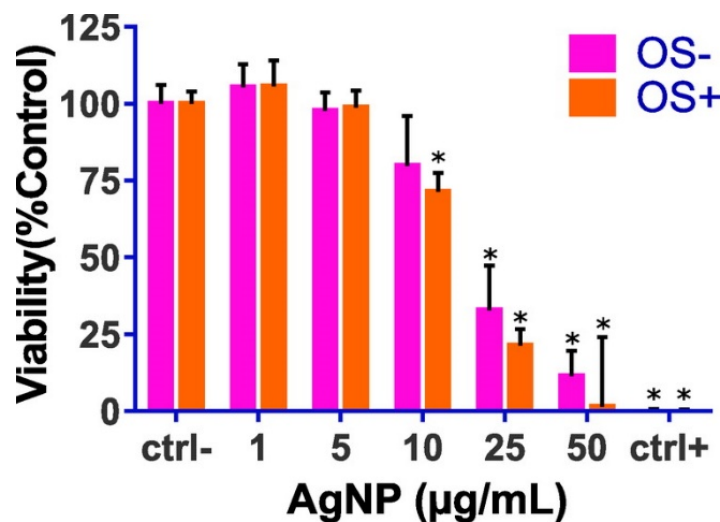


Figure 7.3 - Viability of hBMSC (MTT assay) cultured for 24 hours in the absence (OS-) or presence (OS+) of osteogenic supplements. Cells were exposed to various concentrations of 10 nm PVP-coated AgNP. Cells grown in media alone or media with 3 mmol/L AgNO₃ were used as the negative (ctrl-) and positive (ctrl+) controls, respectively. Values represent (n = 3 replicate experiments). Bars with asterisks are significantly different from the negative control (p < 0.05). SD, standard deviation.

Cell proliferation Proliferation was assessed with the PicoGreen assay in which dsDNA concentrations can be quantitatively measured. The dsDNA concentration is proportional to the number of live cells remaining in the culture; dead cells detach from the plate and are removed with regular media changes. For easier data visualization, proliferation data were organized in two graphs; as a time course (**Figure 7.4**) and individually by timepoint to more clearly show the dose–response and statistically significant differences (**Figure 7.5**).

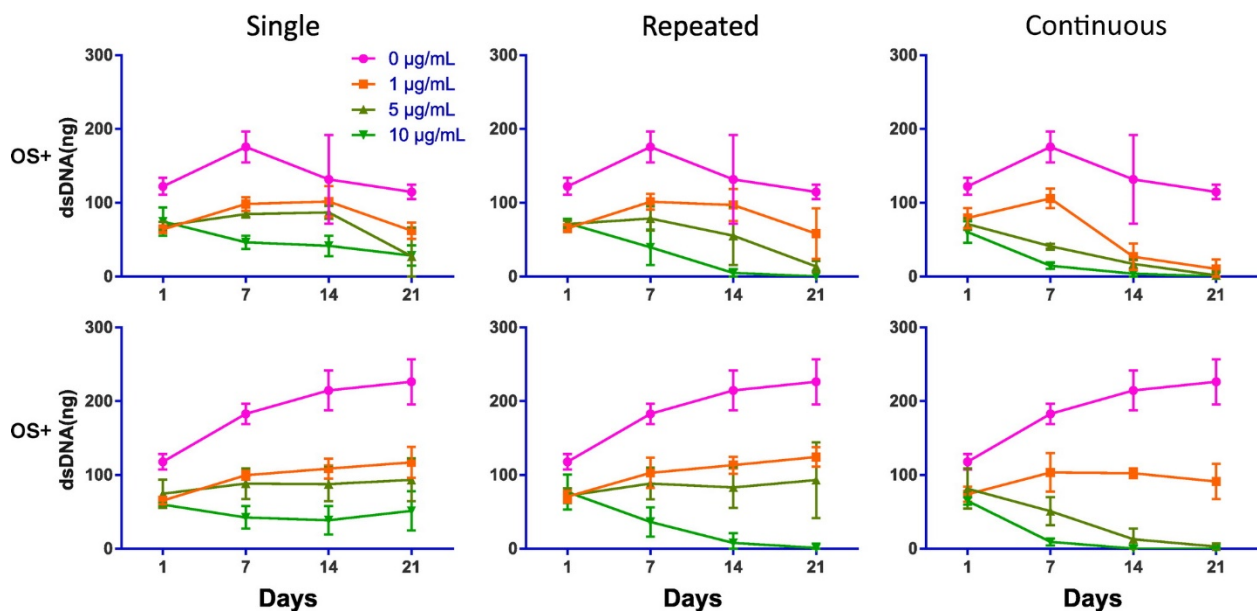


Figure 7.4 - Time-course responses for the proliferation of hBMSC (PicoGreen dsDNA assay) cultured in the absence (OS–) or presence (OS+) of osteogenic supplements under single, repeated, or continuous exposure (Fig. 1) to 1, 5, or 10 µg/mL of 10 nm PVP-coated AgNP. Note that hBMSC not exposed to OS (OS–) or AgNP proliferated over the entire 21-day period, whereas the proliferation of hBMSC exposed to OS (OS+) peaked around day 7 and then declined. Values represent (n = 3 replicate experiments). Statistical analysis of these data is displayed in Figure 7.5.

The behavior of undifferentiated and differentiating hBMSC is observed when considering the proliferation data as a time course (**Figure 7.4**). Long-term cell culture of hBMSC without osteogenic supplements (OS–) was supported over the 21-day study with

increasing proliferation observed at all timepoints under control conditions, which is as expected for a stem cell population. This increasing proliferation was also observed after single exposure to 1 $\mu\text{g}/\text{mL}$ AgNP. No change in proliferation was observed after single exposure to 10 $\mu\text{g}/\text{mL}$, single or repeated exposure to 5 $\mu\text{g}/\text{mL}$, or with repeated exposure to 1 $\mu\text{g}/\text{mL}$ AgNP. In contrast, hBMSC exposed to osteogenic supplements (OS+) under control conditions proliferated between day 1 and 7 after which the amount of dsDNA decreased at day 14 and 21. In general, differentiated cells do not proliferate; as such, the decrease in dsDNA mass was expected for a differentiated culture. Cell proliferation under all exposure conditions of 1 or 5 $\mu\text{g}/\text{mL}$ AgNP responded similarly as the control with high proliferation apparent at day 7. Proliferation under continuous exposure to 1 $\mu\text{g}/\text{mL}$ AgNP also shows some proliferation at day 7; however, no increase in proliferation is observed at single or repeated exposure at 10 $\mu\text{g}/\text{mL}$ or continuous exposure at 5 or 10 $\mu\text{g}/\text{mL}$.

At day 1, no statistically significant difference in dsDNA content was found between any AgNP concentration or exposure scenario (**Figure 7.5**). By day 7, evidence of a dose-related response was becoming evident, with proliferation in the 1 $\mu\text{g}/\text{mL}$ AgNP treatment group being significantly higher than that in the 10 $\mu\text{g}/\text{mL}$ group for both the OS+ supplemented and OS- cells. This dose-response was also observed at day 14 and 21 within each exposure scenario. Proliferation resulting from continuous exposure tended to be lower at all AgNP concentrations than the single or repeated exposure scenarios, although the differences between exposure scenarios using the same AgNP concentration were not statistically significant.

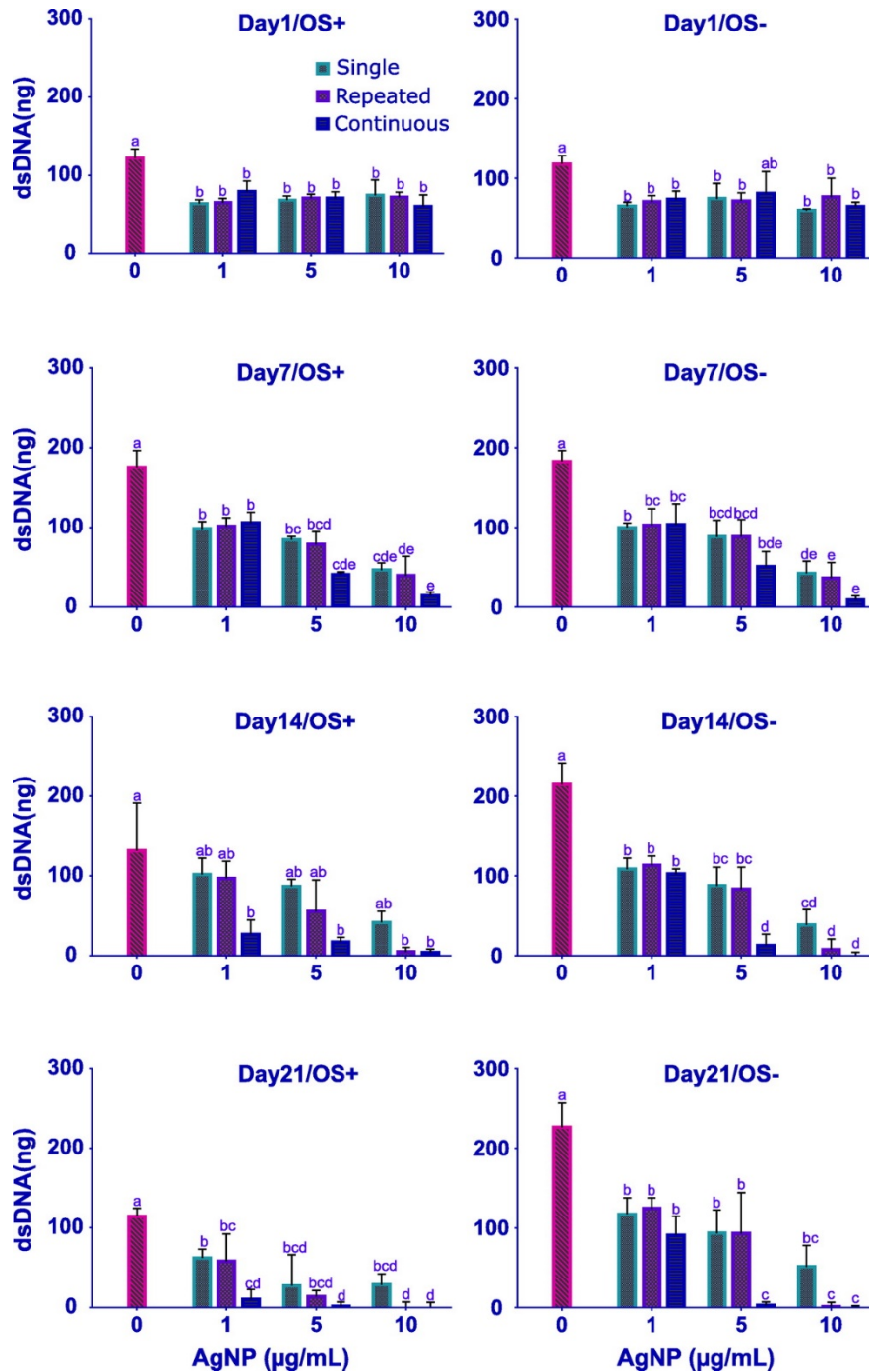


Figure 7.5 - Cell proliferation data from Figure 4 plotted separately for days 1, 7, 14, and 21 of culture to more clearly show statistical differences of exposure (single, repeated, continuous) scenarios and AgNP dose. Values represent (n = 3). Bars with no matching letters are statistically different ($p < 0.05$).

Assessment of early and late osteogenic differentiation markers ALP expression as an early marker of osteogenic differentiation and hydroxyapatite content as a late marker of differentiation are displayed in **Figure 7.6** and **Figure 7.7**, respectively. In both assays, the intensity of the signal should only be used to detect whether osteogenic differentiation was taking place at a certain timepoint. This is due to the coarse nature of the timepoints preventing precise measurement of when the signal is first observed. For example, ALP expression should increase until around day 14 and decrease afterward, but the exact time of the peak is unknown; comparison of one treatment group at the ALP expression peak and a second that had expressed it slightly earlier and has a smaller signal would yield false conclusions. Therefore, the ALP or hydroxyapatite signal for the OS+ supplemented cells were only compared with the corresponding OS- group for statistical analysis. ALP and hydroxyapatite signals were also near the baseline for all cells not exposed to osteogenic supplements, so the data were displayed as the difference between the two groups for clarity.

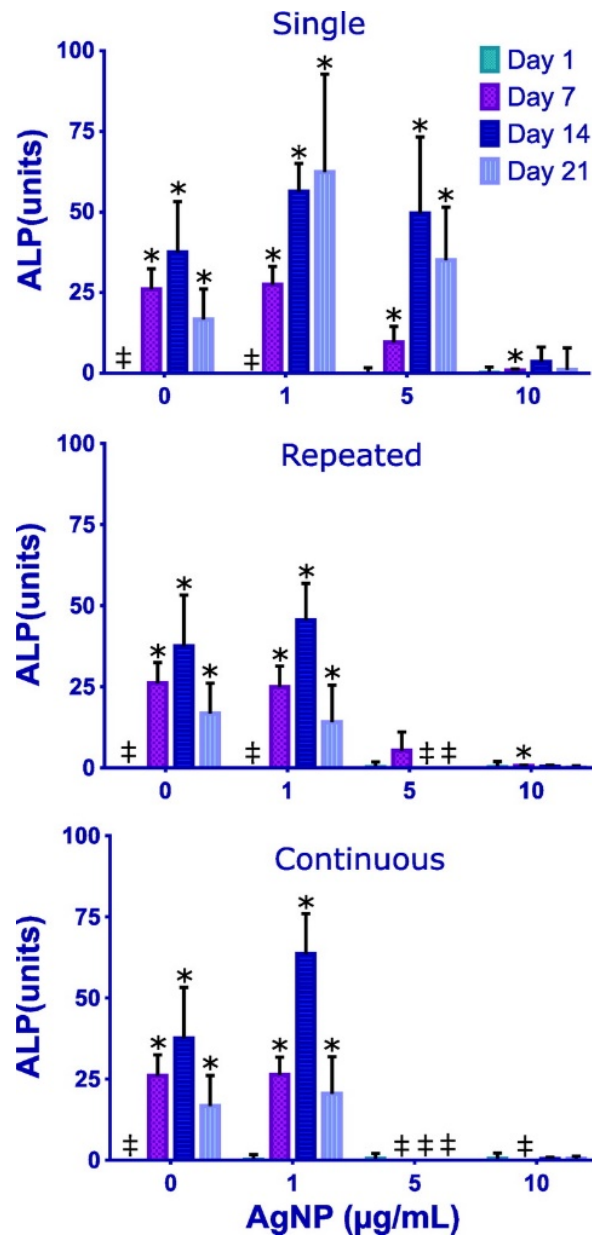


Figure 7.6 - Differences in ALP expression in hBMSC cultured in the presence (OS+) and absence of (OS-) of osteogenic supplements under single, repeated, or continuous exposure (Fig. 1) to 1, 5, or 10 µg/mL of 10 nm PVP-coated AgNP. Elevated ALP expression is an early marker of osteogenic differentiation. Values plotted were derived by subtracting the signal values from OS- cells from the signals from OS+ supplemented cells. Therefore, the values represent calculated as for n = 3 replicate experiments. Bars with asterisks denote a statistically significant ($p < 0.05$) increase in ALP expression of OS+ supplemented cells over the corresponding OS- cells. Absent bars marked with ‡ are the result of negative values due to subtracting the signal values from OS- cells from near-baseline signals from OS+ supplemented cells. ALP, alkaline phosphatase.

In hBMSC cultured in the presence of osteogenic supplements under control conditions, ALP expression reached a peak after 14 days in culture with detectable increases by day 7 (**Figure 7.6**). hBMSC exposed to 1 $\mu\text{g}/\text{mL}$ in all exposure scenarios or exposed to a single exposure to 5 $\mu\text{g}/\text{mL}$ had significantly increased ALP levels at day 7 and expressed detectable levels of hydroxyapatite at day 21 (**Figure 7.7**). Of these, all treatment groups except for single exposure to 5 $\mu\text{g}/\text{mL}$ AgNP and repeated exposure to 1 $\mu\text{g}/\text{mL}$ had detectable hydroxyapatite at day 14; the corresponding fluorescence images of mineralized substrates after 21 days in culture are displayed in **Figure 7.8**. Thus, detection of ALP at day 7 is highly predictive of eventual mineralization of the substrate.

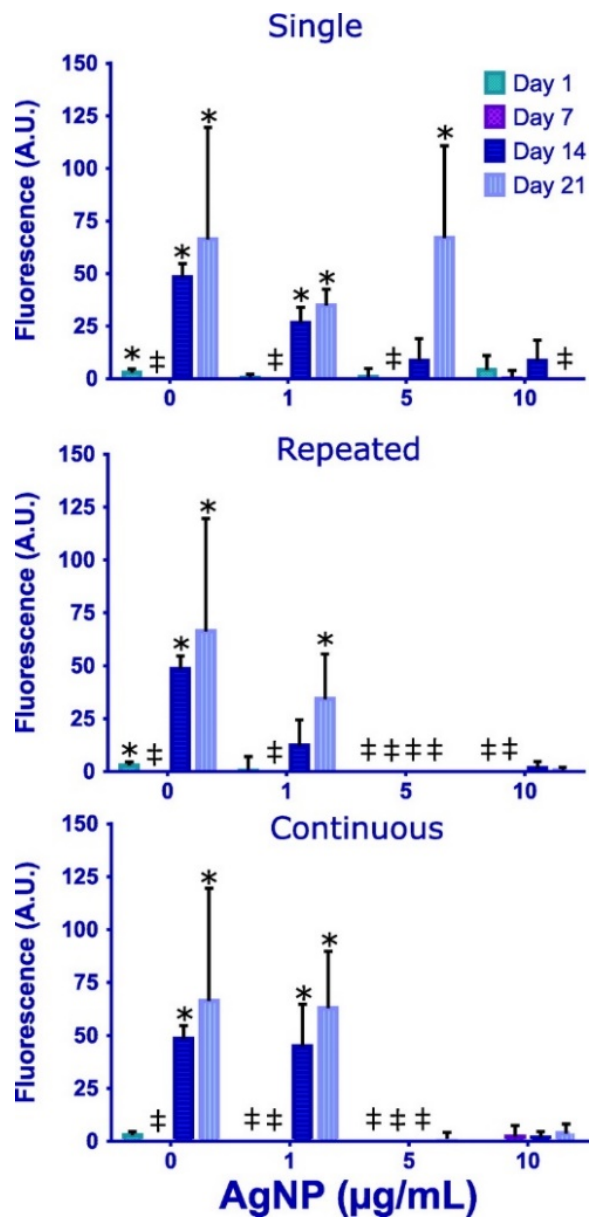


Figure 7.7 - Differences in hydroxyapatite content (OsteoImage Mineralization Assay) between TCPS with hBMSC cultured in the presence of osteogenic supplements (OS+) subtracted from TCPS with hBMSC cultured in the absence of osteogenic supplements (OS-) under single, repeated, or continuous exposure to 1, 5, or 10 µg/mL of 10 nm PVP-coated AgNP. Mineralization of the substrate is a late marker of osteogenic differentiation. Values plotted were derived by subtracting the signal values from OS- cells from the signals from OS+ supplemented cells. Therefore, the values plotted represent calculated as for n = 3 replicate experiments. Bars with asterisks denote a significant (p < 0.05) increase in mineralization of the substrate from OS+ supplemented cells over the corresponding OS- cells. Absent bars marked with ‡ are the result of negative values due to subtracting signal values from OS- cells from near-baseline signal values from OS+ supplemented cells. TCPS, tissue culture polystyrene surfaces.

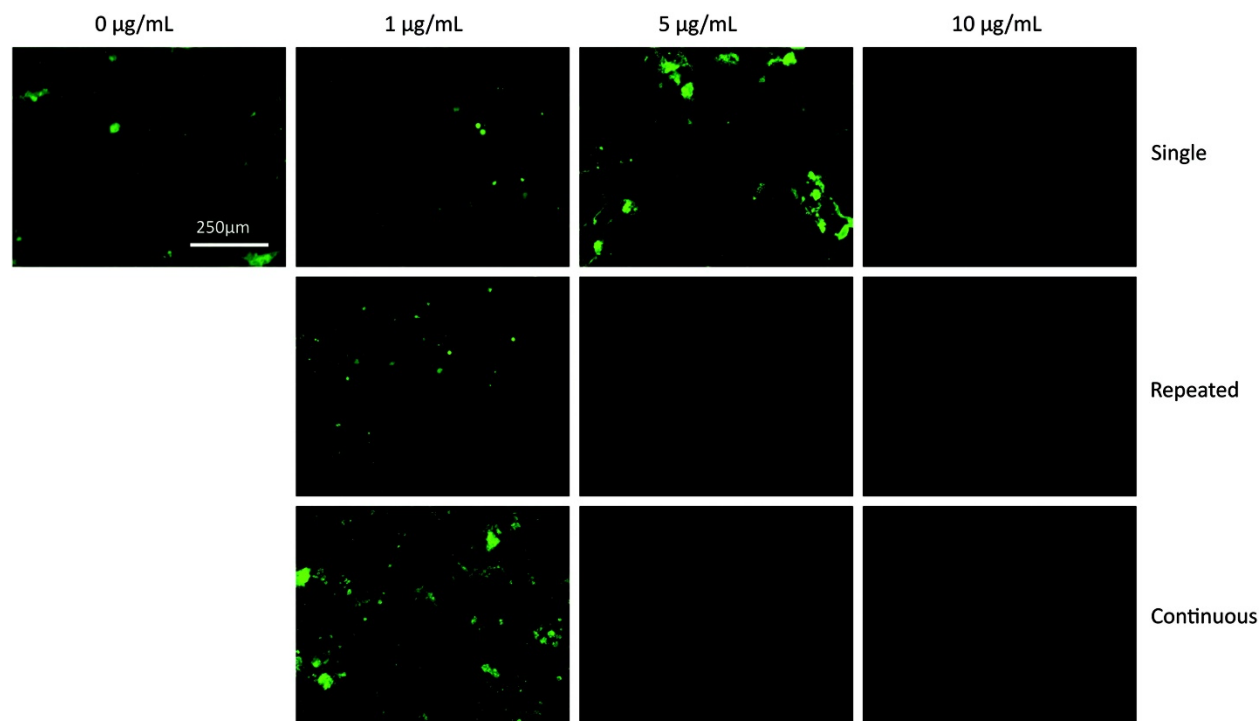


Figure 7.8 - Fluorescence microscopy images corresponding to the OsteoImage mineralization data summarized in Figure 7 for OS+ supplemented hBMSC cultured for 21 days and exposed to AgNP under single, repeated, or continuous exposure scenarios. No hydroxyapatite was detected with repeated or continuous exposure to 5 µg/mL AgNP or for any exposure to 10 µg/mL AgNP.

Discussion

The broad antimicrobial properties of AgNP make them attractive for use in medical device materials; however, these benefits must be balanced with the potential effects on surrounding tissue. In this study, physiologically relevant AgNP concentrations were first evaluated for their cytotoxicity after 24-hour exposure. Sussman et al. investigated ionic Ag⁺ and AgNP content in multiple commercially available medical devices by extracting the devices in multiple solvents, including citrated human plasma. The total silver concentration was ~300 µg/mL in water extract (using a 3 mL/cm² extraction ratio) or ~10 µg/mL in human plasma [31]. AgNP in these products were bound to the device surfaces; therefore, the 1–50 µg/mL range used in the 24-hour exposure in the present study would represent an appropriate

concentration range approximating AgNP eluted from medical device surfaces. No cytotoxicity was detected in hBMSC in either medium (OS+ and OS-) after 24 hours of exposure to 1 or 5 µg/mL AgNP. As for the 10 µg/mL concentration, traditional cytotoxicity testing as described in the ISO 10993 Part 5 standard [160] specifies that a 70% viability after 24 hours of exposure is considered as having “cytotoxic potential”; the average viability of hBMSC exposed to 10 µg/mL in either media was above this threshold and was therefore included in the 21-day study.

The mechanism of AgNP cytotoxicity is an active area of research with particle parameters such as diameter, surface charge, geometry, and ion dissolution playing a role [247, 248, 250]. Thus, one would expect different degrees of cytotoxicity responses when considering particles of different diameters and/or coatings. For example, Sengstock et al. reported no observable change in hBMSC viability in 50 nm PVP-coated AgNP over 24 hours of exposure to 10 µg/mL AgNP [251], whereas the current study demonstrated a decrease in the viability of hBMSC to the 70% viability threshold when 10 nm PVP-coated AgNP were used, which suggests that smaller diameter nanoparticles are more cytotoxic. Rosario et al. reported a viability reduction to 90% of control for MG-63 human osteosarcoma cells exposed to 10 µg/mL 10 nm PVP-coated AgNP exposure and reached the 70% viability threshold at 50 µg/mL [252]. The current study using primary stem cells exposed to 10 nm PVP-coated AgNP from the same supplier resulted in the 70% viability threshold at 10 µg/mL. Similarly, a 24-hour exposure of immortalized human skin keratinocyte cells [253] and MCF-7 breast cancer cells [254] to 10 µg/mL of uncoated 20 nm AgNP resulted in cell viabilities of 67% and 76%, respectively. Exposure of various cell types for 24 hours to 10 µg/mL of both PVP and uncoated AgNP was found to have no observed cytotoxic effect or meets the threshold as a potential cytotoxicant.

These results support the findings in the current study that identify 1 and 5 $\mu\text{g}/\text{mL}$ 10 nm PVP-coated AgNP concentrations as subcytotoxic and 10 $\mu\text{g}/\text{mL}$ as a concentration with borderline cytotoxic potential.

Prolonged or permanent exposure to a medical device implant requires further evaluation beyond 24-hour cytotoxicity testing and includes, but is not limited to, longer term animals tests for systemic toxicity, skin sensitization and irritation, and implantation. In this study, in vitro exposure of hBMSC to AgNP up to 21 days revealed significant differences in proliferation and markers of osteogenic differentiation. Castiglioni et al. reported dose-dependent cytotoxicity to 35 nm uncoated AgNP with a decrease in Saos-2 osteoblast-like cell viability to $\sim 90\%$ of control after a 5-day exposure to 1 and 5 $\mu\text{g}/\text{mL}$ and a similar decrease to $\sim 70\%$ for 10 $\mu\text{g}/\text{mL}$ exposures [255]. In addition, these AgNP were not found to affect the differentiation of hBMSC into osteoblasts after 15 days in culture as judged by Alizarin Red staining of calcium deposits. Nanoparticle size plays a significant role in many in vitro endpoints except for DNA damage; exposed particle surface area was identified as a major factor influencing biological responses [247] and could explain some of the discrepancies between these studies. Since 10 nm AgNP has 3.5 times the surface area of 35 nm AgNP per unit mass, the surface area of 5 $\mu\text{g}/\text{mL}$ concentration of 10 nm AgNP would therefore roughly corresponds to the surface area in 17.5 $\mu\text{g}/\text{mL}$ of 35 nm AgNP; this is within the range of 10–25 $\mu\text{g}/\text{mL}$ 35 nm AgNP used by Castiglioni et al. showing calcium deposition after 15 days. Continuous exposure to 5 $\mu\text{g}/\text{mL}$ AgNP in this study resulted in cytotoxicity at the 7-day timepoint, and no evidence of osteogenic differentiation was observed; thus, factors in addition to the surface area appear to play a role in predicting toxicity.

One possible explanation is that particle size affects uptake and intracellular localization that can have location-dependent toxic effects. Uptake studies in human fibroblasts revealed that 30 nm gold nanoparticles are retained within the cytoplasm while 5 nm gold nanoparticles were found within the nucleus [256]. Particle uptake studies in human mesenchymal stem cells exposed to 70 nm AgNP demonstrated perinuclear localization [257]. Studies have shown that both uncoated [258] and PVP-coated 10 nm AgNP [259] were also localized within lysosomes in multiple cell lines. Uptake of 10 nm PVP-coated AgNP in L929 fibroblasts exposed to 50 $\mu\text{g}/\text{mL}$ AgNP was found to be 5 $\mu\text{g}/\text{cell}$ after 24 hours of exposure [259]. Nanoscale ionic silver crystals were also found to form using TEM imaging and EDXS elemental analysis. Crystal formation was attributed to the dissolution of ionic silver from AgNP due to the acidic environment within lysosomes; silver ions could precipitate due to the presence of intracellular chloride and thiol-containing compounds.

Dissolution of silver ions from AgNP plays a major role in AgNP toxicity. Rosario et al. reported a greater cytotoxic response in MG-63 cells from AgNO₃ compared with the corresponding mass of AgNP for exposures up to 48 hours but noted that by 7 days of exposure to 5 $\mu\text{g}/\text{mL}$ 10 nm AgNP, MG-63 cells lost all proliferative capacity determined by the clonogenic assay while the corresponding 5 $\mu\text{g}/\text{mL}$ of Ag⁺ ions had significantly reduced proliferative capacity [252]. In the present study, it is possible that cytotoxicity observed in the continuous exposure scenario could have been due to a larger contribution from intracellular particles compared with the single or repeated exposures. This conjecture is supported by the proliferation of hBMSC in the single and repeated exposures at 1 $\mu\text{g}/\text{mL}$ being statistically different from the proliferation in the continuous exposure at day 14 for hBMSC cultured with

osteogenic supplements. The trend appears to continue for day 21, although the difference between 1 $\mu\text{g}/\text{mL}$ repeated and continuous exposures was not statistically significant.

Other studies support that the effect on AgNP on hBMSC proliferation could be partially attributed to early molecular initiating events, such as the dysregulation of genes related to cell metabolism or reactive oxygen species (ROS) defense, which lead to cytotoxicity. Genes related to osteogenesis were upregulated after 24-hour exposure to 20 $\mu\text{g}/\text{mL}$ of 20 nm AgNP to the MC3T3-E1 mouse osteoblast cell line [260]. Similarly, a decrease in proliferation in hBMSC and upregulation of markers related to endoplasmic reticulum and ROS stresses were found, but no changes to osteogenic differentiation markers were found in hBMSC [261]. Calcium deposition can be considered a definitive marker of successful osteogenic differentiation; hBMSC exposure to 10 and 25 $\mu\text{g}/\text{mL}$ 35 nm AgNP over 5 days in another study did not cause a change in calcium deposition [255]. In contrast, ALP and mineralization in the current study were significantly impaired for most of the investigated concentrations and exposure scenarios. These effects occurred concomitantly with a marked decrease in proliferation, which may represent a cytotoxic response rather than impairment of differentiation.

Although repeated and continuous exposures at 5 $\mu\text{g}/\text{mL}$ or higher prevented deposition of hydroxyapatite, this marker was not affected under the single exposure scenario and may hold promise as an antimicrobial in orthopedic surgeries. Prophylactic use of antibiotics in orthopedic surgeries includes a single preoperative dose and a possible re-dosing 24 or 48 hours after the operation [262, 263]. In a similar manner to prophylactic antibiotic use, Gao et al. demonstrated that the majority of silver from 70 nm AgNP on the surface of a PEEK implant were released within 24 hours, yielding a 5 $\mu\text{g}/\text{mL}$ extract; the cumulative silver release curve plateaued after 5 days [264]. A reduction in viability of MC3T3-E1 osteoblast precursor cells was observed, but

this difference versus the control was eliminated by day 5 due to dilution of the silver with repeated media changes. Implantation of this material into rats demonstrated antimicrobial activity and was observed to osseointegrate similar to the materials without AgNP after 2 weeks of implantation.

Conclusions

The present study examines the effect of different exposure scenarios on the proliferation and osteocyte function of differentiated hBMSC. Notably, a cytotoxic threshold of 10 $\mu\text{g/mL}$ PVP-coated 10 nm AgNP for hBMSC was determined, but this single 24-hour exposure caused a loss of osteocyte function in the 21-day culture. The viability of hBMSC exposed to 5 $\mu\text{g/mL}$ was not significantly different from controls in the 24-hour exposure, but this single 24-hour exposure caused a delay in the observation of ALP. This marker and subsequent mineralization were not observed after repeated 24-hour exposures at the 5 $\mu\text{g/mL}$ concentration. hBMSC exposed to the 1 $\mu\text{g/mL}$ AgNP concentration were observed to express ALP and deposit hydroxyapatite in all exposure scenarios, but continuous exposure caused significantly lower proliferation rates than the other two exposure scenarios at day 14. Differences in proliferation, ALP expression, and hydroxyapatite deposition were detected in the different exposure scenarios at AgNP concentrations identified as subcytotoxic in a 24-hour exposure assay.

The well-known ability of silver to prevent the growth of a broad spectrum of infectious organisms without the use of antibiotics makes it an attractive additive to medical device implants. However, AgNP exposure at sufficient concentrations and/or exposure durations does have an adverse effect on hBMSC osteogenic differentiation and subsequent function as osteocytes. AgNP-containing medical device materials must be carefully formulated and

evaluated to determine the benefit of infection control versus the risk of adverse effects on bone marrow [265].

Evaluating nanomaterials with biomedical applications presents challenges due to the vast number of nanoparticle physical and chemical parameters (e.g., size, shape, and coating) that influence biological and toxicological effects. For example, assumptions about the safety and performance of AgNP might not be supportable if there is a change in one or more of these parameters. Due to the vast number of nanomaterials with varying sizes, shapes, surface coatings and chemistries, and routes of exposure, in vitro human stem cell models that offer prolonged exposure scenarios compared with traditional in vitro models represent a potentially valuable component of integrated test strategies to evaluate nanomaterials.

Effects of Subcytotoxic Exposure of Silver Nanoparticles on Osteogenic Differentiation of Human Bone Marrow Stem Cells

Alexander K. Nguyen,^{1,2} Reema Patel,² Jade M. Noble,³ Jiwen Zheng,² Roger J. Narayan,¹ Girish Kumar,² and Peter L. Goering²

Abstract

Introduction: *In vitro* toxicology evaluations utilizing human stem cell models represent attractive alternatives to conventional animal models, which are not always predictive of human responses. Silver nanoparticles (AgNP) are a potent antimicrobial for use in orthopedic devices. However, AgNP exposure may alter the behavior of stem cells within the bone marrow. The aim of this study was to determine if differences in cell proliferation, early, and late osteogenic differentiation markers can be detected in osteogenically differentiating human bone marrow mesenchymal stem cells (hBMSC) over a 21-day period at AgNP concentrations that are not considered cytotoxic after 24-hour exposure per ISO 10993-5 cytotoxicity testing guidelines.

Materials and Methods: Polyvinylpyrrolidone (PVP)-coated 10 nm AgNP were evaluated for their short-term (24-hour) cytotoxicity to hBMSC using the MTT assay to determine subcytotoxic concentrations for the subsequent long-term study investigating osteogenic differentiation. hBMSC were exposed to 1, 5, or 10 $\mu\text{g}/\text{mL}$ AgNP in three different exposure scenarios: single (24-hour), repeated (24-hour at 1, 7, and 14 days), or continuous (21-day) exposure. Alkaline phosphatase (early osteogenic differentiation marker), hydroxyapatite deposition (late marker), and cell proliferation were measured at days 1, 7, 14, and 21.

Results: AgNP exposure reduced cell proliferation for all treatments. Neither differentiation marker expression was observed at any timepoint in hBMSC exposed to AgNP at 10 $\mu\text{g}/\text{mL}$ for any exposure scenario or in cells exposed to 5 $\mu\text{g}/\text{mL}$ in the repeated or continuous exposure scenarios.

Conclusions: Differences in proliferation and osteogenic marker expression were detected in the different exposure scenarios at AgNP concentrations identified as subcytotoxic in a 24-hour exposure assay.

Keywords: human bone marrow stem cell, hydroxyapatite, osteogenic differentiation, prolonged exposure, silver nanoparticle

Introduction

INFECTIONS ASSOCIATED with medical devices such as orthopedic implants are a common complication, which often necessitates explantation of the device. Recently published statistics for total knee arthroplasty performed between 1999 and 2015 revealed infection in 1.0%–1.5% of all orthopedic surgeries and was a close-second cause of revision surgeries.¹ *Staphylococcus* was found to be the leading organism in orthopedic surgeries at 29%.² This also

includes methicillin-resistant *Staphylococcus aureus*, which does not respond well to antibiotic treatment. Due to the increasing risk of antibiotic resistance, silver as an alternate mechanism for infection control would be advantageous. Incorporation of silver into medical devices is shown to reduce concentrations of various microbes, including *S. aureus*, and inhibit the formation of biofilms.^{3,4} Both ionic and particulate forms of silver are used in skin-contacting medical devices, such as wound dressings⁵ or dermal reconstruction matrices,⁶ and multiple external-communicating

¹University of North Carolina/North Carolina State University Joint Department of Biomedical Engineering, Raleigh, North Carolina.
²Office of Science and Engineering Laboratories, Center for Devices and Radiological Health, U.S. Food and Drug Administration, Silver Spring, Maryland.
³Office of Generic Drugs, Center for Drug Evaluation and Research, U.S. Food and Drug Administration, Silver Spring, Maryland.

devices, such as Foley catheters containing silver are commercially available.

Despite the beneficial antimicrobial properties, silver could have adverse effects on human cells if released in sufficient doses to the systemic circulation. For example, uncoated 35 nm silver nanoparticles (AgNP) were found to exceed the 5% hemolysis threshold in ASTM E2524-08 at 70 $\mu\text{g}/\text{mL}$.⁷ AgNP (12.5 nm diameter) were also found to significantly alter several hematologic parameters at a 30 $\mu\text{g}/\text{mL}$ threshold concentration in a blood loop model.⁸

Long-term silver exposure resulting from device implantation could raise the possibility of adverse local responses in the surrounding tissue. Stem cells in bone marrow play a role in a wide array of tissue regeneration tasks, such as the growth of new bone, fat, and blood cells. While impairment of any of these functions might negatively influence patient treatment outcomes, adverse effects on differentiation into the osteocyte lineage would slow or prevent osseointegration of the implant. This could lead to loosening, which is the leading cause of revision surgery.¹

AgNP characteristics such as size, coating type, and surface chemistry influence biological outcomes such as cytotoxicity, nanoparticle uptake, and intracellular localization,^{9,10} and the change of any one of these parameters can have drastic effects. For example, equimolar concentrations of 3, 10, 50, and 100 nm diameter AgNP had different effects on zebrafish mortality and a number of sublethal effects such as malformation of different parts.¹¹ Thus, the large number of possible combinations would be a challenge to test with conventional animal models. An alternative *in vitro* model using human stem cells and allowing for long-term exposure to the toxicant of interest would not only be more relevant to human biological and toxicological responses but also be more practical to evaluate a large number of potential toxicants.

Therefore, the objective of this study was to assess the effect of prolonged AgNP exposure on osteogenic differentiation of human bone marrow mesenchymal stem cells (hBMSC) at subcytotoxic AgNP concentrations. Additionally, different exposure scenarios up to 21 days were investigated to model various degrees of duration (e.g., acute, moderate, and prolonged) of implant tissue contact. Thus, the hypothesis that differences in cell proliferation, early, and late osteogenic differentiation markers can be detected in differentiating hBMSC over a 21-day period at AgNP concentrations that are not considered cytotoxic after 24-hour exposure per ISO 10993-5 cytotoxicity testing guidelines was tested. Findings from this *in vitro* model can help inform further understanding of how human stem cells respond to subcytotoxic AgNP concentrations for extended exposures with additional benefits of (1) reducing the necessity of some animal testing and (2) contributing to understanding risks and benefits of this material for medical device implant applications.

Materials and Methods

hBMSC (PCS-500-012; ATCC, Manassas, VA) were cultured in mesenchymal stem cell basal medium (PCS-500-030; ATCC) supplemented with the mesenchymal stem cell growth kit (PCS-500-041; ATCC) and incubated at 37°C, 5.0% CO₂, and 90% relative humidity. Osteogenic differenti-

ation was performed using the Osteocyte Differentiation Tool (PCS-500-052; ATCC) in place of the medium. The mesenchymal stem cell medium and Osteogenic Differentiation Tool are referred to as osteogenic supplement negative (OS⁻) and positive (OS⁺) respectively in this study. Other reagents included Trypsin-EDTA (9002-07-7; Sigma-Aldrich, St. Louis, MO), Dulbecco's phosphate-buffered saline (PBS; 14190-xxx; Thermo Scientific, Waltham, MA), Triton X-100 (Sigma-Aldrich), 37% formaldehyde (252549; Sigma-Aldrich), and ultrapure water from a NANOpure Diamond water purifier (APS Water Services Corp., Van Nuys, CA).

AgNP characterization

Polyvinylpyrrolidone (PVP)-coated, 10 nm diameter AgNP (BioPure; NanoComposix, San Diego, CA) were used in this study. AgNP stock solutions were received as a 1 mg/mL solution in water and were characterized using a JEM 2010F (JEOL, Tokyo, Japan) transmission electron microscope (TEM). AgNP were also diluted in cell culture medium immediately before application to the cryo-TEM grids and the cells per experimental design.

Dynamic light scattering analysis was performed with a Zetasizer Nano ZS (Malvern Panalytical, Malvern, United Kingdom). Hydrodynamic diameter measurements were performed on 20 $\mu\text{g}/\text{mL}$ AgNP in 0.02 μm filtered ultrapure water (MilliporeSigma, Burlington, MA). Zeta potential measurements were performed on 100 $\mu\text{g}/\text{mL}$ AgNP in 10 mM NaCl inside a DTS1070-folded capillary cell (Malvern Panalytical).

Cryo-TEM was performed on a JEOL 1400 (JEOL USA, Inc., Acworth, GA) operated at 80 kV and equipped with an Orius SC1000 CCD camera (Gatan, Pleasanton, CA). Aliquots (5 μL) of 100 $\mu\text{g}/\text{mL}$ AgNP in ultrapure water, OS⁻ media, or OS⁺ media were pipetted onto glow discharged copper Quantifoil (Electron Microscopy Sciences, Hatfield, PA) grids and plunge-frozen using a Leica EM GP automatic plunge freezer (Leica Microsystems, Wetzlar, Germany). Images were binned by 1, resulting in pixel sizes of 0.4 nm.

Cell culture

For each experiment replicate, 1×10^6 hBMSC stored in liquid nitrogen at passage 4 were thawed and seeded into a T-150 flask and incubated overnight. A media change was performed the following day to remove the dimethylsulfoxide cryopreservative and dead/unattached cells and then allowed to divide for ~ 1 week to reach 80% confluence. Cells were trypsinized, centrifuged at 200 g for 5 minutes, and resuspended in media. The hBMSC suspension cell density was measured with a hemocytometer and diluted to 5.0×10^4 cells/mL for seeding. Cells used in both the 24-hour exposure and 21-day culture procedures were therefore used at passage 5; passage 6 is the highest passage recommended by ATCC for osteogenic differentiation with the Osteocyte Differentiation Tool.

Viability of hBMSC after a single 24-hour exposure to AgNP

Cytotoxicity of AgNP in a single 24-hour exposure was measured via the MTT assay (CellTiter 96 Non-radioactive Cell Proliferation Assay, G4000; Promega, Madison, WI)

and read with an OptiMax plate reader (Molecular Devices, Sunnyvale, CA). Three wells per treatment in a 96-well plate were seeded with 1.0×10^4 cells per well in 200 μ L medium and allowed to attach over 24 hours. Cells were then exposed to 1, 5, 10, 25, or 50 μ g/mL AgNP for 24 hours in either OS- or OS+ media. Medium alone and medium with 3 mM AgNO₃ were used as negative and positive controls, respectively. Cell-free wells of the corresponding solution were used as the background. An aliquot of 15 μ L MTT dye was added to each well and allowed to metabolize for 3 hours. The kit surfactant solution was used to stop the reaction and dissolve the colored metabolite. The plates were read after 30 minutes of incubation and 30 minutes on a shake plate. For each well, absorbance at 650 nm was subtracted from the absorbance at 570 nm. Viability is calculated as a percent of the negative control and reported as the means and standard deviations (SD) of three independent replicate experiments.

Long-term hBMSC culture using three dosing/exposure scenarios

Three long-term subcytotoxic exposure scenario studies involved monitoring hBMSC with a combination of the following treatment conditions: (1) exposure to one of the three AgNP dosing/exposure scenarios, (2) exposure to one of the three different AgNP concentrations, and (3) culture in media with or without osteogenic supplements. The exposure scenarios are summarized in Figure 1: a single 24-hour exposure (single), three 24-hour exposures performed on days 1, 7, and 14 (repeated), and continuous exposure to AgNP for 21 days with AgNP refreshed 3 \times per week (continuous). AgNP concentrations of 1, 5, or 10 μ g/mL in media with (OS+) or without (OS-) osteogenic supplements were prepared immediately before exposure to the cells.

For each of four sampling timepoints (1, 7, 14, and 21 days), six 96-well plates were used corresponding to one of the three exposure conditions, and the use of media with or without osteogenic supplements. On each plate, two wells per AgNP concentration (1, 5, or 10 μ g/mL) for each of the planned assays were seeded with 1.0×10^4 cells per well in 200 μ L medium and incubated for 24 hours before starting the prescribed exposure scenario; hBMSC at the day 1 AgNP exposure was \sim 50% confluent. hBMSC grown with or without osteogenic supplements and in the absence of AgNP

were used as the negative controls. Data from the negative controls are shared between all exposure scenarios but are included on all subcharts in Figures 4–7 for ease of comparison. Media were changed three times a week for the 21-day culture period with either media or media with AgNP applied to the cells according to the relevant exposure scenario (Fig. 1). If a well in the single or repeated exposure scenarios received media with AgNP, the particles were removed 24 hours later and replaced with the corresponding media.

For each timepoint, plates were processed for the different assays: Quant-iT PicoGreen, Alkaline Phosphatase (ALP) Liquicolor, and OsteoImage Mineralization assays. ALP was measured immediately at each timepoint, but PicoGreen and OsteoImage assays were performed in bulk after all plates had been harvested. In preparation for storage, media were aspirated from all wells; OsteoImage wells were fixed with 3.7% formaldehyde in PBS for 30 minutes, rinsed 2 \times with PBS, and then, the PBS aspirated before storage at -80°C .

PicoGreen assay. Cells designated for the PicoGreen assay (Quant-iT PicoGreen dsDNA assay kit, P7589; Thermo Scientific) were previously frozen at -80°C at each timepoint so were thawed to room temperature before digestion with a papain suspension (lot 32J13550, LS003127; Worthington, Lakewood, NJ). Papain was dissolved at a 0.21 U/mL concentration in 1.75 mg/mL L-cysteine in PBS, and 200 μ L of this solution was added to each well. The entire plate was sealed with aluminum sealing tape and heated at 60°C for 18 hours. After digestion, the plates were cooled to room temperature over 1 hour. From each well, three aliquots of 50 μ L were transferred to three wells on a separate 96-well plate for measurement in triplicate. A double-stranded DNA concentration series (0, 40, 100, 200, 400, 600, 1000, 1400, 1600, and 2000 ng/mL) was prepared by diluting the kit dsDNA stock solution in Tris-EDTA buffer. For each dsDNA ladder concentration, 50 μ L was added to two wells for measurement in duplicate. PicoGreen dye in Tris-EDTA buffer was mixed according to the manufacturer's specifications, and 50 μ L was added to all wells and the samples stained for 5–10 minutes. The plate was read in a fluorescent plate reader using 485 nm excitation and 538 nm emission wavelengths. For each set of three measurement wells corresponding to a single well on the initial plate, the average fluorescence intensity was fit to the DNA standard curve and multiplied by the 200- μ L volume used in the papain digestion to calculate the DNA mass within the well.

ALP assay. ALP was measured using the Alkaline Phosphatase Liquicolor kit (2900-430; Stanbio, Boerne, TX) using SER-T-FY 1 Level 1 Control Serum (lot 151631, G427-86; Stanbio) for controls. Kinetic measurements for this assay were performed on a SpectraMax 190 plate reader (Molecular Devices). Media from ALP assay wells were aspirated and replaced with 100 μ L 0.2% Triton X-100 in PBS for 20 minutes. A new 96-well plate was prepared where three wells each were allocated for negative and positive controls: 0.2% Triton X-100, 5 μ L serum, 15 μ L serum, and 35 μ L serum. These control wells were diluted to 75 μ L total volume with additional 0.2% Triton X-100. The permeabilized cells were diluted with an additional 100 μ L of 0.2% Triton X-100 and mixed thoroughly. Two 75 μ L aliquots from each of

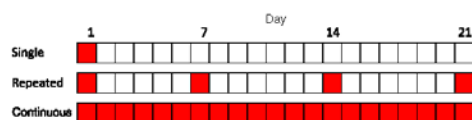


FIG. 1. Schedule of AgNP dosing of hBMSC cultures for three separate exposure scenarios: single 24-hour exposure, repeated weekly 24-hour exposures, or continuous exposure. Each square represents a 24-hour period with red squares indicating periods of AgNP exposure. Cell proliferation, alkaline phosphatase expression, and hydroxyapatite content were measured on days 1, 7, 14, and 21 for all exposure scenarios. Fluorescence imaging of hydroxyapatite was performed on day 21 only. hBMSC, human bone marrow mesenchymal stem cells. Color images are available online.

these solutions were added to two wells on the new plate for measurement in duplicate. A 75 μ L aliquot of the kit working reagent was added to each well; the plate was then immediately placed into a fluorescent plate reader for kinetic measurements. Absorbance at 405 nm was read once per minute over 5 hours. The rate of generation of the colored compound is initially linear and proportional to the ALP content. For each well, the linear region of the curve was determined between the start of data collection and the timepoint when the R^2 value of the linear regression was greater than 0.98. The slope of the linear region was compared with the slope of the serum control wells to calculate the ALP concentration.

OsteoImage fluorescent microscopy/mineralization quantification assay. Mineralization quantification was performed with the OsteoImage Mineralization Assay (PA-1503; Lonza, Walkersville, MD) that specifically stains hydroxyapatite; fluorescence quantification using a plate reader and fluorescence microscopy was performed in the same well. The hBMSC were previously fixed in 3.7% formaldehyde and stored frozen at -80°C . OsteoImage dye was diluted 1:100 in the supplied wash buffer per the manufacturer's instructions; 100 μ L was added to each well, the samples stained for 30 minutes, and then washed $3\times$ with the wash buffer. The hydroxyapatite fluorescence signal was read at 492 nm excitation and 520 nm emission wavelengths. Fluorescent images of the wells after 21 days in culture were obtained using an Eclipse TE2000-U fluorescence microscope (Nikon, Tokyo, Japan).

Statistical analysis

Statistical analysis and graphing were performed using GraphPad Prism 6 (San Diego, CA). Cytotoxicity after 24-hour AgNP exposure was analyzed by multiple Student's t -tests comparing each treatment with the negative control. Proliferation during the 21-day study measured by the PicoGreen DNA assay was analyzed using two-way analysis of var-

iance between AgNP concentrations and exposure scenarios within each timepoint; statistical significance was determined using the Tukey *post hoc* analysis ($p < 0.05$). Detection of ALP and mineralization, early and late markers of osteogenic differentiation, respectively, was analyzed by comparing OS+ supplemented cells with the corresponding OS- treatment for each timepoint using a one-tailed Student's t -test. Since both ALP expression and hydroxyapatite deposition were near baseline levels for all OS- cells, data were summarized as the difference between the OS+ and OS- supplemented groups for clarity. Thus, the resulting means and SDs were calculated using $\bar{X}_{\text{OS}+} - \bar{X}_{\text{OS}-} \pm \sqrt{\text{SD}_{\text{OS}+}^2 + \text{SD}_{\text{OS}-}^2}$.

Results

AgNP characterization

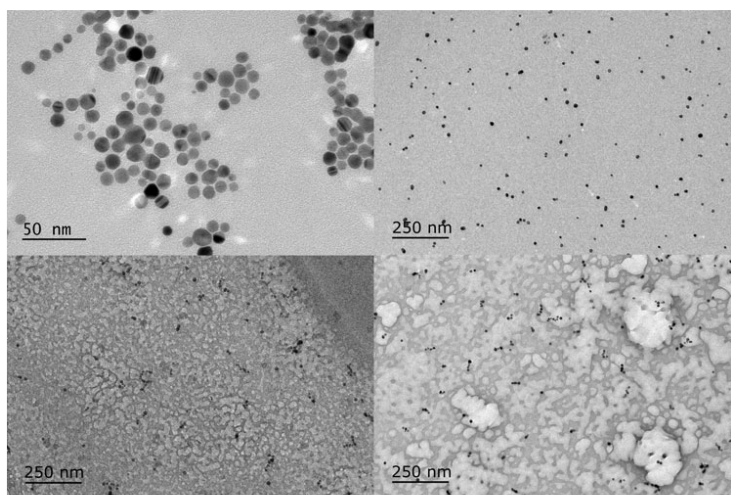
Particles ($n=140$) in one TEM image (Fig. 2) were analyzed using the ImageJ (NIH, Bethesda, MD). Particle diameter averaged 9.95 nm with a SD of 2.22 nm. The morphology was approximately circular with average major and minor elliptical axes of 10.52 and 9.44 nm, respectively. AgNP Z-average hydrodynamic diameter was measured to be 18.33 nm, with a SD of 0.73 nm over six measurements. Zeta potential was measured to be -15.6 mV , with a SD of 0.95 mV over four measurements.

Cryo-TEM (Fig. 2) was performed on AgNP in both OS- and OS+ media to image the state of AgNP that the hBMSC were exposed to. AgNP dispersed in water was found to be monodisperse. In both media types, AgNP appeared as single particles or as small agglomerates of less than 10 particles.

Dose-finding for cytotoxicity of AgNP after a single 24-hour exposure

An AgNP concentration-dependent decrease in hBMSC viability was observed using the MTT assay (Fig. 3). Based on the international standard ISO 10993-5,¹² a chemical is noted to have cytotoxic potential if the viability falls

FIG. 2. Representative TEM image (top left) of 10 nm PVP-coated AgNP. AgNP core diameter was determined to be 9.95 nm with a 2.22 nm SD by image analysis of $n=140$ particles. Cryo-TEM images of AgNP diluted in water (top right), OS- media (bottom left), and OS+ media (bottom right). AgNP, silver nanoparticles; SD, standard deviation; TEM, transmission electron microscope.



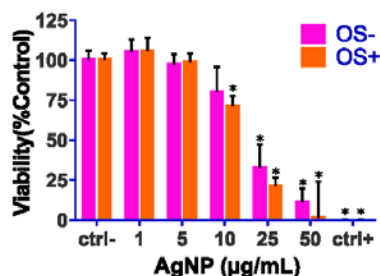


FIG. 3. Viability of hBMSC (MTT assay) cultured for 24 hours in the absence (OS-) or presence (OS+) of osteogenic supplements. Cells were exposed to various concentrations of 10 nm PVP-coated AgNP. Cells grown in media alone or media with 3 mmol/L AgNO₃ were used as the negative (ctrl-) and positive (ctrl+) controls, respectively. Values represent $\bar{x} \pm SD$ ($n=3$ replicate experiments). Bars with asterisks are significantly different from the negative control ($p < 0.05$). SD, standard deviation. Color images are available online.

below 70%. The viability of hBMSC exposed to 1 or 5 μg/mL AgNP for 24 hours was not statistically different from the negative control. hBMSC exposed to 10 μg/mL AgNP exhibited viabilities of 80% and 71% of control when cultured in the absence and presence of osteogenic supplements, respectively. Concentrations of 25 and 50 μg/mL resulted in statistically significant decreases in viability, and the values were below the 70% cytotoxicity threshold. Therefore, concentrations of 1 and 5 μg/mL were included

in the 21-day study as concentrations with no detected 24 hours of cytotoxicity, and 10 μg/mL AgNP included as the concentration that meets the criteria for nonsignificant cytotoxic potential according to the ISO 10993-5 standard.

Cell proliferation

Proliferation was assessed with the PicoGreen assay in which dsDNA concentrations can be quantitatively measured. The dsDNA concentration is proportional to the number of live cells remaining in the culture; dead cells detach from the plate and are removed with regular media changes. For easier data visualization, proliferation data were organized in two graphs; as a time course (Fig. 4) and individually by timepoint to more clearly show the dose-response and statistically significant differences (Fig. 5).

The behavior of undifferentiated and differentiating hBMSC is observed when considering the proliferation data as a time course (Fig. 4). Long-term cell culture of hBMSC without osteogenic supplements (OS-) was supported over the 21-day study with increasing proliferation observed at all timepoints under control conditions, which is as expected for a stem cell population. This increasing proliferation was also observed after single exposure to 1 μg/mL AgNP. No change in proliferation was observed after single exposure to 10 μg/mL, single or repeated exposure to 5 μg/mL, or with repeated exposure to 1 μg/mL AgNP. In contrast, hBMSC exposed to osteogenic supplements (OS+) under control conditions proliferated between day 1 and 7 after which the amount of dsDNA decreased at day 14 and 21. In general, differentiated cells do not proliferate; as such, the decrease in dsDNA mass was expected for a differentiated culture. Cell proliferation under all exposure conditions of 1 or

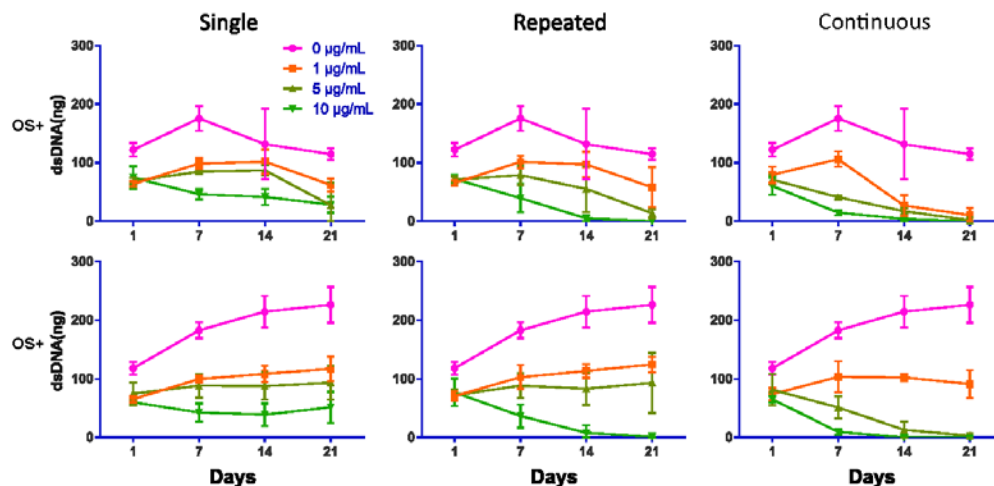


FIG. 4. Time-course responses for the proliferation of hBMSC (PicoGreen dsDNA assay) cultured in the absence (OS-) or presence (OS+) of osteogenic supplements under single, repeated, or continuous exposure (Fig. 1) to 1, 5, or 10 μg/mL of 10 nm PVP-coated AgNP. Note that hBMSC not exposed to OS (OS-) or AgNP proliferated over the entire 21-day period, whereas the proliferation of hBMSC exposed to OS (OS+) peaked around day 7 and then declined. Values represent $\bar{x} \pm SD$ ($n=3$ replicate experiments). Statistical analysis of these data is displayed in Figure 5. Color images are available online.

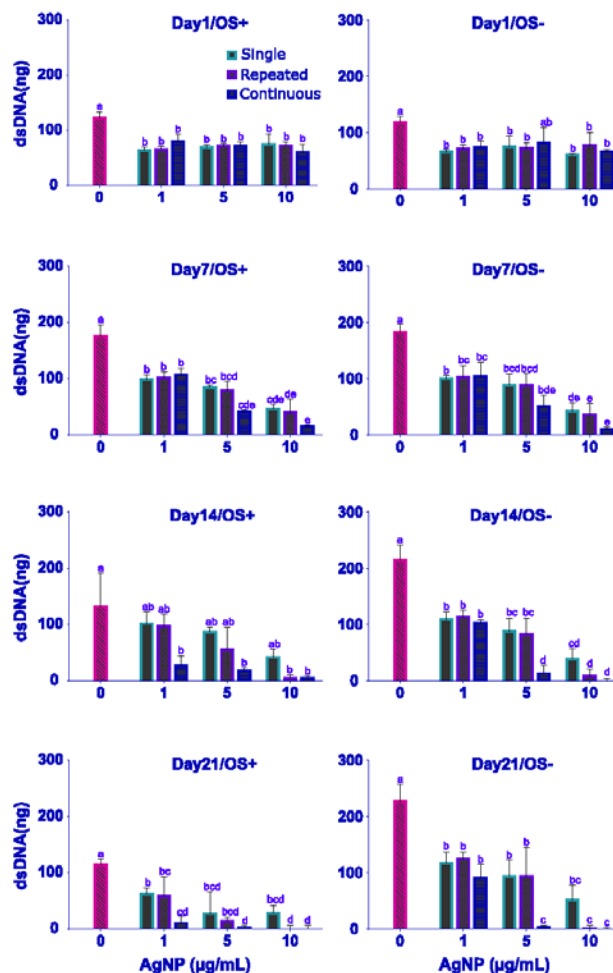


FIG. 5. Cell proliferation data from Figure 4 plotted separately for days 1, 7, 14, and 21 of culture to more clearly show statistical differences of exposure (single, repeated, continuous) scenarios and AgNP dose. Values represent $\bar{x} \pm SD$ ($n=3$). Bars with no matching letters are statistically different ($p < 0.05$). Color images are available online.

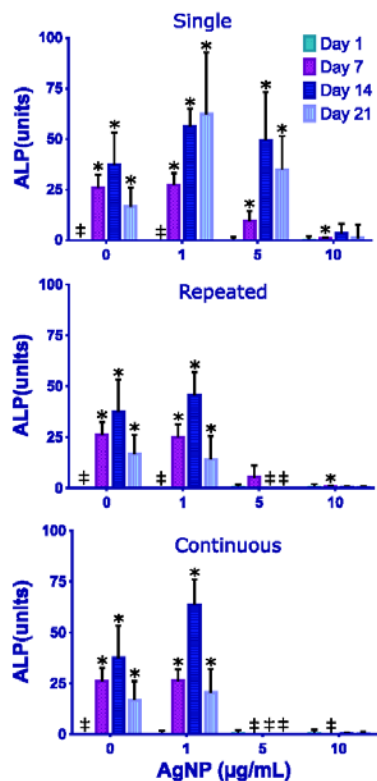
5 µg/mL AgNP responded similarly as the control with high proliferation apparent at day 7. Proliferation under continuous exposure to 1 µg/mL AgNP also shows some proliferation at day 7; however, no increase in proliferation is observed at single or repeated exposure at 10 µg/mL or continuous exposure at 5 or 10 µg/mL.

At day 1, no statistically significant difference in dsDNA content was found between any AgNP concentration or exposure scenario (Fig. 5). By day 7, evidence of a dose-related response was becoming evident, with proliferation in the 1 µg/mL AgNP treatment group being significantly higher than that in the 10 µg/mL group for both the OS+ supplemented and OS- cells. This dose-response was also observed at day 14 and 21 within each exposure scenario. Proliferation resulting from continuous exposure tended to

be lower at all AgNP concentrations than the single or repeated exposure scenarios, although the differences between exposure scenarios using the same AgNP concentration were not statistically significant.

Assessment of early and late osteogenic differentiation markers

ALP expression as an early marker of osteogenic differentiation and hydroxyapatite content as a late marker of differentiation are displayed in Figures 6 and 7, respectively. In both assays, the intensity of the signal should only be used to detect whether osteogenic differentiation was taking place at a certain timepoint. This is due to the coarse nature of the timepoints preventing precise measurement of when



Downloaded by FDA FOOD AND DRUG ADMINISTRATION MULTISITE from www.liebertpub.com at 09/25/19. For personal use only.

FIG. 6. Differences in ALP expression in hBMSC cultured in the presence (OS+) and absence (OS-) of osteogenic supplements under single, repeated, or continuous exposure (Fig. 1) to 1, 5, or 10 µg/mL of 10 nm PVP-coated AgNP. Elevated ALP expression is an early marker of osteogenic differentiation. Values plotted were derived by subtracting the signal values from OS- cells from the signals from OS+ supplemented cells. Therefore, the values represent $\bar{x} \pm SD$ calculated as $\bar{X}_{OS+} - \bar{X}_{OS-} \pm \sqrt{SD_{OS+}^2 + SD_{OS-}^2}$ for $n=3$ replicate experiments. Bars with asterisks denote a statistically significant ($p < 0.05$) increase in ALP expression of OS+ supplemented cells over the corresponding OS- cells. Absent bars marked with ‡ are the result of negative values due to subtracting the signal values from OS- cells from near-baseline signals from OS+ supplemented cells. ALP, alkaline phosphatase. Color images are available online.

the signal is first observed. For example, ALP expression should increase until around day 14 and decrease afterward, but the exact time of the peak is unknown; comparison of one treatment group at the ALP expression peak and a second that had expressed it slightly earlier and has a smaller signal would yield false conclusions. Therefore, the ALP or hydroxyapatite signal for the OS+ supplemented cells were only compared with the corresponding OS- group for statistical analysis. ALP and hydroxyapatite signals were also near the baseline for all cells not exposed to osteogenic supple-

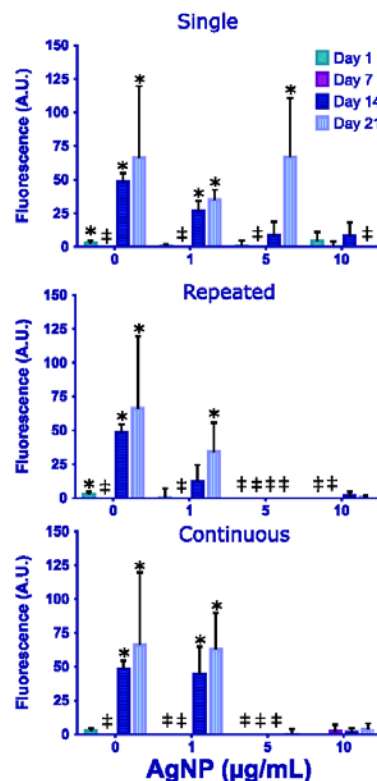


FIG. 7. Differences in hydroxyapatite content (OsteoImage Mineralization Assay) between TCPS with hBMSC cultured in the presence of osteogenic supplements (OS+) subtracted from TCPS with hBMSC cultured in the absence of osteogenic supplements (OS-) under single, repeated, or continuous exposure to 1, 5, or 10 µg/mL of 10 nm PVP-coated AgNP. Mineralization of the substrate is a late marker of osteogenic differentiation. Values plotted were derived by subtracting the signal values from OS- cells from the signals from OS+ supplemented cells. Therefore, the values plotted represent $\bar{x} \pm SD$ calculated as $\bar{X}_{OS+} - \bar{X}_{OS-} \pm \sqrt{SD_{OS+}^2 + SD_{OS-}^2}$ for $n=3$ replicate experiments. Bars with asterisks denote a significant ($p < 0.05$) increase in mineralization of the substrate from OS+ supplemented cells over the corresponding OS- cells. Absent bars marked with ‡ are the result of negative values due to subtracting signal values from OS- cells from near-baseline signal values from OS+ supplemented cells. TCPS, tissue culture polystyrene surfaces. Color images are available online.

ments, so the data were displayed as the difference between the two groups for clarity.

In hBMSC cultured in the presence of osteogenic supplements under control conditions, ALP expression reached a peak after 14 days in culture with detectable increases by day 7 (Fig. 6). hBMSC exposed to 1 µg/mL in all exposure scenarios or exposed to a single exposure to 5 µg/mL had

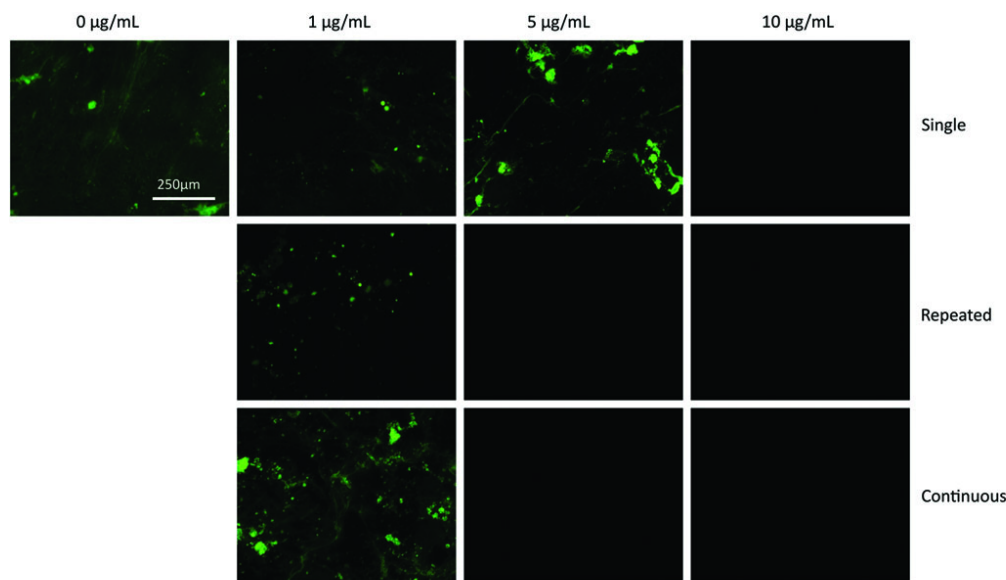


FIG. 8. Fluorescence microscopy images corresponding to the OsteoImage mineralization data summarized in Figure 7 for OS+ supplemented hBMSC cultured for 21 days and exposed to AgNP under single, repeated, or continuous exposure scenarios. No hydroxyapatite was detected with repeated or continuous exposure to 5 µg/mL AgNP or for any exposure to 10 µg/mL AgNP. Color images are available online.

significantly increased ALP levels at day 7 and expressed detectable levels of hydroxyapatite at day 21 (Fig. 7). Of these, all treatment groups except for single exposure to 5 µg/mL AgNP and repeated exposure to 1 µg/mL had detectable hydroxyapatite at day 14; the corresponding fluorescence images of mineralized substrates after 21 days in culture are displayed in Figure 8. Thus, detection of ALP at day 7 is highly predictive of eventual mineralization of the substrate.

Discussion

The broad antimicrobial properties of AgNP make them attractive for use in medical device materials; however, these benefits must be balanced with the potential effects on surrounding tissue. In this study, physiologically relevant AgNP concentrations were first evaluated for their cytotoxicity after 24-hour exposure. Sussman et al. investigated ionic Ag⁺ and AgNP content in multiple commercially available medical devices by extracting the devices in multiple solvents, including citrated human plasma. The total silver concentration was ~300 µg/mL in water extract (using a 3 mL/cm² extraction ratio) or ~10 µg/mL in human plasma.¹³ AgNP in these products were bound to the device surfaces; therefore, the 1–50 µg/mL range used in the 24-hour exposure in the present study would represent an appropriate concentration range approximating AgNP eluted from medical device surfaces. No cytotoxicity was detected in hBMSC in either medium (OS+ and OS–) after 24 hours of exposure to 1 or 5 µg/mL AgNP. As for the 10 µg/mL concentration,

traditional cytotoxicity testing as described in the ISO 10993 Part 5 standard¹² specifies that a 70% viability after 24 hours of exposure is considered as having “cytotoxic potential”; the average viability of hBMSC exposed to 10 µg/mL in either media was above this threshold and was therefore included in the 21-day study.

The mechanism of AgNP cytotoxicity is an active area of research with particle parameters such as diameter, surface charge, geometry, and ion dissolution playing a role.^{9,10,14} Thus, one would expect different degrees of cytotoxicity responses when considering particles of different diameters and/or coatings. For example, Sengstock et al. reported no observable change in hBMSC viability in 50 nm PVP-coated AgNP over 24 hours of exposure to 10 µg/mL AgNP,¹⁵ whereas the current study demonstrated a decrease in the viability of hBMSC to the 70% viability threshold when 10 nm PVP-coated AgNP were used, which suggests that smaller diameter nanoparticles are more cytotoxic. Rosario et al. reported a viability reduction to 90% of control for MG-63 human osteosarcoma cells exposed to 10 µg/mL 10 nm PVP-coated AgNP exposure and reached the 70% viability threshold at 50 µg/mL.¹⁶ The current study using primary stem cells exposed to 10 nm PVP-coated AgNP from the same supplier resulted in the 70% viability threshold at 10 µg/mL. Similarly, a 24-hour exposure of immortalized human skin keratinocyte cells¹⁷ and MCF-7 breast cancer cells¹⁸ to 10 µg/mL of uncoated 20 nm AgNP resulted in cell viabilities of 67% and 76%, respectively. Exposure of various cell types for 24 hours to 10 µg/mL of both PVP

and uncoated AgNP was found to have no observed cytotoxic effect or meets the threshold as a potential cytotoxicant. These results support the findings in the current study that identify 1 and 5 $\mu\text{g}/\text{mL}$ 10 nm PVP-coated AgNP concentrations as subcytotoxic and 10 $\mu\text{g}/\text{mL}$ as a concentration with borderline cytotoxic potential.

Prolonged or permanent exposure to a medical device implant requires further evaluation beyond 24-hour cytotoxicity testing and includes, but is not limited to, longer term animal tests for systemic toxicity, skin sensitization and irritation, and implantation. In this study, *in vitro* exposure of hBMSC to AgNP up to 21 days revealed significant differences in proliferation and markers of osteogenic differentiation. Castiglioni et al. reported dose-dependent cytotoxicity to 35 nm uncoated AgNP with a decrease in Saos-2 osteoblast-like cell viability to $\sim 90\%$ of control after a 5-day exposure to 1 and 5 $\mu\text{g}/\text{mL}$, and a similar decrease to $\sim 70\%$ for 10 $\mu\text{g}/\text{mL}$ exposures.¹⁹ In addition, these AgNP were not found to affect the differentiation of hBMSC into osteoblasts after 15 days in culture as judged by Alizarin Red staining of calcium deposits. Nanoparticle size plays a significant role in many *in vitro* endpoints except for DNA damage; exposed particle surface area was identified as a major factor influencing biological responses⁹ and could explain some of the discrepancies between these studies. Since 10 nm AgNP has 3.5 times the surface area of 35 nm AgNP per unit mass, the surface area of 5 $\mu\text{g}/\text{mL}$ concentration of 10 nm AgNP would therefore roughly correspond to the surface area in 17.5 $\mu\text{g}/\text{mL}$ of 35 nm AgNP; this is within the range of 10–25 $\mu\text{g}/\text{mL}$ 35 nm AgNP used by Castiglioni et al. showing calcium deposition after 15 days. Continuous exposure to 5 $\mu\text{g}/\text{mL}$ AgNP in this study resulted in cytotoxicity at the 7-day timepoint, and no evidence of osteogenic differentiation was observed; thus, factors in addition to the surface area appear to play a role in predicting toxicity.

One possible explanation is that particle size affects uptake and intracellular localization that can have location-dependent toxic effects. Uptake studies in human fibroblasts revealed that 30 nm gold nanoparticles are retained within the cytoplasm while 5 nm gold nanoparticles were found within the nucleus.²⁰ Particle uptake studies in human mesenchymal stem cells exposed to 70 nm AgNP demonstrated perinuclear localization.²¹ Studies have shown that both uncoated²² and PVP-coated 10 nm AgNP²³ were also localized within lysosomes in multiple cell lines. Uptake of 10 nm PVP-coated AgNP in L929 fibroblasts exposed to 50 $\mu\text{g}/\text{mL}$ AgNP was found to be 5 $\mu\text{g}/\text{cell}$ after 24 hours of exposure.²³ Nanoscale ionic silver crystals were also found to form using TEM imaging and EDXS elemental analysis. Crystal formation was attributed to the dissolution of ionic silver from AgNP due to the acidic environment within lysosomes; silver ions could precipitate due to the presence of intracellular chloride and thiol-containing compounds.

Dissolution of silver ions from AgNP plays a major role in AgNP toxicity. Rosario et al. reported a greater cytotoxic response in MG-63 cells from AgNO_3 compared with the corresponding mass of AgNP for exposures up to 48 hours but noted that by 7 days of exposure to 5 $\mu\text{g}/\text{mL}$ 10 nm AgNP, MG-63 cells lost all proliferative capacity determined by the clonogenic assay while the corresponding 5 $\mu\text{g}/\text{mL}$ of Ag^+ ions had significantly reduced proliferative capacity.¹⁶

In the present study, it is possible that cytotoxicity observed in the continuous exposure scenario could have been due to a larger contribution from intracellular particles compared with the single or repeated exposures. This conjecture is supported by the proliferation of hBMSC in the single and repeated exposures at 1 $\mu\text{g}/\text{mL}$ being statistically different from the proliferation in the continuous exposure at day 14 for hBMSC cultured with osteogenic supplements. The trend appears to continue for day 21, although the difference between 1 $\mu\text{g}/\text{mL}$ repeated and continuous exposures was not statistically significant.

Other studies support that the effect on AgNP on hBMSC proliferation could be partially attributed to early molecular initiating events, such as the dysregulation of genes related to cell metabolism or reactive oxygen species (ROS) defense, which lead to cytotoxicity. Genes related to osteogenesis were upregulated after 24-hour exposure to 20 $\mu\text{g}/\text{mL}$ of 20 nm AgNP to the MC3T3-E1 mouse osteoblast cell line.²⁴ Similarly, a decrease in proliferation in hBMSC and upregulation of markers related to endoplasmic reticulum and ROS stresses were found, but no changes to osteogenic differentiation markers were found in hBMSC.²⁵ Calcium deposition can be considered a definitive marker of successful osteogenic differentiation; hBMSC exposure to 10 and 25 $\mu\text{g}/\text{mL}$ 35 nm AgNP over 5 days in another study did not cause a change in calcium deposition.¹⁹ In contrast, ALP and mineralization in the current study were significantly impaired for most of the investigated concentrations and exposure scenarios. These effects occurred concomitantly with a marked decrease in proliferation, which may represent a cytotoxic response rather than impairment of differentiation.

Although repeated and continuous exposures at 5 $\mu\text{g}/\text{mL}$ or higher prevented deposition of hydroxyapatite, this marker was not affected under the single exposure scenario and may hold promise as an antimicrobial in orthopedic surgeries. Prophylactic use of antibiotics in orthopedic surgeries includes a single preoperative dose and a possible re-dosing 24 or 48 hours after the operation.^{26,27} In a similar manner to prophylactic antibiotic use, Gao et al. demonstrated that the majority of silver from 70 nm AgNP on the surface of a PEEK implant were released within 24 hours, yielding a 5 $\mu\text{g}/\text{mL}$ extract; the cumulative silver release curve plateaued after 5 days.²⁸ A reduction in viability of MC3T3-E1 osteoblast precursor cells was observed, but this difference versus the control was eliminated by day 5 due to dilution of the silver with repeated media changes. Implantation of this material into rats demonstrated antimicrobial activity and was observed to osseointegrate similar to the materials without AgNP after 2 weeks of implantation.

Conclusions

The present study examines the effect of different exposure scenarios on the proliferation and osteocyte function of differentiated hBMSC. Notably, a cytotoxic threshold of 10 $\mu\text{g}/\text{mL}$ PVP-coated 10 nm AgNP for hBMSC was determined, but this single 24-hour exposure caused a loss of osteocyte function in the 21-day culture. The viability of hBMSC exposed to 5 $\mu\text{g}/\text{mL}$ was not significantly different from controls in the 24-hour exposure, but this single 24-hour exposure caused a delay in the observation of ALP. This marker and

subsequent mineralization were not observed after repeated 24-hour exposures at the 5 $\mu\text{g}/\text{mL}$ concentration. hBMSC exposed to the 1 $\mu\text{g}/\text{mL}$ AgNP concentration were observed to express ALP and deposit hydroxyapatite in all exposure scenarios, but continuous exposure caused significantly lower proliferation rates than the other two exposure scenarios at day 14. Differences in proliferation, ALP expression, and hydroxyapatite deposition were detected in the different exposure scenarios at AgNP concentrations identified as subcytotoxic in a 24-hour exposure assay.

The well-known ability of silver to prevent the growth of a broad spectrum of infectious organisms without the use of antibiotics makes it an attractive additive to medical device implants. However, AgNP exposure at sufficient concentrations and/or exposure durations does have an adverse effect on hBMSC osteogenic differentiation and subsequent function as osteocytes. AgNP-containing medical device materials must be carefully formulated and evaluated to determine the benefit of infection control versus the risk of adverse effects on bone marrow.²⁹

Evaluating nanomaterials with biomedical applications presents challenges due to the vast number of nanoparticle physical and chemical parameters (e.g., size, shape, and coating) that influence biological and toxicological effects. For example, assumptions about the safety and performance of AgNP might not be supportable if there is a change in one or more of these parameters. Due to the vast number of nanomaterials with varying sizes, shapes, surface coatings and chemistries, and routes of exposure, *in vitro* human stem cell models that offer prolonged exposure scenarios compared with traditional *in vitro* models represent a potentially valuable component of integrated test strategies to evaluate nanomaterials.

Acknowledgments

The authors acknowledge Brendan Casey and the CDRH Advanced Characterization Facility for TEM imaging of the AgNP. This study was supported by funds from the U.S. Food and Drug Administration.

Disclaimer

The findings and conclusions in this article have not been formally disseminated by the Food and Drug Administration and should not be construed to represent any agency determination or policy. The mention of commercial products, their sources, or their use in connection with material reported herein is not to be construed as either an actual or implied endorsement of such products by the Department of Health and Human Services.

Author Disclosure Statement

No competing financial interests exist.

References

- Chua HS, Whitehouse SL, Lorimer M, et al. Mortality and implant survival with simultaneous and staged bilateral total knee arthroplasty experience from the Australian Orthopaedic Association National Joint Replacement Registry. *J Arthroplasty* 2018;33:3167–3173.
- Al-Mulhim FA, Baragbah MA, Sadat-Ali M, et al. Prevalence of surgical site infection in orthopedic surgery: A 5-year analysis. *Int Surg* 2014;99:264–268.
- Goel A, Meher MK, Gupta P, et al. Microwave assisted κ -carrageenan capped silver nanocomposites for eradication of bacterial biofilms. *Carbohydr Polym* 2019;206:854–862.
- Khalid HF, Tehseen B, Sarwar Y, et al. Biosurfactant coated silver and iron oxide nanoparticles with enhanced antibiofilm and anti-adhesive properties. *J Hazard Mater* 2019;364:441–448.
- Liu M, Liu T, Chen X, et al. Nano-silver-incorporated biomimetic polydopamine coating on a thermoplastic polyurethane porous nanocomposite as an efficient antibacterial wound dressing. *J Nanobiotechnol* 2018;16:89.
- Chen Y, Dan N, Dan W, et al. A novel antibacterial acellular porcine dermal matrix cross-linked with oxidized chitosan oligosaccharide and modified by *in situ* synthesis of silver nanoparticles for wound healing applications. *Mater Sci Eng C Mater Biol Appl* 2019;94:1020–1036.
- Choi J, Reipa V, Hitchins VM, et al. Physicochemical characterization and *in vitro* hemolysis evaluation of silver nanoparticles. *Toxicol Sci* 2011;123:133–143.
- Krajewski S, Prucek R, Panacek A, et al. Hemocompatibility evaluation of different silver nanoparticle concentrations employing a modified Chandler-loop *in vitro* assay on human blood. *Acta Biomater* 2013;9:7460–7468.
- Ahmed KBR, Nagy AM, Brown RP, et al. Silver nanoparticles: Significance of physicochemical properties and assay interference on the interpretation of *in vitro* cytotoxicity studies. *Toxicol In Vitro* 2017;38:179–192.
- Akter M, Sikder MT, Rahman MM, et al. A systematic review on silver nanoparticles-induced cytotoxicity: Physicochemical properties and perspectives. *J Adv Res* 2018;9:1–16.
- Bar-Ilan O, Albrecht RM, Fako VE, et al. Toxicity assessments of multisized gold and silver nanoparticles in zebrafish embryos. *Small* 2009;5:1897–1910.
- International Organization for Standardization. Biological Evaluation of medical devices. (ISO Standard No. 10993:2009). <https://www.iso.org/standard/36406.html> (last accessed Apr. 27, 2012).
- Sussman EM, Jayanti P, Dair BJ, et al. Assessment of total silver and silver nanoparticle extraction from medical devices. *Food Chem Toxicol* 2015;85:10–19.
- De Matteis V, Cascione M, Toma CC, et al. Silver nanoparticles: Synthetic routes, *in vitro* toxicity and therapeutic applications for cancer disease. *Nanomaterials (Basel)* 2018;8:319.
- Sengstock C, Diendorf J, Epple M, et al. Effect of silver nanoparticles on human mesenchymal stem cell differentiation. *Beilstein J Nanotechnol* 2014;5:2058–2069.
- Rosario F, Hoet P, Santos C, et al. Death and cell cycle progression are differently conditioned by the AgNP size in osteoblast-like cells. *Toxicology* 2016;368:103–115.
- Kreeinthong S, Uawithya P. Effects of Short-term silver nanoparticle exposure on proliferative signaling pathway in human skin keratinocyte. *J Physiol Biomed Sci* 2014;27:48–53.
- Çiftçi H, Türk M, Tamer U, et al. Silver nanoparticles: Cytotoxic, apoptotic, and necrotic effects on MCF-7 cells. *Turkish J Biol* 2013;37:573–581.
- Castiglioni S, Cazzaniga A, Locatelli L, et al. Silver nanoparticles in orthopedic applications: New insights on their

- effects on osteogenic cells. *Nanomaterials (Basel)* 2017;7:124.
20. Berry CC, de la Fuente JM, Mullin M, et al. Nuclear localization of HIV-1 tat functionalized gold nanoparticles. *IEEE Trans Nanobioscience* 2007;6:262–269.
 21. Ahlberg S, Antonopoulos A, Diendorf J, et al. PVP-coated, negatively charged silver nanoparticles: A multi-center study of their physicochemical characteristics, cell culture and in vivo experiments. *Beilstein J Nanotechnol* 2014;5:1944–1965.
 22. Hsiao I-L, Hsieh Y-K, Chuang C-Y, et al. Effects of silver nanoparticles on the interactions of neuron- and glia-like cells: Toxicity, uptake mechanisms, and lysosomal tracking. *Environ Toxicol* 2017;32:1742–1753.
 23. Wildt BE, Celedon A, Maurer EI, et al. Intracellular accumulation and dissolution of silver nanoparticles in L-929 fibroblast cells using live cell time-lapse microscopy. *Nanotoxicology* 2016;10:710–719.
 24. Qing T, Mahmood M, Zheng Y, et al. A genomic characterization of the influence of silver nanoparticles on bone differentiation in MC3T3-E1 cells. *J Appl Toxicol* 2018;38:172–179.
 25. Pauksch L, Hartmann S, Rohnke M, et al. Biocompatibility of silver nanoparticles and silver ions in primary human mesenchymal stem cells and osteoblasts. *Acta Biomater* 2014;10:439–449.
 26. Backes M, Dingemans SA, Dijkgraaf MGW, et al. Effect of antibiotic prophylaxis on surgical site infections following removal of orthopedic implants used for treatment of foot, ankle, and lower leg fractures: A Randomized Clinical Trial. *JAMA* 2017;318:2438–2445.
 27. Gans I, Jain A, Sirisreerex N, et al. Current practice of antibiotic prophylaxis for surgical fixation of closed long bone fractures: A survey of 297 members of the Orthopaedic Trauma Association. *Patient Saf Surg* 2017;11:2.
 28. Gao C, Wang Y, Han F, et al. Antibacterial activity and osseointegration of silver-coated poly(ether ether ketone) prepared using the polydopamine-assisted deposition technique. *J Mater Chem B* 2017;5:9326–9336.
 29. Petrochenko PE, Zheng J, Casey BJ, et al. Nanosilver-PMMA composite coating optimized to provide robust antibacterial efficacy while minimizing human bone marrow stromal cell toxicity. *Toxicol In Vitro* 2017;44:248–255.

Address correspondence to:

*Dr. Peter L. Goering
Office of Science and Engineering Laboratories
Center for Devices and Radiological Health
US Food and Drug Administration
10903 New Hampshire Avenue
Silver Spring, MD 20993*

E-mail: peter.goering@fda.hhs.gov

CHAPTER 8 – Sintered Tape-cast 3YSZ Supports Human Bone Marrow Derived Stem Cell Osteogenic Differentiation

Alexander K. Nguyen^{1,2}, Peter L. Goering², John A. Olenick³, Kathy Olenick³, and Roger J. Narayan¹

1. UNC/NCSU Joint Department of Biomedical Engineering, North Carolina State University, Raleigh, NC
2. Division of Biology Chemistry and Materials Science, US Food and Drug Administration, Silver Spring, MD
3. ENrG Inc., Buffalo, NY

Reference: Nguyen, A.K.; Goering, P.L.; Olenick, J.A.; Olenick, K.; Narayan, R.J. Sintered Tape-cast 3YSZ Supports Human Bone Marrow Derived Stem Cell Osteogenic Differentiation. *MRS Advances* **2019**, *4*, 2541-2549, doi:10.1557/adv.2019.335.

Abstract

Tape-cast yttria stabilized zirconia (YSZ) was evaluated for its elemental composition, crystal structure, and imaged with atomic force microscopy (AFM) and scanning electron microscopy (SEM). Human bone marrow stem cells (hBMSC) were cultured on the ceramic and differentiated into the osteoblast lineage and alkaline phosphatase (ALP) activity tracked as a differentiation marker. The YSZ was composed of purely tetragonal grains with a median equivalent circular diameter of 283 nm. Zirconium, yttrium, oxygen, and adventitious carbon was detected on the substrate with no other elements in significant quantities detected. YSZ samples had a RMS roughness of 26.852 nm, elastic modulus of 206.27 ± 13.95 GPa, and hardness of 14.15 ± 1.54 GPa. hBMSC were observed to attach and proliferate on the YSZ surfaces and had significantly increased ALP versus the undifferentiated control. This method

for producing a YSZ ceramic yields a typical material of this type and supports attachment and differentiation of hBMSC which makes this a possible material for a bone implant.

Introduction

Zirconia has low cytotoxicity, chronic toxicity, carcinogenicity[266], among other properties that make it an attractive medical device material. Chemical and radiological impurities can be of toxicological concern but even unpurified zirconia was not found to be mutagenic or carcinogenic.[267] It has also found use in the dental field as an orthodontic retainer material since it has superior esthetics versus stainless steel wire and has bonding protocols with better clinical outcomes versus stainless steel bonding.[268] In addition, zirconia is chemically stable; accelerated aging in 4% acetic acid at 80°C for 168 hours had no effect on flexural strength or sample mass.[269] The zirconia surface also exhibits superior tribological properties versus other materials. Zirconia femoral heads reduced the volumetric wear of polyethylene liners by a third versus cobalt chrome heads.[270] A 2 μm thick layer of yttria-stabilized zirconia on titanium reduced volumetric wear of ultra-high molecular weight polyethylene by 18% versus bare titanium.[271] Volumetric wear of zirconia-on-alumina was comparable to that of alumina-on-alumina but the zirconia surface had smaller, more uniform, scratches versus larger scratches on the alumina-on-alumina surfaces.[270]

For these reasons, zirconia was a popular material for femoral heads until a large proportion of them fractured after installation with a combined fracture rate of 2.2% over the affected batches; one batch had a 24% fracture rate.[272] This is due to a change from using a batch sintering furnace to a tunnel furnace; typical monoclinic-phase zirconia content after steam sterilization is <5% but was found to be 74% on the interior surfaces contacting the taper portion of the femoral implant.[272] Partially stabilized zirconia undergoes transformation toughening

where the metastable tetragonal phase transforms to monoclinic; the volume change inhibits crack propagation. Insufficient concentration of tetragonal-phase zirconia would prevent this process and make the ceramic prone to fracture. Addition of yttria to stabilize the tetragonal-zirconia lattice is a common strategy to maintain this structure at room temperature. During sintering, the monoclinic-tetragonal phase change occurs around 1000°C with the tetragonal-cubic phase change occurring around 2200°C.[273] However sintering at 1550°C with 3 mol% yttria caused cubic grains to form that were stabilized by depleting the yttria from, and thereby destabilizing, the surrounding grains.[274]

Although zirconia as a medical device material is well established, product from new manufacturing methods must be evaluated to ensure the properties are as expected from tetragonal zirconia. ENrG developed a sintered tape-cast 3YSZ with various potential applications such as flexible substrates for electronics[275], or as an infrared transparent window[276], and is shown to have no monoclinic phase after autoclaving for 5 hr at 200°C.[277] This manufacturing process should be evaluated to determine its cytocompatibility and mechanical properties for use in orthopedic applications. In this study, sintered tape-cast zirconia was evaluated for its elemental composition, crystal structure, topography, mechanical properties, and its ability to retain osteogenic differentiation ability of hBMSC.

Materials and Methods

Thin E-Strate sintered tape-cast YSZ wafers (15 mm diameter x 0.02 mm thick) were received from ENrG (ENrG Inc., Buffalo, NY).

Physical Characterization X-ray photoelectron spectra (XPS) were collected using the Phoibos 150 hemispherical analyzer (SPECS Surface Nano Analysis GmbH, Berlin, Germany) using Mg K_α radiation (1254 eV). X-ray incidence angle was 30° and the x-ray source to

analyzer angle was 60°; photoelectron takeoff angle was normal to the sample surface. Energy calibration within each spectrum was established by referencing to adventitious carbon (C 1s line at 285.0 eV binding energy). Pressure in the analysis chamber was maintained in the 10⁻¹⁰ mbar range.

X-ray diffraction (XRD) data were collected using a Panalytical Empyrean X-ray diffractometer using Cu K- α 1 radiation ($\lambda = 0.15418$ nm). Samples were scanned at a 2 θ range between 10 to 90 degrees at a 0.026 degree step size and 96 seconds per step.

AFM was performed using an Asylum MFP-3D (Asylum Research, Morrisville, NC) on a 10.00 μ m region and 1.00 μ m sub-region in tapping mode with 256 scan lines at a 0.75 Hz scan rate. Height data was determined on the retrace.

Nanoindentation was performed on a Bruker Hysitron TI980 TriboIndenter (Bruker, Billerica, MA) using a diamond indenter with Berkovich geometry (50 nm tip radius) at multiple locations spaced 10 μ m apart. A 20 second loading segment to a maximum load of 3, 4, 5, or 6 mN, a 10 second hold at maximum load, and a 20 second unloading segment to 0 mN was performed at each location.

Human bone marrow stem cell alkaline phosphatase expression hBMSC (ATCC, Manassas, VA) expression of ALP was determined by normalizing the ALP activity measured using the Alkaline Phosphatase Liquicolor kit (Stanbio, Boerne, TX) to cell count measured using the Pico Green assay (ThermoFisher Scientific, Waltham, MA).

Three YSZ wafers and six glass coverslips (10x10 mm) were UV-sterilized for 30 minutes per side under germicidal UV-C light in a biosafety hood and placed into a 24-well plate. hBMSC at passage 4 were sub-cultured, re-suspended in media, then seeded at a 3.0x10⁵ cells/cm² density and incubated at 37°C, 95% RH, 5.0% CO₂ for 4 hr for cell attachment. Media

from the YSZ wafers and half the glass coverslips were aspirated and replaced with 0.5 mL of the Osteocyte Differentiation Tool (ATCC, Manassas, VA), which is media containing proprietary osteogenic supplements. Three plates per replicate were seeded for both assays at days 7, 14, and 21 after seeding.

Cell lysate used in both biological assays were produced from the samples and from a hBMSC suspension of known cell density to be used as the cell count standards. Samples were dipped 3x in PBS and transferred to a new 24 well plate to eliminate signal from cells attached to the tissue culture treated polystyrene. A solution (0.5 mL) of 0.2% w/w Triton X-100 was added to each sample and the plate agitated at room temperature for 30 min to produce the cell lysates. Cell standards solutions containing 100000, 50000, 25000, 10000, 7500, 5000, and 2500 cells/mL in 0.2% Triton X-100 were also produced.

Three 50 μ L aliquots of each lysate was transferred to two 96-well plates designated for the ALP Liquicolor and PicoGreen assays for measurement in triplicate. ALP Liquicolor standard was produced using SER-T-FY level 1 control serum (Stanbio, Boerne, TX) to produce a solution containing 48 U/L ALP and 0.2% Triton X-100; three 50 μ L aliquots of this solution and 0.2% Triton X-100 were added to the ALP Liquicolor plate as the serum standard and blank respectively.

PicoGreen working reagent was mixed according to manufacturer specifications and 50 μ L added to each well. After 5 minutes for staining, fluorescence at 485 nm excitation and 538 nm emission wavelengths were read on a fluorescence plate reader (SpectraMAX Gemini EM, Molecular Devices, San Jose, CA). Fluorescence readings from the lysate generated from each sample was normalized to the cell standard ladder to determine the cell count. ALP Liquicolor working reagent was mixed according to manufacturer specifications and 50 μ L added to each

well. The plate was immediately read on a plate reader (SpectraMAX190, Molecular Devices, San Jose, CA); the absorbance at 405 nm was read every 15 seconds for 15 minutes. ALP converts the colorless substrate into a colored compound at a constant rate, so the reaction rate determined from each lysate was compared to the reaction rate of the serum control to calculate the ALP activity. Three independent experimental replicates of the described procedure were performed.

Scanning Electron Microscopy hBMSC were cultured on YSZ wafers or tissue-culture treated polyester Thermanox coverslips (ThermoFisher Scientific, Waltham, MA). All samples were rinsed 2x in PBS, fixed for 30 min in 2.5% glutaraldehyde in PBS, then rinsed 3x in PBS. Samples were dehydrated using an ethanol gradient by immersing samples in 0%, 25%, 50%, 75%, and 95% ethanol in ultrapure water for 5 min each, 3x in 100% ethanol, 2x in a 50% v/v hexamethyldisilazane (HMDS) in ethanol solution, and 2x in HMDS for 10 minutes each. A YSZ wafer, wafer with hBMSC, and Thermanox with hBMSC were sputter coated with gold and imaged at 10.0 kV using a Mira3 scanning electron microscope (Tecan, Maennedorf, Switzerland).

Image analysis of a SEM image with a 10.00 μm view field was performed in ImageJ (National Institutes of Health, Bethesda, MD). In short, watershed segmentation was used to delineate particles with thresholding used to exclude regions of low signal where segmentation was unreliable. Descriptive statistics of 815 grains were summarized.

Results and Discussion

XPS determined presence of carbon (20.2 at%), oxygen (58.2 at%), zirconium (18.3 at%), and yttrium (3.2 at%). Presence of carbon is attributed to adventitious carbon. XRD data is presented in Figure 8.1; major peaks at 30.13°, 50.12°, and 60.00° are consistent with the

tetragonal (PDF 04-016-1792, ICDD, 2019) and cubic (PDF 00-030-1468, ICDD, 2019) lattices but not the monoclinic (PDF 00-036-0420, ICDD, 2019) lattice. Peaks at approximately 35°, 50°, and 60° are present as doublets which is consistent with a tetragonal lattice and not a cubic lattice. In addition, the peak intensities match the t-ZrO₂ reference spectrum, so this material exhibits a pure tetragonal lattice with undetectable levels of monoclinic or cubic lattices.

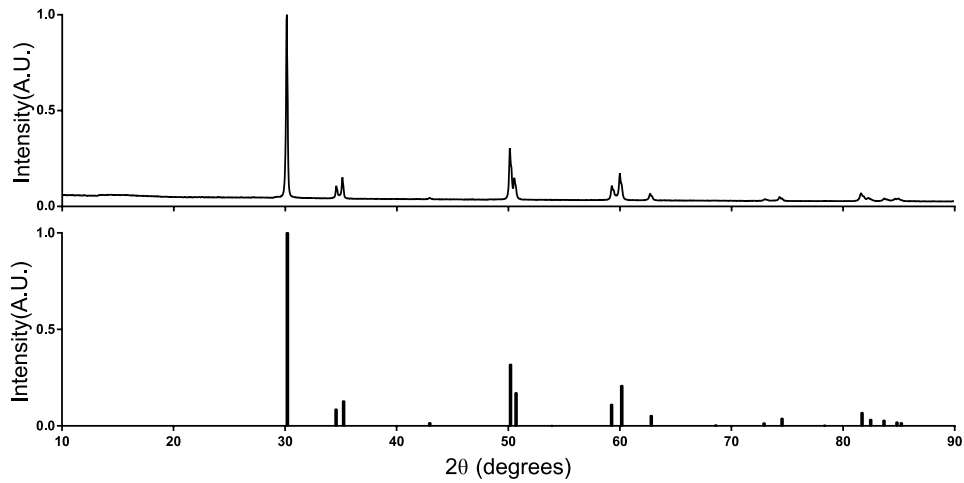


Figure 8.1 - X-ray diffraction spectra of a YSZ wafer (top), and the tetragonal ZrO₂ reference spectrum (bottom) from PDF Card 04-016-1792.

Considering the zirconium to yttrium ratio and the high fidelity of the sample to the reference XRD spectrum, these data are consistent with a fully stabilized (8 mol% Y₂O₃) zirconia with purely tetragonal grains. However, zirconia with Y₂O₃ concentrations beyond 3 mol% should contain cubic grains.[273] While >8 mol% YSZ with a high proportion of tetragonal phase is possible, it is commonly achieved using the sol-gel synthesis method where high-temperatures conducive to the formation of cubic phases can be avoided [278-280] In addition, formation of a cubic phase during sintering at high temperatures is visible at the micro-scale. For example, 3 mol% YSZ sintered at 1550°C for 5 hours formed large micron-scale yttria-rich cubic grains with sub-micron yttria-depleted tetragonal grains at the edges.[274] Since

the observed XRD spectra matches the t-ZrO₂ spectra and no micron-scale grains were detected in SEM (Figure 8.2), the observation of a pure tetragonal phase in this sample is accurate. Detection of a high proportion of yttrium in this sample can be attributed to the adventitious carbon; presence of this layer attenuates high binding energy photoelectrons more than low binding energy electrons [281] and would therefore overestimate yttria content relative to other elements. Thus, elements consistent with a YSZ ceramic were detected.

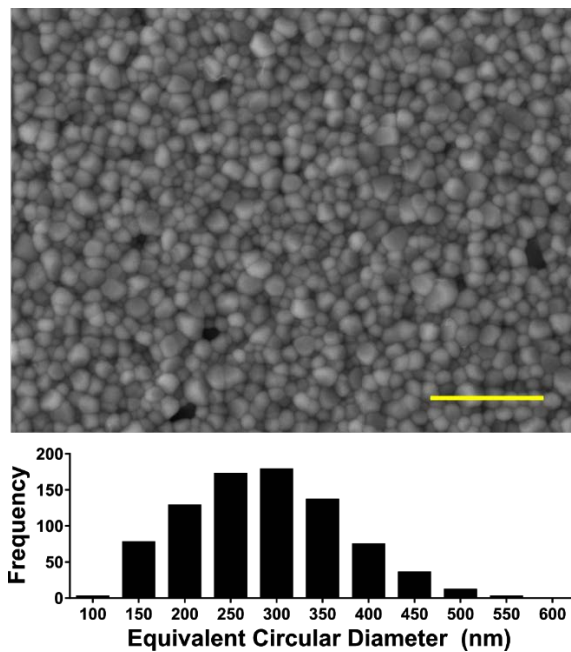


Figure 8.2 - Scanning electron microscopy image analysis of ENrG tape-cast zirconia (top). Scale bar = 2 μ m. Summary data from 815 particles (bottom) reported a median grain size of 283 nm.

Topography of a YSZ wafer was measured with AFM (Figure 8.3). The surface was smooth with an RMS roughness of 26.852 nm measured over a 10.00 μ m x 10.00 μ m area and 20.799 nm measured over a 1.00 μ m x 1.00 μ m sub-section. Image analysis of 815 grains in an SEM image (Figure 8.2) determined a median equivalent circular diameter of 283.221 nm with an interquartile range between 222.837 nm and 342.254 nm. Wafers had a reduced modulus of

206.27 ± 13.95 GPa (mean ± SD) and hardness of 14.15 ± 1.54 measured at multiple locations with varying maximum indentation forces. These values are consistent with elastic modulus [282, 283] and hardness [283, 284] values reported in the literature.

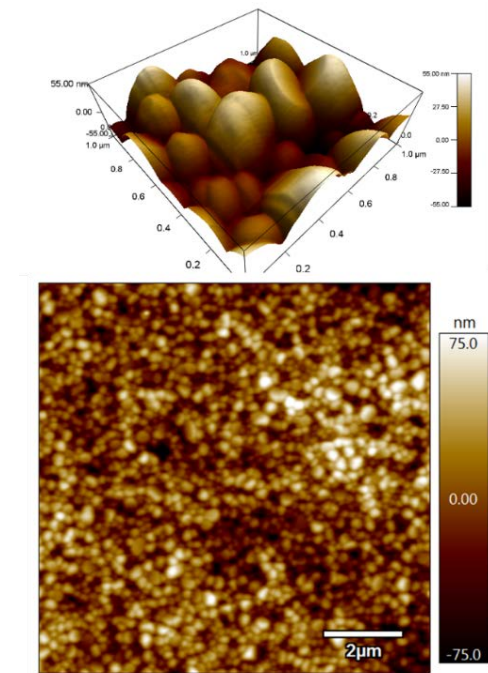


Figure 8.3 - Atomic Force Microscopy of a YSZ wafer. Topographical image of a 10.00 μm scan size (bottom) and 3D rendering of a 1.0 μm region (top). RMS roughness values were 26.852 nm and 20.799 nm for the 10.00 μm and 1.0 μm regions respectively.

hBMSC cultured on YSZ wafers and tissue-culture treated polyester (Figure 8.4) had qualitative differences in morphology; cells on YSZ wafers were observed to have rolled edges which suggest inferior cell attachment versus the tissue-culture treated polyester surface. ALP activity (Figure 8.5) of cell lysate obtained from hBMSC cultured on YSZ wafers with osteogenic media, or hBMC cultured on glass with osteogenic media (positive control) were elevated above ALP activity of cell lysate obtained from hBMSC cultured on glass in the absence of osteogenic supplements (negative control) indicating differentiation to the osteocyte

lineage is taking place. ALP is expressed early during differentiation but declines at the later stages of osteogenic differentiation [285] Because this study investigated specific timepoints, the ALP expression peak cannot be identified so elevated ALP levels per cell only shows that osteogenic differentiation is taking place.

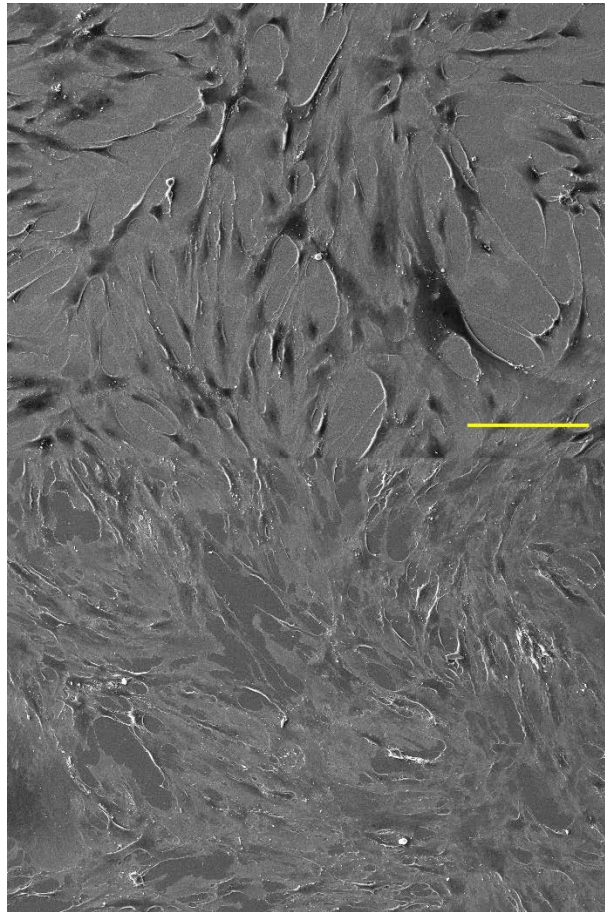


Figure 8.4 - Scanning electron micrographs of ENrG with hBMSC (top), and tissue-culture treated polyester with hBMSC (bottom). Scale bar = 200 μm

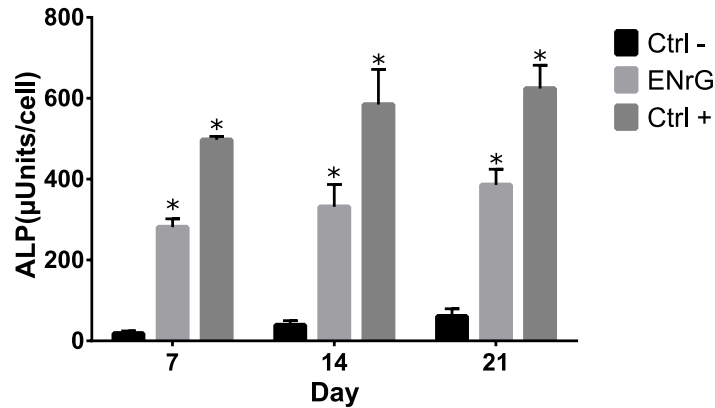


Figure 8.5 - ALP activity per cell hBMSC cultured on glass without osteogenic media (Ctrl -), tape-cast zirconia (ENrG) with osteogenic media, and glass with osteogenic media (Ctrl +). Bars with asterisks (*) are significantly higher than the negative control. Values represent $\bar{x} \pm SD$ of $n = 3$ independent experimental replicates.

Conclusion

Manufacturing methods of YSZ ceramics influence the physical properties and inadvertent manufacturing defects can have disastrous effects especially in implanted orthopedic devices. Maintenance of the meta-stable tetragonal phase necessary for the transformation-toughening properties of YSZ ceramics must be maintained. Physical characterization of the elemental composition, crystal structure, elastic modulus, hardness, and topography determined properties consistent with a YSZ ceramic with pure tetragonal crystal structure. In addition, the YSZ wafers maintained cytocompatibility and supported hBMSC osteogenic differentiation.

MRS Advances © 2019 Materials Research Society
DOI: 10.1557/adv.2019.335



Sintered Tape-cast 3YSZ Supports Human Bone Marrow Derived Stem Cell Osteogenic Differentiation

Alexander K. Nguyen^{1,2}, Peter L. Goering², John A. Olenick³, Kathy Olenick³, and Roger J. Narayan¹

¹North Carolina State University, UNC/NCSU Joint Department of Biomedical Engineering, 911 Oval Drive, Raleigh, NC 27695

²US Food and Drug Administration, Center for Devices and Radiological Health, Office of Science and Engineering Laboratories, Division of Biology, Chemistry, and Materials Science, 10903 New Hampshire Ave., Silver Spring, MD 20993

³ENrG Inc., Buffalo, NY 14207

ABSTRACT

Sintered tape-cast yttria-stabilized zirconia (YSZ) was evaluated for its elemental composition, crystal structure, and imaged with atomic force microscopy (AFM) and scanning electron microscopy (SEM). Human bone marrow stem cells (hBMSC) were cultured on the ceramic and differentiated into the osteoblast lineage; alkaline phosphatase (ALP) activity was tracked as a differentiation marker. The YSZ was composed of purely tetragonal grains with a median equivalent circular diameter of 283 nm. Zirconium, yttrium, oxygen, and adventitious carbon was detected on the substrate with no other elements in significant quantities detected. YSZ samples had an RMS roughness value of 27 nm, elastic modulus of 206 ± 14 GPa, and hardness of 14 ± 2 GPa. hBMSC were observed to attach and proliferate on the YSZ surfaces and had significantly increased ALP versus the undifferentiated control cultured on glass. This method for producing a YSZ ceramic yields a typical material of this type and supports attachment and differentiation of hBMSC; thus, making it useful as a bone implant material.

INTRODUCTION:

Zirconia exhibits low cytotoxicity, chronic toxicity *in vivo*, and carcinogenicity[1], properties that make it an attractive medical device material. Chemical and radioactive impurities in zirconium sands, such as uranium and thorium, can be of toxicological concern but even unpurified zirconia was not found to be mutagenic or carcinogenic.[2] It has also found use in the dental field as an orthodontic retainer material since it has superior esthetics versus stainless steel wire and has bonding protocols with better clinical outcomes versus stainless steel bonding.[3] In addition, zirconia is chemically stable; accelerated aging in 4% acetic acid at 80°C for 168 hours had no effect on flexural strength or sample mass.[4] The zirconia surface also exhibits superior tribological properties versus other materials for use as

joint replacements. Zirconia femoral heads reduced the volumetric wear of polyethylene liners by a third versus cobalt chrome heads.[5] A 2- μm thick layer of yttria-stabilized zirconia on titanium reduced volumetric wear of ultra-high molecular weight polyethylene by 18% versus bare titanium.[6] Volumetric wear of zirconia-on-alumina was comparable to that of alumina-on-alumina but the zirconia surface had smaller, more uniform, scratches versus larger scratches on the alumina-on-alumina surfaces.[5]

For these reasons, zirconia was a popular material for femoral heads until a large proportion of them fractured after implantation with a combined fracture rate of 2.2% over the affected batches; one batch had a 24% fracture rate.[7] This was due to a change from using a batch sintering furnace to a tunnel furnace; typical monoclinic-phase zirconia content after steam sterilization should be <5% but was found to be 74% on the interior surfaces contacting the taper portion of the femoral implant.[7] Partially stabilized zirconia undergoes transformation toughening where the metastable tetragonal phase transforms to monoclinic; the volume change inhibits crack propagation. Insufficient concentration of tetragonal-phase zirconia would prevent this process and make the ceramic prone to fracture. Addition of yttria to stabilize the tetragonal-zirconia lattice is a common strategy to maintain this structure at room temperature. During sintering, the monoclinic-tetragonal phase change occurs around 1000°C with the tetragonal-cubic phase change occurring around 2200°C.[8] However, sintering at 1550°C with 3 mol% yttria caused cubic grains to form that were stabilized by depleting the yttria from, and thereby destabilizing, the surrounding grains.[9]

Although zirconia as a medical device material is well-established, products from new manufacturing methods must be evaluated to ensure material properties are as expected from tetragonal zirconia. A sintered tape-cast 3YSZ was developed with various potential applications such as flexible substrates for electronics[10], or as an infrared transparent window[11], and is shown to have no monoclinic phase after autoclaving for 5 hr at 200°C.[12] This manufacturing process should be evaluated to determine its cytocompatibility and mechanical properties for use in orthopedic applications. In this study, sintered tape-cast zirconia was evaluated for its elemental composition, crystal structure, topography, mechanical properties, and its ability to support osteogenic differentiation ability of hBMSC.

METHODS AND MATERIALS:

Thin E-Strate sintered tape-cast YSZ wafers (15 mm diameter \times 0.02 mm thick) were received from ENrG (ENrG Inc., Buffalo, NY).

Physical characterization

X-ray photoelectron spectra (XPS) were collected using the Phoibos 150 hemispherical analyzer (SPECS Surface Nano Analysis GmbH, Berlin, Germany) using Mg K α radiation (1254 eV). X-ray incidence angle was 30° and the x-ray source to analyzer angle was 60°; photoelectron takeoff angle was normal to the sample surface. Energy calibration within each spectrum was established by referencing to adventitious carbon (C 1s line at 285.0 eV binding energy). Pressure in the analysis chamber was maintained in the 10⁻¹⁰ mbar range.

X-ray diffraction (XRD) data were collected using a Panalytical Empyrean X-ray diffractometer (Malvern Panalytical Ltd., Royston, UK) using Cu K- α 1 radiation ($\lambda = 0.15418$ nm). Samples were scanned at a 2 θ range between 10 to 90 degrees at a 0.026 degree step size and 96 seconds per step.

AFM was performed using an Asylum MFP-3D (Asylum Research, Morrisville, NC) using a Tap300 tip (Budget Sensors, Sofia, Bulgaria) on a 10.00- μm region and 1.00- μm sub-region in tapping mode with 256 scan lines at a 0.75 Hz scan rate. Height data were determined on the retrace.

Nanoindentation was performed on a Bruker Hysitron TI980 TriboIndenter (Bruker, Billerica, MA) using a diamond indenter with Berkovich geometry (50 nm tip radius) at multiple locations spaced 10 μm apart. A 20-sec loading segment to a maximum load of 3, 4,

5, or 6 mN, a 10-sec hold at maximum load, and a 20-sec unloading segment to 0 mN were performed at each location.

Human bone marrow stem cell alkaline phosphatase expression

hBMSC (ATCC, Manassas, VA) expression of ALP was determined by normalizing the ALP activity measured using the Alkaline Phosphatase Liquicolor kit (Stanbio, Boerne, TX) to cell count measured using the Pico Green assay (ThermoFisher Scientific, Waltham, MA).

Three YSZ wafers and six glass coverslips (10x10 mm) were UV-sterilized for 30-min per side under germicidal UV-C light in a biosafety hood and placed into a 24-well plate. hBMSC at passage 4 were sub-cultured, re-suspended in media, then seeded at a 3.0×10^5 cells/cm² density and incubated at 37°C, 95% RH, 5.0% CO₂ for 4 hr for cell attachment. Media from the YSZ wafers and half the glass coverslips were aspirated and replaced with 0.5 mL of the Osteocyte Differentiation Tool (ATCC, Manassas, VA), which is media containing proprietary osteogenic supplements. Three plates per replicate were seeded for both assays at days 7, 14, and 21 after seeding.

Cell lysate used in both biological assays were produced from the samples and from an hBMSC suspension of known cell density to be used as the cell count standards. Samples were rinsed 3x in PBS and transferred to a new 24 well plate to eliminate signal from cells attached to the tissue culture treated polystyrene. A solution (0.5 mL) of 0.2% w/w Triton X-100 was added to each sample and the plate agitated at room temperature for 30 min to produce the cell lysates. hBMSC lysate solutions containing 100000, 50000, 25000, 10000, 7500, 5000, and 2500 cells/mL in 0.2% Triton X-100 were also produced for the PicoGreen standard curve. Three 50- μ L aliquots of each lysate were transferred to two 96-well plates designated for the ALP Liquicolor and PicoGreen assays for measurement in triplicate.

PicoGreen working reagent was mixed according to manufacturer specifications and 50 μ L added to each well in one plate. After 5 min for staining, fluorescence at 485 nm excitation and 538 nm emission wavelengths were read on a fluorescence plate reader (SpectraMAX Gemini EM, Molecular Devices, San Jose, CA). Fluorescence readings from the lysate generated from each sample were normalized to the cell standard curve to determine the cell count.

ALP Liquicolor standard was produced using SER-T-FY level 1 control serum (Stanbio, Boerne, TX) to produce a solution containing 48 U/L ALP and 0.2% Triton X-100; three 50- μ L aliquots of this solution and 0.2% Triton X-100 were added to the ALP Liquicolor plate as the serum standard and blank, respectively. ALP Liquicolor working reagent was mixed according to manufacturer specifications and 50 μ L added to each well. The plate was immediately read on a plate reader (SpectraMAX190, Molecular Devices, San Jose, CA); the absorbance at 405 nm was read every 15 seconds for 15 minutes. ALP converts the colorless substrate into a colored compound at a constant rate, so the reaction rate determined from each lysate was compared to the reaction rate of the serum control to calculate the ALP activity.

ALP activity was normalized to the cell count determined by the PicoGreen assay for each well. Three independent experimental replicates of the described procedure were conducted, and the normalized ALP activity of hBMSC on YSZ and glass cultured with osteogenic supplements compared to that of hBMCS cultured in the absence of osteogenic media using the Students t-test.

Scanning Electron Microscopy

hBMSC were cultured on YSZ wafers or tissue-culture treated polyester Thermanox coverslips (ThermoFisher Scientific, Waltham, MA). All samples were rinsed 2x in PBS, fixed for 30 min in 2.5% glutaraldehyde in PBS, then rinsed 3x in PBS. Samples were dehydrated using an ethanol gradient by immersing samples in 0%, 25%, 50%, 75%, and 95% ethanol in ultrapure water for 5 min each, 3x in 100% ethanol, 2x in a 50% v/v

hexamethyldisilazane (HMDS) in ethanol solution, and 2x in HMDS for 10 minutes each. A YSZ wafer, YSZ wafer with hBMSC, and Thermanox coverslip with hBMSC were sputter coated with gold and imaged at 10.0 kV using a Mira3 scanning electron microscope (Tecan, Maennedorf, Switzerland).

Image analysis of an SEM image with a 10.00- μm view field was performed in ImageJ (National Institutes of Health, Bethesda, MD). In short, watershed segmentation was used to delineate particles with thresholding used to exclude regions of low signal where segmentation was unreliable. Descriptive statistics of 815 grains were summarized.

RESULTS AND DISCUSSION:

XPS determined the presence of carbon (20.2 at%), oxygen (58.2 at%), zirconium (18.3 at%), and yttrium (3.2 at%). Presence of carbon is attributed to adventitious carbon. XRD data is presented in Figure 1; major peaks at 30.13°, 50.12°, and 60.00° are consistent with the tetragonal (PDF 04-016-1792, ICDD, 2019) and cubic (PDF 00-030-1468, ICDD, 2019) lattices but not the monoclinic (PDF 00-036-0420, ICDD, 2019) lattice. Peaks at approximately 35°, 50°, and 60° are present as doublets which is consistent with a tetragonal lattice and not a cubic lattice. In addition, the peak intensities match the t-ZrO₂ reference spectrum, so this material exhibits a pure tetragonal lattice with undetectable levels of monoclinic or cubic lattices.

Considering the zirconium to yttrium ratio and the high fidelity of the sample to the reference XRD spectrum, these data are consistent with a fully stabilized (8 mol% Y₂O₃) zirconia with purely tetragonal grains. However, zirconia with Y₂O₃ concentrations beyond 3 mol% should contain cubic grains.[8] While >8 mol% YSZ with a high proportion of tetragonal phase is possible, it is commonly achieved using the sol-gel synthesis method where high-temperatures conducive to the formation of cubic phases can be avoided [13-15] In addition, formation of a cubic phase during sintering at high temperatures is visible at the micro-scale. For example, 3 mol% YSZ sintered at 1550°C for 5 hours formed large micron-scale yttria-rich cubic grains with sub-micron yttria-depleted tetragonal grains at the edges.[9] Since the observed XRD spectra matches the t-ZrO₂ spectra and no micron-scale grains were detected in SEM (Figure 3), the observation of a pure tetragonal phase in this sample is accurate. Detection of a high proportion of yttrium in this sample can be attributed to the adventitious carbon; presence of this layer attenuates high binding energy photoelectrons more than low binding energy electrons [16] and would, therefore, overestimate yttria content relative to other elements. Thus, elements consistent with a YSZ ceramic were detected.

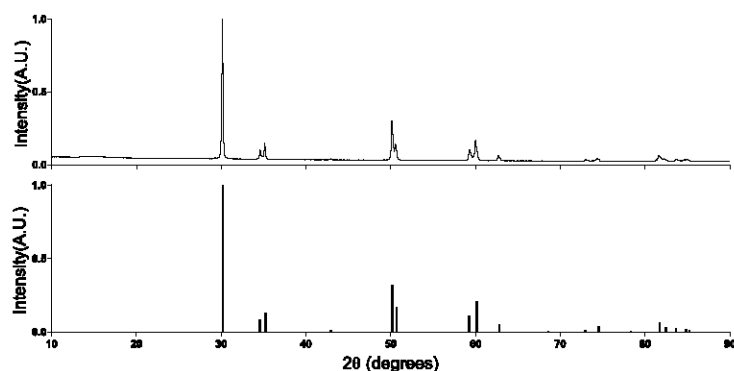


Figure 1 – X-ray diffraction spectra of a YSZ wafer (top), and the tetragonal ZrO₂ reference spectrum (bottom) from PDF Card 04-016-1792.

Topography of a YSZ wafer was measured with AFM (Figure 2). The surface was smooth with an RMS roughness of 27 nm measured over a 10.00 μm \times 10.00 μm area and 21 nm measured over a 1.00 μm \times 1.00 μm sub-section. Image analysis of 815 grains in an SEM image (Figure 3) determined a median equivalent circular diameter of 283 nm with an interquartile range between 223 nm and 342 nm. Wafers had a reduced modulus of 206 ± 14 GPa (mean \pm SD) and hardness of 14 ± 2 GPa measured at multiple locations with varying maximum indentation forces. These values are consistent with elastic modulus [17, 18] and hardness [18, 19] values reported in the literature.

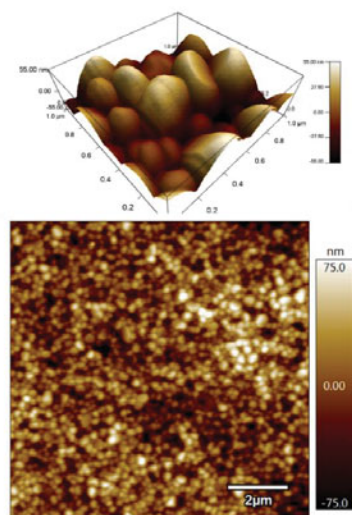


Figure 2 – Atomic force microscopy of a YSZ wafer. Topographical image of a 10.00 μm scan size (bottom) and 3D rendering of a 1.0 μm region (top). RMS roughness values were 27 nm and 21 nm for the 10.00 μm and 1.0 μm regions, respectively.

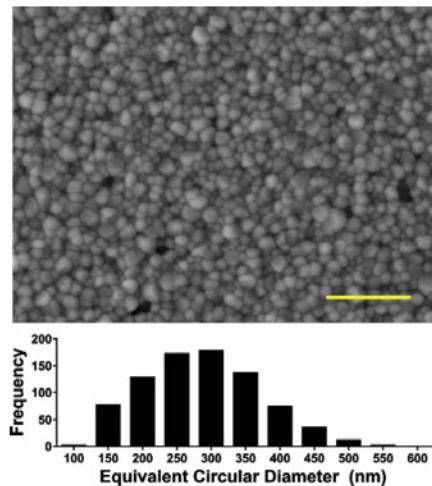


Figure 3 – Scanning electron microscopy image analysis of a YSZ wafer (top). Scale bar = 2 μ m. Summary data from 815 particles (bottom) reported a median grain size of 283 nm.

hBMSC cultured on YSZ wafers and tissue-culture treated polyester (Figure 4) had qualitative differences in morphology; cells on YSZ wafers were observed to have rolled edges which suggest inferior cell attachment versus the tissue-culture treated polyester surface. ALP activity (Figure 5) in cell lysate obtained from hBMSC cultured on YSZ wafers with osteogenic media, or hBMSC cultured on glass with osteogenic media (positive control), were elevated above ALP activity of cell lysate obtained from hBMSC cultured on glass in the absence of osteogenic supplements (negative control), indicating differentiation to the osteocyte lineage is taking place. ALP is expressed early during differentiation but declines at the later stages of osteogenic differentiation.[20] Because this study investigated specific timepoints, the exact timepoint of the ALP expression peak cannot be identified so elevated ALP levels per cell only determine that osteogenic differentiation is occurring.

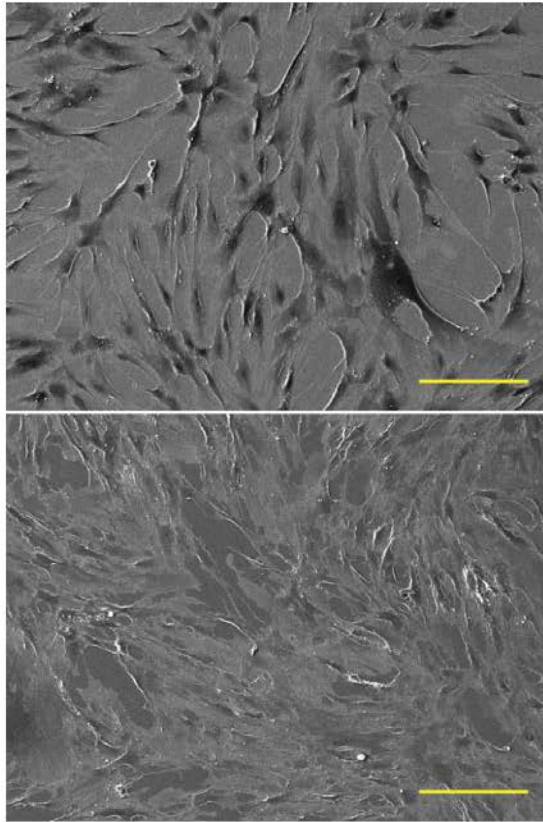


Figure 4 – Scanning electron micrographs of a YSZ wafer with hBMSC (top), and tissue-culture treated polyester with hBMSC (bottom). Scale bar = 200 μm

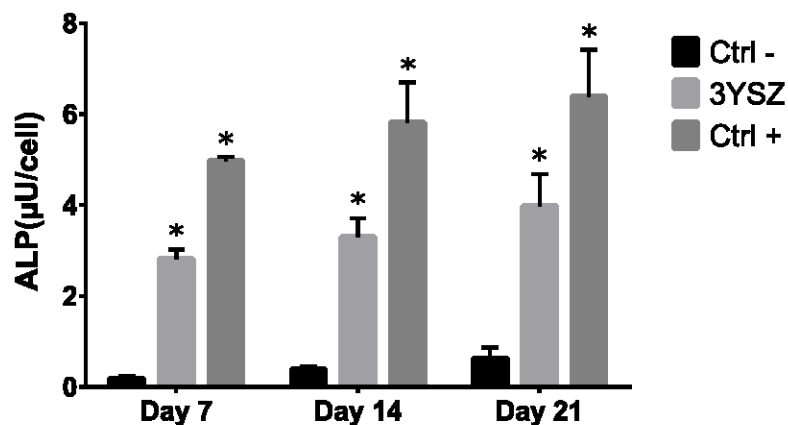


Figure 5 – ALP activity per cell hBMSC cultured on glass without osteogenic media (Ctrl -), YSZ wafer with osteogenic media, and glass with osteogenic media (Ctrl +). Asterisks (*) indicate mean values that are statistically significantly increased compared to the negative control. Values represent $\bar{x} \pm SD$ of $n = 3$ independent experimental replicates.

CONCLUSION:

Manufacturing methods of YSZ ceramics control the physical properties and inadvertent manufacturing defects can cause earlier than expected material failure during the intended use life of a device leading to adverse events in implanted orthopedic devices; maintenance of the meta-stable tetragonal phase necessary for the transformation-toughening properties of YSZ ceramics must be controlled during the manufacturing process by routine physicochemical characterization. For this reason, the present study confirmed the elemental composition, crystal structure, elastic modulus, hardness, and topography of the ceramic fabricated with a new manufacturing method was consistent with a YSZ ceramic with purely tetragonal crystal structure. In addition, the YSZ wafers maintained cytocompatibility and supported hBMSC osteogenic differentiation and would be suitable as a bone implant material.

ACKNOWLEDGMENTS:

The authors acknowledge Charles Mooney (AFM), Fred Stevie (XPS), Phillip Strader (nanoindentation), and Ching-Chang Chung (XRD) from North Carolina State University Advanced Characterization Facility for their expertise.

DISCLAIMER:

The findings and conclusions in this paper have not been formally disseminated by the Food and Drug Administration and should not be construed to represent any agency determination or policy. The mention of commercial products, their sources, or their use in connection with material reported herein is not to be construed as either an actual or implied endorsement of such products by Department of Health and Human Services.

References:

- [1] Takamura, K., K. Hayashi, N. Ishinishi, T. Yamada, and Y. Sugioka, *J. Biomed. Mater. Res.* **28** (5), 583-589. (1994)
- [2] Covacci, V., N. Bruzzese, G. Maccauro, C. Andreassi, G.A. Ricci, C. Piconi, E. Marmo, W. Burger, and A. Cittadini, *Biomaterials.* **20** (4), 371-376. (1999)
- [3] Stout, M.M., B.K. Cook, D.D. Arola, H. Fong, A.J. Raigrodski, and A.M. Bollen, *Am J Orthod Dentofacial Orthop.* **151** (1), 63-73. (2017)
- [4] Ardlin, B.I., *Dental Materials.* **18** (8), 590-595. (2002)
- [5] Cales, B., *Clin Orthop Relat Res.* **379**, 94-112. (2000)
- [6] Berni, M., N. Lopomo, G. Marchiori, A. Gambardella, M. Boi, M. Bianchi, A. Visani, P. Pavan, A. Russo, and M. Marcacci, *Materials Science and Engineering: C.* **62**, 643-655. (2016)
- [7] Masonis, J.L., R.B. Boume, M.D. Ries, R.W. McCalden, A. Salehi, and D.C. Kelman, *The Journal of Arthroplasty.* **19** (7), 898-905. (2004)
- [8] Scott, H.G., *Journal of Materials Science.* **10** (9), 1527-1535. (1975)
- [9] Chevalier, J., S. Deville, E. Münch, R. Jullian, and F. Lair, *Biomaterials.* **25** (24), 5539-5545. (2004)
- [10] Kim, S.H., S. Singh, S.K. Oh, D.K. Lee, K.H. Lee, S. Shervin, M. Asadirad, V. Venkateswaran, K. Olenick, J.A. Olenick, S. Lee, J.S. Kwak, A. Mavrokefalos, and J. Ryou, *IEEE Electron Device Letters.* **37** (5), 615-617. (2016)
- [11] Gopalan, K.K., D. Rodrigo, B. Paulillo, K.K. Soni, and V. Pruneri, *Advanced Optical Materials.* **7** (2), 1800966. (2019)
- [12] Burlingame, N., *Accelerated Life Testing of Thin Ceramic Substrates.* 2014(unpublished work).
- [13] Heshmatpour, F., Z. Khodaiy, and R.B. Aghakhanpour, *Powder Technology.* **224**, 12-18. (2012)
- [14] Viuzzi, C., J.-P. Bonino, F. Ansart, and A. Barnabé, *Journal of Alloys and Compounds.* **452** (2), 377-383. (2008)
- [15] Barad, C., G. Shekel, M. Shandalov, H. Hayun, G. Kimmel, D. Shamir, and Y. Gelbstein, *Materials.* **10** (12), 1440. (2017)
- [16] Moulder, J., W. Stickle, P. Sobol, and K. Bomben, *Handbook of X-ray Photoelectron Spectroscopy*, ed. J. Chastain. (Perkin-Elmer Corporation, Eden Prairie, Minnesota, 1992).
- [17] Adams, J.W., R. Ruh, and K.S. Mazdīyasni, *Journal of the American Ceramic Society.* **80** (4), 903-908. (1997)
- [18] Stollberg, D.W., J.M. Hampikian, L. Riestler, and W.B. Carter, *Materials Science and Engineering: A.* **359** (1), 112-118. (2003)
- [19] Tong, H., C.B. Tanaka, M.R. Kaizer, and Y. Zhang, *Ceramics international.* **42** (1 Pt B), 1077-1085. (2016)
- [20] E Golub, E. and K. Boesze-Battaglia, *Current Opinion in Orthopedics.* **18** (5), 444-448. (2007)

CHAPTER 9 - Physical characterization and in vitro evaluation of 3D printed hydroxyapatite, tricalcium phosphate, zirconia, alumina, and SiAlON structures made by lithographic ceramic manufacturing

Alexander K. Nguyen^{1,2}, Peter L. Goering², Shelby A. Skoog², and Roger J. Narayan¹

1. UNC/NCSU Joint Department of Biomedical Engineering, North Carolina State University, Raleigh, NC
2. Division of Biology Chemistry and Materials Science, US Food and Drug Administration, Silver Spring, MD

Reference: Nguyen, A.K.; Goering, P.L.; Skoog, S.A.; Narayan, R.J. Physical characterization and in vitro evaluation of 3D printed hydroxyapatite, tricalcium phosphate, zirconia, alumina, and SiAlON structures made by lithographic ceramic manufacturing. *MRS Advances* **2020**, 10.1557/adv.2020.229, 1-10, doi:10.1557/adv.2020.229.

Abstract

In this study, lithographic ceramic manufacturing was used to create solid chips out of hydroxyapatite, tricalcium phosphate, zirconia, alumina, and SiAlON ceramic. X-ray powder diffraction of each material confirmed that the chips were crystalline, with little amorphous character that could result from remaining polymeric binder, and were composed entirely out of the ceramic feedstock. Surface morphologies and roughnesses were characterized using atomic force microscopy. Human bone marrow stem cells cultured with osteogenic supplements on each material type expressed alkaline phosphatase levels, an early marker of osteogenic differentiation, on par with cells cultured on a glass control. However, cells cultured on the tricalcium phosphate-containing material expressed lower levels of ALP suggesting that osteoinduction was impaired on this material. Further analyses should be conducted with these materials to identify underlying issues of the combination of material and analysis method.

Introduction

As noted by Schwentenwein et al., ceramic parts created by conventional 3D printing approaches such as selective laser sintering often suffer from insufficient densities and poor mechanical properties [286]. A vat photopolymerization-based 3D printing approach known as lithographic ceramic manufacturing (LCM) from Lithoz GmbH (Vienna, Austria) has been developed to 3D print bioceramic parts [287]. Unlike other 3D printing approaches, vat polymerization-based 3D printing methods are known for providing parts with superior mechanical properties and surface quality, a high level of precision and homogeneity, and isotropic microstructure [288].

In LCM, the photoactive slurry is solidified in a layer-by-layer manner by exposure to blue light from a light emitting diode, which is patterned by a digital micromirror device. The photoactive slurry used in LCM includes a ceramic powder with particle size in the range of 0.01-50 μm , which is uniformly dispersed in a matrix containing a commercial acrylate- or methacrylate-based monomer, nonreactive organic diluents, dispersing agent, organic solvent, inert light absorber, and photoinitiator.

Unlike many other 3D printing approaches, the part in LCM is built in an “upside-down” orientation. The “upside down” build orientation significantly reduces the amount of slurry that is used in the 3D printing process. Since nearly all of the precursor material that is fed into the instrument is solidified, the LCM process is efficient in terms of resource utilization and cost [288].

The 3D printing process involves the following steps: (a) a thin layer of photoactive slurry is coated on the transparent vat, (b) the building platform approaches the vat, leaving a micrometer-level gap for the photoactive slurry, (c) a recoating system that includes a static wiper blade and a rotating vat is used to spread a fresh layer of the photoactive slurry and create

a thin slurry film, and (d) a pattern of blue LED light from the digital micromirror device is used to selectively polymerize regions of the photoactive slurry layer. Since the bottom of the vat is transparent, a light source can illuminate the photoactive slurry through the rotating vat from below. The cured layer then becomes attached to the building platform. The building platform, which is located above the vat, subsequently moves upwards to polymerize the next layer of photoactive slurry. The steps mentioned above are repeated until the 3D printing process is completed.

The resulting green body is a composite that consists of ceramic particles held together by the photoactive polymer matrix [289]. This part is then cleaned with pressurized air and LithaSol 20 (Lithoz GmbH, Vienna, Austria) solvent, which dissolves the slurry without damaging the photopolymerized part. After cleaning, the green part then undergoes a conventional ceramic forming thermal treatment to (a) remove the solvent, (b) decompose the polymeric binder, as well as (c) densify and sinter the remaining material. The thermal treatment leaves no residual organic component in the 3D printed parts. After the thermal treatment, the 3D printed part exhibits high density, high strength, and similar mechanical properties to ceramic parts made from powder precursors using conventional approaches [288]. For example, zirconia parts made by LCM show high density (>99.8 % relative density) [288]. Other benefits of the LCM process include the ability to prepare implants with complex shapes otherwise impossible with other fabrication methods such as CNC milling, and high geometric fidelity to the initial design. LCM is able to prepare geometries similar to orthopedic implants prepared by stereolithography [290-292] but composed out of ceramics currently used clinically.

Several researchers have previously examined medical applications for LCM technology. For example, Chen et al. showed that tricalcium phosphate (TCP)-based scaffolds successfully

regenerated bone and bridged a bony defect over four weeks in a noncritical-size defect that was created in a rabbit calvarium [287]. However, the conventionally-produced titanium scaffold showed better functionality and mechanical stability versus the TCP scaffold for a critical-size defect [287]. Ghayor and Weber showed that 3D printed TCP scaffolds in a rabbit calvarial bone defect model provided optimal osteoconductivity with pore diameters between 0.7-1.2 mm and bottlenecks between 0.5-1.2 mm [289].

The objective of this study was to evaluate additional LCM materials for potential use in orthopedic devices. LCM was used to create 10 mm diameter chips with a thickness of 1.5 mm out of various ceramic materials. X-ray diffraction was used to evaluate the composition of the materials. *In vitro* assays were performed with commercially-obtained human bone marrow-derived stem cells cultured on the LCM chips and in the presence of osteogenic supplements; alkaline phosphatase (ALP) levels, an early marker of osteogenic differentiation, were assessed, to detect any effect on osteogenic differentiation.

Methods

LCM chip processing and sterilization LCM of 10 mm diameter, 1.5 mm thick chips of eight different Lithoz materials where the primary ceramic components were 1) alumina-toughened zirconia (ATZ), 2) 3 mol% yttria-stabilized zirconia (3YSZ), 3) zirconia-toughened alumina (ZTA), 4) 99.99% purity aluminum oxide (Al_2O_3 99.99%), 5) 99.8% purity aluminum oxide (Al_2O_3 99.8%), 6) SiAlON, 7) hydroxyapatite (HA), and 8) TCP (Lithoz GmbH, Vienna, Austria) was performed as described previously [286, 288]. In brief, a ceramic slurry composed primarily of ceramic particles (typically 75 – 85% w/w) and a liquid methacrylate-based photocrosslinkable resin were additively manufactured on a CeraFab 7500 lithography ceramic manufacturing printer (Lithoz GmbH, Vienna, Austria). A LED light engine coupled with a

digital micromirror chip projects a cross-section of the object onto the bottom of a photopolymer vat, adhering the layer onto the build platform. Subsequent layers are produced by peeling the build platform off the bottom, blade coating additional slurry, then contacting the structure to the vat bottom before additional illumination takes place. The ceramic green body is heated in a debinding furnace to 900 °C to remove the acrylate component, then sintered at a temperature between 1300-1750 °C (depending on the requirements of the different ceramics) to produce the final structure.

Physical Characterization X-ray diffraction (XRD) analysis was used to determine the chemical composition and crystal structure of each ceramic type by peak-matching with reference spectra from the International Centre for Diffraction Data (ICDD) Powder Diffraction File (PDF) database. All samples were scanned from $2\theta = 0$ to 90° on a Panalytical Empyrean X-ray Diffractometer (Malvern PANalytical, Royston, UK) using Cu K- α 1 X-ray radiation. Signal was collected using a 0.026 degree step size at 96 sec per step. XRD spectra were matched with reference spectra in the ICDD PDF4+ database (ICDD, Newtown Square, PA) using the HighScore Plus software (Malvern PANalytical, Royston, UK). The topography of each sample was imaged on an Asylum MFP-3D (Asylum Research, Morrisville, NC) Atomic Force Microscope. In the AFM analysis, $10 \times 10 \mu\text{m}$ and $2 \times 2 \mu\text{m}$ regions were scanned using 256 scan lines measuring at 256 points per line at a 0.75 Hz scan rate.

Cell Culture Nine chips of each material type and 18 x 10 mm square borosilicate glass coverslips were washed 2x in isopropanol for 2 minutes per wash, 1x in acetone, and then autoclaved before biological assays. Human bone marrow-derived stem cells (hBMSC) were cultured in mesenchymal stem cell basal medium with the bone marrow-derived mesenchymal stem cell growth kit (ATCC, Manassas, VA). hBMSC at passage 5 were seeded at a density of

3.1×10^4 cells/cm² on the ceramic chips and glass coverslips; ATCC recommends passage 6 as the maximum passage for osteogenic differentiation procedures. All samples were incubated for 4 hr for cell attachment before the media was replaced with the Osteocyte Differentiation Tool (PCS-500-052, ATCC, Manassas, VA) which are media containing osteogenic supplements (OS). Samples were incubated at 37 °C, 5% CO₂, and 95% humidity.

Collection of Cell Lysate for PicoGreen® and ALP Liquicolor® Assays During days 7, 14, and 21, samples were removed from the plate, rinsed 3x in excess PBS, and placed into a new 24-well plate to minimize interference from cells attached to the plate surfaces and from serum in the cell culture medium. hBMSC were lysed in 0.5 mL of 0.2% w/w Triton X-100 (Sigma Aldrich, St. Louis, MO) in ultrapure water (>18.2 MΩ·cm; Millipore, St. Louis, MO) for 30 minutes on a shaker. The resulting cell lysate was used immediately in both the PicoGreen® dsDNA assay (Thermo Fisher Scientific, Waltham, MA) and the Alkaline Phosphatase Liquicolor® assay (EKF Diagnostics, Boerne, TX).

Cell lysate generated from a solution of known cell density was produced to correlate dsDNA content in this assay to cell number. hBMSC were trypsinized (Sigma Aldrich, St. Louis, MO) and centrifuged at 200 x g for 5 minutes and the supernatant discarded. The pellet was resuspended in 10 mL of ultrapure water and the cell density was measured to be 2.16×10^5 cells/mL. Triton X-100 was added to produce a 0.2% w/w solution and then the solution was agitated for 30 minutes. Cell lysate was aliquoted and stored at -70°C until use for the cell ladder control. For each timepoint, cell lysate was diluted in appropriate volumes of 0.2% Triton X-100 to produce 8 solutions ranging from 0 to 1.0×10^5 cells/mL.

Cell lysate (50 µL) from hBMSC cultured on the 8 materials, glass control without osteogenic supplements (OS-), glass control with osteogenic supplements (OS+), and 8 cell

ladder solutions were transferred in triplicate to a 96-well plate. PicoGreen® dye working solution (50 µL) in TE buffer (Quality Biological Inc., Gaithersburg, MD) was added to each well and stained for at least 5 minutes before reading in a fluorescence plate reader at 480 nm and 500 nm excitation and emission wavelengths respectively. Final concentrations of Triton X-100 would be 0.1% in all wells during staining which is the maximum acceptable concentration for the PicoGreen® assay as specified by the manufacturer.

For the ALP assay, SER-T-FY Level 1 Control Serum (EKF Diagnostics Inc., Boerne, TX) from lot 24474 was rehydrated in 5.000 g of ultrapure water on an analytical balance. Serum was diluted 1:1 with 0.4% Triton X-100 in ultrapure water as the serum control containing 48 U/L ALP. Cell lysate (50 µL) from the 8 materials, OS- glass control, OS+ glass control, 50 µL of the serum solution, and blank 0.2% Triton X-100 were transferred in triplicate to a 96-well plate. Liquicolor® dye solution (50 µL) was added and immediately measured in a plate reader using absorbance at 405 nm four times per minute for 15 minutes. The change in absorbance over time was correlated to the change in serum control wells to calculate the ALP activity of lysate from each sample.

For cell lysate from each sample, the ALP activity measured by the ALP Liquicolor® assay was normalized to cell count determined by the PicoGreen® assay. Three independent replicates were performed and the detection of ALP expression increase was determined by comparing the normalized ALP signal for cell lysate from each sample versus the signal from the corresponding OS- and OS+ glass controls for that timepoint using a two-tailed Student's t-test; results were deemed statistically significant at the $p < 0.05$ level.

Results and Discussion

XRD spectra of each ceramic material are presented in Figure 9.1. ATZ, 3YSZ, and ZTA all contained tetragonal ZrO_2 (Powder Diffraction File# 00-050-1089). ATZ, ZTA, Al_2O_3 99.99%, and Al_2O_3 99.8% contained α - Al_2O_3 (Powder Diffraction File# 04-007-4873). LithaNite 720 contained β -SiAlON [293, 294]. HA-MS8F and TCP-MS8F were HA (PDF# 04-014-8416) and TCP (Powder Diffraction File# 04-001-7220) respectively. All ceramics except for ATZ had excellent fits with their respective reference spectra in peak location and intensity. The β -SiAlON spectra agree with previous data collected on this material including peaks at 29.5° and 31.1° which were attributed to Y_2O_3 and Si_3N_4 respectively [24]. A similar diffraction pattern is also identified in the Joint Committee on Powder Diffraction Standards (JCPDS) card 48-1615 as β -SiAlON [293] and more specifically as either Si_5AlON_7 or $\text{Si}_4\text{Al}_2\text{O}_2\text{N}_6$ [294]. Aluminum oxide peaks were present but almost undetectable in ATZ, suggesting a very low proportion of this material. XRD analysis confirms that all materials except for ZTA were primarily composed of a single crystalline material with low proportions of sintering aids; ZTA contains both tetragonal ZrO_2 and rhombohedral Al_2O_3 with no other detected peaks.

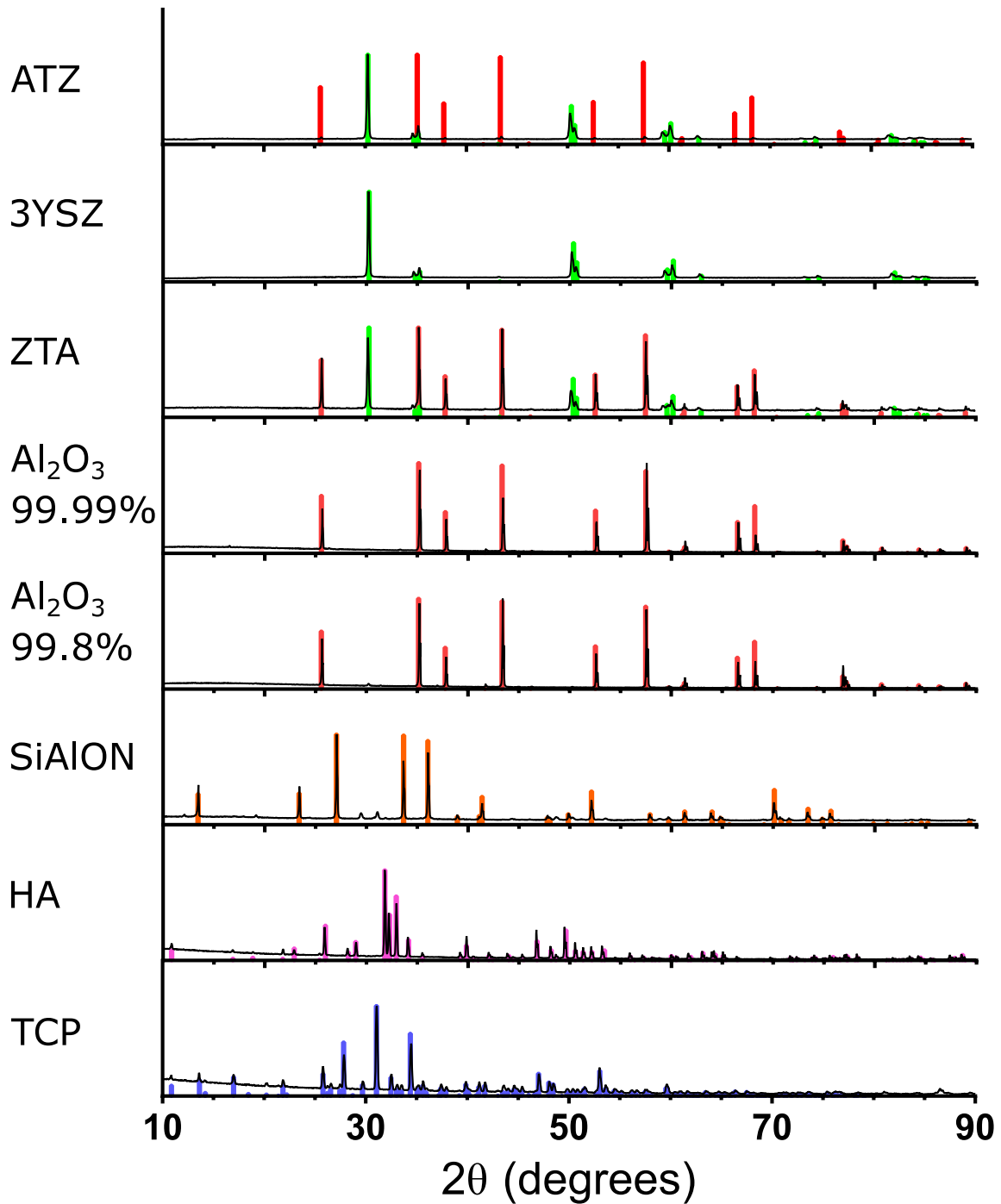


Figure 9.1 - XRD spectra (black line) of the LCM ceramics after sintering. Colored highlights correspond to the reference spectra of tetragonal zirconia (green, ZrO_2 , Powder Diffraction File# 00-050-1089), alumina (red, $\alpha\text{-Al}_2\text{O}_3$, Powder Diffraction File# 04-007-4873), silicon nitride (orange, $\beta\text{-Si}_3\text{N}_4$, Powder Diffraction File# 00-033-1160), HA (purple, $\text{Ca}_5(\text{PO}_4)_3(\text{OH})$, Powder Diffraction File# 04-014-8416), and TCP (blue, $\text{Ca}_3(\text{PO}_4)_2$, Powder Diffraction File# 04-001-7220).

AFM images (Figure 9.2) of the ceramic materials revealed widely varying grain morphologies and surface roughness; composition and RMS roughness values for each ceramic are summarized in Table 9.1. The RMS roughness values from 10 x 10 μm and 2 x 2 μm regions of each material were measured from AFM data. ATZ and 3YSZ, both primarily yttria-stabilized zirconia, consisted of sub-micron grains and had similar RMS roughness when measured between the 10 μm and 2 μm regions.

Table 9.1 – Composition and RMS Roughness of Sintered LCM Ceramics

Material	Identified phases	RMS Roughness (nm)	
		10x10 μm Area	2x2 μm Area
ATZ	t-ZrO ₂	57	32
	α -Al ₂ O ₃		
3YSZ	t-ZrO ₂	111	104
ZTA	t-ZrO ₂	483	105
	α -Al ₂ O ₃		
Al ₂ O ₃ 99.99%	α -Al ₂ O ₃	199	6
Al ₂ O ₃ 99.8%	α -Al ₂ O ₃	489	17
SiAlON	β -Si ₃ N ₄	604	120
HA	Ca ₅ (PO ₄) ₃ (OH)	483	187
TCP	Ca ₃ (PO ₄) ₂	159	60

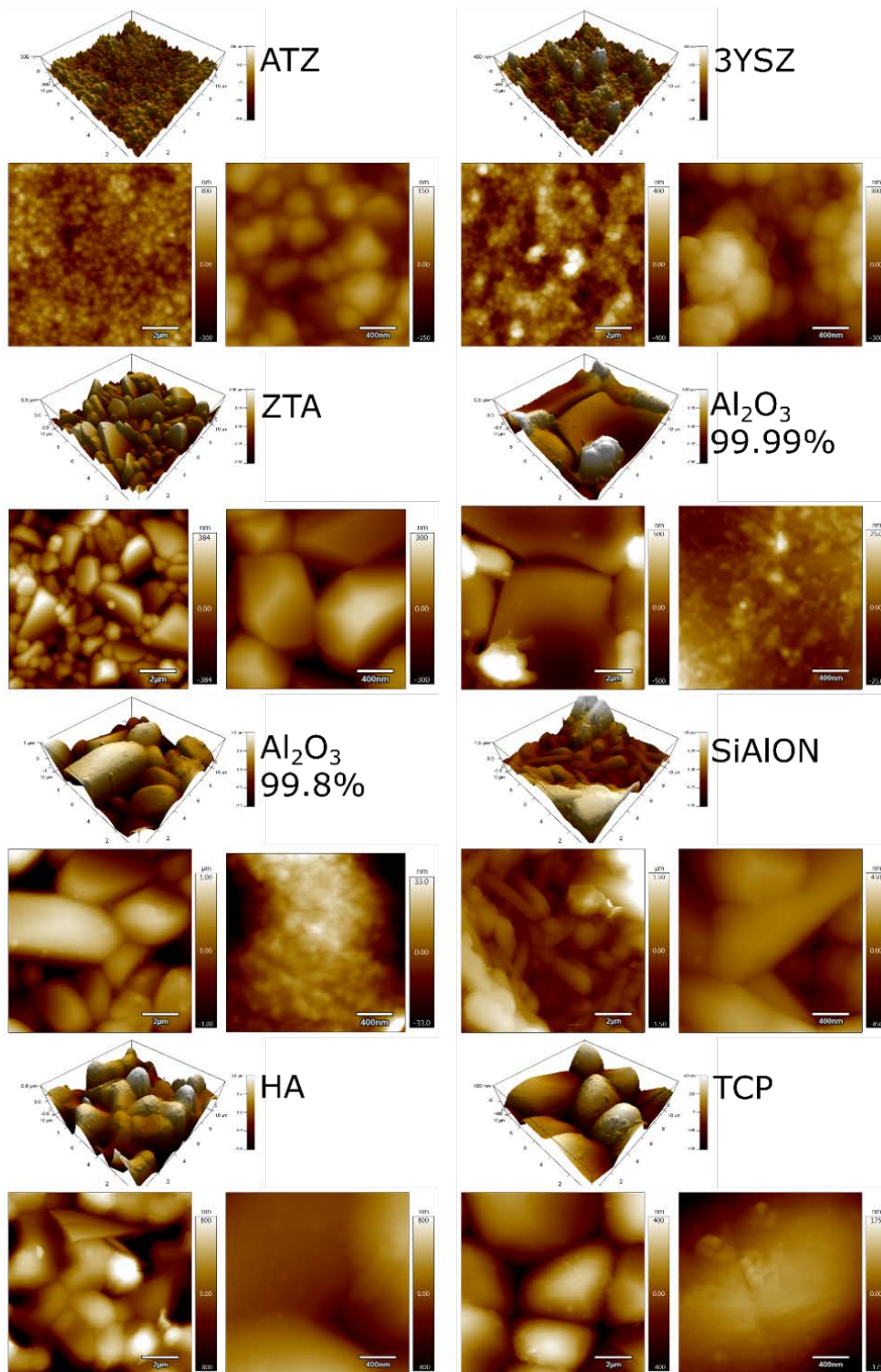


Figure 9.2 - 3D renderings and topographical maps from AFM data from the sintered LCM ceramics. Scale bars are 2 μm for the left image and 400 nm for the right image for each material. Roughness data is summarized in Table 9.1.

ALP was measured as an early marker of osteogenic differentiation; ALP expression normalized to cell count is depicted in Figure 9.3. hBMSC exposed to osteogenic supplements and grown on any surface exhibited elevated ALP levels compared to hBMSC cultured on glass in the absence of osteogenic supplements. However, hBMSC cultured on some of the materials exhibited different ALP levels when compared to hBMSC cultured on glass in the presence of osteogenic supplements.

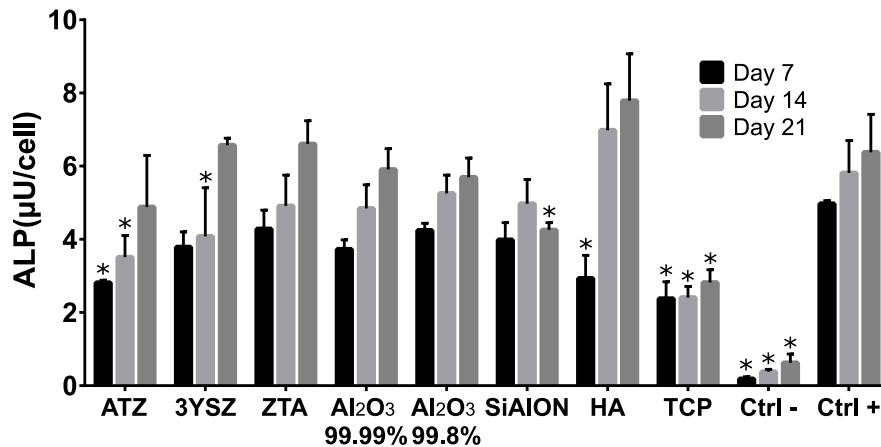


Figure 9.3 - ALP expression of hBMSC grown in the presence of osteogenic supplements and cultured on sintered LCM ceramics or glass and assayed at day 7 (black), day 14 (light gray), and day 21 (gray). ALP measured from the ALP Liquicolor® assay was normalized to cell count determined from the PicoGreen® assay. hBMSC cultured on borosilicate glass coverslips and grown in mesenchymal stem cell media and osteogenic media were used as the negative (Ctrl -) and positive (Ctrl +) controls respectively. Asterisks (*) represent values significantly different ($p < 0.05$) from the corresponding positive control at the same timepoint. Values represent the means and standard deviations of $N = 3$ independent replicates (except for ATZ day 14, which has $N = 2$).

Compared to hBMSC cultured on glass and exposed to osteogenic supplements, hBMSC on ATZ had lower ALP expression on day 7 and 14 but was not significantly different by day 21. hBMSC on 3YSZ had lower ALP expression on Day 14 although this timepoint had an outlier; statistics were calculated from $N = 2$ independent replicates instead of 3 as with all other groups. hBMSC on SiAlON had lower expression at Day 21 and TCP-MS8F had lowered ALP

expression at all timepoints. Thus, most materials did not have a significant effect on hBMSC osteoinduction except for TCP-MS8F, the material composed of TCP. TCP is noted in the literature to be an osteoinductive material [28, 295] so other processes may be responsible for the drop in ALP expression.

One possible factor for the reduced ALP expression for the TCP material could be the cleaning of the chips with isopropanol and acetone before sterilization which may have remained after autoclaving. The TCP material may be more porous than the other materials and may have absorbed solvent. Acetone, in particular, may have effects on the bone marrow and may cause bone loss. Recent studies investigating the effects of a ketogenic diet have noted lower bone mineral content in rats, [296] mice, [297] and humans [298]; acetone is a metabolite generated during ketosis and can be used as a biomarker of ketoacidosis [299]. A study investigating the effects of acetone in drinking water noted bone marrow hypoplasia in rats dosed with high levels of acetone [300]. In this study, differences in surface morphology or porosity were not controlled, so it is possible that residual acetone from the cleaning process may have caused a drop in ALP expression.

ALP is linked with mineralization via multiple possible mechanisms such as the generation of inorganic phosphates for HA growth or the hydrolysis of pyrophosphates which inhibit HA growth [301] so the reduction of this marker could have a negative effect on osseointegration of orthopedic implants. One example case investigated by Bonsignore et al. found that machine oil contamination of Ti-6AL-4V implants inhibited ALP expression among other osteogenic markers in MC3T3-E1 pre-osteoblasts and was also associated with reduced bone-implant contact and pullout force in screws implanted in a murine model [302].

Surface roughness also affects ALP as a marker of osteogenic differentiation and could have played a role in ALP expression in this study. Faia-Torres et al. investigated the effects of surface roughness on osteogenic differentiation of human primary bone marrow stem cells on polycaprolactone substrates in the presence and absence of OS; R_a values around 2.1 – 3.1 μm [303] and 0.93 – 1.53 μm [304] determined using optical profilometry were found to increase ALP expression along with other markers of osteogenic differentiation. These roughness values may be underestimated compared to values measured using AFM [305]. Thus, the materials in this study with R_{rms} values one or two orders of magnitude lower than values determined by Faia-Torres et al. should be far under the optimal roughness, so roughness in this study should not be a significant factor in ALP expression. No correlation between surface roughness measured from either the 10 μm or 2 μm area with ALP expression from a linear regression was observed with R^2 values of 0.06 and 0.19 respectively.

Conclusions

LCM and subsequent sintering of additively manufactured ceramic parts yield pure crystalline ceramic parts with little evidence of residual polymeric binder and are highly similar to their respective feedstock material composition. When potentially applied to orthopedic implants, all tested materials except for TCP were found to not interfere with osteogenic differentiation. As TCP is known to be an osteoconductive material, an unidentified property of the finished TCP ceramic or steps during handling causes a drop in early osteogenic differentiation markers. Future work should be focused on determining which post-processing parameters and sterilization methods have significant effects on osteoinduction.



Physical characterization and in vitro evaluation of 3D printed hydroxyapatite, tricalcium phosphate, zirconia, alumina, and SiAlON structures made by lithographic ceramic manufacturing

Alexander K. Nguyen^{1,2}, Peter L. Goering², Shelby A. Skoog², Roger J. Narayan^{1*}

¹ Joint UNC/NCSU Department of Biomedical Engineering, North Carolina State University, Raleigh, North Carolina, United States

² Center for Devices and Radiological Health, U.S. Food and Drug Administration, Silver Spring, MD

Abstract

In this study, lithographic ceramic manufacturing was used to create solid chips out of hydroxyapatite, tricalcium phosphate, zirconia, alumina, and SiAlON ceramic. X-ray powder diffraction of each material confirmed that the chips were crystalline, with little amorphous character that could result from remaining polymeric binder, and were composed entirely out of the ceramic feedstock. Surface morphologies and roughnesses were characterized using atomic force microscopy. Human bone marrow stem cells cultured with osteogenic supplements on each material type expressed alkaline phosphatase levels, an early marker of osteogenic differentiation, on par with cells cultured on a glass control. However, cells cultured on the tricalcium phosphate-containing material expressed lower levels of ALP suggesting that osteoinduction was impaired on this material. Further analyses should be conducted with these materials to identify underlying issues of the combination of material and analysis method.

INTRODUCTION:

As noted by Schwentenwein et al., ceramic parts created by conventional 3D printing approaches such as selective laser sintering often suffer from insufficient densities and poor mechanical properties [1]. A vat photopolymerization-based 3D printing approach known as lithographic ceramic manufacturing (LCM) from Lithoz

GmbH (Vienna, Austria) has been developed to 3D print bioceramic parts [2]. Unlike other 3D printing approaches, vat polymerization-based 3D printing methods are known for providing parts with superior mechanical properties and surface quality, a high level of precision and homogeneity, and isotropic microstructure [3].

In LCM, the photoactive slurry is solidified in a layer-by-layer manner by exposure to blue light from a light emitting diode, which is patterned by a digital micromirror device. The photoactive slurry used in LCM includes a ceramic powder with particle size in the range of 0.01-50 μm , which is uniformly dispersed in a matrix containing a commercial acrylate- or methacrylate-based monomer, nonreactive organic diluents, dispersing agent, organic solvent, inert light absorber, and photoinitiator.

Unlike many other 3D printing approaches, the part in LCM is built in an “upside-down” orientation. The “upside down” build orientation significantly reduces the amount of slurry that is used in the 3D printing process. Since nearly all of the precursor material that is fed into the instrument is solidified, the LCM process is efficient in terms of resource utilization and cost [3].

The 3D printing process involves the following steps: (a) a thin layer of photoactive slurry is coated on the transparent vat, (b) the building platform approaches the vat, leaving a micrometer-level gap for the photoactive slurry, (c) a recoating system that includes a static wiper blade and a rotating vat is used to spread a fresh layer of the photoactive slurry and create a thin slurry film, and (d) a pattern of blue LED light from the digital micromirror device is used to selectively polymerize regions of the photoactive slurry layer. Since the bottom of the vat is transparent, a light source can illuminate the photoactive slurry through the rotating vat from below. The cured layer then becomes attached to the building platform. The building platform, which is located above the vat, subsequently moves upwards to polymerize the next layer of photoactive slurry. The steps mentioned above are repeated until the 3D printing process is completed.

The resulting green body is a composite that consists of ceramic particles held together by the photoactive polymer matrix [4]. This part is then cleaned with pressurized air and LithaSol 20 (Lithoz GmbH, Vienna, Austria) solvent, which dissolves the slurry without damaging the photopolymerized part. After cleaning, the green part then undergoes a conventional ceramic forming thermal treatment to (a) remove the solvent, (b) decompose the polymeric binder, as well as (c) densify and sinter the remaining material. The thermal treatment leaves no residual organic component in the 3D printed parts. After the thermal treatment, the 3D printed part exhibits high density, high strength, and similar mechanical properties to ceramic parts made from powder precursors using conventional approaches [3]. For example, zirconia parts made by LCM show high density (>99.8 % relative density) [3]. Other benefits of the LCM process include the ability to prepare implants with complex shapes otherwise impossible with other fabrication methods (e.g., CNC milling), and high geometric fidelity to the initial design. LCM is able to fabricate structures with geometries similar to orthopedic implants that are commonly fabricated using stereolithography [5-7]; with LCM, the structures can be created out of clinically-used ceramics.

Several researchers have previously examined medical applications for LCM technology. For example, Chen et al. showed that tricalcium phosphate (TCP)-based scaffolds successfully regenerated bone and bridged a bony defect over four weeks in a noncritical-size defect that was created in a rabbit calvarium [2]. However, the conventionally-produced titanium scaffold showed better functionality and mechanical stability versus the TCP scaffold for a critical-size defect [2]. Ghayor and Weber showed that 3D printed TCP scaffolds in a rabbit calvarial bone defect model provided optimal osteoconductivity with pore diameters between 0.7-1.2 mm and bottlenecks between 0.5-1.2 mm [4].

The objective of this study was to evaluate additional LCM materials for potential use in orthopedic devices. LCM was used to create 10 mm diameter chips with a thickness of 1.5 mm out of various ceramic materials. X-ray diffraction was used to evaluate the composition of the materials. *In vitro* assays were performed with commercially-obtained human bone marrow-derived stem cells cultured on the LCM chips and in the presence of osteogenic supplements; alkaline phosphatase (ALP) levels, an early marker of osteogenic differentiation, were assessed to detect any effect on osteogenic differentiation.

METHODS:

LCM Chip Processing and Sterilization

LCM of 10 mm diameter, 1.5 mm thick chips of eight different Lithoz materials where the primary ceramic components were 1) alumina-toughened zirconia (ATZ), 2) 3 mol% yttria-stabilized zirconia (3YSZ), 3) zirconia-toughened alumina (ZTA), 4) 99.99% purity aluminum oxide (Al_2O_3 99.99%), 5) 99.8% purity aluminum oxide (Al_2O_3 99.8%), 6) SiAlON, 7) hydroxyapatite (HA), and 8) TCP (Lithoz GmbH, Vienna, Austria) was performed as described previously [1, 3]. In brief, a ceramic slurry composed primarily of ceramic particles (typically 75 – 85% w/w) and a liquid methacrylate-based photocrosslinkable resin were additively manufactured on a CeraFab 7500 lithography ceramic manufacturing printer (Lithoz GmbH, Vienna, Austria). A LED light engine coupled with a digital micromirror chip projects a cross-section of the object onto the bottom of a photopolymer vat, adhering the layer onto the build platform. Subsequent layers are produced by peeling the build platform off the bottom, blade coating additional slurry, then contacting the structure to the vat bottom before additional illumination takes place. The ceramic green body is heated in a debinding furnace to 900 °C to remove the acrylate component, then sintered at a temperature between 1300-1750 °C (depending on the requirements of the different ceramics) to produce the final structure.

Physical Characterization

X-ray diffraction (XRD) analysis was used to determine the chemical composition and crystal structure of each ceramic type by peak-matching with reference spectra from the International Centre for Diffraction Data (ICDD) Powder Diffraction File (PDF) database. All samples were scanned from $2\theta = 0$ to 90° on a Panalytical Empyrean X-ray Diffractometer (Malvern PANalytical, Royston, UK) using Cu K- α X-ray radiation. Signal was collected using a 0.026 degree step size at 96 sec per step. XRD spectra were matched with reference spectra in the ICDD PDF4+ database (ICDD, Newtown Square, PA) using the HighScore Plus software (Malvern PANalytical, Royston, UK). The topography of each sample was imaged on an Asylum MFP-3D (Asylum Research, Morrisville, NC) Atomic Force Microscope. In the AFM analysis, $10 \times 10 \mu\text{m}$ and $2 \times 2 \mu\text{m}$ regions were scanned using 256 scan lines measuring at 256 points per line at a 0.75 Hz scan rate.

Cell Culture

Nine chips of each material type and 18 x 10 mm square borosilicate glass coverslips were washed 2x in isopropanol for 2 minutes per wash, 1x in acetone, and then autoclaved before biological assays. Human bone marrow-derived stem cells

(hBMSC) were cultured in mesenchymal stem cell basal medium with the bone marrow-derived mesenchymal stem cell growth kit (ATCC, Manassas, VA). hBMSC at passage 5 were seeded at a density of 3.1×10^4 cells/cm² on the ceramic chips and glass coverslips; ATCC recommends passage 6 as the maximum passage for osteogenic differentiation procedures. All samples were incubated for 4 hr for cell attachment before the media was replaced with the Osteocyte Differentiation Tool (PCS-500-052, ATCC, Manassas, VA) which are media containing osteogenic supplements (OS). Samples were incubated at 37 °C, 5% CO₂, and 95% humidity.

Collection of Cell Lysate for PicoGreen® and ALP Liquicolor® Assays

During days 7, 14, and 21, samples were removed from the plate, rinsed 3x in excess PBS, and placed into a new 24-well plate to minimize interference from cells attached to the plate surfaces and from serum in the cell culture medium. hBMSC were lysed in 0.5 mL of 0.2% w/w Triton X-100 (Sigma Aldrich, St. Louis, MO) in ultrapure water (>18.2 MΩ-cm; Millipore, St. Louis, MO) for 30 minutes on a shaker. The resulting cell lysate was used immediately in both the PicoGreen® dsDNA assay (Thermo Fisher Scientific, Waltham, MA) and the Alkaline Phosphatase Liquicolor® assay (EKF Diagnostics, Boerne, TX).

Cell lysate generated from a solution of known cell density was produced to correlate dsDNA content in this assay to cell number. hBMSC were trypsinized (Sigma Aldrich, St. Louis, MO) and centrifuged at 200 x g for 5 minutes and the supernatant discarded. The pellet was resuspended in 10 mL of ultrapure water and the cell density was measured to be 2.16×10^5 cells/mL. Triton X-100 was added to produce a 0.2% w/w solution and then the solution was agitated for 30 minutes. Cell lysate was aliquoted and stored at -70°C until use for the cell ladder control. For each timepoint, cell lysate was diluted in appropriate volumes of 0.2% Triton X-100 to produce 8 solutions ranging from 0 to 1.0×10^5 cells/mL.

Cell lysate (50 µL) from hBMSC cultured on the 8 materials, glass control without osteogenic supplements (OS-), glass control with osteogenic supplements (OS+), and 8 cell ladder solutions were transferred in triplicate to a 96-well plate. PicoGreen® dye working solution (50 µL) in TE buffer (Quality Biological Inc., Gaithersburg, MD) was added to each well and stained for at least 5 minutes before reading in a fluorescence plate reader at 480 nm and 500 nm excitation and emission wavelengths respectively. Final concentrations of Triton X-100 would be 0.1% in all wells during staining which is the maximum acceptable concentration for the PicoGreen® assay as specified by the manufacturer.

For the ALP assay, SER-T-FY Level 1 Control Serum (EKF Diagnostics Inc., Boerne, TX) from lot 24474 was rehydrated in 5.000 g of ultrapure water on an analytical balance. Serum was diluted 1:1 with 0.4% Triton X-100 in ultrapure water as the serum control containing 48 U/L ALP. Cell lysate (50 µL) from the 8 materials, OS-glass control, OS+ glass control, 50 µL of the serum solution, and blank 0.2% Triton X-100 were transferred in triplicate to a 96-well plate. Liquicolor® dye solution (50 µL) was added and immediately measured in a plate reader using absorbance at 405 nm four times per minute for 15 minutes. The change in absorbance over time was correlated to the change in serum control wells to calculate the ALP activity of lysate from each sample.

For cell lysate from each sample, the ALP activity measured by the ALP Liquicolor® assay was normalized to cell count determined by the PicoGreen® assay. Three independent replicates were performed and the detection of ALP expression increase was determined by comparing the normalized ALP signal for cell lysate from each sample versus the signal from the corresponding OS- and OS+ glass controls for

that timepoint using a two-tailed Student's t-test; results were deemed statistically significant at the $p < 0.05$ level.

RESULTS & DISCUSSION:

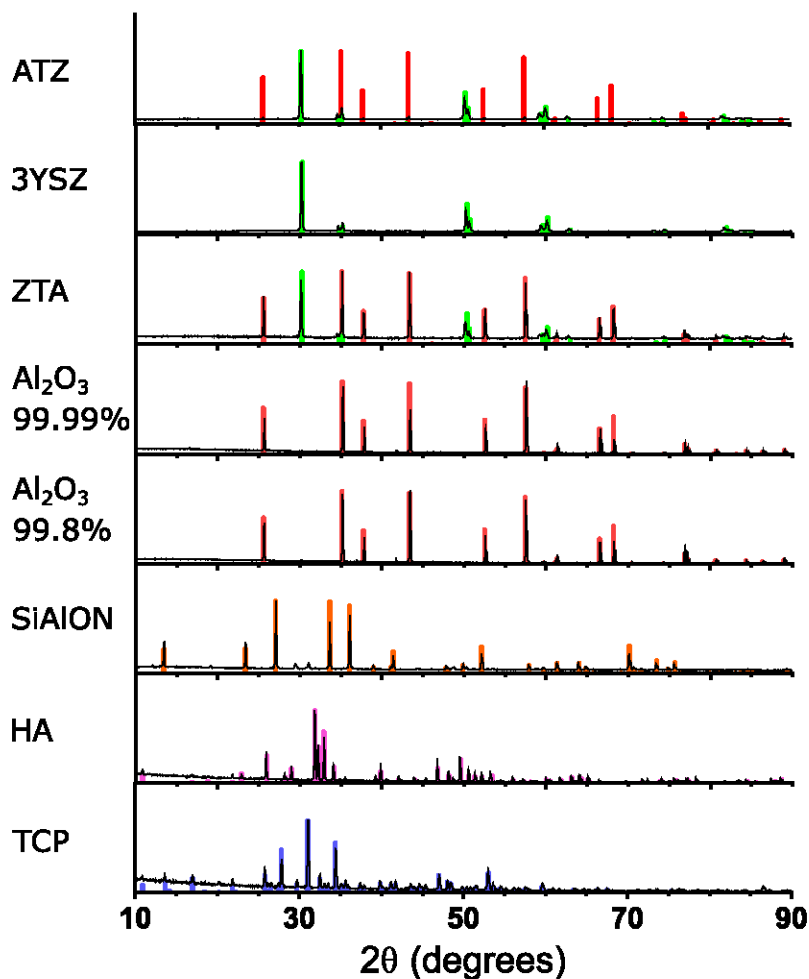


Figure 1 – XRD spectra (black line) of the LCM ceramics after sintering. Colored highlights correspond to the reference spectra of tetragonal zirconia (green, ZrO_2 , Powder Diffraction File# 00-050-1089), alumina (red, $\alpha\text{-Al}_2\text{O}_3$, Powder Diffraction File# 04-007-4873), silicon nitride (orange, $\beta\text{-Si}_3\text{N}_4$, Powder Diffraction File# 00-033-1160), HA (purple, $\text{Ca}_5(\text{PO}_4)_3(\text{OH})$, Powder Diffraction File# 04-014-8416), and TCP (blue, $\text{Ca}_3(\text{PO}_4)_2$, Powder Diffraction File# 04-001-7220).

XRD spectra of each ceramic material are presented in Figure 1. ATZ, 3YSZ, and ZTA all contained tetragonal ZrO_2 (Powder Diffraction File# 00-050-1089). ATZ, ZTA, Al_2O_3 99.99%, and Al_2O_3 99.8% contained $\alpha\text{-Al}_2\text{O}_3$ (Powder Diffraction File# 04-007-4873). LithaNite 720 contained $\beta\text{-SiAlON}$ [8, 9]. HA-MS8F and TCP-MS8F were

HA (PDF# 04-014-8416) and TCP (Powder Diffraction File# 04-001-7220) respectively. All ceramics except for ATZ had excellent fits with their respective reference spectra in peak location and intensity. The β -SiAlON spectra agree with previous data collected on this material, including peaks at 29.5° and 31.1° , which were attributed to Y_2O_3 and Si_3N_4 respectively [10]. A similar diffraction pattern is also identified in the Joint Committee on Powder Diffraction Standards (JCPDS) card 48-1615 as β -SiAlON [8] and more specifically as either Si_5AlON_7 or $Si_4Al_2O_2N_6$ [9]. Aluminum oxide peaks were present but almost undetectable in ATZ, suggesting a very low proportion of this material. XRD analysis confirms that all materials except for ZTA were primarily composed of a single crystalline material with low proportions of sintering aids; ZTA contains both tetragonal ZrO_2 and rhombohedral Al_2O_3 with no other detected peaks.

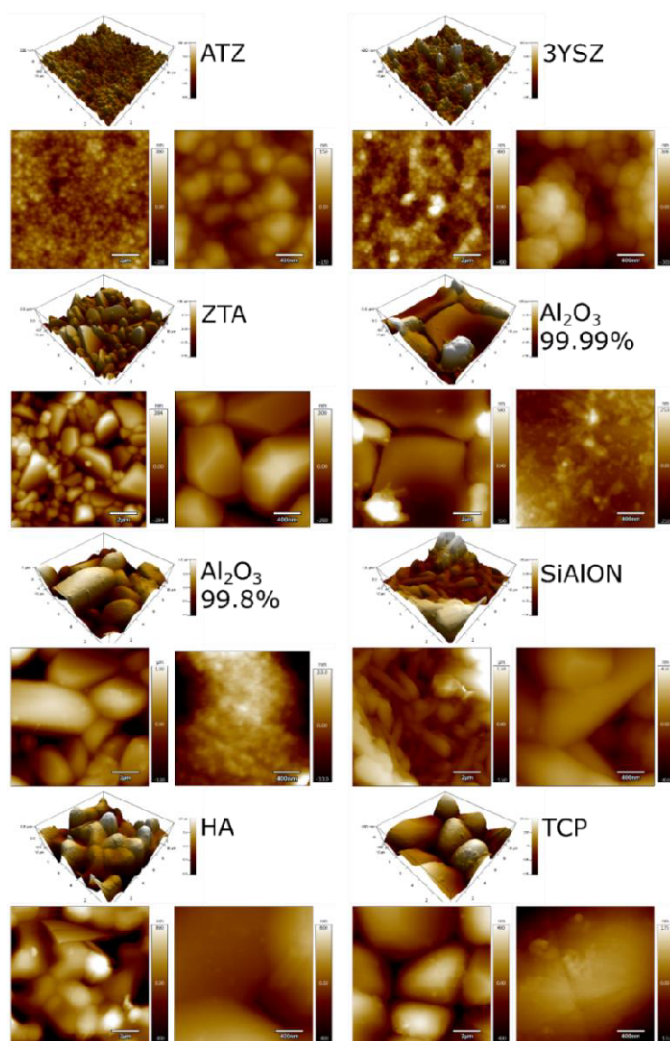


Figure 2 – 3D renderings and topographical maps from AFM data from the sintered LCM ceramics. Scale bars are $2\ \mu\text{m}$ for the left image and $400\ \text{nm}$ for the right image for each material. Roughness data is summarized in Table 1.

AFM images (Figure 2) of the ceramic materials revealed widely varying grain morphologies and surface roughness; composition and RMS roughness values for each ceramic are summarized in Table 1. The RMS roughness values from 10 x 10 μm and 2 x 2 μm regions of each material were measured from AFM data. ATZ and 3YSZ, both primarily yttria-stabilized zirconia, consisted of sub-micron grains and had similar RMS roughness when measured between the 10 μm and 2 μm regions.

Table 1 - Composition and RMS Roughness of Sintered LCM ceramics

Material	Identified phases	RMS Roughness (nm)	
		10x10 μm Area	2x2 μm Area
ATZ	t-ZrO ₂	57	32
	α -Al ₂ O ₃		
3YSZ	t-ZrO ₂	111	104
ZTA	t-ZrO ₂	483	105
	α -Al ₂ O ₃		
Al ₂ O ₃ 99.99%	α -Al ₂ O ₃	199	6
Al ₂ O ₃ 99.8%	α -Al ₂ O ₃	489	17
SiAlON	β -Si ₃ N ₄	604	120
HA	Ca ₅ (PO ₄) ₃ (OH)	483	187
TCP	Ca ₃ (PO ₄) ₂	159	60

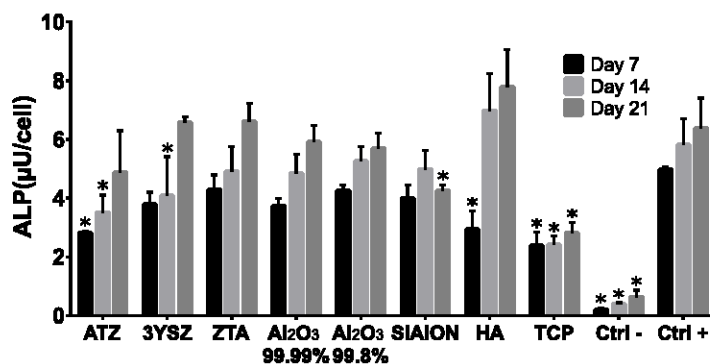


Figure 3 – ALP expression of hBMSC grown in the presence of osteogenic supplements and cultured on sintered LCM ceramics or glass and assayed at day 7 (black), day 14 (light gray), and day 21 (gray). ALP measured from the ALP Liqicolor® assay was normalized to cell count determined from the PicoGreen® assay. hBMSC cultured on borosilicate glass coverslips and grown in mesenchymal stem cell media and osteogenic media were used as the negative (Ctrl -) and positive (Ctrl +) controls respectively. Asterisks (*) represent values significantly different ($p < 0.05$) from the corresponding positive control at the same timepoint. Values represent the means and standard deviations of $N = 3$ independent replicates (except for ATZ day 14, which has $N = 2$).

ALP was measured as an early marker of osteogenic differentiation; ALP expression normalized to cell count is depicted in Figure 3. hBMSC exposed to osteogenic supplements and grown on any surface exhibited elevated ALP levels compared to hBMSC cultured on glass in the absence of osteogenic supplements. However, hBMSC cultured on some of the materials exhibited different ALP levels when compared to hBMSC cultured on glass in the presence of osteogenic supplements.

Compared to hBMSC cultured on glass and exposed to osteogenic supplements, hBMSC on ATZ had lower ALP expression on day 7 and 14 but was not significantly different by day 21. hBMSC on 3YSZ had lower ALP expression on Day 14 although this timepoint had an outlier; statistics were calculated from $N = 2$ independent replicates instead of 3 as with all other groups. hBMSC on SiAlON had lower expression at Day 21 and TCP-MS8F had lowered ALP expression at all timepoints. Thus, most materials did not have a significant effect on hBMSC osteoinduction except for TCP-MS8F, the material composed of TCP. TCP is noted in the literature to be an osteoinductive material [11, 12] so other processes may be responsible for the drop in ALP expression.

One possible factor associated with reduced ALP expression for the TCP material could be the cleaning of the chips with isopropanol and acetone before sterilization, which may have remained after autoclaving. The TCP material may be more porous than the other materials and may have absorbed solvent. Acetone, in particular, may have effects on the bone marrow and may cause bone loss. Recent studies investigating the effects of a ketogenic diet have noted lower bone mineral content in rats, [13] mice, [14] and humans [15]; acetone is a metabolite generated during ketosis and can be used as a biomarker of ketoacidosis [16]. A study investigating the effects of acetone in drinking water noted bone marrow hypoplasia in rats dosed with high levels of acetone [17]. In this study, differences in surface morphology or porosity were not controlled, so it is possible that residual acetone from the cleaning process may have caused a drop in ALP expression.

ALP is linked with mineralization via multiple possible mechanisms such as the generation of inorganic phosphates for HA growth or the hydrolysis of pyrophosphates that inhibit HA growth [18]; areduction of this marker could have a negative effect on osseointegration of orthopedic implants. One example is a study by Bonsignore et al., which found that machine oil contamination of Ti-6Al-4V implants inhibited ALP expression among other osteogenic markers in MC3T3-E1 pre-osteoblasts; this finding was also associated with reduced bone-implant contact and pullout force in screws implanted in a murine model [19].

Surface roughness also affects ALP as a marker of osteogenic differentiation and could have played a role in ALP expression in this study. Faia-Torres et al. investigated the effects of surface roughness on osteogenic differentiation of human primary bone marrow stem cells on polycaprolactone substrates in the presence and absence of OS; R_a values around $2.1 - 3.1 \mu\text{m}$ [20] and $0.93 - 1.53 \mu\text{m}$ [21] determined using optical profilometry were found to increase ALP expression along with other markers of osteogenic differentiation. These roughness values may be underestimated compared to values measured using AFM [22]. Thus, the materials in this study with R_{rms} values one or two orders of magnitude lower than values determined by Faia-Torres et al. should be far under the optimal roughness; as such, roughness in this study should not be a significant factor in ALP expression. No correlation between surface roughness measured from either the $10 \mu\text{m}$ or $2 \mu\text{m}$ area with ALP expression from a linear regression was observed with R^2 values of 0.06 and 0.19, respectively.

CONCLUSIONS:

LCM and subsequent sintering of additively manufactured ceramic parts yield pure crystalline ceramic parts with little evidence of residual polymeric binder and are highly similar to their respective feedstock material composition. When potentially applied to orthopedic implants, all tested materials except for TCP were found to not interfere with osteogenic differentiation. As TCP is known to be an osteoconductive material, an unidentified property of the finished TCP ceramic or steps during handling causes a drop in early osteogenic differentiation markers. Future work should be focused on determining the post-processing parameters and sterilization methods that have significant effects on osteoinduction.

ACKNOWLEDGEMENTS:

Martin Schwentenwein and Daniel Bomze from Lithoz GmbH for donating the LCM samples. Ching-Chang Chung and Charles Mooney from North Carolina State University Advanced Characterization Facility for expertise in XRD and AFM respectively. Funding for this project was provided by National Science Foundation Award #1762202.

DISCLAIMER:

The findings and conclusions in this paper have not been formally disseminated by the Food and Drug Administration and should not be construed to represent any agency determination or policy. The mention of commercial products, their sources, or their use in connection with material reported herein is not to be construed as either an actual or implied endorsement of such products by Department of Health and Human Services.

References:

1. Schwentenwein, M., P. Schneider, and J. Homa, *Lithography-Based Ceramic Manufacturing: A Novel Technique for Additive Manufacturing of High-Performance Ceramics*. *Advances in Science and Technology*, 2014. **88**: p. 60-64.
2. Chen, T.-H., et al., *Lattice Microarchitecture for Bone Tissue Engineering from Calcium Phosphate Compared to Titanium*. *Tissue Engineering Part A*, 2018. **24**(19-20): p. 1554-1561.
3. Bomze, D. and A. Ioannidis, *3D-Printing of High-Strength and Bioresorbable Ceramics for Dental and Maxillofacial Surgery Applications-the LCM Process*. *Ceramic Applications*, 2019. **7**(1): p. 38-43.
4. Ghayor, C. and F.E. Weber, *Osteoconductive Microarchitecture of Bone Substitutes for Bone Regeneration Revisited*. *Frontiers in physiology*, 2018. **9**: p. 960-960.
5. Kim, K., et al., *Stereolithographic Bone Scaffold Design Parameters: Osteogenic Differentiation and Signal Expression*. *Tissue Engineering Part B: Reviews*, 2010. **16**(5): p. 523-539.
6. Melchels, F.P.W., et al., *Mathematically defined tissue engineering scaffold architectures prepared by stereolithography*. *Biomaterials*, 2010. **31**(27): p. 6909-6916.
7. Kebede, M.A., et al., *Stereolithographic and molding fabrications of hydroxyapatite-polymer gels applicable to bone regeneration materials*. *Journal of the Taiwan Institute of Chemical Engineers*, 2018. **92**: p. 91-96.
8. Dong, P.L., et al., *The Preparation and Characterization of beta-SiAlON Nanostructure Whiskers*. *Journal of Nanomaterials*, 2008.
9. Seymour, V.R. and M.E. Smith, *Distinguishing between Structural Models of beta '-Stalons Using a Combined Solid-State NMR, Powder XRD, and Computational Approach*. *Journal of Physical Chemistry A*, 2019. **123**(45): p. 9729-9736.

10. Altun, A., et al., *Dense, Strong, and Precise Silicon Nitride-Based Ceramic Parts by Lithography-Based Ceramic Manufacturing*. Applied Sciences, 2020. **10**: p. 996.
11. Li, Y., et al., *Osteogenic differentiation of mesenchymal stem cells (MSCs) induced by three calcium phosphate ceramic (CaP) powders: A comparative study*. Materials Science and Engineering: C, 2017. **80**: p. 296-300.
12. Schmidleithner, C., et al., *Application of high resolution DLP stereolithography for fabrication of tricalcium phosphate scaffolds for bone regeneration*. Biomedical Materials, 2019. **14**(4): p. 045018.
13. Ding, J., et al., *Bone loss and biomechanical reduction of appendicular and axial bones under ketogenic diet in rats*. Experimental and therapeutic medicine, 2019. **17**(4): p. 2503-2510.
14. Wu, X., et al., *Ketogenic Diet Compromises Both Cancellous and Cortical Bone Mass in Mice*. Calcified Tissue International, 2017. **101**(4): p. 412-421.
15. Bergqvist, A.G.C., et al., *Progressive bone mineral content loss in children with intractable epilepsy treated with the ketogenic diet*. The American Journal of Clinical Nutrition, 2008. **88**(6): p. 1678-1684.
16. Prabhakar, A., et al., *Acetone as biomarker for ketosis buildup capability—a study in healthy individuals under combined high fat and starvation diets*. Nutrition journal, 2015. **14**: p. 41-41.
17. DIETZ, D.D., et al., *Toxicity Studies of Acetone Administered in the Drinking Water of Rodents*. Toxicological Sciences, 1991. **17**(2): p. 347-360.
18. Whyte, M.P., *Physiological role of alkaline phosphatase explored in hypophosphatasia*. Annals of the New York Academy of Sciences, 2010. **1192**(1): p. 190-200.
19. Bonsignore, L.A., V.M. Goldberg, and E.M. Greenfield, *Machine oil inhibits the osseointegration of orthopaedic implants by impairing osteoblast attachment and spreading*. Journal of Orthopaedic Research, 2015. **33**(7): p. 979-987.
20. Faia-Torres, A.B., et al., *Differential regulation of osteogenic differentiation of stem cells on surface roughness gradients*. Biomaterials, 2014. **35**(33): p. 9023-9032.
21. Faia-Torres, A.B., et al., *Osteogenic differentiation of human mesenchymal stem cells in the absence of osteogenic supplements: A surface-roughness gradient study*. Acta Biomaterialia, 2015. **28**: p. 64-75.
22. Poon, C.Y. and B. Bhushan, *Comparison of surface roughness measurements by stylus profiler, AFM and non-contact optical profiler*. Wear, 1995. **190**(1): p. 76-88.

CHAPTER 10 – Conclusions

Photopolymer-based additive manufacturing of medical devices was demonstrated in this work to have down to micron-scale resolution, compatibility with materials ranging from hydrogels to ceramics, and can be cytocompatible. The main concern was the potential toxicity of the photoinitiator but multiple medical device types were demonstrated that either removed the photopolymer from the final medical device, post-processed the fabricated part to lower toxicity, or were characterized to better understand the risk to embedded cells.

2PP fabrication of a microneedle array master structure was demonstrated where fine needles with micron-scale tip radii were directly printed in a single step. Replication using soft lithography was able to rapidly generate hundreds of needles. These needle arrays were used to investigate the feasibility of amphotericin B delivery directly to the site of a leishmaniasis lesion using a “poke-and-apply” approach. It was demonstrated that the small lesions caused by *L. Mexicana* were effectively treated using this approach but the larger, ulcerated lesions caused by *L. major* were not effectively treated perhaps due to the uneven surface. In addition, 750 μm needles were found to be the most effective versus the 1000 and 500 μm needle lengths; precise control of needle geometry would not only be important to achieve good tip sharpness, but also to deliver drugs to the proper depth. Since 2PP can achieve throughput on par with SLA while improving the needle morphology and be a more facile process than other lithographic processes involving etching, the strategy of using 2PP for master fabrication followed by replication in the desired material is an extremely feasible method to produce large numbers of devices with micron-scale features.

Certain features such as porous objects cannot be replicated in this strategy and would be directly fabricated out of photopolymers. Generally speaking, tissue engineering can proceed with

either acellular scaffolds that are subsequently seeded or with constructs that are fabricated with cells *in situ*. In the former case, 2PP fabricated PEGda ring scaffolds photoinitiated with a mixture of riboflavin and triethanolamine were successfully seeded with GM-7373 bovine aortic endothelial cells and supported their attachment and proliferation. Extracts of PEGda photoinitiated with the riboflavin mixture was also less cytotoxic and genotoxic versus PEGda photoinitiated with Irgacure 369 or Irgacure 2959. This came at the cost of greatly increased laser power requirements with the riboflavin photoinitiator requiring 244 mW of average laser power versus 90 mW for Irgacure 369. Photoinitiator extracts would retain residual photoinitiator and photo-byproducts which could remain phototoxic. Extracts of GelMA photoinitiated with LAP, a common photoinitiator used in bioprinting, was confirmed to be non-cytotoxic but the photocatalytic properties towards NADH photo-oxidation were inversely proportional to the crosslinking time; under-crosslinking photopolymer to achieve lower elastic moduli would yield higher potential for phototoxicity. In addition, exposing photopolymer well beyond what is required for crosslinking did not significantly change the elastic modulus versus the moderate light exposure condition so exhaustive light exposure would lower phototoxicity while retaining predictable mechanical properties of photopolymeric devices.

In the case where cells are present *in situ* during the crosslinking process, neither strategy of micromolding to avoid photopolymer use in the final device, or post-processing to reduce photopolymer toxicity would be applicable. To address this, the cytotoxicity and mutagenic potential of LAP exposed to light were evaluated to better understand the risks. LAP was evaluated under light exposure conditions that would fully crosslink GelMA as determined using photorheology. Without light exposure, confluent M-1 collecting duct cells exhibited 100% viability at 0.5 wt% LAP, a common concentration used in GelMA hydrogels for bioprinting.

However, light exposure caused 0.1 wt%, the lowest LAP concentration investigated, to be cytotoxic. It was hypothesized that this significant phototoxicity caused by free-radical generation would also be mutagenic. However, an Ames assay battery with multiple *S. typhimurium* strains and an *E. coli* strain specifically mentioned to detect oxidizing mutagens did not detect mutagenic potential. Although it was demonstrated that the crosslinking reaction can be significantly cytotoxic, the results did not support the hypothesis that these free radicals would also be mutagenic.

Additive manufacturing for orthopedic applications would involve many feedstock material types and additives. In particular, AgNP were investigated as a potential additive with antimicrobial properties to combat infections of the bone-implant interface. AgNP exposure at concentrations not acutely cytotoxic after 24 hr exposure reduced hBMSC proliferation in all investigated exposure scenarios. Notably, a single 24 hr exposure to 10 $\mu\text{g/mL}$ 10 nm PVP-coated AgNP eliminated hBMSC ALP expression and substrate mineralization. When considering continuous exposure, 1 $\mu\text{g/mL}$ AgNP, the lowest concentration investigated, did not significantly impair ALP expression or mineralization. While the anti-microbial properties of AgNP are well known and documented, great care must be taken when applying this material to orthopedic devices.

LCM of orthopedic devices would retain the resolution and patient-specific treatment options of SLA but generate a ceramic part composed purely of the feedstock material with no remaining photopolymer component. XRD analysis of ceramic parts confirms that the manufacturing process is highly similar in both peak position and intensity to their reference spectra in the ICDD PDF database. Sharp peak morphology consistent with a highly crystalline material was observed in all materials which imply the absence of residual photopolymer.

However, nanoindentation measurement of these materials was hampered by many “pop-in” events which may be indicative of sub-surface voids. All materials supported the osteogenic differentiation of hBMSCs, but certain materials had reduced ALP activity per cell. Of particular note, tricalcium phosphate, a known osteoconductive material, caused lower ALP expression versus the control. Since nanoindentation of this material had an especially large number of “pop-in” events versus the other materials, one hypothesis is that solvents, such as acetone, used to wash and sterilize the samples remained within pores of this material. Although the LCM process was shown to generate a pure ceramic material, post-processing and sterilization processes may have caused an impairment of osteogenic differentiation.

Outlook and Future Directions

2PP is a highly attractive technology that could generate micron-scale features and be comparable in speed to other AM technologies for specific geometries. Fabrication logic used in this study are effective at producing the simple geometry of microneedles but should be improved to be compatible with arbitrary geometries and take full advantage of the truly 3D fabrication capability; the layer-by-layer paradigm should be broken. At the minimum, trajectory generation logic used in FDM printers could be adapted to 2PP to maintain the benefits of vector printing. This could be expanded to form 3D infills and contours that would increase the fabrication speed of arbitrary structures while eliminating the staircase artifact. Micromolding of these structures has been demonstrated in another photopolymer but can ostensibly be any material. Since the molds are already available, micromolding using soluble materials could create microneedles that deliver pharmaceuticals to a target depth and dissolve away.

Photopolymers for tissue engineering scaffolds have demonstrated the ability to be non-cytotoxic given some post-processing steps but phototoxicity is still a concern. In the worst case where encapsulated cells are exposed directly to the photoinitiator and light, reduced cell viability can be expected but was not definitively mutagenic. Although the Ames assay results were negative, the bioprinting field would benefit from studies focusing specifically on the mutagenicity of free-radical photoinitiators used in bioprinting. Other variables such as shear rate during printing, presence of mechanical strain during culture, etc. could also affect cell behavior. The results of these studies are a promising first step into the non-mutagenicity of photopolymers which should invite more involved studies to increase confidence towards clinical use.

REFERENCES

1. Song, C., A. Wang, Z. Wu, Z. Chen, Y. Yang, and D. Wang, *The design and manufacturing of a titanium alloy beak for Grus japonensis using additive manufacturing*. Materials & Design, 2017. **117**: p. 410-416.
2. Kuo, E. and R.J. Miller, *Automated custom-manufacturing technology in orthodontics*. American Journal of Orthodontics and Dentofacial Orthopedics, 2003. **123**(5): p. 578-581.
3. Cassetta, M., L.V. Stefanelli, M. Giansanti, and S. Calasso, *Accuracy of implant placement with a stereolithographic surgical template*. Int J Oral Maxillofac Implants, 2012. **27**(3): p. 655-63.
4. Gür, Y., *Additive Manufacturing of Anatomical Models from Computed Tomography Scan Data*. Mol Cell Biomech, 2014. **11**(4): p. 249-58.
5. Saunders, R.E. and B. Derby, *Inkjet printing biomaterials for tissue engineering: bioprinting*. International Materials Reviews, 2014. **59**(8): p. 430-448.
6. Skoog, S.A., P.L. Goering, and R.J. Narayan, *Stereolithography in tissue engineering*. Journal of Materials Science: Materials in Medicine, 2014. **25**(3): p. 845-856.
7. Saunders, R., J. Gough, and B. Derby, *Piezoelectric Inkjet Printing of Cells and Biomaterials*, in *Cell and Organ Printing*, B.R. Ringeisen, B.J. Spargo, and P.K. Wu, Editors. 2010, Springer Netherlands: Dordrecht. p. 35-50.
8. Di Biase, M., R.E. Saunders, N. Tirelli, and B. Derby, *Inkjet printing and cell seeding thermoreversible photocurable gel structures*. Soft Matter, 2011. **7**(6): p. 2639-2646.
9. Koch, L., A. Deiwick, S. Schlie, S. Michael, M. Gruene, V. Coger, D. Zychlinski, A. Schambach, K. Reimers, P.M. Vogt, and B. Chichkov, *Skin tissue generation by laser cell printing*. Biotechnology and Bioengineering, 2012. **109**(7): p. 1855-1863.
10. Panwar, A. and L.P. Tan, *Current Status of Bioinks for Micro-Extrusion-Based 3D Bioprinting*. Molecules, 2016. **21**(6): p. 685.
11. Suntornnond, R., E.Y.S. Tan, J. An, and C.K. Chua, *A Mathematical Model on the Resolution of Extrusion Bioprinting for the Development of New Bioinks*. Materials, 2016. **9**(9): p. 756.
12. Lim, K.S., R. Levato, P.F. Costa, M.D. Castilho, C.R. Alcalá-Orozco, K.M.A. van Dorenmalen, F.P.W. Melchels, D. Gawlitta, G.J. Hooper, J. Malda, and T.B.F. Woodfield, *Bio-resin for high resolution lithography-based biofabrication of complex cell-laden constructs*. Biofabrication, 2018. **10**(3): p. 034101.

13. Tromayer, M., A. Dobos, P. Gruber, A. Ajami, R. Dedic, A. Ovsianikov, and R. Liska, *A biocompatible diazosulfonate initiator for direct encapsulation of human stem cells via two-photon polymerization*. *Polymer Chemistry*, 2018. **9**(22): p. 3108-3117.
14. Ning, L. and X. Chen, *A brief review of extrusion-based tissue scaffold bio-printing*. *Biotechnology Journal*, 2017. **12**(8): p. 1600671.
15. Correia Carreira, S., R. Begum, and A.W. Perriman, *3D Bioprinting: The Emergence of Programmable Biodesign*. *Advanced Healthcare Materials*. **n/a**(n/a): p. 1900554.
16. Premi, S., S. Wallisch, C.M. Mano, A.B. Weiner, A. Bacchiocchi, K. Wakamatsu, E.J. Bechara, R. Halaban, T. Douki, and D.E. Brash, *Photochemistry. Chemiexcitation of melanin derivatives induces DNA photoproducts long after UV exposure*. *Science*, 2015. **347**(6224): p. 842-7.
17. Shanmugam, S., J. Xu, and C. Boyer, *Photoinduced Oxygen Reduction for Dark Polymerization*. *Macromolecules*, 2017. **50**(5): p. 1832-1846.
18. Perdiz, D., P. Grof, M. Mezzina, O. Nikaido, E. Moustacchi, and E. Sage, *Distribution and repair of bipyrimidine photoproducts in solar UV-irradiated mammalian cells. Possible role of Dewar photoproducts in solar mutagenesis*. *J Biol Chem*, 2000. **275**(35): p. 26732-42.
19. Agar, N.S., G.M. Halliday, R.S. Barnetson, H.N. Ananthaswamy, M. Wheeler, and A.M. Jones, *The basal layer in human squamous tumors harbors more UVA than UVB fingerprint mutations: a role for UVA in human skin carcinogenesis*. *Proceedings of the National Academy of Sciences of the United States of America*, 2004. **101**(14): p. 4954-4959.
20. Mohamed, M.G.A., H. Kumar, Z. Wang, N. Martin, B. Mills, and K. Kim, *Rapid and Inexpensive Fabrication of Multi-Depth Microfluidic Device using High-Resolution LCD Stereolithographic 3D Printing*. *Journal of Manufacturing and Materials Processing*, 2019. **3**(1): p. 26.
21. Gallego, D., N. Ferrell, Y. Sun, and D.J. Hansford, *Multilayer micromolding of degradable polymer tissue engineering scaffolds*. *Materials Science and Engineering: C*, 2008. **28**(3): p. 353-358.
22. Giedre, G., B. Daiva, B. Evaldas, J. Linas, and M. Mangirdas. *Fabrication of flexible microporous 3D scaffolds via stereolithography and optimization of their biocompatibility*. in *Proc.SPIE*. 2018.
23. Barry, J.J.A., A.V. Evseev, M.A. Markov, C.E. Upton, C.A. Scotchford, V.K. Popov, and S.M. Howdle, *In vitro study of hydroxyapatite-based photocurable polymer composites prepared by laser stereolithography and supercritical fluid extraction*. *Acta Biomaterialia*, 2008. **4**(6): p. 1603-1610.

24. Altun, A., T. Prochaska, T. Konegger, and M. Schwentenwein, *Dense, Strong, and Precise Silicon Nitride-Based Ceramic Parts by Lithography-Based Ceramic Manufacturing*. Applied Sciences, 2020. **10**: p. 996.
25. Koroleva, A., A. Deiwick, A. Nguyen, S. Schlie-Wolter, R. Narayan, P. Timashev, V. Popov, V. Bagratashvili, and B. Chichkov, *Osteogenic Differentiation of Human Mesenchymal Stem Cells in 3-D Zr-Si Organic-Inorganic Scaffolds Produced by Two-Photon Polymerization Technique*. Plos One, 2015. **10**(2).
26. Li, Y., H. Zhang, R. Yang, Y. Laffitte, U. Schmill, W. Hu, M. Kaddoura, E.J.M. Blondeel, and B. Cui, *Fabrication of sharp silicon hollow microneedles by deep-reactive ion etching towards minimally invasive diagnostics*. Microsystems & Nanoengineering, 2019. **5**(1): p. 41.
27. Johnson, A.R. and A.T. Procopio, *Low cost additive manufacturing of microneedle masters*. 3D Printing in Medicine, 2019. **5**(1): p. 2.
28. Schmidleithner, C., S. Malferrari, R. Palgrave, D. Bomze, M. Schwentenwein, and D.M. Kalaskar, *Application of high resolution DLP stereolithography for fabrication of tricalcium phosphate scaffolds for bone regeneration*. Biomedical Materials, 2019. **14**(4): p. 045018.
29. Chua, H.S., S.L. Whitehouse, M. Lorimer, R. De Steiger, L. Guo, and R.W. Crawford, *Mortality and implant survival with simultaneous and staged bilateral total knee arthroplasty experience from the Australian Orthopaedic Association National Joint Replacement Registry*. The Journal of arthroplasty, 2018. **33**(10): p. 3167-3173.
30. Prokopovich, P., M. Köbrick, E. Brousseau, and S. Perni, *Potent antimicrobial activity of bone cement encapsulating silver nanoparticles capped with oleic acid*. Journal of Biomedical Materials Research Part B: Applied Biomaterials, 2015. **103**(2): p. 273-281.
31. Sussman, E.M., P. Jayanti, B.J. Dair, and B.J. Casey, *Assessment of total silver and silver nanoparticle extraction from medical devices*. Food and Chemical Toxicology, 2015. **85**: p. 10-19.
32. Deng, L., Y. Deng, and K. Xie, *AgNPs-decorated 3D printed PEEK implant for infection control and bone repair*. Colloids and Surfaces B: Biointerfaces, 2017. **160**: p. 483-492.
33. Jia, Z., M. Li, P. Xiu, X. Xu, Y. Cheng, Y. Zheng, T. Xi, S. Wei, and Z. Liu, *A novel cytocompatible, hierarchical porous Ti6Al4V scaffold with immobilized silver nanoparticles*. Materials Letters, 2015. **157**: p. 143-146.
34. Emons, M., K. Obata, T. Binhammer, A. Ovsianikov, B.N. Chichkov, and U. Morgner, *Two-photon polymerization technique with sub-50 nm resolution by sub-10 fs laser pulses*. Optical Materials Express, 2012. **2**(7): p. 942-947.
35. Wu, D., J. Xu, L.G. Niu, S.Z. Wu, K. Midorikawa, and K. Sugioka, *In-channel integration of designable microoptical devices using flat scaffold-supported femtosecond-*

- laser microfabrication for coupling-free optofluidic cell counting*. Light-Science & Applications, 2015. **4**.
36. Hjorto, G.M., M.H. Olsen, I.M. Svane, and N.B. Larsen, *Confinement dependent chemotaxis in two-photon polymerized linear migration constructs with highly definable concentration gradients*. Biomedical Microdevices, 2015. **17**(2).
 37. Miller, P.R., X.Y. Xiao, I. Brener, D.B. Burckel, R. Narayan, and R. Polsky, *Microneedle-Based Transdermal Sensor for On-Chip Potentiometric Determination of K⁺*. Advanced Healthcare Materials, 2014. **3**(6): p. 876-881.
 38. Turunen, S., E. Kapyla, M. Lahteenmaki, L. Yla-Outinen, S. Narkilahti, and M. Kellomaki, *Direct laser writing of microstructures for the growth guidance of human pluripotent stem cell derived neuronal cells*. Optics and Lasers in Engineering, 2014. **55**: p. 197-204.
 39. Marino, A., C. Filippeschi, G.G. Genchi, V. Mattoli, B. Mazzolai, and G. Ciofani, *The Osteoprint: A bioinspired two-photon polymerized 3-D structure for the enhancement of bone-like cell differentiation*. Acta Biomaterialia, 2014. **10**(10): p. 4304-4313.
 40. Gittard, S.D., A. Ovsianikov, N.A. Monteiro-Riviere, J. Lusk, P. Morel, P. Minghetti, C. Lenardi, B.N. Chichkov, and R.J. Narayan, *Fabrication of polymer microneedles using a two-photon polymerization and micromolding process*. J Diabetes Sci Technol, 2009. **3**(2): p. 304-11.
 41. Koroleva, A., S. Gittard, S. Schlie, A. Deiwick, S. Jockenhoevel, and B. Chichkov, *Fabrication of fibrin scaffolds with controlled microscale architecture by a two-photon polymerization-micromolding technique*. Biofabrication, 2012. **4**(1).
 42. Malinauskas, M., A. Zukauskas, G. Bickaускаite, R. Gadonas, and S. Juodkazis, *Mechanisms of three-dimensional structuring of photo-polymers by tightly focussed femtosecond laser pulses*. Optics Express, 2010. **18**(10): p. 10209-10221.
 43. Ong, B.H., X. Yuan, S. Tao, and S.C. Tjin, *Photothermally enabled lithography for refractive-index modulation in SU-8 photoresist*. Opt Lett, 2006. **31**(10): p. 1367-9.
 44. Seet, K.K., S. Juodkazis, V. Jarutis, and H. Misawa, *Feature-size reduction of photopolymerized structures by femtosecond optical curing of SU-8*. Applied Physics Letters, 2006. **89**(2).
 45. Baldacchini, T., S. Snider, and R. Zadoyan, *Two-photon polymerization with variable repetition rate bursts of femtosecond laser pulses*. Optics Express, 2012. **20**(28): p. 29890-29899.
 46. Waller, E. and G. von Freymann, *Spatio-Temporal Proximity Characteristics in 3D μ -Printing via Multi-Photon Absorption*. Polymers, 2016. **8**(8): p. 297.

47. Sheikbahae, M., A.A. Said, T.H. Wei, D.J. Hagan, and E.W. Vanstryland, *Sensitive Measurement of Optical Nonlinearities Using a Single Beam*. Ieee Journal of Quantum Electronics, 1990. **26**(4): p. 760-769.
48. Ajami, A., W. Husinsky, R. Liska, and N. Pucher, *Two-photon absorption cross section measurements of various two-photon initiators for ultrashort laser radiation applying the Z-scan technique*. Journal of the Optical Society of America B-Optical Physics, 2010. **27**(11): p. 2290-2297.
49. Cumpston, B.H., S.P. Ananthavel, S. Barlow, D.L. Dyer, J.E. Ehrlich, L.L. Erskine, A.A. Heikal, S.M. Kuebler, I.Y.S. Lee, D. McCord-Maughon, J.Q. Qin, H. Rockel, M. Rumi, X.L. Wu, S.R. Marder, and J.W. Perry, *Two-photon polymerization initiators for three-dimensional optical data storage and microfabrication*. Nature, 1999. **398**(6722): p. 51-54.
50. Pawlicki, M., H.A. Collins, R.G. Denning, and H.L. Anderson, *Two-Photon Absorption and the Design of Two-Photon Dyes*. Angewandte Chemie-International Edition, 2009. **48**(18): p. 3244-3266.
51. Aydin, M., N. Arsu, and Y. Yagci, *One-component bimolecular photoinitiating systems, 2 - Thioxanthone acetic acid derivatives as photoinitiators for free radical polymerization*. Macromolecular Rapid Communications, 2003. **24**(12): p. 718-723.
52. Nazir, R., P. Danilevicius, A.I. Ciuciu, M. Chatzinikolaidou, D. Gray, L. Flamigni, M. Farsari, and D.T. Gryko, *π -Expanded Ketocoumarins as Efficient, Biocompatible Initiators for Two-Photon-Induced Polymerization*. Chemistry of Materials, 2014. **26**(10): p. 3175-3184.
53. Orellana, B., A.M. Rufs, M.V. Encinas, C.M. Previtali, and S. Bertolotti, *The photoinitiation mechanism of vinyl polymerization by riboflavin/triethanolamine in aqueous medium*. Macromolecules, 1999. **32**(20): p. 6570-6573.
54. Nguyen, A.K., S.D. Gittard, A. Koroleva, S. Schlie, A. Gaidukeviciute, B.N. Chichkov, and R.J. Narayan, *Two-photon polymerization of polyethylene glycol diacrylate scaffolds with riboflavin and triethanolamine used as a water-soluble photoinitiator*. Regenerative Medicine, 2013. **8**(6): p. 725-738.
55. Li, Z.Q., J. Torgersen, A. Ajami, S. Muhleder, X.H. Qin, W. Husinsky, W. Holnthoner, A. Ovsianikov, J. Stampfl, and R. Liska, *Initiation efficiency and cytotoxicity of novel water-soluble two-photon photoinitiators for direct 3D microfabrication of hydrogels*. Rsc Advances, 2013. **3**(36): p. 15939-15946.
56. Pawar, A.A., G. Saada, I. Cooperstein, L. Larush, J.A. Jackman, S.R. Tabaei, N.J. Cho, and S. Magdassi, *High-performance 3D printing of hydrogels by water-dispersible photoinitiator nanoparticles*. Sci Adv, 2016. **2**(4): p. e1501381.

57. Song, L., Q. Ye, X. Ge, A. Misra, and P. Spencer, *Tris(trimethylsilyl)silane as a co-initiator for dental adhesive: Photo-polymerization kinetics and dynamic mechanical property*. Dent Mater, 2016. **32**(1): p. 102-13.
58. Denis, A.B., C.A. Diagone, A.M.G. Plepis, and R.B. Viana, *Kinetic Parameters during Bis-GMA and TEGDMA Monomer Polymerization by ATR-FTIR: The Influence of Photoinitiator and Light Curing Source*. Journal of Spectroscopy, 2016. **2016**: p. 1-8.
59. Salgado, V.E., D. Cavassoni, A.P.R. Gonçalves, C. Pfeifer, R.R. Moraes, and L.F. Schneider, *Photoinitiator system and water effects on C=C conversion and solubility of experimental etch-and-rinse dental adhesives*. International Journal of Adhesion and Adhesives, 2017. **72**: p. 6-9.
60. Randolph, L.D., J. Steinhaus, B. Moginger, B. Gallez, J. Stansbury, W.M. Palin, G. Leloup, and J.G. Leprince, *Photopolymerization of highly filled dimethacrylate-based composites using Type I or Type II photoinitiators and varying co-monomer ratios*. Dent Mater, 2016. **32**(2): p. 136-48.
61. Cicha, K., Z.Q. Li, K. Stadlmann, A. Ovsianikov, R. Markut-Kohl, R. Liska, and J. Stampfl, *Evaluation of 3D structures fabricated with two-photon-photopolymerization by using FTIR spectroscopy*. Journal of Applied Physics, 2011. **110**(6).
62. Kufelt, O., A. El-Tamer, C. Sehring, M. Meissner, S. Schlie-Wolter, and B.N. Chichkov, *Water-soluble photopolymerizable chitosan hydrogels for biofabrication via two-photon polymerization*. Acta Biomaterialia, 2015. **18**: p. 186-195.
63. Kufelt, O., A. El-Tamer, C. Sehring, S. Schlie-Wolter, and B.N. Chichkov, *Hyaluronic Acid Based Materials for Scaffolding via Two-Photon Polymerization*. Biomacromolecules, 2014. **15**(2): p. 650-659.
64. Van den Bulcke, A.I., B. Bogdanov, N. De Rooze, E.H. Schacht, M. Cornelissen, and H. Berghmans, *Structural and rheological properties of methacrylamide modified gelatin hydrogels*. Biomacromolecules, 2000. **1**(1): p. 31-38.
65. Ovsianikov, A., A. Deiwick, S. Van Vlierberghe, M. Pflaum, M. Wilhelmi, P. Dubruel, and B. Chichkov, *Laser Fabrication of 3D Gelatin Scaffolds for the Generation of Bioartificial Tissues*. Materials, 2011. **4**(1): p. 288-299.
66. Koroleva, A., A.A. Gill, I. Ortega, J.W. Haycock, S. Schlie, S.D. Gittard, B.N. Chichkov, and F. Claeysens, *Two-photon polymerization-generated and micromolding-replicated 3D scaffolds for peripheral neural tissue engineering applications*. Biofabrication, 2012. **4**(2).
67. Kloxin, A.M., M.W. Tibbitt, and K.S. Anseth, *Synthesis of photodegradable hydrogels as dynamically tunable cell culture platforms*. Nature Protocols, 2010. **5**(12): p. 1867-1887.
68. Mastropasqua, L., *Collagen cross-linking: when and how? A review of the state of the art of the technique and new perspectives*. Eye Vis (Lond), 2015. **2**: p. 19.

69. Kuetemeyer, K., G. Kensah, M. Heidrich, H. Meyer, U. Martin, I. Gruh, and A. Heisterkamp, *Two-photon induced collagen cross-linking in bioartificial cardiac tissue*. Optics Express, 2011. **19**(17): p. 15996-16007.
70. Kaehr, B., N. Ertas, R. Nielson, R. Allen, R.T. Hill, M. Plenert, and J.B. Shear, *Direct-write fabrication of functional protein matrixes using a low-cost Q-switched laser*. Analytical Chemistry, 2006. **78**(9): p. 3198-3202.
71. Kaehr, B. and J.B. Shear, *Multiphoton fabrication of chemically responsive protein hydrogels for microactuation*. Proceedings of the National Academy of Sciences of the United States of America, 2008. **105**(26): p. 8850-8854.
72. Khripin, C.Y., C.J. Brinker, and B. Kaehr, *Mechanically tunable multiphoton fabricated protein hydrogels investigated using atomic force microscopy*. Soft Matter, 2010. **6**(12): p. 2842-2848.
73. Skoog, S.A., A.K. Nguyen, G. Kumar, J.W. Zheng, P.L. Goering, A. Koroleva, B.N. Chichkov, and R.J. Narayan, *Two-photon polymerization of 3-D zirconium oxide hybrid scaffolds for long-term stem cell growth*. Biointerphases, 2014. **9**(2).
74. Lin, C.Y., C.H. Lien, K.C. Cho, C.Y. Chang, N.S. Chang, P.J. Campagnola, C.Y. Dong, and S.J. Chen, *Investigation of two-photon excited fluorescence increment via crosslinked bovine serum albumin*. Optics Express, 2012. **20**(13): p. 13669-13676.
75. Hilario, P.L., M.J. Villangca, and G. Tapang, *Independent light fields generated using a phase-only spatial light modulator*. Optics Letters, 2014. **39**(7): p. 2036-2039.
76. Yang, L., J.W. Li, Y.L. Hu, C.C. Zhang, Z.X. Lao, W.H. Huang, and J.R. Chu, *Projection two-photon polymerization using a spatial light modulator*. Optics Communications, 2014. **331**: p. 82-86.
77. Zalesskii, A.D., N.A. Danil'chenko, Y.V. Barbashov, B.I. Zapadinskii, and O.M. Sarkisov, *Multiphoton polymerization with the holographic control of femtosecond and continuous laser radiation*. Russian Journal of Physical Chemistry B, 2012. **6**(3): p. 357-361.
78. Gittard, S.D., A. Nguyen, K. Obata, A. Koroleva, R.J. Narayan, and B.N. Chichkov, *Fabrication of microscale medical devices by two-photon polymerization with multiple foci via a spatial light modulator*. Biomedical Optics Express, 2011. **2**(11): p. 3167-3178.
79. Neghina, R. and A.M. Neghina, *Leishmaniasis, a global concern for travel medicine*. Scandinavian Journal of Infectious Diseases, 2010. **42**(8): p. 563-570.
80. Murray, H.W., J.D. Berman, C.R. Davies, and N.G. Saravia, *Advances in leishmaniasis*. The Lancet, 2005. **366**(9496): p. 1561-1577.
81. Jacobson, R.L., *Leishmaniasis in an Era of Conflict in the Middle East*. Vector-Borne and Zoonotic Diseases, 2010. **11**(3): p. 247-258.

82. Ameen, M., *Cutaneous leishmaniasis: advances in disease pathogenesis, diagnostics and therapeutics*. Clinical and Experimental Dermatology, 2010. **35**(7): p. 699-705.
83. Matheson, A., R. Williams, and M. Bailey, *Cutaneous Leishmaniasis in Royal Marines from Oruzgan, Afghanistan*. Journal of the Royal Army Medical Corps, 2012. **158**(3): p. 221-224.
84. David, C.V. and N. Craft, *Cutaneous and mucocutaneous leishmaniasis*. Dermatologic Therapy, 2009. **22**(6): p. 491-502.
85. Torres-Guerrero, E., M. Quintanilla-Cedillo, J. Ruiz-Esmenjaud, and R. Arenas, *Leishmaniasis: a review [version 1; peer review: 2 approved]*. F1000Research, 2017. **6**(750).
86. Bari, A.U. and S.B. Rahman, *A Therapeutic update on Cutaneous leishmaniasis*. Journal of the College of Physicians and Surgeons--Pakistan : JCPSP, 2003. **13**(8): p. 471-476.
87. Carneiro, G., M.G. Aguiar, A.P. Fernandes, and L.A.M. Ferreira, *Drug delivery systems for the topical treatment of cutaneous leishmaniasis*. Expert Opinion on Drug Delivery, 2012. **9**(9): p. 1083-1097.
88. López, L., M. Robayo, M. Vargas, and I.D. Vélez, *Thermotherapy. An alternative for the treatment of American cutaneous leishmaniasis*. Trials, 2012. **13**(1): p. 58.
89. Frézard, F. and C. Demicheli, *New delivery strategies for the old pentavalent antimonial drugs*. Expert Opinion on Drug Delivery, 2010. **7**(12): p. 1343-1358.
90. Aronson, N.E., G.W. Wortmann, S.C. Johnson, J.E. Jackson, R.A. Gasser, Jr., A.J. Magill, T.P. Endy, P.E. Coyne, M. Grogl, P.M. Benson, J.S. Beard, J.D. Tally, J.M. Gambel, R.D. Kreutzer, and C.N. Oster, *Safety and Efficacy of Intravenous Sodium Stibogluconate in the Treatment of Leishmaniasis: Recent U.S. Military Experience*. Clinical Infectious Diseases, 1998. **27**(6): p. 1457-1464.
91. Aronson, N.E., G.W. Wortmann, W.R. Byrne, R.S. Howard, W.B. Bernstein, M.A. Marovich, M.E. Polhemus, I.-K. Yoon, K.A. Hummer, R.A. Gasser, Jr., C.N. Oster, and P.M. Benson, *A Randomized Controlled Trial of Local Heat Therapy Versus Intravenous Sodium Stibogluconate for the Treatment of Cutaneous Leishmania major Infection*. PLOS Neglected Tropical Diseases, 2010. **4**(3): p. e628.
92. Solomon, M., F. Pavlotsky, E. Leshem, M. Ephros, H. Trau, and E. Schwartz, *Liposomal amphotericin B treatment of cutaneous leishmaniasis due to Leishmania tropica*. Journal of the European Academy of Dermatology and Venereology, 2011. **25**(8): p. 973-977.
93. Mosimann, V., A. Neumayr, D.H. Paris, and J. Blum, *Liposomal amphotericin B treatment of Old World cutaneous and mucosal leishmaniasis: A literature review*. Acta Tropica, 2018. **182**: p. 246-250.

94. Glasser, J.S. and C.K. Murray, *Central Nervous System Toxicity Associated with Liposomal Amphotericin B Therapy for Cutaneous Leishmaniasis*. The American Journal of Tropical Medicine and Hygiene, 2011. **84**(4): p. 566-568.
95. Hervás, J.A., A. Martín-Santiago, D. Hervás, E. Rojo, A. Mena, V. Rocamora, and J. Dueñas, *Old World Leishmania infantum Cutaneous Leishmaniasis Unresponsive to Liposomal Amphotericin B Treated With Topical Imiquimod*. The Pediatric Infectious Disease Journal, 2012. **31**(1).
96. Henry, S., D.V. McAllister, M.G. Allen, and M.R. Prausnitz, *Microfabricated Microneedles: A Novel Approach to Transdermal Drug Delivery*. Journal of Pharmaceutical Sciences, 1998. **87**(8): p. 922-925.
97. Gittard, S.D., A. Ovsianikov, B.N. Chichkov, A. Doraiswamy, and R.J. Narayan, *Two-photon polymerization of microneedles for transdermal drug delivery*. Expert Opinion on Drug Delivery, 2010. **7**(4): p. 513-533.
98. Schönian, G., A. Nasereddin, N. Dinse, C. Schweynoch, H.D.F.H. Schallig, W. Presber, and C.L. Jaffe, *PCR diagnosis and characterization of Leishmania in local and imported clinical samples I Part of this work has been presented at the Second World Congress on Leishmaniosis in Crete, Greece, May 2001*. Diagnostic Microbiology and Infectious Disease, 2003. **47**(1): p. 349-358.
99. Fine, D., A. Grattoni, R. Goodall, S.S. Bansal, C. Chiappini, S. Hosali, A.L. van de Ven, S. Srinivasan, X. Liu, B. Godin, L. Brousseau Iii, I.K. Yazdi, J. Fernandez-Moure, E. Tasciotti, H.-J. Wu, Y. Hu, S. Klemm, and M. Ferrari, *Silicon Micro- and Nanofabrication for Medicine*. Advanced Healthcare Materials, 2013. **2**(5): p. 632-666.
100. Wolf Nassif, P., T.F.P. De Mello, T.R. Navasconi, C.A. Mota, I.G. Demarchi, S.M.A. Aristides, M.V.C. Lonardoni, J.J.V. Teixeira, and T.G.V. Silveira, *Safety and efficacy of current alternatives in the topical treatment of cutaneous leishmaniasis: a systematic review*. Parasitology, 2017. **144**(8): p. 995-1004.
101. Ben Salah, A., N. Ben Messaoud, E. Guedri, A. Zaatour, N. Ben Alaya, J. Bettaieb, A. Gharbi, N. Belhadj Hamida, A. Boukthir, S. Chlif, K. Abdelhamid, Z. El Ahmadi, H. Louzir, M. Mokni, G. Morizot, P. Buffet, P.L. Smith, K.M. Kopydlowski, M. Kreishman-Deitrick, K.S. Smith, C.J. Nielsen, D.R. Ullman, J.A. Norwood, G.D. Thorne, W.F. McCarthy, R.C. Adams, R.M. Rice, D. Tang, J. Berman, J. Ransom, A.J. Magill, and M. Grogil, *Topical Paromomycin with or without Gentamicin for Cutaneous Leishmaniasis*. New England Journal of Medicine, 2013. **368**(6): p. 524-532.
102. Golenser, J., S. Frankenburg, T. Ehrenfreund, and A.J. Domb, *Efficacious Treatment of Experimental Leishmaniasis with Amphotericin B-Arabinogalactan Water-Soluble Derivatives*. Antimicrobial Agents and Chemotherapy, 1999. **43**(9): p. 2209-2214.
103. Iman, M., Z. Huang, S.H. Alavizadeh, F.C. Szoka, and M.R. Jaafari, *Biodistribution and *In Vivo* Antileishmanial Activity of 1,2-Distigmasterylhemisuccinoyl-*

- sn-Glycero-3-Phosphocholine Liposome-Intercalated Amphotericin B. *Antimicrobial Agents and Chemotherapy*, 2017. **61**(9): p. e02525-16.
104. Corware, K., D. Harris, I. Teo, M. Rogers, K. Naresh, I. Müller, and S. Shaunak, *Accelerated healing of cutaneous leishmaniasis in non-healing BALB/c mice using water soluble amphotericin B-polymethacrylic acid*. *Biomaterials*, 2011. **32**(31): p. 8029-8039.
 105. El-On, J., G.P. Jacobs, E. Witztum, and C.L. Greenblatt, *Development of topical treatment for cutaneous leishmaniasis caused by Leishmania major in experimental animals*. *Antimicrobial Agents and Chemotherapy*, 1984. **26**(5): p. 745-751.
 106. Frankenburg, S., D. Glick, S. Klaus, and Y. Barenholz, *Efficacious Topical Treatment for Murine Cutaneous Leishmaniasis with Ethanolic Formulations of Amphotericin B*. *Antimicrobial Agents and Chemotherapy*, 1998. **42**(12): p. 3092-3096.
 107. Varikuti, S., S. Oghumu, N. Saljoughian, M.S. Pioso, B.E. Sedmak, A. Khamesipour, and A.R. Satoskar, *Topical treatment with nanoliposomal Amphotericin B reduces early lesion growth but fails to induce cure in an experimental model of cutaneous leishmaniasis caused by Leishmania mexicana*. *Acta Tropica*, 2017. **173**: p. 102-108.
 108. Yardley, V. and S.L. Croft, *Activity of liposomal amphotericin B against experimental cutaneous leishmaniasis*. *Antimicrobial Agents and Chemotherapy*, 1997. **41**(4): p. 752-756.
 109. Grogl, M., M. Hickman, W. Ellis, T. Hudson, J.S. Lazo, E.R. Sharlow, J. Johnson, J. Berman, and R.J. Sciotti, *Drug Discovery Algorithm for Cutaneous Leishmaniasis*. *The American Journal of Tropical Medicine and Hygiene*, 2013. **88**(2): p. 216-221.
 110. Fortin, A., D.P. Caridha, S. Leed, F. Ngundam, J. Sena, T. Bosschaerts, S. Parriott, M.R. Hickman, T.H. Hudson, and M. Grogl, *Direct Comparison of the Efficacy and Safety of Oral Treatments with Oleylphosphocholine (OlPC) and Miltefosine in a Mouse Model of L. major Cutaneous Leishmaniasis*. *PLOS Neglected Tropical Diseases*, 2014. **8**(9): p. e3144.
 111. Caridha, D., S. Parriot, T.H. Hudson, T. Lang, F. Ngundam, S. Leed, J. Sena, M. Harris, M. O'Neil, R. Sciotti, L. Read, H. Lecoer, M. Hickman, and M. Grogl, *Use of Optical Imaging Technology in the Validation of a New, Rapid, Cost-Effective Drug Screen as Part of a Tiered In Vivo Screening Paradigm for Development of Drugs To Treat Cutaneous Leishmaniasis*. *Antimicrobial Agents and Chemotherapy*, 2017. **61**(4): p. e02048-16.
 112. Grevelink, S.A. and E.A. Lerner, *Leishmaniasis*. *Journal of the American Academy of Dermatology*, 1996. **34**(2, Part 1): p. 257-272.
 113. Venkataram, M., M. Moosa, and L. Devi, *Histopathological spectrum in cutaneous leishmaniasis: a study in Oman*. *Indian J Dermatol Venereol Leprol*, 2001. **67**(6): p. 294-8.

114. Calabro, K., A. Curtis, J.-R. Galarneau, T. Krucker, and I. Bigio, *Gender variations in the optical properties of skin in murine animal models*. Journal of Biomedical Optics, 2011. **16**(1): p. 011008.
115. Wei, J.C.J., G.A. Edwards, D.J. Martin, H. Huang, M.L. Crichton, and M.A.F. Kendall, *Allometric scaling of skin thickness, elasticity, viscoelasticity to mass for micro-medical device translation: from mice, rats, rabbits, pigs to humans*. Scientific Reports, 2017. **7**(1): p. 15885.
116. Schilling, S. and N. Glaichenhaus, *T Cells That React to the Immunodominant *Leishmania major* LACK Antigen Prevent Early Dissemination of the Parasite in Susceptible BALB/c Mice*. Infection and Immunity, 2001. **69**(2): p. 1212-1214.
117. Laskay, T., I. Wittmann, A. Diefenbach, M. Röllinghoff, and W. Solbach, *Control of Leishmania major infection in BALB/c mice by inhibition of early lymphocyte entry into peripheral lymph nodes*. The Journal of Immunology, 1997. **158**(3): p. 1246-1253.
118. Blum, J., P. Buffet, L. Visser, G. Harms, M.S. Bailey, E. Caumes, J. Clerinx, P.P.A.M. van Thiel, G. Morizot, C. Hatz, T.P.C. Dorlo, and D.N.J. Lockwood, *LeishMan Recommendations for Treatment of Cutaneous and Mucosal Leishmaniasis in Travelers, 2014*. Journal of Travel Medicine, 2013. **21**(2): p. 116-129.
119. Mears, E.R., F. Modabber, R. Don, and G.E. Johnson, *A Review: The Current In Vivo Models for the Discovery and Utility of New Anti-leishmanial Drugs Targeting Cutaneous Leishmaniasis*. PLOS Neglected Tropical Diseases, 2015. **9**(9): p. e0003889.
120. Aguilar Torrentera, F., M.-A. Lambot, J.D. Laman, M. Van Meurs, R. Kiss, J.-C. Noël, and Y. Carlier, *Parasitic load and histopathology of cutaneous lesions, lymph node, spleen, and liver from BALB/c and C57BL/6 mice infected with Leishmania mexicana*. The American Journal of Tropical Medicine and Hygiene, 2002. **66**(3): p. 273-279.
121. Žukauskas, A., K.K. Tikuišis, M. Ščiuka, A. Melninkaitis, R. Gadonas, C. Reinhardt, and M. Malinauskas. *Single-step direct laser fabrication of complex shaped microoptical components*. in *Micro-Optics 2012*. 2012. International Society for Optics and Photonics.
122. Stoneman, M., M. Fox, C. Zeng, and V. Raicu, *Real-time monitoring of two-photon photopolymerization for use in fabrication of microfluidic devices*. Lab on a Chip, 2009. **9**(6): p. 819-827.
123. Ovsianikov, A., B. Chichkov, O. Adunka, H. Pillsbury, A. Doraiswamy, and R. Narayan, *Rapid prototyping of ossicular replacement prostheses*. Applied surface science, 2007. **253**(15): p. 6603-6607.
124. Gittard, S.D., A. Ovsianikov, H. Akar, B. Chichkov, N.A. Monteiro-Riviere, S. Stafslie, B. Chisholm, C.C. Shin, C.M. Shih, and S.J. Lin, *Two Photon Polymerization-Micromolding of Polyethylene Glycol-Gentamicin Sulfate Microneedles*. Advanced Engineering Materials, 2010. **12**(4): p. B77-B82.

125. Kasko, A.M. and D.Y. Wong, *Two-photon lithography in the future of cell-based therapeutics and regenerative medicine: a review of techniques for hydrogel patterning and controlled release*. *Future medicinal chemistry*, 2010. **2**(11): p. 1669-1680.
126. Farsari, M. and B.N. Chichkov, *Two-photon fabrication*. *Nature photonics*, 2009. **3**(8): p. 450-452.
127. Narayan, R.J., A. Doraiswamy, D.B. Chrisey, and B.N. Chichkov, *Medical prototyping using two photon polymerization*. *Materials Today*, 2010. **13**(12): p. 42-48.
128. Ovsianikov, A., A. Deiwick, S. Van Vlierberghe, P. Dubruel, L. Möller, G. Dräger, and B. Chichkov, *Laser fabrication of three-dimensional CAD scaffolds from photosensitive gelatin for applications in tissue engineering*. *Biomacromolecules*, 2011. **12**(4): p. 851-858.
129. Raimondi, M.T., S.M. Eaton, M.M. Nava, M. Laganà, G. Cerullo, and R. Osellame, *Two-photon laser polymerization: from fundamentals to biomedical application in tissue engineering and regenerative medicine*. *Journal of applied biomaterials & functional materials*, 2012. **10**(1): p. 56-66.
130. Ovsianikov, A., M. Gruene, M. Pflaum, L. Koch, F. Maiorana, M. Wilhelmi, A. Haverich, and B. Chichkov, *Laser printing of cells into 3D scaffolds*. *Biofabrication*, 2010. **2**(1): p. 014104.
131. Weiß, T., R. Schade, T. Laube, A. Berg, G. Hildebrand, R. Wyrwa, M. Schnabelrauch, and K. Liefelth, *Two-Photon Polymerization of Biocompatible Photopolymers for Microstructured 3D Biointerfaces*. *Advanced Engineering Materials*, 2011. **13**(9): p. B264-B273.
132. Koskela, J.E., S. Turunen, L. Ylä-Outinen, S. Narkilahti, and M. Kellomäki, *Two-photon microfabrication of poly (ethylene glycol) diacrylate and a novel biodegradable photopolymer—comparison of processability for biomedical applications*. *Polymers for Advanced Technologies*, 2012. **23**(6): p. 992-1001.
133. Gittard, S., *Light-based Rapid Prototyping of Micro-and Nanoscale Medical Devices for Drug Delivery and Regenerative Medicine*. 2011.
134. Raimondi, M.T., S.M. Eaton, M. Laganà, V. Aprile, M.M. Nava, G. Cerullo, and R. Osellame, *Three-dimensional structural niches engineered via two-photon laser polymerization promote stem cell homing*. *Acta biomaterialia*, 2013. **9**(1): p. 4579-4584.
135. Gittard, S.D., A. Koroleva, A. Nguyen, E. Fadeeva, A. Gaidukeviciute, S. Schlie-Wolter, R.J. Narayan, and B. Chichkov, *Two-photon polymerization microstructuring in regenerative medicine*. *Frontiers in bioscience (Elite edition)*, 2013. **5**: p. 602.
136. Ovsianikov, A., M. Malinauskas, S. Schlie, B. Chichkov, S. Gittard, R. Narayan, M. Löbler, K. Sternberg, K.-P. Schmitz, and A. Haverich, *Three-dimensional laser micro-*

- and nano-structuring of acrylated poly (ethylene glycol) materials and evaluation of their cytotoxicity for tissue engineering applications.* Acta biomaterialia, 2011. **7**(3): p. 967-974.
137. Arcaute, K., B.K. Mann, and R.B. Wicker, *Stereolithography of three-dimensional bioactive poly (ethylene glycol) constructs with encapsulated cells.* Annals of biomedical engineering, 2006. **34**(9): p. 1429-1441.
 138. Williams, C.G., A.N. Malik, T.K. Kim, P.N. Manson, and J.H. Elisseeff, *Variable cytocompatibility of six cell lines with photoinitiators used for polymerizing hydrogels and cell encapsulation.* Biomaterials, 2005. **26**(11): p. 1211-1218.
 139. Rouillard, A.D., C.M. Berglund, J.Y. Lee, W.J. Polacheck, Y. Tsui, L.J. Bonassar, and B.J. Kirby, *Methods for photocrosslinking alginate hydrogel scaffolds with high cell viability.* Tissue Engineering Part C: Methods, 2011. **17**(2): p. 173-179.
 140. Lu, C.-Y., W.-F. Wang, W.-Z. Lin, Z.-H. Han, S.-D. Yao, and N.-Y. Lin, *Generation and photosensitization properties of the oxidized radical of riboflavin: a laser flash photolysis study.* Journal of Photochemistry and Photobiology B: Biology, 1999. **52**(1-3): p. 111-116.
 141. Encinas, M., A. Rufs, S. Bertolotti, and C. Previtali, *Free radical polymerization photoinitiated by riboflavin/amines. Effect of the amine structure.* Macromolecules, 2001. **34**(9): p. 2845-2847.
 142. Turunen, S., E. Käpylä, K. Terzaki, J. Viitanen, C. Fotakis, M. Kellomäki, and M. Farsari, *Pico- and femtosecond laser-induced crosslinking of protein microstructures: evaluation of processability and bioactivity.* Biofabrication, 2011. **3**(4): p. 045002.
 143. Husain, E. and I. Naseem, *Riboflavin-mediated cellular photoinhibition of cisplatin-induced oxidative DNA breakage in mice epidermal keratinocytes.* Photodermatology, Photoimmunology & Photomedicine, 2008. **24**(6): p. 301-307.
 144. Hardwick, C.C., T.R. Herivel, S.C. Hernandez, P.H. Ruane, and R.P. Goodrich, *Separation, Identification and Quantification of Riboflavin and its Photoproducts in Blood Products using High-performance Liquid Chromatography with Fluorescence Detection: A Method to Support Pathogen Reduction Technology.* Photochemistry and photobiology, 2004. **80**(3): p. 609-615.
 145. Wollensak, G., M. Wilsch, E. Spoerl, and T. Seiler, *Collagen fiber diameter in the rabbit cornea after collagen crosslinking by riboflavin/UVA.* Cornea, 2004. **23**(5): p. 503-507.
 146. Spoerl, E., M. Mrochen, D. Sliney, S. Trokel, and T. Seiler, *Safety of UVA-riboflavin cross-linking of the cornea.* Cornea, 2007. **26**(4): p. 385-389.
 147. Hovakimyan, M., R. Guthoff, S. Knappe, A. Zhivov, A. Wree, A. Krüger, A. Heisterkamp, and O. Stachs, *Short-term corneal response to cross-linking in rabbit eyes assessed by in vivo confocal laser scanning microscopy and histology.* Cornea, 2011. **30**(2): p. 196-203.

148. Knappe, S., O. Stachs, A. Zhivov, M. Hovakimyan, and R. Guthoff, *Results of confocal microscopy examinations after collagen cross-linking with riboflavin and UVA light in patients with progressive keratoconus*. *Ophthalmologica*, 2011. **225**(2): p. 95-104.
149. Liao, H., D. Munoz-Pinto, X. Qu, Y. Hou, M.A. Grunlan, and M.S. Hahn, *Influence of hydrogel mechanical properties and mesh size on vocal fold fibroblast extracellular matrix production and phenotype*. *Acta biomaterialia*, 2008. **4**(5): p. 1161-1171.
150. Bulick, A.S., D.J. Muñoz-Pinto, X. Qu, M. Mani, D. Cristancho, M. Urban, and M.S. Hahn, *Impact of endothelial cells and mechanical conditioning on smooth muscle cell extracellular matrix production and differentiation*. *Tissue Engineering Part A*, 2009. **15**(4): p. 815-825.
151. Munoz-Pinto, D.J., A.S. Bulick, and M.S. Hahn, *Uncoupled investigation of scaffold modulus and mesh size on smooth muscle cell behavior*. *Journal of Biomedical Materials Research Part A: An Official Journal of The Society for Biomaterials, The Japanese Society for Biomaterials, and The Australian Society for Biomaterials and the Korean Society for Biomaterials*, 2009. **90**(1): p. 303-316.
152. Musumeci, G., C. Loreto, M.L. Carnazza, I. Strehin, and J. Elisseeff, *OA cartilage derived chondrocytes encapsulated in poly (ethylene glycol) diacrylate (PEGDA) for the evaluation of cartilage restoration and apoptosis in an in vitro model*. *Histology and histopathology*, Vol. 26, n°10 (2011), 2011.
153. Lin, S., N. Sangaj, T. Razafiarison, C. Zhang, and S. Varghese, *Influence of physical properties of biomaterials on cellular behavior*. *Pharmaceutical research*, 2011. **28**(6): p. 1422-1430.
154. Bahney, C., T. Lujan, C. Hsu, M. Bottlang, J. West, and B. Johnstone, *Visible light photoinitiation of mesenchymal stem cell-laden bioresponsive hydrogels*. *European cells & materials*, 2011. **22**: p. 43.
155. Williams, C.G., T.K. Kim, A. Taboas, A. Malik, P. Manson, and J. Elisseeff, *In vitro chondrogenesis of bone marrow-derived mesenchymal stem cells in a photopolymerizing hydrogel*. *Tissue engineering*, 2003. **9**(4): p. 679-688.
156. Lee, S.-H., J.J. Moon, and J.L. West, *Three-dimensional micropatterning of bioactive hydrogels via two-photon laser scanning photolithography for guided 3D cell migration*. *Biomaterials*, 2008. **29**(20): p. 2962-2968.
157. Browning, M.B. and E. Cosgriff-Hernandez, *Development of a biostable replacement for PEGDA hydrogels*. *Biomacromolecules*, 2012. **13**(3): p. 779-786.
158. Xin, A.X., C. Gaydos, and J.J. Mao. *In vitro degradation behavior of photopolymerized PEG hydrogels as tissue engineering scaffold*. in *2006 International Conference of the IEEE Engineering in Medicine and Biology Society*. 2006. IEEE.

159. Patel, P.N., C.K. Smith, and C.W. Patrick Jr, *Rheological and recovery properties of poly (ethylene glycol) diacrylate hydrogels and human adipose tissue*. Journal of Biomedical Materials Research Part A: An Official Journal of The Society for Biomaterials, The Japanese Society for Biomaterials, and The Australian Society for Biomaterials and the Korean Society for Biomaterials, 2005. **73**(3): p. 313-319.
160. International Organization for Standardization, see: <https://www.iso.org/standard/36406.html> for "Biological Evaluation of Medical Devices (ISO Standard No. 10993:2009).".
161. Schlie, S., A. Ngezahayo, A. Ovsianikov, T. Fabian, H.-A. Kolb, H. Haferkamp, and B.N. Chichkov, *Three-dimensional cell growth on structures fabricated from ORMOCER® by two-photon polymerization technique*. Journal of biomaterials applications, 2007. **22**(3): p. 275-287.
162. Shu, X.Z., Y. Liu, F.S. Palumbo, Y. Luo, and G.D. Prestwich, *In situ crosslinkable hyaluronan hydrogels for tissue engineering*. Biomaterials, 2004. **25**(7-8): p. 1339-1348.
163. Yeh, J., Y. Ling, J. Karp, J. Gantz, A. Chandawarkar, G. Eng, and J. Blumling, *IIIrd, Langer R and Khademhosseini A 2006 Micromolding of shape-controlled, harvestable cell-laden hydrogels*. Biomaterials. **27**: p. 5391-8.
164. Lim, K.S., R. Levato, P.F. Costa, M.D. Castilho, C.R. Alcalá-Orozco, K.M. van Dorenmalen, F.P. Melchels, D. Gawlitta, G.J. Hooper, and J. Malda, *Bio-resin for high resolution lithography-based biofabrication of complex cell-laden constructs*. Biofabrication, 2018. **10**(3): p. 034101.
165. Wang, Z., H. Kumar, Z. Tian, X. Jin, J.F. Holzman, F. Menard, and K. Kim, *Visible light photoinitiation of cell-adhesive gelatin methacryloyl hydrogels for stereolithography 3D bioprinting*. ACS applied materials & interfaces, 2018. **10**(32): p. 26859-26869.
166. Pepelanova, I., K. Kruppa, T. Scheper, and A. Lavrentieva, *Gelatin-Methacryloyl (GelMA) hydrogels with defined degree of functionalization as a versatile toolkit for 3D cell culture and extrusion bioprinting*. Bioengineering, 2018. **5**(3): p. 55.
167. McBeth, C., J. Lauer, M. Ottersbach, J. Campbell, A. Sharon, and A.F. Sauer-Budge, *3D bioprinting of GelMA scaffolds triggers mineral deposition by primary human osteoblasts*. Biofabrication, 2017. **9**(1): p. 015009.
168. Liu, W., M. Heinrich, Y. Zhou, A. Akpek, N. Hu, X. Liu, X. Guan, Z. Zhong, X. Jin, and A. Khademhosseini, *Extrusion bioprinting of shear-thinning gelatin methacryloyl bioinks*, *Adv. Healthc. Mater.* **6** (2017) 1–11.
169. Govindarajan, S.R., T. Jain, J.-W. Choi, A. Joy, I. Isayeva, and K. Vorvolakos, *A hydrophilic coumarin-based polyester for ambient-temperature initiator-free 3D printing: Chemistry, rheology and interface formation*. Polymer, 2018. **152**: p. 9-17.

170. Lin, Y., C. Gao, D. Gritsenko, R. Zhou, and J. Xu, *Soft lithography based on photolithography and two-photon polymerization*. *Microfluidics and Nanofluidics*, 2018. **22**(9): p. 97.
171. Bertlein, S., G. Brown, K.S. Lim, T. Jungst, T. Boeck, T. Blunk, J. Tessmar, G.J. Hooper, T.B. Woodfield, and J. Groll, *Thiol-ene clickable gelatin: a platform bioink for multiple 3D biofabrication technologies*. *Advanced materials*, 2017. **29**(44): p. 1703404.
172. Ooi, H.W., C. Mota, A.T. Ten Cate, A. Calore, L. Moroni, and M.B. Baker, *Thiol-ene alginate hydrogels as versatile bioinks for bioprinting*. *Biomacromolecules*, 2018. **19**(8): p. 3390-3400.
173. Zheng, S., M. Zlatin, P.R. Selvaganapathy, and M.A. Brook, *Multiple modulus silicone elastomers using 3D extrusion printing of low viscosity inks*. *Additive Manufacturing*, 2018. **24**: p. 86-92.
174. Shirahama, H., B.H. Lee, L.P. Tan, and N.-J. Cho, *Precise Tuning of Facile One-Pot Gelatin Methacryloyl (GelMA) Synthesis*. *Scientific Reports*, 2016. **6**(1): p. 31036.
175. Mironi-Harpaz, I., D.Y. Wang, S. Venkatraman, and D. Seliktar, *Photopolymerization of cell-encapsulating hydrogels: crosslinking efficiency versus cytotoxicity*. *Acta biomaterialia*, 2012. **8**(5): p. 1838-1848.
176. Ikehata, H., S. Higashi, S. Nakamura, Y. Daigaku, Y. Furusawa, Y. Kamei, M. Watanabe, K. Yamamoto, K. Hieda, and N. Munakata, *Action spectrum analysis of UVR genotoxicity for skin: the border wavelengths between UVA and UVB can bring serious mutation loads to skin*. *Journal of Investigative Dermatology*, 2013. **133**(7): p. 1850-1856.
177. Fairbanks, B.D., M.P. Schwartz, C.N. Bowman, and K.S. Anseth, *Photoinitiated polymerization of PEG-diacrylate with lithium phenyl-2,4,6-trimethylbenzoylphosphinate: polymerization rate and cytocompatibility*. *Biomaterials*, 2009. **30**(35): p. 6702-6707.
178. Severus, W., N. Kleindienst, F. Seemüller, S. Frangou, H. Möller, and W. Greil, *What is the optimal serum lithium level in the long-term treatment of bipolar disorder—a review?* *Bipolar disorders*, 2008. **10**(2): p. 231-237.
179. Baird-Gunning, J., T. Lea-Henry, L.C.G. Hoegberg, S. Gosselin, and D.M. Roberts, *Lithium Poisoning*. *J Intensive Care Med*, 2017. **32**(4): p. 249-263.
180. EI, M.D.C.S.C., P. Ottosen, and S. Nielsen, *Lithium-induced downregulation of aquaporin-2 water channel expression*. *J Clin Invest*, 1995. **95**: p. 1838-1845.
181. Hodgkins, K.S. and H.W. Schnaper, *Tubulointerstitial injury and the progression of chronic kidney disease*. *Pediatric nephrology*, 2012. **27**(6): p. 901-909.

182. Lee, N.A., S.J. Kim, B.-J. Park, H.M. Park, M. Yoon, B.H. Chung, and N.W. Song, *Development of multiplexed analysis for the photocatalytic activities of nanoparticles in aqueous suspension*. Photochemical & Photobiological Sciences, 2011. **10**(12): p. 1979-1982.
183. Johnson, K.L. and K.L. Johnson, *Contact mechanics*. 1987: Cambridge university press.
184. Oliver, W.C. and G.M. Pharr, *An improved technique for determining hardness and elastic modulus using load and displacement sensing indentation experiments*. Journal of Materials Research, 1992. **7**(6): p. 1564-1583.
185. Qian, L. and H. Zhao, *Nanoindentation of soft biological materials*. Micromachines, 2018. **9**(12): p. 654.
186. Karshafian, R., P.D. Bevan, R. Williams, S. Samac, and P.N. Burns, *Sonoporation by ultrasound-activated microbubble contrast agents: effect of acoustic exposure parameters on cell membrane permeability and cell viability*. Ultrasound in medicine & biology, 2009. **35**(5): p. 847-860.
187. Molavian, H.R., A. Goldman, C.J. Phipps, M. Kohandel, B.G. Wouters, S. Sengupta, and S. Sivaloganathan, *Drug-induced reactive oxygen species (ROS) rely on cell membrane properties to exert anticancer effects*. Scientific reports, 2016. **6**: p. 27439.
188. Bacellar, I.O., M.S. Baptista, H.C. Junqueira, M. Wainwright, F. Thalmann, C.M. Marques, and A.P. Schroder, *Permeability of DOPC bilayers under photoinduced oxidation: Sensitivity to photosensitizer*. Biochimica et Biophysica Acta (BBA)- Biomembranes, 2018. **1860**(11): p. 2366-2373.
189. Duchi, S., C. Onofrillo, C.D. O'Connell, R. Blanchard, C. Augustine, A.F. Quigley, R.M. Kapsa, P. Pivonka, G. Wallace, and C. Di Bella, *Handheld co-axial bioprinting: application to in situ surgical cartilage repair*. Scientific reports, 2017. **7**(1): p. 1-12.
190. O'Connell, C.D., B. Zhang, C. Onofrillo, S. Duchi, R. Blanchard, A. Quigley, J. Bourke, S. Gambhir, R. Kapsa, and C. Di Bella, *Tailoring the mechanical properties of gelatin methacryloyl hydrogels through manipulation of the photocrosslinking conditions*. Soft matter, 2018. **14**(11): p. 2142-2151.
191. Eng, G., B.W. Lee, H. Parsa, C.D. Chin, J. Schneider, G. Linkov, S.K. Sia, and G. Vunjak-Novakovic, *Assembly of complex cell microenvironments using geometrically docked hydrogel shapes*. Proceedings of the National Academy of Sciences, 2013. **110**(12): p. 4551-4556.
192. Wang, Z., Z. Tian, F. Menard, and K. Kim, *Comparative study of gelatin methacrylate hydrogels from different sources for biofabrication applications*. Biofabrication, 2017. **9**(4): p. 044101.
193. Zhao, X., Q. Lang, and L. Yildirimer, *Photocrosslinkable gelatin hydrogel for epidermal tissue engineering*. Adv Healthc Mater 5: 108–118. 2016.

194. Stampfl, J., S. Baudis, C. Heller, R. Liska, A. Neumeister, R. Kling, A. Ostendorf, and M. Spitzbart, *Photopolymers with tunable mechanical properties processed by laser-based high-resolution stereolithography*. Journal of Micromechanics and Microengineering, 2008. **18**(12): p. 125014.
195. Larsen, E.K.U., N.B. Larsen, K. Almdal, E.K.U. Larsen, N.B. Larsen, and K. Almdal, *Multimaterial hydrogel with widely tunable elasticity by selective photopolymerization of PEG diacrylate and epoxy monomers*. Journal of Polymer Science Part B: Polymer Physics, 2016. **54**(13): p. 1195-1201.
196. Jeon, O., K.H. Bouhadir, J.M. Mansour, and E. Alsberg, *Photocrosslinked alginate hydrogels with tunable biodegradation rates and mechanical properties*. Biomaterials, 2009. **30**(14): p. 2724-2734.
197. Crivello, J.V. and E. Reichmanis, *Photopolymer Materials and Processes for Advanced Technologies*. Chemistry of Materials, 2014. **26**(1): p. 533-548.
198. Pereira, R.F. and P.J. Bártolo, *3D Photo-Fabrication for Tissue Engineering and Drug Delivery*. Engineering, 2015. **1**(1): p. 090-112.
199. Lin, C.-C., C.S. Ki, and H. Shih, *Thiol-norbornene photo-click hydrogels for tissue engineering applications*. Journal of applied polymer science, 2015. **132**(8): p. 41563.
200. OECD, *Test No. 442D: In Vitro Skin Sensitisation*. 2018.
201. OECD, *Test No. 442E: In Vitro Skin Sensitisation*. 2018.
202. Strickland, J., Q. Zang, M. Paris, D.M. Lehmann, D. Allen, N. Choksi, J. Matheson, A. Jacobs, W. Casey, and N. Kleinstreuer, *Multivariate models for prediction of human skin sensitization hazard*. Journal of applied toxicology : JAT, 2017. **37**(3): p. 347-360.
203. Sabnis, A., M. Rahimi, C. Chapman, and K.T. Nguyen, *Cytocompatibility studies of an in situ photopolymerized thermoresponsive hydrogel nanoparticle system using human aortic smooth muscle cells*. J Biomed Mater Res A, 2009. **91**(1): p. 52-9.
204. Leonhardt, S., M. Klare, M. Scheer, T. Fischer, B. Cordes, and M. Eblenkamp, *Biocompatibility of photopolymers for additive manufacturing*, in *Current Directions in Biomedical Engineering*. 2016. p. 113.
205. Moody, C.S. and H.M. Hassan, *Mutagenicity of oxygen free radicals*. Proceedings of the National Academy of Sciences of the United States of America, 1982. **79**(9): p. 2855-2859.
206. Rookmaaker, M.B., H.A.J.M. van Gerven, R. Goldschmeding, and W.H. Boer, *Solid renal tumours of collecting duct origin in patients on chronic lithium therapy*. Clinical kidney journal, 2012. **5**(5): p. 412-415.

207. Trepiccione, F., T. Pisitkun, J.D. Hoffert, S.B. Poulsen, G. Capasso, S. Nielsen, M.A. Knepper, R.A. Fenton, and B.M. Christensen, *Early targets of lithium in rat kidney inner medullary collecting duct include p38 and ERK1/2*. *Kidney International*, 2014. **86**(4): p. 757-767.
208. Roque, A., V. Herédia, M. Ramalho, R. de Campos, A. Ferreira, R. Azevedo, and R. Semelka, *MR findings of lithium-related kidney disease: preliminary observations in four patients*. *Abdominal Imaging*, 2012. **37**(1): p. 140-146.
209. Aiff, H., P.-O. Attman, M. Aurell, H. Bendz, B. Ramsauer, S. Schön, and J. Svedlund, *Effects of 10 to 30 years of lithium treatment on kidney function*. *Journal of Psychopharmacology*, 2015. **29**(5): p. 608-614.
210. Christensen, B.M., A.M. Zuber, J. Loffing, J.-C. Stehle, P.M.T. Deen, B.C. Rossier, and E. Hummler, *α ENaC-Mediated Lithium Absorption Promotes Nephrogenic Diabetes Insipidus*. *Journal of the American Society of Nephrology*, 2011. **22**(2): p. 253-261.
211. Davis, J., M. Desmond, and M. Berk, *Lithium and nephrotoxicity: Unravelling the complex pathophysiological threads of the lightest metal*. *Nephrology (Carlton)*, 2018. **23**(10): p. 897-903.
212. Hiatt, M.J. and D.G. Matsell, *Chapter 25 - Plasticity within the Collecting Ducts: What Role Does This Play in Response to Injury?*, in *Kidney Development, Disease, Repair and Regeneration*, M.H. Little, Editor. 2016, Academic Press: San Diego. p. 335-350.
213. Efrati, S., M. Averbukh, S. Berman, L. Feldman, V. Dishy, L. Kachko, J. Weissgarten, A. Golik, and Z. Averbukh, *N-Acetylcysteine ameliorates lithium-induced renal failure in rats*. *Nephrol Dial Transplant*, 2005. **20**(1): p. 65-70.
214. Benedikt, S., J. Wang, M. Markovic, N. Moszner, K. Dietliker, A. Ovsianikov, H. Grützmacher, and R. Liska, *Highly efficient water-soluble visible light photoinitiators*. *Journal of Polymer Science Part A: Polymer Chemistry*, 2016. **54**(4): p. 473-479.
215. Korbmacher, C., A.S. Segal, G. Fejes-Toth, G. Giebisch, and E.L. Boulpaep, *Whole-cell currents in single and confluent M-1 mouse cortical collecting duct cells*. *J Gen Physiol*, 1993. **102**(4): p. 761-93.
216. Gillman, N., D. Lloyd, R. Bindra, R. Ruan, and M. Zheng, *Surgical applications of intracorporal tissue adhesive agents: current evidence and future development*. *Expert Review of Medical Devices*, 2020. **17**(5): p. 443-460.
217. Sun, A., X. He, L. Li, T. Li, Q. Liu, X. Zhou, X. Ji, W. Li, and Z. Qian, *An injectable photopolymerized hydrogel with antimicrobial and biocompatible properties for infected skin regeneration*. *NPG Asia Materials*, 2020. **12**(1): p. 25.
218. Duchi, S., C. Onofrillo, C.D. O'Connell, R. Blanchard, C. Augustine, A.F. Quigley, R.M.I. Kapsa, P. Pivonka, G. Wallace, C. Di Bella, and P.F.M. Choong, *Handheld Co-*

- Axial Bioprinting: Application to in situ surgical cartilage repair*. Sci Rep, 2017. **7**(1): p. 5837.
219. OECD, *Test No. 471: Bacterial Reverse Mutation Test*. OECD Guidelines for the Testing of Chemicals, Section 4. 1997.
220. Fairbanks, B.D., M.P. Schwartz, C.N. Bowman, and K.S. Anseth, *Photoinitiated polymerization of PEG-diacrylate with lithium phenyl-2,4,6-trimethylbenzoylphosphinate: polymerization rate and cytocompatibility*. Biomaterials, 2009. **30**(35): p. 6702-7.
221. Lim, K.S., B.S. Schon, N.V. Mekhileri, G.C.J. Brown, C.M. Chia, S. Prabakar, G.J. Hooper, and T.B.F. Woodfield, *New Visible-Light Photoinitiating System for Improved Print Fidelity in Gelatin-Based Bioinks*. ACS Biomaterials Science & Engineering, 2016. **2**(10): p. 1752-1762.
222. Monteiro, N., G. Thirivikraman, A. Athirasala, A. Tahayeri, C.M. França, J.L. Ferracane, and L.E. Bertassoni, *Photopolymerization of cell-laden gelatin methacryloyl hydrogels using a dental curing light for regenerative dentistry*. Dental Materials, 2018. **34**(3): p. 389-399.
223. Duchi, S., C. Onofrillo, C.D. O'Connell, R. Blanchard, C. Augustine, A.F. Quigley, R.M.I. Kapsa, P. Pivonka, G. Wallace, C. Di Bella, and P.F.M. Choong, *Handheld Co-Axial Bioprinting: Application to in situ surgical cartilage repair*. Scientific Reports, 2017. **7**(1): p. 5837.
224. Lee, T.Y., C.A. Guymon, E.S. Jönsson, and C.E. Hoyle, *The effect of monomer structure on oxygen inhibition of (meth)acrylates photopolymerization*. Polymer, 2004. **45**(18): p. 6155-6162.
225. López de Arbina, L., L.M. Gugliotta, M.J. Barandiaran, and J. Asua, *Effect of oxygen on emulsion polymerisation kinetics: a study by reaction calorimetry*. Polymer, 1998. **39**(17): p. 4047-4055.
226. Godar, D.E., C. Gurunathan, and I. Ilev, *3D Bioprinting with UVA1 Radiation and Photoinitiator Irgacure 2959: Can the ASTM Standard L929 Cells Predict Human Stem Cell Cytotoxicity?* Photochemistry and Photobiology, 2019. **95**(2): p. 581-586.
227. Ding, H., N.P. Illsley, and R.C. Chang, *3D Bioprinted GelMA Based Models for the Study of Trophoblast Cell Invasion*. Sci Rep, 2019. **9**(1): p. 18854.
228. Lee, C., C.D. O'Connell, C. Onofrillo, P.F.M. Choong, C. Di Bella, and S. Duchi, *Human articular cartilage repair: Sources and detection of cytotoxicity and genotoxicity in photo-crosslinkable hydrogel bioscaffolds*. Stem Cells Transl Med, 2020. **9**(3): p. 302-315.

229. Erden, A., H. Karagöz, M. Başak, S. Karahan, A. Cetinkaya, D. Avci, and I. Bugğday, *Lithium intoxication and nephrogenic diabetes insipidus: a case report and review of literature*. International journal of general medicine, 2013. **6**: p. 535-539.
230. de Groot, T., M. Alsady, M. Jaklofsky, I. Otte-Höller, R. Baumgarten, R.H. Giles, and P.M.T. Deen, *Lithium causes G2 arrest of renal principal cells*. Journal of the American Society of Nephrology : JASN, 2014. **25**(3): p. 501-510.
231. Datta, S., A. Das, A.R. Chowdhury, and P. Datta, *Bioink formulations to ameliorate bioprinting-induced loss of cellular viability*. Biointerphases, 2019. **14**(5): p. 051006.
232. Stockley, J.H., K. Evans, M. Matthey, K. Volbracht, S. Agathou, J. Mukanowa, J. Burrone, and R.T. Káradóttir, *Surpassing light-induced cell damage in vitro with novel cell culture media*. Scientific reports, 2017. **7**(1): p. 849-849.
233. Fedorovich, N.E., M.H. Oudshoorn, D. van Geemen, W.E. Hennink, J. Alblas, and W.J.A. Dhert, *The effect of photopolymerization on stem cells embedded in hydrogels*. Biomaterials, 2009. **30**(3): p. 344-353.
234. Utesch, D. and J. Splittgerber, *Bacterial photomutagenicity testing: Distinction between direct, enzyme-mediated and light-induced events*. Mutation Research/Environmental Mutagenesis and Related Subjects, 1996. **361**(1): p. 41-48.
235. Wang, L., J. Yan, P.P. Fu, K.A. Parekh, and H. Yu, *Photomutagenicity of cosmetic ingredient chemicals azulene and guaiazulene*. Mutation Research/Fundamental and Molecular Mechanisms of Mutagenesis, 2003. **530**(1): p. 19-26.
236. Williams, R.V., D.M. DeMarini, L.F. Stankowski, P.A. Escobar, E. Zeiger, J. Howe, R. Elespuru, and K.P. Cross, *Are all bacterial strains required by OECD mutagenicity test guideline TG471 needed?* Mutation Research/Genetic Toxicology and Environmental Mutagenesis, 2019. **848**: p. 503081.
237. Zeiger, E., *The test that changed the world: The Ames test and the regulation of chemicals*. Mutation Research/Genetic Toxicology and Environmental Mutagenesis, 2019. **841**: p. 43-48.
238. Cimino, M.C., *Comparative overview of current international strategies and guidelines for genetic toxicology testing for regulatory purposes*. Environmental and Molecular Mutagenesis, 2006. **47**(5): p. 362-390.
239. Lilienblum, W. and Rapporteur, *Scientific Committee on Consumer Safety (SCCS). Opinion on the Safety of Trimethylbenzoyl-diphenylphosphineoxide (TPO) in Cosmetic Products, 27 March 2014, SCCS/1528/14*. 2014.
240. Manojlovic, D., M.D. Dramićanin, V. Miletic, D. Mitić-Ćulafić, B. Jovanović, and B. Nikolić, *Cytotoxicity and genotoxicity of a low-shrinkage monomer and monoacylphosphine oxide photoinitiator: Comparative analyses of individual toxicity and combination effects in mixtures*. Dental Materials, 2017. **33**(4): p. 454-466.

241. Al-Mulhim, F.A., M.A. Baragbah, M. Sadat-Ali, A.S. Alomran, and M.Q. Azam, *Prevalence of surgical site infection in orthopedic surgery: a 5-year analysis*. International surgery, 2014. **99**(3): p. 264-268.
242. Goel, A., M.K. Meher, P. Gupta, K. Gulati, V. Pruthi, and K.M. Poluri, *Microwave assisted κ -carrageenan capped silver nanocomposites for eradication of bacterial biofilms*. Carbohydrate polymers, 2019. **206**: p. 854-862.
243. Khalid, H.F., B. Tehseen, Y. Sarwar, S.Z. Hussain, W.S. Khan, Z.A. Raza, S.Z. Bajwa, A.G. Kanaras, I. Hussain, and A. Rehman, *Biosurfactant coated silver and iron oxide nanoparticles with enhanced anti-biofilm and anti-adhesive properties*. Journal of hazardous materials, 2019. **364**: p. 441-448.
244. Liu, M., T. Liu, X. Chen, J. Yang, J. Deng, W. He, X. Zhang, Q. Lei, X. Hu, and G. Luo, *Nano-silver-incorporated biomimetic polydopamine coating on a thermoplastic polyurethane porous nanocomposite as an efficient antibacterial wound dressing*. Journal of nanobiotechnology, 2018. **16**(1): p. 1-19.
245. Chen, Y., N. Dan, W. Dan, X. Liu, and L. Cong, *A novel antibacterial acellular porcine dermal matrix cross-linked with oxidized chitosan oligosaccharide and modified by in situ synthesis of silver nanoparticles for wound healing applications*. Materials Science and Engineering: C, 2019. **94**: p. 1020-1036.
246. Krajewski, S., R. Prucek, A. Panacek, M. Avci-Adali, A. Nolte, A. Straub, R. Zboril, H.P. Wendel, and L. Kvitek, *Hemocompatibility evaluation of different silver nanoparticle concentrations employing a modified Chandler-loop in vitro assay on human blood*. Acta Biomaterialia, 2013. **9**(7): p. 7460-7468.
247. Ahmed, K.B.R., A.M. Nagy, R.P. Brown, Q. Zhang, S.G. Malghan, and P.L. Goering, *Silver nanoparticles: Significance of physicochemical properties and assay interference on the interpretation of in vitro cytotoxicity studies*. Toxicology in Vitro, 2017. **38**: p. 179-192.
248. Akter, M., M.T. Sikder, M.M. Rahman, A.A. Ullah, K.F.B. Hossain, S. Banik, T. Hosokawa, T. Saito, and M. Kurasaki, *A systematic review on silver nanoparticles-induced cytotoxicity: Physicochemical properties and perspectives*. Journal of advanced research, 2018. **9**: p. 1-16.
249. Bar-Ilan, O., R.M. Albrecht, V.E. Fako, and D.Y. Furgeson, *Toxicity assessments of multisized gold and silver nanoparticles in zebrafish embryos*. Small, 2009. **5**(16): p. 1897-1910.
250. De Matteis, V., M. Cascione, C.C. Toma, and S. Leporatti, *Silver nanoparticles: Synthetic routes, in vitro toxicity and theranostic applications for cancer disease*. Nanomaterials, 2018. **8**(5): p. 319.

251. Sengstock, C., J. Diendorf, M. Epple, T.A. Schildhauer, and M. Köller, *Effect of silver nanoparticles on human mesenchymal stem cell differentiation*. Beilstein journal of nanotechnology, 2014. **5**(1): p. 2058-2069.
252. Rosário, F., P. Hoet, C. Santos, and H. Oliveira, *Death and cell cycle progression are differently conditioned by the AgNP size in osteoblast-like cells*. Toxicology, 2016. **368**: p. 103-115.
253. Kreeinthong, S. and P. Uawithya, *Effects of short-term silver nanoparticle exposure on proliferative signaling pathway in human skin keratinocyte*. J. Physiol. Biomed. Sci, 2014. **27**: p. 48-53.
254. Ciftci, H., M. TÜRK, U. TAMER, S. Karahan, and Y. Menemen, *Silver nanoparticles: cytotoxic, apoptotic, and necrotic effects on MCF-7 cells*. Turkish Journal of Biology, 2013. **37**(5): p. 573-581.
255. Castiglioni, S., A. Cazzaniga, L. Locatelli, and J.A. Maier, *Silver nanoparticles in orthopedic applications: New insights on their effects on osteogenic cells*. Nanomaterials, 2017. **7**(6): p. 124.
256. Berry, C., J. De La Fuente, M. Mullin, S.W.L. Chu, and A. Curtis, *Notice of violation of IEEE publication principles nuclear localization of HIV-1 Tat functionalized gold nanoparticles*. IEEE transactions on nanobioscience, 2007. **6**(4): p. 262-269.
257. Ahlberg, S., A. Antonopoulos, J. Diendorf, R. Dringen, M. Epple, R. Flöck, W. Goedecke, C. Graf, N. Haberl, and J. Helmlinger, *PVP-coated, negatively charged silver nanoparticles: A multi-center study of their physicochemical characteristics, cell culture and in vivo experiments*. Beilstein journal of nanotechnology, 2014. **5**(1): p. 1944-1965.
258. Hsiao, I.L., Y.K. Hsieh, C.Y. Chuang, C.F. Wang, and Y.J. Huang, *Effects of silver nanoparticles on the interactions of neuron-and glia-like cells: Toxicity, uptake mechanisms, and lysosomal tracking*. Environmental toxicology, 2017. **32**(6): p. 1742-1753.
259. Wildt, B.E., A. Celedon, E.I. Maurer, B.J. Casey, A.M. Nagy, S.M. Hussain, and P.L. Goering, *Intracellular accumulation and dissolution of silver nanoparticles in L-929 fibroblast cells using live cell time-lapse microscopy*. Nanotoxicology, 2016. **10**(6): p. 710-719.
260. Qing, T., M. Mahmood, Y. Zheng, A.S. Biris, L. Shi, and D.A. Casciano, *A genomic characterization of the influence of silver nanoparticles on bone differentiation in MC3T3-E1 cells*. Journal of Applied Toxicology, 2018. **38**(2): p. 172-179.
261. Pauksch, L., S. Hartmann, M. Rohnke, G. Szalay, V. Alt, R. Schnettler, and K.S. Lips, *Biocompatibility of silver nanoparticles and silver ions in primary human mesenchymal stem cells and osteoblasts*. Acta biomaterialia, 2014. **10**(1): p. 439-449.

262. Backes, M., S.A. Dingemans, M.G. Dijkgraaf, H.R. van den Berg, B. van Dijkman, J.M. Hoogendoorn, P. Joosse, E.D. Ritchie, W.H. Roerdink, and J.P. Schots, *Effect of antibiotic prophylaxis on surgical site infections following removal of orthopedic implants used for treatment of foot, ankle, and lower leg fractures: a randomized clinical trial*. *Jama*, 2017. **318**(24): p. 2438-2445.
263. Gans, I., A. Jain, N. Sirisreetreerux, E.R. Haut, and E.A. Hasenboehler, *Current practice of antibiotic prophylaxis for surgical fixation of closed long bone fractures: a survey of 297 members of the Orthopaedic Trauma Association*. *Patient safety in surgery*, 2017. **11**(1): p. 1-6.
264. Gao, C., Y. Wang, F. Han, Z. Yuan, Q. Li, C. Shi, W. Cao, P. Zhou, X. Xing, and B. Li, *Antibacterial activity and osseointegration of silver-coated poly (ether ether ketone) prepared using the polydopamine-assisted deposition technique*. *Journal of Materials Chemistry B*, 2017. **5**(47): p. 9326-9336.
265. Petrochenko, P.E., J. Zheng, B.J. Casey, M.R. Bayati, R.J. Narayan, and P.L. Goering, *Nanosilver-PMMA composite coating optimized to provide robust antibacterial efficacy while minimizing human bone marrow stromal cell toxicity*. *Toxicology In Vitro*, 2017. **44**: p. 248-255.
266. Takamura, K., K. Hayashi, N. Ishinishi, T. Yamada, and Y. Sugioka, *Evaluation of carcinogenicity and chronic toxicity associated with orthopedic implants in mice*. *J. Biomed. Mater. Res.*, 1994. **28**(5): p. 583-589.
267. Covacci, V., N. Bruzzese, G. Maccauro, C. Andreassi, G.A. Ricci, C. Piconi, E. Marmo, W. Burger, and A. Cittadini, *In vitro evaluation of the mutagenic and carcinogenic power of high purity zirconia ceramic*. *Biomaterials*, 1999. **20**(4): p. 371-376.
268. Stout, M.M., B.K. Cook, D.D. Arola, H. Fong, A.J. Raigrodski, and A.M. Bollen, *Assessing the feasibility of yttria-stabilized zirconia in novel designs as mandibular anterior fixed lingual retention after orthodontic treatment*. *Am J Orthod Dentofacial Orthop*, 2017. **151**(1): p. 63-73.
269. Ardlin, B.I., *Transformation-toughened zirconia for dental inlays, crowns and bridges: chemical stability and effect of low-temperature aging on flexural strength and surface structure*. *Dental Materials*, 2002. **18**(8): p. 590-595.
270. Cales, B., *Zirconia as a Sliding Material: Histologic, Laboratory, and Clinical Data*. *Clin Orthop Relat Res.*, 2000. **379**: p. 94-112.
271. Berni, M., N. Lopomo, G. Marchiori, A. Gambardella, M. Boi, M. Bianchi, A. Visani, P. Pavan, A. Russo, and M. Marcacci, *Tribological characterization of zirconia coatings deposited on Ti6Al4V components for orthopedic applications*. *Materials Science and Engineering: C*, 2016. **62**: p. 643-655.

272. Masonis, J.L., R.B. Bourne, M.D. Ries, R.W. McCalden, A. Salehi, and D.C. Kelman, *Zirconia femoral head fractures: A clinical and retrieval analysis*. The Journal of Arthroplasty, 2004. **19**(7): p. 898-905.
273. Scott, H.G., *Phase relationships in the zirconia-yttria system*. Journal of Materials Science, 1975. **10**(9): p. 1527-1535.
274. Chevalier, J., S. Deville, E. Münch, R. Jullian, and F. Lair, *Critical effect of cubic phase on aging in 3mol% yttria-stabilized zirconia ceramics for hip replacement prosthesis*. Biomaterials, 2004. **25**(24): p. 5539-5545.
275. Kim, S.H., S. Singh, S.K. Oh, D.K. Lee, K.H. Lee, S. Shervin, M. Asadirad, V. Venkateswaran, K. Olenick, J.A. Olenick, S. Lee, J.S. Kwak, A. Mavrokefalos, and J. Ryou, *Visible Flip-Chip Light-Emitting Diodes on Flexible Ceramic Substrate With Improved Thermal Management*. IEEE Electron Device Letters, 2016. **37**(5): p. 615-617.
276. Gopalan, K.K., D. Rodrigo, B. Paulillo, K.K. Soni, and V. Pruneri, *Ultrathin Yttria-Stabilized Zirconia as a Flexible and Stable Substrate for Infrared Nano-Optics*. Advanced Optical Materials, 2019. **7**(2): p. 1800966.
277. Burlingame, N., *Accelerated Life Testing of Thin Ceramic Substrates*. 2014. p. (unpublished work).
278. Heshmatpour, F., Z. Khodaiy, and R.B. Aghakhanpour, *Synthesis and characterization of pure tetragonal nanocrystalline sulfated 8YSZ powder by sol-gel route*. Powder Technology, 2012. **224**: p. 12-18.
279. Viazzi, C., J.-P. Bonino, F. Ansart, and A. Barnabé, *Structural study of metastable tetragonal YSZ powders produced via a sol-gel route*. Journal of Alloys and Compounds, 2008. **452**(2): p. 377-383.
280. Barad, C., G. Shekel, M. Shandalov, H. Hayun, G. Kimmel, D. Shamir, and Y. Gelbstein, *Internal Nano Voids in Yttria-Stabilised Zirconia (YSZ) Powder*. Materials, 2017. **10**(12): p. 1440.
281. Moulder, J., W. Stickle, P. Sobol, and K. Bomben, *Handbook of X-ray Photoelectron Spectroscopy*, ed. J. Chastain. 1992, Eden Prairie, Minnesota: Perkin-Elmer Corporation.
282. Adams, J.W., R. Ruh, and K.S. Mazdizyani, *Young's Modulus, Flexural Strength, and Fracture of Yttria-Stabilized Zirconia versus Temperature*. Journal of the American Ceramic Society, 1997. **80**(4): p. 903-908.
283. Stollberg, D.W., J.M. Hampikian, L. Riester, and W.B. Carter, *Nanoindentation measurements of combustion CVD Al₂O₃ and YSZ films*. Materials Science and Engineering: A, 2003. **359**(1): p. 112-118.

284. Tong, H., C.B. Tanaka, M.R. Kaizer, and Y. Zhang, *Characterization of three commercial Y-TZP ceramics produced for their high-translucency, high-strength and high-surface area*. *Ceramics international*, 2016. **42**(1 Pt B): p. 1077-1085.
285. E Golub, E. and K. Boesze-Battaglia, *The role of alkaline phosphatase in mineralization*. *Current Opinion in Orthopedics*, 2007. **18**(5): p. 444-448.
286. Schwentenwein, M., P. Schneider, and J. Homa, *Lithography-Based Ceramic Manufacturing: A Novel Technique for Additive Manufacturing of High-Performance Ceramics*. *Advances in Science and Technology*, 2014. **88**: p. 60-64.
287. Chen, T.-H., C. Ghayor, B. Siegenthaler, F. Schuler, J. Rüegg, M. De Wild, and F.E. Weber, *Lattice Microarchitecture for Bone Tissue Engineering from Calcium Phosphate Compared to Titanium*. *Tissue Engineering Part A*, 2018. **24**(19-20): p. 1554-1561.
288. Bomze, D. and A. Ioannidis, *3D-Printing of High-Strength and Bioresorbable Ceramics for Dental and Maxillofacial Surgery Applications-the LCM Process*. *Ceramic Applications*, 2019. **7**(1): p. 38-43.
289. Ghayor, C. and F.E. Weber, *Osteoconductive Microarchitecture of Bone Substitutes for Bone Regeneration Revisited*. *Frontiers in physiology*, 2018. **9**: p. 960-960.
290. Kim, K., A. Yeatts, D. Dean, and J.P. Fisher, *Stereolithographic Bone Scaffold Design Parameters: Osteogenic Differentiation and Signal Expression*. *Tissue Engineering Part B: Reviews*, 2010. **16**(5): p. 523-539.
291. Melchels, F.P.W., K. Bertoldi, R. Gabbriellini, A.H. Velders, J. Feijen, and D.W. Grijpma, *Mathematically defined tissue engineering scaffold architectures prepared by stereolithography*. *Biomaterials*, 2010. **31**(27): p. 6909-6916.
292. Kebede, M.A., K.S. Asiku, T. Imae, M. Kawakami, H. Furukawa, and C.M. Wu, *Stereolithographic and molding fabrications of hydroxyapatite-polymer gels applicable to bone regeneration materials*. *Journal of the Taiwan Institute of Chemical Engineers*, 2018. **92**: p. 91-96.
293. Dong, P.L., X.D. Wang, M. Zhang, M. Guo, and S. Seetharaman, *The Preparation and Characterization of beta-SiAlON Nanostructure Whiskers*. *Journal of Nanomaterials*, 2008.
294. Seymour, V.R. and M.E. Smith, *Distinguishing between Structural Models of beta '-Sialons Using a Combined Solid-State NMR, Powder XRD, and Computational Approach*. *Journal of Physical Chemistry A*, 2019. **123**(45): p. 9729-9736.
295. Li, Y., T. Jiang, L. Zheng, and J. Zhao, *Osteogenic differentiation of mesenchymal stem cells (MSCs) induced by three calcium phosphate ceramic (CaP) powders: A comparative study*. *Materials Science and Engineering: C*, 2017. **80**: p. 296-300.

296. Ding, J., X. Xu, X. Wu, Z. Huang, G. Kong, J. Liu, Z. Huang, Q. Liu, R. Li, Z. Yang, Y. Liu, and Q. Zhu, *Bone loss and biomechanical reduction of appendicular and axial bones under ketogenic diet in rats*. Experimental and therapeutic medicine, 2019. **17**(4): p. 2503-2510.
297. Wu, X., Z. Huang, X. Wang, Z. Fu, J. Liu, Z. Huang, G. Kong, X. Xu, J. Ding, and Q. Zhu, *Ketogenic Diet Compromises Both Cancellous and Cortical Bone Mass in Mice*. Calcified Tissue International, 2017. **101**(4): p. 412-421.
298. Bergqvist, A.G.C., J.I. Schall, V.A. Stallings, and B.S. Zemel, *Progressive bone mineral content loss in children with intractable epilepsy treated with the ketogenic diet*. The American Journal of Clinical Nutrition, 2008. **88**(6): p. 1678-1684.
299. Prabhakar, A., A. Quach, H. Zhang, M. Terrera, D. Jackemeyer, X. Xian, F. Tsow, N. Tao, and E.S. Forzani, *Acetone as biomarker for ketosis buildup capability--a study in healthy individuals under combined high fat and starvation diets*. Nutrition journal, 2015. **14**: p. 41-41.
300. DIETZ, D.D., J.R. LEININGER, E.J. RAUCKMAN, M.B. THOMPSON, R.E. CHAPIN, R.L. MORRISSEY, and B.S. LEVINE, *Toxicity Studies of Acetone Administered in the Drinking Water of Rodents*. Toxicological Sciences, 1991. **17**(2): p. 347-360.
301. Whyte, M.P., *Physiological role of alkaline phosphatase explored in hypophosphatasia*. Annals of the New York Academy of Sciences, 2010. **1192**(1): p. 190-200.
302. Bonsignore, L.A., V.M. Goldberg, and E.M. Greenfield, *Machine oil inhibits the osseointegration of orthopaedic implants by impairing osteoblast attachment and spreading*. Journal of Orthopaedic Research, 2015. **33**(7): p. 979-987.
303. Faia-Torres, A.B., S. Guimond-Lischer, M. Rottmar, M. Charnley, T. Goren, K. Maniura-Weber, N.D. Spencer, R.L. Reis, M. Textor, and N.M. Neves, *Differential regulation of osteogenic differentiation of stem cells on surface roughness gradients*. Biomaterials, 2014. **35**(33): p. 9023-9032.
304. Faia-Torres, A.B., M. Charnley, T. Goren, S. Guimond-Lischer, M. Rottmar, K. Maniura-Weber, N.D. Spencer, R.L. Reis, M. Textor, and N.M. Neves, *Osteogenic differentiation of human mesenchymal stem cells in the absence of osteogenic supplements: A surface-roughness gradient study*. Acta Biomaterialia, 2015. **28**: p. 64-75.
305. Poon, C.Y. and B. Bhushan, *Comparison of surface roughness measurements by stylus profiler, AFM and non-contact optical profiler*. Wear, 1995. **190**(1): p. 76-88.